Experimental investigation on suspended sediment, hydro-abrasive erosion and efficiency reductions of coated Pelton turbines

Versuchsanstalt für Wasserbau
Hydrologie und Glaziologie
der Eidgenössischen
Technischen Hochschule Zürich

Mitteilungen **238**

Experimental investigation on suspended sediment, hydro-abrasive erosion and efficiency reductions of coated Pelton turbines

David Felix

Zürich, 2017

Herausgeber: Prof. Dr. Robert Boes

ETH zürich

Zitiervorschlag für VAW-Mitteilungen:

Felix, D. (2017).
Experimental investigation on suspended sediment, hydro-abrasive erosion and efficiency reductions of coated Pelton turbines.
VAW-Mitteilungen 238, Versuchsanstalt für Wasserbau, Hydrologie und Glaziologie (VAW), (R. M. Boes, ed.), ETH Zürich, Schweiz.

Im Eigenverlag der
Versuchsanstalt für Wasserbau,
Hydrologie und Glaziologie
ETH Zürich
CH-8093 Zürich

Tel.: +41 - 44 - 632 4091
Fax: +41 - 44 - 632 1192
e-mail: info@vaw.baug.ethz.ch

Zürich, 2017

ISSN 0374-0056

PREFACE

Medium- and high-head hydropower plants (HPPs) often feature Pelton turbines. For very high-heads above some 800 meters, this turbine type is practically the one and only alternative. Medium- and high-head schemes represent an important backbone of the Swiss electricity production which is highly relying on renewable hydropower. In the context of the Swiss Energy Strategy 2050 the efficiency of the existing hydropower infrastructure is aimed at being optimized. However, sediments compromise this target because they cause wear, increased maintenance and refurbishment cost, as well as efficiency reductions of turbines, resulting in production and revenue losses. According to the rare literature on this topic the annual maintenance cost for both Pelton and Francis turbines in Switzerland was estimated to some 20 Mio. CHF (as of 1988), corresponding to some 2% of the annual revenue.

Dr. Felix conducted a multi-year experimental investigation on the interrelations between suspended sediments, hydro-abrasive wear and efficiency losses of coated Pelton turbines. There are a number of options to reduce the negative effects of turbine erosion on the HPP's cost-effectiveness and energy efficiency. Among these, the economic potential of temporary turbine shutdowns during severe sediment conditions such as during storm runoff as an operational option was aimed at being analyzed in detail from the beginning. An important sub-goal was to investigate and further develop techniques for continuous suspended sediment monitoring in real-time as a prerequisite for turbine shutdowns.

To reach these goals, Dr. Felix conducted both laboratory experiments at the Competence Center for Fluid Mechanics and Hydro Machines of Hochschule Luzern (HSLU) and a comprehensive field study at the HPP Fieschertal, operated by Gommerkraftwerke AG, in the Canton of Valais. Because the behavior and the effects of suspended sediment particles in high-head HPPs cannot be easily simulated in small-scale physical models, but would require a complex high-pressure test rig, it was decided to study the thesis topic at a prototype facility featuring high suspended sediment loads. The capabilities and limits of various instruments for suspended sediment monitoring were systematically investigated in a laboratory tank under controlled conditions. A variety of instruments was then installed in Fieschertal and tested over up to three sediment seasons. In collaboration with

our mechanical engineering partners from HSLU, the HPP operator and BKW engineering, the turbine erosion was measured periodically and efficiency changes were monitored based on both sliding needle index efficiency tests and on continuous data from the HPP's control system.

Thanks to the acquired data series which are unique worldwide and are also most valuable for numerical modelling, Dr. Felix succeeded in adapting an analytical turbine erosion model to runners of coated Pelton turbines, thereby distinguishing between two stages of erosion, namely erosion of mainly coating and base material, respectively. He obtained calibration coefficients for a number of locations within the runner bucket (splitter width and height, cut-out depth, splitter tip, inner side of bucket), mostly showing surprisingly high correlation quality. His findings also result in the determination of a suspended sediment concentration for temporary shutdown of the study HPP and in a methodology on how to determine such a threshold value for a given HPP. Moreover, the study of Dr. Felix provides guidance to adequately select instrumentation for continuous suspended sediment monitoring in real-time at HPPs and in rivers.

My sincere thanks go to a number of institutions that enabled this comprehensive research project through their funding, namely Swisselectric research, the Swiss Federal Office of Energy (SFOE, grant numbers SI/500638 and 500960), Gommerkraftwerke AG, and the Swiss Committee on Dams. The support of Endress+Hauser, Sigrist-Photometer and Rittmeyer by freely placing instrumentation at Dr. Felix' disposal is gratefully acknowledged. The good collaboration with A. Abgottspon and Prof. Dr. T. Staubli from HSLU as well as B. Truffer and M. Perren from Gommerkraftwerke and U. Aebi from BKW is much appreciated.

The co-reviews of Prof. Dr. T. Staubli, Competence Center for Fluid Mechanics and Hydro Machines at HSLU, Prof. Dr. H. Habersack, Institute for Water Management, Hydrology and Hydraulic Engineering at the University of Natural Resources and Life Sciences (BOKU), Vienna, and of Dr. I. Albayrak, VAW, are gratefully acknowledged.

Zürich, June 2017 Prof. Dr. Robert M. Boes

ABSTRACT

The water driving the turbines in many hydro-electric power plants (HPPs) contains sediment particles. At high flow velocities, hard and in particular angular, relatively coarse particles cause hydro-abrasive erosion on turbine parts. This problem is most severe in high-head HPPs equipped with Pelton turbines. Although the application of hard-coatings (tungsten carbide) contributes to increase the times between overhauls, turbine erosion cannot be fully prevented in severe conditions. The consequences are reduced turbine efficiency and lower electricity generation as well as higher costs for maintenance and spare parts. Hence, the energy efficiency and profitability of HPPs are negatively affected.

For the mitigation of these negative effects, data on sediment load, turbine erosion, efficiency reductions and costs are required as a basis. However, complete data sets are rarely available in literature, and measuring the relevant quantities with sufficiently low uncertainty is challenging.

In the present interdisciplinary research project, quantitative relations between sediment load, turbine erosion and efficiency reductions as well as relevant measuring techniques were investigated. The project comprised a preliminary laboratory study on various instruments for suspended sediment monitoring and a long-term field study at the HPP Fieschertal in the Canton of Valais, Switzerland. The suspended sediment mass concentration (*SSC*) and the particle size distributions (PSD) were continuously measured from 2012 to 2014/2015 using an innovative combination of five techniques including Laser *In-Situ* Scattering and Transmissometry (LISST) and a Coriolis Flow- and Density meter. The erosion on the buckets of the Pelton runners was quantified by optical 3D-surveys and systematic coating thickness measurements before and after the sediment seasons. The changes in the turbine's efficiencies were monitored with periodic sliding-needle measurements as well as daily evaluation of operation data.

The combined use of several techniques for sediment monitoring allowed *SSC* measurements in a wide range and an assessment of the instruments' performances. The detailed *SSC* and PSD results gave new insights into the sediment dynamics depending on natural events and operational conditions. The *SSC* and the median particle size d_{50} varied independently and ranged from 0 to 50 g/l and 10 to 100 μm (medium silt to fine sand), respectively. The maximum *SSC* was measured in a flood event with a return period of ~20 years in July 2012. The suspended sediment load in that year was more than twice

the average of the other years, and coarser particles were transported. This led to considerable erosion on the runners and an efficiency reduction of ~0.9%.

The analytical erosion model described in IEC 62364 (2013) was adapted for coated Pelton buckets and calibrated based on the field data for six cases, i.e. locations on the bucket. A threshold particle load characterizing the initiation of systematic base material erosion was introduced and quantified. Below this threshold, mainly the coating on the splitters and cut-out edges was eroded; these zones can be repaired on-site between the sediment seasons with limited effort. Moreover, efficiency reductions were evaluated as a function of the relative splitter width increase or radial splitter tip erosion.

Based on the combined results, the study demonstrates that it is economic to shut down a HPP in periods of high erosion potential. In the major flood event in July 2012, a benefit corresponding to almost 3% of the value of the annually generated electricity would have resulted from closing the intake for 16 h when the *SSC* was above 10 g/l.

Further investigations at the HPP Fieschertal and other high-head HPPs at sediment-laden rivers are recommended in parallel with laboratory studies and numerical simulations to extend the data base and improve erosion and efficiency prediction models.

ZUSAMMENFASSUNG

In vielen Wasserkraftanlagen (WKA) wird Wasser genutzt, welches Sedimentpartikel enthält. Harte und insbesondere kantige, relativ grobkörnige Partikel verursachen bei hohen Fliessgeschwindigkeiten so genannten Hydroabrasiv-Verschleiss an Turbinenbauteilen. Dieses Problem ist in Hochdruck-WKA mit Peltonturbinen am ausgeprägtesten und kann auch mit Wolframkarbid-Hartbeschichtungen nicht bei allen Anlagen vollständig vermieden werden. Die Folgen sind tiefere Wirkungsgrade und Erzeugungseinbussen sowie höhere Kosten für Unterhalt und Ersatzteile, was die Energieeffizienz und die Wirtschaftlichkeit solcher WKA beeinträchtigt.

Um diese negativen Folgen zu mindern, sind verlässliche Grundlagendaten erforderlich. Solche Daten sind aber in der Literatur kaum verfügbar und die messtechnische Erfassung der relevanten Grössen mit ausreichend kleiner Unsicherheit ist anspruchsvoll.

Im vorliegenden interdisziplinären Forschungsprojekt wurden quantitative Beziehungen zwischen dem Schwebstoffaufkommen, dem Turbinenverschleiss und Wirkungsgradminderungen sowie entsprechende Messtechniken untersucht. Das Projekt beinhaltete eine vorgängige Untersuchung von Schwebstoffmessgeräten im Labor und eine mehrjährige Prototypstudie am Kraftwerk Fieschertal im Kanton Wallis in der Schweiz. Die Schwebstoffkonzentration (*SSC*) und die Partikelgrössenverteilungen (PSD) wurden in den Jahren 2012 bis 2014/2015 mittels einer innovativen Kombination von fünf verschiedenen Messtechniken kontinuierlich gemessen. Unter anderem wurden *in-situ* Laserdiffraktometrie (LISST) und ein Corolis-Durchfluss– und Dichtemessgerät eingesetzt. Der Verschleiss an den Pelton-Laufrädern wurde mittels wiederholter optischer 3D-Vermessungen und systematischer Schichtdickenmessungen erfasst. Die Wirkungsgradänderungen wurden mittels periodisch durchgeführter *Sliding-Needle*-Messungen und durch tägliche Auswertung von Leitsystemdaten quantifiziert.

Die detaillierten *SSC*- und PSD-Messungen zeigten eine grosse Dynamik im Schwebstoffaufkommen je nach natürlichen und betrieblichen Bedingungen. Die *SSC* und der Median-Partikeldurchmesser d_{50} variierten unabhängig voneinander zwischen 0 und 50 g/l bzw. 10 und 100 µm (Mittelsilt bis Feinsand). Die maximale *SSC* trat während eines etwa 20-jährlichen Hochwasserereignisses anfangs Juli 2012 auf. In diesem Jahr war die Schwebstofffracht mehr als doppelt so hoch als im Durchschnitt der andern Jahre

und es wurden grössere Partikel transportiert. Dies führte zu beträchtlichem Verschleiss an den Laufrädern und zu einer Wirkungsgradeinbusse von ~0.9%.

Das analytische Turbinenabrasionsmodell gemäss IEC 62364 (2013) wurde für beschichtete Peltonlaufräder angepasst und aufgrund der Felddaten für sechs Anwendungsfälle innerhalb der Becher kalibriert. Ein Schwellenwert der sogenannten *Particle Load*, ab welchem das Grundmaterial systematisch erodiert wird, wurde eingeführt und quantifiziert. Unterhalb dieses Schwellenwerts können lokale Erosionen auf den Mittelschneiden und an den Bechereintrittskanten mit beschränktem Aufwand vor Ort repariert werden. Weiter wurden Wirkungsgradabnahmen in Funktion der relativen Mittelschneidenbreite und der radialen Erosion an den Mittelschneidenspitzen ausgewertet.

Die kombinierte Auswertung der Felddaten zeigte, dass das Betriebsergebnis im Jahr 2012 um gegen 3% des Werts der jährlich produzierten elektrischen Energie hätte verbessert werden können, wenn die WKA im Hochwasser vom Juli 2012 bei SSC = 10 g/l für 16 Stunden ausser Betrieb genommen worden wäre.

Weitere Untersuchungen an der WKA Fieschertal und weiteren Pelton-WKA an sedimentreichen Flüssen werden zusammen mit Laborversuchen und numerischen Simulationen empfohlen, um die Datenbasis zu erweitern und Modelle für die Vorhersage von Turbinenerosion und Wirkungsgradänderungen zu verbessern.

RÉSUMÉ

Les eaux motrices des centrales hydroélectriques contiennent souvent des particules minérales en suspension. Entraînées à grande vitesse, ces particules abîment les turbines par érosion hydroabrasive. Ce type d'usure est important dans les turbines Pelton installées dans les aménagements à haute chute, notamment si les particules dures et à angles vifs sont relativement grosses (sable). Dans des conditions sévères, même des revêtements durs à base de carbure de tungstène n'empêchent pas totalement l'érosion. Il s'en suit une baisse des rendements hydrauliques et de la production électrique, ainsi qu'une hausse des coûts d'entretien et de remplacements, bref, des pertes d'efficacité énergétique et de rentabilité financière.

Une meilleure connaissance des causes et des conséquences de l'érosion hydroabrasive des turbines, basée sur des données fiables, permettrait de mieux gérer les aménagements hydroélectriques par rapport aux impacts négatifs des sédiments. Mais les informations nécessaires sont lacunaires dans la littérature publiée et le mesurage précis des quantités concernées est un véritable défi technique à relever.

Dans le présent projet de recherche interdisciplinaire, des techniques de mesurage et des relations quantitatives entre la charge des particules, l'érosion des turbines Pelton et les différences de leurs rendements ont été investiguées. Les techniques de mesurage pour les sédiments en suspension ont été expérimentées en laboratoire, avant de procéder à l'étude de cas à l'aménagement hydraulique de Fieschertal dans le Canton du Valais en Suisse. La concentration et la distribution des tailles des particules ont été mesurées en continu dans les années 2012–2014/2015 en utilisant cinq instruments, y compris un diffractomètre laser et un débitmètre à effet Coriolis mesurant aussi la densité de l'eau chargée de sédiments. L'érosion des augets des roues Pelton a été quantifiée par des relevés optiques tridimensionnels et des mesurages systématiques de l'épaisseur du revêtement. Les différences de rendements ont été quantifiées par (i) mesurages périodiques en ouvrant et fermant progressivement les injecteurs des turbines, ainsi que (ii) par l'analyse journalière des données enregistré par le système de contrôle pendant l'exploitation normale.

Les résultats des mesurages détaillés des concentrations et des tailles des particules ont montré une haute variabilité en fonction des conditions hydrométéorologiques et d'exploitation. Le diamètre moyen des particules d_{50} a varié entre 10 et 100 μm (limon moyen

à sable fin). Au début de juillet 2012, la concentration des sédiments a atteint 50 g/l lors d'une crue avec une probabilité de retour d'environ 20 ans. Dû à cet événement singulier, la charge sédimentaire des turbines en 2012 était largement doublée et consistait de particules plus grandes par rapport aux autres années. Donc, l'érosion et la réduction du rendement (~0.9%) en 2012 étaient plus importantes.

Le modèle analytique pour la prédiction de l'érosion selon IEC 62364 (2013) a été adapté pour des roues Pelton revêtues. En utilisant les résultats de la présente étude, le modèle a été calibré pour six cas d'application, c'est-à-dire pour des endroits spécifiques dans les augets. Une valeur seuil de la charge en particules a été introduite et quantifiée, au-delà de celle-ci le matériel de base (acier inoxydable) est systématiquement érodé. Au-dessous de ce seuil, des érosions locales – sur les arêtes médianes et les bords d'attaque des échancrures des augets – peuvent être réparés sur place à des frais limités. En outre, des corrélations entre la géométrie émoussée des arêtes des augets et la réduction du rendement hydraulique ont été analysées.

L'étude de cas a montré qu'un avantage financier de presque 3% de la valeur de la production électrique annuelle aurait résulté en 2012 si l'exploitation de l'aménagement avait été interrompue lors de la crue majeure pendant 16 heures quand la concentration des sédiments dépassait 10 g/l.

Il est recommandé de poursuivre les investigations sur les sujets traités à l'aménagement de Fieschertal, à d'autres aménagements à haute chute, en laboratoire et par simulation numérique afin d'améliorer les modèles pour la prédiction (i) de l'érosion des turbines et (ii) des réductions de leurs rendements.

TABLE OF CONTENTS

1 INTRODUCTION

1.1 Problem outline

If hydraulic turbines and pumps are operated in sediment-laden water (Fig. 1-1), their components and other parts along waterways may be subject to hydro-abrasive erosion. Factors for severe erosion are:

- High relative velocities between the flow and the exposed surface, and
- High concentrations of relatively coarse, hard and angular suspended sediment particles.

High flow velocities prevail in medium- and high-head hydro-electric power plants (HPPs), where Francis and Pelton turbines are employed. High-head Pelton turbines are particularly prone to hydro-abrasive erosion (Fig. 1-2). For example at a head of 500 m, the velocity of a jet in a Pelton turbine is 100 m/s. High concentrations of harmful silt and fine sand particles are typically found in the turbine water of run-of-river HPPs using water originating from catchment areas with high specific sediment yields. High sediment yields are typical for currently or formerly glaciated catchments and relatively young geological formations, and are reported from the Himalaya, the European Alps, the Andes and the Rocky Mountains. In many of these areas, the percentage of hard minerals – such as quartz and feldspar – is relatively high. The concentration and sizes of sediment particles vary with the season, the weather (flood events) and the HPP operation (e.g. reservoir drawdowns).

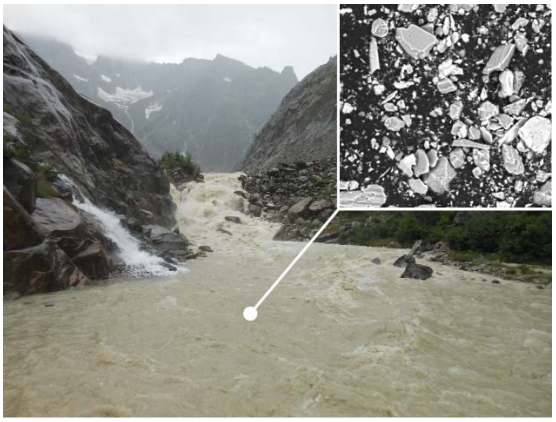

Figure 1-1 Example of a sediment-laden mountain river (upstream of HPP Fieschertal, Switzerland) and microscopic image of particles.

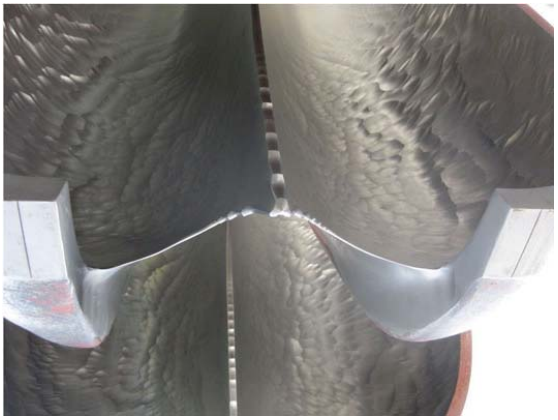

Figure 1-2 Example of a Pelton turbine with damages mainly due to hydro-abrasive erosion (at display at Emosson dam, Switzerland).

Erosion in hydraulic machines causes (i) increased roughness on parts in contact with the water and (ii) degrades their shapes, i.e. the so-called hydraulic profiles. This leads to reductions in efficiency and may affect the mechanical stability and integrity of machine parts. In order to maintain hydraulic machines in good condition, frequent maintenance and repair works as well as replacements of eroded parts are required. This results in increased costs as well as in losses in electricity generation and revenues due to reduced efficiency and downtimes during works. The causes and consequences of hydro-abrasive erosion are schematically summarized in the left part of Figure 1-3. All in all, hydro-abrasive erosion negatively affects the energy efficiency, cost effectiveness, availability and eventually safety of HPPs. The problem of erosion in hydraulic machines is expected to become more severe in the future due to the following reasons:

- The sediment availability is expected to increase in many mountainous catchments due to the retreat of glaciers and permafrost (climate change);
- More sediment is expected to be transported in rivers due to more intense precipitations and run-off;
- Sediment concentrations in the turbine water might increase due to reservoir sedimentation, or as a consequence of additional legal regulations regarding ecology (in Switzerland: GSchG 2009) and landscape protection which may restrict sediment trapping, removal and flushing operations;
- As a consequence of an increased worldwide demand in sustainable energy and a lack of alternative sites, additional medium- and high-head run-of-river HPPs are expected to be constructed in regions with high specific sediment yield;
- Market situations and energy policies may demand further economic and energetic optimizations of HPPs, requiring more detailed knowledge on relevant processes and the erosion status of hydraulic machines.

In the design, operation and maintenance of HPPs, various types of measures can be taken to reduce hydro-abrasive erosion and its negative consequences (e.g. Naidu 1999):

- Use of materials and coatings with high resistance to erosion;
- Optimizations of turbine design and maintenance schedule;
- Construction and operation of facilities for partial sediment exclusion (storage reservoirs, gravel and sand traps, etc.);
- Temporary closing of intakes and pausing of turbine operation (HPP shutdowns) in periods with exceptionally high erosion potential.

The first measure increases the resistance to erosion, whereas the last two reduce the sediment “loading” on the machine parts. Despite considerable advances in material sciences, hydro-abrasive erosion cannot be fully prevented at medium- and high-head HPPs with high sediment loads. Moreover, fine sediments cannot be fully excluded from the turbine

water. Thus, a combination of measures is generally adopted, involving the design, operation and maintenance of civil structures and electro-mechanical equipment.

For an overall optimization of a HPP with respect to fine sediment and its consequences, information on the costs and benefits as well as the energetic losses and gains of the measures are required. Currently, only a part of the information required to solve the optimization problem is available. Firstly, there is a lack of practically prooven measurement techniques and reliable measurement data on suspended sediment load, turbine erosion and efficiency changes. Secondly, generally applicable quantitative relations between these three elements are rare in literature.

1.2 Goal and objectives

The present study aims to contribute to the sustainable and energy-efficient use of the hydropower potential in high-head HPPs at sediment-laden rivers by extending the knowledge on hydro-abrasive erosion, its causes and consequences. To reach this goal, the following objectives have been defined:

- Investigation of techniques and instruments for continuous real-time suspended sediment measurements (concentration and particle size);
- Investigation of relevant processes and relations between suspended sediment load, turbine erosion and efficiency changes based on field measurements in a high-head HPP during several sediment seasons;
- Application, adaptation and calibration of erosion prediction models based on the field data;
- Recommendations on the operation of HPPs with respect to fine sediment, in particular to investigate the option of HPP shutdowns in periods of exceptionally high erosion potential;
- Recommendations on instrumentation for continuous and real-time suspended sediment monitoring (SSM).

1.3 Research methodology

For the investigation of physical phenomena – in particular in fluid mechanics, hydraulic engineering and hydraulic structures – analytical approaches, physical model tests (at reduced scale), field measurements (at prototype scale), numerical simulations, or a combination of these are generally applied. In this study, the method of measurements at prototype scale, i.e. at an existing high-head HPP, was adopted for the following reasons:

The problem cannot be solved purely analytically and some parameters need to be determined *in-situ*. Small scale model tests on hydro-abrasive erosion are potentially affected by scale effects; large scale model tests are unaffordable or unfeasible. Due to a lack of suitable mathematical models and data for calibration and validation, not all relevant processes can be numerically simulated yet.

The following approach structured in six tasks was adopted (Fig. 1-3):

- Task A Investigation of techniques for SSM in the laboratory;
- Task B Monitoring of suspended sediment in the case study HPP;
- Task C Monitoring of turbine erosion in the case study HPP;
- Task D Monitoring of turbine efficiency changes in the case study HPP;
- Task E Evaluation of the relations between the results from the tasks B to D;
- Task F Investigation of HPP shutdowns in periods of high erosion potential.

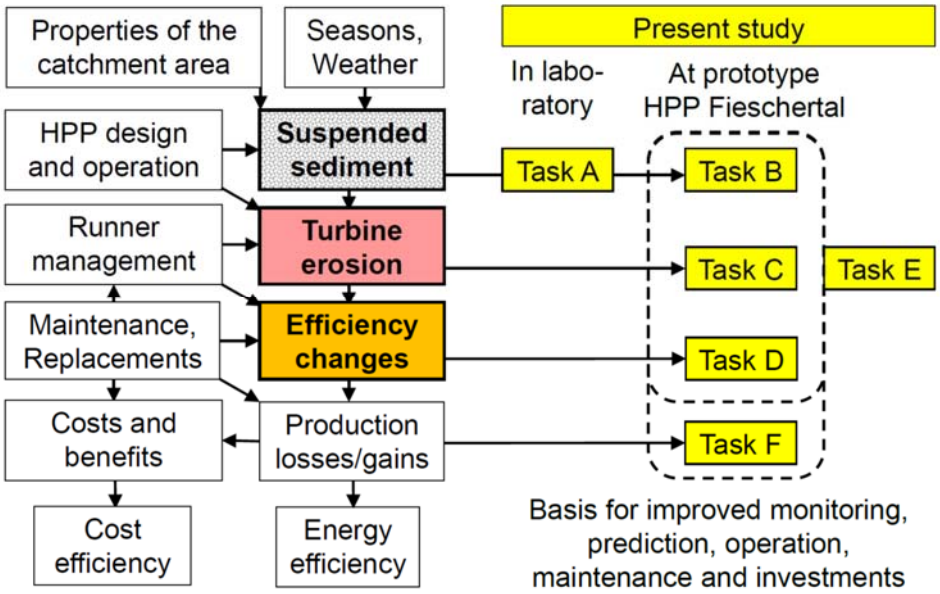

Figure 1-3 Causes and consequences of hydro-abrasive erosion in hydraulic turbines and overview on the six tasks in the present study.

1.4 Timeline and project organisation

The laboratory investigation (Task A) was conducted in the first semester of 2012 prior to the installation of the SSM instruments at the case study HPP. Data acquisition at the case study HPP for Tasks B, C and D began in summer 2012. The data evaluation was done partly in parallel to the laboratory and field work as well as mainly in 2015 and 2016. In the frame of the present thesis, field data from 2012 to 2014 were evaluated; results of a further year of turbine efficiency monitoring are reported in addition.

To tackle the interdisciplinary problem, VAW of ETH Zürich collaborated with the Competence Center for Fluid Mechanics and Hydro Machines (CC FMHM) of Hochschule Luzern (HSLU) as a research partner. While VAW treated mainly the aspects of hydrology, sedimentology and hydraulics (civil and environmental engineering), the CC FMHM covered mainly the 3D-erosion measurements, efficiency monitoring and turbine technology (mechanical engineering). Moreover, CC FMHM provided laboratory infrastructure and support for Task A and contributed to the project in the area of sediment monitoring, particularly regarding the acoustic technique.

Furthermore, various industry partners contributed to the project, i.e. mainly the operator of the case study HPP (Gommerkraftwerke GKW), its engineering consultant (BKW), a turbine manufacturer (Andritz Hydro) and various measuring equipment manufacturers (Rittmeyer, Endress+Hauser, Sigrist Photometers, and Sequoia Scientific).

1.5 Outline of the thesis

Chapter 2 gives an overview on processes, relevant physical properties, known relations, and state-of the-art techniques in the fields of suspended sediment, turbine erosion and efficiency monitoring. In Chapter 3, the facilities, experimental setups, instrumentation, materials and methods used in the laboratory and field investigations are treated. In Chapters 4 to 7 the results of the tasks A to D, respectively, are presented and discussed. The relations between suspended sediment, turbine erosion and efficiency are evaluated in Chapter 8. In particular, an erosion model is adapted and calibrated for coated Pelton runner buckets. In Chapter 9 the option of temporary HPP shutdowns in periods of exceptionally high erosion potential is investigated. Finally, conclusions and recommendations are given in Chapter 10.

2 FUNDAMENTALS AND STATE OF THE ART

In this Chapter, information on the physical background and state of the art are given with respect to (i) suspended sediment yield, properties, transport and management, (ii) Pelton turbines, erosion damages, countermeasures and modelling approaches, as well as (iii) turbine efficiency reductions due to erosion. For each of the three topics, available monitoring techniques are described, too.

2.1 Sediment origin, properties, transport and management

2.1.1 Origin of sediment

2.1.1.1 Rock and soil erosion

Rock or soil particles are eroded from the earth's surface by the action of glaciers, flowing water and wind. Among other factors, erosion rates depend on rock/soil properties, precipitation height and intensity, hill slope and vegetation cover. In the present study, the transport of eroded fine sediment by flowing water is relevant.

2.1.1.2 Sediment yield

The long-term denudation rate in the crystalline central Alps of Switzerland has been estimated as 0.9 ±0.3 mm/year based on the analysis of cosmogenic nuclides (Wittmann *et al.* 2007). The average corresponds to 900 $m^3/(km^2 \cdot year)$ or ~2400 $tons/(km^2 \cdot year)$ with an assumed sediment density of 2650 kg/m^3. For streams in the Himalayas, Wulf *et al.* (2012) reported specific suspended sediment yields of 0.1 to 2 mm/year, corresponding to a few 100 to several 1000 $tons/(km^2 \cdot year)$.

Glacier retreat due to climate change generally leads to increased sediment yield (Geilhausen *et al.* 2013). The actual flux of sediment transported by a river may differ considerably from the long term erosion rate because of sediment deposition (e.g. in proglacial lakes) or mobilisation (e.g. slope failure) within the catchment area.

2.1.2 Particle properties

Sediment particles are characterized by the following main parameters:

2.1.2.1 Particle size

Figure 2-1 shows the two systems to classify sediment particles by size (diameter) commonly used in Europe and the United States of America, respectively. In the latter, the logarithmically spaced limits of the size classes are also defined by the normalized particle diameter ϕ according to Krumbein (1937). In the present study, the terminology according to DIN EN ISO 14688-1 (2013) is adopted.

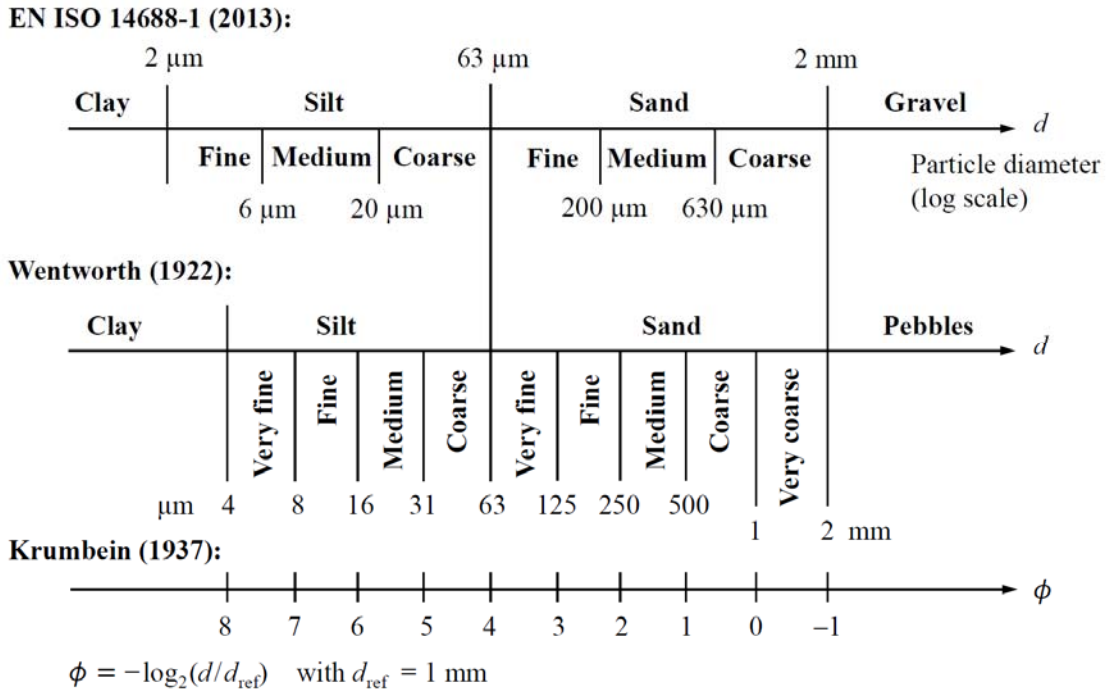

Figure 2-1 Common systems for classification of sediment particles by size.

Silt and clay particles are cohesive and may form flocs which are larger than the primary particles. For turbine erosion, the size of the primary particles is relevant because flocs are disaggregated before and during the turbine passage.

2.1.2.2 Particle dimensions and shapes

The size of a spherical particle is clearly defined by its diameter d. For the size of non-spherical particles, the volume-equivalent sphere diameter d_{es} serves as a simple and comparable parameter.

For non-spherical particles, three lengths in the three dimensions of space can be measured, a being in the direction of the longest extension of the particle, b the intermediate and c the shortest. These three numbers are the side lengths of an enveloping cuboid (Fig. 2-2a). Alternatively, the enveloping cuboid can be orientated according to the plane of maximum stability (Fig. 2-2b).

The aspect ratios, *b*/*a* and *c*/*b* (both ranging between 0 and 1) indicate the basic particle shapes, which can be cubic (equant), platy (discoid, flaky), blade- or rod-like (Fig. 2-2a). The ratio *b*/*a* is related to the elongation, *c*/*b* to the flatness. Mineral particles with isotropic strength (e.g. quartz) usually have the first type of shape with no preferred dimension. Minerals of the sheet silicates group (e.g. mica), however, are usually flaky due to their layer structure.

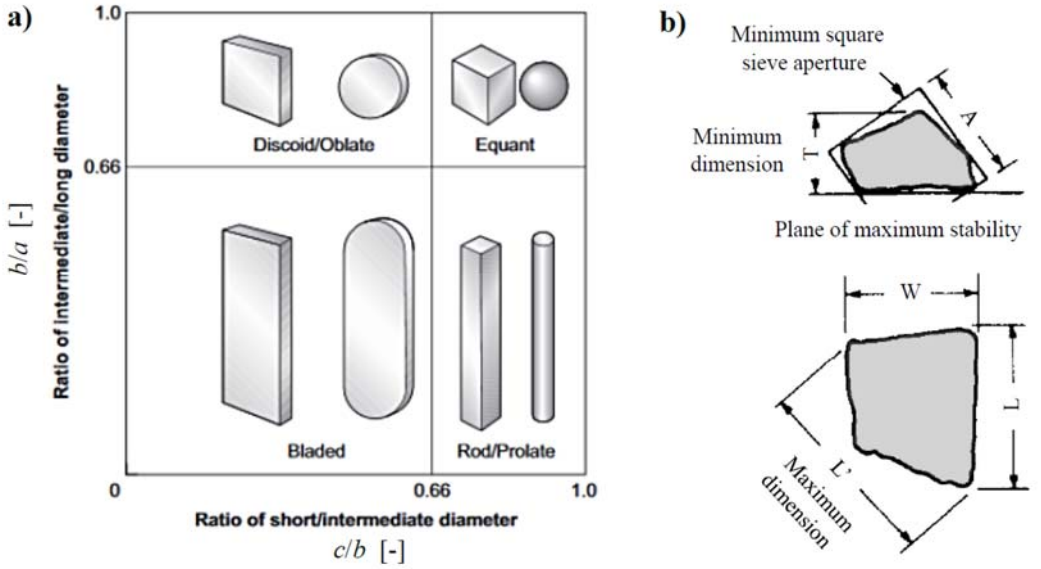

Figure 2-2 a) Characterization of basic particle shapes (Nichols 2009), b) particle dimensions according to Bahadur & Badruddin (1990)

The Corey (1949) Shape Factor, defined as

$$CSF = \frac{c}{\sqrt{ab}} \qquad [-] \qquad (2\text{-}1)$$

considers all three dimensions and is used e.g. in the context of settling velocity of non-spherical particles. For natural (irregular and rounded) sand particles, $CSF \approx 0.7$.

In a second step, the particle shape can be characterized by the degree of rounding of its primary shape. Bouwman *et al.* (2004) and Al-Rousan *et al.* (2007) summarized methods for the quantification of particle shape, angularity and texture, mainly based on image analysis. The Cox (1927) Roundness Factor (also called circularity) is determined from particle images, with A = projected area and P_g = perimeter length:

$$CRF = \frac{4\pi A}{P_g^{\,2}} \qquad [-] \qquad (2\text{-}2)$$

This factor is 1 for spheres (or particles appearing as a disk), and lower for elongated or angular particles. Diepenbroek (1992) and Poudel *et al.* (2012) used Fourier analysis to parameterize morphological properties of sediment particles in 2D.

For the erosion potential of particles, their angularity is more important than their elongation. On microscopic images, particles can be visually classified in some sub-classes between rounded and very angular, e.g. according to Krumbein (1941). Advanced methods to characterize the angularity have been proposed by Hamblin & Stachowiak (1995). They calculated a 'spike parameter' from the heights and the apex angles of the particles' protrusions measured from 2D microscopic images.

Mineral particles in the water of medium- and high-head HPPs are typically angular, because such HPPs are usually located in upper river reaches, where particles have not yet been well-rounded by long fluvial transport. Glaciers are a major source of small angular particles because particles are fragmented (comminuted) on their beds.

2.1.2.3 Particle size distribution (PSD)

In monodisperse suspensions all particles have the same diameter. For graded particles however, their size distribution can be characterized by volume or mass fractions falling into certain size classes. In environmental and civil engineering, cumulative PSDs are typically represented as obtained from sieve curves: The d_x denotes the diameter of graded particles which is not exceeded by x % of the particle mass. The d_{50} is the median particle diameter, i.e. in half of the particle mass the particles have smaller or larger diameters, respectively. In hydraulic engineering the so-called (geometric) spreading of a PSD is used to quantify its width:

$$\sigma_g = \sqrt{\frac{d_{84}}{d_{16}}} \qquad [-] \qquad (2\text{-}3)$$

If the specific area of graded, especially non-spherical particles is relevant, the Mean Sauter Diameter *SMD* is used:

$$SMD = \frac{6\,V_p}{A_{s,p}} \qquad [\mu m] \qquad (2\text{-}4)$$

where V_p = particle volume and $A_{s,p}$ = surface area of an ensemble of particles (Sauter 1926). For non-graded spherical particles, *SMD* corresponds to the sphere diameter d.

2.1.2.4 Particle density and organic content

The density of the primary particles can be measured with a pycnometer in the laboratory. In case of aggregated particles (flocs), their bulk density is lower than the density of the primary particles. The organic content of a sample can be measured in the laboratory via

mass reduction on ignition. In the present study, the focus lies on mineral particles with negligible organic content.

2.1.2.5 Mineralogical composition and hardness

The mineralogical composition of particle material can be quantified in the laboratory using Rietveld X-ray diffraction analysis. The hardness of the particles is assigned based on the mineralogy using tables from petrographic literature. The Mohs scale, a non-linear rather qualitative scale introduced in 1812 is commonly used in the present context. The scale ranges from 1 (chalk) to 10 (diamond). High fractions of hard particles, e.g. of quartz and feldspar (Mohs hardness 7 and 6, respectively) are typical for igneous rocks, whereas sedimentary rocks are generally softer.

2.1.3 Sediment transport in water

2.1.3.1 Drag force and settling velocity

A basic parameter for the transport of a sediment particle in water is its settling velocity. The terminal settling velocity in stagnant water $v_{s,\infty}$ results from the forces due to gravity, buoyancy and drag. For a small particle, the flow around the particle is laminar (viscous drag), whereas it is turbulent for larger particles (wake behind the particle). The drag force F_D is

$$F_D = \frac{1}{2}\,\rho_w\, v_p^{\,2}\, C_D\, A \qquad [\mathrm{N}] \qquad (2\text{-}5)$$

where ρ_w = density of water, v_p = relative velocity between the particle and the flow, A = projected area. The drag coefficient C_D is a function of the particle shape and the particle Reynolds number $\mathrm{Re}_p = v_p\, d / \upsilon$, where υ = kinematic viscosity of the fluid.

The settling velocity $v_{s,\infty}$ varies with d^2 for small particles, whereas it varies with $d^{0.5}$ for larger particles (Fig. 2-3). Ferguson & Church (2004) presented an equation applicable for all particle sizes:

$$v_{s,\infty} = \frac{\left(\frac{\rho_s}{\rho_w} - 1\right) g\, d^{\,2}}{C_1\, \upsilon + \left(0.75\, C_2 \left(\frac{\rho_s}{\rho_w} - 1\right) g\, d^{\,3}\right)^{0.5}} \qquad [\mathrm{m/s}] \qquad (2\text{-}6)$$

where ρ_s = solid density of the particle material, g = gravitational acceleration; C_1 = 18 for spherical, 20 for natural sand and 24 for very angular particles; C_2 = 0.4 for spherical, 1.1 for natural sand and 1.2 for very angular particles.

Equation (2-6) can be rearranged as an explicit equation for the drag coefficient (Ferguson & Church 2004):

$$C_D = \left[\frac{2\ C_1\ v}{3\left(\left(\frac{\rho_s}{\rho_w} - 1\right) g\ d^3\right)^{0.5}} + \sqrt{C_2} \right]^2 \qquad [-] \qquad (2\text{-}7)$$

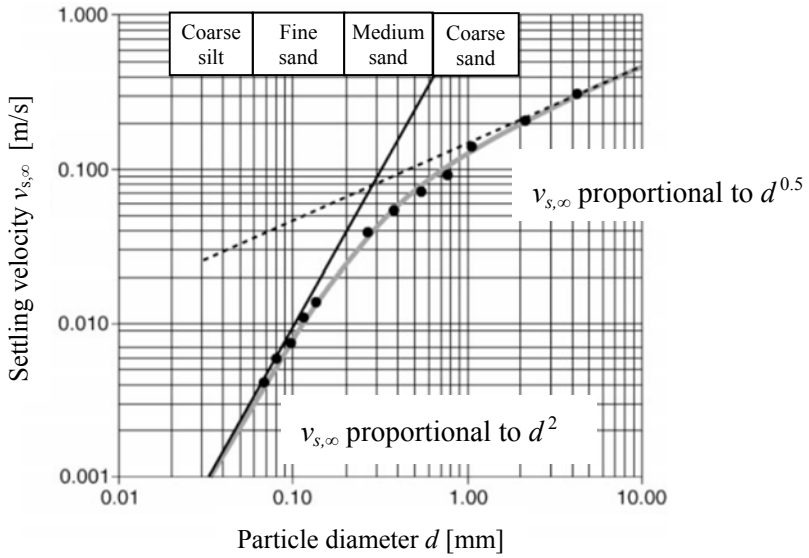

Figure 2-3 Settling velocity of river sediment particles in stagnant water as a function of their diameter (Ferguson & Church 2004).

The settling velocity is reduced for rough and non-spherical particles, higher concentrations and/or in flowing water (due to turbulent lift forces). With several particles and close to walls, complex interactions may occur in the settling process.

2.1.3.2 Incipient motion of sediment particles on the bed

A sediment particle lying on a river bed or a channel invert is moved if the drag force exerted by the flow is higher than the retaining forces. Sediment particles are moved if the non-dimensional shear stress θ (Shields 1936) exceeds a critical value:

$$\theta = \frac{U_*^2}{\left(\frac{\rho_s}{\rho_w} - 1\right) g\ d} > \theta_c \qquad [-] \qquad (2\text{-}8)$$

$$\text{with} \quad U_* = \sqrt{g\ R_h\ S_e} \qquad [\text{m/s}] \qquad (2\text{-}9)$$

where U_* = friction velocity, R_h = hydraulic radius, S_e = slope of the energy line.

For non-cohesive particles, θ_c lies typically in the range of 0.04 to 0.06 for rough beds and is smaller for transitionally rough and smooth beds (Auel 2014).

The adhesive forces acting between small particles and the bed can be modelled with an apparent increase of the relative density of the suspended sediment ρ_s'. This increase is represented by the last term of the following equation (Zanke 1982):

$$\rho'_s = \frac{\rho_s}{\rho_w} - 1 + \frac{0.009}{d^2 \rho_w} \qquad [-] \qquad (2\text{-}10)$$

with d in [mm], ρ_w and ρ_s in [g/cm^3], for quartz particles in water. For $d > 1$ mm, the effect of cohesion on the initiation of motion is negligible. For $d = 100$ µm, the increase of ρ_s' is about 50%. For $d = 20$ µm, ρ_s' is about 15 times ρ_s.

2.1.3.3 Bedload and suspended sediment transport

Depending on sediment availability, flow conditions and sediment properties, sediment particles of various sizes are transported in flowing water. The following transport modes are typically distinguished: sliding, rolling, saltation and suspension (García 2008). In saltation, a particle's trajectory contains a single up- and downward motion, whereas the trajectory in suspension is wavy and the distances between subsequent bed contacts are longer or indefinite (Francis 1973). Particle transport by sliding, rolling and saltation is called bedload transport, and is typical for the transport of gravel. Transport in suspension is typical for silt particles. The transport of even finer particles (clay) is also called wash-load. In many rivers, the transport of fine sediment in suspension makes up the major part of the long-term sediment flux (e.g. Sommer 1980).

The threshold of suspension can be modelled by comparing the vertical velocity fluctuations v' in a turbulent flow to the settling velocity of a particle in stagnant water $v_{s,\infty}$. With v' being related to U_*, Van Rijn (1984) expressed the (upper) threshold for sediment transport in suspension as

$$\frac{U_*}{v_{s,\infty}} \gtrsim 0.4 \quad . \qquad [-] \qquad (2\text{-}11)$$

The Rouse number Z is proportional to the inverse of this ratio, and can also be used to express the threshold of sediment transport in suspension (e.g. Celik & Rodi 1991):

$$Z = \frac{v_{s,\infty}}{\beta \kappa U_*} \lesssim 6 \qquad [-] \qquad (2\text{-}12)$$

where β = coefficient relating eddy viscosity to eddy diffusivity ≈ 1, κ = von Kármán constant ≈ 0.4. Because U_* is related to U, and $v_{s,\infty}$ is a function of d (Fig. 2-3), the threshold of suspension can approximately be expressed as

$$d \approx \frac{U^2}{360\, g} \qquad \text{[m]} \qquad (2\text{-}13)$$

where U = depth-averaged main flow velocity (Kresser 1964). At a flow velocity of e.g. 1 m/s, particles smaller than 280 µm are thus estimated to be transported in suspension.

The threshold of suspension can also be expressed in terms of the Shields parameter e.g. according to Celik & Rodi (1991) for shear Reynolds numbers $\mathrm{Re}_* = U_*\, d / \upsilon > 0.6$:

$$\theta \gtrsim 0.25 \qquad \text{[-]} \qquad (2\text{-}14)$$

Comparing with Equation (2-8), the required θ for transport in suspension is at least about five times as high as that for the inception of particle motion.

It should be recalled that the process of sediment transport is highly stochastic due to the random nature of the turbulent velocity fluctuations. The mentioned thresholds are thus only indicative. Local instantaneous suspended sediment concentrations are influenced by coherent flow structures (large eddies) and bed roughness. Parsons *et al.* (2015) pointed out that (i) sediment transport is intermittent also in steady-state flow and (ii) the various modes of sediment transport can be seen as a continuum of particle movements with increasing hop lengths.

2.1.4 Suspended sediment concentration (*SSC*)

2.1.4.1 Definition

The Suspended Sediment mass Concentration (*SSC*) is defined as the ratio between the mass of solid particles and the corresponding volume of the water-particle mixture. In this study, the unit [g/l] is adopted; other frequently used units are 'ppm by mass' or mg/l. *SSC* does not include the concentration of dissolved minerals.

2.1.4.2 Typical SSC in rivers

SSC greatly varies in space and time (seasonally, diurnally, event-based). *SSC* in rivers ranges from a few mg/l (in the low-flow season, with snow/ice cover in the catchment area) to e.g. 100 g/l during floods or reservoir flushing events. *SSC* of several g/l during monsoon months, > 10 g/l for a few times per year, and peaks of e.g. 70 g/l are reported from India (Sidhu 1999, Winkler *et al.* 2011b). *SSC* may increase within minutes and decrease usually less quickly.

2.1.4.3 Spatial SSC gradients

Due to gravity, *SSC* is generally higher in lower parts of water columns. In steady-state 2D-open channel flow and dilute suspensions, the vertical *SSC* distribution is usually described according to the approach by Rouse (1937). Figure 2-4 shows a good agreement of measured *SSC* and fits by Rouse-type curves. Such curves are also shown in Figure 2-5a with a linear scaling of the *SSC*-axis. The vertical *SSC* profile is more uniform if the Rouse number Z (Eq. 2-12) is low, i.e. U_* is high and the particles are small. Rouse profiles do not apply to the region close to the bed, where typically bedload is transported.

In horizontal or inclined pipes, *SSC* also increases towards the bottom as shown in Figure 2-5b. These *SSC* profiles of graded ash particles ($d_{50} \approx 50$ µm) were measured in a horizontal DN 250 mm pipe at increasing flow velocities of 0.28, 0.40, 1.00 and 1.84 m/s corresponding to decreasing Z. With high *SSC* and high Z, a slurry flow may form on the pipe invert.

In rivers, *SSC* may vary considerably not only in the vertical, but also in the horizontal (transversal) direction. Hence, a cross-section averaged *SSC* needs to be determined from measurements in several verticals over the river width (Grasso *et al.* 2014, Haimann *et al.* 2014). In quasi-horizontal pipes, measurements by Vlasak *et al.* (2015) showed that *SSC* varies less in transversal than in vertical direction. Experimental data on spatial *SSC* gradients of dilute suspensions in large pipes (penstocks) are scarce.

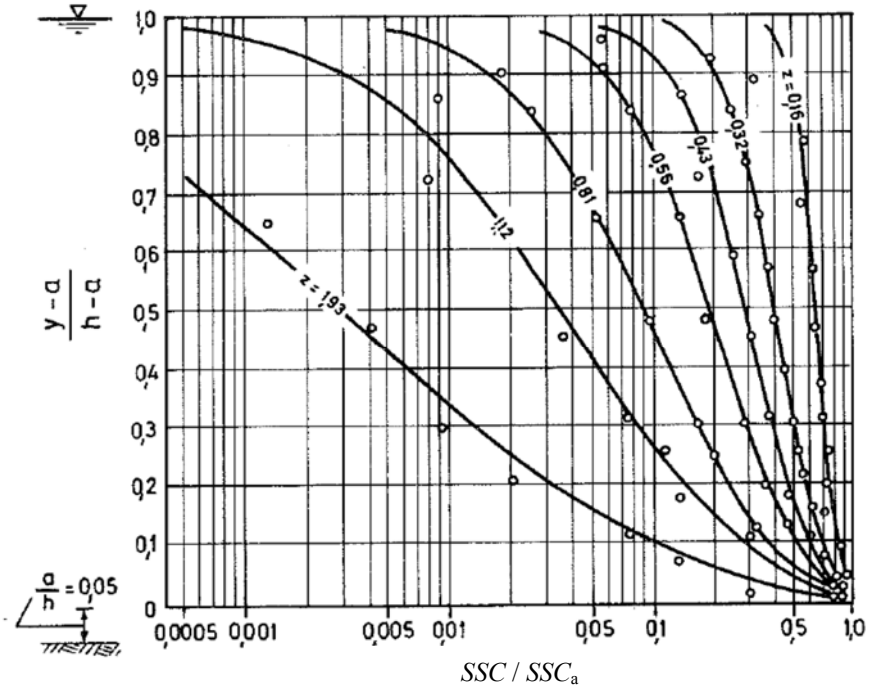

Figure 2-4 Vertical *SSC* profiles in open-channel flow measured by Vanoni (1946) and adjusted Rouse-type curves (DVWK 125 1986, García 2008); SSC_a is the *SSC* at 5% of the water depth above the bed (reference elevation $a/h = 0.05$).

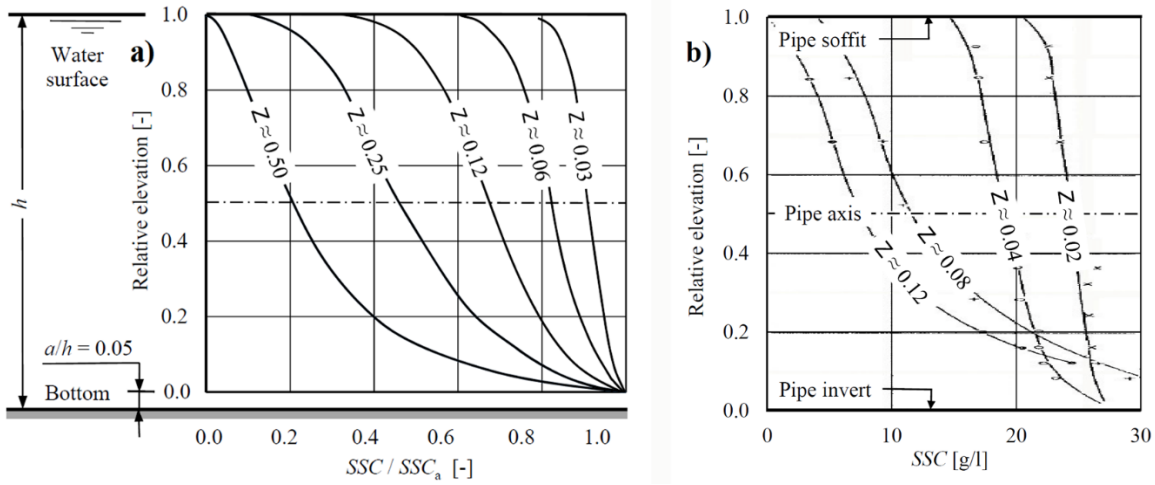

Figure 2-5 Vertical *SSC* profiles a) in 2d-open channel flow (modified from Vanoni 2006) and b) in a horizontal pipe (modified from Durand 1951).

At given flow conditions, the concentration of coarser particles is higher in the lower part of a water column, as can be seen from the profiles in Fig. 2-4a for increasing Z. Hence, vertical PSD gradients have to be expected with graded particles.

2.1.5 Suspended sediment flux and load

In a one-dimensional flow, the transport rate of suspended sediment, i.e. the solid mass flux, results from the integration of the product of the local *SSC* and the local flow velocity *u* over the cross-section *A* (e.g. Shah-Fairbank & Julien 2015). With the cross-section averaged velocity *U* and homogeneous *SSC*, the Suspended Sediment transport Rate *SSR* is

$$SSR(t) = SSC(t) \cdot U(t) \cdot A = SSC(t) \cdot Q(t) \qquad \text{[kg/s]} \qquad (2\text{-}15)$$

where *Q* denotes the discharge, i.e. the volumetric flow rate [m^3/s], of the water-sediment mixture. The suspended sediment load (*SSL*) results from the integration of the *SSR* over a certain time.

2.1.6 Sediment processes and sediment-related management of HPPs

2.1.6.1 Partial sediment exclusion in reservoirs

Many HPP schemes comprise lakes impounded by dams. Such in-stream reservoirs serve for balancing water inflow and production, and contribute to the difference in elevation

exploited by the HPP. Sediment transported by rivers accumulates partly in such reservoirs. Coarser sediment particles settle close to the inflows forming deltas, while finer sediments are transported towards the dam, e.g. by turbidity currents.

The percentage of sediment which settles in a reservoir, i.e. the trap efficiency, depends mainly on the reservoir's storage volume compared to the mean volume of annual inflows, i.e. the Capacity-Inflow-Ratio (Morris & Fan 1998). This ratio reflects the mean residence time of the stored water. If this ratio is high, finer sediment particles settle. The sediment exclusion by reservoirs is favourable to reduce turbine erosion, as long as the progressing reservoir sedimentation does not lead to higher *SSC* and coarser particles in the turbine water. From an overall and medium to long-term perspective, reservoir sedimentation is a growing worldwide problem, because the active storage volumes of reservoirs and their save operation may be compromised (ICOLD 2009, Schleiss *et al.* 2010, Annandale 2013).

2.1.6.2 Partial sediment exclusion on power waterways

When the turbine water is not taken from a reservoir, one or several of the following facilities may be built and operated in medium- and high-head HPPs to reduce *SSC* and particle size in the turbine water:

- Sand traps, mostly in the form of long, flushable basins, open-air or sub-surface; possibly preceded by a gravel trap (Vischer & Huber 2002; Ortmanns 2006);
- Flushable intake areas, compensation basins/chambers or storage tunnels;
- Coanda-effect screens: typically if the intake discharge is smaller than a few m3/s and if it is sufficient to exclude grains with diameters > 0.5 or 1 mm;
- Hydro-cyclones in penstocks with moderate discharges (under development): according to numerical simulations, particles larger than 60 µm and some particles > 20 µm can be excluded (Doujak & Götsch 2010).

The extracted sediments together with some flushing water are usually returned to the river in the intake area. For economic, technical and other reasons, it is not possible to exclude all sediments from the turbine water. Typically, sediment particles with $d > 300$ µm are excluded. The design particle size should be adjusted to the head of the HPP, the hardness and angularity of the particles.

At HPPs with unlined waterways or with water adductions from simple intake structures into the power waterway, additional sediment traps (often called 'rock traps') should be provided.

2.1.6.3 Operational measures to reduce sediment loads on turbines

The sediment load in water adductions, power waterways and/or turbines can also be limited by temporary closing of intakes and pausing of turbine operation (HPP shutdowns) during floods or other events with high sediment load or erosion potential (Müller & De Cesare 2009, Boes 2010, Singh *et al.* 2013, Wedmark 2014, Winkler 2014).

Hydro-abrasive erosion can also be reduced by avoiding partial-load operation because the amount of erosion per generated kWh is lower at full load (Wedmark 2014).

Moreover, highly sediment-laden water may be released through Pelton turbines without erosion on the runner and without electricity generation when the jet deflectors are activated (as during an emergency closure). Such operation is an option for rare situations with very high *SSC*, e.g. due to re-suspension of settled sediment, as may occur during the emptying of upstream storage facilities or dewatering of the power waterway.

In most hydraulic schemes worldwide, *SSC* and especially PSD are not continuously monitored in real-time. The operation of reservoirs and turbines is mostly not based on quantitative information of actual fine sediment load.

2.2 Techniques for suspended sediment monitoring

2.2.1 Monitoring of *SSC*

2.2.1.1 Overview

Guidelines for measuring *SSC* in rivers are provided in DVWK 125 (1986) and Habersack *et al.* (2008). The practice of *SSC* measurements in Swiss rivers is described in Spreafico *et al.* (2005). Various techniques for *SSC* measurements are treated in Wren *et al.* (2000) and ISO 11657 (2014). A literature review on *SSC* measuring techniques and references to recent studies are given by Rai & Kumar (2015).

Techniques for *SSC* measurements are grouped in direct and indirect ones:

- The direct technique consists of taking water samples, transporting them to the laboratory and carrying out gravimetrical analyses. Such measurements are discontinuous and results are available only after a few hours or days. This technique offers high accuracy but requires a lot of man hours.
- Most of the indirect (also called ‘surrogate’) techniques, however, can be used *in-situ*, are able to provide *SSC* data at high temporal resolution or continuously and/or in real-time. A major drawback of indirect techniques is the requirement of calibration and/or validation.

Taking representative samples of water containing suspended particles is not evident. Larger particles may separate from streamlines before entering into a bottle or sampling line. If the velocity of the sampling flow is lower than that of the approaching flow, *SSC* and particle sizes are overestimated, essentially for particles coarser than silt (Edwards & Glysson 1999). To avoid such biases, both flows should have the same velocity, and the sampling flow should be taken in the direction of the approaching flow (*isokinetic* sampling).

In the context of sediment management at HPPs, turbine erosion and environmental monitoring, reliable measurements of higher *SSC* (up to e.g. 100 g/l), especially of coarser particles, are important. In the following, a selection of measuring techniques used in this context is described.

2.2.1.2 Gravimetrical analysis

The mass of the sediments in relation to the volume of the sample is determined by weighing of the dried residues, which are obtained by (i) filtration or (ii) evaporation of the water. In the first case, particles smaller than the pore size of the filter are not captured. In the second case, the concentration of the minerals which were dissolved in the water before its evaporation needs to be accounted for. Gravimetrical analysis is the reference for the indirect techniques.

2.2.1.3 Imhoff cone measurements

In practice of HPP operation, e.g. for SSM in a river downstream of a dam during reservoir flushing, Imhoff cones are traditionally used (in Europe). River water is taken and poured into a conical, transparent beaker. The bulk volume concentration of sediments is read from the top level of the settled, unconsolidated solids after e.g. 15 or 60 minutes. Uncertainty on *SSC* obtained from Imhoff cones arises from the variation of the bulk volume concentration as a function of the particle size, the solid density of the particles and the settling time.

2.2.1.4 Turbidity (optical transmission and optical backscatter)

The presence of solid particles in water leads to a reduction of transparency, i.e. turbidity as treated in DIN EN ISO 7027 (2000). For turbidity measurements, a collimated beam of visible or near infrared light (wave length 0.3 to 1 μm) is sent into a sample volume and light is scattered by the particles. With suspended mineral particles in the range of clay to fine sand, the wave length is not much different from the particle diameters. This

scattering regime is described by the theory of Mie (1908) for spherical particles. Depending on the type of turbidimeter, the received light intensity is measured at a different angle α (Fig. 2-6), which leads to different characteristics:

- $\alpha > 90°$, i.e. optical backscatter (often abbreviated as OBS): the signal suffers less from saturation at high turbidities;
- $\alpha = 90°$, called 'nephelometric': the signal is less dependent on particle size;
- $0° < \alpha < 90°$, i.e. optical forward scatter: suitable to measure low turbidities;
- $\alpha = 0°$, called through-light or transmission measurement: suitable to measure higher turbidities.

In some turbidimeters, measurements at several angles are combined to increase their measuring range.

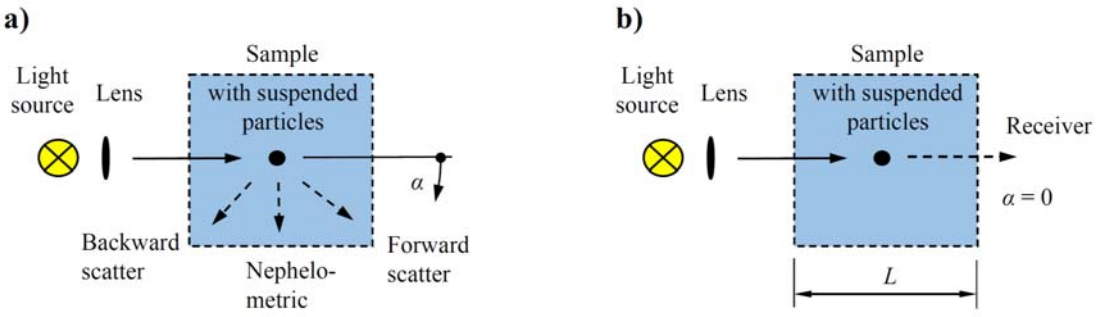

Figure 2-6 Turbidity measurements by a) scattering at $\alpha > 0°$ or by b) through-light (α=0°).

For dilute suspensions, turbidity is usually proportional to *SSC*. The specific turbidity, i.e. turbidity/*SSC*, depends on PSD, particle shapes and material properties such as density, colour, refractive index, surface roughness etc. (Gippel 1995, Sutherland *et al.* 2000, Downing 2006). Changes in the particle diameter *d* significantly affect the specific turbidity: For monodisperse suspensions with spherical particles in the size range relevant for SSM and with the usual wavelengths, specific turbidity is approximately proportional to 1/*d*. For graded and/or non-spherical particles, specific turbidity is well-correlated with the Sauter Mean Diameter *SMD*. Furthermore, turbidity readings are sensitive to contamination on the optics (so-called fouling) and to air bubbles.

For $\alpha = 0°$, the equation of Bouguer-Lambert-Beer applies

$$\lg\left(\frac{I_0}{I_1}\right) = \beta \cdot SSC \cdot L \qquad [-] \qquad (2\text{-}16)$$

where I_0 and I_1 are the incident and the received light intensities, respectively, β = coefficient accounting for the absorption and scattering, depending on the above mentioned

particle properties and the wave length, and L = optical path length. Equation (2-16) shows that the measurable *SSC* increases if the optical path length L is reduced.

For $\alpha > 0°$, the measured specific turbidity may decrease at high turbidities because not all particles are fully exposed to the incident light and a smaller fraction of the scattered light reaches the receiver (effects of shadows caused by the high number of particles).

Turbidimeters are usually factory-calibrated for certain suspensions. There are various units for turbidity, the most common being Formazine Nephelometric Units [FNU] in Europe and Nephelometric Turbidity Units [NTU] in the USA. Formazine is an insoluble polymer of which aqueous suspensions are prepared with high reproducibility.

A widely used approach to quantify *SSC* in surface waters consists of continuously measuring turbidity and to convert these measurements to *SSC* based on a calibration curve obtained from comparison of turbidity measurements to gravimetrically determined *SSC* of occasionally taken bottle samples (Grasso *et al.* 2011, Haimann *et al.* 2014, Müller *et al.* 2014). However, turbidity-based *SSC* may be biased if particle properties as mentioned above change in time and are not correlated to *SSC*.

2.2.1.5 Acoustic techniques

Overview

Information on *SSC* can be obtained from the forward- and/or backscatter of pulsed ultrasonic signals (Gruber *et al.* 2016). Their frequency f is mostly between 300 kHz and 8 MHz. In this range, the wavelengths of sound in water are ~4.7 to 0.18 mm. With clay to medium silt particles, the wavelength is long compared to d. In the so-called Long Wavelength Regime, the visco-inertial effects dominate, and the attenuation can be modelled e.g. according to Atkinson & Kytömaa (1992). For larger particles (sand) and higher frequencies, more complex models including also the backscattering effects need to be applied (e.g. Faran 1951).

Backscatter

Ultrasonic signals are mostly used for SSM in connection with Acoustic Doppler Current Profilers (ADCPs). The use of ADCPs offers the advantage of obtaining spatially distributed information on *SSC* in cross-sections of surface water bodies. Besides classical vertical profiling, ADCPs can also be installed horizontally (side-looking) to monitor *SSC* across a river at a certain elevation (Moore 2011). *SSC* are inferred from backscattered signals and their correlation with gravimetrical *SSC* from bottle samples. Agrawal *et al.*

(2016) favour using $f = 8$ MHz because of a relatively low particle-size sensitivity for $60 \leq d \leq 500$ µm.

The simultaneous use of two transducers with different frequencies reduces the sensitivity of estimated *SSC* to PSD variations or allows retrieving information on the median particle size d_{50} (Guerrero *et al.* 2013, Jourdin *et al.* 2014). Further multiple-frequency acoustic backscatter techniques for measurements of *SSC* and d_{50} are under development. Skripalle *et al.* (2016) use $f = 0.5$, 1, 2 and 4 MHz and presented laboratory and field measurements compared to reference techniques. The inversion of acoustic data is challenging due to a low signal-to-noise-ratio and the generally ill-posed inversion problem (Gruber *et al.* 2016).

Forwardscatter (attenuation)

With two transducers installed at the ends of an acoustic path in water, acoustic forwardscatter, i.e. attenuation, can be exploited for SSM. Such acoustic paths are used in Acoustic Discharge Measurement (ADM) based on the acoustic transit time method (also called time-of-flight method). For the determination of the average axial flow velocity U and consequently the discharge Q in channels and penstocks, ultrasonic pulses are sent through the water. If the water contains sediment particles, the received signal is weaker due to the so-called 'excess attenuation' (Costa *et al.* 2012). Therefore, such ADM installations can also serve to monitor *SSC* (Felix *et al.* 2013b). The amplitude of the acoustic signal A at a distance x from the transducer is

$$A(x) = \frac{K_T}{x} e^{-a\,x} \qquad \text{e.g. [V]} \qquad (2\text{-}17)$$

where K_T is a transducer constant and α the attenuation coefficient [1/m]. For dilute suspensions, α can be modelled as the attenuation due to the water α_w and the excess attenuation due to the interaction of the water with the suspended solid particles a_{ex}. The latter is approximately proportional to *SSC* with otherwise constant parameters (Gruber *et al.* 2016). For a given signal frequency and particle type, *A(x)* and *SSC* are related by

$$\frac{A(x)}{A_w(x)} = e^{-\beta\ SSC\,x} \qquad [-] \qquad (2\text{-}18)$$

where $A_w(x)$ is the amplitude in clear water and β is a constant. For a certain path length x, the measured amplitude $A(t)$ and *SSC* are related by

$$\frac{A(t)}{A_w} = e^{-\varepsilon\,SSC(t)} \qquad [-] \qquad (2\text{-}19)$$

where ε is the specific attenuation which can be determined by comparison to gravimetrical *SSC*. Similarly to through-light turbidimeters (Eq. 2-16), ε depends on the PSD, particle shapes, particle density and potentially (micro) air bubbles in the water or attached to solid particles. For $f = 1$ MHz and monodisperse suspensions with spherical particles in the size range of $2 < d < 60$ µm, ε decreases approximately linearly with $1/d$ due to visco-inertial effects (Guerrero *et al.* 2016). For larger particles, i.e. sand, scattering becomes more important and ε increases with d.

2.2.1.6 Laser In-Situ Scattering and Transmissometry (LISST)

Since 1995, portable laser diffraction (LD) instruments have become available under the trademark LISST, standing for 'Laser In-situ Scattering and Transmissometry'. The principles of LD, the construction of LISST-instruments and the mathematical approach used in the data analysis are described in Agrawal & Pottsmith (2000). Besides marine science, LISST instruments have been used in a few HPPs outside Switzerland (Boes 2009, 2010; Agrawal *et al.* 2012, 2016) and in reservoir sedimentation studies (Haun *et al.* 2013).

In LISST instruments, the scattering (diffraction) of a laser beam ($\lambda = 670$ nm) at small angles (< 9°) and its attenuation, caused by suspended particles, are measured. From these light intensities, the particle volume concentrations in 32 logarithmically spaced size classes (also called size bins) are computed with a software provided by the manufacturer. The volume concentrations in the size bins are termed *BVC*. With most LD instruments, this inversion is based on the assumption that particles have spherical shape (Mie theory). More recently, Agrawal *et al.* (2008) developed an additional inversion mode for so-called 'random shaped' particles and added it to the software for LISST data analysis. The term 'random' refers to particles with no preferred axes, i.e. elongated and platy particles were not considered. Although the latter types of particles exist in natural environments, no specific inversion mode is available. In this thesis, the two available inversion modes are referred to as IMS for the spherical and IMR for the 'random shaped' particles.

The total volume concentration (*TVC*) is calculated from the BVC at each time step. Finally, the *TVC* is converted to *SSC* (concentration by mass). In contrast to turbidimeters and single-frequency acoustic techniques, effects of temporal variations of particle sizes on the concentration are considered in LISST.

LISST instruments allow for measuring *SSC* as low as some mg/l, thus the lower limit of their measuring range is of no concern for SSM in the context of turbine erosion. How-

ever, the upper limit of the *SSC*-measuring range of a LISST, termed SSC_{lim} in the following, is an important aspect. If the optical transmission τ is too low (i.e. the water is too turbid), the inversion of the raw data to *BVC* is not possible, and hence no PSD and *SSC* are obtained. Generally, it is recommended to perform LD measurements at $\tau \geq 0.3$ to avoid increased measurement uncertainty due to multiple scattering. According to the manufacturer (Sequoia 2008), SSC_{lim} can be estimated by

$$SSC_{lim} = \frac{\alpha \ SMD \ \rho_p}{1.13 \cdot 10^3 \cdot 2.65} = \frac{-ln(\tau) \ SMD \ \rho_p}{2995 \ L} \qquad [g/l] \qquad (2\text{-}20)$$

where *SMD* [µm] is the Sauter Mean Diameter (Eq. 2.4), ρ_p = particle density [g/cm^3], $\alpha = -\ln(\tau)/L$ is the attenuation coefficient [1/m], and L is the optical path length [m].

To measure higher *SSC* with given particle properties, there are two options: (i) reduction of the optical path length and/or (ii) sample dilution with clear water prior to measurements. With the first option, SSC_{lim} scales with $1/L$ (Eq. 2-20). The practical possibilities are limited; the shortest optical path of currently available LISST models is 3 mm (standard *LISST-Hydro* and *LISST-Infinite*). With the second option, SSC_{lim} can be increased by an order of magnitude or more, depending on the dilution ratio (Agrawal *et al.* 2011, 2012). Such models have a built-in mixing chamber for automatic sample dilution, a clear water tank, a pump and additional controls, and are accordingly more costly.

2.2.1.7 Densimetry

High *SSC* can be measured via the density of the water-sediment mixture. Le Boursicaud *et al.* (2015) determined the mixture density by weighing of a known volume of pumped river water in a cyclic process. More conveniently, the mixture density can be measured continuously on a sampling line using 'Vibrating Tube Density Meters' (also called 'oscillating U-tubes') or 'Coriolis Flow– and Density Meters' (CFDM). In such devices, the fluid flows through one (or two parallel) straight or bent measuring tubes, which are forced by electromagnetic transducers to oscillate laterally. The oscillation is controlled in such a way that its frequency corresponds to the natural frequency of the liquid-filled tube. The natural frequency is related to the weight of the fluid in the tube (Holcomb & Outcalt 1998, Kalotay 1999). With the known volume of the fluid in the tube, the fluid density is calculated. Furthermore, temperature is measured and thermal expansion is compensated in the internal data processing.

In CFDMs, the Coriolis effect is used to determine the mass flow rate through the tubes by evaluating a phase shift along the oscillating tubes (Wang & Baker 2014). Together

with the density measurement, CFDMs are also able to display volumetric flow rates Q. Although Vibrating Tube Density Meters and CFDMs are widely used in the process industry, they have been rarely used for *in-situ* SSM (Bishwakarma & Støle 2008).

Vibrating Tube Density Meters and CFDMs overestimate the density and thus *SSC* if debris, sediment or biofilms accumulate inside the measuring tubes. On the contrary, the density and *SSC* may be underestimated if the measuring tubes are eroded or if so-called 'phase decoupling' occurs in particulate fluids (Zhu 2009, Basse 2014). In the latter case, particles do not strictly follow the motion of the fluid in the oscillating tubes. This effect on the density measurement is known to be more important with larger particles, but has not yet been experimentally quantified for sediment particles in water.

2.2.1.8 Differential pressure

The mixture density and hence *SSC* are determined from pressure measurements at a fluid column at two levels with a known difference in elevation. If this technique is applied at the penstock of a HPP, the headwater level and the static pressure upstream of the turbines are measured. If the water in the penstock contains suspended sediment, the pressure difference between the upper and the lower sensor is higher than in clear water conditions. Knowing the density of the clear water (as a function of temperature) and the density of the particles, these pressure deviations are converted to *SSC* in quasi-steady state. The relative uncertainty of the technique decreases with high *SSC*, large difference in elevation between the two sensors and small pressure fluctuations (Hsu & Cai 2010).

2.2.1.9 Radiometry and other techniques

Another option to measure *SSC* is by radiometry (nuclear gauges). Similar to turbidimeters, attenuation (or backscatter) from gamma radiation or X-rays can be correlated with gravimetrical *SSC* (Le Boursicaud *et al.* 2015). For gamma rays, permanent sources may be used (e.g. ^{137}Cs), while X-rays are generated in an electrically powered device. With adequate radiation intensity, *SSC* measurements are not affected by particle size variations. These techniques are however not practical for many HPP operators because staff with special training on radiation safety and/or licenses are required.

Further techniques for indirect *SSC* measurements, which are not established in the context of SSM in HPPs and at rivers, comprise

- Electrical conductivity / capacitance (Hsu *et al.* 2010);
- Focused beam reflectance;
- Microwave density meter (Le Boursicaud *et al.* 2015).

2.2.2 Monitoring of suspended sediment sizes

2.2.2.1 Laboratory techniques and instruments for PSD

From bottle samples of sediment-laden water, particle size distributions (PSDs) can be obtained in the laboratory by one of the following techniques:

Dry or wet sieving of dried residue (mainly for sand and coarser particles): The percentages of particle mass passing through a series of sieves with decreasing mesh sizes is determined by weighing. Sieving is considered as the primary technique for particles commonly > 62 µm; wet sieving is possible down to 20 µm. Note that the intermediate particle diameter *b* may differ from the size of the square mesh depending on the particle shapes.

Pipette, hydrometer, or 'visual accumulation tube' analysis (for silt and clay): The PSD (mass of percentage finer) is inferred from calculated settling velocities, presuming a certain particle density and shape. With pipette analysis, the mass fraction of solids remaining in suspension after a certain time is repeatedly determined by weighing of dried residues. With hydrometer analysis, the density of the sediment-water mixture is repeatedly measured by a partly immerged floating body. With a visual accumulation tube, the height of unconsolidated settled sediment is measured as a function of time and hence settling velocity.

Laser diffraction (LD): PSDs are obtained from light intensities scattered at various angles. Smaller particles cause scattering at larger angles. LD has been widely used in laboratories since the 1970ies to characterize powders (e.g. cement).

Focused beam reflectance: A rotating laser beam is sent inside a suspension through a small window. When there is a particle in the laser's path close to the window, light is reflected and sensed. The so-called 'chord lengths' of the particles are calculated from these binary signal and information on the PSD is obtained by statistical methods. This technique is mainly used in process engineering and pharmaceutics.

Coulter Counter: Particles suspended in an electrolyte are pumped through a small orifice while the electric current is measured. The passage of a particle through the orifice causes a change in impedance which is proportional to the particle's volume. Like this, the number and size of particles are determined. This technique is common in biology and medicine for the investigation of cells.

Analysis of microscopic images: Dimensions and 2D shapes of dry particles can be quantified in detail. 3D-systems based on stereo imaging are under development (e.g. Schorsch *et al.* 2014).

Digital holography: 3D-surface shapes are reconstructed based on interferograms. Dimensions and shapes of particles can be analysed in detail.

For SSM, frequent PSD measurements in the laboratory are generally not affordable due to the relatively high effort for collection, transport and analyses of bottle samples. A further drawback is that the results are not available in real-time.

2.2.2.2 Techniques for in-situ PSD measurements at high SSC

The first two techniques mentioned in the previous Section, i.e. sieving and analyses relying on the particle-size dependent settling velocity, are not possible for continuous measurements. For focused beam reflectance and Coulter Counter, no devices for long-term field measurements are known to the author. Particle imaging and holography require rather low turbidity and are thus not suitable for SSM in the context of HPPs.

With LISST instruments mentioned in Section 2.2.1.6, if required with automatic dilution, *in-situ* PSD measurements of suspended sediment at high temporal resolution (e.g. every minute) became feasible. The nominal size range of the latest model (*LISST-200X*) is 1 to 500 µm with spherical particles (IMS). PSDs are calculated from the *BVC* in 32 logarithmically spaced size classes.

Acoustic techniques have the potential to work under opaque conditions. Acoustic multi-frequency techniques for the *in-situ* characterization of particle size(s) are under development (Skripalle *et al.* 2016), but so far these techniques yield less detailed and mostly less accurate PSDs than LD.

2.3 Erosion in hydraulic turbines

2.3.1 Hydraulic turbines

2.3.1.1 Turbine types

In a HPP, hydraulic turbines convert potential and kinetic energy of water into essentially mechanical rotation energy, which is further converted to electric energy by generators. There are three main types of hydraulic turbines: Kaplan, Francis and Pelton. Their application ranges depend basically on the hydraulic head, i.e. the difference in elevation exploited by the HPP. Pelton turbines are used at the highest heads (currently up to ~1900 m), whereas Kaplan turbines are used at low heads <70 m (Giesecke *et al.* 2014). Francis turbines are employed at medium heads up to ~700 m. Within these head ranges, turbine types are selected based on further criteria such as operational efficiency, ease of maintenance and cost-effectiveness.

In Kaplan and Francis turbines, i.e. *reaction* turbines, the runner is fully in the water. In Pelton turbines, however, the runner in an air-filled housing is driven by up to six water jets emerging from nozzles (also called injectors). Pelton turbines are classified as *action* turbines. The present study focuses on hydro-abrasive erosion in Pelton turbines.

2.3.1.2 Turbine materials

Early hydraulic turbine runners were made of cast iron. Nowadays, a martensitic stainless steel with 13% chrome and 4% nickel is mainly used (IEC 62364 2013). Such steel has a density of about 7.7 g/cm^3 and a Mohs hardness of ~4.5, i.e. is softer than quartz and feldspar particles present at many sites worldwide. The possibilities of increasing the erosion resistance of turbine parts are limited, because these need to have not only high hardness, but also high toughness, resistance to fatigue and good machinability. For needle tips of Pelton nozzles or for welded hard-facing layers in buckets, different steel grades and alloys with higher erosion resistance have been used (e.g. steel-cobalt-alloys such as ‘stellite’).

2.3.1.3 Surface treatments and coatings

Various surface treatments and e.g. chrome coatings were developed and tested over decades, but erosion was not much reduced in cases with harder particles.

Soft-coatings based on polyurethane or epoxy resin have been applied on Kaplan and Francis runners (Engelhardt *et al.* 2001). Hard filler materials such as aluminum oxide

and ceramics can be used (Espinoza 2016, Flanagan 2016). Soft-coatings have high bonding strengths and are reported to contribute to reducing cavitation erosion.

Thermally sprayed hard-coatings made of tungsten carbide, cobalt and chrome (WC-CoCr) have been increasingly applied since the 1980s (Kalberer 1988, Karimi *et al.* 1995, Sidhu 1999, Engelhardt *et al.* 2001). Such coatings are applied by High Velocity Oxy Fuel (HVOF) and form a so-called '*cermet*'. They have become state-of the art for medium- and high-head turbines operated in sediment-laden water (Winkler 2014). WC-CoCr-coatings have a Vikers' hardness of 900 to 1200 HV (at 0.3 kg loading, Winkler *et al.* 2011b); hence they are harder than feldspar (Mohs' hardness 6) and can reach similar hardness as quartz (Mohs' hardness 7). Hard-coatings are sensitive to impacts e.g. of stones (splintering). Usually, the coating thickness is 300 to 500 µm. A drawback of coating is that it may hinder the detection of potential cracks in the base material.

Coatings reduce the extent of erosion and increase the time between overhauls *TBO*. However, even hard-coatings may be damaged in severe conditions at least locally. The quality of coatings differs among suppliers due to the properties of the coating material, the preparations, the spraying process and the ambient conditions (e.g. air humidity).

Hard-coated runners have generally a smaller initial efficiency than uncoated ones due to higher roughness and potentially different hydraulic profiles, but the reduction of turbine efficiency is slower, resulting in higher revenues depending on site conditions (Dahlhaug *et al.* 2010, Winkler 2014). After installation of hard-coated runners, the turbine efficiency may slightly increase due to polishing of the coating by sediment-laden water, before efficiency decreases due to damages (IEC 62364 2013).

2.3.2 Pelton turbines

2.3.2.1 Parts and operation principle

The main parts and the operation principle of a) an 'improved water wheel' according to L.A. Pelton in 1880 and b) a today's horizontal-axis Pelton turbine are shown in Figure 2-7. Pelton turbines are classified by the orientation of their axis (vertical or horizontal) and by their number of nozzles (z_0 = 1 to 6). The jets lie in the plane of the runner. The flow rate and thus the turbine power are regulated by the degree of opening of the nozzles. In turbines having several nozzles, more nozzles are opened with increasing power and the degree of opening is usually the same for all nozzles in operation. In this way, the turbine efficiency is generally higher at partial load than if all nozzles had the same, smaller degree of opening. Apart from the start-up and shut-down periods, the rotational

speed n is constant (irrespective of the power) in accordance with the generators' number of pole pairs and the grid frequency.

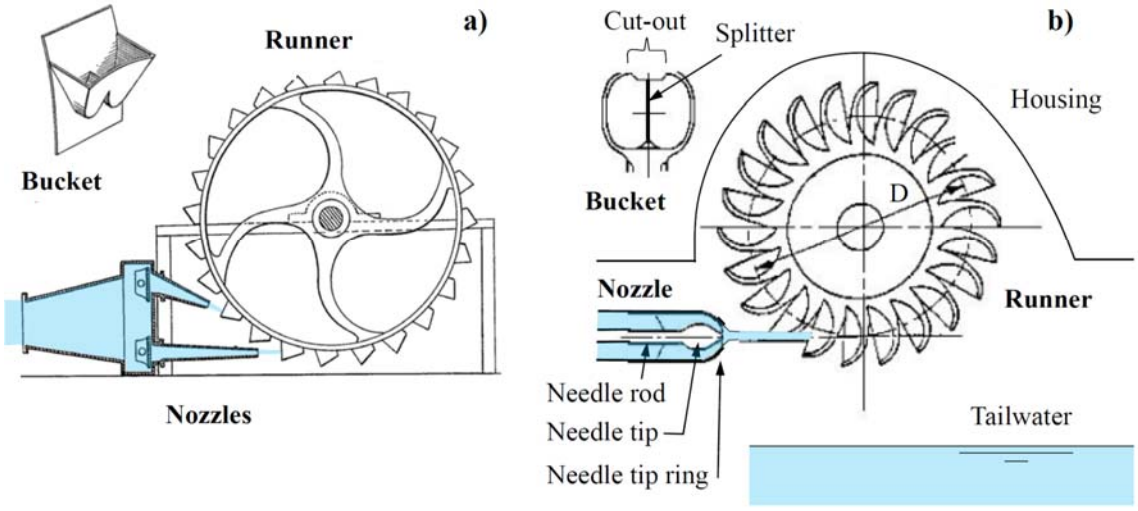

Figure 2-7 Vertical sections of horizontal-axis Pelton turbines with details of buckets, a) according to Patent US233692 (1880) and b) schematic example of a turbine with one nozzle in contemporary design.

2.3.2.2 Hydraulics and main features of Pelton turbine design

A certain portion (longitudinal piece) of the water jet enters each bucket at the periphery of the runner (Fig. 2-8a). The jet is cut by the cut-out edges of the buckets (Fig. 2-9a). In each bucket, the jet is divided by its splitter in the plane of symmetry (Fig. 2-9b). The water flows through both half-buckets and is redirected by $\beta_2 \approx 170°$ (Figs. 2-8b and 2-9c). Firstly the water leaves the bucket close to its root (Fig. 2-9a), then mainly on its sides, and towards the end of a cycle close to the cut-outs (Fig. 2-9d). In addition, splashing water and strings of droplets may occur depending on the bucket design (Bachmann *et al.* 1990). After the bucket passage, a part of the water interacts with the turbine housing. Finally, the decelerated water falls into the tailwater channel.

In Pelton turbines, the jet velocity depends on the net head h_n

$$w_{inj} \approx \sqrt{2\,g\,h_n} \qquad \text{[m/s]} \qquad (2\text{-}21)$$

The velocity of the runner at the pitch circle diameter D (Fig. 2-7b) is typically 45% to 48% of w_{inj} (Zhang 2016). This velocity ratio (<50%) yields a suitable residual flow velocity of the water emerging from the buckets. Hence, the relative velocity w between the jet and the buckets is 52% to 55% of w_{inj}.

The net head varies according to the upstream water level and the head losses which depend on the actual turbine discharge Q. However, the h_n-variations of Pelton turbines are

typically <10%. Hence, w_{inj} and w are practically constant. In contrast, the nozzles' degree of opening, the jet diameter d_0 and the thickness of the water sheets in the buckets are smaller at partial load.

The inner bucket width B is usually ~3 d_0 at design discharge Q_d. The shape of a Pelton runner, i.e. mainly the ratios D/B and D/d_0, are related to the specific speed

$$n_q = n \frac{Q_{1j*}^{0.5}}{h_{n*}^{0.75}} \qquad [1/\text{min}] \qquad (2\text{-}22a)$$

where n = rotational speed usually in revolutions per minute in this context, Q_{1j*} = design discharge (rated discharge) of one jet normalized by 1 m^3/s, and h_{n*} = net head normalized with 1 m (e.g. reported by Zhang 2016). Alternatively, a non-dimensional specific speed has been defined (IEC 60193 1999)

$$n_{QE} = n \frac{Q_{1j}^{0.5}}{(g\, h_n)^{0.75}} \qquad [-] \qquad (2\text{-}22b)$$

where n = rotational speed in revolutions per second and Q_{1j} = design discharge per jet.

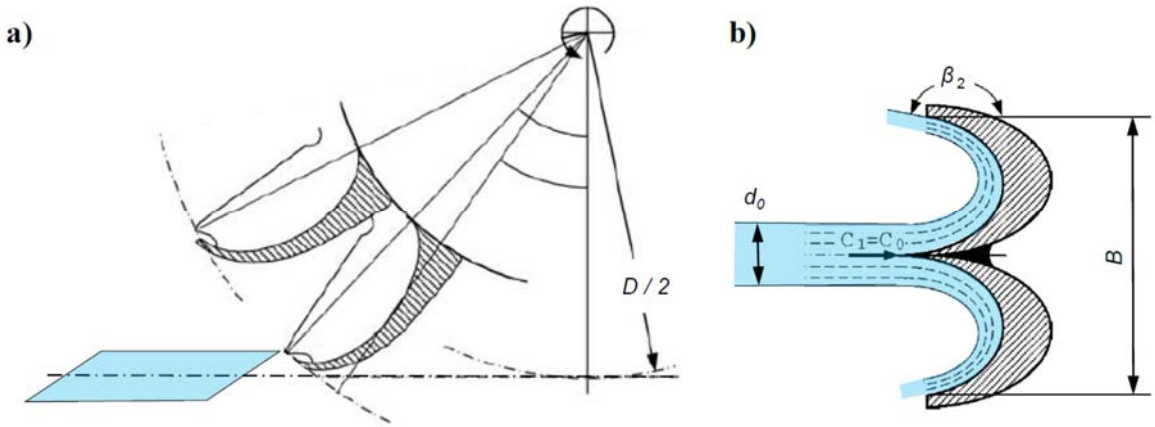

Figure 2-8 Schematics showing a) the jet portion entering a bucket of a Pelton runner and b) the splitting and redirection of the jet in the bucket (Zhang 2016).

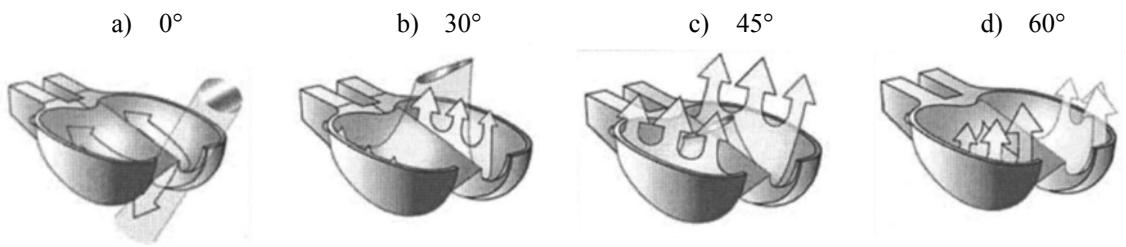

Figure 2-9 Illustrations of the flow in a Pelton bucket at selected relative angular positions of the runner based on photographs and numerical modelling of the 3D free-surface-flow (Perrig *et al.* 2006).

2.3.2.3 Typical erosion damages

The following parts of Pelton turbines are mainly affected by erosion (Faletti 1934, Gummer 2009, Neopane *et al.* 2011, IEC 62364 2013, Winkler 2014):

- Needle tips (Fig. 2-10) and needle tip rings;
- Runner buckets (Figs. 1-2 and 2-11);
- Jet deflector (eroded inside if deflector is activated, outside by splash water);
- Nozzle shields (in turbines with several nozzles);
- Inner side of runner housing (potentially with baffles);
- Grating below the runner (platform for inspection and maintenance).

Material losses lead to increased roughness and changes in hydraulic profiles, and may affect the mechanical stability and integrity of turbine parts, the HPPs' availability, electricity generation, and eventually safety. Erosion leads to undulated or scaly surfaces inside buckets of uncoated runners. Erosion is usually most severe on leading edges, i.e. on splitter crests and at cut-outs of Pelton buckets.

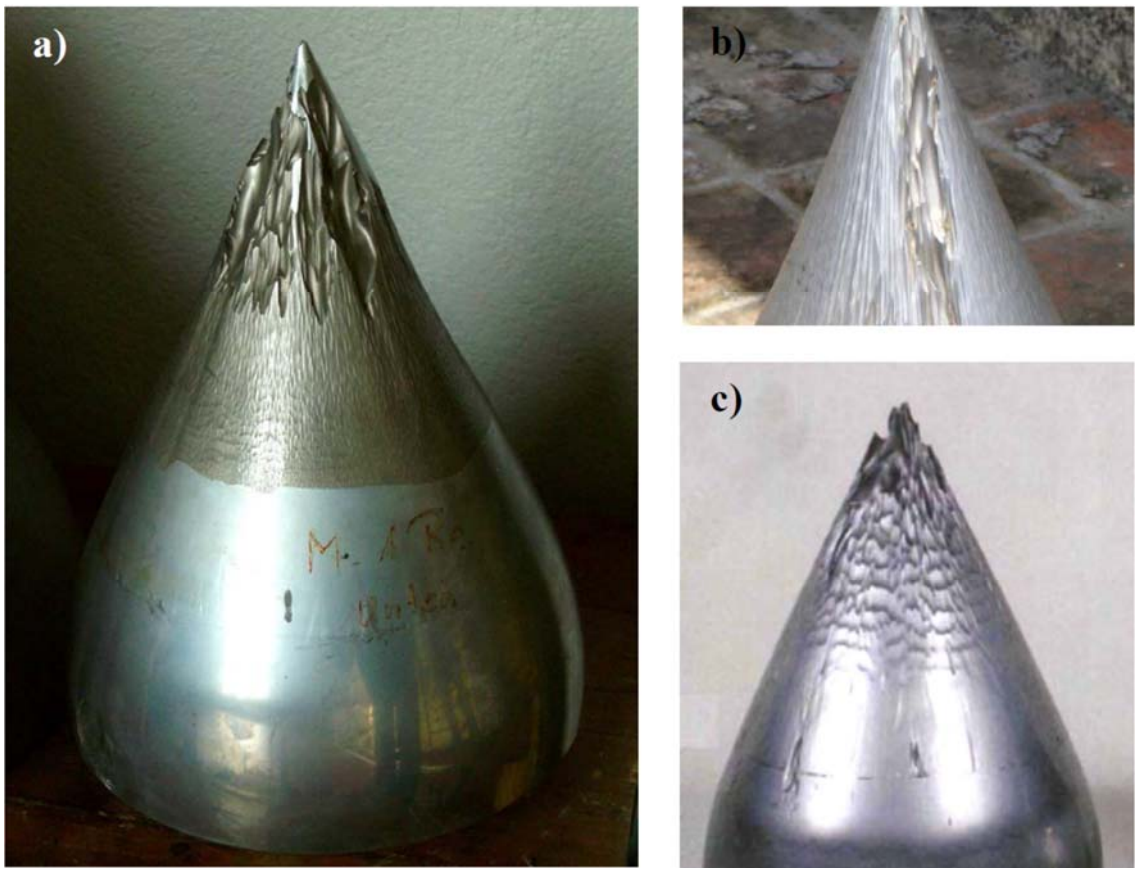

Figure 2-10 Eroded uncoated needle tips of Pelton turbines a) HPP Rabiusa-Realta, Switzerland (courtesy A. Abgottspon), b) Chilime HPP, Nepal (Bajracharya *et al.* 2008), and c) example reported by Cateni *et al.* (2008) / Hamerak (2016).

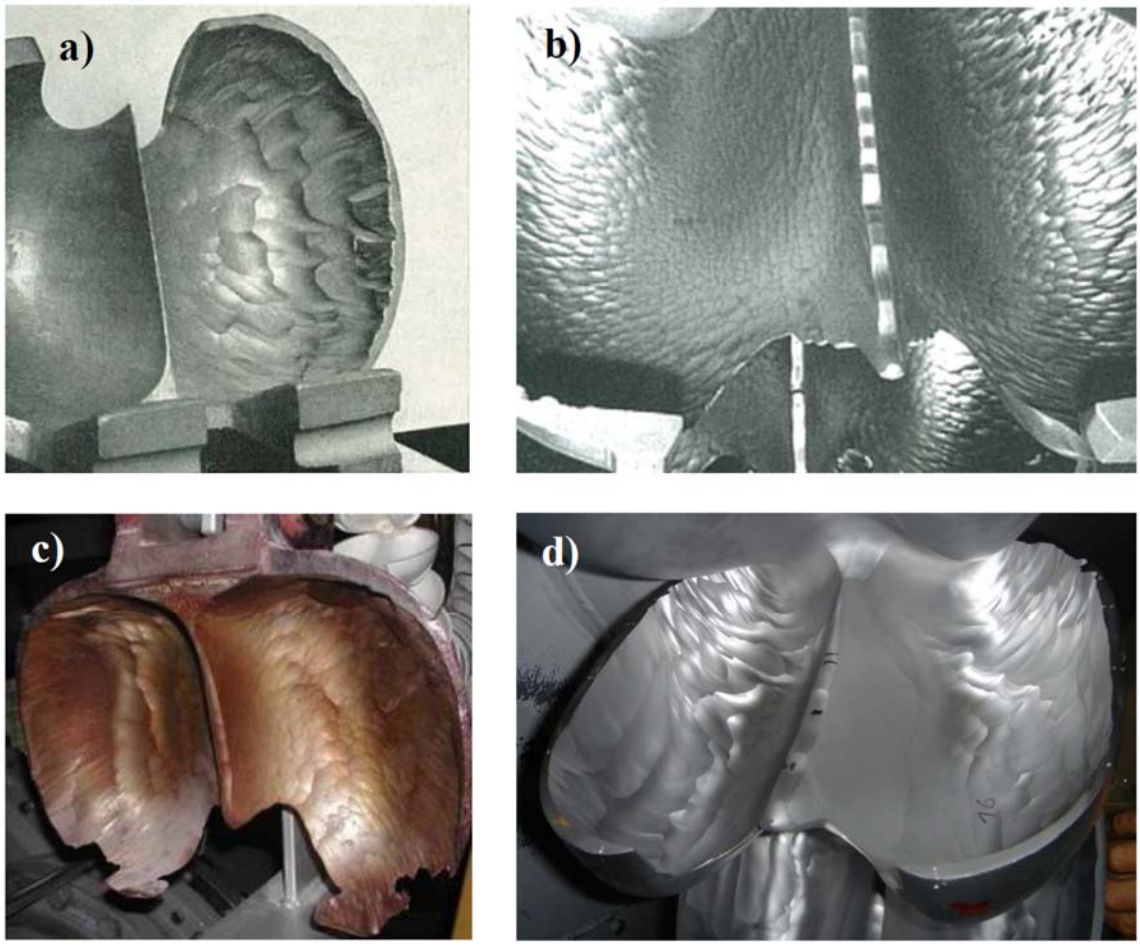

Figure 2-11 Eroded uncoated buckets of Pelton turbine runners: a) early example with the left half-bucket reconstructed by welding (Bovet 1958), b) from HPP Alfalfal, Chile (Krause & Grein 1996), c) severe erosion having affected the integrity of the bucket (Thapa 2004), and d) from HPP Dorferbach, Austria (courtesy of TIWAG-Tiroler Wasserkraft, in Zhang 2016).

2.3.2.4 Typical repair works

Repair works and condition testing of Pelton turbine runners comprises typically:

(i) Small revision on-site, if required every year in the low-flow season:
- Grinding (rounding) of splitter crests and leading edges in the cut-outs,
- Possibly with small repairs by manual welding (induces residual stresses),
- Check for cracks (magnetic particles test) in particular at the bucket root,
- For coated runners: if required local re-coating (inside the runner housing).

(ii) Major overhaul in factory, after several small revisions (Thomann 1988):
- For coated runners: complete removal of coating by special sand blasting,
- Checking for cracks (magnetic particles test, dye penetrant test),
- Reconstruction of eroded material by welding (manually or by robot),
- Pre-grinding or machining to approach the planned geometry,
- Checking for cracks and pores,

- Heat treatment for stress relieve,
- Dynamic balancing,
- Completion of grinding for restoration of planned geometry and polishing,
- For coated runners: apply coating inside the buckets (usually by spray robot),
- Final check.

A Pelton runner can undergo many on-site revisions and several major factory overhauls in its lifetime. Because Pelton runners are not submerged, the effort for runner inspections and replacements is lower than with Francis or Kaplan turbines. Pelton runners can be replaced in less than one day. Thus, downtimes are relatively low if spare parts and qualified staff are available on-site.

2.3.3 Erosion processes

2.3.3.1 Overview

Tribology is a field of science dealing with the contact of primarily solid material surfaces in relative motion; the contact can also be between solids and fluids. Important tribological phenomena are friction and wear. A form of wear is erosion (from Latin: *to gnaw*), i.e. gradual material loss from surfaces of solids (Preece & Macmillan 1977). The term 'erosion' is also used in other fields, e.g. geology (Section 2.1.1). The material loss leads to alteration of roughness and geometry. Causes for erosion are (Fig. 2-12):

a) Flowing fluids (i.e. at the boundaries of gas or liquid flow);
b) Droplets (liquid particles, also called 'rain erosion');
c) Solid particles, mostly contained in a fluid (two-phase flow); and
d) Imploding gas bubbles in a fluid close to solid surfaces, i.e. cavitation.

The particles causing erosion are called 'erodent'. The wear process due to mechanical contact between solids is frequently called abrasion.

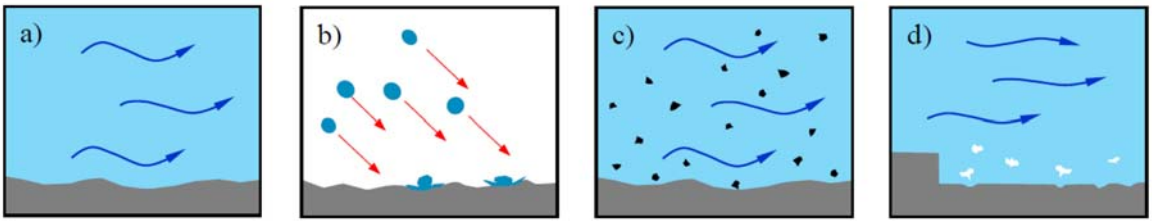

Figure 2-12 Schematics of erosion processes a) to d) (modified from Uetz 1986).

In the context of hydraulic machines, all these processes – and combinations of them – are relevant. In the present study, the focus lies on c); the fluid is water and the solid

particles consist of minerals. The phenomenon is also called sand or silt erosion (or abrasion), slurry erosion (at high solid concentrations), abrasive erosion (Duan & Karelin 2002) or hydro-abrasive erosion. The latter term is used in DIN 50320 (1979, withdrawn), in IEC 62364 (2013) and in the present study.

Because erosion is a discrete and cumulative process, it can be quantified by analysing the impacts of single particles and adding up their effects. The different effects of the impacts on ductile and brittle target materials are adressed in the following.

2.3.3.2 Erosion due to solid particle impact on ductile materials

If a solid sphere impacts on ductile material, a crater is formed (Fig. 2-13). The crater consists of a central depression and a peripheral rim of displaced and possibly loosened material. Thereby, the angle of attack α, i.e. the angle between the trajectory of an incident particle and the target surface is an important parameter, because it determines the ratio of the velocity components perpendicular (normal) and parallel to the surface. According to Wellinger (1949), two sub-mechanisms are commonly distinguished depending on α (Finnie 1960, Bitter 1963):

(i) Cutting of surface material due to sliding or impingement of particles at low α (‘cutting erosion’, ‘scratching out of material’); and

(ii) Plastic deformation of surface material and/or crack formation due to (repeated) particle impacts at higher α, leading to breaking loose of material pieces (‘deformation erosion’ or ‘impact erosion’).

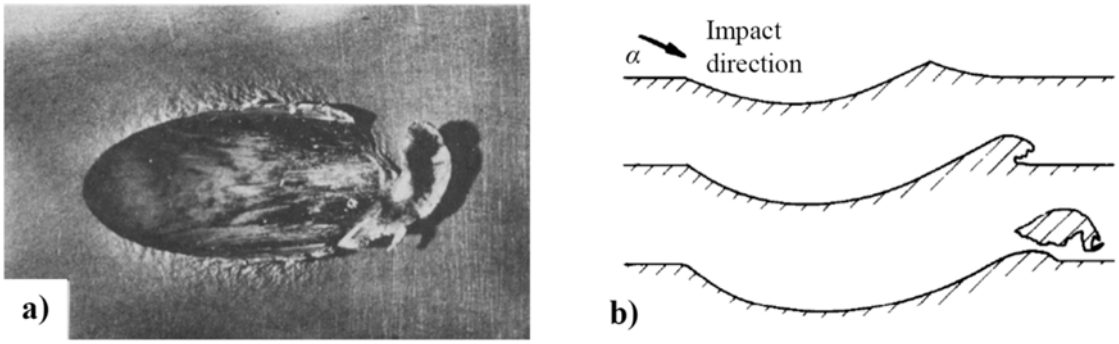

Figure 2-13 Effects of low-angle solid particle impact on ductile material: a) crater shape in aluminium at $\alpha = 19°$ (Hutchings & Winter 1974) and b) schematic of surface deformation and material removal at increasing velocities (Winter & Hutchings 1974).

For (i), Finnie (1960) considered the cutting action of an angular grain striking an ideally ductile material. He assumed that the stress between the particle and the deformed target material is constant and exceeds the yield strength, i.e. plastic deformation occurs. He distinguished two cases depending whether the particle motion ceases while cutting or

not. Combining the two cases he obtained an equation for the relative mass loss of the target material as a non-linear function of α, the velocity and the size of the particles. Finnie's erosion model is summarized e.g. in Meng & Ludema (1995).

For (ii), i.e. deformation erosion, Bitter (1963) considered an elastic sphere impacting on an elasto-plastic target surface. Assuming a constant elastic stress limit (no work hardening) and using Hertz' theory of elastic contact, he postulated that the eroded volume is proportional to

$$\frac{1}{2} m_p \left(w_p \sin \alpha - w_{p,el} \right)^2 \qquad [J] \qquad (2\text{-}23)$$

where m_p = mass of particles, w_p = relative velocity of particles before impact, $w_{p,el}$ is the w_p up to which the collisions are purely elastic. The term '$w_p \sin \alpha$' is the velocity component normal to the original target surface. If this term is smaller than $w_{p,el}$, no erosion results because there are no permanent deformations. The erosion rates due to (i) 'cutting' and (ii) 'deformation' can be added to consider both mechanisms which may occur simultaneously.

2.3.3.3 Erosion due to solid particle impact on brittle materials

If the target material is ideally brittle and behaves elastically, the stresses in the target material due to the contact of an elastic sphere can be calculated according to Hertz (1881) reported by Lawn & Wilshaw (1975): The maximum tensile stress acts radially in the target surface at the periphery of the contact circle, the maximum compression stress acts normal to the target at its surface in the centre of the contact circle, and the maximum shear stress acts in the target material below the centre of the contact circle. Hertz' theory has been extended to account for elastic anisotropy, combined normal and tangential loading, and friction. In many brittle materials, the tensile strength is an order of magnitude lower than the compression strength and thus decisive for failure.

The principal damage feature arising from the described stresses is a curved crack having a shape similar to a cone frustum (Fig. 2-14). Such a crack generally develops from a random surface flaw just outside the contact surface. The depth of the crack depends on the magnitude and duration of the impact load. If several cracks form due to particle impacts at other locations, chips of the target material may be loosened. The chip formation does not only depend on the number and the magnitude of the impacts, but also on the flaws on the target surface (Preece & Macmillan 1977).

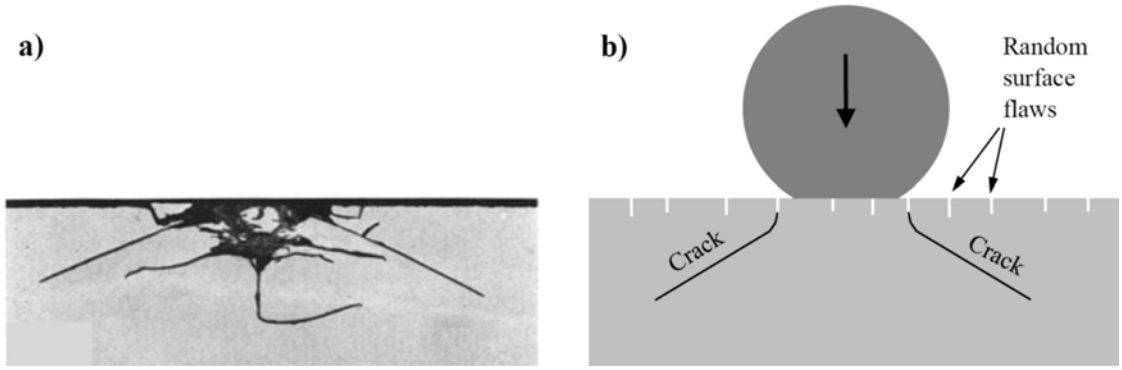

Figure 2-14 Effects of solid particle impact on brittle material: a) etched section of a soda-lime glass impacted by a tungsten carbide sphere of d = 0.5 mm (Lawn & Wilshaw 1975) and b) schematic of crack formation (Hertzian cone crack, modified from Lawn & Wilshaw 1975).

2.3.3.4 Formation of ripples

Smeltzer *et al.* (1970) analysed the patterns on the surfaces of ductile materials eroded at low α and did not find grooves parallel to the flow direction (as expected from the model of cutting erosion), but ripples running perpendicular to the flow direction. The formation of ripples was also observed by Karimi & Schmid (1992) both on ductile and brittle materials, and also in tests without erodent particles in the flow. They explained the formation of ripples as follows: When a fluid – containing optionally erodent particles – flows along a wall with some roughness resulting from machining, there are small eddies in the turbulent boundary layer (Fig. 2-15a). Then, ripples of increasing size develop and reach a steady pattern while the erosion continues perpendicularly to the original surface (Fig. 2-15b). In an extreme stage (Fig. 2-15c), cavitation may occur on the lee-side of ripples, leading to material loss and the redevelopment of a stable pattern.

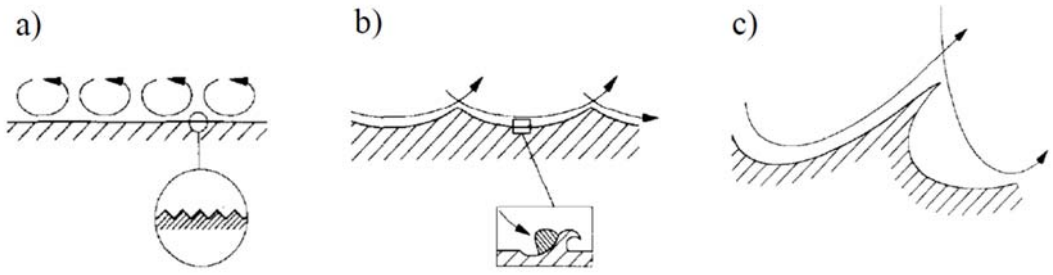

Figure 2-15 Schematic illustration of ripple formation: a) initial stage, b) intermediate stage, c) extreme stage with occurrence of cavitation on the lee-side of ripples (modified from Karimi & Schmid 1992).

2.3.3.5 Erosion due to cavitation and solid particles

Avoiding cavitation is an important objective in the design of turbine parts, which is usually met for parts with as-planned geometries in standard situations. Cavitation often occurs as a consequence of erosion, i.e. as a secondary damage. Cavitation may in turn

increase erosion (synergistic effect). Hydro-abrasive erosion and its combination with cavitation are well distinguishable in (i) the middle and (ii) the upper region of the Pelton needle tip in Figure 2-10a, respectively. Erosion features with razor-sharp edges are generally a sign of cavitation (Prof. Dr. H. Brekke, reported in Thapa 2004). At some Pelton buckets, cavitation is observed on the backsides of buckets close to the cut-outs (Grein 1990). With heavy erosion on the splitters, cavitation may also occur at the splitter flanks and at other locations inside the bucket. The complex interaction between erosion and cavitation is beyond the scope of this thesis.

2.3.4 Influence of main parameters on solid particle erosion

2.3.4.1 Overview

The influences of the main parameters governing the erosion processes have been identified and investigated for decades based on field observations and measurements, analytical considerations and laboratory tests. Literature reviews on erosion processes, relevant parameters and models have been given by Preece & Macmillan (1977) and Meng & Ludema (1995), as well as more specifically for hydraulic machines by Truscott (1971) and Padhy & Saini (2008).

The parameters influencing hydro-abrasive erosion can be grouped as follows:

- Erodent particle properties: size, shape, hardness, density;
- Parameters describing the flow and the loading: velocity, angle of attack (location within the turbine, flow field), *SSC*, operating hours;
- Parameters describing the turbine: type and geometry of the turbine, resistance of the material (base material and possibly coating)

In the following, the effects of selected main parameters are discussed.

2.3.4.2 SSC

At moderate *SSC* and with a given PSD, the erosion rate is approximately proportional to *SSC*, because the number of particles per unit volume of the carrier flow or per unit surface of the target material increases with *SSC*. At high *SSC*, the erosion rate may increase sub-proportionally to *SSC* because an increasing number of particles impact on other particles instead of the target material (cover effect).

2.3.4.3 Angle of attack

For ductile target materials, the erosion rate is usually highest between $\alpha \approx 20°$ and 40° (Fig. 2-16a). For brittle materials such as glass however, the erosion rate is highest at

$\alpha \approx 90°$ and decreases pronouncedly with smaller α (e.g. Finnie 1960, Bitter 1963). Most metals and steels are ductile at temperatures above 0 °C and atmospheric pressure. However, for martensitic steel, i.e. hardened steel with a heat treatment similar to that of usual turbine steel, the curve of the erosion rate as a function of α is closer to that of brittle materials (Fig. 2-16b). Hard-coatings consist of brittle mineral particles in a ductile metal matrix. Overall, hard-coatings show brittle behaviour.

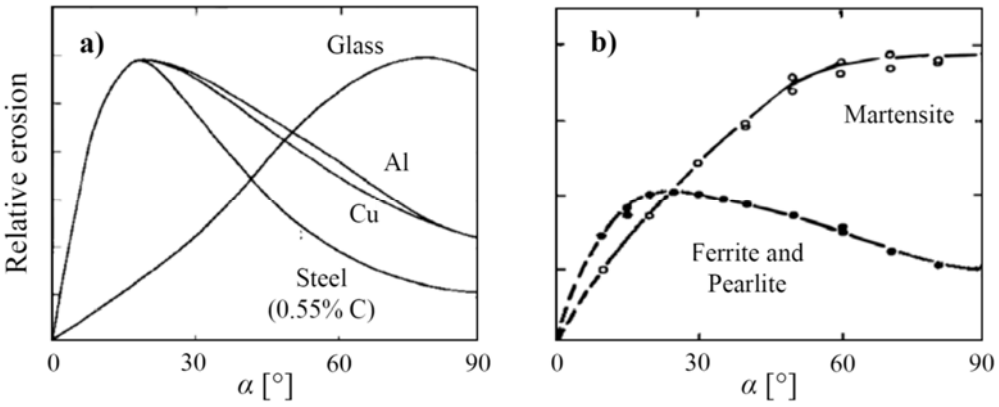

Figure 2-16 Relative erosion rates as a function of the angle of attack α; a) typical curves of three ductile materials (metals) and a brittle material (glass) according to Smelzer *et al.* (1970), and b) for two types of steel (0.55% C) differing only by heat treatment (Finnie 1960).

2.3.4.4 Relative velocity

With flow velocities above several m/s in medium- and high-head turbines, and particles with $d \leq 300$ µm, the velocity of particles before impact is assumed to correspond to the average velocity of the flow (no slip). The relative velocity w, i.e. the velocity between the flowing water and a turbine part, is known to have a very strong effect on the erosion rate. This can be understood by the following analytical considerations for impact and sliding wear, respectively:

For impact wear, Bergeron (1950) postulated that the eroded mass is proportional to the difference in kinetic energy of a particle before and after the impact. For a single particle, the erosion is thus approximately proportional to w^2 before the impact. The number of impacts per unit time increases with w. Thus, the eroded mass per unit time is approximately proportional to w^3 according to analytical considerations.

For erosion due to particles sliding along a curved wall with constant radius of curvature r, Bergeron (1950) – and Bovet (1958) – also derived a relation between the erosion rate and w. Particles travel on circular paths due to the centripetal acceleration:

$$a_c = \frac{w^2}{r} \qquad [\mathrm{m/s^2}] \qquad (2\text{-}24)$$

In Pelton buckets, a_c is typically several 10 000 m/s^2 (Neopane *et al.* 2011). Assuming hydrostatic pressure, Bergeron (1950) estimated the force between a submerged particle and the wall as

$$F_c = \frac{V_p \left(\rho_s - \rho_w\right) w^2}{r} \qquad [\mathrm{N}] \qquad (2\text{-}25)$$

where V_p = particle volume. The erosion rate was assumed to be proportional to the friction power P_f of each particle. With the friction coefficient μ, the friction force is μF_c. The friction power is the friction force times w:

$$P_f = \frac{\mu\ V_p \left(\rho_s - \rho_w\right) w^3}{r} \qquad [\mathrm{W}] \qquad (2\text{-}26)$$

Also with this approach, the erosion rate is proportional to w^3. This is in line with many laboratory investigations, in which a velocity exponent $x \approx 3$ was found (Truscott 1971). Depending on specific configurations x ranges between 2 and 4 for metals, and even between 2 and 6.5 for glasses, ceramics, polymers and composites (Preece & Macmillan 1977). For flat specimens subjected to a sediment-laden jet, x = 2.5 to 2.75 were experimentally determined in a jet-type test rig (Ilgaz 1952, Winkler *et al.* 2011a). For uncoated Pelton splitter crest specimes, x = 2.8 to 3 was found with a jet diameter d_o = 10 mm (Winkler *et al.* 2011a).

2.3.4.5 Particle size

The particle size d has multiple effects on the erosion rate. It is proposed to distinguish direct and indirect effects. The first are related to material science, the latter to hydrodynamics.

Direct effects: If d is high, there are fewer particles at a given *SSC*. With the higher energy of large particles, a lower number of stronger impacts results. Due to non-linear effects mainly in the behaviour of the target material, a small number of strong impacts may cause more erosion than many low-energy impacts. For example, a certain threshold energy is required for the erosion of ductile targets (Eq. 2-23). For small particles impacting on brittle materials, an erosion behavior similar to that of ductile targets has been observed. Preece & Macmillan (1977) explained this by the lower probability of a critical surface flaw being present within the stressed area.

Indirect effects: In addition to the direct effects of d, the erosion rate is affected by the particle-size dependent behaviour of the particles in the flow. One such effect is that the local *SSC* in the vicinity of a curved turbine part deviates from the cross-section averaged

SSC depending on *d*. The local *SSC* is decisive for the number of impacts whereas the average *SSC* serves as the reference. An example of an indirect effect of *d* on the erosion rate is at leading edges of turbine blades: Numerical simulations reported by Winkler *et al.* (2011a) showed that particles approaching the splitter of a Pelton bucket impinge on the splitter when they had a diameter of 80 µm (Fig. 2-17a), whereas smaller particles (20 µm) rather follow the streamlines around the splitter with a smaller probability of hitting it (Fig. 2-17b).

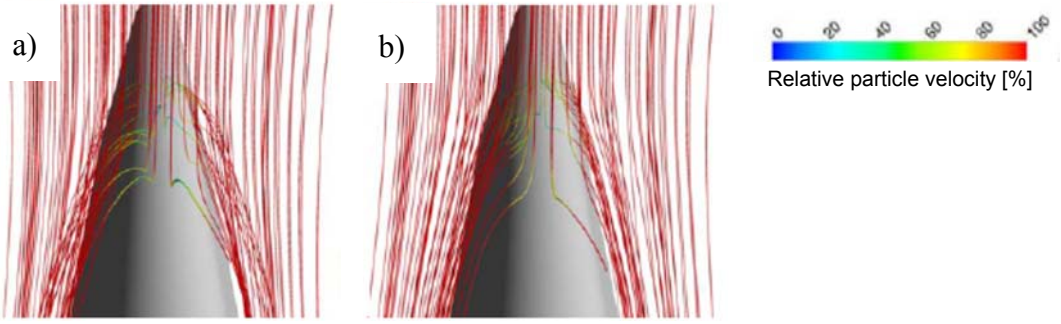

Figure 2-17 3D-view on particle trajectories at the splitter of a Pelton bucket according to numerical simulations with particle diameters of a) 80 µm and b) 20 µm (Winkler *et al.* 2011a).

The relation between erosion rate and particle size depends thus on many factors such as turbine type, location inside the turbine, curvature, size of the turbine, and material properties. Various relations between the relative erosion rate *RER* and the particle size have been proposed in the literature:

a) Nozaki (1990) postulated that *RER* in Francis and Pelton turbines increases linearly with particle size and considered $d = 50$ µm as the reference (Fig. 2-18a);

b) Asarin *et al.* (2001) indicated the *RER* in some particle size classes shown in Figure 2-18b, where the dashed line represents the midpoints of the steps;

c) According to erosion tests in the laboratory with particle-laden turbulent flow in the gap between a rotating shaft and its housing (Grein & Krause 1994), the *RER* was found to depend non-linearly on *d* as in Figure 2-18c (Sulzer Hydro 1996 partly published in DWA 2006);

d) According to more recent laboratory tests (Winkler *et al.* 2011a), particles larger than ~100 µm cause considerably more erosion on Pelton splitters than smaller particles (Fig. 2-18d);

e) In a field investigation at Chilime HPP in Nepal, Bajracharya *et al.* (2008) found the relation of Figure 2-18e for the erosion on Pelton splitters, which refers to a quartz content of 60%;

f) Padhy & Saini (2009) found that the *RER* slightly increases with *d* (Fig. 2-18f), based on laboratory investigations on a model Pelton turbine made of brass exposed to natural sediment with a quartz content of e.g. 60%;

g) Mei (1996) considered particles with $d > 50$ µm as relevant for turbine erosion, which corresponds to a step function for *RER*. He further refers to other Chinese researchers who classified $d > 20$ µm as relevant for erosion.

The relations in Figure 2-18 indicate that *RER* generally increases with particle size and no formulation exists which would be correct for all locations in all types of hydraulic turbines in various configurations.

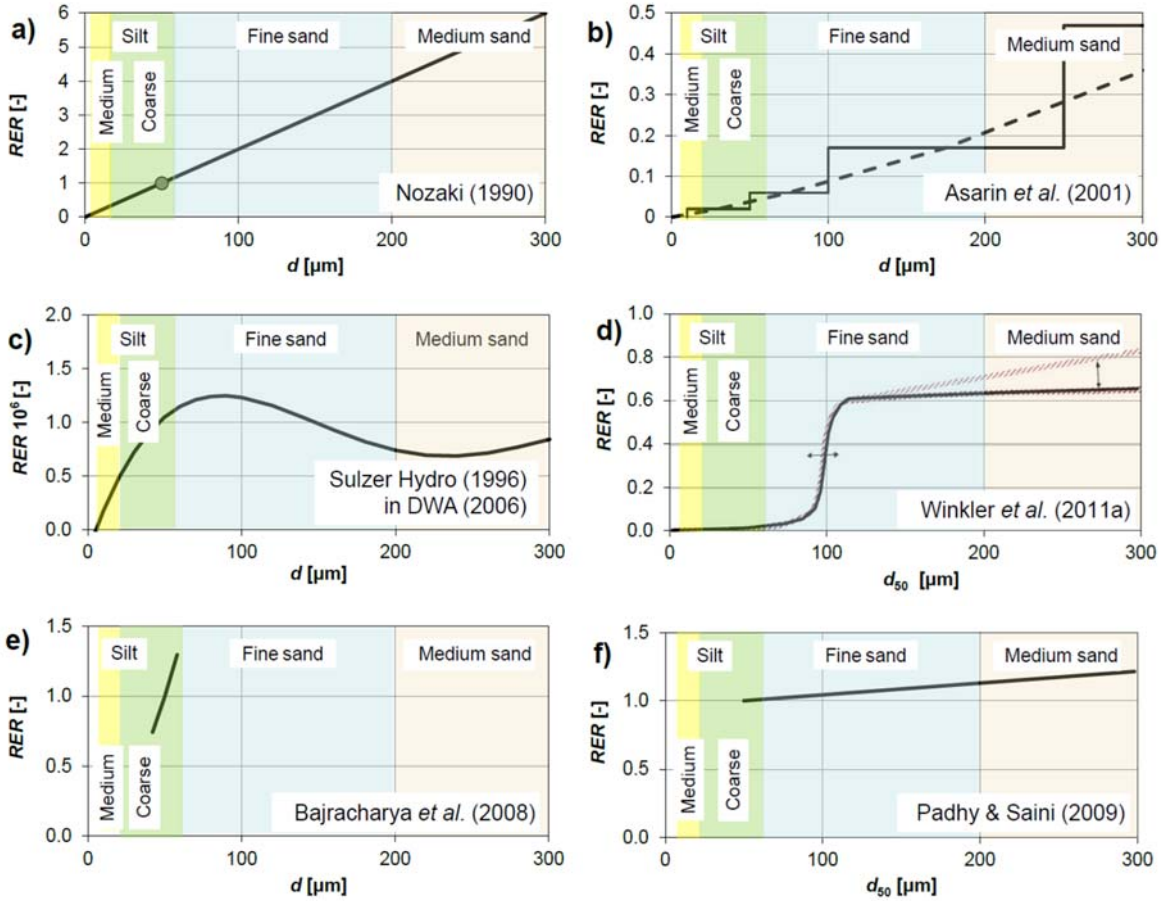

Figure 2-18 Relative erosion rate (*RER*) as a function of the particle diameter (d or d_{50}) according to six literature sources (a–f).

2.3.4.6 Particle shape (angularity)

Angular particles cause more erosion than rounded particles because of higher local stresses on target materials (Bitter 1963). Winter & Hutchings (1974) observed that angular particles either cut into ductile surfaces (micro machining) or displace material by ploughing depending on the particle orientation, whereas rounded particles do ploughing only.

Levy & Chik (1983) experimentally determined that angular steel particles impinging on a carbon steel plate caused four times more erosion than spherical ones. They explained this based on their observation that the angular erodent particles caused deeper and sharper craters and produced more extruded platelets.

Desale *et al.* (2006) showed that the angularity of particles has more effect on the erosion rate if α is small (Fig. 2-19). This can be explained by the fact that the angularity is more relevant for 'cutting erosion' than for 'deformation erosion', and cutting erosion occurs at small α. To quantify angularity, they used a modified shape factor based on Cox' shape factor (Section 2.1.2.2).

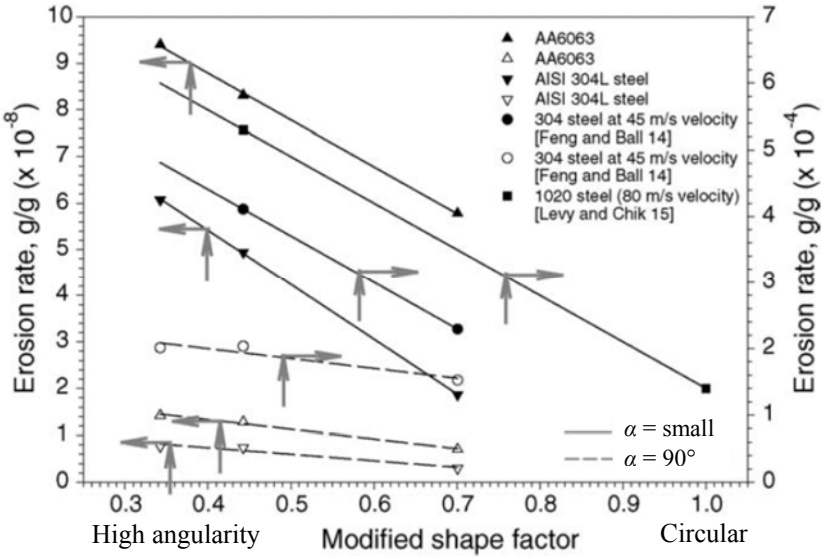

Figure 2-19 Effect of erodent particle shape on the erosion rate of ductile materials at different impact angles α; the horizontal arrows indicate the corresponding y-axis on the left and right sides, respectively (Desale *et al.* 2006).

In erosion tests with recirculation of particles, the erosion rate decreased due to a reduction of the particles' angularity: On a steel plate impinged by a jet of water with quartz fine sand, a reduction of the erosion rate by 20% was measured without having reached a steady state (Ilgaz 1952). In experiments with a model Pelton turbine made of brass (Mohs hardness 3 to 4) and natural sediment particles (90% quartz), Padhy *et al.* (2012) measured a reduction of the erosion rate by a factor of 2.5, possibly also including other factors. Nozaki (1990) proposed values of 0.75, 1.0 and 1.25 for the relative erosion potential of rounded, angular and sharp-edged particles, respectively.

2.3.4.7 Particle hardness

Levy & Chik (1983) observed that apatite particles with a relatively low hardness of 5 on the Mohs scale broke upon impact on a carbon steel plate, while alumina particles with a Mohs hardness of 9 did not break and produced almost five times more erosion.

The erosion rate as a function of the erodent hardness is typically similar to a step function (Uetz 1986): if the erodent particles are less hard than the target surface (e.g. mica vs. steel), the erosion is low or even negligible. In the opposite case, the erosion rate is constantly high, i.e. does not increase with harder erodent. Between the low and the high level of erosion rate, there is a transition in the range of both materials having similar hardness. An indenter is generally able to cause scratches if its hardness is at least 20% higher than that of the target.

2.3.4.8 Target material properties

The erosion rate depends further on the target material's erosion resistance. Various relations between the erosion resistance and combinations of the following parameters were investigated: Young's or bulk modulus, Poisson's ratio, density, hardness (Mohs, Vickers or Brinell), toughness, yield strength, linear thermal expansion coefficient, melting point, specific heat, micro and crystal structure or hardening behaviour (Preece & Macmillan 1977). However, no general formulation valid for a wide range of materials is well established. So far, empirical constants are used to quantify the material-dependent effects on the erosion rate for certain combinations of target and erodent materials.

On a jet-type erosion test rig, Winkler *et al.* (2011a) measured eroded masses on uncoated and coated Pelton splitter specimens as a function of time. With otherwise constant parameters, the mass-based erosion rate of mainly coating material was ~1/10 compared to only base material. Assuming a homogeneous erosion in the coating on the splitter crest and considering the higher density of the coating material, the geometrical erosion rate in the coating was hence ~1/15 compared to base material. When the coating on the splitter crest was eroded, the mass-based erosion rate increased, but was still ~1/3 compared to the uncoated splitters. This means that the remaining coating on the splitter flanks still contributed to reduce the erosion.

2.3.4.9 Turbine type, part and geometry

The erosion rate depends further on the type of turbine, the part and the location within the turbine, the radii of curved parts (e.g. in buckets, thus the turbine size) or the radii of leading edges (e.g. on splitter crests and in cut-outs of Pelton buckets). These variations

of the erosion rates are mainly related to the angle of attack and potential deviations of close-to-wall *SSC* from average *SSC* (Section 2.3.4.5).

2.3.5 Modelling hydro-abrasive erosion

2.3.5.1 General considerations

Erosion can be quantified as

- Erosion depth d_e per unit time Δt (geometric erosion rate or erosion velocity, e.g. in µm/h) assuming homogeneous erosion in a certain zone;
- Volume loss per unit time (volumetric erosion rate, e.g. in mm^3/h) referring to a certain part of a turbine (e.g. a runner or a nozzle tip);
- Mass loss Δm per unit time Δt (gravimetric erosion rate, e.g. in g/s) also referring to a certain part of a turbine;
- The dimensionless ratio M of eroded mass Δm to erodent mass (here *SSL*).

The quantification and modelling of erosion is complex due to the following reasons (Preece & Macmillan 1977):

- Simultaneous occurrence of many processes and types of impact events;
- Great number of relevant and interdependent parameters;
- Dynamic and localized nature of the loading;
- Impact parameters (α, number of impacts) resulting from the flow are not fully known;
- Feedback of eroded surface on the erosion (self-intensifying process).

For engineering purposes, there is an interest in easily applicable equations. Such semi-empirical equations are limited to specific applications and comprise typically some calibration parameters obtained from laboratory investigations and/or measurements at prototypes.

2.3.5.2 Laboratory investigations

Many test procedures and apparatuses for the investigation of the erosion resistance of materials in the laboratory were developed; selected ones are described in the appendix of IEC 62364 (2013). Most tests yield a relative erosion resistance compared to a reference material. The erosion resistances obtained from various test procedures may differ considerably among each other and from those in real-scale turbines. The type of erosion depends also on the locations within Francis or Pelton turbines. Hence specific test setups are required to realistically investigate a certain type of turbine erosion in the laboratory.

Numerous erosion tests have been conducted over decades (Table 2-1). Such laboratory tests gave valuable information on the effects of single parameters on the erosion rate.

Table 2-1: Selected experimental laboratory investigations on hydro-abrasive erosion (Felix *et al.* 2016b)

Investigators and reference	Type of test rig, velocity range	Remarks
Ilgaz (1952)	Jet-type, 26 to 44 m/s	Tests on metal plates with varying angle; one of the first jet-type test rigs with sand and water found in the literature
Grein & Krause (1994)	Rotating shaft, up to 80 m/s	Highly turbulent flow in gap between rotating shaft and specimens fixed on its housing; laboratory results were compared to field data (erosion depths on uncoated Pelton buckets)
Thapa (2004)	Jet-type, up to 80 m/s	Tests on plates with varying angle and on specimens having a splitter and a certain curvature, also with soft- and hard-coatings
Winkler *et al.* (2011a)	Jet-type, 40 to 85 m/s	Tests on plates and real-scale splitter specimens (with reduced jet diameter), also with hard-coatings
Grewal *et al.* (2013)	Jet-type, 4 and 16 m/s	Tests on plates with varying angle; references given to ten other laboratory studies of erosion on 13Cr4Ni-steel

Based on the laboratory investigations by Grein & Krause (1994), a formula for the erosion rate on martensitic stainless steel was developed at Sulzer Hydro in 1996 and has been partly published in DWA (2006):

$$\frac{\Delta d_e}{\Delta t} = 1.6 \cdot 10^{-10} \;\; w^{3.0} \; SSC \;\; q \;\; f\left(d_{50}\right) \;\; \frac{z_0}{z_2} \qquad [\mu m/h] \qquad (2\text{-}27)$$

where q = mass fraction of quartz [-], z_0 = number of jets [-], z_2 = number of buckets per runner [-], with w in [m/s] and SSC in [g/l]. The quotient z_0 / z_2 is applicable for Pelton runners and resulted from analytical considerations. The dimensionless factor $f(d_{50})$ has a maximum of $1.25 \cdot 10^6$ at about 80 µm (Fig. 2-18c). A velocity exponent of 3.4 was proposed alternatively by Krause & Grein (1996).

2.3.5.3 Field investigations

Nozaki (1990) compiled field data on turbine erosion of 18 HPPs in South America. He proposed a modified or equivalent *SSC* to consider the following effects on the erosion rate: particle size, shape (angularity), hardness, and the resistance of the turbine material, respectively.

$$SSC_{\mathrm{eq}} = SSC \;\; k_{\mathrm{size}} \; k_{\mathrm{shape}} \; k_{\mathrm{hardness}} \; K_{\mathrm{m}} \qquad [g/l] \qquad (2\text{-}28)$$

He established outstanding diagrams indicating the time between overhauls *TBO* of uncoated Francis and Pelton turbine parts as a function of the time-averaged SSC_{eq} and the net head h_{n}. These diagrams are e.g. published in Ortmanns (2006). However, the applica-

bility of the diagrams is limited because (i) it is not clear which extent of erosion or efficiency reduction had been accepted until turbine overhauls, and (ii) coated turbine parts were not treated at that time.

Mei (1996) investigated turbine erosion in HPPs in China and classified the extent of erosion as a function of *SSC* (considering particles with $d > 50$ µm) and the head *H*. He considered a value of the product $SSC \cdot H > 7$ [g/l · m] as 'severe erosion'. $SSC \cdot H$ is proportional to the potential energy of the particles. Because *w* varies with $h_n^{0.5}$ (Section 2.3.2.2), the approach by Mei (1996) corresponds to modelling erosion proportional to w^2, which is a rather low velocity exponent.

Mann (2000) investigated turbine erosion in 27 HPPs in India and classified them depending on the *TBO*:

a) Very severe erosion: $TBO \leq 2$ years (monsoon seasons);
b) Severe erosion: $TBO \leq 4$ years;
c) Considerable erosion: $TBO \leq 8$ years.

Boes (2009) reported on *SSC*, PSD and splitter width measurements at HPP Dorferbach in Austria. He applied Equation (2-27) to the field data, used a correlation between *SSC* and d_{50}, and calibrated the model by adjusting the constant. Using the measured *SSC* time series, he found a reasonable agreement between predicted and observed splitter widths as a function of time.

In earlier field studies, e.g. by Strübin & Bussy (1988), Thomann (1988), Nozaki (1990), Krause & Grein (1996) and Bajracharaja *et al.* (2008), the sediment load and the extent of Pelton turbine erosion were either not quantified in detail or not fully published, and hard-coated runners have yet been rarely treated.

2.3.6 IEC erosion model

2.3.6.1 Erosion rate

A working group of the International Electrotechnical Commission (IEC) formulated a concept for the modeling of hydro-abrasive erosion (without cavitation) in hydraulic turbines for applied engineering purposes (Winkler *et al.* 2010). This concept and general design recommendations have been published in IEC 62364 (2013), i.e. the first edition of this guideline. Based on a literature review of various erosion models, the following equation for the erosion rate has been proposed:

$$\frac{\Delta d_e}{\Delta t} = \frac{K_f}{RS^p}\ K_m\ w^x\ SSC\ \ k_{size}\ k_{shape}\ k_{hardness} \qquad \text{[mm/h]} \qquad (2\text{-}29)$$

where
- Δt Exposure period [h];
- Δd_e Depth of erosion [mm] during Δt;
- K_f Coefficient reflecting the flow pattern, i.e. angle of attack and turbulence intensity (units as resulting from calibration), intended to be constant for each turbine component, see note below;
- RS Reference size (length) of a turbine [m]; for Francis turbines RS = runner diameter D, for Pelton turbines RS = inner bucket width B;
- p Exponent [-], intended to be a constant for each turbine component, for consideration of curvature-dependent effects, see note below;
- K_m Coefficient for the material at the surface of a turbine part [-], $K_m = 1$ for martensitic stainless steel with 13% Cr and 4% Ni; $K_m < 1$ for coating material;
- w Characteristic relative velocity [m/s] between the flow (or the particles) and the turbine part; for Pelton injectors see Eq. (2-21), for buckets $w = 0.5\sqrt{2\,g\,h_n}$
- x Exponent [-], IEC suggests 3.4, literature values see Section 2.3.4.4;
- SSC Suspended sediment mass concentration [g/l] = [kg/m^3], for Pelton turbines $SSC = 0$ if no flow;
- k_{size} Coefficient for particle size [-], IEC suggests $k_{size} = d_{50}/1000$ µm (with d_{50} in µm);
- k_{shape} Coefficient for particle shape [-], IEC suggests $k_{shape} = 1$ for rounded or 2 for angular;
- $k_{hardness}$ Coefficient for particle hardness with respect to the hardness of the surface material [-], IEC suggest to take the mass fraction of particles harder than the surface material.

Note: Numerical values for K_f and p are given in IEC for five locations (parts) within uncoated Francis turbines. These values resulted from the evaluation of field data of up to seven HPPs mainly in China. The standard deviation σ of the relative prediction error was estimated as 26 to 42% depending on the turbine part. For Pelton turbines, no K_f- and p-values are given in IEC due to the scarcity of field data.

2.3.6.2 Concept of the 'Particle Load'

To obtain the erosion depth Δd_e over a time interval Δt, Equation (2-29) is multiplied by Δt. The erosion depths in the time intervals of Δt from the start time t_0 to the time t are summed up to obtain the cumulated erosion depth $d_e(t)$ as follows:

$$d_e(t) = \frac{K_f}{RS^p}\ K_m\ w^x \underbrace{\sum_{i=1}^{(t-t_0)/\Delta t} SSC_i\ \ k_{size,i}\ k_{shape,i}\ k_{hardness,i}\ \Delta t}_{= PL(t)} \qquad \text{[mm]} \qquad (2\text{-}30)$$

The time step number is denoted as i. The parameters K_f, RS, p, K_m, w and x are constant or are assumed to be constant. In Equation 2-30, the integral of the product of the particle-related factors over the exposure period is termed 'particle load' (PL). $PL(t)$ reflects the

cumulated erosion potential of the particles (at unit velocity) passing through a turbine as a function of t since t_0. PL has units of [h · g/l] = [h · kg/m^3]; the unit 'hour' was taken with reference to the widely used 'operation hours' although it is not a SI-unit. In contrast to SSL, the PL is not a function of the discharge and does hence not depend on the turbine design flow.

According to Equations (2-29) and (2-30), the erosion depth is proportional to SSC and the exposure time. Thus, the same erosion depth is expected when a turbine runs e.g. for 1000 h at 0.5 g/l or for 100 h at 5 g/l (with the same particle properties), and the PL is the same in both cases.

2.3.6.3 Adaptation of the PL for Pelton runners

In contrast to reaction turbines or nozzles of Pelton turbines, the erosion on a Pelton bucket takes place during only a part of the operation time (intermittent process). The erosion on a bucket decreases proportionally to the number of buckets z_2 because of the shorter exposure time per bucket. On the contrary, the erosion increases approximately proportional to the number of jets z_0 because more buckets are simultaneously in contact with the sediment-laden water. The effects of z_0 and z_2 on the erosion rate or depth were already stated in Equation (2-27) and are included in the so-called 'reference model' for Pelton turbines in IEC 62364 (2013). To account for these effects, an adapted PL for Pelton buckets is introduced here:

$$PL_\mathrm{b} = \frac{z_0}{z_2}\, PL \qquad [\mathrm{h \cdot g/l}] = [\mathrm{h \cdot kg/m^3}] \qquad (2\text{-}31)$$

2.3.6.4 Relative erosion model

As mentioned at the end of Section 2.3.6.1, IEC 62364 (2013) does not give K_f- and p-values for Pelton turbines. Hence, erosion depths or TBO cannot be directly estimated so far. Indirect estimates are possible if the erosion depth or TBO from a comparable reference turbine with the same overhaul criteria is known together with additional relevant parameters of both turbines and the respective sediment properties. For such indirect estimates, the ratios of the factors in Equations (2-30) and (2-31) for the target and the reference turbine are considered (proportional conversion).

2.3.7 Further approaches for erosion modelling

2.3.7.1 Investigation of particle trajectories in Pelton bucket cross-sections

Thapa & Brekke (2004) discussed the acceleration of particles during the passage in a Pelton bucket from the splitter to its outlet. According to Equation (2-24), the acceleration towards the bucket surface is

(i) proportional to the square of w, i.e. proportional to the net head (Eq. 2-21), and
(ii) inversely proportional to the radius of curvature r.

Assuming that the erosion rate in a bucket increases with the acceleration of particles towards the bucket surface, not only runners of Pelton turbines with a high head, but also with a small bucket width are more prone to erosion. Moreover, Thapa & Brekke (2004) stated that larger particles reach the bucket surface within a shorter distance than fine ones starting at the same distance off the jet axis (Fig. 2-20). Higher *SSC* close to the bucket surfaces and hence more intense erosion are expected towards the outlets.

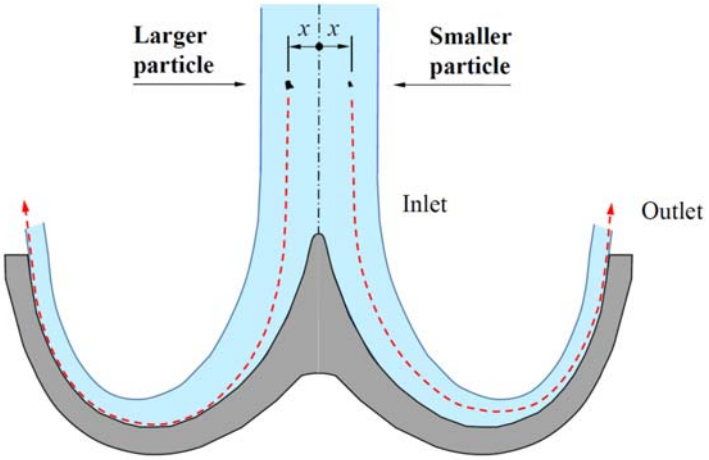

Figure 2-20 Cross section of Pelton bucket with conceived trajectories of particles of different sizes (modified from Thapa and Brekke 2004).

Rai *et al.* (2016) analytically studied the following forces acting on a submerged sediment particle during the passage of a Pelton bucket in the rotating system (relative reference frame, rotating around the turbine axis and moving with the flow through the bucket):

- Coriolis force;
- Centrifugal force due to the rotation around the turbine axis;
- Centrifugal force due to the curvature of the bucket;
- Drag force.

Their investigation shows that the centrifugal force due to the curvature, mentioned by Thapa & Brekke (2004), is the major contribution. The first two forces act in radial direction of the runner and thus do not contribute to the acceleration of the particles towards the bucket surface in a central cut of the bucket. Rai *et al.* (2016) defined the 'separation angle' as the angle between a streamline and the particle trajectory and gave an analytical expression for the same based on the ratio of w and the particle's velocity normal to the bucket surface.

Zhang (2016) also treated the equation of motion of a suspended particle in a cross-section of a Pelton bucket. He considered (i) a stationary bucket with a realistic non-circular cross-section geometry, (ii) the decrease of the water sheet thickness due to its lateral spreading, and (iii) the pressure gradient due to the curvature (non-hydrostatic). According to his calculations for one configuration (Fig. 2-21, w = 61 m/s), less than half of the particles with $d \leq 60$ µm reach the bucket surface. At a higher relative velocity of w = 81 m/s for example, a similar trajectory was found, because the force ratios remained similar. In smaller buckets with higher curvature, the particle velocity normal to the bucket surface is higher as mentioned above, but the time of passage through the bucket is shorter. Therefore, the probability of particles hitting the bucket does not linearly increase with the particles' normal velocity.

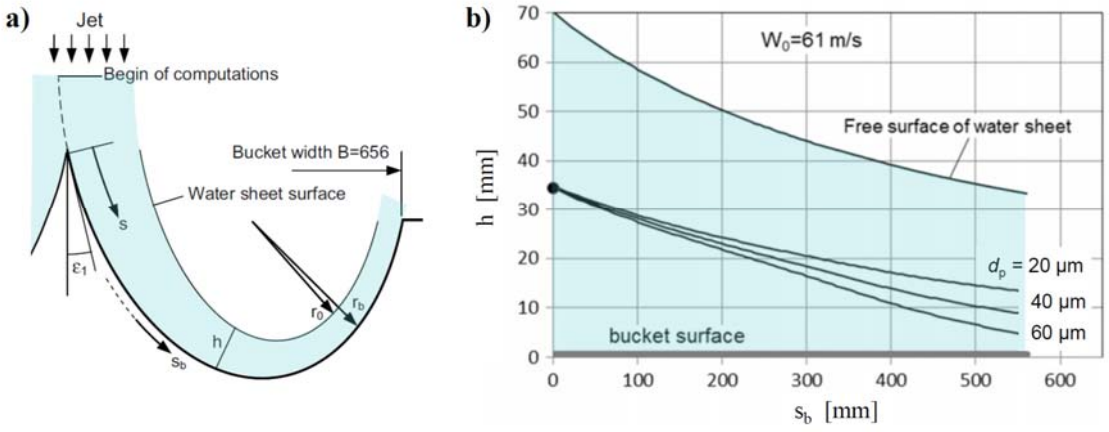

Figure 2-21 a) Cross section of a Pelton half-bucket with definition of coordinates s_b and h; b) exemplary result of modelled trajectories of particles with three different diameters entering the bucket at a relative water depth of 0.5h (Zhang 2016).

It should be noted that in the three approaches described in this Section, the effect of the flow turbulence on the particle motion, i.e. local flow velocities normal to the bucket surface due to the presence of eddies, was neglected. Due to the high shearing of the flow close to the bucket surface, i.e. in the region where the particles interact with the bucket, flow turbulence is considered to have an important effect on the probability of particles

hitting the bucket surface and hence on erosion. However, there is the phenomenon of so-called flow 'relaminarization', leading to reduced turbulence in accelerated flows due to high pressure gradients. The term relaminarization is used in the wider sense of the word, referring to 'near-zero values of intermittency', although the turbulence intensities are still high (Escudier *et al.* 1998).

2.3.7.2 Numerical simulations

More recently, mechanistic or semi-empirical erosion equations have been implemented in numerical simulation codes. The numerical simulation involves the determination of flow velocities (flow field) and *SSC* close to turbine parts. Depending on the implemented erosion model, the particle impingement rate and angle of attack, as well as the material removal are determined. This last step depends on the properties and the behaviour of materials; the latter is reflected by constitutive models (Leguizamón *et al.* 2016).

For Francis turbines, spatially distributed relative erosion rates on runner blades have been simulated (Neopane 2010, Guangjie *et al.* 2013), using the erosion model by Finnie (1960). Moreover, numerical simulations of relative erosion rates were used to optimize the shapes of Francis runner blades (Khanal *et al.* 2016).

For Pelton turbines, the simulation of the flow field is particularly challenging because of the 3D-free-surface flow (Fig. 2-22a). This has been modelled using a two-phase homogeneous model for example (Perrig *et al.* 2006). Besides grid-based methods (e.g. Volume Of Fluid VOF), also mesh-free methods such as Smoothed Particle Hydrodynamics (SPH) or Finite Particle Volume Method (FPVM) were further developed. The latter has been used to simulate the flow in Pelton buckets (Fig. 2-22a), as well as the flow, the particle movements and the erosion of a stationary plate due to an inclined particle-laden jet (Fig. 2-22b).

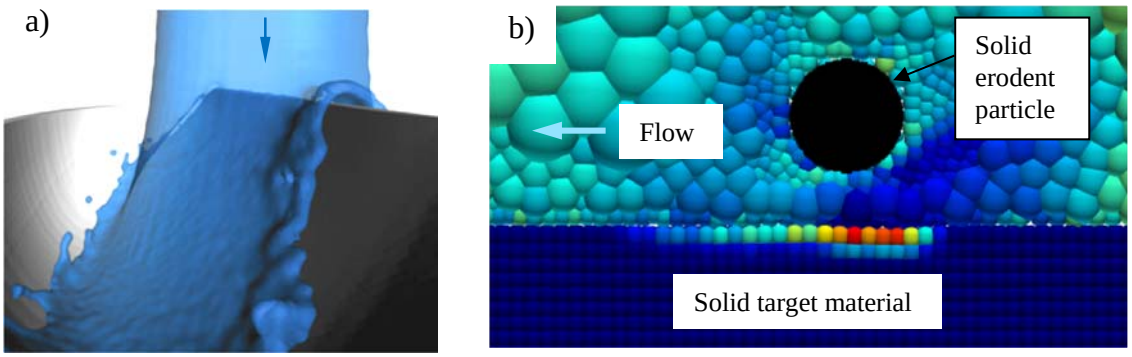

Figure 2-22 Examples of numerical simulations a) 3D-view on the flow at the splitter of a Pelton bucket (Vessaz *et al.* 2015), b) vertical section of solid-particle laden flow causing erosion on bottom plate simulated by FPVM, the colors represent the velocities of the fluid and the plastic strain of the target material, respectively (Jahanbakhsh 2014).

So far, not all processes can be simulated numerically, e.g. erosion on coated parts with local loss of coating and subsequent erosion of base material including secondary damages due to cavitation. Moreover, numerical models need calibration based on data obtained from measurements at prototypes if erosion depths are to be predicted quantitatively.

2.4 Techniques for monitoring of turbine erosion

2.4.1 Discontinuous erosion monitoring

2.4.1.1 Inspections and photographs

The basic technique for erosion monitoring of turbine parts is repeated visual inspections during standstill, at least during the low-flow season when not all turbines are permanently in operation. Surface structures, zones with completely eroded coating, and local erosion features are documented by photographs, preferably with a ruler as size reference and a clear labelling of the bucket number. Whereas the buckets of Pelton runners and the needle tips are well accessible in the turbine housing, not all parts of the nozzle can be inspected without dewatering and disassembling.

2.4.1.2 Geometrical measurements (surveys)

Geometrical changes due to erosion in Pelton buckets are typically determined using a set of metallic 2D templates. With appropriate illumination, the difference between the actual and the planned bucket cross-section is visualized.

The splitter width is considered to be an important indicator of the erosion status of a runner (Maldet 2008, Boes 2009). The actual width of eroded splitters of Pelton buckets and the radial position of the splitter tip (nose) can be measured with a ruler or a custom-made simple template. Measuring the actual cut-out depth requires an advanced template.

The actual 3D-geometry of Pelton buckets or needle tips can be surveyed using optical digitizing systems, laser scanners, or coordinate measuring arms. Handheld camera-based systems (structure-from-motion techniques) are judged to be not accurate enough.

2.4.1.3 Weighing

The total mass reduction of a runner can be determined by weighing. Padhy & Saini (2009) and others used this technique to quantify the erosion on model Pelton runners. Mass reductions of 100 and 1500 kg were reported from uncoated 10 MW-Pelton and

75 MW-Francis runners, respectively (Maldet 2008, Singh *et al.* 2013). The weighing method is suitable for laboratory investigations and when runners need to be replaced. Otherwise, the effort of dismounting and re-mounting a runner appears too high just for the determination of the eroded mass.

2.4.1.4 Coating thickness measurements

Coating thickness (*CT*) meters based on magnetic induction allow measuring the thickness of a non-magnetisable coating on a magnetisable base material (ISO 2178 2016). This constellation is present with soft- and hard-coatings on the mostly used turbine steel. Because *CT* meter readings depend on the magnetic permeability of the base material, they need to be calibrated on the respective material. With *CT* meters, measurements on plane and mildly curved surfaces are possible, but not on edges. Typically, local *CT*s are measured with a handheld probe at visually selected locations. Guangjie *et al.* (2013) measured *CT*s on a Kaplan turbine blade on marked grid points with a spacing of several centimetres.

2.4.2 Continuous erosion monitoring

Continuous automatic monitoring of the erosion on turbine runners would be an advantage, but is not available so far due to technical challenges. However, stationary sensors for continuous monitoring of erosion depths are used in the process industry, e.g. in pipelines. For example, the actual length of a small rod protruding into a particle-laden flow is measured via electrical resistance. Another possibility is to monitor the actual thickness of a pipe's wall by acoustic signal reflection.

2.5 Efficiency reductions due to erosion on Pelton turbines

2.5.1 Efficiency and efficiency differences

Efficiency η is the ratio between power output and input, the latter being the hydraulic power P_{hydr}:

$$\eta_{\mathrm{MG}} = \frac{P_{\mathrm{el}}}{P_{\mathrm{hydr}}} = \frac{P_{\mathrm{el}}}{\rho\, g\, h_{\mathrm{n}}\, Q} \qquad [-] \qquad (2\text{-}32)$$

where ρ is the density of the working fluid (water, temporarily containing sediment particles). The power output is measured in terms of the electrical active power P_{el} at the generator. Hence, η based on practically measurable parameters includes the energy

losses of the generator, and refers to a machine group (MG) consisting of a turbine and a generator. An MG is also called a 'Unit'.

The energy losses of the generator are small compared to those of the turbine. Moreover, the losses of the generator are quite constant, provided that it is not operated at very low loads or at variable high percentages of virtual (blind) power. Thus, changes in η_{MG} can be taken as a good indicator for changes in turbine efficiency.

Turbine efficiency varies with the discharge and the net head (so-called hill chart). For a given head, the efficiency varies as a function of the discharge and thus power (i.e. a section in the hill chart).

Efficiency differences $\Delta\eta$ over time are evaluated from efficiencies measured repeatedly in the same operating conditions (on the whole hill chart or at selected operation points).

2.5.2 Extent of efficiency reductions

Figure 2-23 shows examples of efficiency curves of Pelton turbines as a function of the normalized power or discharge. The powers and discharges were normalized with their design values, also called rated power P_{rated} (nominal capacity) or rated discharge Q_{rated}. The efficiency curves were measured at various times before and after operation in temporarily sediment-laden water. The initial shape of the η-curve of a Pelton turbine depends on its design, in particular on the number of jets. As the erosion progresses, the shape of the η-curves changes (Fig. 2-23), and the efficiency decrease is more pronounced (Bajracharya *et al.* 2008). With respect to Fig. 2-23d, Cateni *et al.* (2008) gave the following descriptions of the runner status in three progressive stages of erosion:

(i) Erosion inside buckets, splitter tips slightly lowered, cut-outs slightly rounded;
(ii) Erosion on root zones which modifies the exit angle;
(iii) Heavy erosion in buckets with lowering of cut-outs and consequent water losses.

Further examples of measured $\Delta\eta$ due to hydro-abrasive erosion published in literature are given in Table 2-2. Considerable $\Delta\eta$ of several percent per year (or sediment season) were common with uncoated runners at sites with high erosion potential. Also in recent examples with uncoated and even with coated runners, efficiency reductions of several percent per year are reported in severe cases.

Only little data on measured efficiency changes are available and published. From the literature, no general relations can be obtained, because the sediment load and the extent of the erosion in corresponding time intervals are often not known. Kalberer (1988) estimated the average efficiency reduction for Pelton turbines in Swiss HPPs as 0.5% per

year. For an updated, more precise and worldwide estimate, more data from efficiency reductions based on measurements are required.

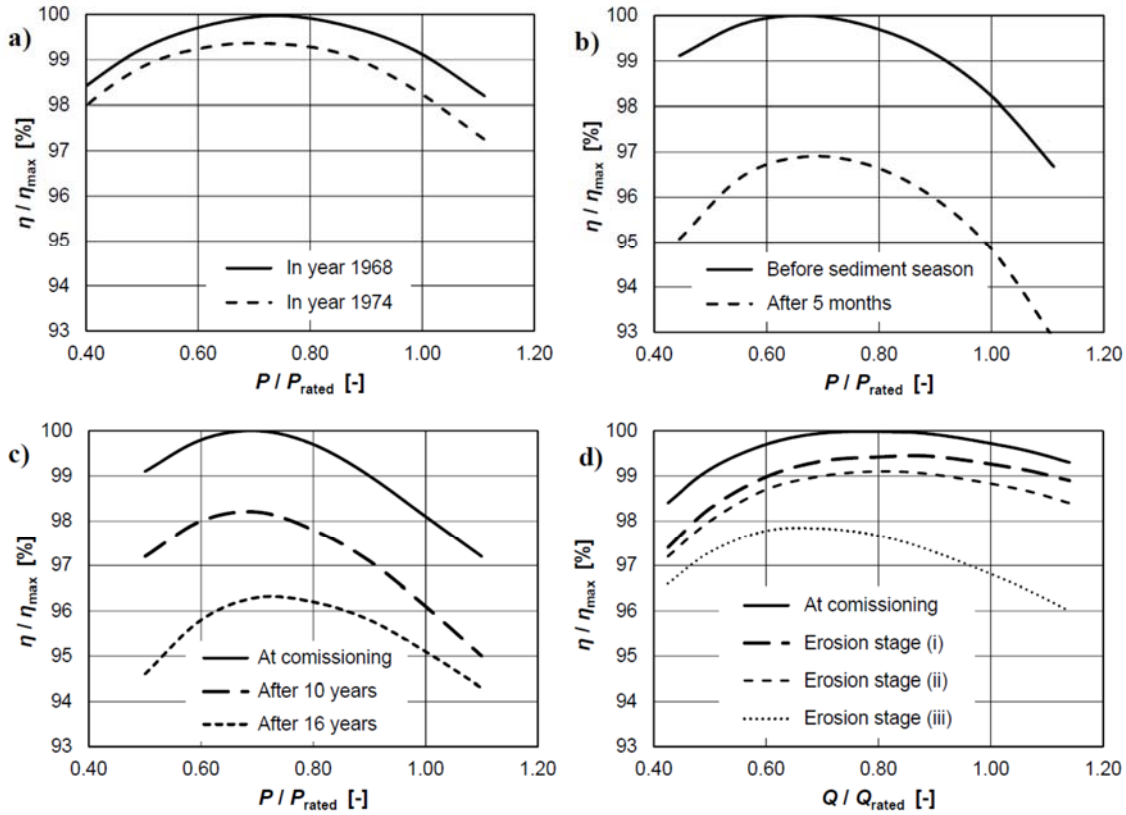

Figure 2-23 Measured efficiency reductions of Pelton turbines due to hydro-abrasive erosion: Examples compiled from a) Brekke *et al.* (2002), b) Strübin & Bussi (1988), c) Lazzaro & Rossi (1995), and d) Cateni *et al.* (2008).

Table 2-2: Absolute efficiency changes $\Delta\eta$ of Pelton turbines due to hydro-abrasive erosion.

HPP, country	Head [m]	$\Delta\eta$ [%]	Coated runner	Available information on time, sediment load	Reference
Klösterli (dismantled), Switzerland	218	−8	no	3.5 months, at average *SSC* = 0.2 g/l	Dufour (1921)
Mörel (Aletsch), Switzerland	700	−3	no	5 months	Strübin & Bussy (1988), Fig. 2-23b
Dorferbach, Austria	686	−6	no	4 months	Maldet (2008)
Alfalfal, Chile	690	−5	yes	3 months, approx. 100 000 t of sediment	Winkler (2014)

2.5.3 Effect of turbine erosion on turbine efficiency

2.5.3.1 Overview

In Pelton turbines, erosion on the nozzles is expected to have a negative effect on turbine efficiency due to a reduced jet quality (e.g. momentum deficit in the jet axis, jet spreading). With respect to the runner buckets, the turbine efficiency can be affected due to changes in

- Surface roughness and
- Geometry of the splitter crests, cut-out edges and other locations (outer walls and root zone) in severe cases.

Erosion generally increases the roughness of eroded parts, except for newly hard-coated turbines in which the roughness may temporarily slightly decrease due to polishing. Faletti (1934) mentioned an increased roughness as a reason for reduced turbine efficiency. Lazzaro & Rossi (1995) reported $\Delta\eta \approx -1\%$ due higher roughness simulated by applying paint in the buckets of a model Pelton runner. On the contrary, Karimi & Schmid (1992) argued that the formation of ripples not always significantly increases the flow resistance, similar to the phenomenon of friction/drag reduction along surfaces with favourable textures.

Padhy & Saini (2011) experimentally investigated correlations between (i) $\Delta\eta$ and the mass loss as well as (ii) $\Delta\eta$, SSC, d_{50}, w and exposure time on a model Pelton runner made of brass with quite round splitters and cut-outs. It is however not clear, how these correlations would need to be adapted to prototype conditions (different bucket geometries and material).

The relations between $\Delta\eta$ and the erosion on nozzles, splitters, cut-outs or inside the buckets have not yet been investigated systematically. The individual effects are thus not quantitatively known. For example, it is not clear if the $\Delta\eta$ is always higher at partial load (Figure 2-23). In the following, available correlations between $\Delta\eta$ and normalized geometrical changes on the buckets, mainly based on field data, are presented.

2.5.3.2 Effect of blunt splitters

The degradation of splitter crests, i.e. increased width and a blunter shape, causes flow disturbance and is seen as an important factor for $\Delta\eta$ of Pelton turbines. Bozic *et al.* (2004) reported $\Delta\eta$ as a function of the splitter width s normalized with B (Fig. 2-24). They distinguished between (i) erosion only on the splitter crests and (ii) also in the buckets. Note that the curves in Figure 2-24b do not start from the origin of the axes because the splitters

have a certain initial width s. A minimal splitter crest radius is selected for mechanical reasons and in case of coated runners for the applicability of the coating (e.g. $r \geq 2$ mm). Hence the initial s/B tends to be lower for wide buckets.

Maldet (2008) reported an over-proportional increase of $\Delta\eta$ as s increased (Fig 2-25), but the variation among the three investigated runners shows that s is not the only influencing parameter. According to Brekke *et al.* (2002), Bozic *et al.* (2004) and Maldet (2008), $\Delta\eta$ may reach several percent if s/B increases to a few percent. This means that $\Delta\eta$ and s/B have usually the same order of magnitude.

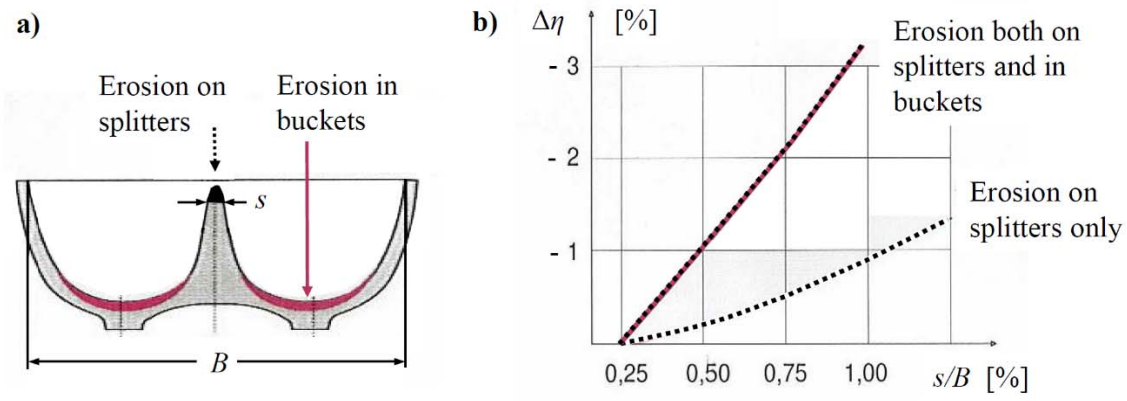

Figure 2-24 a) Definition of the relative splitter width s/B and b) efficiency reductions at Pelton turbines as a function of s/B according to Bozic *et al.* (2004)

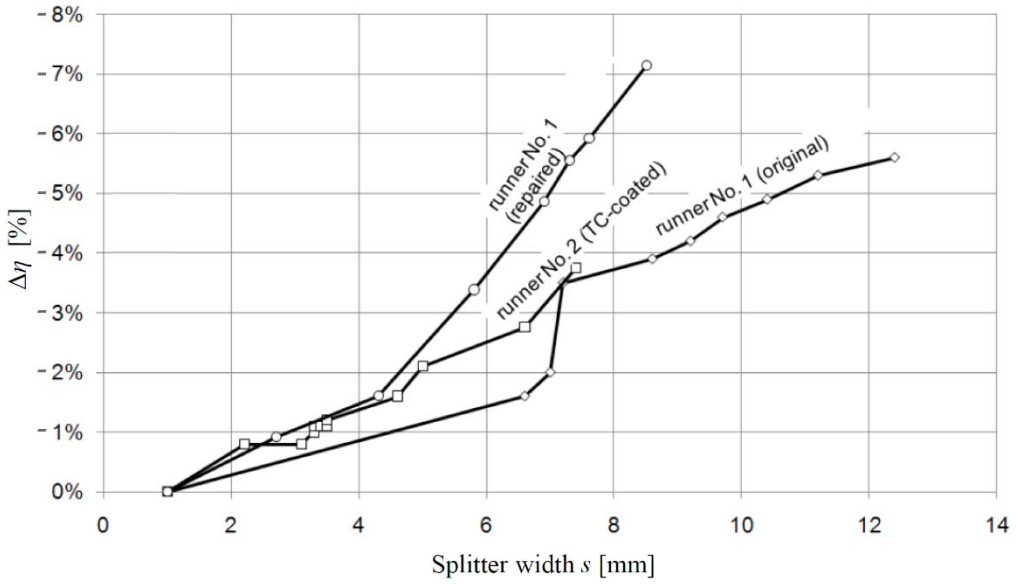

Figure 2-25 Reductions in absolute efficiency $\Delta\eta$ at the Pelton turbine of HPP Dorferbach with B = 228 mm as a function of the splitter width (Maldet 2008).

Zhang (2016) proposed an analytical, physically-based, conceptual model for $\Delta\eta$ of a Pelton turbine as a function of s/B and the degree of load Q/Q_d. He postulated that the

flow detachment at the splitters renders a part of the flow ineffective for torque generation. The effect of flow detachment is more important if s increases due to erosion and if the jet width is reduced (Figures 2-26a & b). The latter is the case during partial load operation and in splitter cross-sections lying off the jet axis (in radial runner direction). The critical deflection angle, above which the water is assumed to be ineffective for torque generation, can be used as a calibration parameter. He applied the model to exemplary data of HPP Dorferbach and found a reasonable agreement with the range of reported field data (Fig. 2-26c). The model and the field data indicate that the relation between $\Delta\eta$ and s/B is non-linear, which was also stated by Bajracharya *et al.* (2008).

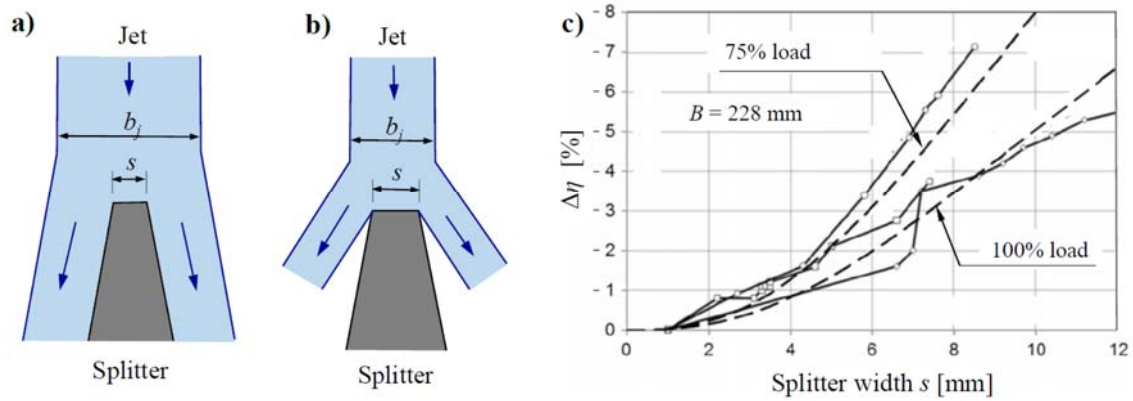

Figure 2-26 a) Attached and b) detached flow (with large angle) at the splitter of a Pelton bucket (Zhang 2016); c) Efficiency reduction as a function of the splitter width at HPP Dorferbach modelled by Zhang (2016; dashed lines) compared to field data (solid lines according to Maldet 2008 from Fig. 2-25).

2.5.3.3 Effects of cut-out and splitter tip erosion

Based on the evaluation of pressure measurements and numerical simulations, Perig *et al.* (2006) showed that the bucket regions outside the pitch circle diameter D (Fig. 2-7b) contribute most to the torque and hence turbine power. Erosion on the cut-out edges and the splitter tips affects the interaction of the jet with the runner, in particular the torque generation, and is thus another reason for efficiency reductions besides degraded splitters.

Hassler & Schnablegger (2006) proposed the radial erosion on the splitter tip Δy_t (Fig. 2-27a) as an easily measurable indicator for the erosion status of an uncoated runner. They normalized Δy_t by the jet diameter d_0 and found an approximately linear relation between some measured $\Delta y_t/d_0$ and $\Delta\eta$ (Fig. 2-27b). Because d_0 is usually one third of B (Section 2.3.2.2), the normalized radial erosion depth on the splitter tip can also be expressed as a fraction of B, as indicated on the top horizontal axis in Fig. 2-27b). The $\Delta\eta$ and the $\Delta y_t/B$ in this Figure are similar. Considering the previous paragraph, this means that the $\Delta\eta$, the s/B and the $\Delta y_t/B$ have usually the same order of magnitude.

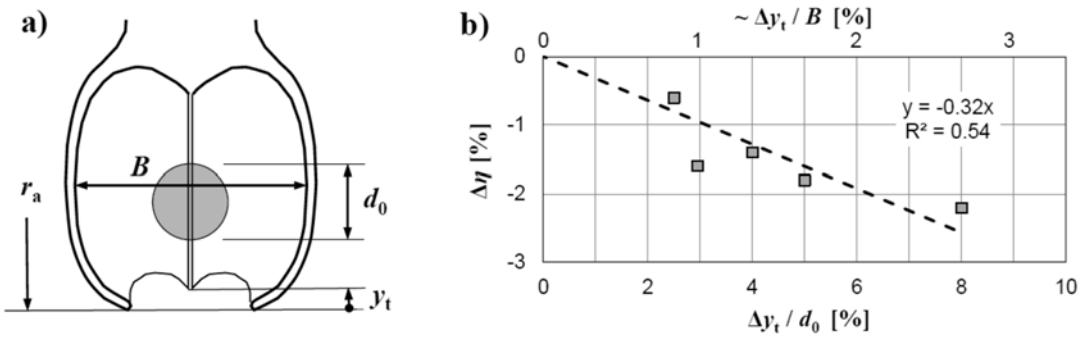

Figure 2-27 a) Definition of the radial splitter tip position y_t as an indicator for the erosion status of a runner and b) measured reductions in absolute index efficiencies $\Delta\eta$ as a function of the splitter tip erosion Δy_t normalized with the jet diameter d_0 (modified from Hassler & Schnablegger 2006).

2.6 Techniques for monitoring of turbine efficiency

2.6.1 Periodic efficiency monitoring

2.6.1.1 Absolute vs. index efficiency measurements

Procedures for efficiency measurements of hydraulic turbines are described in IEC 60041 (1991). Thermodynamic efficiency measurements yield absolute efficiencies, and the discharge results from the evaluation of the measurements. Thermodynamic measurements are most accurate for medium- and high-head HPP, but are generally not affordable for frequent repetitions because they require quite a high effort (installation of probes etc.).

For the determination of $\Delta\eta$, which is the main interest in the context of turbine erosion, no absolute efficiencies are needed. A series of index efficiency measurements is sufficient. These are calculated from electric output, discharge and pressure (Eq. 2-32) measured with instruments permanently installed in most HPPs. The results of such measurements may be systematically biased due to inaccurate calibration of the instruments. Thus, index efficiencies may be systematically biased, but are proportional to absolute efficiencies. An important prerequisite for efficiency monitoring is a good reproducibility of the measurements over several years. To achieve this, long-term stable sensors are required, and modifications on the instruments, the data transmission and acquisition system as well as the evaluation procedure should be avoided.

In classical index efficiency measurements, the relevant parameters are measured at a series of operation points (from partial load to overload) with constant operating conditions at each load level. Accordingly, such measurements are time-consuming and may hinder the flexible operation of HPPs.

2.6.1.2 Sliding-needle measurements (SNM)

Almquist *et al.* (1995) introduced the so-called 'sliding gate method'. In this method the guide vanes of a Kaplan turbine are continuously opened and closed while acquiring data for efficiency evaluation. This method has been adapted for Pelton turbines and is accordingly called 'sliding-needle method' (Abgottspon *et al.* 2013a, 2013b, 2014). In a Sliding-Needle Measurement (SNM), the nozzles of a Pelton turbine are gradually opened and closed to operate the MG from partial to full load (or even overload) and back to partial load. The test duration needs to be long enough to achieve quasi-steady conditions. Nevertheless, the SNM takes less time than a series of classical index efficiency measurements. Each SNM yields a continuous curve of the turbine's index efficiency as a function of the power, in contrast to the classical method with a series of discrete points.

2.6.2 Continuous efficiency monitoring (CEM)

In some HPPs, the decrease of turbine efficiency can directly be seen from the time series of the power output displayed in the HPP's control system, as in the example of Figure 2-28, if the following conditions are met:

- The efficiency decrease is high, say several percent;
- There is only one turbine or identical turbines operated similarly, frequently run at a constant discharge, e.g. at full load typically during the wet season;
- The head water level is approximately constant, resulting in an almost constant net head for Pelton turbines;
- Turbine regulation is based on discharge (not on power output).

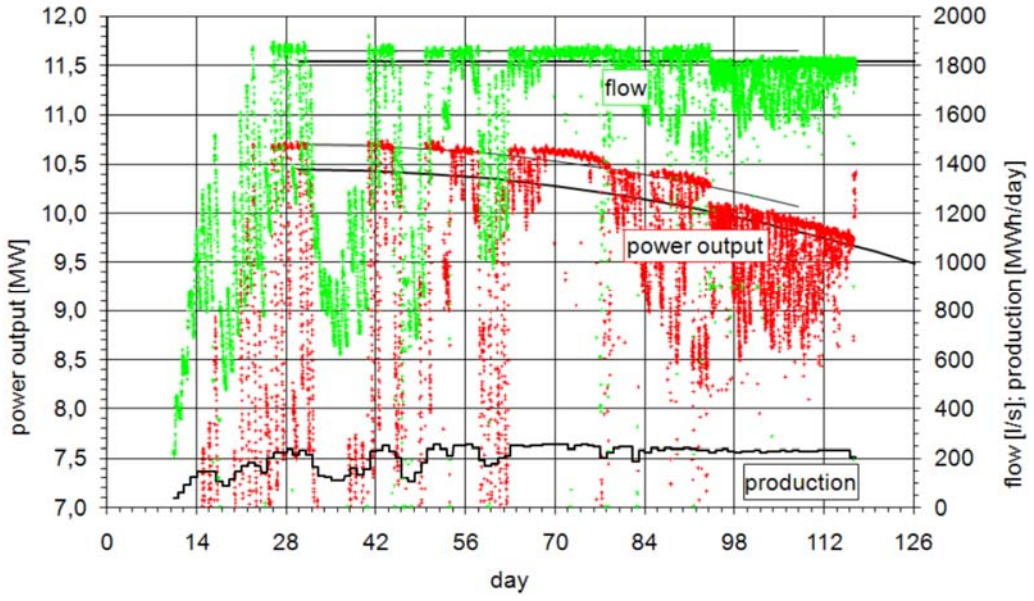

Figure 2-28 Decreasing power output at full load and constant head as an indicator for decreasing turbine efficiency (Maldet 2008).

If these conditions are not met, i.e. in most cases and particularly for larger HPPs, this indicative type of continuous turbine efficiency monitoring is not sufficient, and more advanced methods are required, which are so far not described in the literature. Such methods are based on the evaluation of continuously acquired operation data.

2.7 Economic aspects of turbine erosion

2.7.1 Turbine refurbishment costs

Only few data on the cost of turbine refurbishments due to hydro-abrasive erosion have been published. For the Pelton and Francis turbines operated in Switzerland, Kalberer (1988) estimated these costs as 20 Mio. CHF/year. At that time, coatings were not yet widely applied. With 19 TWh of produced electricity per year, the specific turbine refurbishment cost due to erosion was on average 0.001 CHF/kWh. Assuming an electricity price of 0.05 CHF/kWh, this cost corresponded to ~2% of the annual revenue.

Table 2-3 shows published data on turbine refurbishment costs of some HPPs with their estimated percentages on the annual revenues. These examples show that the refurbishment cost varies considerably also in relation to the annual revenue, depending on the HPP layout, site conditions, sediment transport events, operation regime, size of turbines, salary levels, market situation, electricity prices, etc.

Table 2-3: Examples of turbine refurbishment costs in relation to the annual revenue.

HPP, country	Turbines	Characteristics	Annual refurbishment costs	% of annual revenue (estimated)	Reference (for refurbishment costs)
Dharasu (Maneri Bhali Stage-II), Uttarakhand, India	4 x 76 MW Francis	Net head = 248 m, *SSC* up to 12 g/l	~1 Mio. €, probably before coating	~2%	Singh *et al.* (2013)
Cahua, Peru	2 x 22 MW Francis	Gross head = 215 m, *SSC* ≥ 3 g/l during 15 to 30 days/year	0.58 Mio US$*, before improved runner coating	~6%	Espinoza (2016)
Nathpa Jhakri, Himachal Pradesh, India	6 x 250 MW Francis	Head = 428 m, *SSC* up to 70 g/l (Satluj River)	~0.5 Mio. € mainly for welding repairs, before coating	~0.3%	Winkler *et al.* (2011b)

* in addition: generation losses due to downtimes of 20 days per year.

2.7.2 Economic importance of reduced turbine efficiency

Besides refurbishment costs, electricity generation losses due to reduced efficiency negatively affect the cost-efficiency of HPPs in sediment-laden rivers (Section 2.5.2). In the management of runner repairs and replacements with repect to turbine efficiency, the cost of these actions are balanced against the avoided revenue decreases due to efficiency reductions. With annual repair costs in the range of some 0.1% to several % of the annual revenue, and considering that not all repairs are related to efficiency, $\Delta\eta$ in the range of 0.1% can be economically relevant. This poses high exigencies on the efficiency monitoring.

For the screening of several HPPs with respect to the importance of economically optimized runner management, Hassler & Schnablegger (2006) proposed to consider the cost of a new runner in relation to 1% of the annual revenue from the corresponding generated electricity. This key figure expresses a duration in years, over which a new runner could be payed solely by the avoided $\Delta\eta$ of −1% on temporal average. For HPPs where this figure is low, a greater effort for keeping high turbine efficiency is adequate (monitoring, repairs and replacements).

2.7.3 HPP shutdowns in periods of high erosion potential

The erosion potential may vary considerably depending on *SSC* and PSD in the turbine water. In a period with high *SSC* and relatively coarse particles, the direct and consequential damages on turbines and other elements of HPPs may exceed the revenues from electricity sales. These damages include (i) the costs of repair works and replacement investments due to hydro-abrasive erosion, and (ii) losses of revenue due to reduced turbine efficiency or due to downtimes during revision works. When *SSC* and particle sizes exceed threshold values, it may hence be more economical to close water intakes and to pause turbine operation, if this is possible from the regulatory framework, production obligations and load compensations within a group of HPPs.

Because the effect of PSD on turbine erosion is not yet fully known and real-time PSD measurements are not standard, shutdown decisions are so far based on *SSC* only. In the following, the threshold *SSC* at which turbines are taken out of operation for the mentioned economical reasons is referred to as ‘shutdown *SSC*’. Table 2-4 shows examples of shutdown *SSC* in some run-of-river HPPs. Economically based HPP shutdowns during exceptionally high erosion potential are not practiced systematically. Reasons for this are

in some cases the incompatibility with the regulatory framework and production obligations, but in most cases the lack of real-time SSM systems and insufficient information on shutdown *SSC*.

Table 2-4: Examples of shutdown *SSC* in some run-of-river HPPs.

HPP, country	Turbine characteristics	Particle characteristics	Shutdown *SSC*	Remarks	Reference
Dharasu (Maneri Bhali Stage-II), India	4 x 76 MW Francis, Net head = 248 m	Quartz and feldspar content = 72%, 90% ≤ 150 µm, mostly angular	3 g/l in river water at intake	Firstly uncoated, then coated runners	Singh *et al.* (2013)
Jhimruk, Nepal	3 x 4 MW Francis Net head = 202 m	Quartz and feldspar content = 83%, 80% < 100 µm	3 g/l	Uncoated runners	Elkvik (2013), Pradhan (2004)
Cahua, Peru (Pativilca river)	2 x 22 MW Francis Gross head = 215 m	Quartz content = 78%, 82% ≤ 60 µm silt	3 g/l vs. 10 g/l in power water	Before vs. after improved runner design and coating	Espinoza (2016)
Dorferbach, Austria	1 x 10 MW Pelton, Gross head = 686 m, 4 nozzles	Quartz content = 50%, often $12 \leq d_{50} \leq 60$ µm, mostly angular	1.1 g/l in power water	Firstly uncoated, then coated runners	Boes (2009, 2010)

3 EXPERIMENTAL SETUPS, INSTRUMENTATION AND METHODS

In this chapter, the facilities, experimental setups, instrumentation, materials and methods used in the laboratory and field investigations are treated for all parts of the research project (suspended sediment, turbine erosion and efficiency monitoring). In particular, the layout, the Pelton turbines and the operation experience of HPP Fieschertal are described.

3.1 Instruments for suspended sediment monitoring (SSM)

The instruments for SSM used in this study and their main specifications are listed in Table 3-1. All instruments except the automatic water sampler serve for continuous real-time measurements of *SSC*. The water sampler is used for discontinuous *SSC* reference measurements (Boes *et al.* 2013). In addition, PSDs are obtained from LISST.

The turbidimeters (1) and (2) are standard instruments for SSM in waste water treatment plants and rivers in accordance with DIN EN ISO 7027 (2000). They use near-infrared light to measure turbidity with two receivers at 90° (Endress+Hauser 2003, Hach Lange 2005). The optical path of the second receiver is longer than that of the first one; the signals of both receivers are combined in the internal data processing (Endress+Hauser 2003). In addition, temperature is measured in (1) which can be useful to detect if the probe was submerged in case of varying water levels. The turbidimeter models (1) and (2) have wipers to prevent fouling (Fig. A-5b in Appendix A1).

The turbidimeters (3) and (4) are mainly used in the process industry, whereas (5) was originally developed for quality control in water supply systems. The latter measures turbidity at a free-falling water jet (Fig. A-2b in Appendix A1). Turbidimeters (3) and (5) measure at $\alpha = 90°$. The turbidimeter (3) has a second output channel from a receiver at $\alpha = 25°$. The turbidimeter (4) measures at $\alpha = 0°$; its measuring cell with an optical path length of only 10 mm was selected to measure high turbidity.

The turbidimeters (1), (2), (3) and (5) have been factory-calibrated to FNU. The output of the 25°-channel of (3) is also displayed in FNU, although the unit FNU is actually defined with $\alpha = 90°$ (nephelometric). The through-light turbidimeter (4) has been factory-calibrated to so-called ‘Concentration Units’ CU.

With respect to LISST (6) a multi-purpose, submersible model without dilution chamber was used. To increase the upper limit of measureable *SSC*, the instrument's optical path length was reduced from 50 to 5 mm by inserting the strongest available path reduction module consisting of a glass cylinder (Fig. A-5a in Appendix A1). The nominal range of measurable particle sizes is 2.5 to 500 µm for IMS or 1.9 to 380 µm for IMR, respectively (Sequoia 2011). The LISST's volume conversion constant has been factory-calibrated with spherical particles and IMS.

The acoustic technique (7) is based on standard ADM equipment with 1 MHz transducers (Fig. A-4 in Appendix A1). This system is not factory-calibrated regarding SSM.

The selected CFDM (8) contains two parallel bent tubes with 8 mm inner diameter. It has been factory-calibrated and the accuracy of its density measurement was specified by the manufacturer as ±0.5 g/l, which is a common value (Kalotay 1999). The pressure transmitters (9) are factory-calibrated standard devices for HPP instrumentation. The water sampler (10) is a portable standard device for automatic collection of pumped, bottled samples for water quality monitoring in surface waters and sewerage systems.

Table 3-1 Investigated instruments for SSM (modified from Felix *et al.* 2013b).

No.	Instrument type		Instrument model, manufacturer	Instrument output, measuring range	Derived quantities
(1)	Turbidimeter, submerged, with wipers		*TurbiMax W CUS 41* Endress+Hauser	Turbidity (α = 90° dual) 0 … 10 000 [FNU]	*SSC*
(2)			*Solitax ts-line sc* Hach Lange	Turbidity (α = 90° dual) 0 … 4 000 [FNU]	*SSC*
(3)	Turbidi-meter, in-line	Pressure flow (in flow-cells), without wipers	*TurBiScat* Sigrist Photometer	Turbidity (α = 90°, 25°) 0 … 4 000 [FNU]	*SSC*
(4)			*TF16-N* with *F20* Optek Danulat	Turbidity (Transmission) 0 … 5 [CU] (α = 0°)	*SSC*
(5)		Free-falling jet	*AquaScat WTM A* Sigrist Photometer	Turbidity (α = 90°) 0 … 4 000 [FNU]	*SSC*
(6)	Laser In-Situ Scattering and Transmissometry instrument (LISST)		*LISST-100X*, Type C, with 90% path reduction module Sequoia Scientific	Volume concentrations [ppm] in 32 size classes (2 to 380 µm)	*SSC* and PSD
(7)	Acoustic technique (based on ADM installation)		*Risonic Modular* Rittmeyer	Received amplitude [V] (acoustic damping at 1 MHz)	*SSC*
(8)	Coriolis Flow– and Density Meter (CFDM)		*Promass 83 F15* DN15 Endress+Hauser	Volumetric flow rate [l/s], Density [kg/m^3]; Temperature [°C]	*SSC*
(9)	Differential pressure (u/s and d/s of penstock)		*2088, 1151* Rosemount	Static pressure [0 … 55 bar]	*SSC*
(10)	Automatic water sampler		*Isco 3700* Isco-Teledyne	Bottled water samples (24 x 1 liter)	*SSC*

3.2 Laboratory investigations on SSM (Task A)

3.2.1 Scope and instruments

The SSM instruments (1) to (7) listed in Table 3-1 were investigated in the laboratory prior to their use at the case study site. The *SSC*-measuring ranges, the conversions of instrument outputs to *SSC* (calibrations), and the measurement uncertainties were investigated under controlled conditions in various dilute suspensions made of water and seven types of mineral particles.

3.2.2 Mineral particles

The properties of the seven particle types are listed in Table 3-2 and their microscopic images are shown in Figure 3-1. Glass beads were chosen for their ideal shape and served as reference. Quartz, feldspar and mica particles, i.e. the main components of granite rock, were selected with reference to the case study. The first five particle types (G to M) were purchased from commercial applications. The particle types N1 and N2, however, are natural fine sediments collected from deposits in the tailwater channels at the case study HPP Fieschertal and at another HPP in the Canton of Valais, Switzerland. Note that these sediments are coarser than the usually transported mineral particles, because the finer ones did not settle in the tailwater channels. The solid densities ρ_s of the particle materials were measured using a helium expansion pycnometer and are also listed in Table 3-2 together with descriptions of the particle shapes and colours.

Table 3-2 Mineral particles used in the laboratory investigation.

Itenti-fier	Particle type (material, grading)	Manufacuring / origin, product name	Shape (qualitative)	Color	ρ_s [g/cm^3]
G	Glass beads	Sand blasting agent	Spherical, smooth	White	2.42
Q3	Quartz fine sand	Natural, washed, (*Geba '0.06–0.3 mm'*)	Irregular, rounded	Whitish	2.66
Q2	Quartz powder	Milled (for ceramics) (*Dorsilit 1.600*)	Angular	White	2.67
F	Feldspar powder (Na-plagioclase)	Milled (for pottery) (*Feldspat Na LF 90*)	Elongated, angular	White	2.65
M	Mica powder (Muscovite)	Milled (additive for paint) (*Mica Mu 101*)	Flaky	Whitish	2.86
N1	HPP Fieschertal	Natural fine sediment, collected from deposits in tailwater channels	Mixed (angular, elongated and flaky)	Grey	2.70
N2	HPP Stalden			Greenish	2.92

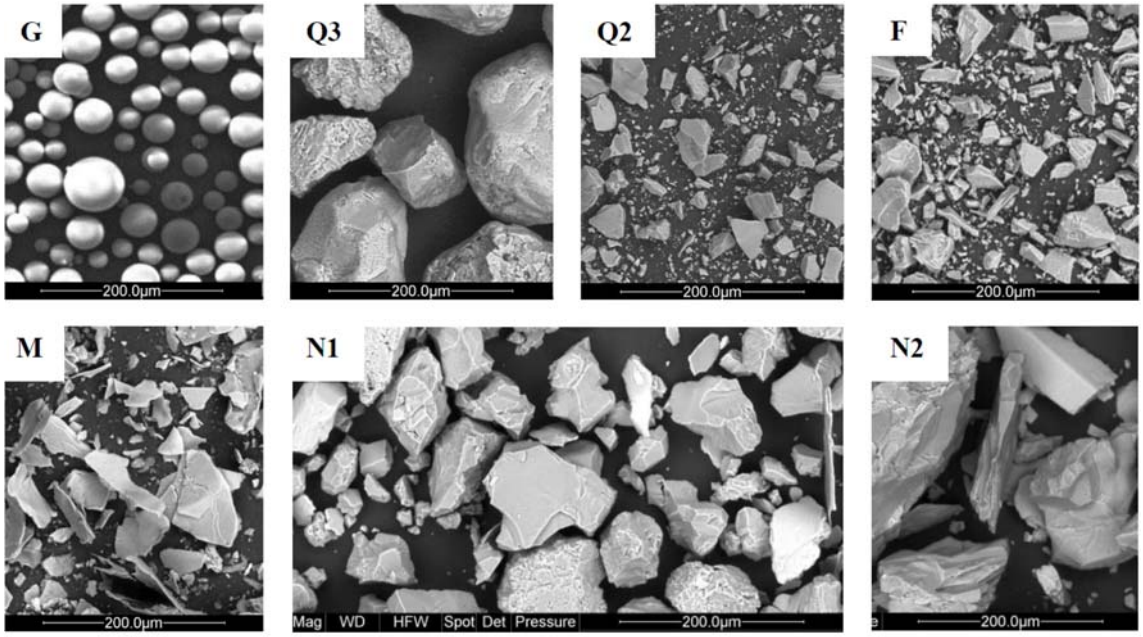

Figure 3-1 Particles used in the experiments, labels refer to Table 3-2 (image G courtesy of HSLU, other images ETH Zürich).

Prior to the laboratory experiments described in the next sections, the PSDs of all particle types shown in Figure 3-2 were measured from suspended samples with adequate dilution using a stationary laser diffractometer (*LA-950* manufactured by Horiba) at the Geotechnical Institute of ETH Zürich. This instrument has a nominal size-measuring range of 0.01 µm to 3 mm, i.e. wider than LISST. Because the software of the laboratory LD assumes spherical particles, the PSDs of highly non-spherical particles, particularly mica, are biased and should be interpreted with care. The PSD of Q3 was mainly in the range of fine sand (63 to 200 µm). The natural sediment particles (N1 and N2) contained almost 80% by mass of fine sand. The particle sizes of the other particle types were mainly in the range of silt. Only Q2 had 10% of particles in the size-range of clay (< 2 µm).

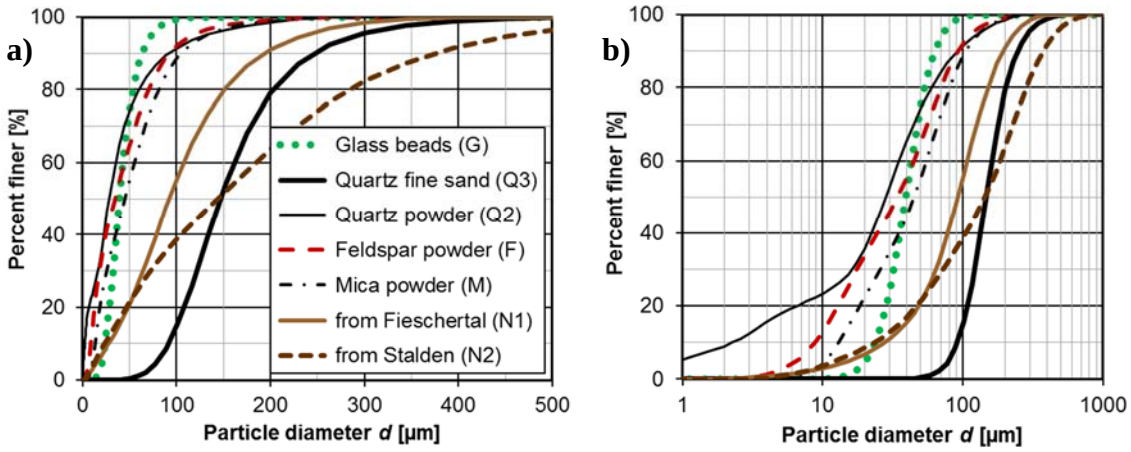

Figure 3-2 PSDs of particles used in the laboratory investigations obtained from the non-portable laser diffractometer (*LA-950*), with a) linear and b) logarithmic scaling of the diameter axis.

For the particle types G, Q3, F and M, the three main particle dimensions (*a*, *b* and *c*-axes according to Section 2.1.2.2) of 50 to 100 particles were measured from microscopic images. Distributions of the *a*-, *b*- and *c*-dimensions as well as of the equivalent sphere diameter d_{es} were evaluated (Felix *et al.* 2013a). In addition, the *SMD* (Eq. 2-4) was determined for each particle type considering the various particle shapes. These results are presented in Section 4.1 and served as a reference for the PSD measurements from LISST.

3.2.3 Mixing tank and pump line

Measurements were carried out on suspensions prepared in a mixing tank (Fig. 3-3 as well as Fig. A-1 in Appendix A1) in the hydraulic laboratory of the CC FMHM, Hochschule Luzern, in Horw. The tank with a length of 2.12 m and a width of 1.13 m was previously used in the investigations of Abgottspon (2011) and Costa *et al.* (2012). The relatively big tank allowed accommodating an acoustic path with a length of 1.73 m similar to typical prototype conditions. The tank was equipped with a central vertical stirrer operated at 280 to 350 revolutions per minute (Fig. A-3a in Appendix A1). In addition, the suspension was circulated by means of a pump line (d_i = 4 cm) connected to the tank.

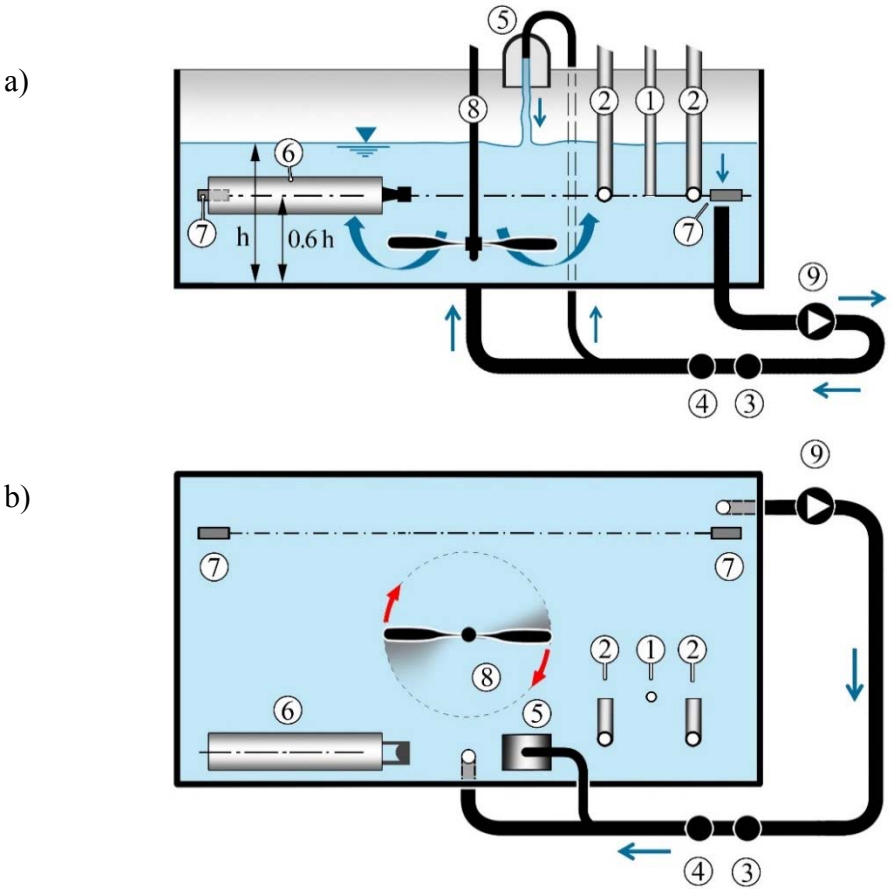

Figure 3-3 Experimental setup in the laboratory investigations a) vertical section and b) plan view; items (1)-(7) refer to the instruments in Table 3-1, (8) stirrer, (9) pump (modified from Felix *et al.* 2013a).

The *in-line* turbidimeters (3) and (4) were installed in the pump line. The other instruments were mounted in the tank at 60% of the water depth above the invert. Because the turbidimeter measuring at the free-falling-jet (5) requires a flow rate of only 0.06 to 0.12 l/s, it was connected with a small hose of 12 mm inner diameter branching off from the main pump line. The branch-off angle was 125°. The small pipe had an oblique end-cut and protruded into the DN40 main pipe.

For one type of submersible turbidimeter (2), two items of the same model were included in the laboratory investigations, as a preparation to installing one probe at each of the two turbines in the case study HPP.

3.2.4 Experimental procedure

3.2.4.1 Measurement series

Eight series of measurements were conducted with step-wise increasing *SSC*. Whereas in seven series the single types of particles listed in Table 3-2 were used, a mixture of 70% by mass of feldspar (F) and 30% mica (M) particles was used in the last series (labelled F-M). This mixture was selected with reference to the case study site, where mainly angular and up to 30% of platy particles were previously measured (Abgottspon 2011).

3.2.4.2 Preparation of suspensions with step-wise increasing SSC

Suspensions were prepared with clear water (from the public water supply) and mineral particles; no dispersant agent was added. At the start of each series, the cleaned tank was filled with water to a depth of h = 0.5 m (Fig. 3-3), i.e. 1.2 m^3.

In each series, *SSC* was stepwise increased from 0.1 to at least 3 g/l. For most types of particles, *SSC* was further increased, as long as some of the devices were able to measure and enough particle material was available. Figure 3-4 shows the nominal *SSC* for the eight series, i.e. the planned *SSC* calculated from the particle mass divided by the volume of the mixture in the tank. *SSC* was increased to the next level by pouring the prepared additional mass of particles into the tank.

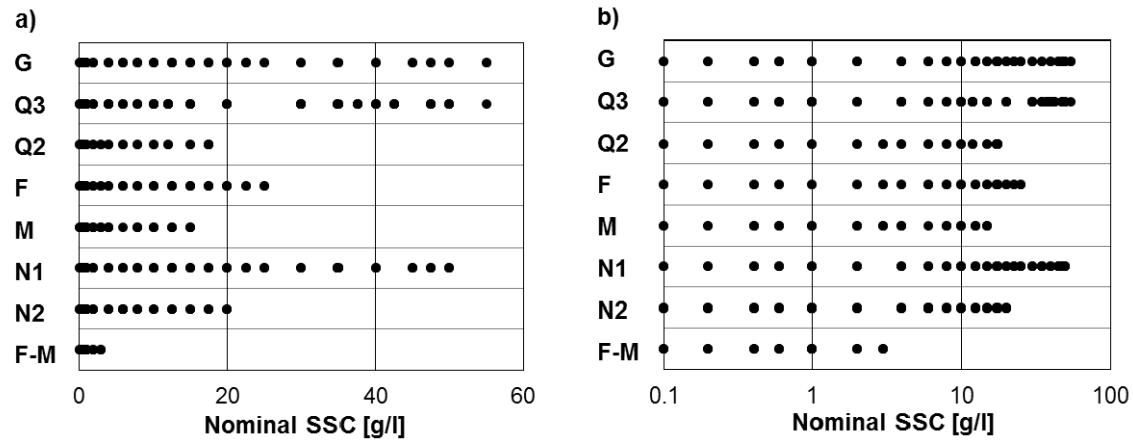

Figure 3-4 Nominal *SSC* in the eight measurement series in the laboratory, with a) linear and b) logarithmic scaling of the *SSC* axis.

3.2.4.3 Measurement Procedure

Before particles were added, 'zero measurements' were performed with all instruments. For the LISST, the so-called 'background scatter' was recorded. This allowed also to check that the path reduction module has been properly installed (no air between it and the receiving window).

At each *SSC* level, measurements with all instruments were performed after a mixing time of at least 10 minutes. For the instruments with an analogue output, i.e. the turbidimeters and the acoustic technique, the signal was recorded during 100 seconds at 1 Hz. For the LISST, 100 single measurements were taken in the real-time mode, i.e. with processing of *BVC* between the measurements. The measuring frequency in this mode was between 0.4 and 0.6 Hz, corresponding to a measuring duration of 3 to 4 minutes at each *SSC* level.

At each *SSC* level, bottle samples of the suspension were taken from (i) the mixing tank at the level of the instruments and (ii) from the jet at the outlet of the turbidimeter above the tank (item no. 5 in Fig. 3-3). For (i), the samples were taken using a plastic bottle with an additional lateral opening close to its bottom (similar to a 'Van Dorn' horizontal water sampler): While both openings were blocked, the empty bottle was brought to the SSM instruments' level in horizontal position with the second opening to the top. Then both openings were unblocked, the suspension flew into the bottle and the air escaped through the second opening. When the required sample volume was reached, both openings were blocked again and the bottle was taken out.

In general, two samples per *SSC* level were taken at the location (i) and one sample at (ii). In total, 370 bottle samples were taken, i.e. 230 at (i) and 140 at (ii). The sample volumes were 0.4 to 0.6 l at nominal $SSC \leq 0.15$ g/l, 0.3 to 0.5 l at 0.15 to 0.5 g/l, and 0.1 to 0.2 l at higher *SSC*. A smaller sample volume was selected at higher *SSC*, because it was

sufficient to achieve a reasonably low relative measurement uncertainty on the gravimetric *SSC*, and a smaller sample volume facilitated the sample treatment (less time required to evaporate the water).

3.2.5 Data acquisition and data treatment

The analogue output signals of the turbidimeters and the acoustic technique were recorded using a data acquisition board (National Instruments) with a resolution of 16 bit connected to a PC. For each *SSC* level, the measured values were averaged.

For the acoustic technique, the damping δ was evaluated as

$$\delta = 1 - \frac{A(t)}{A_w} \ . \qquad [-] \qquad (3\text{-}1)$$

LISST *BVC* were obtained using IMS or IMR, and the background-scatter intensities recorded at the start of each measurement series. The 100 single measurements per nominal *SSC* level were averaged. The *TVC* resulted from summation of the plausible *BVC*. *TVC* were multiplied by the densities listed in Table 3-2 to convert them to *SSC*. These *SSC* obtained from LISST and pycnometer were termed

$$SSC_{L0} = TVC \ \rho_s \ . \qquad [g/l] \qquad (3\text{-}2)$$

3.2.6 Gravimetrical *SSC* from bottle samples

3.2.6.1 Procedure

From the bottled samples, *SSC* was gravimetrically determined as follows: weighing of the sample, evaporation of the water (no filtration), weighing of the dried residue, and calculation of the *SSC* according to the definition in Section 2.1.4.1. The mass of each numbered container was previously determined. Electronic balances (*Kern EG 420-3NM* and *PCB250-3*) with a resolution of 1 mg were employed. From repeated weighing, an expanded measurement uncertainty $U_{2\sigma}$ (at 95% confidence level) of ±6 mg was estimated for the determination of the residues' mass. For the determination of the weight of the sample (plus the container) before the evaporation of the water, a less precise balance was sufficient.

The concentration of minerals which were dissolved in the water before its evaporation was determined on clear water samples and was found to be 0.15 g/l for the drinking water in the laboratory experiments. This concentration was accounted for in the determination of the *SSC*. The the gravimetrically determined *SSC* are termed SSC_G in the following.

3.2.6.2 Measurement uncertainty of reference SSC

With an expanded uncertainty $U_{2\sigma} = \pm 6$ mg on the mass of the dried residues according to the previous Section, $U_{2\sigma}$ on the *SSC* was estimated as <0.01 g/l for 0.5 l, <0.015 g/l for 0.4 l, and <0.05 g/l for 0.1 l samples. The relative uncertainty on *SSC* is higher for low *SSC* and small sample volumes. Considering the higher sample volumes at lower *SSC* according to Section 3.2.4.3, the relative $U_{2\sigma}$ on *SSC* due to weighing is < 10%, reducing to < 1% above 5 g/l.

3.3 The HPP Fieschertal

3.3.1 General layout and catchment

The field investigation was carried out at the high-head HPP Fieschertal in Valais, Switzerland, operated by the Gommerkraftwerke AG (GKW). This run-of-river HPP has a design discharge $Q_d = 15$ m^3/s, a gross head of 520 m, a rated power of 2 x 32 = 64 MW and is equipped with two Pelton turbines. Schematics of the layout of the HPP, intake works, storage tunnel, valve chamber and powerhouse are presented in Appendix B.

The HPP is located on the mountain stream *Wysswasser*, a tributary of the upper *Rhone* River. The HPP's intake at an elevation of 1650 m a.s.l. has been built in 1971 directly at the mouth of the *Fieschergletscher*, which is the second longest and third largest glacier in the Alps. In the meantime, the glacier has been retreating by about 500 m, dead ice is melting in the glacier foreland and small proglacial lakes formed between sediment deposits. The catchment reaches up to 4274 m a.s.l. and has an area of 58.6 km^2 (swisstopo 2015). 57% are covered by glaciers and only 4% are vegetated; the average elevation of the catchment area is about 3000 m a.s.l. (VAW 2011). In the catchment of the *Wysswasser*, there are crystalline rocks of the magmatic (granite, granodiorite and quartz diorite) and metamorphous group (gneiss, mica schist and amphibolite) (swisstopo 2015).

The discharge regime of the *Wysswasser*, i.e. the typical distribution of the monthly run-offs over the year, is '*a-glaciaire*' according to the Swiss classification system (Weingartner & Aschwanden 1992). With this regime, the run-off volumes in the months July and August correspond to 50% of the annual total; those from October to April to only 12% of the annual total.

The vertical intake (Tyrolian weir) has a capacity of 16 m^3/s and is covered by an inclined steel rack with a bar spacing of 85 mm. From the intake, the water flows to underground gravel and sand traps (Figure B-2 in Appendix B). The sand trap is a 50 m-long basin

designed to exclude sediment grains larger than 0.3 mm. It has a sand evacuation system of the type Hochschule Rapperswil (HSR) which allows effective flushing without water level drawdown. The sand-water mixture enters two submerged pipes through many asymmetrically placed inlets, which creates a vortex flow with high sediment transport capacity.

A free-surface flow tunnel connects the headworks with the valve chamber. The tunnel with a length of 2 km, a width of 8 m and an archway cross-section serves for mainly intra-daily balancing of inflows and energy demand. With a water level variation of up to 4 m (between the nominal min. and max. operating level of 1639.00 and 1643.00 m a.s.l., respectively), the active storage volume is 64 000 m^3. This relatively small headwater storage would allow running the turbines at Q_d for only ~1 hour if there is no inflow. From the valve chamber, a buried penstock with a length of 1350 m leads down to the powerhouse. The penstock's inner diameter decreases from 1.95 m to 1.65 m.

The HPP Fieschertal generates some 150 GWh/year, of which more than 80% during the summer season, when both turbines mostly run at full load. In the winter months, the inflow reduces to 0.15 m^3/s and one turbine is run at partial load for only a few hours a day. With a turbine water volume of ~130 Mio. m^3 per year, the average discharge is 4.2 m^3/s, corresponding to 28% of Q_d of the HPP (i.e. plant factor = 0.28).

3.3.2 Turbines

The two horizontal-axes Pelton turbines of HPP Fieschertal have identical design. Each turbine has two nozzles and one runner (Fig. B-5 in Appendix B). Each turbine has Q_d = 7.5 m^3/s, a rated power of 32 MW, and runs at n = 429 revolutions per minute (rpm). With the specified net head of 509 m, the specific speed is n_q = 7.74 rpm (Eq. 2-22a) and the dimensionless specific speed is n_{QE} = 0.0233 (Eq. 2-22b).

The diameter of the nozzle mouths is 290 mm, and the diameter of the jets d_0 = 228 mm at Q_d. All nozzles are equipped with jet deflectors. The lower nozzles have shields to reduce erosion on the main nozzle parts. The jet deflectors and the nozzle shields are uncoated and made of steel with lower erosion resistance compared to the runners. The inspection and maintenance platforms (gratings) below the runners are made of usual, mild construction steel.

The runners have a pitch circle diameter D = 2090 mm, an outer diameter of 2790 mm, and a mass of 8.5 t. Each runner has z_2 = 20 buckets with an inner width B = 650 mm, i.e. D/B = 3.2. There are four runners which are by turns either in the turbine housing

(for operation and during on-site revisions), in the factory (for major overhauls), or in the machine hall (spare runners). These runners were manufactured in the 1970's and 1980's, and have undergone several major overhauls. Since about 2005, WC-CoCr coating has been applied inside the buckets. The needle tips and the needle tip rings have also been hard-coated.

At HPP Fieschertal, the two nozzles are operated at the same degree of opening also at low partial load (except for start-up periods). This operation mode was adopted to avoid erosion damages between the needle tips and their seat rings of a closed nozzle. Such damage occurred in earlier years due to high-speed leakage flow if a nozzle did not close perfectly or has been previously eroded. During standstill of an MG, its upstream spherical valve is closed and potentially imperfect closure of nozzles is of no concern.

3.3.3 Existing instrumentation

The HPP Fieschertal is equipped with a comprehensive measurement and control system. The main instrumentation which is relevant for the determination of the sediment loads and the turbine efficiency is summarized in Table 3-3:

Table 3-3 Pre-existing relevant instrumentation in the HPP Fieschertal.

Measured quantity	Location	Measurement Principle/Type	Instrument, Manufacturer	Variable name
Discharge [m^3/s]	At the weir at the end of the sand trap (see Figs. 3-6 and B-2)	Stage-discharge relation	Pressure gauge	Q_1
Discharge [m^3/s]	At the upper end of the penstock (see Figs. 3-6 and B-4)	ADM (4 path), inside-mount	*Risonic* * Rittmeyer	Q_2
Discharge [m^3/s]	At the lower end of the penstock, upstream of the bifurcation (see Fig. 3-6)	ADM (2 path), clamp-on	*Prosonic 93 PA2* Endress+Hauser	Q_4
Electric output [MW]	At generator terminals of each MG (i = 1, 2) (see Fig. B-5)	Active power	*Sineax M563* Camille Bauer	$P_{el,i}$
Needle position [%]	At each nozzle j = 1, 2 of each turbine i = 1, 2 (see Fig. B-5)	Angular position of actuator **	*Kinax WT707* Camille Bauer	$s_{n,i,j}$
Head water level [m a.s.l.]	In tunnel in front of the intake to the penstock (see Figs. 3-6 and B-4)	Measured via pressure	*Differential 1151* * Rosemount	Z_1
Static pressure [Pa]	Upstream of the spherical valve of each turbine i = 1, 2 (see Fig. B-5)	For net heads	*Gauge 2088* * Rosemount	p_i

* These instruments are the same as used for *SSC* measurements (Table 3-1).

** Converted to relative needle position (stroke): 0% = nozzle closed, 100% = nozzle fully open.

3.3.4 Operation experience

The turbine water in the HPP Fieschertal originates from a glaciated catchment and is known for relatively high *SSC* in the so-called sediment season (SS). In earlier studies or during earlier flood events, *SSC* were occasionally measured by filtration and gravimetry, or by Imhoff cone. According to 265 *SSC* measurements made by the operator in the years 1992 to 2008 (with 0 to 91 samples per year, probably from the tailwater channels) the volumetric sediment concentration was 0.4 ml/l on average and max. 34 ml/l. With an estimated density of unconsolidated sediments of 1.8 g/cm^3, these values correspond to *SSC* = 0.7 and 61 g/l, respectively. The value of 0.7 g/l lies probably above the time-averaged *SSC* because samples were mainly taken at high *SSC*. These measurements showed a high variability of *SSC* even within hours and the need for continuous measurements for a more accurate determination of the sediment loads.

Based on the decreasing annual number of gravel and sand trap flushings in the last 10 to 20 years, the operator noticed a decrease in the coarse sediment load at the intake. This is seen as a temporary effect of the glacier retreat: a greater part of the coarse sediment is probably trapped in the glacier foreland upstream of the intake until these storage areas are filled. The fine sediment load, however, is less affected by this.

A part of the sediment which passes the sand trap accumulates in the storage tunnel if the tunnel water level is high and thus the flow velocity is low. Sediment deposits in the first half of the tunnel (Figure B-3) were usually conveyed back to the river by flushing up to three times per year. In the year 2014 no such flushing was performed mainly due to operational reasons.

Severe turbine erosion has been observed since the commissioning of the HPP in 1975. Although the application of hard-coating contributed significantly to reduce the extent of the erosion, damages cannot be fully prevented. In the years before and during the present study, no systematic turbine shutdowns in periods of high erosion potential were practiced. The HPP operator, BKW (engineering of the hydro-electric equipment), specialists from Hochschule Luzern and other experts have been working on modifications in the turbine, the runner maintenance procedure, as well as on methods for turbine efficiency and *SSC* monitoring in the frame of previous projects.

3.3.5 Operation and refurbishment schedule of runners and nozzles

During the present research project, the runner in MG 1 was never changed, whereas three different runners were used in MG 2 (Fig. 3-5). The runner installed in MG 1 at the start

of the project was in as-new condition because it had undergone a major factory overhaul before. However, the runners no. 2 and 4 which were in operation in MG 2, have already been in operation for three seasons (after the last factory overhaul) when they were installed. Runner no. 3 has been installed after a factory overhaul which was less comprehensive than usual.

In MG 2, runner no. 2 had to be replaced by runner no. 3 on August 13, 2012, as a consequence of the major flood event on July 2 and 3, 2012 (Fig. 3-5). Runner no. 3 was replaced by runner no. 4 on February 21, 2014 due to a mechanical problem (crack close to a bucket root) not related to erosion. From Mai 23 to June 22, 2012, MG 2 was out of order for 30 days due to third-party damage on its high-voltage cable, while MG 1 was operated almost continuously at full load.

The actuators and positions sensors of the nozzles of both MGs were modified in winter/spring 2013 (triangles in Fig. 3-5).

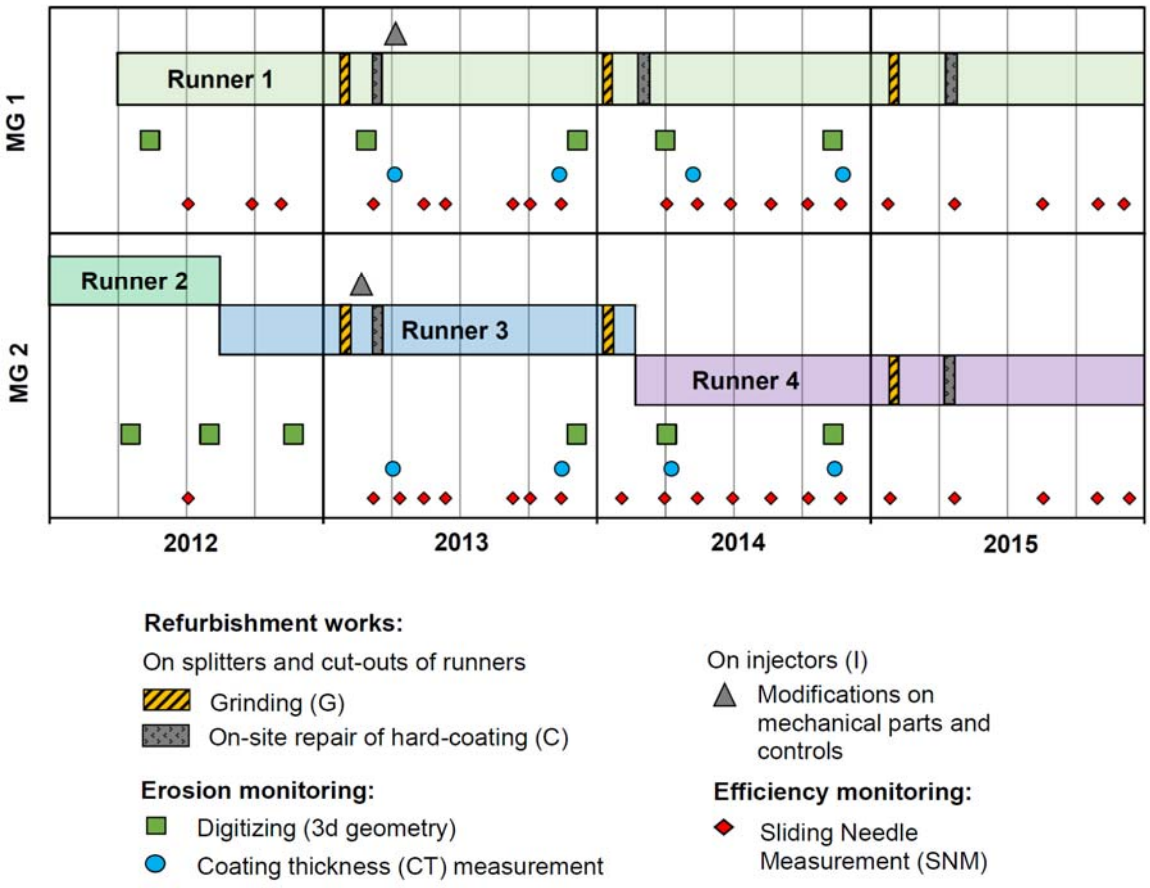

Figure 3-5 Schematic timeline showing the runners in operation, the revision works as well as the erosion and efficiency measurements for both MGs in the HPP Fieschertal.

At HPP Fieschertal, the crests of the splitters and the leading edges in the cut-outs of the runner buckets are usually partially or fully eroded after each sediment season. In winter, these parts are rounded by grinding if required, and the zones in which the coating had been lost are re-coated on site (directly in the turbine housing). Figure 3-5 also shows when these two types of revision works were done. The measurements for erosion and efficiency monitoring are treated in further Sections of this Chapter. The data acquisition period of the present study was from 2012 to 2014. The monitoring has been continued with a reduced measurement program in a follow-up project.

3.4 Suspended sediment monitoring at HPP Fieschertal (Task B)

3.4.1 Setup for SSM

3.4.1.1 Overview

After the laboratory investigations, the instruments for SSM listed in Table 3-1 were installed at the HPP Fieschertal (Fig. 3-6) at the intake, in the valve chamber, and in the powerhouse. Most of the instruments have been operational *in-situ* since the end of June 2012, whereas items (1), (5) and (8) have been taken into service in early summer 2013. The pressure transmitters (9) and the ADM installation (7) have already been in place before the start of the project.

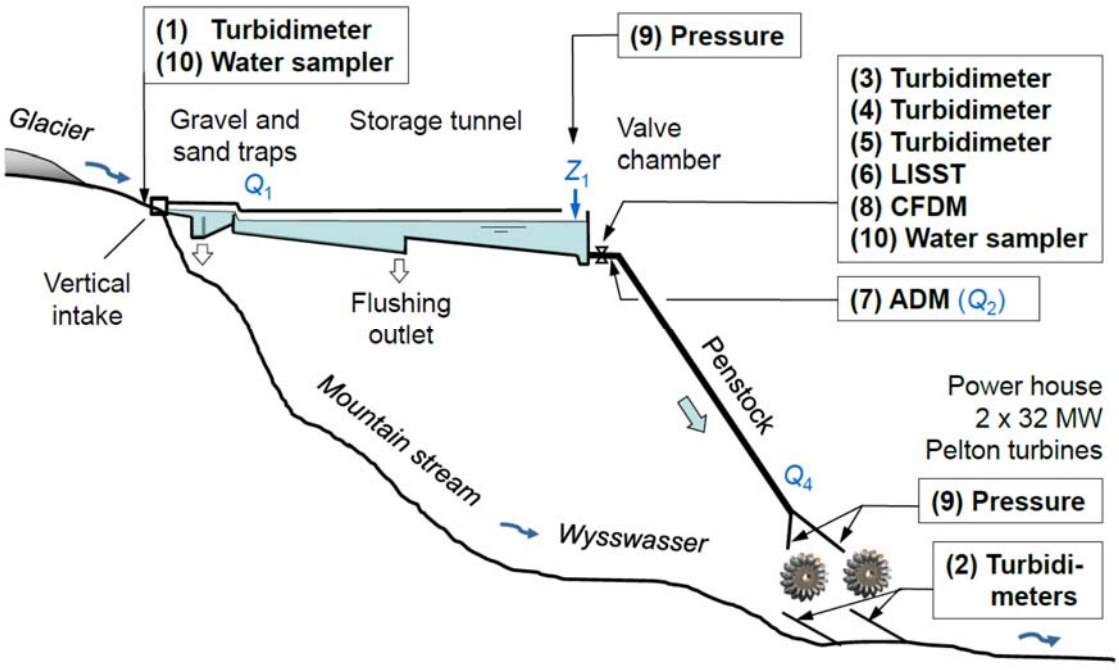

Figure 3-6 Schematic longitudinal profile of HPP Fieschertal with instruments for SSM; the numbers and the variables refer to Tables 3-1 and 3-3, respectively (modified from Felix *et al.* 2016c).

3.4.1.2 Valve chamber

The valve chamber was selected as the main location for SSM for the following reasons:

- For the investigation of turbine erosion, the sediment in the penstock shall be monitored, which may differ from that in the river or at the end of the sand trap;
- At this location no special provisions for handling of high pressure are required (in contrast to the upstream side of the turbines in the powerhouse);
- Downstream of the turbines, air bubbles might disturb the measurements;
- In the present HPP, a SSM installation was easier to realize along the penstock than in the two tailwater channels.

Because it was assumed that the effect of potential particle fragmentation during the turbine passage on PSDs is low (Blaser & Bühler 2001), this was not a decisive argument for the selection of the main measuring location.

In the valve chamber (Fig. B-4 in Appendix B), a sampling pipe protruding by 10 cm into the penstock at the elevation of its axis (detail in Fig. 3-7) was already in place from a previous study (Abgottspon 2011).

The water was conveyed from the penstock to the instruments by the pipe arrangement shown in Figure 3-7. First, the water flows through the CFDM (8), mounted vertically to reduce sediment deposits in the tube bends inside the device (Fig. 3-8a). Then, about two thirds of the sampling pipe discharge flows through the pressurized in-line turbidimeters (3) and (4). The remaining third of the discharge flows through the turbidimeter measuring at the free-falling-jet (5). To avoid bias of *SSC*, the pipe bifurcation was made in such a way that the angles were equal and the branches' cross-sections were proportional to the flow rates (isokinetic).

The measuring head of the LISST (6) was laterally inserted into a bucket with an overflow and a bottom outlet (Fig. 3-8b). The optical path of the LISST was placed immediately below the outlet of the hose at the end of the main sampling line. The outlet of the bucket was partially open to allow continuous sediment evacuation. Since 2014 the bucket has been covered with a black plastic sheet to prevent potential effects of ambient light on the LISST measurements.

No air bubbles which would bias the measurements were observed in the sampling pipe. No provision to prevent clogging of the CFDM was required because the sediment particles at the measuring location ($\leq$ 0.3 mm) were much smaller than the internal diameter of the CFDM's measuring tubes (8 mm) and there was practically no floating debris.

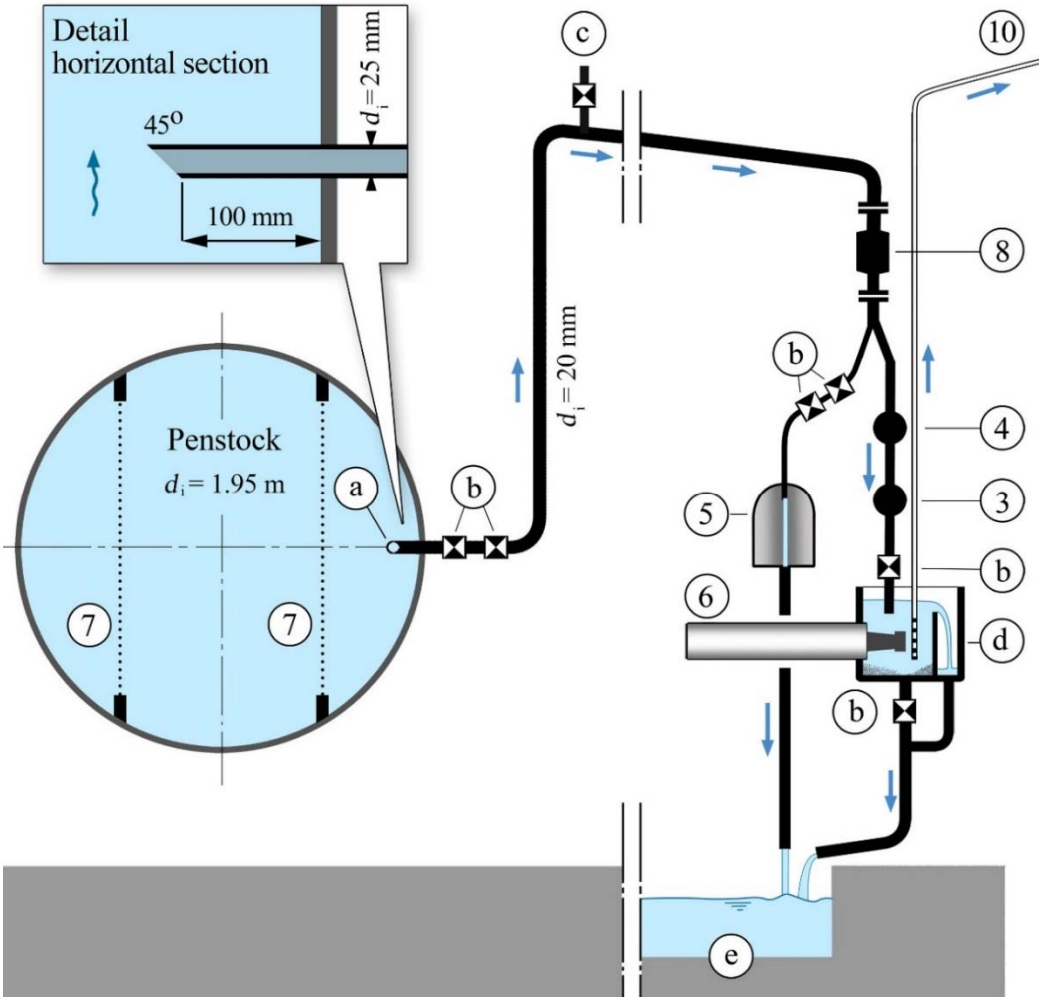

Figure 3-7 Vertical section of the setup for SSM in the valve chamber of HPP Fieschertal; numbers refer to instruments in Table 3-1, a) inlet, b) ball valves, c) de-aeration, d) bucket, e) pump sump (modified from Felix *et al.* 2016c).

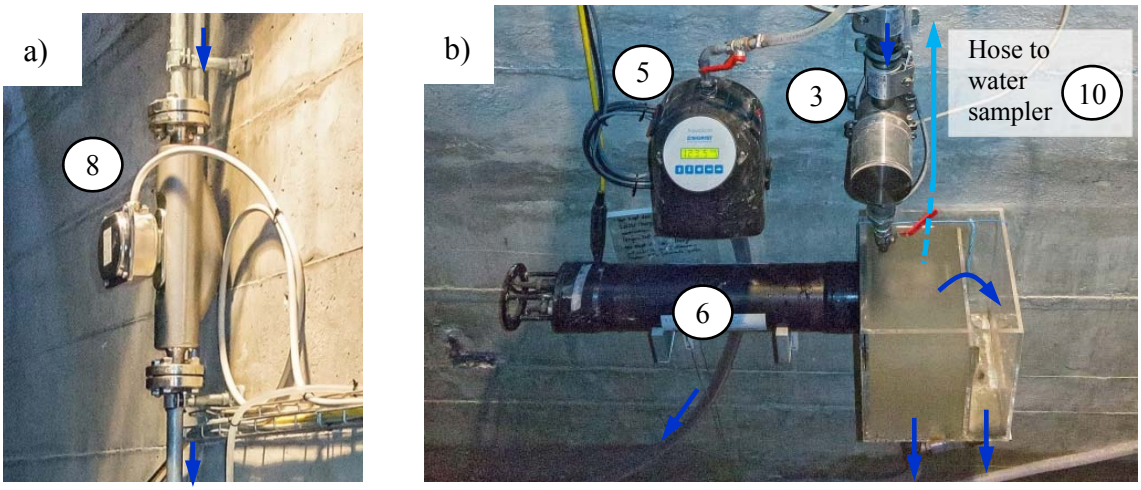

Figure 3-8 Instruments for SSM in the valve chamber of HPP Fieschertal: a) CFDM, b) two in-line turbidimeters and the LISST (numbers refer to Table 3-1).

The end of the aspiration hose of the automatic water sampler (10) was placed in the bucket. The strainer with lateral holes had a front cap to prevent aspiration of sediment deposits. The sampler was controlled by an auxiliary software (developed in this project) running at the local measurement computer. The software allows sending impulses for sample pumping in fixed time intervals and additionally if *SSC* is high (event-based). Initially, turbidity served as trigger signal. After positive operation experience with the CFDM, the mixture density has been used as trigger since autumn 2013.

The discharges in the sampling pipes were regulated by ball valves at their outlets. In the main pipe, a minimum discharge of 0.15 l/s corresponding to a flow velocity ≥ 0.5 m/s was selected to prevent settling of particles in the sampling pipe. With constant valve positions, the discharge in the main sampling pipe increased to 0.25 l/s when the water level in the tunnel was at its maximum. The flow time in the 5.5 m long sampling pipe was about 10 seconds. With a water volume of seven litres in the bucket, the average residence time of the water in the bucket was about one minute.

In spring 2014, the turbidimeter (3) was removed because it was not practical in the present application (signal drift due to fouling, flushing of the sampling pipe was not sufficient for cleaning, manual cleaning of the flow cell required temporary dewatering). A hose was placed instead, giving the additional possibility to manually take bottle samples directly at the outlet of the sampling pipe.

The ADM (Q_2 in Table 3-3) is located in the penstock ~28 m downstream of its inlet (Fig. B-4 in Appendix B). The four paths lie in two vertical planes parallel to the main flow direction, ±0.48 m off the penstock axis (Fig. 3-7). In each plane, two paths are arranged at ±45° from the horizontal (so-called '2E4P' arrangement). The path length is 2.27 m, i.e. 31% longer than that in the laboratory investigation. The 1 MHz transducers are of the same type as those used in the laboratory.

3.4.1.3 Intake

A submersible turbidimeter (item 1 in Table 3-1) was installed in the river *Wysswasser* at the intake in spring 2013, and a turbidimeter *CUS51D* (Endress+Hauser) was added at the end of the sand trap in spring 2014. A second water sampler was operated in 2013 at the intake before it has been moved to the end of the sand trap. Moreover, an air temperature sensor and three radar level gauges (*VegaPuls WL 61*) for the water level upstream of the intake were installed. The latter serve for the determination of the river's natural discharge if it exceeds the HPP's intake capacity.

The turbidimeter at the intake was mounted vertically in a perforated protection pipe on the right abutment upstream of the weir sill (Figure B-2). The measuring head of the turbidimeter was installed 0.15 m below the minimum water level, i.e. about 0.2 m above the river bed. The task of this turbidimeter is to provide information on the natural *SSC*, also in periods when the intake is closed due to floods or revision works. The turbidimeter at the end of the sand trap (Figure B-2) is less exposed to natural hazards.

In typical summer conditions, i.e. when the storage tunnel is full and both MG are operated at full load, the flow velocity in the storage tunnel is about 0.5 m/s. Therefore, both turbidimeters in the intake area (i.e. in the river and at the end of the sand trap) allow detecting high *SSC* approximately one hour before the water enters the penstock.

3.4.1.4 Powerhouse

The two other submersible turbidimeters (items 2 in Table 3-1) were installed in the powerhouse, as foreseen in a previous project: at each turbine, one turbidimeter was mounted in a bucket with an overflow and a small bottom outlet. The buckets have been alimented with raw cooling water pumped from pits in the tailwater channels when the respective turbine is running. An advantage of this sampling location is easy access for maintenance and manual sampling; drawbacks are mainly no pre-warning time for high *SSC* in the turbines and the potentially non-representative sampling due to the existing intake arrangement of the cooling water system.

3.4.2 Data acquisition and general data treatment

At each of the three measuring locations, a compact fan-less computer (*AD Matrix MXE1010*) with a data acquisition board for analogue signals (as in the laboratory investigations) has been installed. The data acquisition system with internet connection was designed to be independent of the HPP's measuring and control system.

The output signals of the instruments for continuous SSM (Table 3-1) and those from the other instruments (Table 3-3) have been recorded at 1 Hz, basically since the end of June 2012. In 2012, the LISST was programmed to take one measurement per minute. Since 2013, it has been set to execute one burst per minute (10 measurements at 1 Hz followed by a break of 50 s).

At the intake and in the valve chamber, water samples of 0.5 l were automatically taken every three to five days, or more frequently if the trigger signals exceeded predefined

threshold values for five minutes. In the powerhouse, occasional water samples were manually taken.

The turbidimeters at the intake and in the powerhouse (items 1 and 2 in Table 3-1) were automatically cleaned with wipers whereas pressurized air purges were used at the turbidimeter at the end of the sand trap. For the LISST and the other turbidimeters, their optical parts in contact with the water were manually cleaned every one to two months. Sediment deposits in buckets and clogged sampling pipes were cleared repeatedly. The flow rate in the sampling pipe in the valve chamber measured by the CFDM was monitored from remote to detect potential clogging and the need for flushing. In the winter months, when the water was clear and *SSC* was not significant for turbine erosion, SSM was paused, except for the ADM which is in operation for discharge measurement anyway.

The measuring system and the data acquisition were improved mainly in the first two years. For the present investigation, the SSM data until the end of 2014 are evaluated. An overview on the data acquired in the valve chamber is given in Figure C-1 in Appendix C1. SSM has been continued in a follow-up project.

LISST raw data were inverted with IMR (Section 2.2.1.6). From the recorded data, minute-by-minute averages were computed. Invalid data, e.g. due to clogging of sampling pipes, instrument failures or power outages, were identified and discarded based on the field protocols and inspection of time series.

3.4.3 Laboratory analyses

From 285 water samples collected in the years 2012 to 2014, the *SSC* were determined in the laboratory by gravimetrical analysis, as described in Section 3.2.6. According to some clear water samples, the concentration of dissolved minerals was ≤ 0.08 g/l.

In addition, the following laboratory analyses were made by the Institutes for Geotechnical Engineering (IGT) and for Building Materials (IfB) of ETH Zürich on dried particle material collected from HPP Fieschertal:

- Solid density (Helium pycnometer, n = 12 samples);
- Quantitative mineralogical composition (X-ray Rietveld diffraction, n = 3);
- Microscopic images (Scanning Electron Microscope, n = 1).

3.4.4 Conversion of the instruments' outputs to *SSC*

3.4.4.1 General

The gravimetrical *SSC* were used as primary reference to convert the instruments' outputs in various units (Table 3-1) to *SSC*. Due to the scarcity of gravimetrical *SSC* above a few g/l, and the relatively low measurement uncertainty of the CFDM technique (as will be shown in Chapter 5), *SSC* obtained from CFDM were also used as a reference for the evaluation of turbidity, LISST and acoustic data, especially at higher *SSC*. Using the *SSC* from CFDM had the advantage that far more data points (> 20 000 per year) were available than from the bottle samples (< 115 samples per year). Note that the gravimetrical *SSC* were used to evaluate the *SSC* from CFDM.

The conversions from the instruments' outputs to *SSC* time series can also be called 'field calibrations' in the wider sense of the word. In the following, these conversions are described for each employed measuring technique.

3.4.4.2 From turbidity to SSC

Turbidity values measured at corresponding times of the bottle samples were plotted as a function of gravimetrical *SSC*. Linear relations were fitted to these data. In the absence of fouling, there is no offset and the result of the fit is a conversion factor. Turbidity data were de-trended if they were affected by fouling and used for further analysis.

3.4.4.3 From acoustic damping to SSC

The damping δ was computed from the measured amplitudes according to Equation (3-1). For each path, the clear water amplitudes A_w were determined as averages in the winter months. The measurements of path no. 2 were discarded because they were affected by a temporally varying offset (probably related to a physical alteration of one of the corresponding transducers). The simultaneous δ-values of the other three paths were averaged and low-pass filtered to reduce noise while maintaining peak values which are of interest in the present study. Similar to turbidimeters, the δ-values were plotted against gravimetrical *SSC* at corresponding times. For conversion of δ to *SSC*, a linear regression was used. Slightly negative *SSC*, which resulted in periods of low *SSC* due to the measurement uncertainty, were set to zero.

3.4.4.4 From LISST volume concentrations to SSC

As a first step of LISST data treatment, the *BVC* were plotted as a function of time and checked for plausibility. Besides the concentrations in size bins well within the LISST's size-measuring range, there were also relatively high concentrations in size bins (i) close to the lower end of the size-measuring range and (ii) sometimes towards its upper end.

Generally there were relatively high concentrations in bins no. 1 to 3 (1.9 to 3.1 µm) decreasing towards a local minimum in bin no. 4. As in the laboratory investigations (Felix *et al.* 2013a), the concentrations in bins no. 1 to 3 were judged to be implausible and were discarded. At the coarse end of the PSDs, the concentrations in the range of bins 25 to 32 (100 to 380 µm) gradually increased during some periods in late summer and autumn (Felix *et al.* 2017). Such implausible concentrations were attributed to fouling, e.g. deposition of larger particles (probably flocs) on the LISST's measuring windows, and were also disregarded in the further data evaluation.

As in the data evaluation of the laboratory measurements, the SSC_{L0} were computed based on *TVC* and ρ_s (Eq. 3-2). To compensate LISST's concentration overestimation for highly non-spherical particles, SSC_{L0} were corrected based on comparison to reference *SSC* from gravimetry and CFDM. SSC_{L1} and SSC_{L2} were obtained by applying a correction factor f_c which was either constant or a function of d_{50}, respectively.

3.4.4.5 From CFDM density to SSC

The *SSC* from the CFDM, termed SSC_C in the following, were determined based on the two measured time series of the mixture density $\rho_m(t)$ and the water temperature $T(t)$ as well as the gravimetric reference *SSC* using Equation (3-3). This equation (except for K) was derived from the definition of *SSC* (Section 2.1.4.1) and is also found in the literature (Morris & Fan 1998). A site-specific and seasonally variable minor offset $K(t)$ was introduced to compensate density offsets due to (i) dissolved substances, (ii) variable biofilm and/or particle deposits inside the measuring tubes, and (iii) potential deviations of the on-site conditions from those at the calibration facility in the factory.

$$SSC_C = \frac{\rho_m(t) - \rho_w(T(t))}{1 - \frac{\rho_w(T(t))}{\rho_s}} + K(t) \approx 1.6\,[\rho_m(t) - \rho_w(T(t))] + K(t) \qquad [\text{g/l}] \qquad (3\text{-}3)$$

The clear water density ρ_w was calculated as a function of the temperature $T(t)$ (Tanaka *et al.* 2001). From the pycnometer measurements, $\rho_s = 2.73$ g/cm^3 was taken as a constant. $K(t)$ was determined by comparing the preliminary SSC_C with the gravimetrical *SSC*. This

corresponds to a periodic *in-situ* calibration. The highest density offsets to be compensated were in autumns 2013 and 2014, and corresponded to an *SSC* difference of ≤ 0.6 g/l. These gradually increasing slight density offsets were attributed to biofilm growth inside the CFDM and correlated with the longer residence time and the higher temperature of the water in the storage tunnel in autumn (Meister 2014, Felix *et al.* 2016g).

The water temperature in the CFDM ranged between 0.1 and 6 °C, leading to a variation of the clear water density by < 0.13 g/l. According to Equation (3-3), this corresponds to a *SSC*-variation < 0.21 g/l.

3.4.4.6 From pressure signals to SSC

As a further technique, *SSC* were determined from pressure and auxiliary measurement signals from the HPP's control system. These *SSC*, termed SSC_P, were determined according to the following steps (Felix *et al.* 2016c):

- Discarding of temporarily implausible pressure measurements;
- Comparison of pressure and head water level measurements in periods of clear water and no flow, and minor correction of pressure data by a scaling factor;
- Determination of the head losses in the penstock as a function of the discharge and the operation mode (one or both turbines running) based on measurements;
- Identification of quasi-steady state periods by analysing the discharge variation;
- Calculation of the density of the sediment-water mixture in the penstock at every time step in quasi-steady-state periods, based on head water level, discharge and pressure measurements and considering the head losses;
- Conversion of the mixture densities to *SSC* according to Equation (3-3) with $K(t) = 0$ (because the pressure data were corrected previously).

3.4.5 Continuous time series of *SSC*, d_{50} and fraction-wise *SSC*

3.4.5.1 Time series of SSC

From the several *SSC* time series obtained from the various measuring techniques, a continuous *SSC* time series covering the years 2012 to 2014 was compiled according to the following order of preferences:

- CFDM if SSC_C was available and > 1 g/l, otherwise
- Pressure-based technique, if SSC_P was available and > 2 g/l, otherwise
- LISST if available and plausible, otherwise
- Turbidimeter (*AquaScat*) if available, otherwise
- Acoustic technique (was always available).

The resulting time series was termed SSC_B, standing for 'best estimate' *SSC*. SSC_P were included in SSC_B only during the major flood event on July 2 and 3, 2012, when the CFDM had not been installed yet.

3.4.5.2 Time series of d_{50}

The time series of the median particle size d_{50} was determined basically from the plausible LISST data by interpolation on the *BVC*. In periods with no LISST data within the sediment season, d_{50} was estimated as follows:

- The *SSC* obtained from CFDM density or from pressure, i.e. SSC_C and SSC_P, depend not – or less – on the particle sizes than the *SSC* from turbidity or the acoustic technique, i.e. SSC_T and SSC_A. Hence the ratio between a *SSC* of the second group and a *SSC* of the first group depends on the particle sizes.
- Correlations between either SSC_T / SSC_C, SSC_A / SSC_C, SSC_T / SSC_P or SSC_A / SSC_P and d_{50} were established in periods when LISST data were available. Such correlations will be shown in Figure 5-19.
- In periods without LISST data, the d_{50} was estimated based on such correlations and available SSC_T, SSC_A, SSC_C and/or SSC_P.

In winter, when the *SSC* and the discharge were low, and the suspended sediment monitoring was paused except for the acoustic technique, a d_{50}-value in the range of medium silt was assumed, as typically measured in late autumn.

3.4.5.3 Time series of fraction-wise SSC

The SSC_B time series was split-up in five particle size classes with the limits of 3, 20, 50, 100, 200 and 380 µm. Such *SSC* are termed fraction-wise *SSC*, because particles of given size classes are also called fractions. The percentages of the *SSC* per size class were computed based on the plausible LISST data when available, otherwise on estimated d_{50} and site-specific correlations. These correlations described the probable percentages of *SSC* per size class as a function of d_{50}. The correlations were stablished in periods when plausible LISST data were available.

3.4.6 Computation of *SSL* and *PL* per turbine

3.4.6.1 Suspended sediment load (SSL)

The suspended sediment load $SSL(t)$ is the suspended sediment mass transported through the penstock or through a turbine from the start time t_0 (beginning of the observation period or of a single year) until the time t. $SSL(t)$ results from integrating the Suspended

Sediment transport Rate $SSR = Q \cdot SSC$ (Eq. 2-15) over time. A constant time step of $\Delta t = 1$ minute was used; i denotes the time step number.

$$SSL(t) = \sum_{i=1}^{(t-t_0)/\Delta t} Q_i \; SSC_i \; \Delta t \quad = \Delta t \sum_{i=1}^{(t-t_0)/\Delta t} Q_i \; SSC_i \qquad [\mathrm{t}] \qquad (3\text{-}4)$$

3.4.6.2 Particle load (PL)

The definition of $PL(t)$ is given in Equation (2-30). The factors k_{hardness} and k_{shape} were assumed to be constant over time (properties of the catchment area). Therefore, these factors were placed in front of the sum in Equation (3-5):

$$PL(t) = \Delta t \; k_{\mathrm{hardness}} \; k_{\mathrm{shape}} \sum_{i=1}^{(t-t_0)/\Delta t} \sum_{j=1}^{5} k_{\mathrm{size},j} \; SSC_{ij} \qquad [\mathrm{h \cdot g/l}] \qquad (3\text{-}5)$$

The product of $k_{\mathrm{size,i}}$ and SSC_{i} in Equation (2-30) was calculated at each time step with the second sum in Equation (3-5) based on the fraction-wise *SSC* in five particle size classes (j = 1 to 5) and the factors $k_{\mathrm{size,j}}$. These factors reflect the relative erosion rate *RER* of the particles in each size class (Section 2.3.4.5). The factors $k_{\mathrm{size},j}$ listed in Table 3-4 were determined from Figure 2-18 as average values within each size class. Note that $k_{\mathrm{size},j}$ are not comparable across the literature sources, because they do not have a common basis. The normalization of the *PL* obtained from the various sets of $k_{\mathrm{size},j}$ according to different literature sources is treated in Section 5.7.4.

Table 3-4 Relative erosion rates *RER* of the particles in five size classes ($k_{\mathrm{size},j}$) according to selected literature sources (compiled in Felix *et al.* 2016d).

Literature source	$k_{\mathrm{size},j}$ [-]				
Particle size class j [-]	1	2	3	4	5
Range of particle diameters d [µm]	3 – 20	20 – 50	50 – 100	100 – 200	200 – 380
a) Baseline case: constant	1.00	1.00	1.00	1.00	1.00
b) IEC 62364 (2013): linear	0.01	0.04	0.08	0.15	0.29
c) Sulzer Hydro (1996) / 10^6	0.21	0.79	1.20	0.99	0.81
d) Winkler *et al.* (2011a)	0.01	0.02	0.08	0.60	0.70

Out of the six literature sources for *RER* as a function of d summarized in Figure 2-18, the following approaches were not selected for the computation of *PL*:

- Nozaki (1990) proposed a linear relation as adopted in IEC 62364 (2013). Hence the *PL* obtained from these two approaches are proportional and lead to the same normalized *PL*.

- The smoothed *RER* according to Asarin *et al.* (2001) (dashed line in Fig. 2-18b) is also approximately linear.
- Bajracharya *et al.* (2008) do not provide information on the *RER* in the size-range of medium silt which is important for the present study.
- The *RER* according to Padhy & Saini (2009) is almost constant and hence close to the baseline case a) in Table 3-4.

The values of SSC_{ij} were set to zero when the respective turbine was not in operation (Section 2.3.6.1). In the calculation of the *SSL* and *PL* of each turbine, it was assumed that the *SSC* in all nozzles correspond to the *SSC* measured in the penstock.

3.4.7 Hydrological data

In addition to the field data acquired in this thesis, precipitation and discharge data were obtained from the Federal Office for Meteorology and Climatology (MeteoSwiss 2014) and the Federal Office for the Environment (FOEN 2014), respectively:

- Daily precipitation heights in Fieschertal at 1095 m a.s.l. (0.5 km from the powerhouse, measured between 06:40 CET and 06:40 on the next day);
- Hourly discharges of the *Massa* River downstream of the *Aletschgletscher* (adjacent to the *Fieschergletscher*) as well as of the upper *Rhone* River in Reckingen and in Brig (up- and downstream of the *Wysswasser* confluence, respectively).

These hydrological data were consulted in the evaluation of the SSM data (e.g. causes for *SSC* peaks, return periods of flood events, etc.). Except for historical data (1904-1913), no discharge measurements in the *Wysswasser* are available from FOEN. From weather stations at higher elevations (*Konkordiahütte* or *Eggishorn*), precipitation data are either not available, incomplete or biased due to wind.

3.5 Turbine erosion monitoring in HPP Fieschertal (Task C)

3.5.1 Coating thickness measurements

3.5.1.1 Data acquisition

The local coating thicknesses (*CT*) in the buckets no. 1 and 2 of the Pelton runners in both MGs of HPP Fieschertal were systematically measured before and after the sediment seasons 2013 and 2014 (see Figure 3-5). Further *CT* measurements were made in the right halves of the buckets no. 1 and 2 of the damaged runner which was taken out of service from MG 2 on 13.08.2012. A hand-held inductive *CT* meter (*Deltascope FMP 30* from Helmut Fischer AG) with a dual-tip probe (*V7FKB4*) was used (Fig. 3-9a). According to

the supplier, this type of probe is more suitable for measurements on rough surfaces (such as WC-CoCr) than a single-tip probe.

For the positioning of the probe inside the buckets, two 3D-templates (Fig. 3-9b) were made in late autumn 2012. Each template for a half-bucket had 152 measuring points, i.e. perforations with a spacing of ≤ 40 mm between their centres. The repeatability of the probe's positioning was observed to be ±0.5 cm in buckets of various runners with different erosion status and revision history.

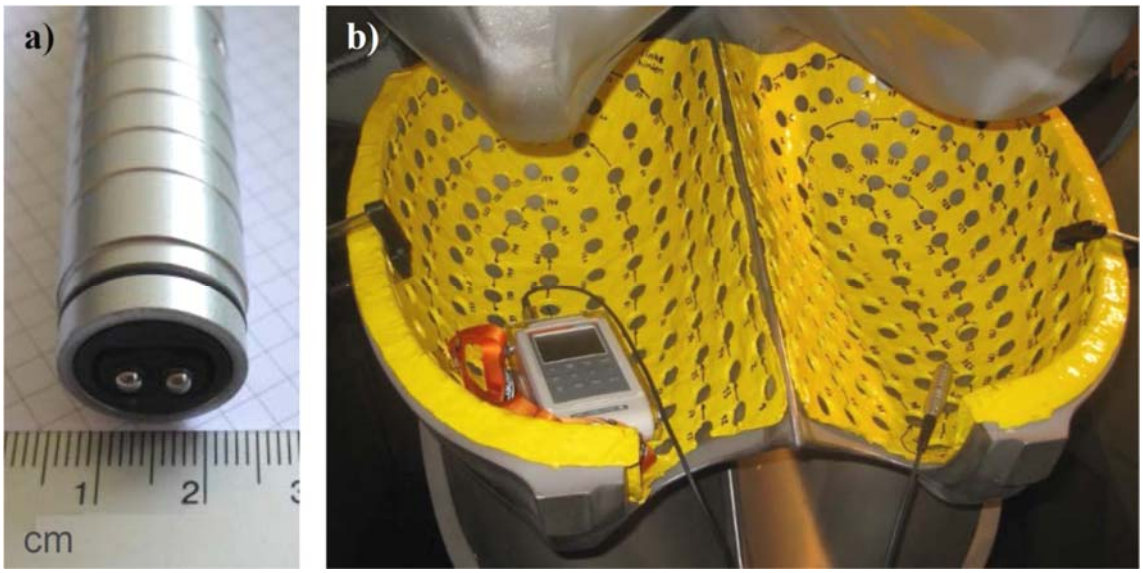

Figure 3-9 a) Detail of the dual-tip probe of the coating thickness meter and b) 3D-templates for the measurements in Pelton buckets in the HPP Fieschertal.

The *CT* meter was calibrated on uncoated, even and smooth locations of the buckets, first without and then with a plastic sheet of known thickness (239 µm) placed beneath the probe tip. This two-point calibration of the instrument was kept during the measurements in this study. To validate the calibration and to check the long-term stability of the thickness meter, reference measurements without and with plastic sheets (9, 125, 239, 286 and 782 µm) were made at the beginning and the end of each measurement campaign on each runner. The systematic *CT* measurements in two buckets of one runner required approximately one working day on site.

According to the specifications of the manufacturer, the accuracy of single *CT* measurements between 100 and 1500 µm is ±1% under favourable conditions and with calibration on the respective base material. Favourable conditions encompass flat, smooth and hard surfaces with *CT* not varying in space, sufficient base material thickness and distance

from edges, and perpendicular positioning of the probe with defined force. In *CT* measurements at Pelton buckets, however, the measurement uncertainty is higher because some of these conditions are not fully met.

On the hard-coated needle tips of the nozzles, *CT* measurements were not possible because the base material was not magnetisable enough.

3.5.1.2 Data evaluation

At each measurement location (i.e. perforation in the template), the average and the standard deviation of the $n = 10$ single *CT* measurements were computed after rejection of outliers (Grubbs 1969). If the standard deviation was >7 µm, the average *CT* value at the respective location was discarded. From four measurement campaigns over two years, local and bucket-averaged *CT* differences were evaluated.

The repeated reference measurements showed that the probe tips were abraded by ~1 µm during the measurements in each half-bucket, i.e. after placing the steel probe 1520 times on the hard-coating with the rough surface. The total abrasion of about 40 µm by the end of 2014 became also visible as a flattening of the formerly semi-spherical probe tips. The erosion of the probe tips was compensated in the data evaluation.

3.5.2 3D-survey by structured-light digitizing system

3.5.2.1 Data acquisition

The 3D-geometries of selected Pelton buckets were repeatedly measured from spring 2012 until November 2014 (see Figure 3-5) by HSLU in collaboration with VAW in order to quantify geometrical changes due to erosion and maintenance works. As for the *CT* measurements, the buckets no. 1 and 2 were measured. At MG 1, runner no. 1 was measured on five dates, while the runners no. 2 to 4 were measured twice each. In order to investigate the reproducibility of the surveying method, one bucket (no. 1 of MG 1) was measured twice on subsequent days in April 2014.

A 3D-optical digitizing system (*Comet L3D 5M*) manufactured by Steinbichler (since 2015: Carl Zeiss Optotechnik) was used. Its operation principle is based on structured-light projection and spatial triangulation (Fig. 3-10). The projector and the camera are combined in one device which is placed on a tripod in free positions at a distance of ~50 cm from the target surface (Fig. 3-11). The measuring system has a resolution of

5 million points per shot. With a target volume of 480 mm · 400 mm · 250 mm, the distance between surface points is thus on average 190 µm. Figure D-5b in Appendix D2 illustrates the high spatial resolution of the triangulated surface (point cloud).

To reduce glare, a whitening spray was applied on the inner and outer sides of the cleaned and dried buckets. Small circular stickers, so-called reference or matching points, were placed in irregular patterns (Fig. 3-11). Due to the geometric conditions (line-of-sight obstructions) and the relatively large size of the Pelton runners in the present case, about 75 shots from adequate angles were needed for one bucket (inside and outside). With the aid of the reference points and using the corresponding software, the partly overlapping single shots were assembled to 3D-models of two buckets per runner (Figure D-5a in Appendix D2). No measurements were possible inside optically hidden erosion features such as narrow and sharp-edged grooves or undercut holes.

The digitizing system has been calibrated and validated in the factory in front of a plate with a pattern of known size. The deviations between corresponding points in two single-shot validation measurements in the factory were only about 10 µm; up to 40 µm is within the specification of this system. After each transport of the digitizing system to the HPP, the validation measurement was repeated after the device has adapted to the prevailing air temperature.

The 3D-survey of two buckets of one runner required about two on-site working days of a two-man team. One person worked on the measurement laptop while the other adjusted the sensor's position and the illumination.

The 3D-models were evaluated and analysed by HSLU as described in the following. The evaluation procedures were developed by HSLU.

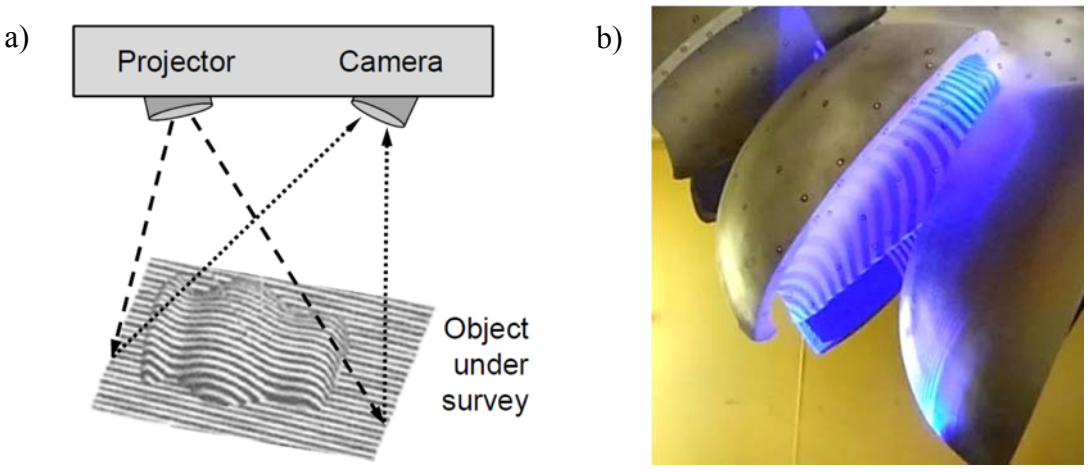

Figure 3-10 a) Working principle of the optical 3D-digitizing system (modified from Gorthi & Rastogi 2010) and b) structured-light projection in a Pelton bucket (HPP Fieschertal).

Figure 3-11 Surveying of the current geometry of selected Pelton runner buckets inside the turbine housing in HPP Fieschertal (Abgottspon *et al.* 2016a).

3.5.2.2 Definition of geometrical reference

As a preparation for the comparison of the repeatedly measured bucket geometries, a reproducible geometrical reference had to be defined. A local Cartesian coordinate system was placed in each bucket (Fig. 3-12): Firstly, the *xy*-plane (A) was set on the top of the outer bucket walls. Then surface B, which is the mid-plane of B1 and B2, served to define the origin of the *x*-coordinate. The origin of the *y*-coordinate was set at the outer radius r_a (Abgottspon *et al.* 2013b). These geometrical features are usually not affected by erosion or by maintenance works.

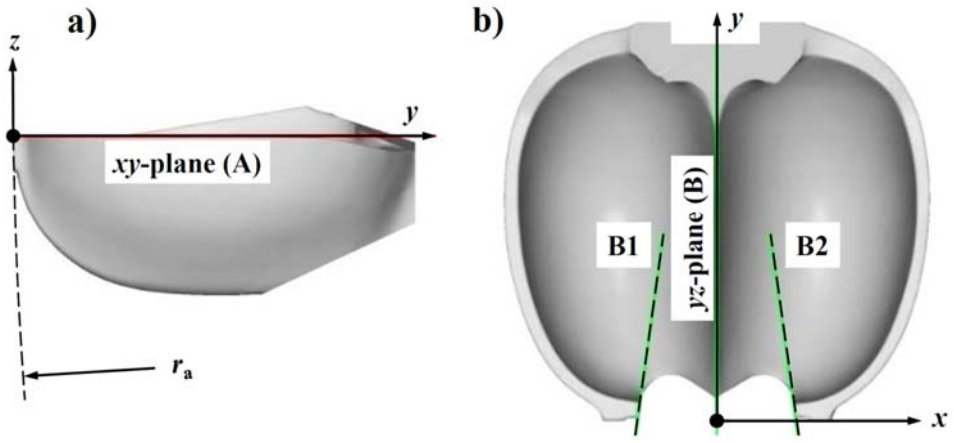

Figure 3-12 Definition of the local coordinate system for the Pelton buckets a) side view, b) top view (modified from Abgottspon *et al.* 2013b)

3.5.2.3 Determination of geometrical changes and volume differences

To quantify the erosion on the splitter crests and on the leading edges of the cut-outs, further geometrical definitions were introduced (Fig. 3-13): The splitter height from the reference crest line h, the splitter width s and the cut-out depth c. The width s of an eroded splitter is clearly defined if the splitter is flat on top and has sharp edges. The selected definition of s using the slopes of tangents according to Abgottspon *et al.* (2013b) allows determining s also for asymmetrically eroded or rounded crests, as shown in Figure D-6 in Appendix D2. The radial splitter tip position y_t is defined in Figure 2-27a. The Δy_t are the Δc in the runner's plane of symmetry ($x = 0$).

Various sections were generated from the 3D-models. From h, s and c computed from the survey results of several dates, the reduction of splitter height Δh, increase of splitter width Δs, increase of cut-out depth Δc and differences in radial splitter tip positions Δy_t were determined for the measured buckets in each year. Furthermore, volume differences on splitter crests and cut-outs were evaluated by comparison of 3D-models.

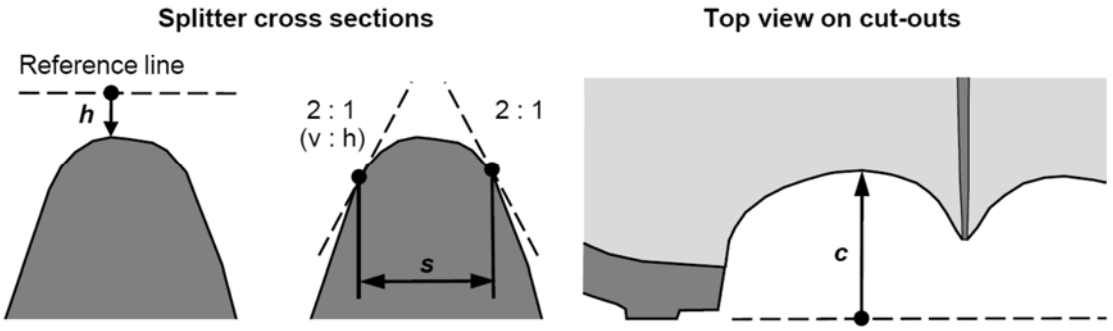

Figure 3-13 Geometrical definitions of splitter height from reference crest line h, splitter width s and cut-out depth c (modified from Abgottspon *et al.* 2013b and 2016b).

3.5.3 Further erosion monitoring

The turbines (runners, nozzles and deflectors) were inspected and documented by photographs during the 3D-survey and *CT*-measurement campaigns, as well as during flushing operations of the reservoir tunnel in August 2012, June 2013 and August 2013. In addition, splitter widths and the extent of local damages were measured during some inspections using a ruler.

3.6 Turbine efficiency monitoring in HPP Fieschertal (Task D)

3.6.1 Sliding-needle measurements (SNM)

3.6.1.1 Data acquisition

Index efficiencies of both MGs of HPP Fieschertal were repeatedly determined by SNM (Section 2.6.1.2). After preliminary tests in 2011, a few SNM were done in 2012. Then about six SNM per year were performed at each MG (Fig. 3-5). The SNM procedure, i.e. basically the gradual opening and closing of the nozzles (Fig. 3-14) was implemented in the HPP's control system. After the setup phase led by the HSLU and BKW engineering, the SNM were performed by the HPP operator and evaluated by HSLU.

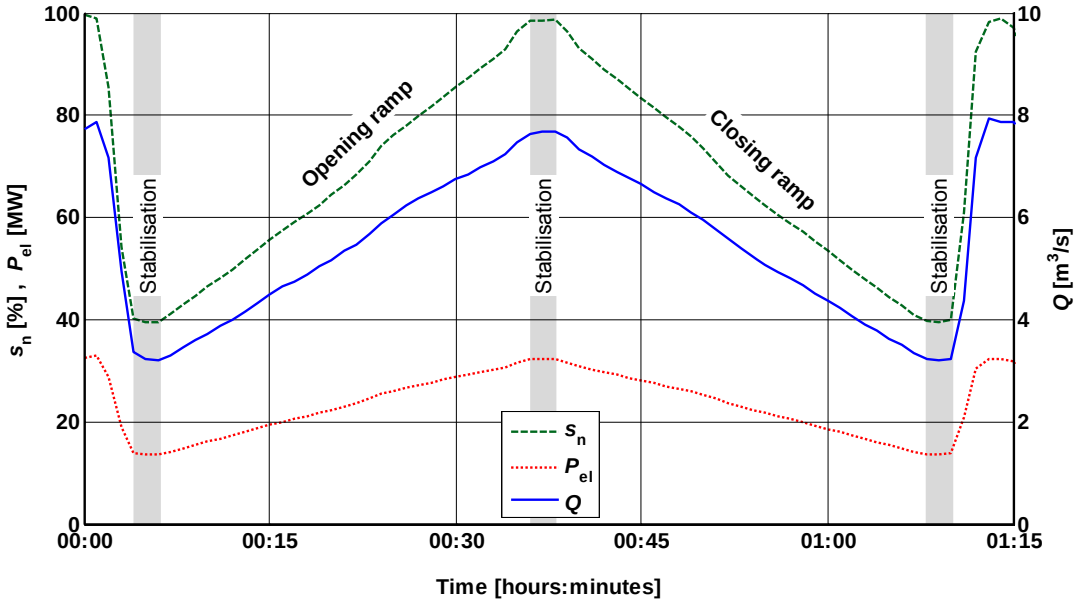

Figure 3-14 Time series of the needle positions s_n, electric active power P_{el} and turbine discharge Q during a SNM (example of MG 1 on June 27, 2014; modified from Abgottspon *et al.* 2013a).

In order to have discharge measurements from the ADMs, the SNM were performed running only one turbine at a time. To improve the quality of the SNM, the following initial conditions were introduced:

- The headwater level shall be at least 2 m above the minimum operation level in order to reduce potential biases in the discharge measurement Q_2 due to low inlet submergence;
- Flushing of the pressure measurement system at the respective MG;
- Run an MG for at least 10 minutes at the initial power level (at about 14 MW ≈ 45% of rated power) in order to stabilize the system before the test;

- In case of leakage flow through the nozzles, close the spherical valve upstream of the MG which is not measured.

During the SNM, the quantities listed in Table 3-3 were measured and recorded at 1 Hz. Typical time series of the needle positions (averaged for both nozzles of an MG), the discharge, and the electric active power are shown in Figure 3-14. The duration of a SNM was ~1 hour. The SNM were planned and announced in the production schedule some days in advance.

3.6.1.2 Determination of discharge

The main difficulty in the accurate determination of turbine efficiency is the measurement of discharge. In HPP Fieschertal, three possibilities are available:

- ADMs at the upper (Q_2) and lower end (Q_4) of the penstock (Fig. 3-6);
- Differential pressure transmitters at Venturi sections upstream of each turbine;
- Needle positions s_n of each nozzle (see Section 3.6.2.2).

Multi-path ADMs are the state-of-the-art system for discharge measurements in channels and penstocks with d_i greater than ~1 m. For the determination of the turbine discharge from a Venturi section, the pressure drop at the flow constriction is correlated to the discharge in the penstock measured with ADM while only one turbine is running.

The discharge measurements of the two ADMs were compared, also to other signals such as power outputs and headwater level. Q_2 was found to be less reliable than Q_4. A possible reason for this is that Q_2 is measured relatively close to the penstock inlet. Discharge measurements of ADMs close to inlets may be more uncertain due to spatial and temporal variations of the velocity field as well as air entrainment at low headwater level and high turbine discharge. Based on this evaluation, preference was given to Q_4. In HPP Fieschertal, the turbine discharges determined from the pressure measurements at the Venturi sections were found to be not reliable enough for efficiency monitoring.

3.6.1.3 Determination of hydraulic power

Another important parameter for the calculation of the hydraulic power in Equation (2-32) is the net head h_n. It is usually determined based on static pressure measurements upstream of the turbine, considering the kinetic energy head in the measuring section as well as the difference in elevation between the pressure sensor and the reference level of the turbine.

However, the evaluation of the pressure data showed that the pressure measurements were implausible or biased in some periods, and sometimes correct. This was mainly attributed

to full or partial clogging of the pressure measurement system by fine sediments. The pipes between the penstock and the transmitters as well as the pressure transmitters can be affected. With the existing system and the temporarily high *SSC*, it was recognized that the pressure data were not suitable for the reliable determination of the hydraulic power over years.

As an alternative, the hydraulic power was calculated from the net head h_n, which is the gross head ($Z_1 - Z_0$) minus the head losses $\Delta p/(\rho g)$:

$$h_{n,i}(t) = Z_1(t) - Z_0 - \frac{\Delta p_i(Q_4(t))}{\rho g} \quad \text{[m]} \qquad (3\text{-}6)$$

where $Z_1(t)$ = head water level at time t, Z_0 = 1123.86 m a.s.l. (average elevation of the intersections of the two jets with the pitch circle diameter), i = operation mode (1 for MG 1 or 2 for MG 2 running not simultaneously). The head losses were modelled as pressure drops [Pa] depending on the measured discharge [m^3/s]:

$$\Delta p_i(t) = C_i \; Q_4(t)^2 \quad \text{[Pa]} \qquad (3\text{-}7)$$

The coefficients C_1 = 797 and C_2 = 719 [kg/m^7] were calculated with a usual roughness inside the penstock (k_s = 0.05 mm) and estimated local losses. In addition, the Δp_i were determined from pressure and discharge measurements obtained during clear water conditions with properly working pressure transmitters (calibrated with the headwater level during no flow). A reasonable agreement was found between calculated and measured head losses. The procedure of calculating the net head instead of using pressure measurements was acceptable in the present case also due to the fact that the head losses in single-turbine operation are less than 1% of the gross head.

In the determination of the hydraulic power of the turbine (Eq. 2-32), the density of the sediment-water mixture ($>\rho_w$) was considered if the *SSC* exceeded 0.3 g/l. The error in turbine efficiency due to density variations is thus < 0.02%. The water temperature in the penstock during the SNM ranged only between 0 and 1 °C. Therefore, the effect of temperature on the density and the turbine efficiency is negligible (< 0.005%).

3.6.1.4 Determination of turbine index efficiency

To make efficiency curves measured at slightly different heads comparable, the electric power output P_{el} (x-axis) was scaled according to the similarity law (IEC 60193 1999)

$$P_{el,ref} = P_{el} \cdot \left(\frac{h_{n,ref}}{h_n} \right)^{1.5} \quad \text{[MW]} \qquad (3\text{-}8)$$

where $h_{n,ref}$ = 509 m is the specified net head (reference). The exponent of 1.5 considers that the power is proportional to both the head (h^1) and the flow rate; the latter is proportional to $h^{0.5}$ for Pelton turbines (Eq. 2-21).

The index efficiency as a function of the power output was calculated according to Equations (2-32) and (3-8) for each SNM. From each efficiency curve, a weighted index efficiency between 16 and 31 MW was calculated with equal weighing factors.

3.6.1.5 Determination of turbine efficiency changes

From weighted index efficiencies $\eta(t)$ at various dates for each MG, absolute differences were evaluated with respect to the initial efficiency η_0 serving as the reference:

$$\Delta\eta(t) = \eta(t) - \eta_0 \qquad [-] \qquad (3\text{-}9)$$

3.6.2 Continuous efficiency monitoring (CEM)

3.6.2.1 Data acquisition and plausibility checks

For CEM, the same signals were used as for the SNM (Table 3-3). These signals have been continuously measured and recorded at 1 Hz partly since July 2012 and fully since 2013. Before, data with a lower temporal resolution (five minutes) were obtained from the archive of the HPP's control system. Data evaluation and further development of the methods for the CEM were carried out by HSLU.

The plausibility of single signals (e.g. pressure) was checked by comparing them with the values computed from physically related signals (e.g. head water level and discharge). Such plausibility checks are elements of a so-called expert system.

3.6.2.2 Determination of discharge

If only one turbine was running, the discharge Q_4 measured in the penstock by the more reliable ADM was taken as the turbine discharge. With two MGs running simultaneously, the discharge of an MG had to be calculated based on the positions of its needles s_n using the latest s_n-Q-curve of this MG. The s_n is the average of the needle positions at the upper and the lower nozzle, which are operated similarly (Section 3.3.2). The s_n-Q-curves were obtained from measured s_n and Q_4 during each SNM which were performed when only one MG was running. The s_n-Q-curve of each MG may be altered due to erosion and revision works on the nozzles, as well as by modifications on their actuators and position sensors.

3.6.2.3 Steady state detection

Variations of discharge and turbine power lead to instationary phenomena (hydraulic transients), including pressure fluctuations (water hammer) in the penstock and surge (waves) in the headwater. The pressure fluctuations decay usually after some minutes and the upstream water level variations are relatively small in the present case (< 0.5 m in storage tunnel). To exclude data of such periods, a steady state detector was implemented. Out of three investigated options, i.e. adaptive moving average, variance and linear regression, the latter type was selected and applied to P_{el}. In a window of 30 values moving over the time series, the slope of a linear regression was calculated and it was evaluated wether it is plausible that the slope is zero. If this was not the case, the data of this period were discarded.

3.6.2.4 Further signal processing

Because efficiency differences of interest are relatively small (~0.1%) and expected to occur within days or longer periods, the measuring signals recorded at 1 Hz were time-averaged and filtered to reduce random fluctuations (noise). In steady state periods, the time series of P_{el}, Q and Z_1 were firstly smoothed with a moving average (window width = 150 values, i.e. 2.5 minutes) and then low-pass filtered to dampen high-frequency oscillations (half power frequency = 0.01 Hz, filter order = 1, no phase shift). The effect of these operations on examples of a discharge time series is illustrated in Figure E-1 in Appendix E.

3.6.2.5 Determination of turbine efficiency changes

For each data set measured at 1 Hz during steady state conditions, the index efficiency was evaluated using Equations (2-32) and (3-8). An averaged difference between these index efficiencies and those from the first SNM (reference curve) was evaluated for each day if at least 100 values per day were available. These daily averages of index efficiencies showed still considerable scatter which was reduced by applying an outlier filter. In this filter, the averages of the five previous and the five subsequent daily values are computed and compared to the current value. If the current value differed more than 0.1% from both averages of the five previous and the five subsequent values, it was discarded. This type of filter avoids removing points directly after sudden and remaining efficiency increases, e.g. due to grinding of splitters and cut-outs.

4 RESULTS AND DISCUSSION OF THE LABORATORY INVESTIGATIONS ON SSM (TASK A)

In this Chapter, the results of the laboratory investigations on the instruments for suspended sediment monitoring (SSM) are reported and discussed. Firstly, the results on PSD measurements (image analysis and laser diffraction) are treated, then the results on *SSC* (turbidimeters, acoustic technique and LISST). Finally, the normalized instrument outputs (sensitivities) are compared and experimental uncertainties are addressed.

4.1 PSD measurements

4.1.1 Image analysis

The longest, intermediate and shortest particle dimensions a, b and c (Section 2.1.2.2) obtained from image analysis for the particle types G, Q3, F and M according to Table 3-2 are listed in Table 4-1 and shown in Figure 4-1. The subscript denotes the mass percentage of particles having a smaller dimension. The particle sizes from image analysis were taken as references.

The fine sand (Q3) particles had close-to-spherical shape, similar to the 'irregular shaped' particles used by Agrawal *et al.* (2008) for the development of IMR. The feldspar powder (F) contained more elongated particles. For the mica particles (M), a and c differed considerably from b or d_{es} (volume-equivalent sphere diameter). The flake thickness was almost constant (~2 μm) and the median value of the aspect ratio c/b was only 0.11. Due to the high specific area and the grading of the mica particles, their *SMD* is about four times smaller than their $d_{es,50}$.

Table 4-1 Particle sizes obtained from image analysis (Felix *et al.* 2013a).

Particle type	Longest diam.			Intermediate diam.			Shortest diam.			Equiv. sphere diam.			*SMD*
	a_{10}	a_{50}	a_{90}	b_{10}	b_{50}	b_{90}	c_{10}	c_{50}	c_{90}	$d_{es,10}$	$d_{es,50}$	$d_{es,90}$	
	μm	μm	μm	μm	μm	μm	μm	μm	μm	μm	μm	μm	μm
G		≈ a		24	39	~55		≈ a			= a		37
Q3	130	200	~270	80	130	~190	~45	~70	~140	87	130	~190	110
F	10	40	~80	6	23	~45	~4	~11	~20	7	25	~50	13
M	16	55	~90	9	24	~48	1	2	3	7	15	~25	4

4.1.2 Non-portable laser diffractometer and LISST

The PSDs obtained from the non-portable LD (*LA-950,* Section 3.2.2) as well as from LISST using both available inversion modes (IMS and IMR) are also shown in Figure 4-1. Characteristic values of LISST PSDs are listed in Table 4-2.

For spherical (G) and close-to-spherical particles (Q3), PSDs from the non-portable LD and the LISST in both inversion modes were in good or reasonable agreement with *b*-axes or d_{es} from image analysis. For these two types of particles, PSDs from LISST using IMS were similar to those from non-portable LD, as expected, because both assume spherical particles. Note that the uncertainty at the coarse ends of the PSDs is higher because graded sediments contain only a relatively low number of large particles.

For the highly non-spherical particles (F and M), PSDs from LISST IMR deviated from *b* or d_{es}, because the particle shape and the degree of non-sphericity are not measured by LD. For these types of particles, IMR yielded PSDs closer to *b* and d_{es} (reference from image analysis) than IMS. Thus IMR was selected for the field measurements.

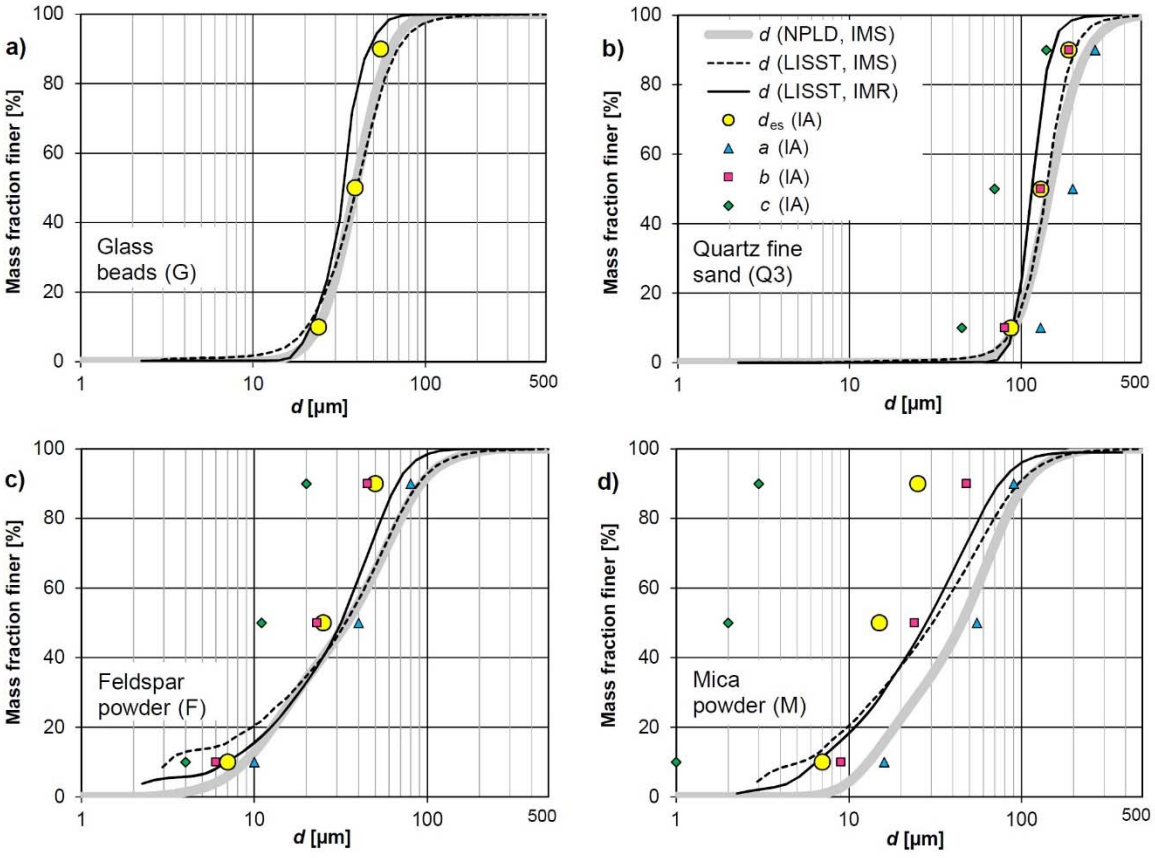

Figure 4-1 PSDs obtained from (i) LISST using both available inversion modes (IMS and IMR), (ii) the non-portable laser-diffractometer (NPLD) and (iii) image analysis (IA), for four types of particles a) to d) (modified from Felix *et al.* 2013a).

With feldspar particles (F) the LISST PSDs did not set in at 0%, i.e. a considerable *BVC* was measured in the first size bin, while the non-portable LD (with the larger size-measuring range down to 0.01 µm) did not measure any significant fraction of particles below 3 µm. Using IMR, this phenomenon was less pronounced than with IMS. Agrawal & Pottsmith (2000), Agrawal *et al.* (2008) and Andrews *et al.* (2011) reported that LISST may overestimate *BVC* mainly in lower size bins due to one or several of the following reasons (Felix *et al.* 2013a):

- Presence of fine out-of-range particles, i.e. particles with *d* smaller than the nominal size-measuring range (2.5 and 1.9 µm for IMS and IMR, respectively);
- Multiple scattering at low optical transmission;
- Effects of refractive index;
- Effects of particle shape.

A pragmatic approach to avoid this effect on LISST PSDs is to discard the *BVC* in selected size bins before calculation of PSD, *TVC* and *SSC*. Based on the position of the local minimum in the *BVC* at the lower end of the size-measuring range, the *BVC* in bins 1 to 3 were judged to be unrealistic and were discarded (Felix *et al.* 2013a). This had no or only a minor effect on the PSD and the spreading of the coarser particle types (G, Q3, N1 and N2), because these *BVC* in bins 1 to 3 were zero or negligibly small.

Table 4-2 Particle sizes and spreading of PSDs obtained from LISST (at nominal *SSC* = 1 g/l) using IMS or IMR and considering or neglecting the *BVC* in bins 1 to 3.

Particle type	Particle sizes [µm]									Spreading σ_g [-]		
	IMS (all 32 bins)			IMR (all 32 bins)			IMR (bins 4 to 32)			IMS 1 to 32	IMR 1 to 32	IMR 4 to 32
	d_{16}	d_{50}	d_{84}	d_{16}	d_{50}	d_{84}	d_{16}	d_{50}	d_{84}			
G	**24**	**40**	**61**	24	33	43	24	33	43	**1.59**	1.33	1.33
Q3	101	141	190	95	116	142	**95**	**116**	**142**	1.37	1.22	**1.22**
Q2	3	20	66	8	20	54	**10**	**22**	**59**	4.62	2.65	**2.36**
F	7	34	75	10	32	59	**13**	**33**	**60**	3.23	2.39	**2.17**
M	8	30	78	9	28	61	**10**	**28**	**62**	3.15	2.63	**2.52**
N1	19	47	92	18	38	70	**19**	**38**	**70**	2.20	1.95	**1.94**
N2	38	110	234	33	94	185	**33**	**94**	**185**	2.49	2.37	**2.37**

Note: The results judged to be closest to reality are printed in bold.

The comparison of the results from image analysis and LISST showed that LISST provides usable PSDs of suspended sediment particles in the size-range of silt to fine sand. For the glass beads (G) the d_{50} = 40 µm from LISST IMS (Table 4-2) was very close to $d_{es,50}$ = 39 µm from image analysis (Table 4-1). For the close-to-spherical fine-sand particles (Q3), the d_{50} from LISST IMR was reasonably accurate, the deviation to $d_{es,50}$ from

image analysis was only 116/130 − 1 = −11%. With highly non-spherical particles, however, particle sizes are overestimated due to the measurement principle of LD: For angular feldspar particles (F) the apparent d_{50} from LISST IMR was 33/25 − 1 = 32% higher than $d_{es,50}$. For mica particles (M) the overestimation of d_{es} by LISST was even 28/15 − 1 = 87%.

4.2 *SSC* measurements

4.2.1 Turbidimeters

The measurement results obtained from the turbidimeters (1) to (5) in Table 3-1 are treated in the following sequence depending on the measuring arrangement:

- Single detector at $\alpha = 90°$ (*AquaScat*, and channel no. 1 of *TurBiScat*)
- Single detector at $\alpha = 25°$ (channel no. 2 of *TurBiScat*)
- Dual detectors at $\alpha = 90°$ (*Solitax ts-line sc* and *TurbiMax W CUS 41*)
- Single detector at $\alpha = 0°$, i.e. through-light (*TF-16N*).

After the presentation of the results of the individual instruments, the turbidity measurements for selected particle types are compared among the instruments and finally the experimentally determined specific turbidities are summarized.

4.2.1.1 AquaScat (scattering at 90°)

Figure 4-2 shows the turbidities obtained from *AquaScat* as a function of SSC_G determined from bottle samples taken at its outlet. Each point represents the time-averaged turbidity at a nominal *SSC* level. Approximately linear relations were found for the suspensions made of each particle type (see Table 3-2) or the mixture of 70% feldspar and 30% mica powders (F-M). The slope of such a linear relation, i.e. turbidity/*SSC* is called specific turbidity. These were quantified by linear fitting in Figure 4-3 for each measurement series. For comparability of the results among most of the turbidimeters, the fits were made on the data points with SSC_G up to 5 g/l for the four suspensions with the highest specific turbidities, and with SSC_G up to 10 g/l for the other suspensions. Linear fits passing through the origins of the axes were selected because the turbidimeters were cleaned before the start of each measurement series and were checked to display less than a few FNU in clear water. As expected, the specific turbidity is higher for particle types with small d_{50}, wide PSDs and/or highly non-spherical shapes (i.e. flaky and/or angular). For most suspensions, the scatter of the measurement points was quite low (high R^2).

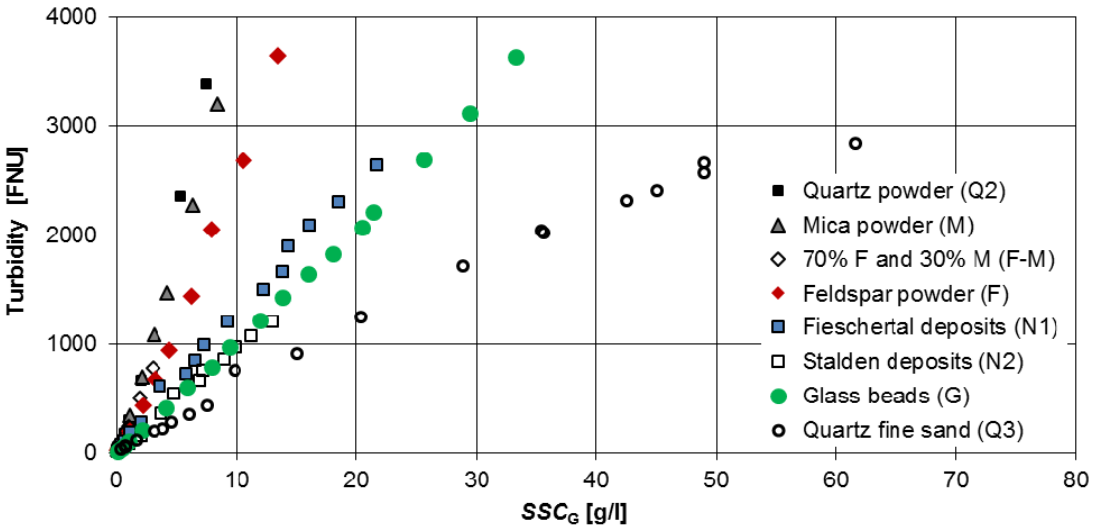

Figure 4-2 Turbidity measured with *AquaScat* at 90° as a function of SSC_G for all measurement series.

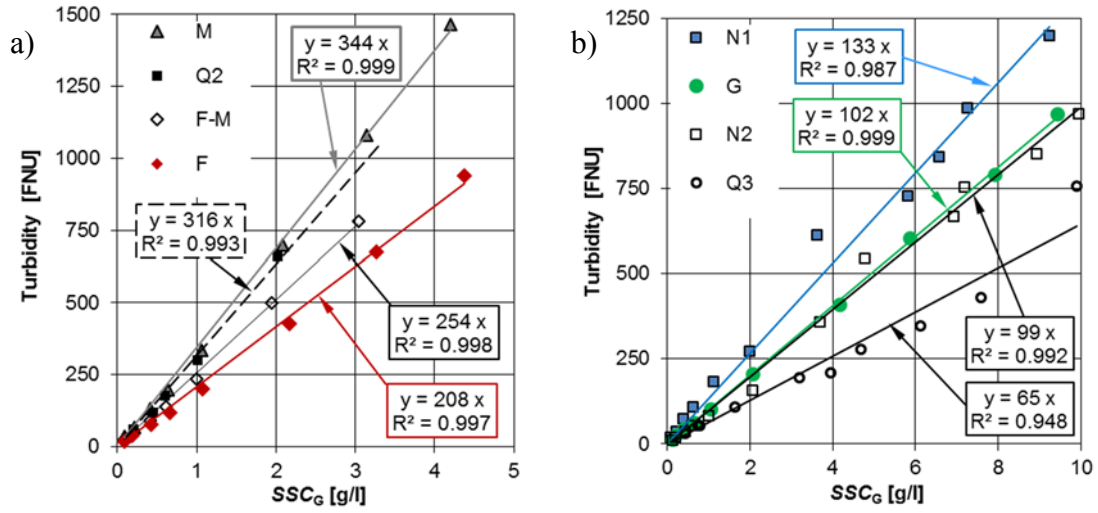

Figure 4-3 Turbidity measured with *AquaScat* at 90° as a function of SSC_G, with linear fits in the ranges up to a) 5 g/l and b) 10 g/l.

4.2.1.2 TurBiScat (scattering at 90° and 25°)

The results obtained from the two independent measuring channels of the *TurBiScat* are shown in Appendix A3 as a function of the SSC_G determined from bottle samples taken from the mixing tank. The latter *SSC* were preferred over the SSC_G determined from bottle samples taken at the outlet of the *AquaScat* to avoid potential bias of *SSC* caused by the oblique branch-off of the *AquaScat*'s small feeding line from the main pump line. Figures A-7 and A-8 show the results of channel no. 1 ($\alpha = 90°$), Figures A-9 and A-10 those of channel no. 2 ($\alpha = 25°$). The results of the *TurBiScat* also showed approximately linear relations depending on the mentioned factors, but the absolute values of the outputs (also at $\alpha = 90°$) differed from the *AquaScat*. As a peculiarity, the points of the glass beads (G)

measured at $\alpha = 25°$ and $SSC > 25$ g/l deviated from a linear relation in contrast to the measurements at $\alpha = 90°$.

The ratios of the turbidities measured with *TurBiScat* at 25° and 90° were evaluated by dividing the corresponding specific turbidities obtained from the fits in Figures A-8 and A-10. These ratios are shown in Figure 4-4 as a function of d_{50} obtained from LISST. A higher ratio was associated with finer particles. This is in agreement with the manufacturer's statement based on Mie theory and experiments that measuring at $\alpha = 25°$ is more sensitive to small particles. According to an unconstrained linear fit, the ratio was 1 at $d_{50} \approx 55$ µm. The scatter in the points is attributed to the different particles shapes, widths of the PSDs and LD's overestimation of d_{50} with highly non-spherical particles.

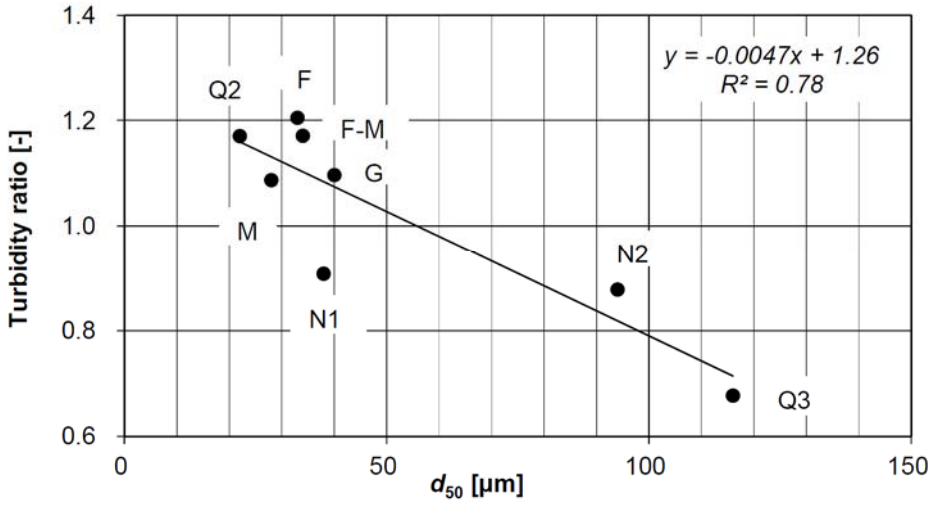

Figure 4-4 Ratio of the turbidities measured with *TurBiScat* at 25° and at 90° as a function of d_{50} obtained from LISST.

4.2.1.3 Solitax ts-line sc (90° dual)

Solitax ts-line sc is the only turbidimeter model of which two probes were used in the laboratory investigations. Despite identical parameter settings, the turbidity signal of probe no. 1 fluctuated more than that of probe no. 2. With time-averaging, the signals of both probes were usable. The measurement results obtained from both probes are shown and compared in Appendix A3 in the Figures A-11 to A-15. The comparison showed that the turbidity readings of two probes of the same model may vary by 10% or sometimes 20%.

With the sediment from the tailwater channel deposits at HPP Fieschertal (N1), decreasing turbidity values were measured for increasing $SSC > 20$ g/l with both *Solitax* probes (Figs. A-11 and A-13). Such behaviour is known for nephelometers at high turbidities

(effects of particles' shadows, Section 2.2.1.4), but was not expected to occur with one particle type only. For unique conversion of turbidity to *SSC*, the probe can thus be used only below 20 g/l with this particle type.

4.2.1.4 TurbiMax W CUS 41 (90° dual)

The results obtained from *TurbiMax W CUS 41* are shown in Figures A-16 and A-17 in Appendix A3.6 as a function of the SSC_G. A peculiarity of this turbidimeter model is its parameter called 'gas bubble threshold'. The laboratory tests were carried out with the default value of this parameter (3%). At turbidities above several 100 FNU, the turbidity signal occasionally rose suddenly because of an internal switching between two measuring modes (below or above 400 FNU) and decayed gradually due to the signal smoothing constant in the signal converter. According to the manufacturer, these sudden signal increases could have been avoided if the 'gas bubble threshold' had been set to 100%. Since a few years, newer turbidimeter models (*CUS51D* and *CUS52*) have become available from the same manufacturer, which do not feature this parameter anymore. The specific turbidities were determined in the range of lower turbidities which were not affected by this technical problem.

4.2.1.5 TF-16N (through-light)

Figure 4-5 shows the results obtained from the *TF-16N*, i.e. the only turbidimeter measuring at $\alpha = 0°$. As for the *TurBiScat*, the SSC_G determined from bottle samples taken from the mixing tank were used as the reference. The relations between turbidity and SSC_G were found to be linear up to ~1 CU. At higher turbidities, the specific turbidities were found to decrease (non-linear relations). The specific turbidities were determined in the linear range (Fig. 4-6).

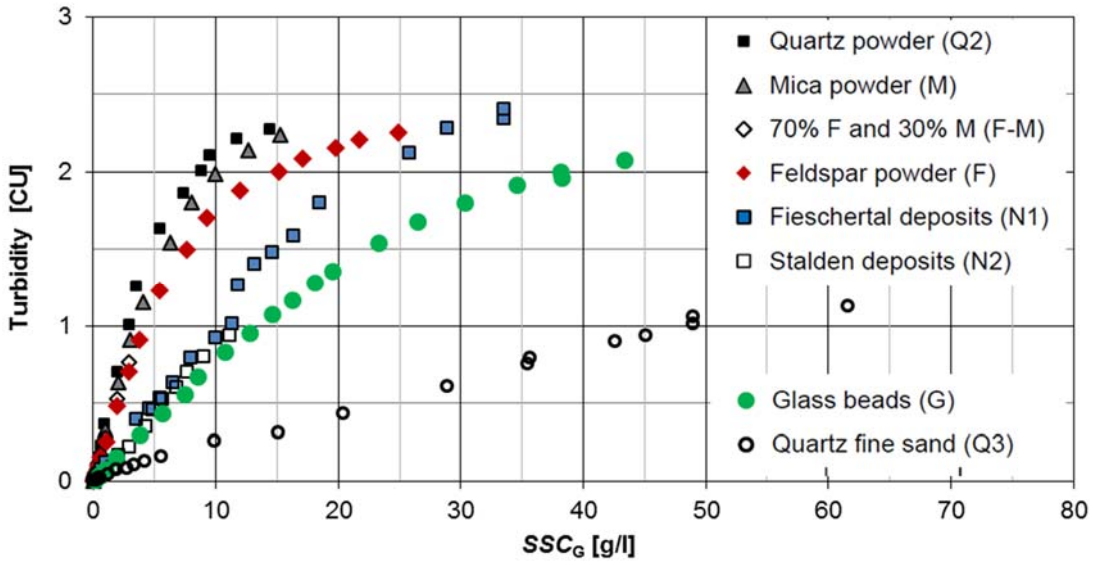

Figure 4-5 Turbidity measured at 0° as a function of SSC_G for all measurement series.

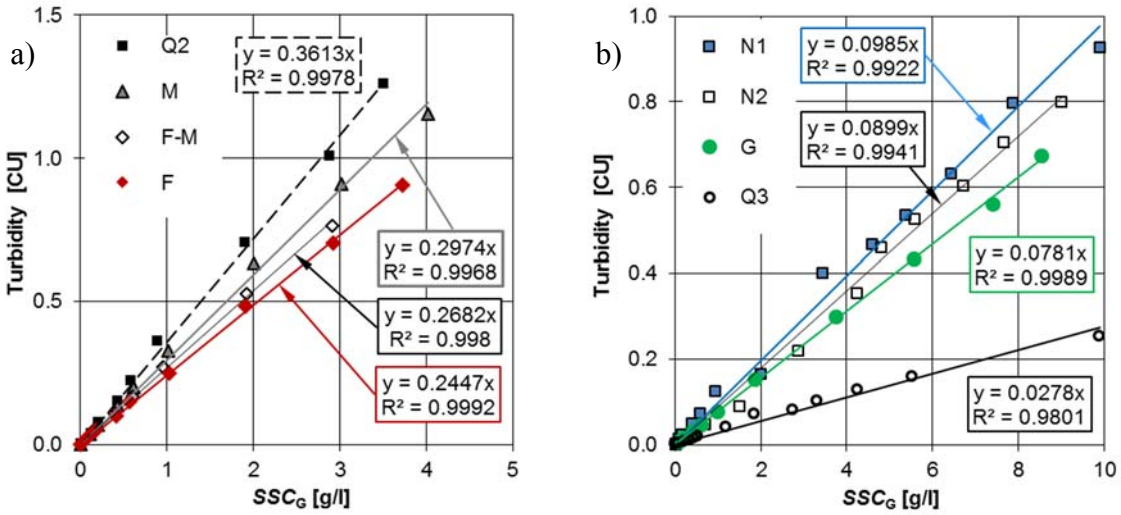

Figure 4-6 Turbidity measured at 0° as a function of SSC_G with linear fits in the ranges up to a) 5 g/l and b) 10 g/l.

4.2.1.6 Comparison of results among instruments

Figures 4-7 and 4-8 show the turbidities measured by the various turbidimeters with output units FNU ($\alpha > 0°$) as a function of the SSC_G for angular feldspar (F) and flaky mica (M) particles, respectively. The instruments' outputs compare as follows:

- Similar results were found for *AquaScat* and channel no. 1 of *TurBiScat* (both measuring at $\alpha = 90°$);
- Turbidities from *TurBiScat* were higher at $\alpha = 25°$ than at 90° for these relatively small particles;
- Both *Solitax ts-line sc* probes yielded higher specific turbidities than *AquaScat* and *TurBiScat*, especially above ~1000 FNU;

– *TurbiMax W CUS 41* yielded even higher turbidities, mostly as a consequence of the inadequate setting of the 'gas bubble threshold'.

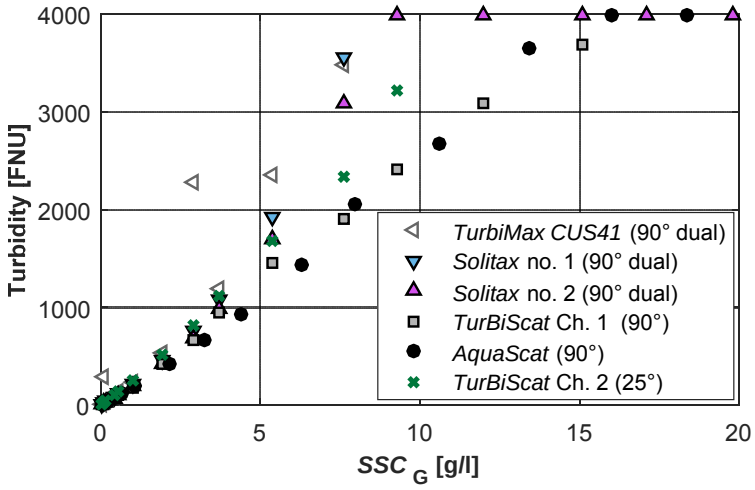

Figure 4-7 Turbidities as a function of SSC_G measured with various turbidimeters in feldspar powder suspension (F).

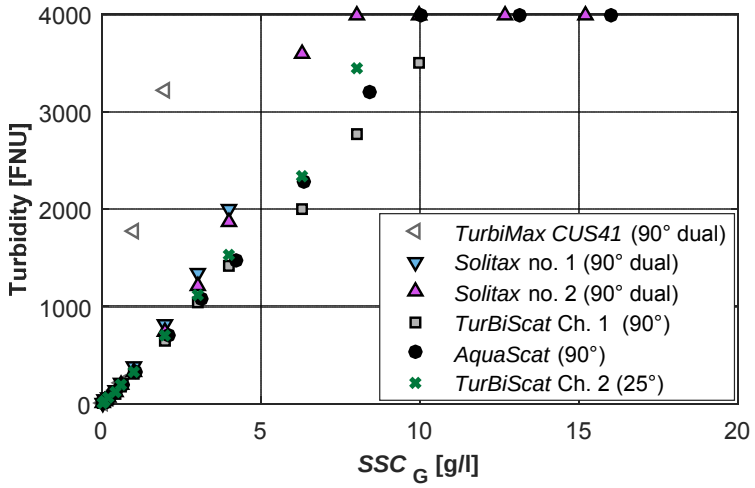

Figure 4-8 Turbidities as a function of SSC_G measured with various turbidimeters in mica powder suspension (M).

The specific turbidities determined with all particle types and turbidimeters are summarized in Table 4-3. The variations of the specific turbidities indicate that the conversions of turbidity values to *SSC*, i.e. the calibrations, need to be established for each particle type or mixture of particle types, for each turbidimeter model and even for each individual probe of the same model. The range of measurable *SSC* for various particle types and instruments can be seen from the Figures of the turbidimeter results. Note that *Turbimax W CUS 41* and its replacement models have a measuring range of 10 000 FNU whereas it is 4000 FNU for most other turbidimeters with $\alpha > 0°$.

Table 4-3 Specific turbidities measured with various turbidimeters in suspensions made of water and various particle types in the laboratory.

Particle Type (Table 3-2)	*SSC* range of linear fit g/l	*AquaScat* (90°)	*TurBiScat*		*Solitax* (dual 90°)		*CUS 41* (dual 90°)	*TF-16N* (0°)
			90°	*25°*	no. 1	no. 2		
		FNU/(g/l)						CU/(g/l)
Q2	< 5	316	402	471	497	441	332	0.3613
M	< 5	344	342	372	463	426	352	0.2974
F-M	< 5	254	256	300	304	276	270	0.2682
F	< 5	208	239	288	272	245	228	0.2447
N1	< 10	133	98	89	166	151	126	0.0985
N2	< 10	99	82	72	129	114	95	0.0899
G	< 10	102	72	79	125	118	92	0.0781
Q3	< 10	65	31	21	66	64	50	0.0278

4.2.1.7 Superposition of turbidity

The specific turbidities measured in the 7:3 mixture of the feldspar (F) and mica (M) powders were as expected between those measured in suspensions made of the individual particle types and water (e.g. Fig. 4-3a). Based on the concept of linear superposition, it was hypothesized that the specific turbidity of a suspension containing a mixture of particle types can be predicted as the sum of the specific turbidities of the components multiplied by their mass fractions (weighted average). With this approach, a specific turbidity of $0.70 \cdot 208 + 0.30 \cdot 344 = 146 + 103 = 249$ FNU/(g/l) was estimated for the investigated mixture and the *AquaScat* for example. This corresponds to 98% of the experimental value of 254 FNU/(g/l). Table 4-4 summarizes the corresponding results for all turbidimeters. This approach allowed predicting the specific turbidities with an error of less than 8%, which is in the range of the overall experimental uncertainty. The findings support the hypothesis that turbidities are superposable.

Table 4-4 Comparison of experimental and estimated specific turbidities for a 7:3 feldspar and mica powder suspension and various turbidimeters.

Turbidimeter (Table 3-1)	Specific turbidity			
	Unit	Experimental	Estimated	Ratio
AquaScat (90°)	FNU/(g/l)	254	249	98%
TurBiScat 90°	FNU/(g/l)	256	270	105%
TurBiScat 25°	FNU/(g/l)	300	313	104%
Solitax (dual 90°) no. 1	FNU/(g/l)	304	329	108%
Solitax (dual 90°) no. 2	FNU/(g/l)	276	299	108%
TurbiMax W CUS 41 (dual 90°)	FNU/(g/l)	270	265	98%
TF-16N (0°)	CU/(g/l)	0.2682	0.2605	97%

4.2.2 Acoustic technique

The acoustic damping δ (Eq. 3-1) as a function of SSC_G measured in the eight series is shown in Figure 4-9. The measurements indicate non-linear relations, particularly at higher *SSC*. The points of the quartz fine sand (Q3), i.e. the coarsest of the investigated particle types, scatter more than the others. This is related to the higher uncertainty on SSC_G, high spatial *SSC* gradients, and possibly to the presence of air in the suspension in the region of the acoustic path (e.g. air-entraining vortices and bubbles due to the faster stirring for Q3). The two Q3-points with the grey background fill were judged as outliers and excluded from the further data evaluation.

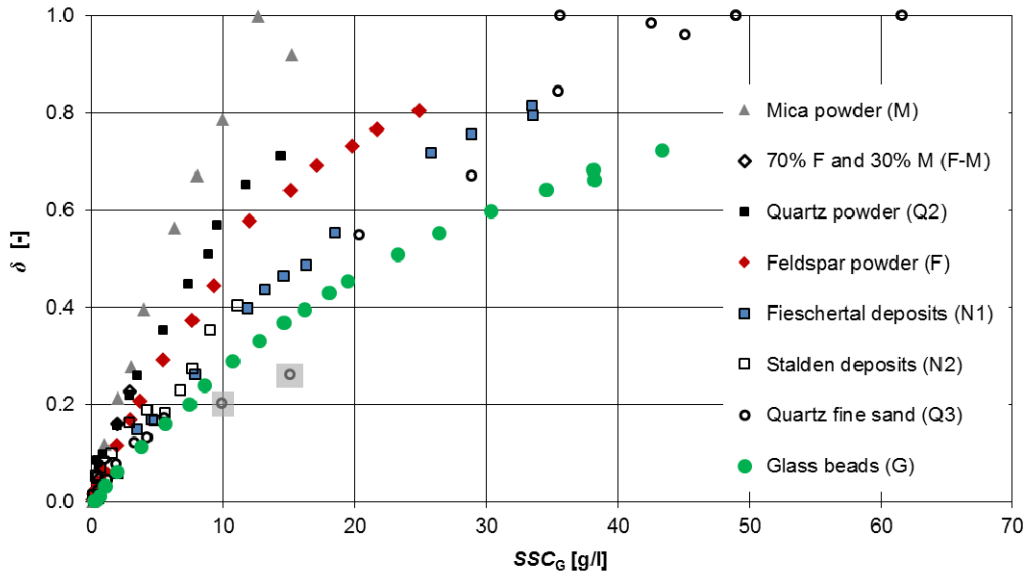

Figure 4-9 Acoustic damping δ as a function of SSC_G for all measurement series.

Non-linear relations as defined in Equation (4-1) were fitted to the data points of each measurement series (Figs. 4-10 and 4-11a). While $\delta = 1$ is reached for infinite *SSC* in Equation (4-1), $\delta = 1$, i.e. no detectable received signal, was measured for finite *SSC* in the experiments. The fits were hence limited to the data with $\delta < 0.8$. Equation (4-1) resulted from the definition of δ (Eq. 3-1) and the relation expected from theory (Eq. 2-19). According to the derivative of Equation (4-1), ε is the specific damping δ/SSC (slope of the curve) at $SSC = 0$.

$$\delta = 1 - e^{-\varepsilon\, SSC} \qquad [-] \qquad (4\text{-}1)$$

Furthermore, linear relations defined in Equation (4-2) were determined for $SSC < 5$ g/l as easily applicable approximations (e.g. Fig. 4-11b).

$$\delta = \varphi\, SSC \qquad [-] \qquad (4\text{-}2)$$

The resulting parameters for both the non-linear and the linear fits, i.e. the specific dampings ε and φ, are listed in Table 4-5. For most particle types, the goodness of the non-linear fits was very high ($R^2 > 0.99$). The ε- and φ-values refer to a path length of $L = 1.73$ m. The corresponding values normalized with L are also listed in Table 4-5, together with information on the *SSC* range.

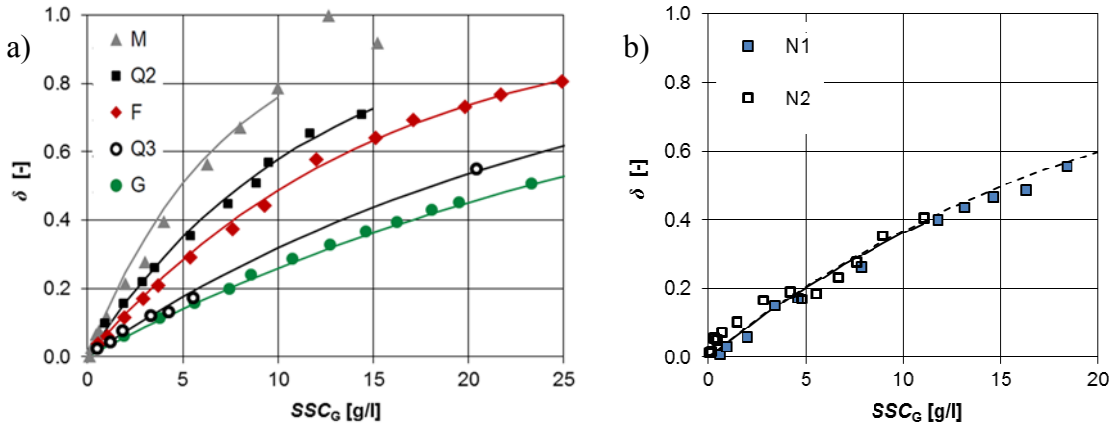

Figure 4-10 Acoustic damping δ as a function of SSC_G with non-linear fits for a) the purchased particles and b) the particles collected from the HPPs.

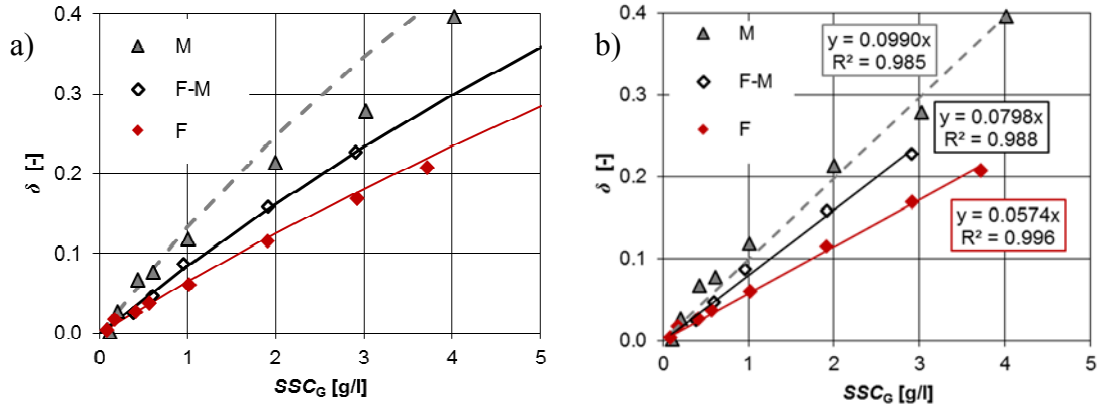

Figure 4-11 Acoustic damping δ as a function of SSC_G for feldspar (F) and mica (M) powders as well as a 7:3 mixture of these components (F-M), with a) non-linear and b) linear fits.

The points of the F-M-mixture in Figure 4-11 (measured up to 3 g/l) were between those of the components as expected. For the mica powder in this *SSC* range, the linear relation (Fig. 4-11b) fits better to the data than the non-linear one (Fig. 4-11a). With the linear fits, φ for the mixture was estimated as 0.0699 using the approach described in Section 4.2.1.7. The estimated φ corresponds to 88% of the experimental φ (0.0798). This deviation is attributed to experimental uncertainty, especially in the specific damping of the mica powder.

Table 4-5 Specific acoustic damping for forward scattering at 1 MHz with a path length of L = 1.73 m based on laboratory investigations.

Particle type (Table 3-2)	Non-linear fits				Linear fits for SSC < 5 g/l		
	ε in Eqs. (4-1) and (2-19)	R^2	$\beta = \varepsilon / L$ in Eq. (2-18)	Valid up to SSC	φ in Eq. (4-2)	R^2	φ / L
	l/g	-	l/(g · m)	g/l	l/g	-	l/(g · m)
Q2	0.0863	0.994	0.0499	15	0.0788	0.918	0.0455
M	0.1420	0.990	0.0821	10	0.0990	0.985	0.0572
F-M	0.0887	0.996	0.0513	(3)	0.0798	0.988	0.0461
F	0.0669	0.999	0.0387	25	0.0574	0.996	0.0332
N1	0.0457	0.995	0.0264	34	0.0374	0.945	0.0216
N2	0.0447	0.959	0.0258	(11)	0.0443	0.773	0.0256
G	0.0300	0.999	0.0173	45	0.0310	0.987	0.0179
Q3	0.0384 *	0.998 *	0.0222	30	0.0342	0.948	0.0198

* After rejection of two outliers (otherwise ε = 0.0350 and R^2 = 0.941).

4.2.3 LISST

4.2.3.1 Concentration overestimation

Figure 4-12 shows the SSC_{L0}, i.e. the SSC obtained from LISST using the solid densities of the particles (Eq. 3-2), as a function of SSC_G from the tank at the instruments' level. The SSC_{L0} were obtained from the BVC in bins 4 to 32 using IMS for the glass beads (G) and IMR for the other particle types. Only with fine sand (Q3), LISST measurements were possible above 12 g/l. No systematic results were obtained above 40 g/l, probably due to high spatial SSC gradients and potentially non-representative SSC_G.

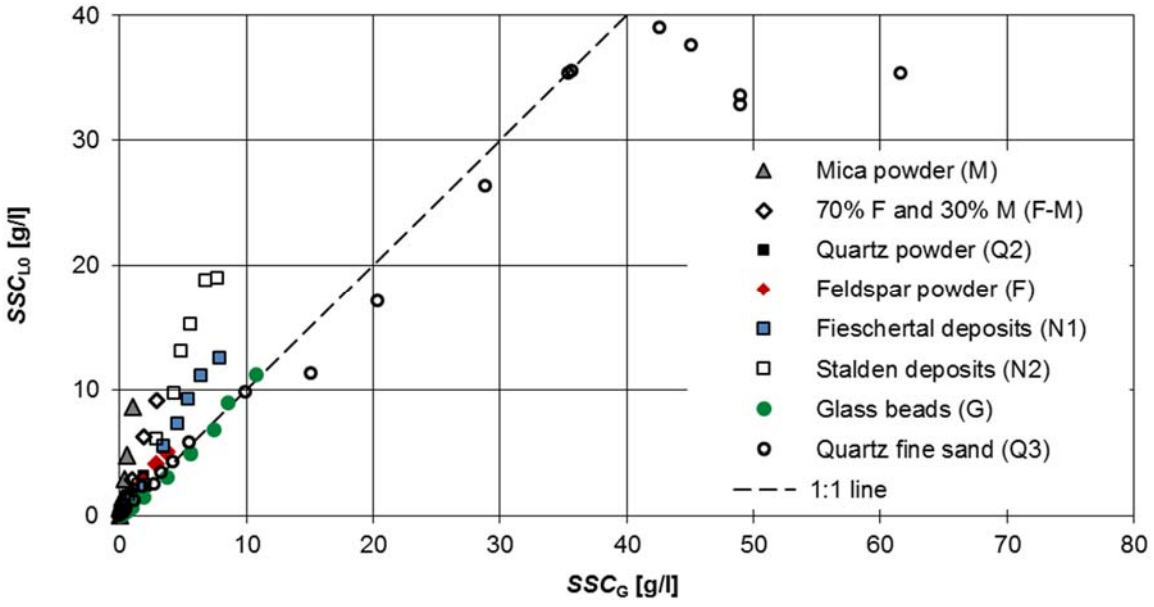

Figure 4-12 SSC_{L0} as a function of gravimetrical SSC in all measurement series.

Figures 4-13 and 4-14 show details of the Figure 4-12 with linear fits for each measurement series for $SSC < 12$ g/l. The fits were constrained to pass through the origins of the axes ($SSC = 0$ in clear water). In the considered range, the R^2 were close to 1. The factors in the equations on Figures 4-13 and 4-14 indicate the slopes of the lines $f_c = SSC_{L0} / SSC_G$. For the glass beads (G) and the rounded fine sand particles (Q3) with close-to-spherical shapes, $f_c \approx 1.0$ was found as expected ($SSC_G < 12$ g/l). This means that the LISST's volume conversion constant has been satisfactorily calibrated by the manufacturer. For the other particle types, f_c was considerably higher, up to $f_c \approx 8$ for the flaky mica particles (M). Assuming that the experimental errors in the determination of the TVC, ρ_s and SSC_G were negligible and that there was no flocculation, f_c was interpreted as the 'concentration overestimation factor' of LISST and was attributed to mainly effects of particle shapes (Felix *et al.* 2013a). The f_c for all investigated particle types are listed in Table 4-6. The considerable difference in f_c of the natural particles N1 and N2 shows that f_c has to be determined site-specifically from reference measurements, unless the particle shapes would be parameterized and known.

In Figure 4-14, the SSC_{L0} of feldspar (F) and mica (M) powders as well as of a 7:3 mixture of these components (F-M) are shown as a function of SSC_G. The $f_c = 3.15$ of the mixture lies between the f_c of the components as expected. Based on linear superposition (Section 4.2.1.7), the f_c of the mixture was estimated as $0.70 \cdot 1.38 + 0.30 \cdot 8.17 = 3.42$. This corresponds to 108% of the experimentally determined value. This supports the hypothesis that the f_c of a mixed-particle type suspension can be estimated by the f_c of the components and their mass ratio.

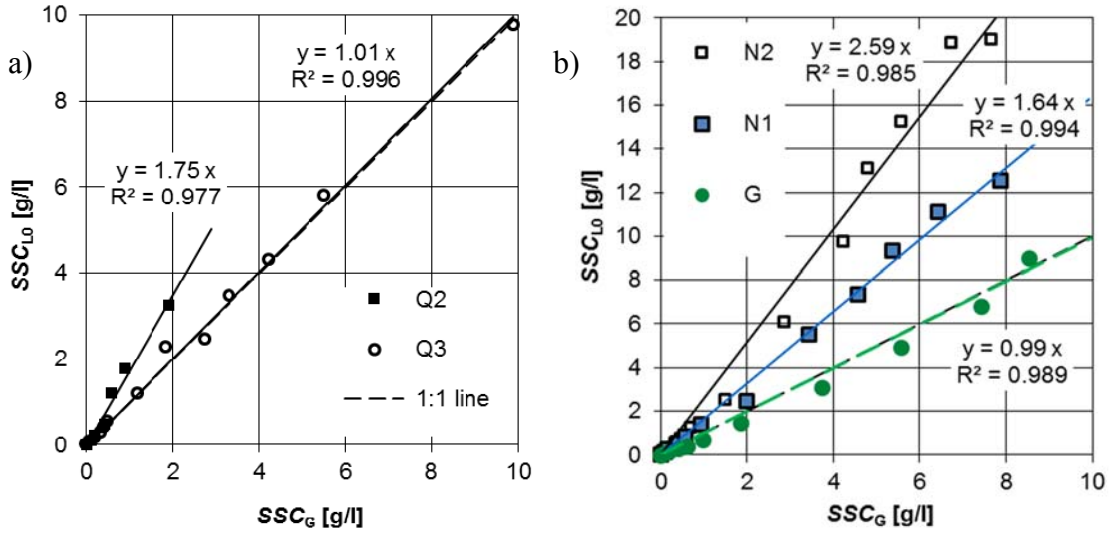

Figure 4-13 SSC_{L0} as a function of gravimetrical SSC for a) quartz powder (Q2) and fine sand (Q3, up to 10 g/l), b) Glass beads (G) and sediments from the HPPs Fieschertal (N1) and Stalden (N2).

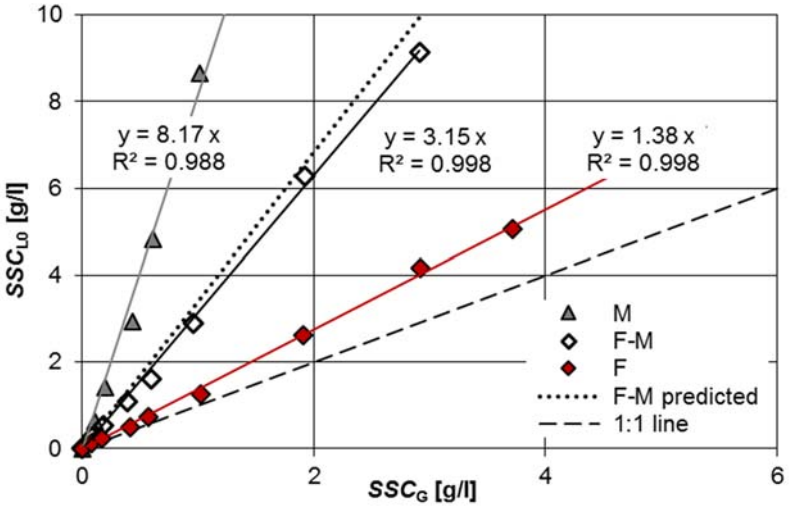

Figure 4-14 SSC_{L0} as a function of gravimetrical *SSC* for feldspar (F) and mica (M) powders as well as a 7:3 mixture of these components (F-M); the dotted line represents the prediction for the mixture (modified from Felix *et al.* 2013a).

4.2.3.2 Upper limit of the SSC-measuring range

As described in Section 2.2.1.6, the upper limit of the *SSC*-measuring range of a LISST, termed SSC_{lim}, depends on the sizes, shapes and density of the particles, as well as on the optical path length. For the path length of 5 mm and densities varying by only ± 9% (2.42 to 2.92 g/cm^3 from Table 3-2), SSC_{lim} depends mainly on the particle sizes and secondly on the particle shapes. SSC_{lim} is related to a minimum optical transmission τ. The values of this auxiliary parameter, internally calculated by LISST from measured intensities of incident and received laser power, are also available in the LISST output.

When τ was higher than the recommended value of 0.3, LISST measurements were always possible. With lower τ, measurements were still possible. When τ was further reduced, some or eventually all of the repeated single measurements at a given nominal *SSC* level were not invertible. The rate of invertible measurements κ was evaluated at all nominal *SSC* levels. For each measurement series, the highest reference SSC_G at which all single measurements were invertible (κ = 1.00) and the next higher SSC_G, i.e. the lowest SSC_G with $\kappa < 1.00$, are listed in Table 4-6. For the latter, also the rate of invertible measurements is indicated. Furthermore, the τ at these two SSC_G per series are given in Table 4-6. At $\tau = 0$, no measurements are possible ($\kappa = 0$).

Figure 4-15 shows the SSC_G listed in Table 4-6 as a function of the median particle diameter d_{50} obtained from LISST (Table 4-2, using IMS for G and IMR for the other particle types, and considering the *BVC* in bins 4 to 32). Because of the discrete values of SSC_G, the exact value of the experimental SSC_{lim} is unknown; however it is known that SSC_{lim}

lies between the two points of each measurement series. Overall, SSC_{lim} increased with d_{50} as expected. The scatter in the points is mainly attributed to different particle shapes.

Table 4-6 Results on LISST concentration overestimation factor f_c and instrument behaviour related to the upper limit of its *SSC*-measuring range; κ denotes the rate of invertible measurements.

Particle Type (Table 3-2)	f_c * [-]	SSC_G [g/l]		κ [-]	τ [-]	
		highest with $\kappa = 1.00$	lowest with $\kappa < 1.00$	at lowest SSC_G with $\kappa < 1.00$	at highest SSC_G with $\kappa = 1.00$	at lowest SSC_G with $\kappa < 1.00$
Q2	1.76	1.9	2.9	0.00	0.10	0.00
M	8.17	1.1	2.0	0.00	0.10	0.00
F-M	3.15	1.9	2.9	0.03	0.15	0.07
F	1.38	2.9	3.7	0.11	0.12	0.07
N1	1.64	6.4	7.9	0.49	0.12	0.08
N2	2.59	5.6	6.7	0.98	0.13	0.09
G	0.99	8.5	10.7	0.28	0.12	0.08
Q3	1.01	20.4	28.9	0.98	0.27	0.16

* with *BVC* of bins 4 to 32, using IMS for G and IMR for the non-spherical particle types; the f_c-value for Q3 refers to $SSC_G \leq 10$ g/l.

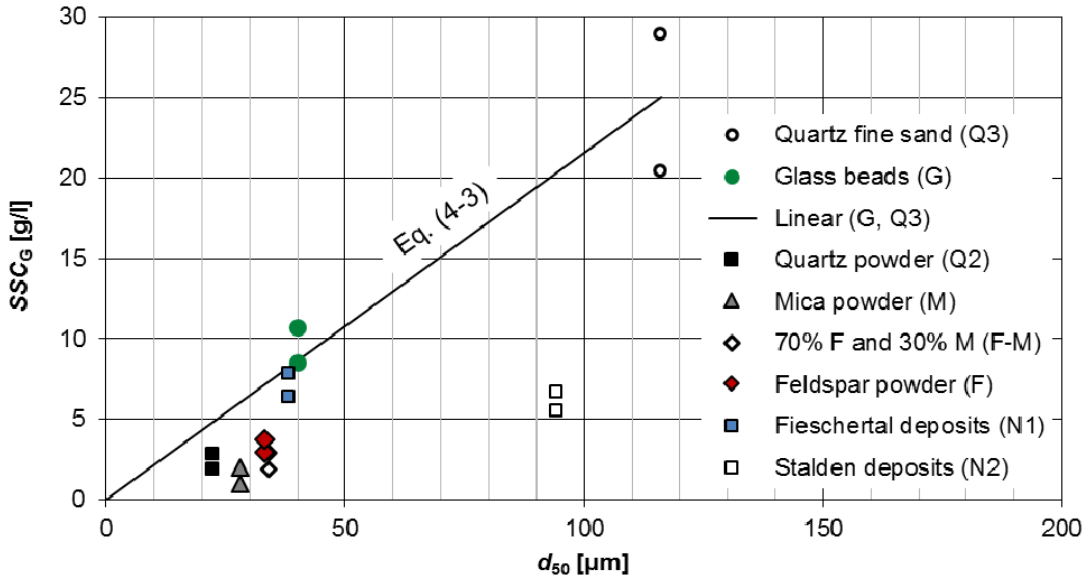

Figure 4-15 Pairs of SSC_G below and above SSC_{lim} of each measurement series as a function of the median particle diameter d_{50} obtained from LISST.

For the spherical glass beads (G) and the irregular, close-to-spherical fine-sand particles (Q3), the $f_c \approx 1$ and d_{50} are reasonably accurate (Section 4.1.2). For these particle types, SSC_{lim} was approximated as

$$SSC_{lim} = 0.21\, d_{50} \qquad [g/l] \qquad (4\text{-}3)$$

where d_{50} in [µm]. This equation resulted from a linear fit on the points of these two particle types and the constraint to pass through the origin of the axes. It should be noted that Equation (4-3) refers to an optical path length of 5 mm, a particle density of 2.42 to 2.66 g/cm^3 (Table 3-2) and no constraint on minimum τ.

However, for the other types of particles with highly non-spherical shapes, τ and SSC_{lim} are relatively low due to $f_c > 1$ (higher specific turbidity) and because LISST over-estimates the particle size ($d_{50} > d_{es,50}$). For the most non-spherical particle type (M), SSC_{lim} was found to be between 0.04 and 0.07 times the apparent d_{50}, i.e. only about 20% of SSC_{lim} estimated with Equation (4-3). For the second-most non-spherical particle type (N2), SSC_{lim} is about 30% of that estimated with Equation (4-3).

Figure 4-16 shows part of the SSC_G data listed in Table 4-6 as a function of *SMD* instead of d_{50}. *SMD*s were determined by image analysis for Q3, G, F and M. For the spherical (G) and close-to-spherical (Q3) particles with narrow PSDs (low σ_g in Table 4-2), the *SMD* was similar to d_{50} (93% and 95% of d_{50}). For the angular and flaky particles with wider PSDs, *SMD* was only 39% and 14% of the apparent d_{50}, respectively. Furthermore, the measured τ-values from Table 4-6 are indicated in Figure 4-16. These experimental results are compared to the nominal SSC_{lim} given by the LISST manufacturer (Eq. 2-20). The equation was evaluated for an optical path length of 5 mm, an average solid density of 2.7 g/cm^3 (Table 3-2), and for three levels of optical transmission:

$$SSC_{lim} = 0.22\ SMD \qquad \text{with } \tau = 0.3 \qquad [\text{g/l}] \qquad (4\text{-}4a)$$

$$SSC_{lim} = 0.29\ SMD \qquad \text{with } \tau = 0.2 \qquad [\text{g/l}] \qquad (4\text{-}4b)$$

$$SSC_{lim} = 0.42\ SMD \qquad \text{with } \tau = 0.1 \qquad [\text{g/l}] \qquad (4\text{-}4c)$$

These equations are shown as three lines in Figure 4-16. The grey area below the line of the generally recommended $\tau = 0.3$ represents the nominal *SSC*-measuring range. The upper limit of the experimentally determined measuring range lies between the pairs of points.

With these four types of particles (Q3, G, F and M), LISST provided measurement results up to SSC_{lim} as predicted by Equation (4-4a). With *SSC* approaching SSC_{lim}, the τ-values in the laboratory measurements decreased however below 0.3, e.g. down to 0.11. If measurement results with $\tau \geq 0.3$ were accepted only, the LISST *SSC*-measuring range would be considerably lower than predicted by Equation (4-4a).

The pairs of points in Figure 4-16 lie approximately on one line. As expected, *SMD* correlates better with SSC_{lim} than d_{50}, because SSC_{lim} also depends on the relative distribution

of the *BVC* (i.e. the shape of the PSD) and the particle shapes, which are considered in *SMD* (Eq. 2-4). However, in many engineering applications, *SMD* is not known and d_{50} is used more frequently. In such cases, the easily applicable Equation (4-3) allows for a rough estimate of SSC_{lim} for spherical or close-to-spherical particles with narrow PSDs. However, for angular and flaky particles and wider PSDs, SSC_{lim} is considerably lower.

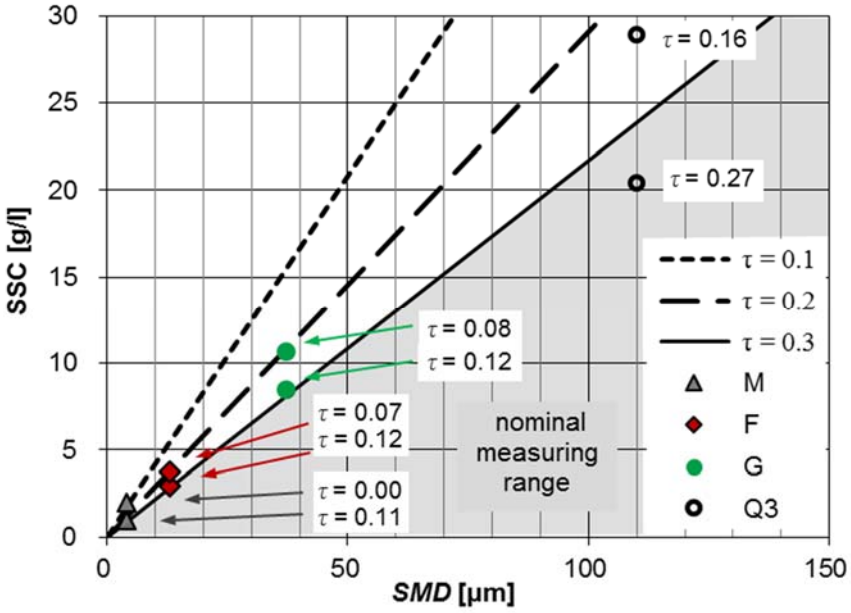

Figure 4-16 Comparison of the nominal and experimental *SSC* measuring range of LISST as a function of the Sauter Mean Diameter *SMD* (modified from Felix *et al.* 2013a).

4.2.4 Comparison of normalized specific instrument outputs

Finally, the specific turbidities determined for all turbidimeters (Table 4-3), the specific acoustic damping (first column of Table 4-5) and the LISST f_c (first column of Table 4-6) were compared for the various particle types. The specific turbidities and dampings were normalized by the respective values obtained for glass beads (G) (Table 4-7). This particle type was chosen as the reference because of the spherical particle shape and the narrow PSD. For the LISST f_c, no normalizing was required because $f_c \approx 1$ for the glass beads.

Figure 4-17 shows the values of Table 4-7 and the LISST f_c (Table 4-6) as a function of d_{50} obtained from LISST. These values indicate the sensitivity of an instrument per unit *SSC* of a certain particle type.

Table 4-7 Normalized specific outputs of the turbidimeters and the acoustic technique with reference to glass beads (G) based on the laboratory measurements.

Particle Type (Table 3-2)	Normalized specific turbidities [-]							Normalized specific acoustic attenuation [-]
	AquaScat (90°)	*TurBiScat*		*Solitax* (dual 90°)		*CUS 41* (dual 90°)	*TF-16N* (0°)	
		90°	25°	no. 1	no. 2			
Q2	3.10	5.58	5.96	3.98	3.74	3.61	4.63	2.54
M	3.37	4.75	4.71	3.70	3.61	3.83	3.81	3.19
F	2.04	3.32	3.65	2.18	2.08	2.48	3.13	1.85
N1	1.30	1.36	1.13	1.33	1.28	1.37	1.26	1.43
N2	0.97	1.14	0.91	1.03	0.97	1.03	1.15	1.21
G (reference)	1.00	1.00	1.00	1.00	1.00	1.00	1.00	1.00
Q3	0.64	0.43	0.27	0.53	0.54	0.54	0.36	1.10

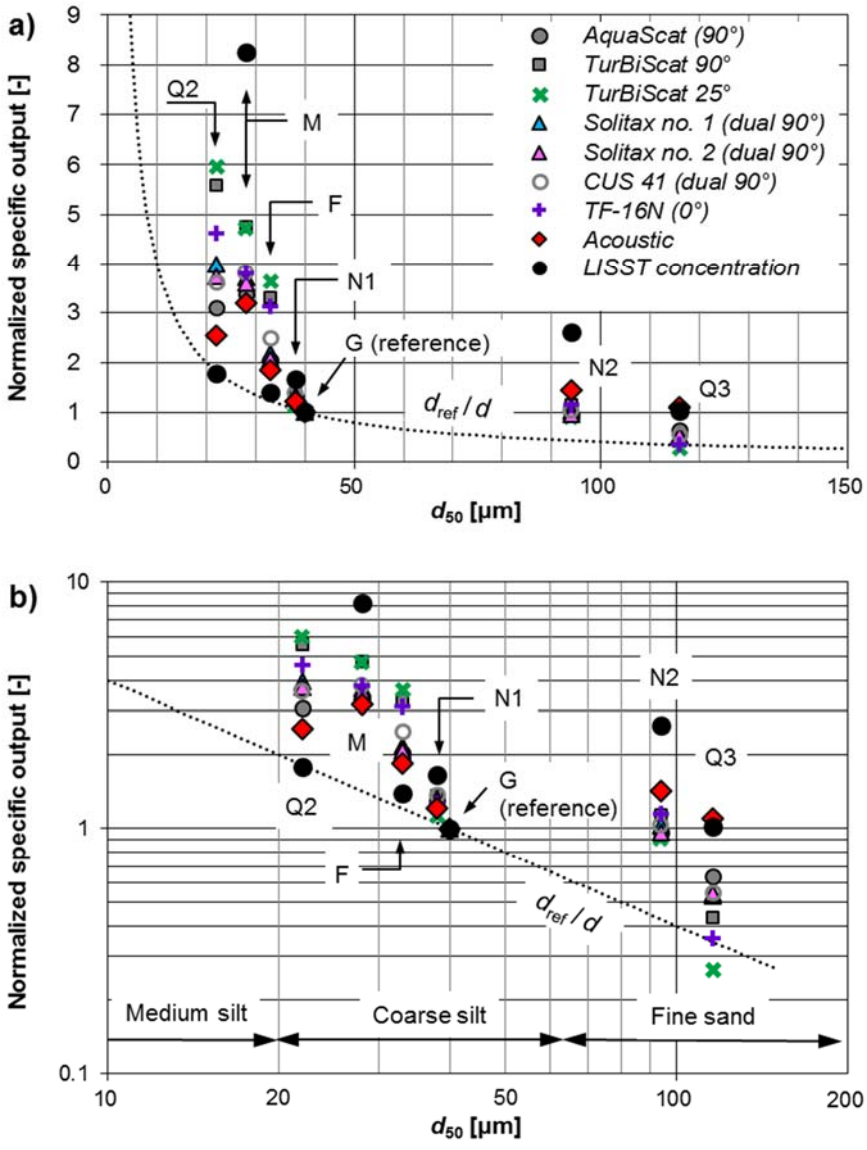

Figure 4-17 Comparison of the normalized specific output of instruments for *SSC* measurements as a function of d_{50} obtained from LISST, with a) linear and b) logarithmic scaling of axes.

Furthermore, the theoretical curve of the diameter-dependency (d_{ref}/d, with d_{ref} = 40 µm for the glass beads) is indicated in Figure 4-17. With logarithmic scaling of the axes, this relation appears as a straight line (Fig. 4-17b). This relation was expected for the turbidimeters and the single-frequency acoustic technique in case of monodisperse spherical particles (Sections 2.2.1.4 and 2.2.1.5). For the acoustic technique, this curve is valid for d < 60 µm only. The LISST concentration outputs should not depend on particle sizes, i.e. f_c should be constantly at unity.

The specific instrument outputs are discussed for each particle type:

- For quartz fine sand (Q3), the LISST f_c was ≈ 1 as expected, and the points of the turbidimeters lie relatively close to the theoretical line. This is attributed to the close-to-spherical particle shapes and the narrow PSD. The Q3-point of the acoustic technique lies considerably above the 1/d-line, which is explained by the fact that the d_{50} = 116 µm of this particle type is > 60 µm, i.e. lies in the size-range in which the specific attenuation increases with size (Section 2.2.1.5).
- For the particles from the tailwater of HPP Stalden (N2), i.e. the second-coarsest particle type, the high LISST f_c ≈ 2.6 is attributed to the flaky and angular particle shapes. The points of the turbidimeters and the acoustic technique lie above the theoretical line. This is attributed to the following reasons: Particles with highly non-spherical shapes produce more scattering and/or attenuation, the *SMD* is lower than d_{50} due to the grading of the particles, and LISST overestimates $d_{50,es}$.
  A further reason for the point of the acoustic technique above the theoretical line is that the majority of the N2-particles (by mass) has a diameter > 60 µm, i.e. in the size-range with increasing specific attenuation as mentioned above.
- For the particles from the tailwater of HPP Fieschertal (N1), the LISST f_c was smaller than for N2, indicating that the before mentioned effects were less pronounced. Similarly, the points of the turbidimeters and the acoustic technique lie closer to the theoretical line as for N2.
- For feldspar powder (F), i.e. angular particles, the LISST f_c is smaller than that of N1 and N2 which is attributed to the absence of flaky particles. Some of the turbidimeters are very sensitive to this particle type, probably due to their higher sensitivity to fine particles, which were absent or scarce in G, Q3, N1 and N2.
- For mica powder (M), i.e. thin flakes, the LISST f_c is about six times as high as for F. The specific outputs of the turbidimeters and the acoustic technique for M are less than twice those for F, indicating that these techniques are less sensitive to extreme particles shapes than LISST. The points of these techniques lie well above the theoretical line, which is explained by the reasons mentioned with N2.
- For quartz powder (Q2), the LISST f_c was higher than for F although both particle types were angular. The degree of angularity might have been different and Q2 contained more fine particles. Some turbidimeters were most sensitive to Q2. However,

the sensitivity of the acoustic technique for N1, F and Q2 varied "only" approximately with $1/d$, and depended less on the other particle properties such as shape.

The following conclusions were drawn from Figure 4-7:

- The specific turbidities varied by a factor of up to 20, depending on d_{50}, the particle shapes and among the tested instruments.
- Except for the thin mica flakes (M), which do not occur in pure form in nature, the specific *SSC* from LISST depended less on particle sizes than the specific turbidities.
- The acoustic technique was less sensitive to variations of particle sizes and shapes than the turbidimeters, and less sensitive to variations in particle shapes than the LISST. Together with a smaller sensitivity to fouling and the path-averaged way of measuring directly in the penstock, these are favourable properties of the acoustic technique for practical SSM in the context of turbine erosion. Despite the lower sensitivity to particle size, the specific output of the acoustic technique varies by a factor of ~2.5 for round to angular particles in the size-range of medium silt to fine sand.

4.3 Experimental errors

4.3.1 Measured and nominal *SSC*

The SSC_G, i.e. the gravimetrically determined *SSC*, were compared with the nominal *SSC* calculated from the particle mass and the water volume (Fig. A-6 in Appendix A2). For mica powder (M), the deviations were smallest. This is explained by the low settling velocity of these relatively small and highly non-spherical particles. For feldspar particles (F), the deviations were also relatively small (less than 10% for $SSC > 7$ g/l). For the relatively fine types of particles (M, F, Q2 and G), the points of SSC_G vs. nominal *SSC* in Figure A-6 show a moderate scatter, indicating a good reproducibility.

For the other types of particles, which (except for Q2) are coarser than F and M, the SSC_G were lower than the nominal *SSC*. This is attributed to mainly vertical *SSC* gradients (Section 2.1.4.3) and settling of a part of the particles. Sediment deposits in the corners and along the lower edges of the tank walls as well as in zones with smaller flow velocity behind installed instruments were detected with a rod, especially with fine sand (Q3). In the Q3 series, the stirrer speed was increased after the detection of sediment deposits, but the setup did not allow keeping the sand particles fully in suspension.

With relatively large particles in the range of fine sand (Q3 and partly N1), the scatter in the SSC_G in Fig. A-6 is larger than with fine particles. With sample volumes of <1 liter

and sampling times <5 s, the scatter in SSC_G may arise not only from measurement uncertainty, but also from real local *SSC* fluctuations within the tank. Coherent structures with locally higher *SSC* (clouds of suspended particles) were observed upwelling and moving around in the tank particularly for fine sand (Q3).

The *SSC* measured at the outlet of the turbidimeter with the free-falling jet were generally higher than those in the tank at the instruments' level (Fig. A-6). These deviations increase with particle size. Possible reasons for this are non-isokinetic conditions (i) in the tank at the vertical intake to the pump line (Fig. 3-3a) and (ii) at the oblique branch-off of the small feeding pipe of the *AquaScat* from the main sampling line.

The deviations between the SSC_G and the nominal *SSC* did not bias the experimental results because SSC_G were taken as the reference.

4.3.2 Measured and actual PSDs

PSDs might have been altered due to preferential setting of coarser particles in cases when it was not possible to keep all particles in suspension. For the coarser particle types, it is expected that the PSDs of the suspended particles in the tank at the level of the instruments were finer than those of the dry particle material (measured based on image analysis and with the non-portable LD prior to the experiments). For the fine particle types however, this deviation is negligible.

4.3.3 Other sources of uncertainty

The stirring induced a high degree of turbulence in the suspension and the formation of vortices which travelled in the tank around the stirrer. If a large vortex formed, it was sometimes air-entraining, which possibly affected the measurements, in particular of the acoustic technique because the acoustic path was arranged over the tank length close to the stirrer (Fig. 3-3b). Moreover, micro-air bubbles sticking to the added particles might have affected the acoustic measurements.

In the present study, flocculation was not prevented nor investigated. It may have played a role with cohesive particles, but not with coarser particles such as fine sand.

5 RESULTS AND DISCUSSION OF SUSPENDED SEDIMENT MONITORING (TASK B)

In this Chapter, the results of the suspended sediment monitoring (SSM) in the power waterway of HPP Fieschertal in the years 2012 to 2014 are reported and discussed. Firstly, the particles' hardness, shape and density is characterized. Secondly, the conversions of the outputs of the various instruments to *SSC* is treated. Thirdly, the variability of *SSC* and PSD and their relation are presented, followed by an analysis of the causes for sediment transport events. Then the performance of the SSM instruments is evaluated based on the field data. Based on the *SSC* and PSD time series, the suspended sediment loads (*SSL*) in the penstock and the particle loads (*PL*) per turbine according to IEC 62364 (2013) are elaborated. Finally, the uncertainties in *PL* and *SSL* are addressed.

5.1 General properties of suspended sediment particles

5.1.1 Mineralogical composition and hardness

According to analyses of the residues of three water samples taken in summer 2012 in the valve chamber, the sediments in the power waterway of HPP Fieschertal consist of the following minerals (in percent by mass):

- 25 to 40% Quartz with Mohs' hardness 7,
- 38 to 42% Feldspars, Epidote and Hornblende with Mohs' hardness 5.5 to ~6.5,
- 21 to 37% of Mica (Muscovite and Biotite), Chlorite and further minerals of the sheet silicates group with Mohs' hardness < 3.

Details of the mineralogical composition of these three samples (no. 1 to 3) as well as of five further samples taken from sediment deposits are presented in Tables C-2 and C-3 in Appendix C2. Sample no. 4 was taken from the particle material originating from the tailwater channel. This relatively coarse material (N1 with d_{50} = 38 µm in Table 4-2) was used in the laboratory investigations of the SSM instruments. In an earlier study by Abgottspon (2011), the samples no. 5 to 8 were taken from sediment deposits in the buckets of the turbidimeters in the powerhouse, which were fed with raw cooling water pumped from the tailrace channel. The results of the eight samples are summarized in Figure 5-1, which shows the cumulated mass fractions as a function of decreasing Mohs hardness.

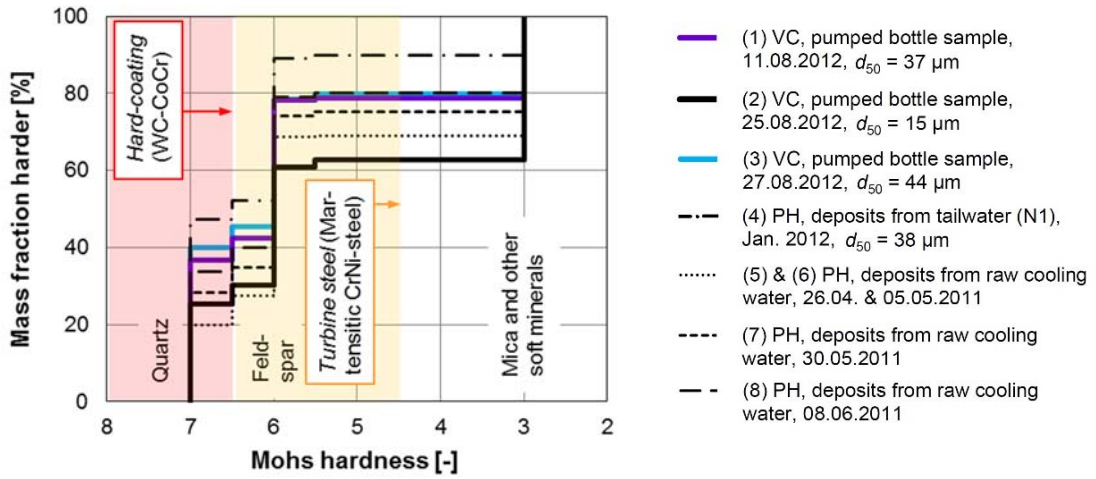

Figure 5-1 Mass fraction and hardness of sediment particles at HPP Fieschertal measured in 2011 and 2012; VC = Valve Chamber, PH = Powerhouse; data of 2011 according to Abgottspon (2011).

The percentage of minerals with a Mohs hardness >4.5, called 'hard minerals' in the following, varied from 63 to 90%. From the eight samples, the percentage of hard minerals was on average 76%; the absolute expanded uncertainty $U_{2\sigma}$ was ±16%. Krause & Grein (1996) reported similarly high percentages of hard particles for other HPPs in the Canton of Valais, Switzerland (Fig. C-2).

The percentage of hard minerals – and particularly the quartz content – were highest for sample no. 4 from the tailwater channel deposit, whereas these values were considerably lower for sample no. 2 with finer particles (d_{50} = 15 µm). For samples no. 5 and 6 with the lowest percentage of hard minerals, the particles were probably also quite fine, as typical for spring and early summer. The measurement results suggest that the fraction of hard minerals is higher if particles are larger. This is attributed mainly to the different properties of hard and soft particles: the latter (sheet silicates) are thin and break easily whereas larger particles consist rather of hard minerals.

According to IEC 62364 (2013), the mass fraction of minerals harder than the material at the surface of a turbine part is relevant for hydro-abrasive erosion and is taken as k_{hardness} (Section 2.3.6.1). For the usual turbine steel and hard-coated surfaces, the Mohs hardness is ~4.5 and ~6.5, respectively (Sections 2.3.1.2 and 2.3.1.3). For Fieschertal, this leads to $k_{\text{hardness}} \approx 0.75$ for base material erosion and $k_{\text{hardness}} \approx 0.31$ for coating erosion (Fig. 5-1 and Table C-2). In the present study, both base material and coating were simultaneously eroded in some periods at different locations within the runner buckets. For the computation of the Particle Loads (PL and PL_b), which are presented later in this Chapter, $\boldsymbol{k_{\text{hardness}} = 0.75}$ was adopted because the erosion of the base material was considered as the basic case.

5.1.2 Solid density

According to pycnometer analyses of the residues of twelve water samples taken in the years 2012 to 2014 at HPP Fieschertal, the solid density of the particles was on average $\boldsymbol{\rho_s = 2.73\ g/cm^3}$ (Table C-1 in Appendix C2). The expanded uncertainty $U_{2\sigma}$ was ±0.07 g/cm^3, corresponding to less than ±3%. The average ρ_s is plausible compared to literature values of the detected minerals' densities and their mass percentages. For example, mica and epidote have higher densities than quartz (2.65 g/cm^3).

5.1.3 Particle shapes

Figure 5-2 shows scanning electron microscopic images of the dried residue of a water sample pumped on August 27, 2012 in the valve chamber (sample no. 3 of mineralogical analyses). The basic particle shapes ranged between compact and elongated and the particles were mainly angular. Flaky particles as expected from the sheet silicates were hard to identify because they lie preferably in the plane of the image and their characteristic small *c*-axis is rarely visible. The flaky sheet silicate particles are of interest for SSM because of their effects on the indirect optical and acoustic *SSC* measurements; however, they are not relevant for turbine erosion. According to IEC 62364 (2013), $\boldsymbol{k_{shape} = 2}$ was set for angular particles (Section 2.3.6.1).

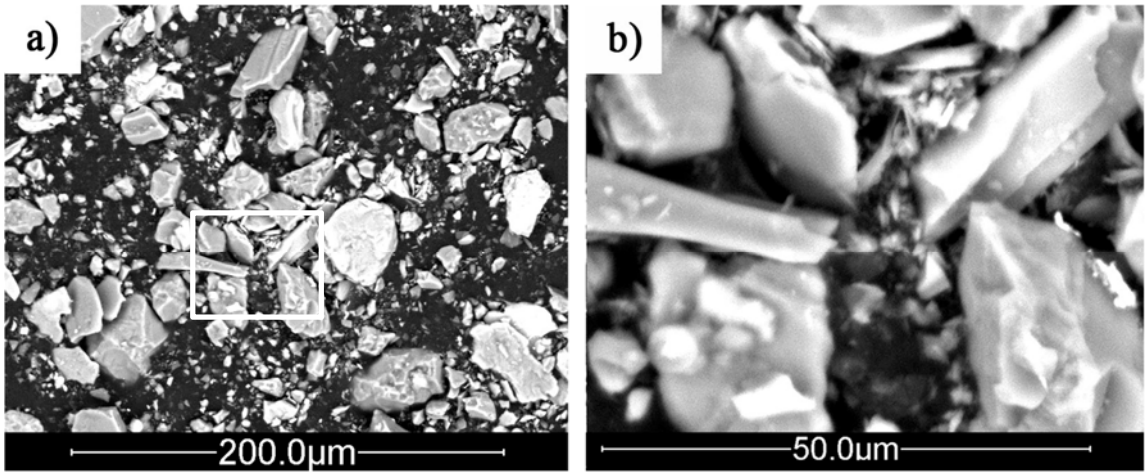

Figure 5-2 Microscopic images of dried sediment particles from a water sample of HPP Fieschertal; b) shows a magnified detail of a).

5.2 *SSC* conversion functions (field calibrations)

5.2.1 General remarks

The time series of the two turbidimeters in the powerhouse had frequent data gaps because their sampling pipes were often clogged. It turned out that the sampling pipe arrangement needs to be improved in order to cope with the intermittent raw water supply depending on turbine operation. The data from these two turbidimeters were not further evaluated. The SSM data evaluation focused hence on the data from the instruments in the valve chamber.

The signals of the turbidimeters *TurBiScat* and *TF-16N* (items no. 3 and 4 in Table 3-1) had strong drift due to fouling (Fig. C-3 in Appendix C3). This showed that occasional cleaning was not sufficient over several months and these turbidimeter models are not practical for SSM in HPPs. Therefore, these signals were not further evaluated, except during the major flood event in July 2012, when the *AquaScat* and the CFDM were not yet installed.

5.2.2 Turbidimeters

The SSC_G and turbidity values measured with *AquaScat* at corresponding times in the sediment seasons 2013 and 2014 are compared in Figure 5-3a ($n = 122$). In some periods, no valid turbidimeter data were available because the small hose feeding the turbidimeter was clogged by fine sediment accumulated upstream of the partially opened ball valves. The relatively high degree of scattering is attributed to mainly temporal PSD variations, and potential variations of particle densities and shapes. The inverse of the relation in Figure 5-3a was used to convert the time series of measured turbidity to SSC_T.

Figure 5-3b shows turbidity values as a function of SSC_C (obtained from CFDM). The points represent all valid results of the minute-by-minute measurements in the sediment seasons 2013 and 2014 when also d_{50}-values from LISST were available ($n \approx 339\,000$). The d_{50} is represented by the colour of the points. The relations between turbidity and SSC_C are quasi-linear for given ranges of d_{50}, and the specific turbidity is smaller for coarser particles. This is as expected from theory (Section 2.2.1.4) and measured in the laboratory (Fig. 4-2).

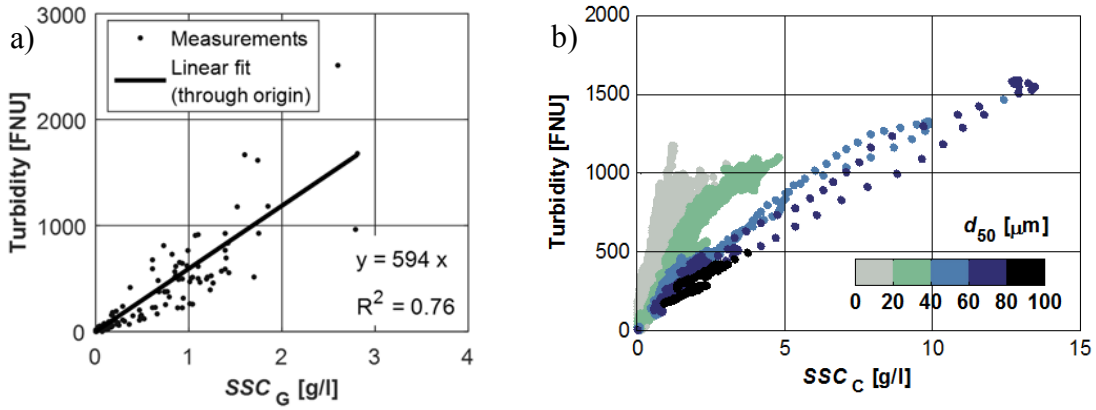

Figure 5-3 Turbidity measured with *AquaScat* in 2013 and 2014 at HPP Fieschertal as a function of a) SSC_G and b) of SSC_C with point colours indicating the d_{50} obtained from LISST (modified from Abgottspon *et al.* 2016a, Felix *et al.* 2016c, Felix *et al.* 2017).

5.2.3 Acoustic technique

The SSC_G and the acoustic damping δ at corresponding times in the sediment seasons 2013 and 2014 are shown in Figure 5-4a (n = 183). The same years as in the previous Section were considered for comparability. The scatter is attributed to the same phenomena as for the turbidimeter. Again a linear relation was determined and applied to convert the time series of δ to SSC_A. A linear relation was selected for simplicity and for direct comparability with turbidimeters. This approximation was acceptable for the determination of SSC_B (best estimate SSC time series) because only low SSC_A (mainly < 1 g/l) were included in SSC_B.

Figure 5-4b shows the δ as a function of SSC_C and d_{50}, in analogy to Figure 5-3b. As for turbidimeters, the specific δ is lower for coarser particles. In contrast to most turbidimeters ($\alpha > 0°$), the relation between δ and SSC_C is non-linear for SSC above some g/l, similar to the laboratory results (Fig. 4-10a) and as expected from theory (Eq. 2-19).

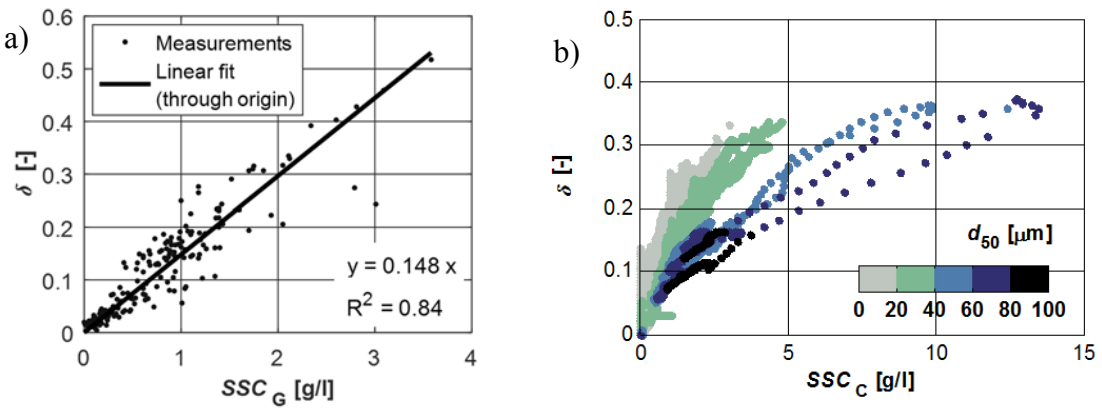

Figure 5-4 Acoustic damping δ measured in 2013 and 2014 at HPP Fieschertal as a function of a) SSC_G and b) SSC_C with point colours indicating d_{50} obtained from LISST (modified from Gruber *et al.* 2016, Felix *et al.* 2017).

5.2.4 LISST concentrations

Figure 5-5a shows the SSC_{L0} compared to the $SSC_G \leq 4$ g/l at corresponding times in the years 2012 to 2014 (n = 248). The SSC_{L0} are the total volume concentrations TVC from LISST multiplied by the average solid density of the particle material ρ_s from the pycnometer (Section 5.1.2). The SSC_{L0} were on average 89% higher than the $SSC_G \leq 4$ g/l. For SSC_G with $d_{50} \leq 15$ µm (n = 184), a similar ratio was found (Fig. 5-5b).

Assuming that the measuring errors of both the SSC_G and ρ_s were negligible, and that there was no flocculation, the overestimation was attributed to effects of highly non-spherical particle shapes. In the laboratory investigations, overestimations of $f_c = 1.38$ and $f_c \approx 8$ were quantified for angular feldspar and relatively thin muscovite flakes, respectively (Table 4-6). With the particle mixture at HPP Fieschertal (mass ratio of ~75% angular and ~25% flaky particles according to Section 5.1.1), and considering that the mica flakes at the study site are probably thicker than those used in the laboratory, the overestimation of $f_c \approx 1.9$ in Figure 5-5 appears plausible.

The scatter in Figure 5-5 is attributed to temporally varying effects of (i) fouling, (ii) particle shapes and (iii) flocculation. The first was partly corrected in the data treatment. These three effects cause SSC overestimations, i.e. explain points above the 1:1-lines. However, also combinations with $SSC_{L0} < SSC_G$ were measured (points below the 1:1-line in Figure 5-5b) at $SSC_G < 0.7$ g/l and $d_{50} < 15$ µm. SSC_G might have been overestimated due to accumulation of sediment particles suspended in the water volume in the LISST bucket, from which the samples were pumped.

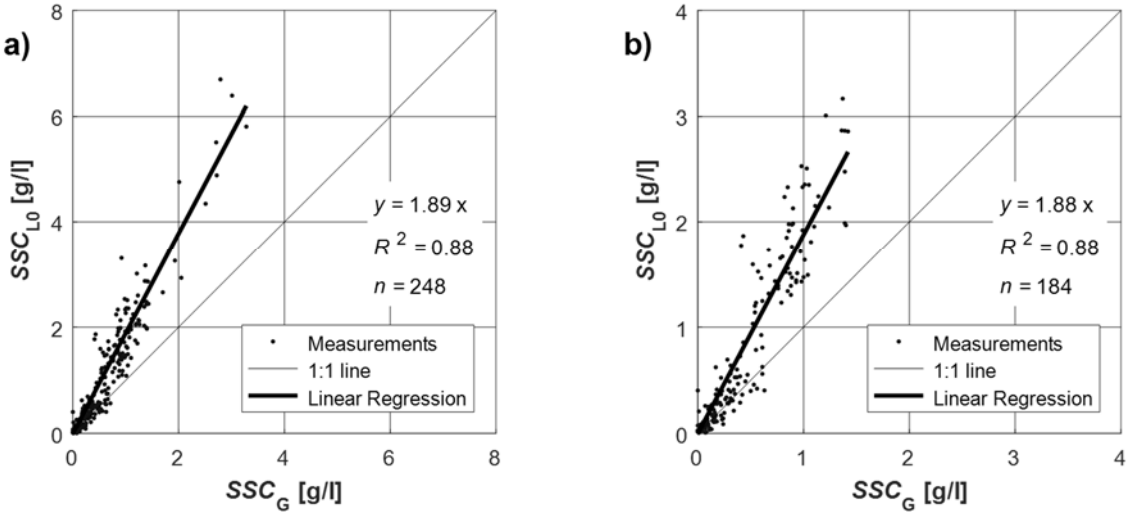

Figure 5-5 SSC_{L0} compared to SSC_G measured at HPP Fieschertal in the years 2012 to 2014 with linear fits for a) $SSC_G \leq 4$ g/l and b) $d_{50} < 15$ µm.

The dependency of f_c on d_{50} was investigated. Given the scarcity of SSC_G with coarse particles, the SSC_C were used as the reference instead of SSC_G. Only data with $SSC_C \geq 1$ g/l were considered in order to limit the relative uncertainty of the reference. It is seen from Figure 5-6 that $SSC_{L0} / SSC_C = f_c$ non-linearly decreases with larger d_{50}. An exponential decay function, above a base value of $f_c = 1.2$, was fitted to the data (Eq. 5-1a). For $d_{50} \leq 12$ µm, where almost no data were available in Figure 5-6, $f_c \approx 1.9$ was taken from Figure 5-5b.

$$f_c = 1.13\, e^{-0.042\, d_{50}} + 1.2 \qquad \text{for } d_{50} > 12 \text{ [µm]} \qquad \text{[-]} \qquad (5\text{-}1a)$$

$$f_c = 1.9 \qquad \text{for } d_{50} \leq 12 \text{ [µm]} \qquad \text{[-]} \qquad (5\text{-}1b)$$

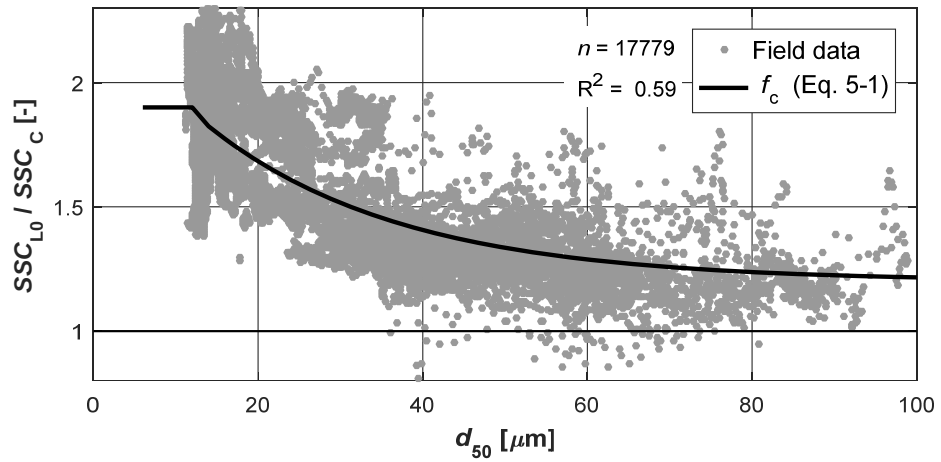

Figure 5-6 *SSC* obtained from LISST and pycnometer (SSC_{L0}) compared to *SSC* from CFDM ($SSC_C \geq 1$ g/l) as a function of d_{50} measured in the power waterway of HPP Fieschertal in the years 2013 to 2014, with fit of a particle size-dependent correction factor f_c.

Possible reasons for the decrease of f_c with larger d_{50} are (i) effects of non-spherical particle shapes on SSC_{L0} and d_{50} from LISST, (ii) effects of the spreading σ_g of the PSD on the d_{50}, and/or (iii) a systematic variation of the particle shapes with increasing particle size. The latter is supported by the smaller percentage of highly non-spherical particles (sheet silicates) at larger sizes (Section 5.1.1).

Equation (5-1) was used to correct the SSC_{L0} (obtained from the LISST and the pycnometer) based on the d_{50} measured by LISST:

$$SSC_{L2} = TVC\ \rho_s / f_c(d_{50}) \qquad \text{[g/l]} \qquad (5\text{-}2)$$

For the turbidimeters and the single-frequency acoustic system, no size-depenent *SSC* correction factor was introduced, because – in contrast to LISST – these instruments do not provide the actual d_{50} which is required to compute such a correction.

If ρ_s is not known or not required, the value of the term ρ_s / f_c can be determined by linear fitting between *TVC* and reference *SSC* data. This conversion factor has units of a density and was called 'effective density' by Czuba *et al.* (2015). In the present study, the term 'apparent density' is used because it does not represent the particle density in case of highly non-spherical particles. The apparent density was 2.73 g/cm^3 / 1.9 = 1.44 g/cm^3 for small particles ($d_{50} \leq 12$ µm) and increased to 2.24 g/cm^3 for particles with d_{50} = 100 µm (f_c = 1.22). In a study at rivers in the USA, Czuba *et al.* (2015) found an average apparent density of 1.24 g/cm^3 which was also considerably lower than the solid density of the particle material (ρ_s = 2.56 to 2.87 g/cm^3).

5.3 *SSC* and PSD in the penstock

5.3.1 Time series of *SSC* (best estimate)

Figure 5-7 shows the time series of SSC_B (best estimate) compiled as described in Section 3.4.5. During the winter months, *SSC* is close to zero, whereas it is higher from April to October, i.e. the sediment season. More detailed *SSC* time series during the sediment seasons 2012 to 2014 are presented in Figures C-5 to C-7 in the Appendix C4. *SSC* exceeded 10 g/l several times a year for some minutes or exceptionally a few hours. The two highest *SSC* peaks, i.e. 50 and 24 g/l, were measured in 2012 during and after the major flood event of July 2 and 3.

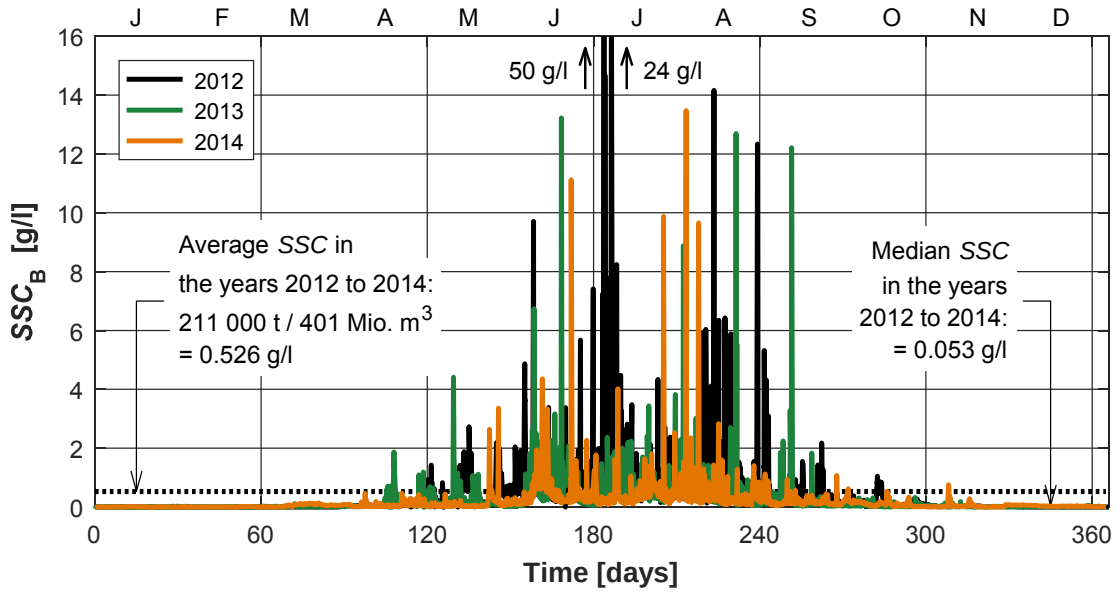

Figure 5-7 Time series of SSC_B in the penstock of HPP Fieschertal in the years 2012 to 2014 (modified from Felix *et al.* 2016d).

Figure 5-8a shows a detail of the SSC_B time series during the major flood event. For this event, SSC_B was computed based on the pressure signals measured upstream of each turbine (Figure 5-8b). While the headwater level and the turbine discharge remained constant, the pressures rose by 17 m of clear water column, i.e. 3.2% of the net head in clear water conditions. The electric outputs of the MGs increased temporarily by the same amount. This was interpreted as an increase of the density of the water-sediment mixture in the penstock up to 1.032 g/cm^3. According to Equation (3-3), this mixture density corresponds to an SSC of 50 g/l. This value was supported by SSC_G of some pumped samples from the valve chamber and by some Imhoff cone measurements of water samples taken by the HPP operator from the tailwater channel.

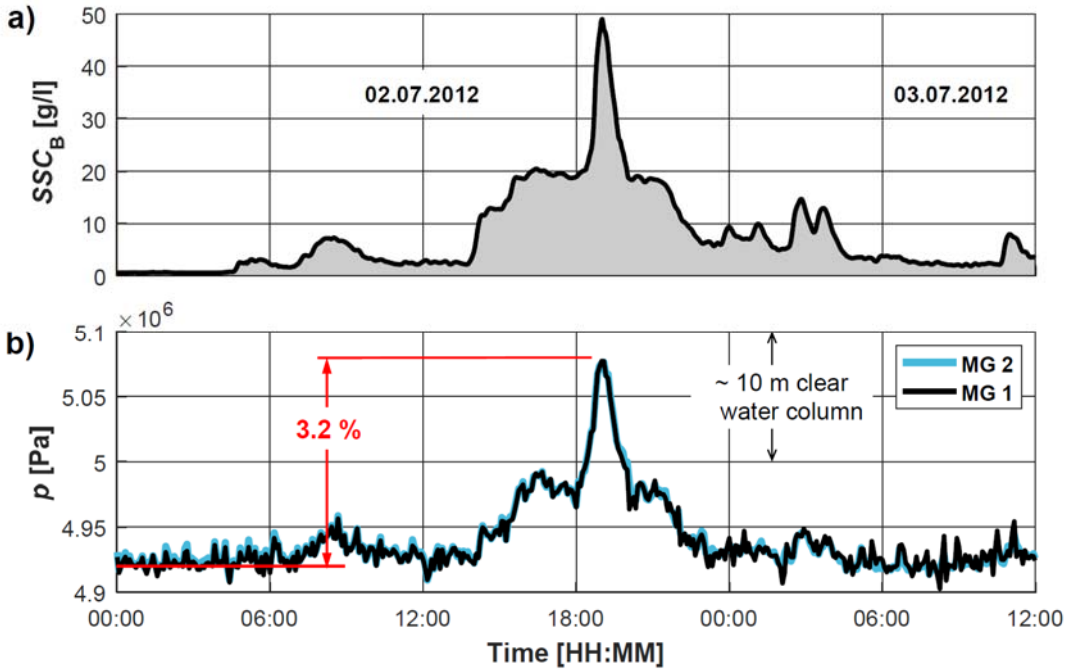

Figure 5-8 a) SSC_B time series in the penstock of HPP Fieschertal during the major flood event on July 2 and 3, 2012 and b) pressures p measured upstream of each turbine in the corresponding period.

5.3.2 PSDs and their spreading

Figure 5-9 shows an example of a fine and coarse PSD measured at two moments on June 30, 2014. On this day, the PSD varied considerably in less than 6 h. In Figures 5-9a and 5-9b, the same data are displayed with a linear and logarithmic scaling of the diameter axes, respectively. All measured PSDs in the years 2012 to 2014 are summarized by the grey areas. A darker grey indicates a higher probability of occurrence P. The P-values were computed from all plausible LISST data in this period ($n \approx 671\,000$ PSDs). The particles were mostly in the size-range of silt.

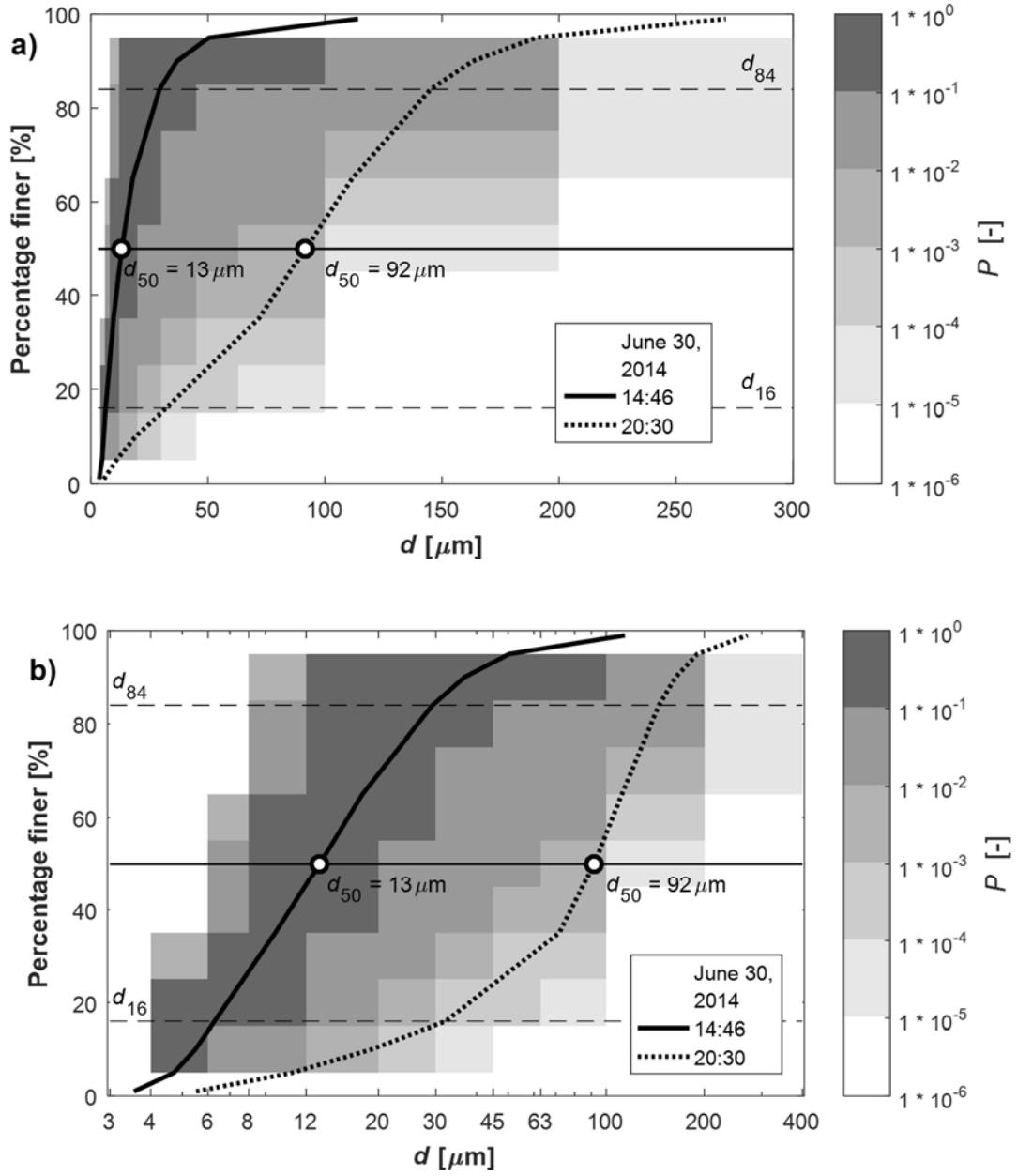

Figure 5-9 PSDs measured in the valve chamber of HPP Fieschertal, with a) linear and b) logarithmic scaling of the diameter axis d (modified from Felix *et al.* 2013c). The lines show examples of a fine and a coarse PSD. A darker shading indicates a higher probability of occurrence in the years 2012 to 2014.

The spreading σ_g of the PSDs was evaluated based on d_{84} and d_{16} (Eq. 2-3). The σ_g was at least 1.5, often below and around 2, and increased occasionally to ~4 on some days. According to Fig. C-4a in Appendix C3, σ_g was generally lower with higher *SSC*. Moreover, σ_g tended to be rather lower for larger d_{50}, i.e. there was a slight trend that fine sand was less graded than silt (Fig. C-4b). This is a possible reason for decreasing f_c for larger particles (Fig. 5-6). The median value of σ_g (dashed lines in Fig. C-4) from all plausible LISST field measurements was 2.15, i.e. slightly higher than σ_g = 1.94 for the particles from the tailwater deposits (N1) used in the laboratory (Table 4-2).

5.3.3 Time series of median particle size d_{50} (best estimate)

Figure 5-10 shows the annual time series of the d_{50} in the three years of measurements (best estimate as described in Section 3.4.5). More detailed d_{50} time series for each sediment season are presented in Figure C-8 in the Appendix C4. The d_{50} was usually in the size-range of medium silt and occasionally increased up to 100 µm, i.e. in the range of fine sand.

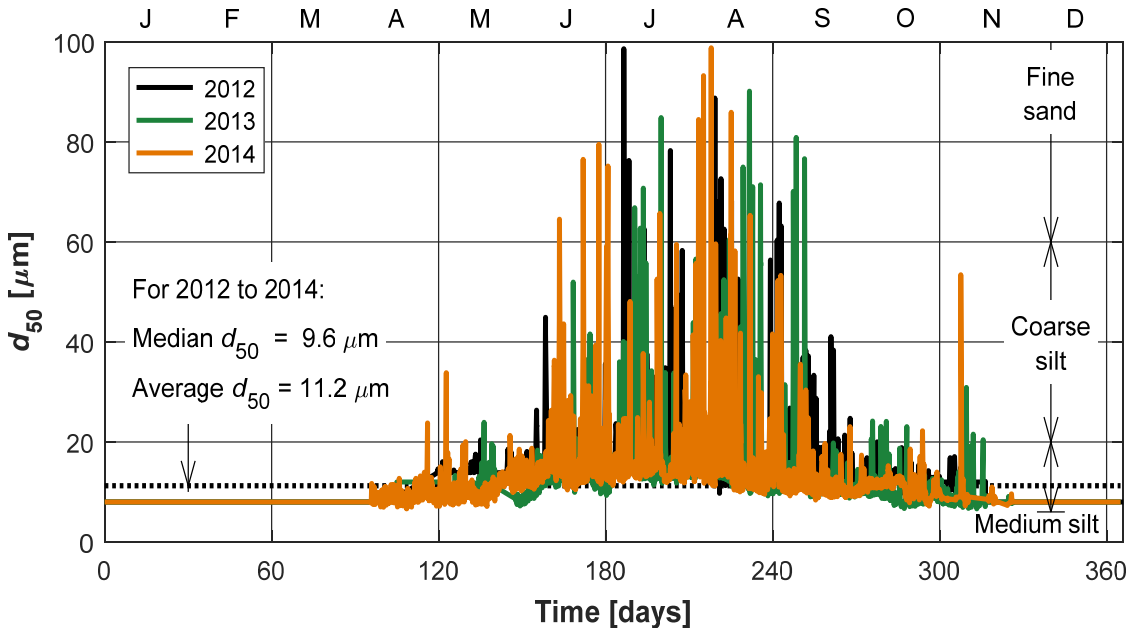

Figure 5-10 Time series of d_{50} in the penstock of HPP Fieschertal in the years 2012 to 2014.

5.3.4 Duration curves of *SSC* and d_{50}

Figure 5-11 shows the duration curves of *SSC* and d_{50} for the period 2012 to 2014. These curves, also called permanence curves, indicate the fraction of time when a certain *SSC* or d_{50} was reached or exceeded. The median values, i.e. which are not exceeded during half of the time, were 0.053 g/l and 9.6 µm, respectively. These median values are also indicated on Figures 5-7 and 5-10, resepectively. The *SSC* exceeded 1 g/l during 12 days per year and 10 g/l during 4 hours per year. The *SSC* was only above 20 g/l during the exceptional flood event in 2012; this part of the duration curve is thus not representative for the three-year period. During 13 days and 14 hours per year, d_{50} exceeded 20 µm and 60 µm, respectively. This means that the d_{50} was in the size-ranges of medium silt, coarse silt and fine sand during 96.44%, 3.40% and 0.16% of the time. The left end of the *SSC* duration curve is sharper than that of d_{50}, i.e. *SSC* varies much more than d_{50}.

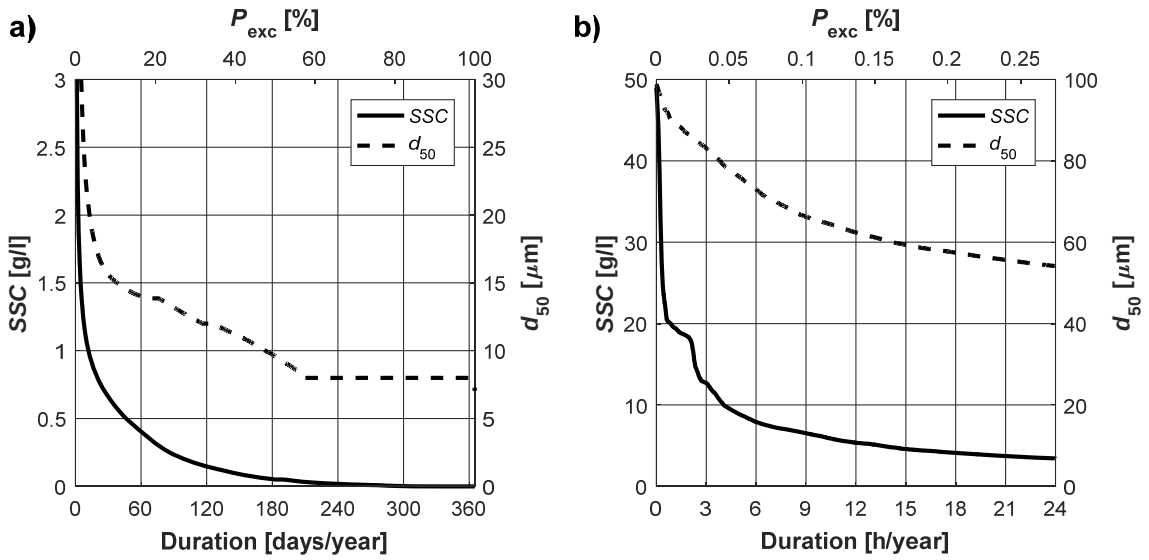

Figure 5-11 Duration curves of SSC_B and d_{50} in the penstock of HPP Fieschertal of the period 2012 to 2014 for a) all days of a year and b) detail of up to one day per year; P_{exc} is the probability of exceedance.

5.3.5 Relation between *SSC* and d_{50}

The median particle diameter d_{50} varied gradually in time and showed a clear relation to SSC_B during single sediment transport events (Fig. 5-12a). Often there was a hysteresis effect between the periods of ascending and falling *SSC*. During two weeks in summer including several events, the scatter was larger (green points in Fig. 5-12b). During another two weeks in autumn, the d_{50} stayed below 20 µm (black points in Fig. 5-12b). Figure 5-13 shows all combinations of the minute-by-minute SSC_B and d_{50} in the years 2012 to 2014 ($n \approx 1.5 \cdot 10^6$ points). With many events, there was only a weak correlation ($R^2 = 0.18$) between d_{50} and *SSC*. The correlation was slightly positive, i.e. there is a trend that coarser particles are transported at higher *SSC*.

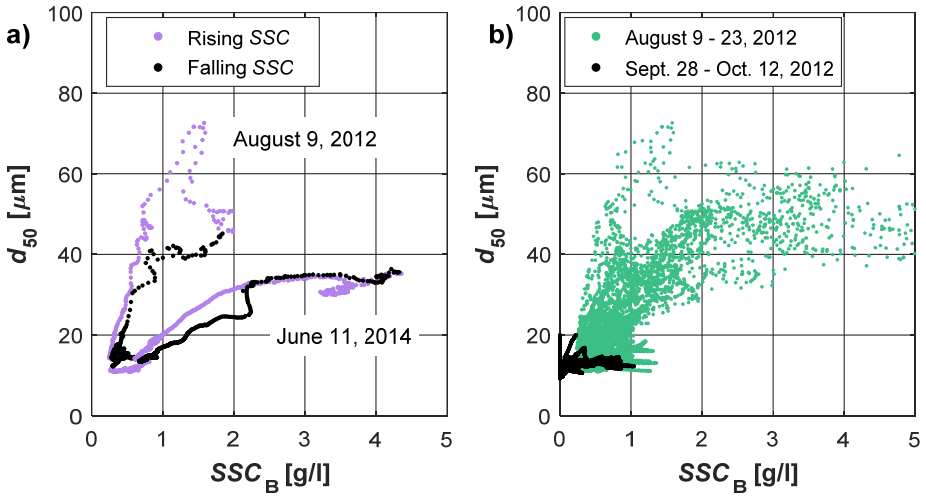

Figure 5-12 Median particle diameter d_{50} and SSC_B in the penstock of HPP Fieschertal measured during a) two selected days and b) two periods of two weeks in summer and autumn 2012 (Felix *et al.* 2014).

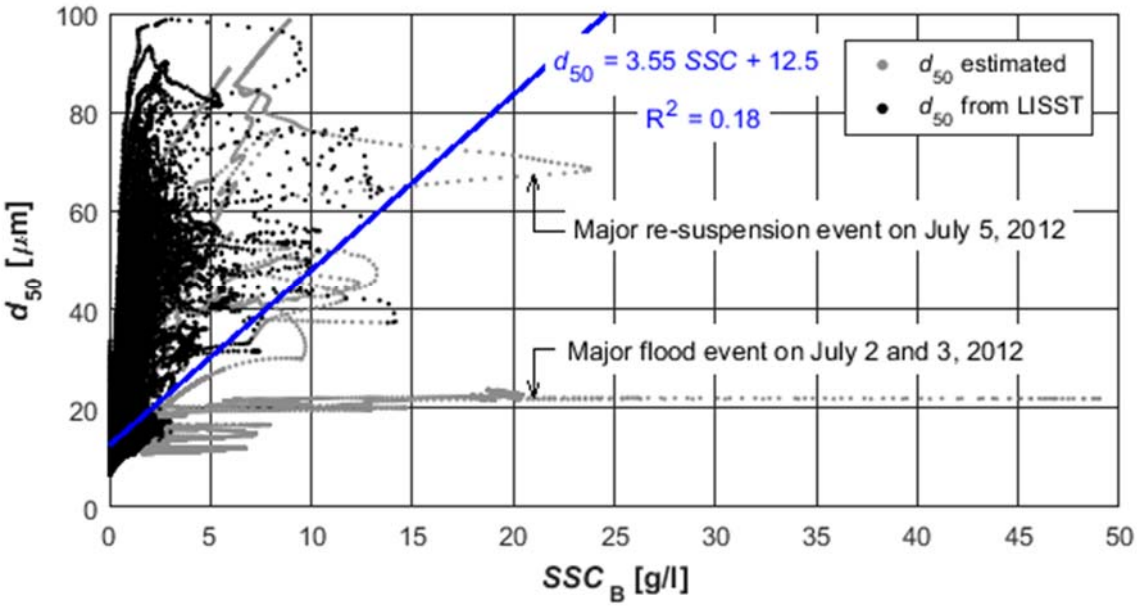

Figure 5-13 All combinations of d_{50} and SSC_B in the penstock of HPP Fieschertal determined from the measurements in the years 2012 to 2014 with linear fit.

Figures 5-14 and 5-15 show the probabilities of occurrence P of certain combinations of SSC_B and d_{50} in the years 2012 to 2014 (bivariate histograms). Classes with widths of 0.1 g/l and 5 µm were defined. The most frequent combination (during 17% of the time) was SSC between 0.1 and 0.2 g/l and d_{50} between 10 and 15 µm (black rectangle in Fig. 5-14). The d_{50} was in this size-range during 62% of the time. Larger particles with $d_{50} > 20$ µm were mainly transported in rather short events with elevated SSC (Fig. 5-16). Such combinations were comparatively rare (e.g. $P = 10^{-4} = 0.01\% \approx 1$ h/year).

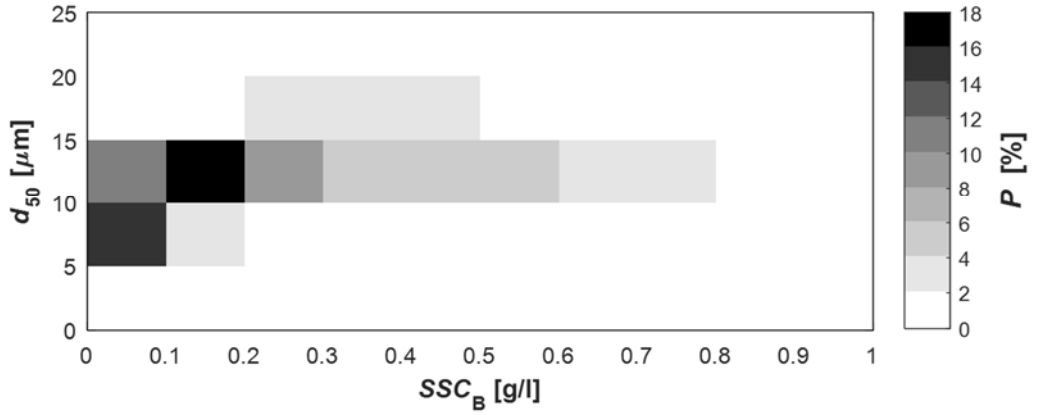

Figure 5-14 Probabilities P of certain combinations of d_{50} and SSC_B in the penstock of HPP Fieschertal based on field data 2012 to 2014, with linear scaling of the probability classes.

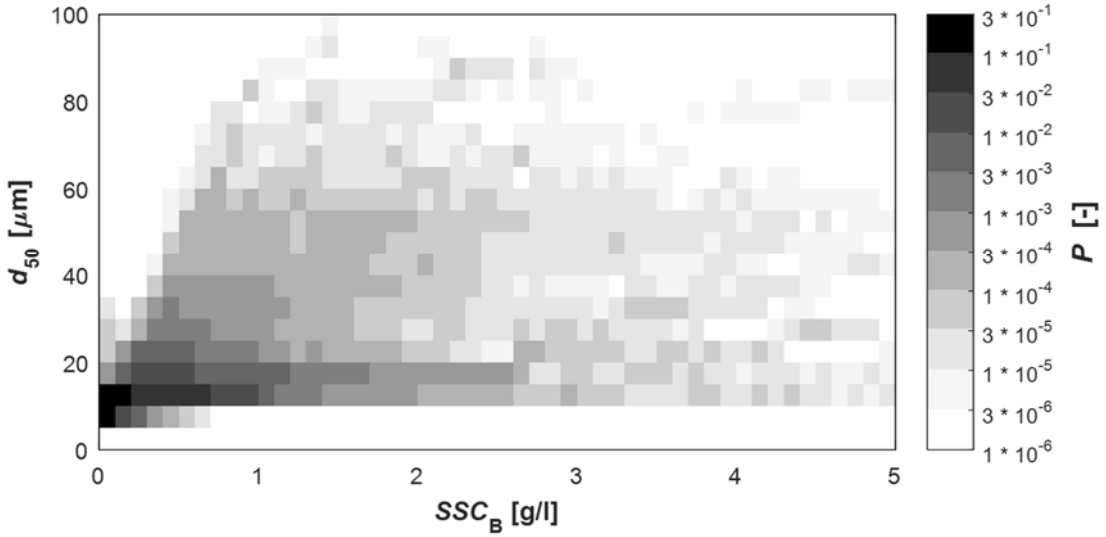

Figure 5-15 Probabilities P of combinations of d_{50} and SSC_B ($\leq$ 5 g/l) in the penstock of HPP Fieschertal based on field data 2012 to 2014, with logarithmic scaling of the probability classes.

5.4 Performance of techniques for continuous SSM

5.4.1 Performance comparison in selected events

The performances of the various techniques and instruments for continuous *SSC* measurements were assessed by evaluating the *SSC* and PSD time series during three years. Based on three examples of these time series (Figs. 5-16 and 5-17), the performance of the instruments is characterized as follows:

- The *SSC* from CFDM up to ~9 g/l were similar to SSC_G. The CFDM measured *SSC* up to 13 g/l.
- The corrected *SSC* from LISST matched reasonably well with those from the CFDM. However, no LISST results were available if the optical transmission was too low. This was the case e.g. above 1.1 g/l with $d_{50} \approx 11$ µm (Fig. 5-17a) or ~5.5 g/l with $d_{50} \approx 36$ µm (Fig. 5-16). However, in the example of Fig. 5-17b with $SSC_{L2} = 15$ g/l and $d_{50} \approx 75$ µm, LISST outputs were not interrupted.
- The *SSC* calculated from turbidity or acoustic single-frequency attenuation considerably deviated from the *SSC* of the other techniques mainly in periods of elevated *SSC*, when the PSD differed from average conditions. The *SSC* from these techniques were determined using linear conversions based on $SSC_G < 4$ g/l (Figs. 5-3a and 5-4a) which are correct for the usually prevailing particles, but lead to *SSC* over- or mainly underestimations if the particles are finer (Fig. 5-17a) or coarser (Figs. 5-16 and 5-17b), respectively. Using non-linear conversion functions to consider a potential correlation between *SSC* and d_{50} and the non-linear behaviour of the acoustic system at higher *SSC* would reduce the *SSC*-deviations of these techniques mainly at high *SSC*. The turbidimeter is more sensitive to finer

particles than the acoustic system (Fig. 5-17a). In Figure 5-17b, no turbidimeter data are available because its feeding pipe was temporarily clogged.

– The pressure-based technique yielded similar *SSC* as the CFDM and bottle samples. The SSC_P were considered only above 2 g/l, because the relative measurement uncertainty was too high at lower *SSC*. The deviations between the SSC_P and SSC_C are mainly attributed to the different measurement volumes: while the CFDM measured *SSC* in a small sampling pipe at the top of the penstock (point measurement), the *SSC* from pressure refers to the volume of the penstock, i.e. is averaged over 3500 m^3 and hence affected by delay and damping.

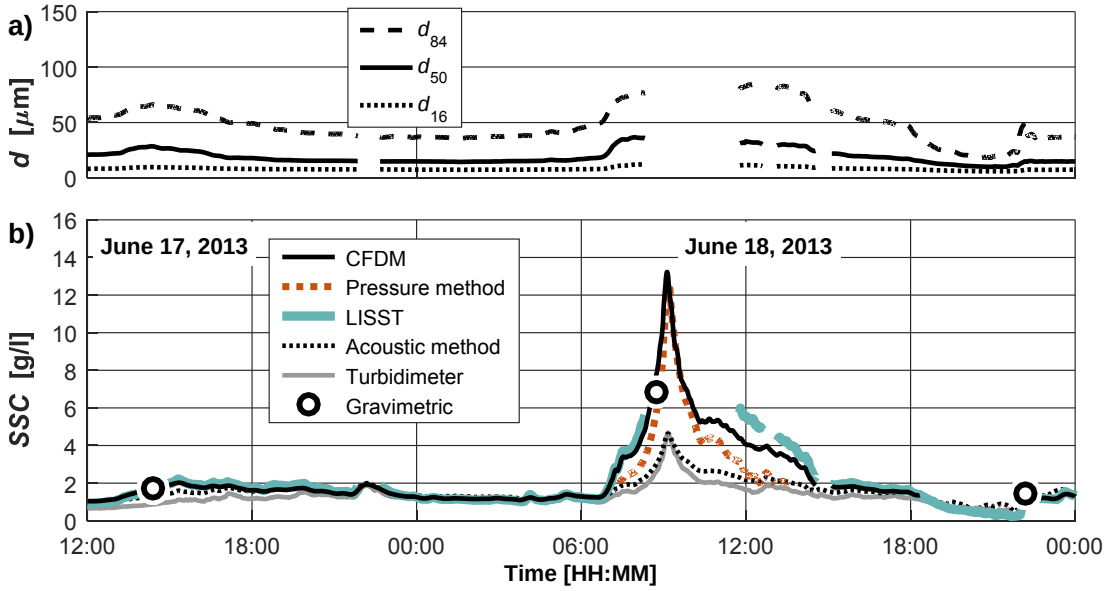

Figure 5-16 Time series of a) particle sizes obtained from LISST as well as of b) *SSC* from five techniques for continuous measurement and reference SSC_G (modified from Felix *et al.* 2016c).

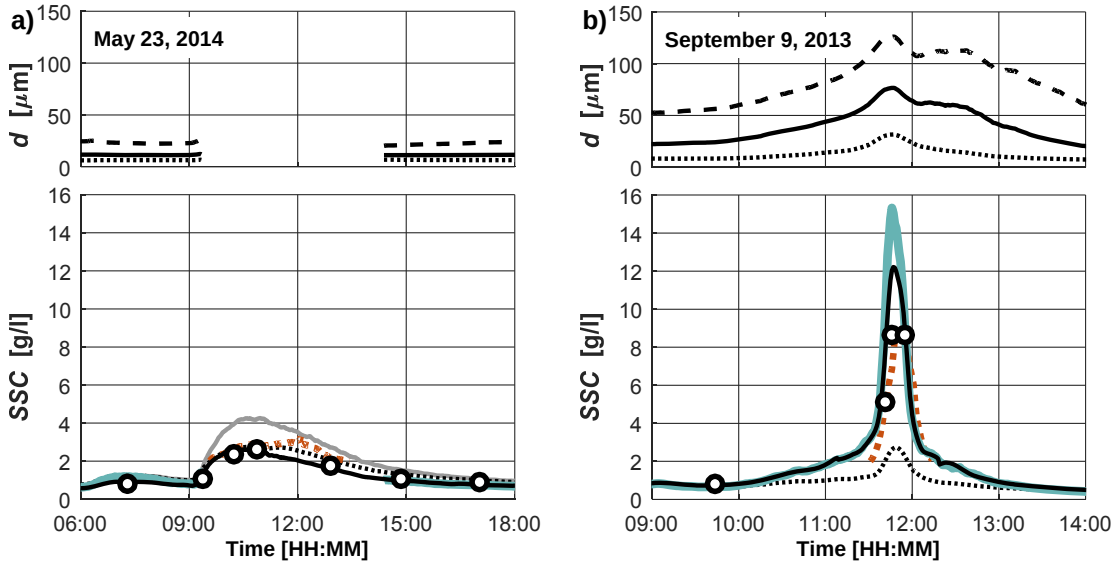

Figure 5-17 Time series of measured particles sizes and *SSC* with two further sediment transport events (modified from Felix *et al.* 2015, 2017); legends as in Figure 5-16.

5.4.2 Measurement uncertainty on *SSC* from CFDM

In Figure 5-18a, the SSC_C are compared to SSC_G ($\leq$ 4 g/l) at corresponding times. The standard deviation of the differences between the *SSC* from both techniques was σ = 0.15 g/l. Assuming that these differences are measuring errors of only the CFDM, the absolute expanded measurement uncertainty on *SSC* from CFDM was estimated as $U_{2\sigma}$ = ±0.3 g/l (dashed lines in Figure 5-18).

According to the operation principle of the CFDM and its specifications, the density measurement uncertainty in the considered range does not increase with *SSC*. E.g. for $SSC \geq 1$ g/l, the relative $U_{2\sigma}$ does not exceed ±30%. The uncertainties on the density and the *SSC* are related by Equation (3-3). Hence the density measurement uncertainty of ±0.5 g/l specified by the manufacturer (Endress+Hauser 2014) corresponds to ±0.8 g/l with respect to *SSC* (dotted lines in Figure 5-18). The *SSC* measurement uncertainty of ±0.3 g/l determined from the field data is thus smaller. The site-specific and temporally variable density offset $K(t)$, i.e. the periodic *in-situ* calibration described in Section 3.4.4.5, contributed to reduce the $U_{2\sigma}$ on the *SSC* from CFDM.

As mentioned in Section 2.2.1.7, so-called phase decoupling may occur with larger particles, which would lead to an underestimation of *SSC* by the CFDM. The ratio of SSC_C to SSC_G was investigated as a function of d_{50} (Figure 5-18b). The SSC_C / SSC_G did not decrease with larger particles, indicating that phase decoupling was not a major issue with mostly silt and occasionally fine sand particles in the water.

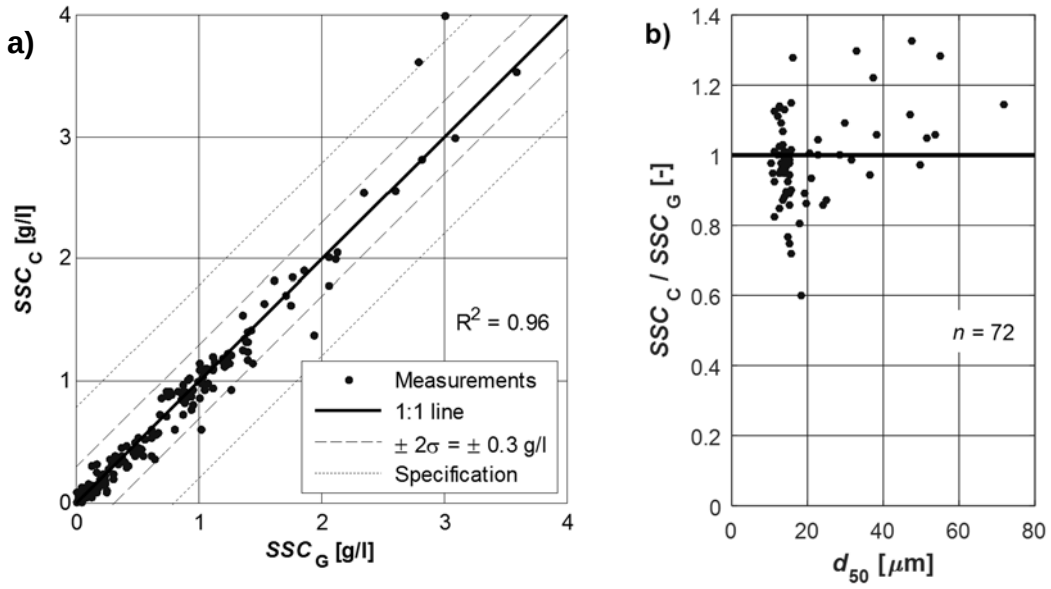

Figure 5-18 a) Comparison of *SSC* from CFDM (SSC_C) and from gravimetry ($SSC_G \leq 4$ g/l) measured at HPP Fieschertal in 2013 and 2014 (Felix *et al*. 2017); b) *SSC*-ratio of the two techniques as a function of d_{50} (for $SSC_C \geq 0.5$ g/l and 0.5 g/l $\leq SSC_G \leq 4$ g/l).

5.4.3 Particle-size sensitivity

Figure 5-19 shows the relative *SSC* obtained from a turbidimeter (*AquaScat*), the acoustic system and the LISST (after the particle-size dependent correction) as a function of d_{50} in the years 2013 to 2014. The *SSC* obtained from the three devices were normalized with SSC_C. Only the measurement points fulfilling the following conditions were selected for Figure 5-19 (n = 12 860):

- Plausible results of the four instruments simultaneously available, and
- $SSC_C \geq 1$ g/l ($U_{2\sigma}$ of the reference not exceeding ±30%, Section 5.4.2).

For the usually prevailing relatively fine particles ($d_{50} \approx 15$ µm), the *SSC* from the turbidimeter and the acoustic system corresponded well to those from the CFDM ($SSC_i / SSC_C \approx 1$) because of the reasons mentioned in Section 5.4.1. For larger particles, the SSC_i / SSC_C decreased. For mono-disperse spherical particles, the specific turbidity and thus SSC_T / SSC_C is expected to decrease with $1/d$ (Section 2.2.1.4), as displayed in Figure 5-19 for a reference diameter of d_{ref} = 15 µm. The field data showed a similar, but less pronounced particle-size dependency. The deviation is attributed to differences between d_{50} and *SMD*, as well as to effects of non-spherical particle shapes. As in the laboratory tests, the acoustic system was less sensitive to particle size variations than the turbidimeters. *SSC* from LISST did not systematically vary with particle size after application of the size-dependent correction factor (Eq. 5-1).

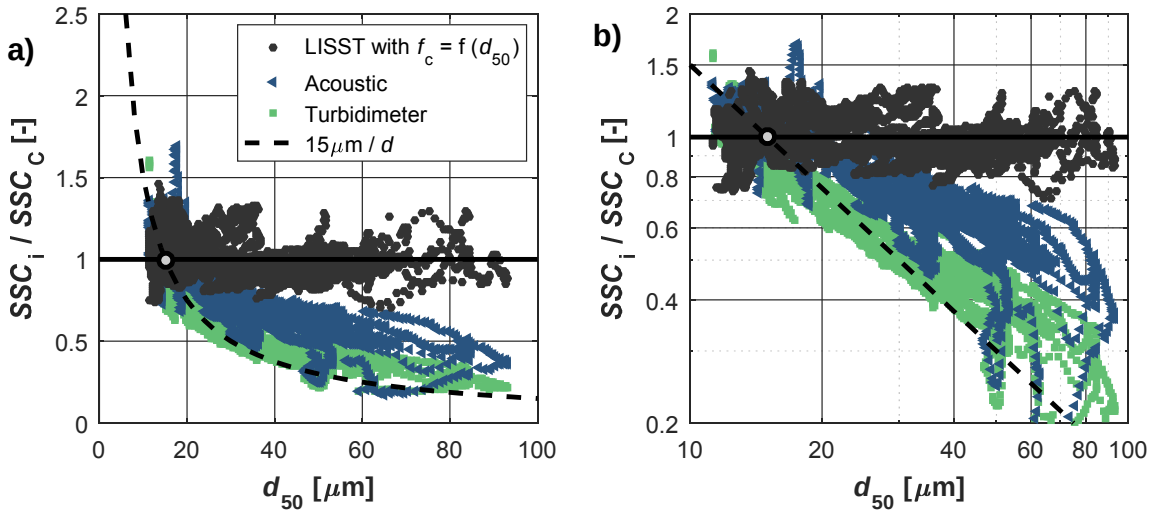

Figure 5-19 Relative *SSC* obtained from turbidimeter (*AquaScat*), acoustic attenuation (1 MHz), and LISST (after correction) compared to SSC_C (≥ 1 g/l) as a function of d_{50} measured in the power waterway of HPP Fieschertal in the years 2013 to 2014; a) with linear and b) with logarithmic scaling of axes.

5.4.4 Performance comparison over two years

In addition to the selected events shown in Figures 5-16 and 5-17, differences and ratios of *SSC* obtained from various instruments were statistically evaluated with respect to reference *SSC* over two years. Data from the years 2013 to 2014 were considered because in these years also data from CFDM and *AquaScat* are available. Table 5-1 summarizes the results with respect to SSC_G, distinguishing two *SSC* ranges:

- Up to 4 g/l, i.e. all SSC_G except those which are potentially biased due to high temporal *SSC* gradients or settling in the LISST bucket;
- Up to 1 g/l, corresponding to the *SSC* range in which LISST, turbidity and acoustic data were used in SSC_B.

SSC_G below 0.1 g/l were excluded because the $U_{2\sigma}$ of these references would be >10%. For comparability, the same data points (moments in time) were considered for all devices, i.e. the bottle samples at which measurement results of the turbidimeter, the acoustic system, LISST and CFDM were available.

For 0.1 g/l ≤ SSC_G ≤ 1 g/l, the average *SSC* of all techniques for continuous SSM were less than 0.09 g/l off the gravimetric reference (Table 5-1). The acoustic system and the CFDM provided *SSC*-values which were on average closer to the SSC_G (< 0.03 g/l) than those from the optical devices. The SSC_i / SSC_G ratios had standard deviations σ between 0.20 and 0.43. Assuming that the deviations were normally distributed, the relative expanded measurement uncertainties $U_{2\sigma}$ of single minute-by-minute *SSC*-values from each technique were hence estimated as

±40% for the CFDM (with periodic field calibration),
±64% for the LISST using the size-dependent correction factor (SSC_{L2}),
±70% for the acoustic system (with linear conversion assuming constant PSD),
±86% for the turbidimeter (with linear conversion assuming constant PSD).

Note that the uncertainty on annual average *SSC* is lower due to partial compensation of temporary over- and underestimations. If SSC_G up to 4 g/l are considered, the absolute deviations were up to 0.14 g/l (turbidimeters) and the relative $U_{2\sigma}$ were slightly lower. The increasing relative $U_{2\sigma}$ of the four techniques in the mentioned sequence is attributed to mainly a higher sensitivity to temporal PSD variations. The relatively high $U_{2\sigma}$ of the LISST in the present setup is attributed to the effects mentioned at the end of Section 5.2.4. Note that these uncertainties refer to 2σ, i.e. a higher confidence level than in many other sediment transport studies. The $U_{2\sigma}$ in the present long-term field measurements are not only a result of the instrument characteristics, but also of varying particle properties,

the selected conversions, the setup, limited maintenance and uncertainty on reference *SSC*.

Table 5-2 summarizes the corresponding results with SSC_C as the reference. Using SSC_C instead of SSC_G increased the number of reference *SSC* considerably. In addition to the two ranges of reference *SSC* mentioned above, a third range with $SSC_C \geq 1$ g/l was considered, in which the $U_{2\sigma}$ of the CFDM is < 30%. The *SSC* ratios in this SSC_C-range were displayed in Figure 5-19 in the previous Section.

For $SSC_C \leq 4$ g/l, the SSC_A were on average again closer to the SSC_G than those from the optical devices (LISST and turbidimeters). For $SSC_C \geq 1$ g/l, the SSC_{L2} were on average closest to the SSC_C because of the size-dependant correction factor. The relative measurement uncertainties with SSC_C as the reference were lower than those with SSC_G, even for the *SSC* range down to 0.1 g/l. This is mainly explaind by the greater number of measurement results in similar conditions and the fact that the *SSC* ratios were computed from smoothed time series (i.e. not fully independent data points).

Table 5-1 Results of absolute and relative *SSC* comparison with respect to gravimetric *SSC* in the years 2013 to 2014.

	0.1 g/l ≤ SSC_G ≤ 1 g/l n = 57 μ = 0.50 g/l, σ = 0.30 g/l				0.1 g/l ≤ SSC_G ≤ 4 g/l n = 81 μ = 0.73 g/l, σ = 0.48 g/l				Explanation of abbreviations:
	$SSC_i - SSC_G$		SSC_i / SSC_G		$SSC_i - SSC_G$		SSC_i / SSC_G		μ = Average σ = Standard deviation T = From turbidity measured with *AquaScat* A = From acoustic system L1 and L2 = from LISST with a constant or a size-dependant correction factor f_c, respectively C = from Coriolis Flow– and Density Meter (CFDM)
i	μ [g/l]	σ [g/l]	μ [-]	σ [-]	μ [g/l]	σ [g/l]	μ [-]	σ [-]	
T	-0.05	0.23	0.80	0.43	-0.14	0.29	0.78	0.38	
A	0.03	0.19	0.99	0.35	-0.01	0.23	0.97	0.31	
L1	-0.09	0.14	0.72	0.31	-0.09	0.17	0.77	0.28	
L2	-0.07	0.13	0.75	0.32	-0.04	0.24	0.82	0.31	
C	-0.01	0.08	0.94	0.20	-0.02	0.14	0.94	0.18	

Table 5-2 Results of absolute and relative *SSC* comparison with respect to *SSC* from CFDM in the years 2013 to 2014; for abbreviations refer to Table 5-1.

	0.1 g/l ≤ SSC_C ≤ 1 g/l n = 226 796 μ = 0.36 g/l, σ = 0.22 g/l				0.1 g/l ≤ SSC_C ≤ 4 g/l n = 239 532 μ = 0.41 g/l, σ = 0.33 g/l				$SSC_C \geq 1$ g/l n = 12 860 μ = 1.42 g/l, σ = 0.71 g/l			
	$SSC_i - SSC_C$		SSC_i / SSC_C		$SSC_i - SSC_C$		SSC_i / SSC_C		$SSC_i - SSC_C$		SSC_i / SSC_C	
i	μ [g/l]	σ [g/l]	μ [-]	σ [-]	μ [g/l]	σ [g/l]	μ [-]	σ [-]	μ [g/l]	σ [g/l]	μ [-]	σ [-]
T	-0.09	0.12	0.74	0.31	-0.11	0.17	0.74	0.31	-0.42	0.65	0.75	0.26
A	0.00	0.09	1.01	0.35	-0.01	0.14	1.00	0.34	-0.20	0.62	0.91	0.24
L1	-0.13	0.07	0.57	0.22	-0.13	0.09	0.58	0.23	-0.18	0.25	0.87	0.14
L2	-0.12	0.07	0.59	0.24	-0.11	0.08	0.61	0.25	0.02	0.22	0.99	0.12

5.4.5 Upper limit of LISST's *SSC* measuring range

The points in Figure 5-20 show all combinations of minute-by-minute SSC_{L2} and d_{50} measured in the sediment seasons 2012 to 2014. The point colours indicate three ranges of optical transmission τ as specified in the legend. The upper limit of the *SSC*-measuring range of the LISST, i.e. SSC_{lim} at the starts and the ends of data gaps in five analysed events and corresponding d_{50}-values are shown by circular markers. The SSC_{lim} strongly depends on d_{50} as expected. A linear fit to these points yielded the relation:

$$SSC_{lim} = 0.22\, d_{50} - 1.9 \qquad (R^2 = 0.956) \qquad [\text{g/l}] \qquad (5\text{-}3)$$

with $d_{50} > 9$ [µm]. Note that Equation (5-3)

- Refers to an optical path length of 5 mm, no dilution and site-specific particle properties (PSD shape, particle shapes and density),
- Includes all available measurement results (also with $\tau < 0.3$ having potentially higher measurement uncertainty), and
- Is the average from a limited number of selected events and no "safety margin" is included.

SSC_{lim} from the field measurements (Eq. 5-3) is slightly lower than SSC_{lim} for glass beads and fine sand particles determined from the laboratory measurements (Eq. 4-3), but higher than SSC_{lim} for pure mica powder in the laboratory. This is in agreement with the degree of non-sphericity of the particle types.

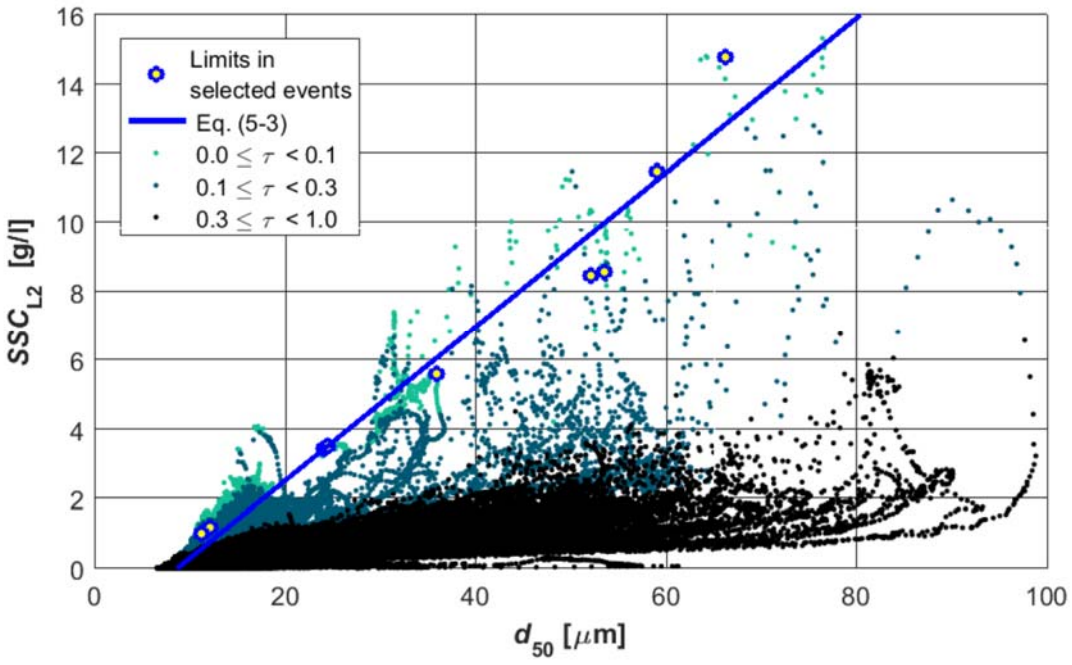

Figure 5-20 *SSC*-measuring range of LISST with particles as in the power waterway of HPP Fieschertal in the years 2012 to 2014 (modified from Felix *et al.* 2017).

5.4.6 Comparative assessment of the instruments for *SSC* measurements

5.4.6.1 Ease of use and maintenance requirements

The acoustic technique based on ADM was the most practical for SSM with the lowest rate of data gaps, because pre-existing sensors inside the penstock were usable and fouling or clogging were of no concern. For the other instruments, the construction and maintenance of a sampling pipe arrangement was required. The turbidity measurements in flow-cells without automatic cleaning were heavily affected by fouling; hence these turbidmeters models were not practical for long-term SSM. With the turbidimeter measuring at the free falling jet, fouling was no issue, but its relatively small feeding pipe with the valves for discharge reduction were prone to clogging in the present setup. Fouling in the measuring tubes of the CFDM affected *SSC* by up to 0.6 g/l; the tubes were not cleaned and the offset was compensated in the data evaluation. With the described sampling arrangement, manual cleaning of the *LISST-100X* every one to two months was not sufficient to prevent fouling. LISST measurements and data treatment were more demanding compared to the other devices.

5.4.6.2 Gravimetric reference SSC

To achieve reasonably low uncertainty, the conversions of measured turbidities and acoustic dampings to *SSC* (i.e. calibrations in the wider sense of the word) need to be established based on SSC_G for each instrument with the prevailing particles. SSC_G were also used to compensate effects of fouling on *SSC* from CFDM. Reference *SSC* from gravimetry or from CFDM are also required to convert apparent *TVC* from LISST to *SSC*. This compensates effects of highly non-spherical particle shapes and/or potential flocculation.

5.4.6.3 Sensitivity to particle properties

SSC from turbidimeters – and to a lesser extent from the acoustic technique – are temporarily biased if particle properties, particularly their size and shapes, deviate from average conditions and are not correlated with *SSC*. Because turbidimeters are more sensitive to fine particles, sand particles in a silt suspension are hardly detectable. Turbidity is hence not always a good indicator for the erosion potential. For the CFDM, no systematic dependency of *SSC* on particle size was measured with mainly silt and occasionally some fine sand particles. With LISST, the particle size is measured, but not the shape. The proposed size-dependent correction factor compensates mainly effects of particle shapes

on *SSC* because there was a trend that coarser particles (washed sand) have a closer-to-spherical shape than finer silt particles containing mica flakes.

5.4.6.4 Measuring ranges

In the context of turbine erosion, mainly the upper limits of the instruments' *SSC* measuring ranges are of interest. With granite particles (quartz, feldspar and mica) having $d_{50} \approx 20$ µm (mainly silt), these upper limits were typically:

- ~5 to 10 g/l for turbidimeters with $\alpha > 0°$ (with a range of 4000 FNU);
- >15 g/l for the through-light turbidimeter (path length = 10 mm); in the laboratory experiments maximum 2.3 CU out of 5 CU were reached;
- ~15 g/l for the acoustic system (1 MHz, path length = 2.3 m, $\delta < 0.8$);
- ~2 g/l for the LISST (with a path length of 5 mm, without dilution);
- >13 g/l for the CFDM (the limit was not reached in the field measurements).

It is expected that a CFDM allows measuring high *SSC*, e.g. 50 g/l as occurred during the flood event in 2012, as long as the measuring tubes are not clogged. The pressure-based technique allowed measuring high $SSC \geq 2$ g/l during quasi-steady state operation, but offers practically no pre-warning time.

5.4.6.5 Representativity

The *SSC* from the pressure-based technique refers to the water-sediment-mixture in the whole penstock. The *SSC* from the acoustic system is averaged over several paths inside the penstock, i.e. is well-averaged in space. The CFDM, the turbidimeters and the LISST measure *SSC* in a sampling pipe which may temporarily deviate from the average *SSC* in the penstock cross-section. However, the consistent results from the LISST, CFDM, turbidimeter and the acoustic system (Figures 5-3b and 5-4b) indicate that the measuring system worked satisfactorily.

5.4.6.6 Measurement uncertainty

With particle properties changing quite independently from *SSC*, the relative measurement uncertainties on *SSC* were highest for tubidimeters, and less for the acoustic technique and the LISST. The periodic field-calibration of the CFDM reduced the expanded *SSC* measurement uncertainty to ±0.3 g/l. For *SSC* above 1 g/l or 10 g/l, the relative uncertainty does not exceed ±30% and ±3%, respectively. The CFDM offers hence the lowest relative uncertainty at high *SSC* which are of particular interest in the context of turbine erosion.

5.5 Analysis of sediment transport events

5.5.1 Types of events

Temporarily elevated *SSC*, i.e. sediment transport events, occurred as expected during and after higher discharges (floods) due to intense and abundant rain in the river catchment (e.g. Fig. 5-21b). Besides such events, sharp *SSC* peaks occurred in periods with only moderate diurnal river discharge variations and without rain (Fig. 5-21a). This type of sediment transport event is related to the operation of the HPP's storage tunnel, as described in the following.

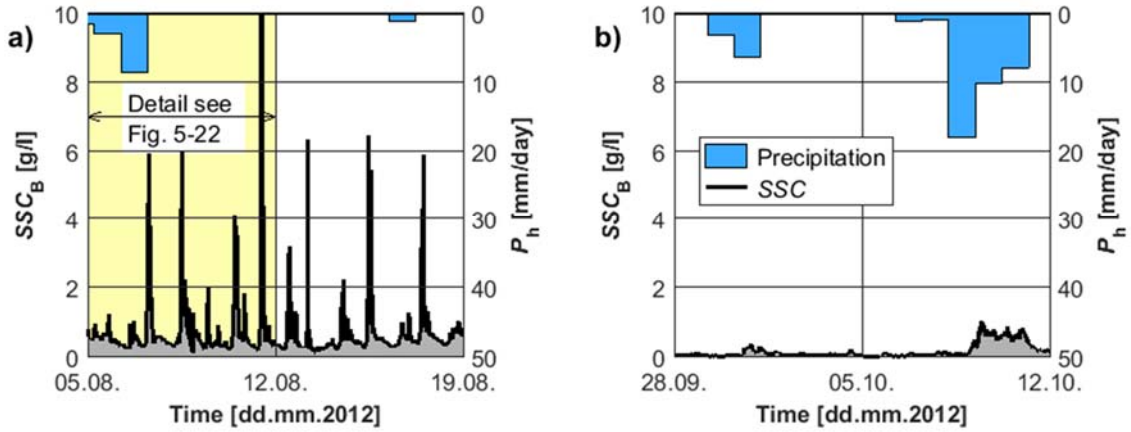

Figure 5-21 Time series of *SSC* and daily precipitation height P_h showing *SSC* peaks a) during dry summer days and b) due to precipitation (modified from Felix *et al.* 2014).

5.5.2 Re-suspension of particles from the storage tunnel

In the free surface flow tunnel between the sand trap and the valve chamber (Fig. 3-6 as well as Fig. B-3 in Appendix B), the water level varies by up to 4 m depending on the HPP operation. In warm and sunny periods in summer, the river discharge is high due to glacier melt and exceeds the design discharge Q_d of the HPP. Hence both turbines are continuously operated at full load while the water level Z_1 measured at the downstream end of the storage tunnel is at its nominal maximum (1643.00 m a.s.l.). If the river discharge falls below Q_d during some hours of the day (usually after midnight), the water level in the storage tunnel is drawn down to use the stored water. Typically, the turbine discharge is adjusted in such a way that the nominal minimum of Z_1 (1639.00 m a.s.l.) is reached when the natural discharge increases again (around midday, Figure 5-22a). With inflows below Q_d, one or two turbines are operated at partial load, in winter during only some hours per day.

SSC- and d_{50}-peaks in the penstock occurred in conjunction with a low tunnel water level, particularly when the turbines were operated close to Q_d = 15 m^3/s (Figure 5-22b). These peaks are explained by the hydraulic conditions in the storage tunnel which were investigated by backwater calculations based on Z_1 and Q_4. When the water level is drawn down, the average flow velocity U and the bottom shear stress τ_b in the storage tunnel at the highest point of the invert were estimated to increase by factors of 4 and 40, respectively (Figure 5-23). At high Z_1 and no (or low) turbine discharge, a part of the suspended sediment particles in the tunnel settle. However, at low Z_1 and particularly at turbine discharge close to Q_d, settled particles are eroded and re-suspended. In this way, sediment deposits mainly from the second half of the storage tunnel are "washed out" via the penstock. The thickness of the sediment deposit on the tunnel invert varies depending on sediment input and HPP operation. The phenomenon of sediment re-suspension at low tunnel water levels has been observed and described earlier by the HPP operator, the responsible engineer (BKW) and Abgottspon (2011).

Imposing operation restrictions (combinations of minimum Z_1 and maximum turbine discharge) to avoid *SSC*- and d_{50}-peaks due to HPP operation would not be a sustainable measure and was hence rejected. Higher sediment deposits – affecting the active storage volume – would build up in the second half of the storage tunnel, in which sediment deposits cannot be flushed to the river via the gate at mid-length of the tunnel.

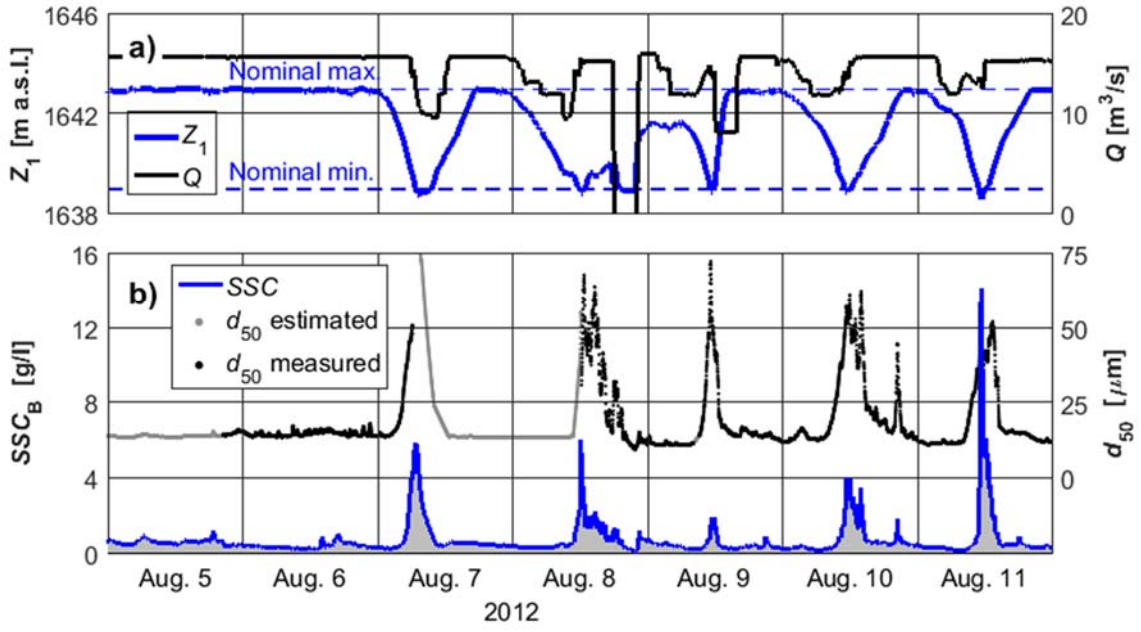

Figure 5-22 Time series of a) the headwater level Z_1 and the turbine discharge Q, as well as b) SSC_B and d_{50} in the penstock of HPP Fieschertal during a week in August 2012 showing *SSC* peaks and transport of coarser particles due to storage tunnel operation (modified from Felix *et al.* 2014).

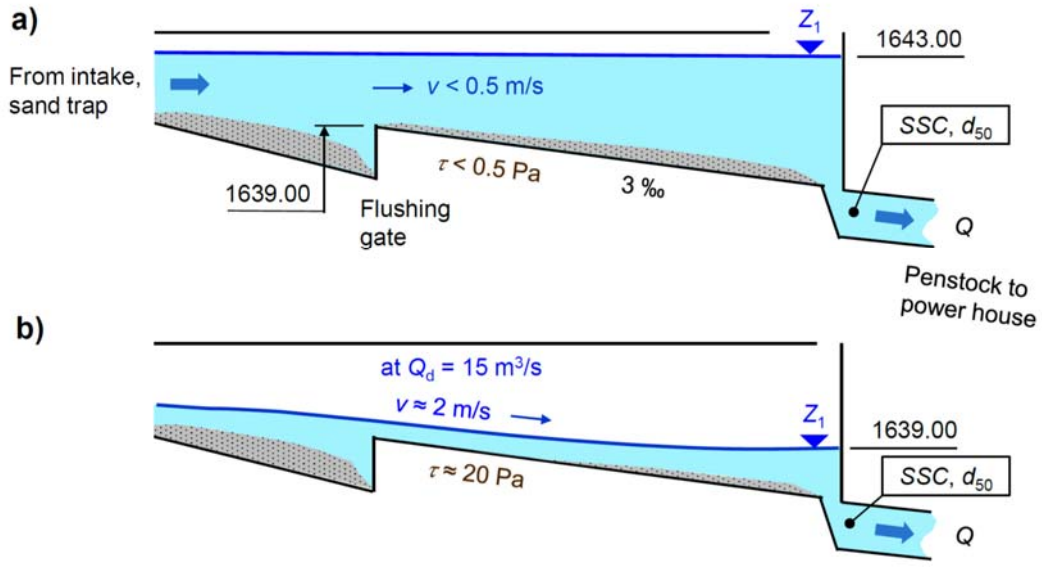

Figure 5-23 Schematic longitudinal sections of the storage tunnel of the HPP Fieschertal with turbine operation at design discharge Q_d and a) high or b) low water level Z_1 leading to sedimentation or re-suspension of particles, respectively.

Figure 5-24 shows the measured *SSC* and d_{50} as a function of the tunnel water level Z_1 in periods of turbine discharge $Q > 0$ and when precipitation was < 5 mm/day on the current and the previous day. More and larger particles were transported when the tunnel water level approached the nominal minimum operation level, or even occasionally fell below it. The increase of bottom shear stress during water level drawdown leads to size-sorting of particles in the power waterway. During the most pronounced re-suspension events, "washed" fine sand was transported into the penstock and through the turbines.

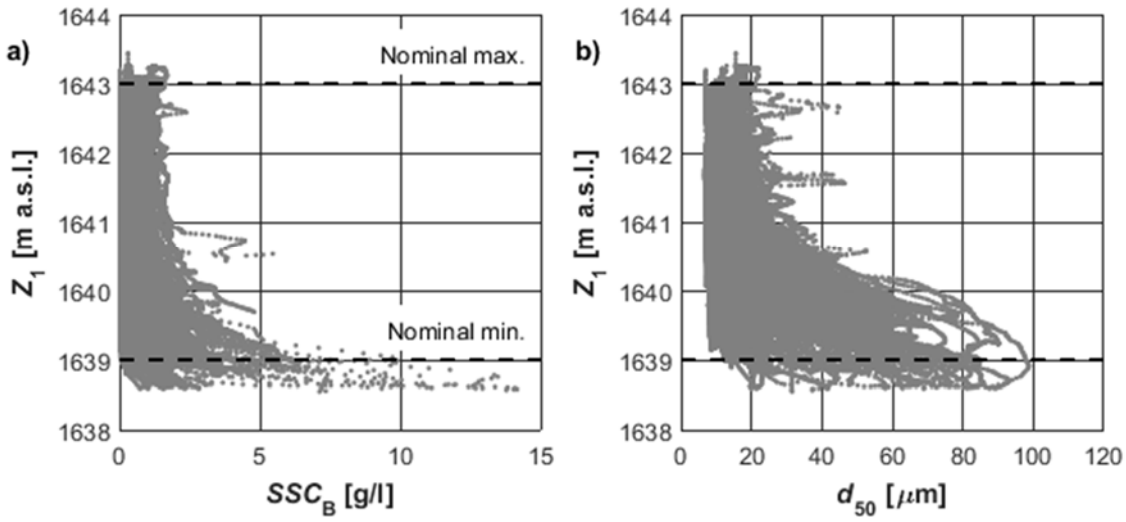

Figure 5-24 a) *SSC* and b) d_{50} in the penstock of HPP Fieschertal in periods without significant rain and during turbine operation in the years 2012 to 2014 as a function of the tunnel water level Z_1 (modified from Felix *et al.* 2014).

5.5.3 Elevated *SSC* due to rain

Examples of a higher and some smaller *SSC* peaks due to rain are shown in Figure 5-25. These peaks occurred in spring when the water level in the storage tunnel was at least 1 m above its nominal minimum and only one MG was running. The particle sizes in the penstock did not increase during the events. Mainly medium silt particles were transported ($d_{50} \approx 12$ µm). The correlation between the daily precipitation height P_h (measured in the village of Fieschertal) and the rain-induced *SSC* peaks is low. This is attributed to the following points: (i) the daily resolution of available precipitation data is not sufficient to characterize intense rainfall events and their consequences, (ii) the precipitation in the catchment area may differ from that measured in the village of Fieschertal (spatial variability), (iii) temperature plays a role (no run-off in case of snow at higher regions of the catchment area), and (iv) the sediment transport from the catchment area to the valve chamber may be delayed and dampened by temporary retention processes in the catchment area and the storage tunnel.

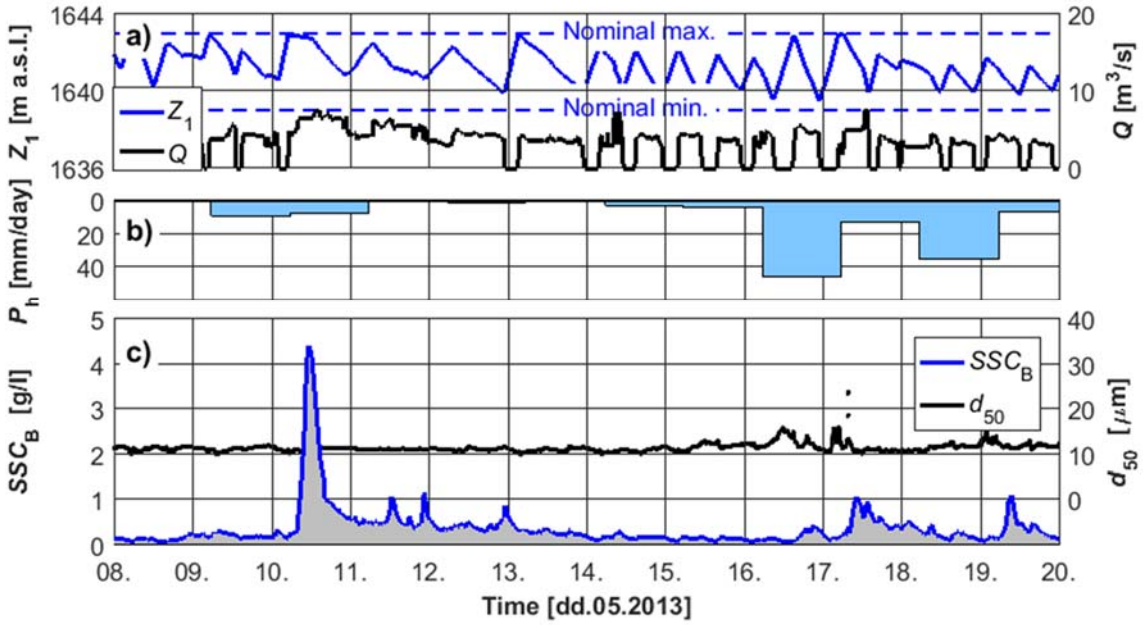

Figure 5-25 Time series of a) the headwater level Z_1 and the turbine discharge Q, b) daily precipitation heights P_h, as well as c) SSC_B and d_{50} in the penstock of HPP Fieschertal in May 2013 with examples of elevated *SSC* due to rain.

5.5.4 Major flood event of July 2 and 3, 2012 and its consequences

Figure 5-26 shows time series of Z_1, Q, *SSC* and d_{50} in the penstock from July 1 to 6, 2012. On July 2 and 3, the mentioned major flood event occurred; two days later the first re-suspension event after the flood took place. The *SSC* peaks in these two events

(50 and 24 g/l) were the highest during the monitoring period (2012 to 2014). Both MGs were operated at full or high load during these events. The return period of the flood event was estimated as ~20 years based on discharge data from gauging stations in the region.

The d_{50} in the penstock was estimated at ≤ 30 µm during the flood event, whereas it increased up to ~100 µm during the first re-suspension event after the flood. This means that the storage tunnel acted as an additional (fine-) sand trap during the flood, and that a part of the sediment which entered the HPP's power waterway during the flood was transported through the turbines later.

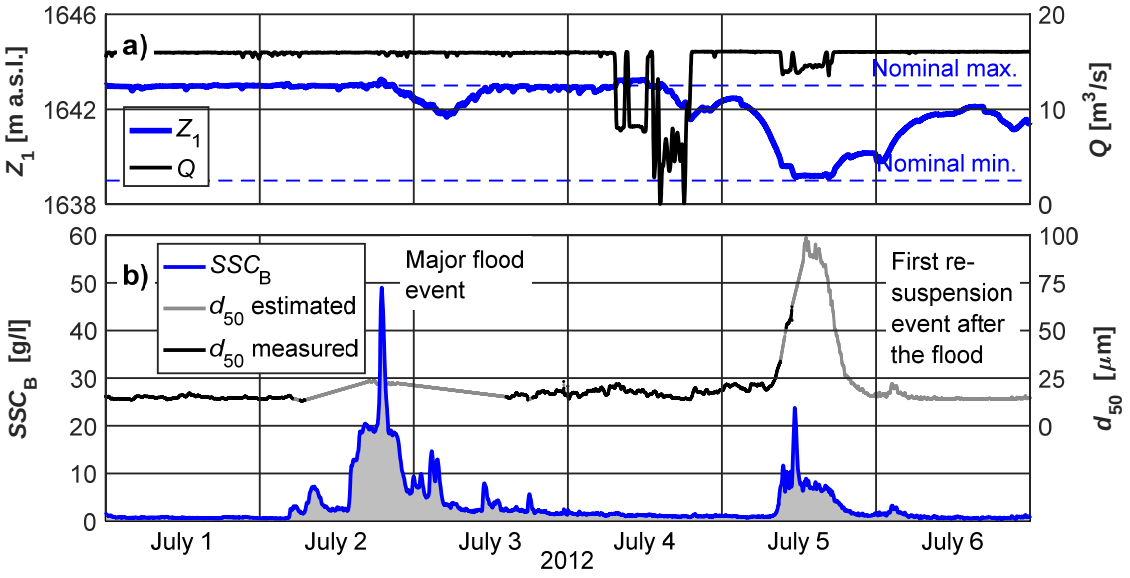

Figure 5-26 Time series of a) the headwater level Z_1 and the turbine discharge Q, as well as b) SSC_B and d_{50} in the penstock of HPP Fieschertal in the beginning of July 2012 (modified from Felix *et al.* 2016d).

5.5.5 Summary of sediment transport events

The sediment transport events in the years 2012 to 2014 are summarized in Table 5-3. The events were classified by their main reason (intense rain or HPP operation). The number of events when SSC_B exceeded 2, 5 or 10 g/l, respectively, were counted in each year. Moreover, the durations of these exceedances t_{exc} (≥ 2 minutes) were determined from the SSC_B time series. The annual mean values $t_{exc,m}$ of the exceedance durations are also listed in Table 5-3.

With respect to the sediment transport events due to intense rain, the major flood event on July 2 and 3, 2012, caused the highest *SSC*. Apart from this event, *SSC* never exceeded 5 g/l due to rain. On average in the years 2013 and 2014, i.e. without a major flood event, *SSC* exceeded 2 g/l for about two hours in only five rain events per year.

HPP operation caused $SSC \geq 10$ g/l several times a year. Exceedances of the mentioned *SSC* thresholds due to HPP operation were about five times more frequent than due to rain. The *SSC* exceedances due to operation were rather short: the annual average durations ranged from 10 minutes to 2 hours. The sediment input into the HPP's power waterway during the major flood caused a much higher number of re-suspension events in 2012.

Table 5-3 Number n and mean duration $t_{exc,m}$ of *SSC* threshold exceedances per year classified by reason.

Period	Mainly due to intense rain						Mainly due to HPP operation					
	> 10 g/l		> 5 g/l		> 2 g/l		> 10 g/l		> 5 g/l		> 2 g/l	
	n [-]	$t_{exc,m}$ [min]	n [-]	$t_{exc,m}$ [min]	n [-]	$t_{exc,m}$ [min]	n [-]	$t_{exc,m}$ [min]	n [-]	$t_{exc,m}$ [min]	n [-]	$t_{exc,m}$ [min]
Year 2012 *	3	185	5	200	20	147	6	17	23	49	98	40
Year 2013	0	-	0	-	7	95	3	13	7	68	19	123
Year 2014	0	-	0	-	2	125	2	10	4	21	13	65
Annual average 2012 to 2014 *	1	185	2	200	10	122	4	13	11	46	43	76
Annual average 2013 to 2014	0	0	0	0	5	110	3	12	6	45	16	94

* including a major flood event with a return period of ~20 years and its consequences.

5.6 Suspended sediment load (*SSL*) in the penstock

5.6.1 Time series of *SSL*

Figure 5-27 shows $SSL(t)$ in the penstock computed according to Equation (3-4) using the time series of SSC_B and Q_4. The annual *SSL* differ considerably for the three years, with the *SSL* in 2012 being the highest mainly due the major flood event of July 2 and 3. In this event ~17 000 t (tons) of sediment were transported through the penstock (Fig. 5-28). This corresponds to 16% of the annual *SSL* in 2012, or 33% of the annual *SSL* in a year without any major flood (average of 2013 and 2014). During the first and largest re-suspension event after the flood, another 4000 t of sediments passed through the penstock and the turbines in only 12 h, corresponding to 4% of the annual *SSL* in 2012.

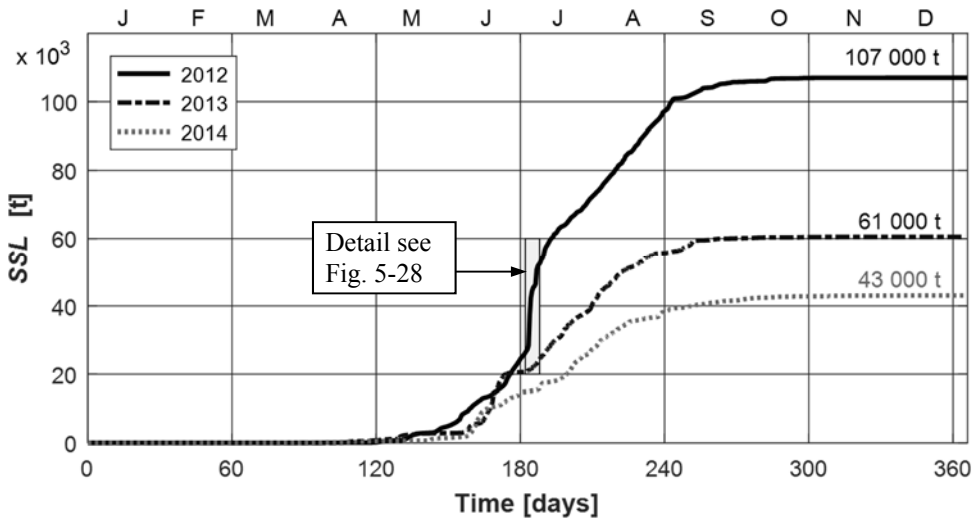

Figure 5-27 *SSL* in the penstock of HPP Fieschertal as a function of time in the years 2012 to 2014.

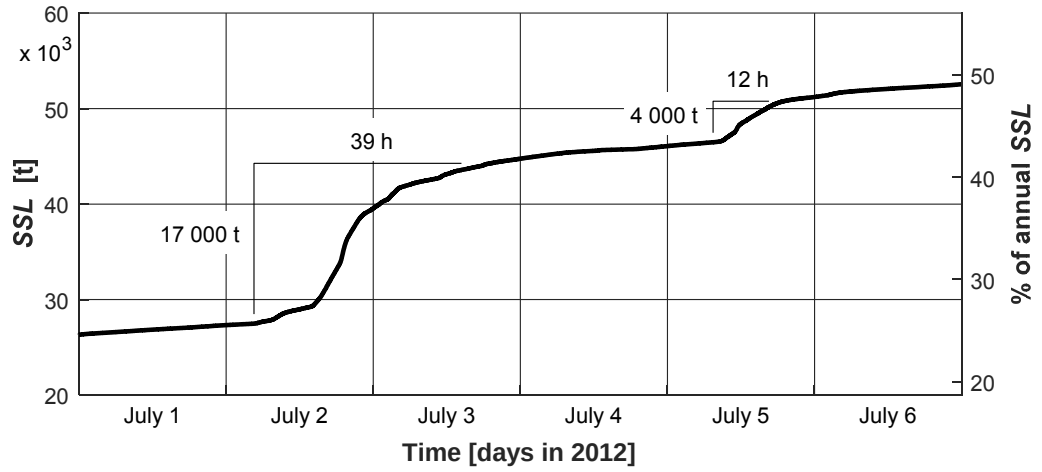

Figure 5-28 *SSL* in the penstock of HPP Fieschertal as a function of time in the beginning of July 2012.

5.6.2 *SSL* by size fractions

In all three years, 55% of the sediment particles transported through the penstock were in the size range of fine and medium silt (≤ 20 µm), about 30% were coarse silt (20 to 63 µm) and about 15% were mainly fine sand (Fig. 5-29a). In 2012 the percentages of fine sand particles were higher than those in the other two years in which no major flood event occurred. These differences are important because coarse particles cause higher turbine erosion per unit mass than fine ones (*RER* in Fig. 2-18).

5.6.3 Effect of runoff on *SSL*

The annual volumes of turbine water (including sediment) in the years 2012, 2013 and 2014 were 143, 130 and 128 Mio m^3, corresponding to annual average penstock discharges of 4.52, 4.13 and 4.07 m^3/s, respectively. The average annual *SSC* in the penstock,

i.e. annual *SSL* divided by the annual volumes, were 0.75, 0.47 und 0.34 g/l. The average *SSC* over the three years was 211 000 t / 401 Mio m^3 = 0.53 g/l, which is displayed in Figure 5-7.

The high *SSL* in 2012 resulted mainly from higher *SSC*, because the annual turbined volume – limited by the available runoff and the HPP's design discharge – was only 11% higher than the average of the other two years. The high sediment input into the HPP system during the major flood event in July 2012 and the elevated transport rate in the following months are apparent in Figure 5-29b. Moreover, a period of elevated *SSC* was detected after the beginning of each sediment season. This is attributed to the phenomenon that fine sediment, which has been eroded on the glacier bed during the winter, is transported out of the glacier through subglacial drainage channels in early summer when the discharge increases due to ice melting.

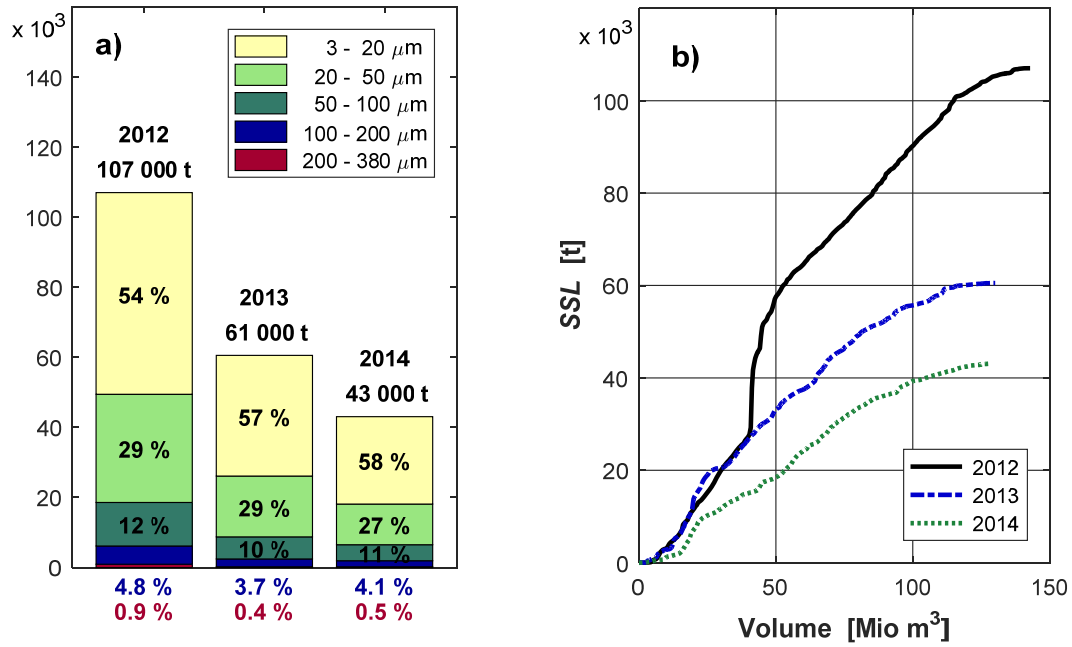

Figure 5-29 a) Annual *SSL* by size classes (Felix *et al*. 2016d) and b) *SSL* as a function of the turbined volume of HPP Fieschertal for the years 2012 to 2014.

5.6.4 Comparison of *SSL* with sediment yield

With respect to the catchment area (59 km^2, Section 3.3.1), the annual *SSL* in the penstock in the years 2012, 2013 and 2014 correspond to specific suspended sediment yields of 0.67, 0.37 and 0.26 mm/year, respectively. These rates, particularly those of 2013 and 2014 (without any major flood event), are lower than the long-term denudation rate in the Swiss crystalline central Alps (Section 2.1.1.2). The *SSL* in the penstock is smaller than that in the river because

- Not all water and sediment is captured at the intake – in particular, the river water in excess of the intake capacity contains typically high *SSC* during floods;
- A part of the sediment contained in the captured water is returned to the river via the flushing outlets of the gravel and sand traps as well as by occasional flushing of the first half of the storage tunnel.

A further reason for the *SSL* in the penstock being lower than the long-term sediment yield is the melting of dead ice and the formation of a proglacial lake in the foreland of the *Fieschergletscher* upstream of the HPP's intake (Section 3.3.1), which is expected to act as a sediment sink (mainly for coarser particles).

5.7 Suspended sediment and particle loads (*SSL* and *PL*) of each MG

5.7.1 *SSL* of each MG

Figure 5-30 shows the *SSL* for each MG as a function of the annual operating hours in the years 2012 to 2014. For MG 1, the annual *SSL* in 2012 was more than twice that of the other two years. The annual *SSL* of MG 2 in 2012 was smaller than that of MG 1, because MG 2 was out of operation from May 23 until June 22 (~30 days) due to a problem at its transmission line while MG 1 was running almost permanently at full load. In 2013 and 2014 the annual *SSL* of both MGs were similar. The annual *SSL* split-up by size-fractions are presented for each MG in Table 5-4. In 2012, the annual mass of sand particles was about 2.5 times that of the average of the other two years (on average for both MGs).

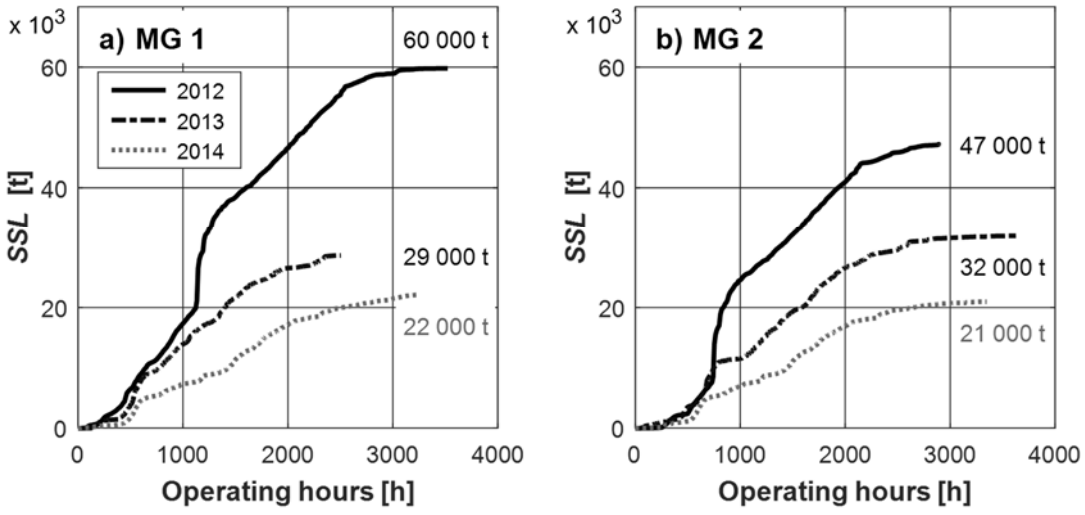

Figure 5-30 Suspended sediment loads *SSL* for each machine group (MG) as a function of the annual operating hours in the years 2012 to 2014 (Felix *et al.* 2016d).

Table 5-4 Annual *SSL* by size-fractions for each MG of HPP Fieschertal in 2012 to 2014.

	Annual *SSL* [t]									
	MG 1					MG 2				
Particle size ranges *d* [µm]	3-20	20-50	50-100	100-200	200-380	3-20	20-50	50-100	100-200	200-380
Year 2012	32544	17206	6718	2782	538	25018	13688	5702	2391	426
Year 2013 §	15991	8320	3102	1099	109	18429	9048	3197	1125	115
Year 2014 §	12936	5894	2291	876	102	12024	5692	2271	876	103
Annual averages										
2012 to 2014	20490	10473	4037	1586	249	18490	9476	3723	1464	214
2013 to 2014 §	14463	7107	2696	987	105	15226	7370	2734	1000	109

§ Periods without any major flood event.

5.7.2 *PL* of each MG

Figure 5-31 shows the *PL* according to IEC 62364 (Eq. 3-5 with $k_{size} = d_{50} / 1000$ µm) for each MG as a function of the annual operating hours in the years 2012 to 2014. The shapes of these curves are similar to those of the *SSL* in Figure 5-30. Table 5-5 summarizes the *SSL* and *PL* with corresponding operating hours for each MG. The ratio of *PL/SSL* is similar for all listed periods except for the first re-suspension event after the major flood. During this event, the ratio of *PL*/*SSL* was more than twice as high as on average because coarser particles with higher k_{size} where transported during this event.

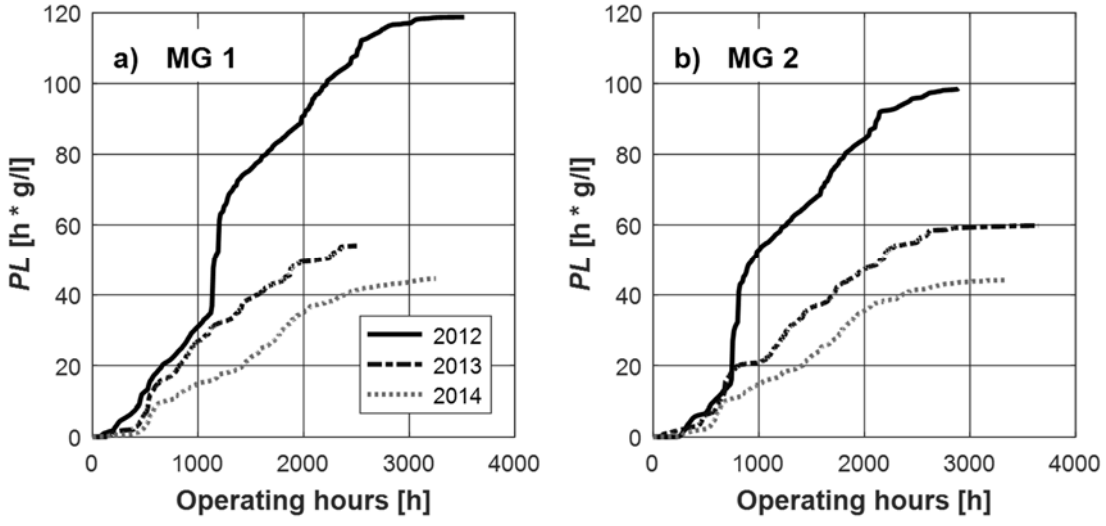

Figure 5-31 Particle loads *PL*s according to IEC 62364 (2013) for each machine group (MG) as a function of the annual operating hours in the years 2012 to 2014.

Table 5-5 Key figures on the operating hours Δt, *SSL*, k_{size} and *PL* for each MG in the HPP Fieschertal in 2012 to 2014.

Period	MG 1				MG 2			
	Δt [h]	*SSL* [10^3 t]	k_{size} # [-]	*PL* * [h · g/l]	Δt [h]	*SSL* [10^3 t]	k_{size} # [-]	*PL* * [h · g/l]
Year 2012	3509	60	0.034	119	2883	47	0.035	98
Year 2013 §	2504	29	0.031	54	3649	32	0.030	60
Year 2014 §	3251	22	0.030	45	3348	21	0.031	44
Total 2012 to 2014	9264	111	-	218	9880	100	-	202
Annual averages								
2012 to 2014	3088	37	0.033	73	3293	33	0.032	67
2013 to 2014§	2878	26	0.031	50	3499	27	0.030	52
Major flood event July 2 and 3, 2012	39	8.4	0.036	15.8	39	8.4	0.036	15.8
First re-suspension event after the flood	12	2.2	0.081	9.8	12	2.2	0.081	9.8

$k_{size} = d_{50}$ / 1000 µm according to IEC 62364 (2013), averages during the operation hours per period.

* According to IEC 62364 (2013) with k_{size} as given above, $k_{hardness} = 0.75$, and $k_{shape} = 2$.

§ Periods without any major flood event.

The average k_{size}-values were computed as the ratios of the *PL* with $k_{size} = f(d_{50})$ and the *PL* with $k_{size} = 1$ in the selected periods. According to the definitions of k_{size} and *PL* in IEC 62364 (2013), these average k_{size}-values correspond to a weighted-average d_{50}, where the *SSC* at corresponding time steps are the weighing factors. Because *SSC* is set to zero if a turbine is not running (Section 2.3.6.1), the weighted average refers only to the periods when the turbines were running. In the present case with $k_{size} \approx 0.032$ for the years 2012 to 2014 (Table 5-5), this means that the *SSC*-weighted average d_{50} was 32 µm during the operating hours, which is considerably higher than the ordinary average $d_{50} = 11$ µm over the whole observation period (Fig. 5-10).

At HPP Fieschertal, the *PL* referring to one bucket, i.e. PL_b, is 1/10 of the *PL* per MG. This factor results from the number of jets (nozzles in operation) $z_0 = 2$ and the number of buckets $z_2 = 20$ (Eq. 2-31).

5.7.3 Comparison of *PL* with *SSL*

In Figure 5-32, the *PL* according to IEC 62364 (2013) are compared with *SSL* for MG 1 as a function of the operating hours over the three years. The curves have similar shapes. Comparing Equation (3-4) to Equation (3-5) with $k_{size} = 1$ yields that the curves would have exactly the same shape if either (i) the discharge Q was constant when $SSC > 0$, or (ii) if $SSC = 0$ (horizontal parts of the curves). In the case of HPP Fieschertal, one of the two conditions is often met for the following reasons:

- The HPP is generally operated at full load during summer when *SSC* is high;
- When the HPP is operated at partial load, the *SSC* is often low or tends to zero.

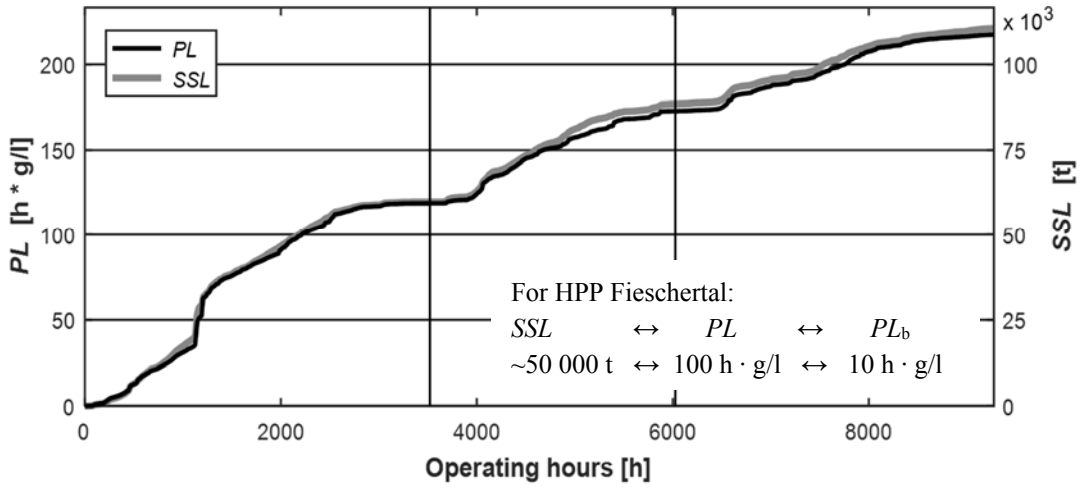

Figure 5-32 Particle load *PL* according to IEC 62364 (2013) and suspended sediment load *SSL* of MG 1 as a function of the operating hours in the years 2012 to 2014 (Felix *et al.* 2016d).

Figure 5-32 shows that in the case of HPP Fieschertal the *PL* is practically proportional to the *SSL* over longer periods such as a year. The *PL* can thus be approximatively converted to *SSL*, which is more familiar to many readers.

5.7.4 Effect of k_{size}-functions on *PL*

Figure 5-33 shows the *PL* of MG 1 calculated based on each of the four sets of the k_{size}-values from Table 3-4. To allow for a visual comparison, the *PLs* were normalized by their total values over the three analysed years. The four curves have generally quite similar shapes. The largest differences among the four curves were identified between the curve calculated with k_{size} according to Winkler *et al.* (2011a) and the curve with $k_{size} = 1$. The main deviations between these two curves were observed (i) during and after the major flood event in 2012, (ii) in late summer, and (iii) in early summer.

The normalized *PL* based on k_{size} according to Winkler *et al*. (2011a) was higher than that with $k_{size} = 1$ in the cases (i) and (ii), whereas it was the contrary in case (iii). These deviations resulted from the high relative erosion rate *RER* of particles above ~100 µm. In cases (i) and (ii), the particles in the turbine water were generally coarser than usual due to the flood and re-suspension events. In case (iii), related to the beginning of the annual ice melting (Section 5.6.3), the particles were generally finer than usual.

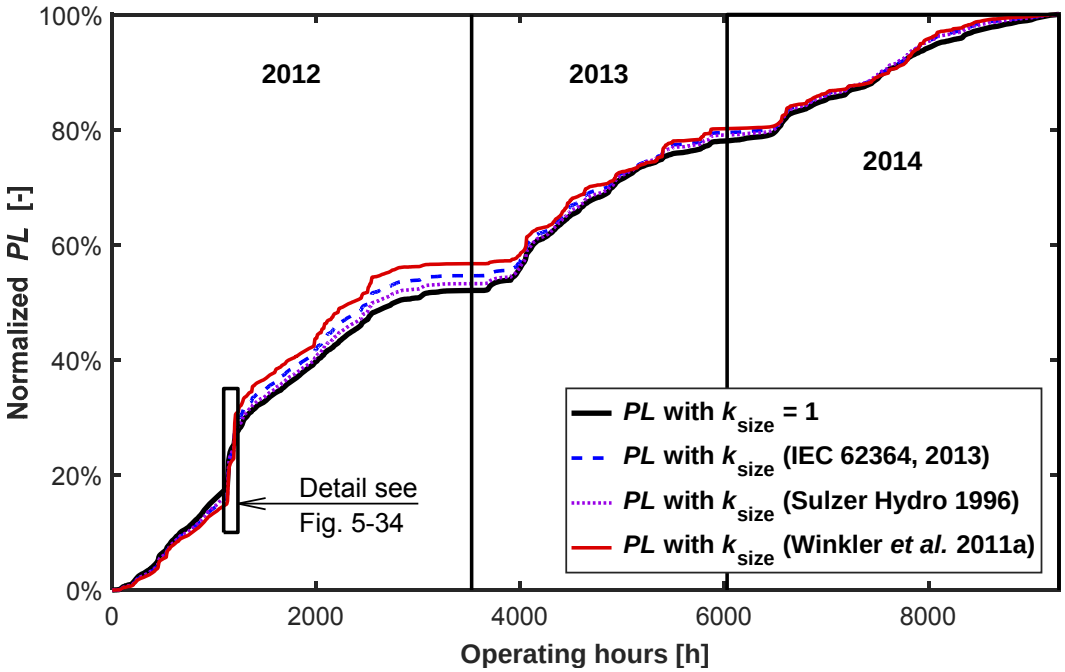

Figure 5-33 Normalized *PL* of MG 1 calculated with four sets of k_{size}-values as a function of the operating hours from 2012 to 2014 (Felix *et al.* 2016d).

Figure 5-34 shows a detail of the previous Figure during the first six days of July 2012. The time range is the same as in Figure 5-28, including the major flood event and the first re-suspension event after the flood. The normalized *PL* calculated with $k_{size} = 1$ increased during these two events by 6% and 2%, respectively. The normalized *PL* during the re-suspension event was thus one third of that during the flood event. With k_{size} according to Winkler *et al.* (2011a) however, the normalized *PL* during the re-suspension event was as high as that during the flood event (7%). This means that the ~4000 tons of mainly fine sand which passed the turbines during the re-suspension event (temporarily at partial load) had a similar erosion potential as the 17 000 tons of mainly silt during the flood event. The normalized *PL*s during the re-suspension event calculated according to IEC and Sulzer Hydro (1996) are higher than with $k_{size} = 1$ as well. The time series of *SSC*, *SSL* and *PL* indicate that this and further re-suspension events after the flood caused considerable erosion in addition to the erosion during the flood itself.

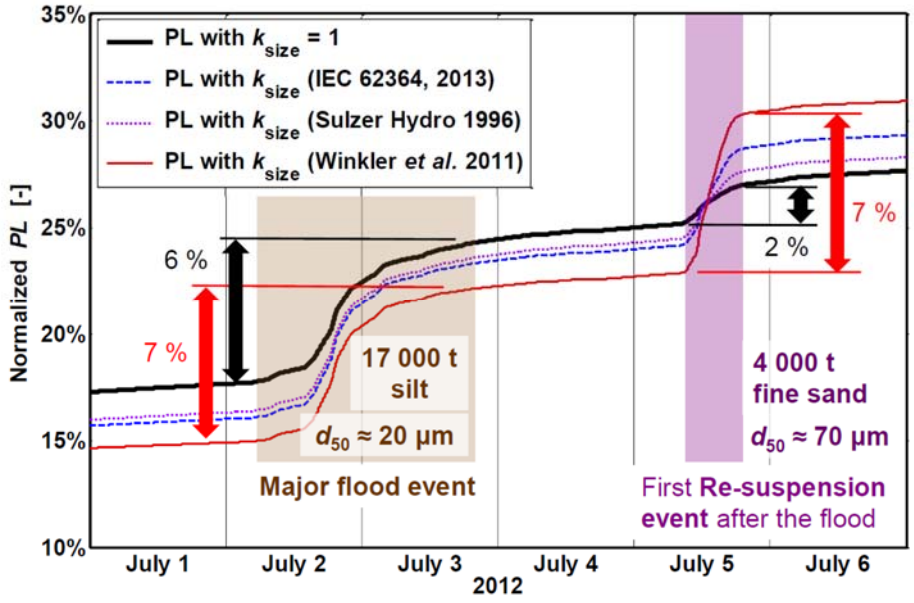

Figure 5-34 Detail of Figure 5-33 in the beginning of July 2012 (modified from Felix *et al.* 2016d).

5.8 Uncertainties and biases in SSM

5.8.1 Overview

The main quantities presented in this Chapter, i.e. *SSC*, d_{50}, *SSL* and *PL*, are affected by random and systematic errors arising from various sources (Fig. 5-35). In Appendix C5, each source of error numbered from 1 to 15 in Figure 5-35 is discussed and uncertainties were quantified as far as relevant information was available.

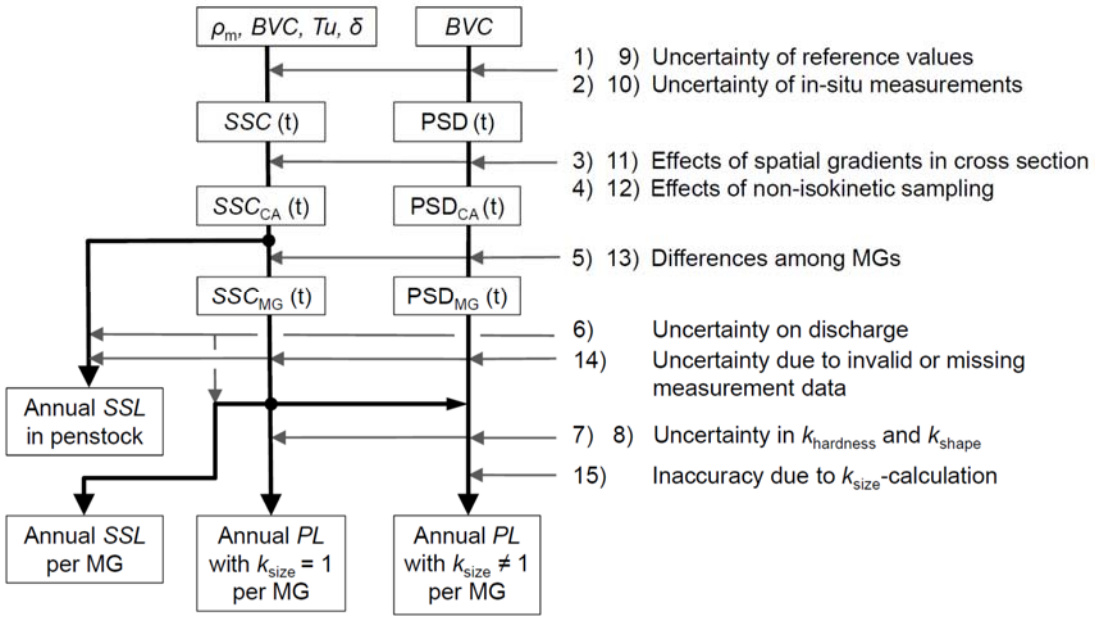

Figure 5-35 Schematic representation of uncertainties in sediment-related quantities for the investigation of turbine erosion; 'Tu' stands for turbidity and 'CA' for cross-section averaged values in the penstock, numbers 1 to 15 refer to sources of error treated in Appendix C5.

5.8.2 Estimated uncertainties and biases in annual *SSL* and *PL*

The estimated relative expanded uncertainties $U_{2\sigma}$ and biases of the annual *SSL* and *PL* (details see Appendix C5) are summarized in Table 5-6. Uncertainty on the *SSL* arises mainly from the indirect *SSC* measurements. The uncertainty on *PL* with $k_{size} = 1$ is higher than in the *SSL* mainly because of the uncertainties associated with the k_{shape} and $k_{hardness}$ factors. In the *PL* with $k_{size} \neq 1$, as according to IEC 62364 (2013), the uncertainty is highest because of the additional uncertainty in the PSD measurements.

It is expected that the *SSL* were underestimated by some percent because the *SSC* was probably underestimated when fine sand was transported during less than a day per year. The same slight bias is expected for the *PL* with $k_{size} = 1$. However, the *PL* according to IEC are expected to be overestimated because the particle sizes were overestimated due to highly non-spherical particles, potential flocculation and fouling. This bias was not compensated because it was not quantitatively known and varies with time.

Table 5-6 Estimated relative expanded uncertainties $U_{2\sigma}$ and biases in annual *SSL* and *PL*.

Quantity (on annual basis)	Uncertainty $U_{2\sigma}$	Estimated bias (qualitatively)
SSL (in penstock and per MG)	± 25%	-
PL and PL_b with $k_{size} = 1$	± 41%	-
PL and PL_b according to IEC with $k_{size} = f(d_{50})$	± 50%	++

6 RESULTS AND DISCUSSION OF TURBINE EROSION MONITORING (TASK C)

In this Chapter, the results of the erosion measurements and the inspections of the turbines in the HPP Fieschertal in the years 2012 to 2014 are reported and discussed, focussing mainly on the runner buckets. This comprises the erosion depths and eroded masses evaluated from the coating thickness (*CT*) measurements and the optical 3D-surveys (HSLU).

6.1 Overview

In all sediment seasons, the inner sides of the buckets remained coated, except for some locations in the buckets of MG 2 in 2012. In each sediment season, the coating at the splitter crests and the leading edges of the cut-outs was either only very locally or systematically removed (Fig. 6-1). In these zones, the base material was visibly eroded.

The results of the measurements and inspections are presented in the following sequence: (i) erosion inside the buckets, (ii) erosion on splitters and cut-outs of the buckets, and (iii) erosion on other turbine parts.

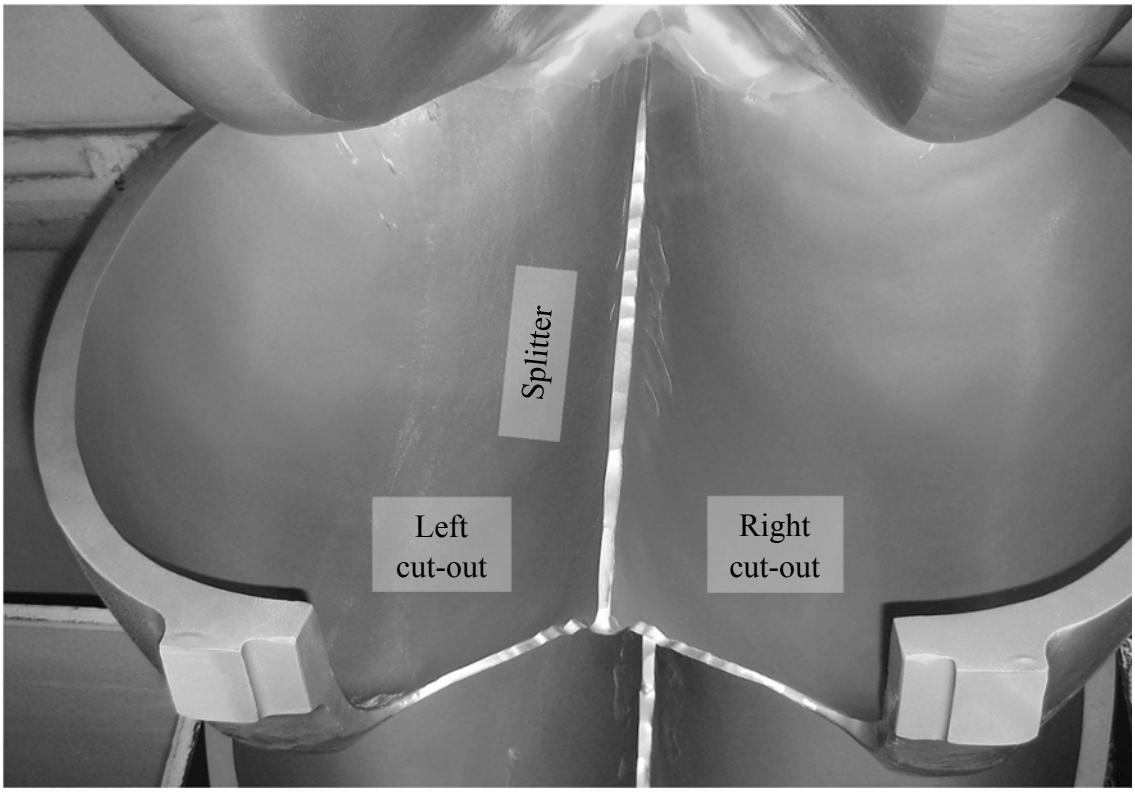

Figure 6-1 Hard-coated Pelton bucket of HPP Fieschertal with typical systematic erosion on the splitter crest and the leading edges of the cut-outs (MG 2, August 8, 2012).

6.2 Erosion inside the runner buckets

6.2.1 Erosion of coating

6.2.1.1 Coating thickness (CT) distributions

Figure 6-2 shows *CT* maps inside selected runner buckets in April 2013, i.e. from the first template-based measurement campaign. These runners have been in operation for at least one sediment season since the last coating in the factory. Each map represents a plane evolution of the inner bucket surface. The *CT* was interpolated between the template's measuring points (black circular markers).

For MG 1, the *CT* varied between 200 und 500 µm and the average *CT* of both buckets was 334 µm. For MG 2, the average *CT* was 364 µm and the *CT* ranged up to 800 µm due to local coating repairs, i.e. on-site re-coating partially on top of the existing coating. Even without such re-coating, the *CT* had high spatial gradients: for example close to the left rim of bucket no. 1 of MG 1, the *CT* varied by 200 µm within a distance of 40 mm. The *CT* maps of both investigated buckets per runner were qualitatively similar.

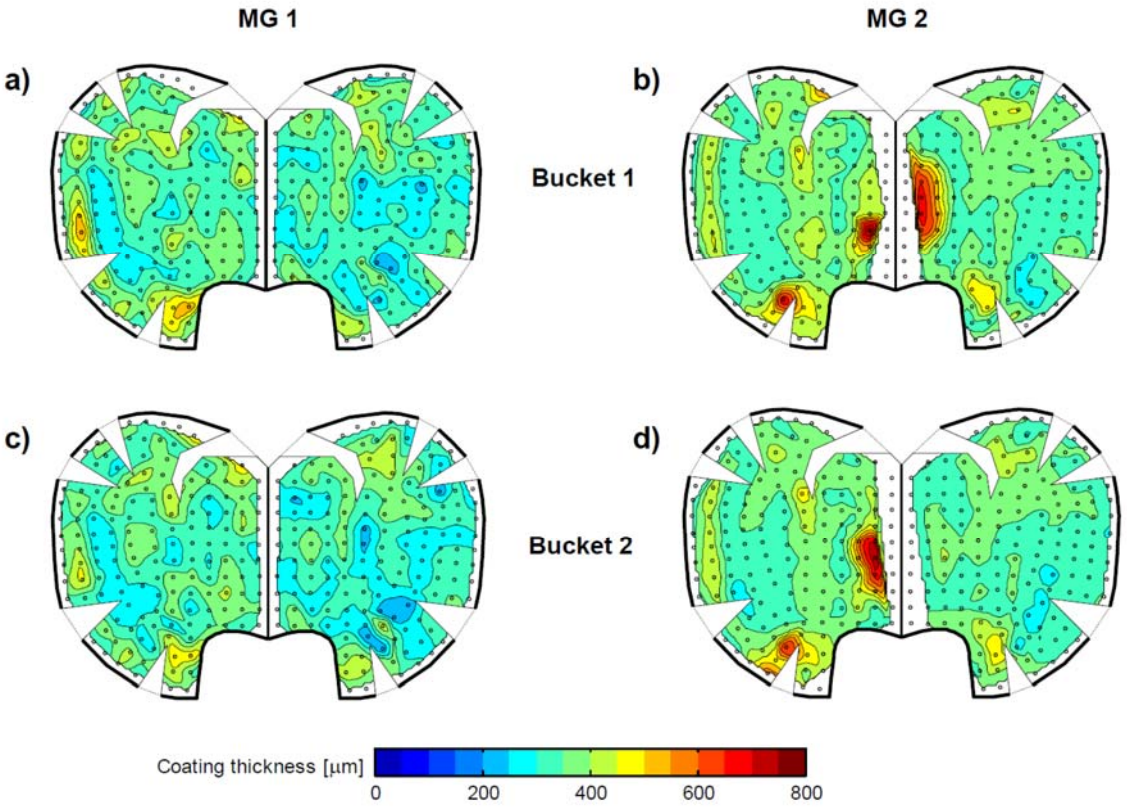

Figure 6-2 Distribution of coating thickness *CT* in buckets no. 1 and 2 of both MGs in the HPP Fieschertal measured in April 2013 (modified from Abgottspon *et al.* 2016b).

On August 8, 2012, i.e. after the major flood event, it was observed that the coating has been locally completely eroded inside some buckets of MG 2 (Fig. D-14 in Appendix D3). The zones with exposed base material (with an area of typically some cm^2) were mainly located in the bottom region of the buckets and towards the bucket roots. In the vicinity of these zones, *CT* of only 50 µm to 100 µm were measured. However, there were no zones with totally eroded coating inside the buckets of MG 1 over the whole observation period.

6.2.1.2 Uncertainty in CT measurements

To quantify the uncertainty of *CT* differences based on template-based measurements, *CT* differences were evaluated from measurements on buckets no. 1 and 2 of MG 1 in November 2013 and Mai 2014 (Fig. D-1 in Appendix D1). In this period, the Δ*CT* were expected to be zero because (i) the *PL* and the erosion in this period (between the sediment seasons) is negligible, (ii) coating repairs were limited to the zones of the splitter crests and cut-out edges (outside the template's measuring points), and (iii) the runner of MG 1 was not changed in that winter. At a few measurement points, the Δ*CT* were up to ±30 µm (red and blue in Figure D-1), whereas they were within ±10 µm at most of the other points (yellow and green). The expanded measurement uncertainty $U_{2\sigma}$ on Δ*CT* at one location was estimated as ±10 µm.

The Δ*CT* in Figure D-1 averaged over the inner bucket surfaces were −2 µm and −4 µm for buckets no. 1 and 2, respectively. These negative differences mean that the *CT* would have increased over time, which is physically not plausible. The $U_{2\sigma}$ of the bucket-averaged Δ*CT* was estimated as ±5 µm.

The uncertainties in the *CT* and Δ*CT* depend on the properties of the instrument, its calibration, the roughness of the coating and the positioning of the probe. In regions with high spatial variability of the *CT*, the latter effect is large compared to the erosion depths of interest (Fig. D-4 in Appendix D1). The *CT* values in Figure D-4 are the averages of $n = 10$ single measurements (Section 3.5.1.2).

6.2.1.3 Reduction of coating thicknesses (CT)

Maps of Δ*CT* over the sediment seasons 2013 and 2014 inside the buckets no. 1 and 2 of the two MGs are shown in Figures D-2 and D-3 in the Appendix D1. Given the $U_{2\sigma} = \pm 10$ µm on the Δ*CT* at one location, the patterns in these maps are mostly not significant. Typical zones of higher erosion within a bucket might be identified after a longer observation period.

The *CT* reductions averaged over the inner bucket surfaces are listed in Table 6-1 and are interpreted as follows:

- The Δ*CT* of MG 1 in 2014 lies within the band of uncertainty, i.e. no significant erosion was measurable.
- The other Δ*CT* were larger than $U_{2\sigma}$. Hence they were interpreted as erosion depths; the relative $U_{2\sigma}$ was ~50%.

Table 6-1 Reductions of *CT* ($\pm U_{2\sigma}$) averaged over the inner bucket surfaces in the sediment seasons 2013 and 2014 in the HPP Fieschertal.

Sediment season	MG 1			MG 2		
	Bucket no. 1 [µm]	Bucket no. 2 [µm]	Average of no. 1 and 2 [µm]	Bucket no. 1 [µm]	Bucket no. 2 [µm]	Average of no. 1 and 2 [µm]
2013	11 ± 5	8 ± 5	10 ± 5	9 ± 5	11 ± 5	10 ± 5
2014	4 ± 5	3 ± 5	3 ± 5	14 ± 5	13 ± 5	13 ± 5

Inside the buckets of MG 2, where the coating was completely eroded in some zones in 2012 (Section 6.2.1.1), the Δ*CT* were locally up to several 100 µm when considering usual initial *CT* of 300 to 500 µm. The average Δ*CT* inside the buckets was thus considerably higher than the values in Table 6-1. The considerable erosion of coating material inside the buckets of MG 2 in 2012 was attributed to the relatively high *PL* and the wide and blunt splitters (s = 8 to 10 mm) which caused a disturbed flow field and probably induced cavitation as a secondary or combined damage mechanism. Local complete erosion of hard-coating in the bottom region of Pelton buckets was also observed by Maldet (2008).

In the sediment seasons 2013 and 2014, the Δ*CT* were small compared to usual initial *CT*. The runner of MG 1 showed that the hard-coating inside the buckets may last for several years despite high *PL* if secondary damages due to degraded splitters and cut-out edges are avoided.

6.2.1.4 Eroded masses of coating

The masses of eroded coating inside the runner buckets Δm_{cb} in Table 6-2 were determined from the bucket-averaged Δ*CT* in the two measured buckets per MG, the area inside a bucket ($5.22 \cdot 10^5$ mm^2), a density of 12 g/cm^3 (according to literature) and the number of buckets z_2 = 20. The $U_{2\sigma}$ = ±5 µm of the bucket-averaged Δ*CT* (Section 6.2.1.2) corresponds to ±31 g per bucket and ±0.63 kg per runner.

In 2012, the Δm_{cb} were not quantified because the templated-based *CT* measurements were begun in 2013 only. According to the much higher erosion depth inside the buckets of MG 2 in 2012 mentioned in the previous Section, the Δm_{cb} of MG 2 in 2012 are estimated to have been considerably higher than the values in Table 6-2.

Table 6-2 Mass of eroded coating in the buckets Δm_{cb} ($\pm U_{2\sigma}$) in 2013 and 2014 in the HPP Fieschertal.

Sediment season	MG 1		MG 2	
	Per bucket [g]	Per runner [kg]	Per bucket [g]	Per runner [kg]
2013	63 ± 31	1.25 ± 0.63	63 ± 31	1.25 ± 0.63
2014	19 ± 31	0.38 ± 0.63	81 ± 31	1.63 ± 0.63

6.2.2 Erosion of base material

6.2.2.1 In zones of completely eroded coating

In contrast to MG 1, local erosion of base material was observed inside some buckets of MG 2 in August 2012 after the major flood event (Fig. D-14 in Appendix D3). These exceptional, up to e.g. 15 mm deep damages are a consequence of the complete erosion of coating at some spots (Section 6.2.1.1) probably due to the disturbed flow field caused by blunt splitters (Section 6.2.1.3). The considerable erosion of base material inside the runners of MG 2 was the main reason to exchange the runner on August 13, 2012. To minimize production losses during the full-load period, the runner was changed as quickly as possible; the MG was back to operation after 17 hours.

6.2.2.2 In uncoated zones

The bucket roots were not coated. One reason for this is to allow non-destructive testing for potential cracks in this highly stressed region. At the bucket roots above the coated area, erosion of base material was observed particularly towards the bucket outlets (Fig. D-19 in Appendix D3). Erosion grooves and sharp edges were rounded by grinding in the winters.

6.3 Erosion on splitters and cut-outs of runner buckets

6.3.1 Results from inspections

6.3.1.1 Erosion on splitters

The erosion process on splitter crests is schematically summarized in Figure 6-3:

(a) At the beginnings of the sediment seasons, the splitter crests were rounded and fully coated.

(b) Erosion of the coating and the underlying base material started on top of the splitter crests with a narrow groove, initially only a few tens of a mm wide (Figs. 6-4b and 6-5a). This type of erosion attack is attributed to the approximately perpendicular impact of particles on the splitter crests and the flow pattern with a stagnation point above the splitter crests.

(c) The erosion groove expanded laterally (Fig. 6-5b).

(d) The erosion progressed often asymmetrically.

(e) The top edges of the coating layers on the splitter flanks broke piecewise on one and the other side (Fig. D-17 in Appendix D3). Such notches lead to flow concentrations resulting in locally increased erosion ("traces") on the splitter flanks approximately perpendicular to the splitter crests (Fig. D-18 in Appendix D3).

(f) The splitter crests were flattened on top and got sharp edges resulting in a blunt shape; the base material was eroded up to ~2 mm below the top edges of the remaining coating layers on the splitter flanks (Fig. 6-4c as well as Figs. D-17 and D-18 in Appendix D3).

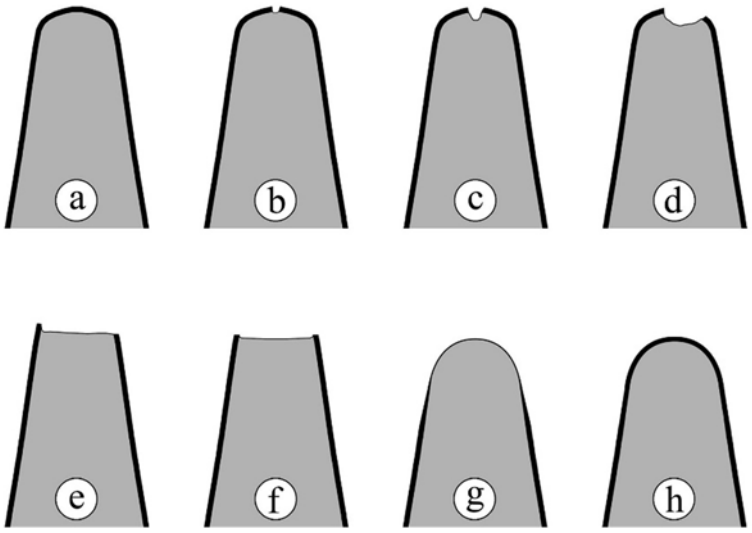

Figure 6-3 Schematic splitter cross-sections of coated Pelton buckets at various stages of erosion and on-site revision works: (a) new, (b) to (f) typical propagation of erosion, (g) after grinding, and (h) after repair of coating in the region of the splitter crest; the bold line represents the coating.

With very blunt splitters (MG 2 in 2012), also the base material on the splitter flanks was locally eroded (Fig. D-7 in Appendix D2). This was attributed to cavitation resulting from the disturbance of the high-spead flow by a bluff body.

The cross-sections (g) and (h) in Figure 6-3 refer to revision works which were usually performed on-site every winter (grinding and coating repair, respectively).

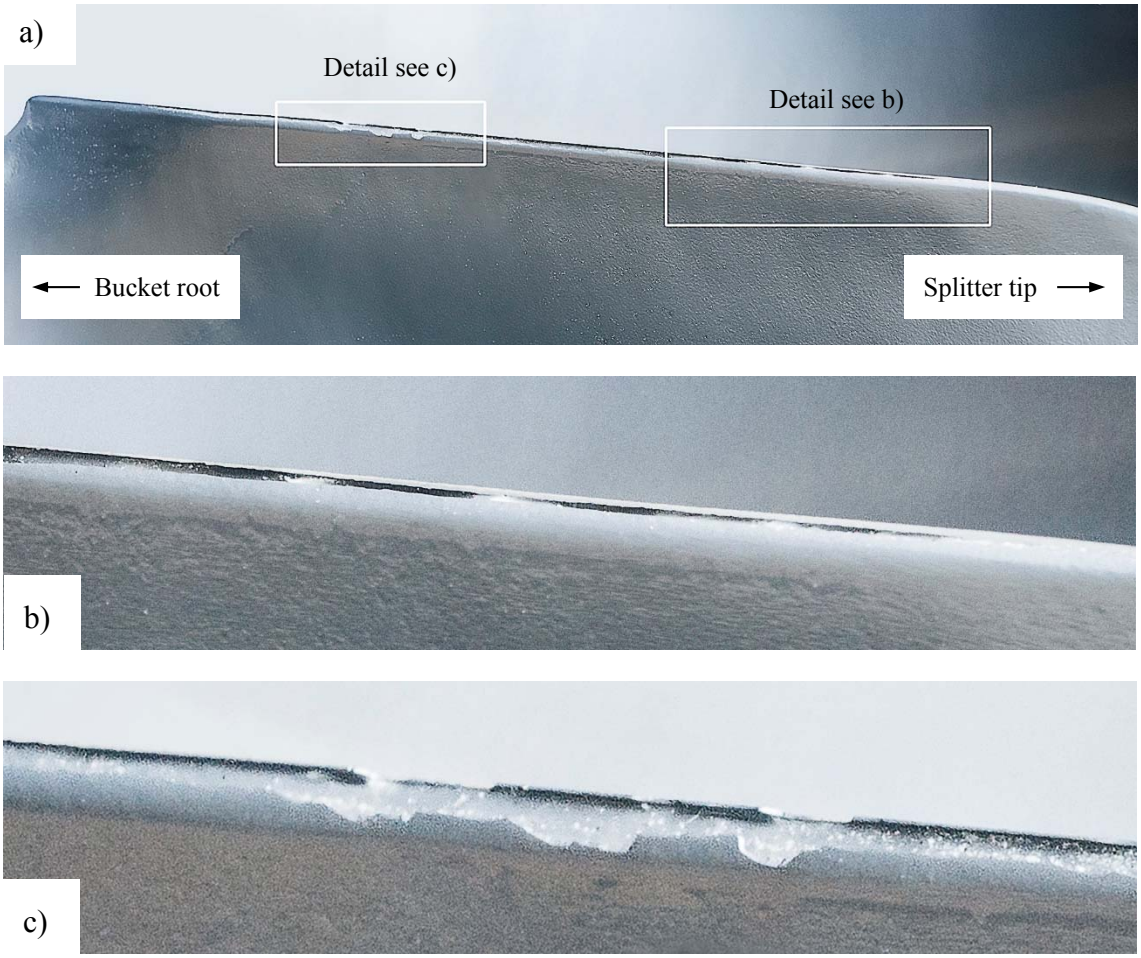

Figure 6-4 Erosion on the splitter crest of a hard-coated Pelton bucket (bucket no. 2 of MG 2 on August 20, 2013): a) overview, b) and c) details.

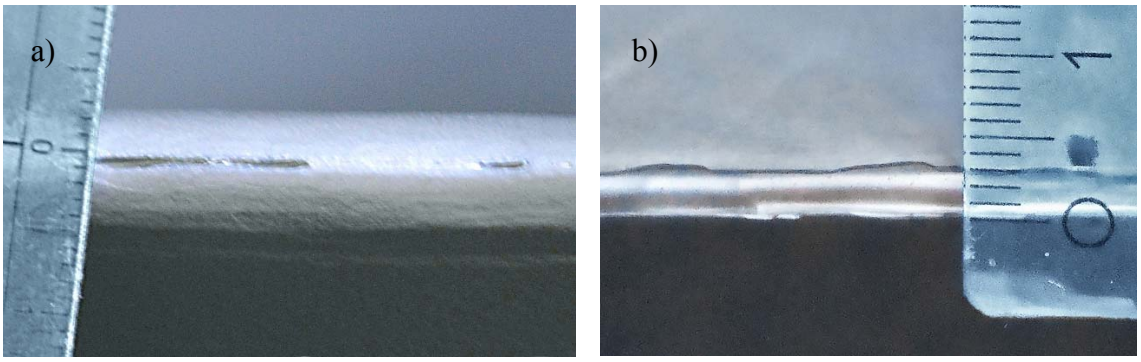

Figure 6-5 Details of erosion on initially coated splitters a) bucket no. 11 of MG 1 on November 26, 2014; b) bucket no. 1 of MG 2 on November 15, 2013; rulers have mm gradation.

The splitter crests of MG 1 in 2013 and of both MGs in 2014 were eroded only locally (Figs. 6-6 and 6-7). Reasons for such local damages on leading edges are (i) splintering of coating due to exceptional impacts of stones (e.g. from the unlined ceiling of the storage tunnel) and (ii) more likely a locally lower quality of the coating and its bonding (coating flaws). An example for the latter is given in Figure 6-7: The lack of coating at one spot on the splitter crest before the sediment season 2014 (Fig. 6-7b) resulted in a local erosion damage with a larger area at the end of the season (Fig. 6-7c). This damage had a depth of ~2.5 mm (Fig. D-10f in Appendix D2) and a volume of ~91 mm^3 (determined from 3D-surveys) corresponding to an eroded mass of ~0.7 g.

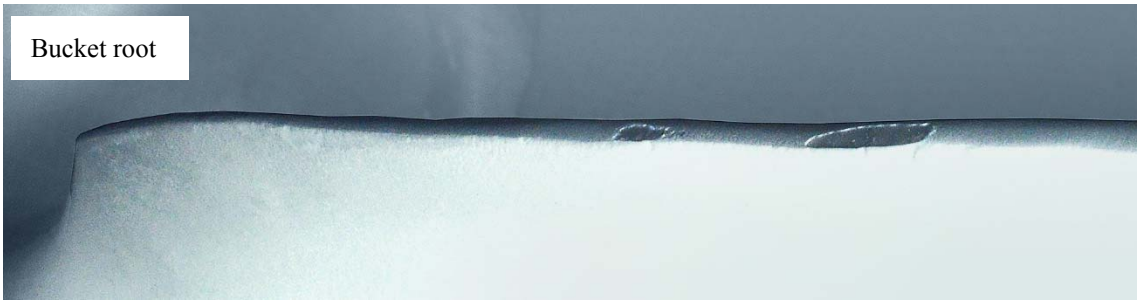

Figure 6-6 Local erosion of coating on the splitter crest of bucket no. 1 of MG 1 on December 5, 2013.

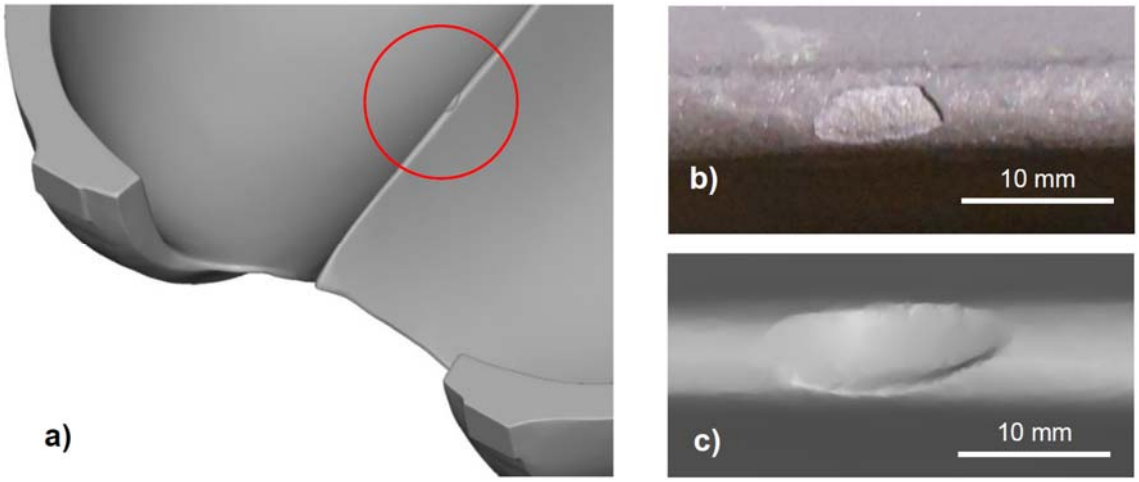

Figure 6-7 Local erosion on the splitter of bucket no. 1 of MG 2 in the sediment season 2014: a) location of the damage in the 3D-model, b) photo of local lack of coating in April 2014 and c) detail of the erosion damage at this location in November 2014 according to the 3D-model.

6.3.1.2 Erosion on cut-outs

Systematic erosion of coating and base material on the leading edges of cut-outs is shown in Figures 6-1 and 6-8. As for the splitters, the erosion of base material usually began with narrow grooves on the leading edges (Fig 6-9a) which expanded to their full width (Fig. 6-9d).

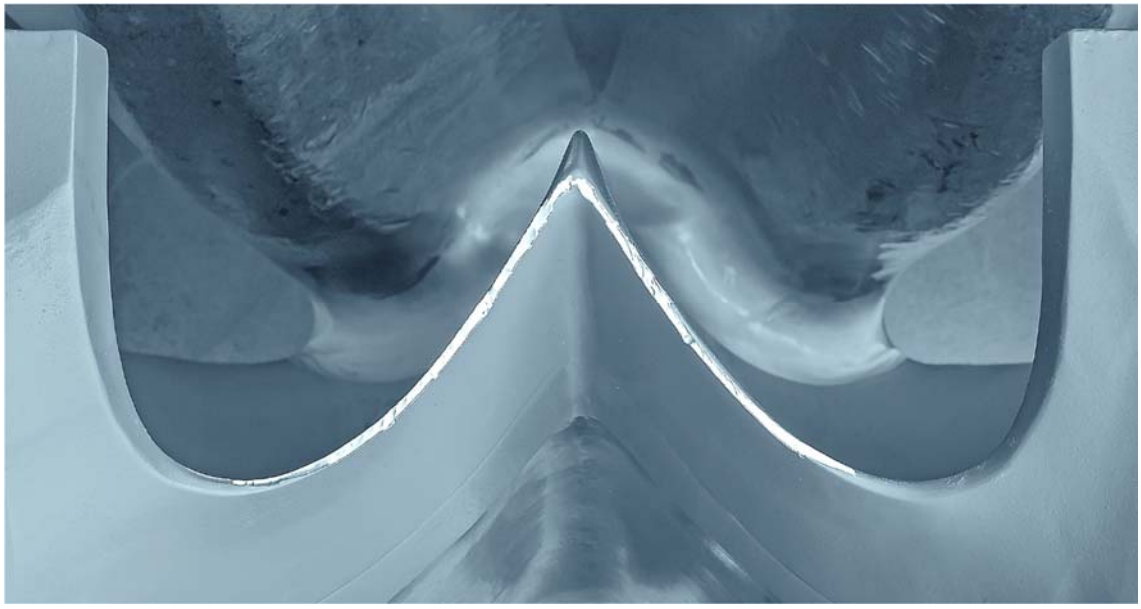

Figure 6-8 Erosion on the leading edges of the cut-outs of a hard-coated Pelton bucket (no. 2 of MG 2 on August 20, 2013).

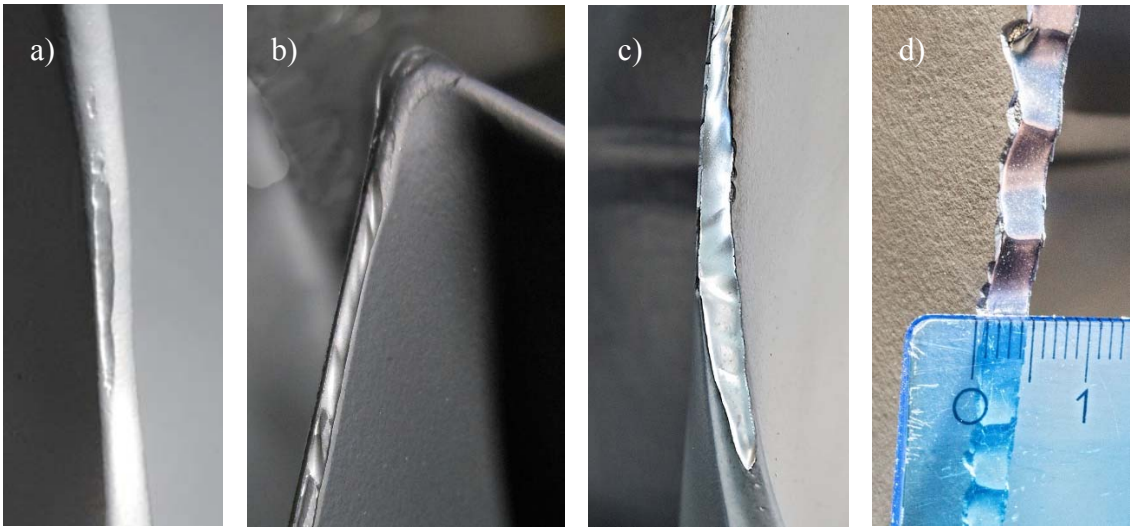

Figure 6-9 Details of cut-outs with local complete erosion of coating and subsequent erosion of base material on leading edges a) bucket no. 1 of MG 1 on November 12, 2013; b) bucket no. 14 of MG 2 on June 18, 2013; c) and d) MG 2 on November 15, 2013.

6.3.2 Results from 3D-surveys

6.3.2.1 Geometrical changes

Super-elevated longitudinal profiles of the splitter crests of buckets no. 1 of MG 1 and MG 2 at the beginning of the observation period in April 2012 and from the next 3D-survey (after the major flood event) are shown in the lower parts of Figure 6-10. The corresponding splitter height reductions Δh are shown in the upper parts of the diagrams. The splitters were generally most eroded in the central third of the splitter length. Erosion caused undulated crest profiles (Figure 6-10b) which were smoothed by grinding after the

sediment seasons (Figure 6-10a). Further diagrams of Δh along the splitter crests for buckets no. 1 and 2 of both MG in the sediment seasons 2012 to 2014 are shown in Figure D-10 in Appendix D2. Except for local damages, the Δh-profiles had a similar character for both investigated buckets.

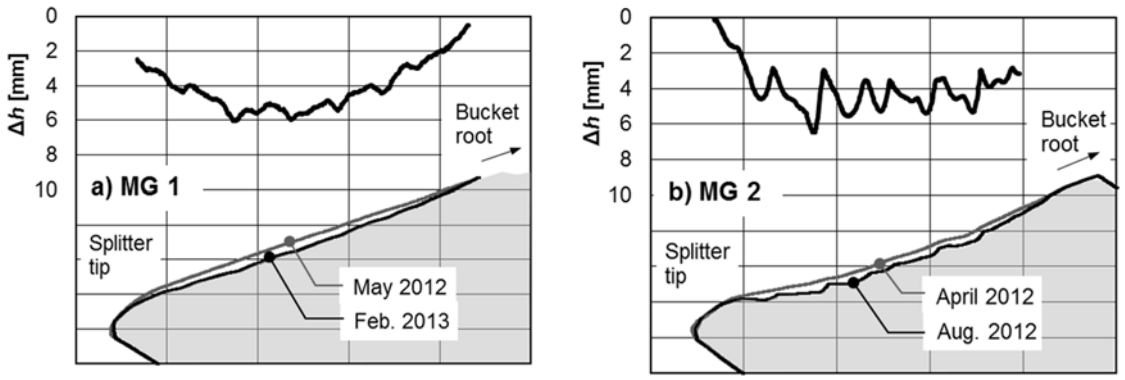

Figure 6-10 Super-elevated longitudinal profiles of the splitter crests of buckets no. 1 of a) MG 1 and b) MG 2 measured in the beginning and the end of periods including the major flood event of July 2012, as well as resulting splitter height reductions Δh displayed above the profiles (modified from Abgottspon *et al.* 2013b, 2016b).

Figure 6-11 shows the cross-sections of the splitter crests of buckets no. 1 of each MG at various dates. The sections are located at half of the splitter length. At the beginning of the observation period, the splitter crest profile of MG 2 was wider than that of MG 1 because of previous erosion and repair works (Section 3.3.5). The shapes of the splitters were altered mainly in 2012 in periods including the major flood event. The blunt splitter profile in Figure 6-11b resulted from erosion; the rounded one in Figure 6-11a from grinding. The maximum splitter width s (definition see Figure 3-13) in the three years was 10 mm (MG 2 in August 2012), corresponding to 1.5% of the inner bucket width B.

The splitter widths s_0 before each sediment season are shown along the splitters in Figure D-11 in Appendix D2. At MG 1, the s_0 decreased from the splitter tips towards the bucket roots. At MG 2 however, where the runners no. 2 to 4 were installed over the three years, the s_0 were either maximal in the central third of the splitter length or approximately constant. The differences in the s_0-profiles among the runners are attributed to their different erosion states and maintenance histories.

The increases in splitter widths Δs along the splitter length are shown in Figure D-12 in Appendix D2. The Δs were similar for both investigated buckets. As for the Δh, the Δs of MG 2 in 2012 varied considerably along the splitter due to the undulations in the crest profiles (Fig. D-12b) and the inclination of the splitter flanks; such variations were smoothed out by grinding (Fig. D-12a).

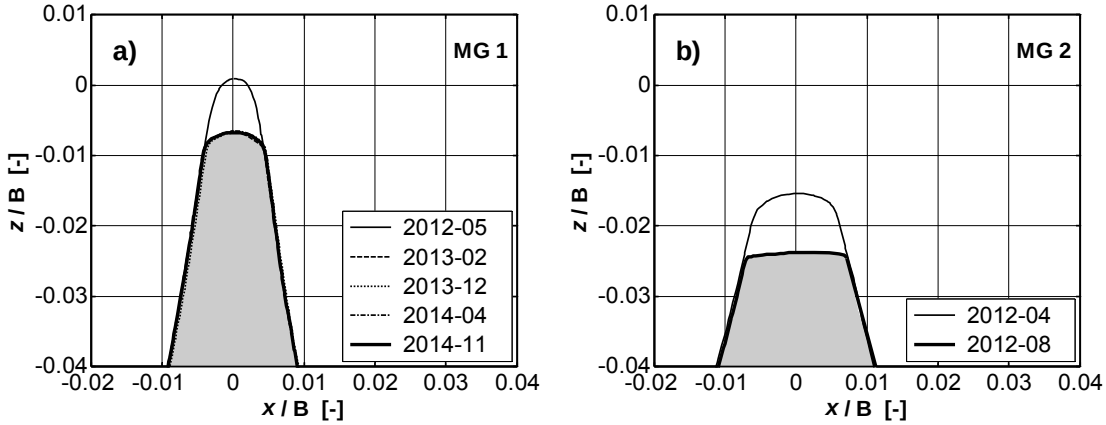

Figure 6-11 Splitter cross-sections of buckets no. 1 of a) MG 1 und b) MG 2 measured at various stages of erosion and maintenance works (Abgottspon *et al.* 2016b).

The top-view geometries of the cut-outs of the buckets no. 1 of MG 1 and MG 2 at the beginning of the observation period in April 2012 and from the next 3D-survey (after the major flood event) are shown in the lower parts of Figure 6-12. The cut-out geometries differed considerably among runners depending on the maintenance histories. The corresponding increases of the cut-out depths Δc (definition of c see Figure 3-13) are shown in the upper parts of the Figure. For MG 2, the cut-out edges were mainly eroded in their central (lowest) parts. For MG 1 with cut-outs closer-to-original geometries, the main erosions were closer to the splitter tips. The top-view width of the mainly eroded zone in the cut-outs was 70 to 90% of the jet diameter (Figure D-8 in Appendix D2.

Further diagrams of Δc along the cut-outs of buckets no. 1 and 2 of both MG in the sediment seasons 2012 to 2014 are shown in Figure D-13 in Appendix D2. The Δc were similar for both investigated buckets. For MG 2 in 2013, the moderate Δc were less symmetrical than the larger Δc in 2012.

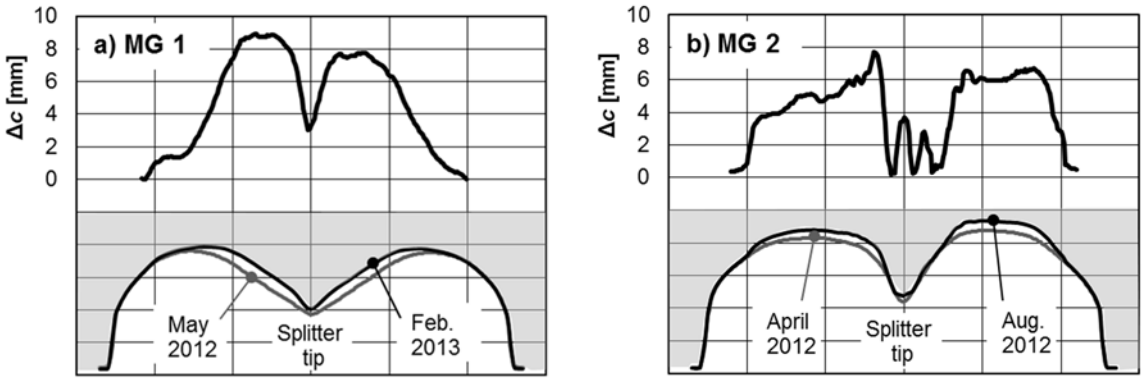

Figure 6-12 Top views of the cut-outs of buckets no. 1 of a) MG 1 and b) MG 2 measured in the beginning and the end of periods including the major flood event of July 2012, as well as resulting increases in cut-out depths Δc displayed above the contours of the cut-outs (modified from Abgottspon *et al.* 2013b, 2016b).

Table 6-3 summarizes characteristic values of the splitter widths $s_{0,centr}$ before each sediment season as well as geometrical changes on the splitters (Δh_{max}, Δs_{centr} and Δy_t) and cut-outs (Δc_{max}) during the years. The $s_{0,centr}$ and Δs_{centr} are rounded average values in the central third of the splitter length of buckets no. 1 and 2. The Δy_t are rounded average values of both measured buckets. The Δh_{max} and Δc_{max} are rounded average values of the maximum differences along the splitters or cut-outs of both measured buckets. Note that the Δc_{max} is not necessarily there where the cut-out depth c is maximal, but rather towards the splitter tip (Fig. 6-12).

The coating on splitter crests and cut-out edges was systematically eroded for both MGs in 2012 and for MG 2 in 2013. This led to erosion of base material and geometrical changes in the range of several millimetres. Otherwise, the coating was removed only locally, and the geometry of the splitters and cut-outs was not significantly altered.

Table 6-3 Characteristic values of splitter widths before the sediment seasons $s_{0,centr}$ and of the geometrical changes on the splitters and cut-outs of the runner buckets; definition of y_t see Figure 2-27a and for the other variables see Figure 3-13.

Year	MG 1						MG 2					
	Runner	RW	$s_{0,centr}$ mm	Δh_{max} mm	Δs_{centr} mm	Δy_t mm	Δc_{max} mm	Runner	RW	$s_{0,centr}$ mm	Δh_{max} mm	Δs_{centr} mm	Δy_t mm	Δc_{max} mm
2012	no. 1	G	3	6.5	3	3.5	9.5	no. 2 §		8	6.5	2	5.5	7
2013	no. 1	C	6	Not significant				no. 3	G, C	4.5	3	1.5	0.5	4
2014	no. 1		6	Not significant				no. 4		7	Not significant			

* RW = Revision works: G = Grinding of splitters and cut-outs, C = On-site re-coating of these parts.
§ From April 18 to August 13 (first half of the sediment season, including the major flood event).

6.3.2.2 Uncertainty in optical 3D-surveys

To investigate the uncertainty of the geometrical differences determined from the optical surveys, the 3D-geometries of bucket surfaces from selected measurements were compared. Figure D-9a in Appendix D2 resulted from two repeated measurements of the same geometry in April 2014. Figures D-9b to D-9d resulted from measurements before and after the sediment season 2014. In 2014, the local ΔCT inside the buckets were <0.04 mm (Figs. D-2 and D-3 in Appendix D1), and the coating was removed only on a few spots on the splitter crests and cut-out edges. Hence, the geometrical differences in Figure D-9 were attributed to measurement uncertainty. The largest differences of up to 0.7 mm were identified inside the buckets. This is considerably more than the optical system's measurement uncertainty in a single shot (<0.04 mm according to Section 3.5.2.1). The experimentally determined higher measurement uncertainty for a large Pelton bucket as in the present case is attributed to the imperfect assembling of some point clouds obtained

from the individual shots. The expanded measurement uncertainties on the geometrical differences on the splitters and the cut-outs were estimated as $U_{2\sigma}$ = ±0.2 mm and ±0.6 mm, respectively.

6.3.2.3 Eroded masses

Figure 6-13 shows the digital 3D-models of the splitters of buckets no. 1 and 2 of MG 2 in August 2012 compared to those before the sediment season (semi-transparent surfaces). The volume differences were converted to mass differences assuming a density of 7.7 g/cm^3 as for the usual turbine base material. The eroded masses on splitters Δm_{sp} and cut-outs Δm_{cu} of all buckets of a runner were estimated from the average mass differences determined on the two measured buckets multiplied by the number of buckets z_2. The eroded masses evaluated from the 3D-surveys are summarized in Tables 6-4 and 6-5 for MG 1 and MG 2, respectively. The absolute expanded uncertainties $U_{2\sigma}$ on the Δm were estimated based on the respective surface areas and the $U_{2\sigma}$ of the geometrical differences of ±0.2 or ±0.6 mm (Section 6.3.2.2). The results showed that the Δm on the cut-outs can exceed those on the splitter crests.

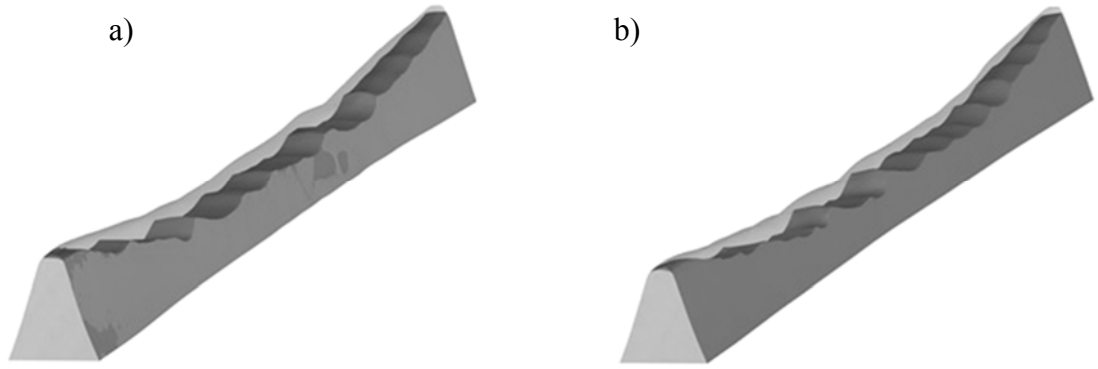

Figure 6-13 3D-views on the eroded splitters of buckets no. 1 and 2 of MG 2 in August 2012 (after the major flood event); semi-transparent surfaces show the geometry before the sediment season (modified from Abgottspon *et al.* 2013b, 2014, 2016a).

Table 6-4 Eroded masses ($\pm U_{2\sigma}$) on runner buckets of MG 1 in 2012 to 2014 based on 3D-surveys.

Period and revision works*	Runner	At splitters Δm_{sp}				At cut-outs Δm_{cu}				$\Delta m_{sp} + \Delta m_{cu}$
		Per bucket			Per runner	Per bucket			Per runner	Per runner
		no. 1 [g]	no. 2 [g]	** [g]	[kg]	no. 1 [g]	no. 2 [g]	** [g]	[kg]	[kg]
2012 G	no. 1	49	58	54	1.07 ±0.25	71	75	73	1.46 ±0.30	2.53 ±0.55
2013 C	no. 1	Insignificant result				Implausible result				-
2014	no. 1	Insignificant result #				Implausible result #				- #

* G = Grinding of splitters and cut-outs, C = On-site re-coating of splitters and cut-outs (Fig. 3-5).

** Average of buckets no. 1 and no. 2.

Eroded masses of base material determined from ruler measurements see Figure 6-14.

Table 6-5 Eroded masses ($\pm U_{2\sigma}$) on runner buckets of MG 2 in 2012 to 2014 based on 3D-surveys.

Period and revision works*	Runner	At splitters Δm_{sp} Per bucket no. 1 [g]	no. 2 [g]	** [g]	Per runner [kg]	At cut-outs Δm_{cu} Per bucket no. 1 [g]	no. 2 [g]	** [g]	Per runner [kg]	$\Delta m_{sp} + \Delta m_{cu}$ Per runner [kg]
2012 §	no. 2	80	79	80	1.59 ±0.25	73	78	76	1.51 ±0.30	3.10 ±0.55
2013 G, C	no. 3	16	No data		0.32 ±0.15	39	No data		0.78 ±0.20	1.10 ±0.35
2014	no. 4	Insignificant result #				Implausible result #				-#

§ From April 18 to August 13 (first half of the sediment season, including the major flood event).
Further explanations see notes below Table 6-4.

6.3.3 Results from damage mapping and ruler measurements

At the end of the sediment season 2014, minor local erosions of coating and base material were observed on splitters and cut-outs which varied among the buckets. These damages were mapped on all buckets of both MGs, in addition to the 3D-surveys of buckets no. 1 and 2. The length, the average width and the average depth of each of the local damages were measured with a ruler or estimated based on reference lengths. The eroded masses were calculated from the dimensions of each damage and assuming again a density of 7.7 g/cm^3. The eroded masses on the splitters and cut-outs of each bucket of both runners are shown in Figure 6-14. The cut-outs of bucket no. 14 of MG 1 were most eroded (Fig. 6-14a as well as Fig. D-15 in Appendix D3). Regarding the splitters, the largest erosion was detected on bucket no. 19 of MG 2 (Fig. 6-14b as well as Fig. D-16 in Appendix D3). The eroded masses per runner in 2014 were 0.071 and 0.049 kg for MG 1 and MG 2, respectively. Note that these are only <3% of the eroded masses in 2012 (Tables 6-4 and 6-5).

With such rather small damages on the coated runners, the location and extent of erosion along the splitter crests and cut-out edges appears to be random. It seems that the variability of the erosion damages on the splitter crests and cut-outs among the buckets reduces, if the erosion progresses and systematic erosion patterns develop at all buckets. For example in 2012 with the maximum erosion of the three years, the eroded masses on the splitter crests and cut-out edges of buckets no. 1 and 2 were similar (Tables 6-4 and 6-5).

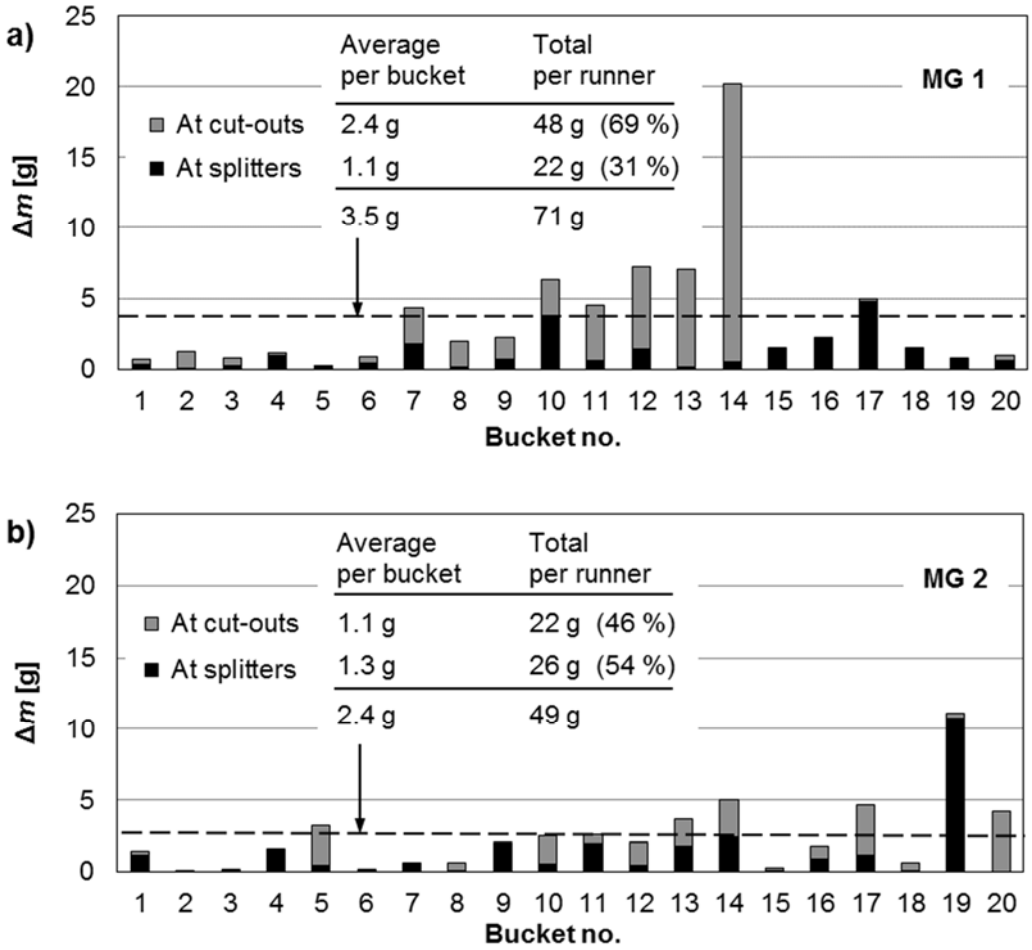

Figure 6-14 Eroded masses on the splitters and cut-outs of all runner buckets of a) MG 1 and b) MG 2 in the sediment season 2014 based on mapping of mainly minor local erosion damages (ruler measurements).

6.4 Erosion on other turbine parts

6.4.1 Needle tips

In the years 2012 to 2014, the base material of the coated needle tips of the nozzles of both MGs was not eroded except for their tips (Fig. 6-15a). The erosion status of a needle tip was approximately described with its radius r in the side-view. The maximum tip erosion over the three years was measured on the lower nozzle of MG 1 in November 2014 with r = 7 mm (Figure 6-15b). The other needle tip radii obtained from measurements by ruler (or estimates based on images) are given in Table 6-6. All in all, the erosions on the needle tips were small during the observation period. The more rounded needle tips of MG 1 resulted mainly from erosion before the observation period. The needle tips of MG 2 stayed in as good as new condition during the observation period.

Table 6-6 Needle tip radii *r* of the nozzles in the HPP Fieschertal in the years 2012 to 2014.

Date	MG 1		MG 2	
	Lower nozzle [mm]	Upper nozzle [mm]	Lower nozzle [mm]	Upper nozzle [mm]
April 2012	(4)	no data	(1.5)	(1.5)
April 2013	(6)	(5)	(1.5)	(1.5)
Nov. 2014	7	6	1.5	1.5

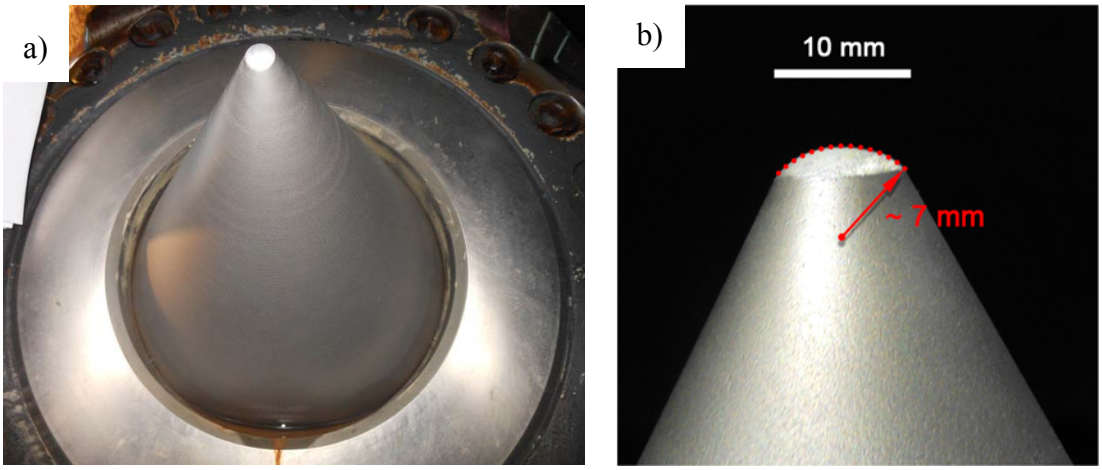

Figure 6-15 Hard-coated needle tip of the lower nozzle of MG 1 in November 2014 with minor tip erosion; a) overview and b) detail.

6.4.2 Jet deflectors, nozzle shields and inspection platforms

The outer side of the deflectors, the top surfaces of the nozzle shields in the vicinity of the runners, and parts of the inspection platforms below the runners (steel gratings) were eroded by typically several millimetres during each sediment season. These uncoated surfaces are not directly exposed to the jet, but to secondary flows after the interaction of the jet with the runner. The erosion was particularly high in 2012 with the major flood event (Figs. D-20b and D-21 in Appendix D3). Undulated and scaly erosion patterns were observed as known from the inner sides of uncoated runner buckets (Section 2.3.2.3).

The erosions on the deflectors, shields and gratings were not relevant for turbine efficiency and not critical for the structural safety of the MGs, but lead to recurring costs. These erosion damages were repaired on-site in every winter by welding and grinding.

7 RESULTS AND DISCUSSION OF TURBINE EFFICIENCY MONITORING (TASK D)

In this Chapter, the results of the turbine efficiency monitoring at HPP Fieschertal performed by HSLU in the years 2012 to 2015 are reported and discussed. Firstly, the sliding-needle measurements (SNM) and secondly the efficiency monitoring based on continuously recorded operation data (CEM) are treated.

7.1 Periodic turbine efficiency monitoring by SNM

7.1.1 Checking for reproducible conditions

In the years 2012 to 2015, twenty SNM were done for each MG (Fig. 3-5). To check if the SNM were performed in reproducible conditions, the following set of criteria was developed:

- The headwater level is above the minimum level specified in Section 3.6.2.1;
- The difference between the average efficiencies computed for the increasing and decreasing ramp does not exceed a threshold value;
- The shapes of the efficiency curves as a function of power computed during the increasing and decreasing ramps are similar to previous ones (threshold values for deviations at 16, 24 and 32 MW were not exceeded).
- The slopes of the best-fits on power and discharge data during the increasing and decreasing ramps differ by less than 1%.

After each SNM, it was checked if these criteria were met. If more than one criterion was not met, the result of the SNM was discarded. Using the discharge measurement Q_4, one SNM (Aug. 17, 2015) was discarded for MG 1 and another one (Feb. 2, 2014) for MG 2. Appling these quality checks, the expanded uncertainty on $\Delta\eta$ was estimated as $U_{2\sigma} = \pm 0.2\%$.

7.1.2 Comparison of efficiency curves

Figure 7-1 shows the index turbine efficiencies for both MGs measured at the beginning of the observation period and after the sediment seasons as a function of the electric active power P_{el}. No absolute efficiencies are indicated on the vertical axes because the absolute scaling of the Q-signal is not exactly known. Irrespective of vertical shifts by up to almost 1% due to erosion, maintenance works, and runner exchanges (for MG 2), the best efficiency point of all curves was at ~20 MW, i.e. ~63% of the rated power (32 MW).

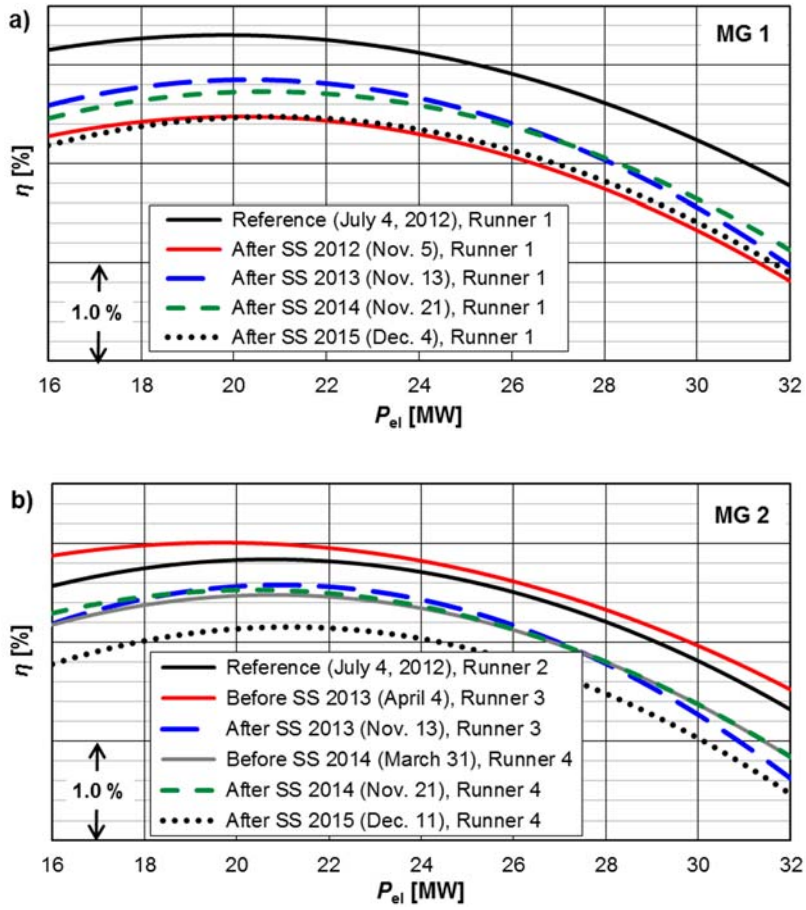

Figure 7-1 Measured index efficiency curves as a function of power obtained from SNM based on Q_4 in the years 2012 to 2015 for a) MG 1 and b) MG 2.

7.1.3 Time series of changes in weighted efficiencies

Figure 7-2 shows time series of the absolute differences of weighted index efficiencies $\Delta\eta$ obtained from SNM in the years 2012 to 2015 for boths MGs (efficiency histories). The available points before and after each sediment season are marked with red ellipses. Table 7-1 summarizes the $\Delta\eta$ between the average efficiencies of the marked points. The expanded uncertainty on these $\Delta\eta$ (resulting mostly from two pairs of points) was estimated as $U_{2\sigma} \approx \pm 0.15\%$. For MG 2, no SNM were possible in the second half of 2012 because of a mechanical problem at the actuator of one nozzle.

During the sediment seasons, efficiency reductions $\Delta\eta$ with an amount of up to 0.9% were measured; the average was 0.3% and the standard deviation $\sigma = 0.3\%$, i.e. there is a high coefficient of variation. These $\Delta\eta$ are attributed to turbine erosion (hydro-abrasive erosion and secondary damages due to cavitation). Note that the operating hours in Table 7-1 are not suitable to explain the $\Delta\eta$ (e.g. 2012 vs. 2014 for MG 1).

Between the sediment seasons, the efficiencies increased by up to 0.6% due to on-site grinding of splitters and cut-out edges (G). The average was 0.2% and σ = 0.25%, i.e. there is a high scatter. These increases are represented by vertical line segments. The beneficial effect of grinding mainly depends on the extent of erosion before the grinding. No significant $\Delta\eta$ due to on-site re-coating (C) were measured.

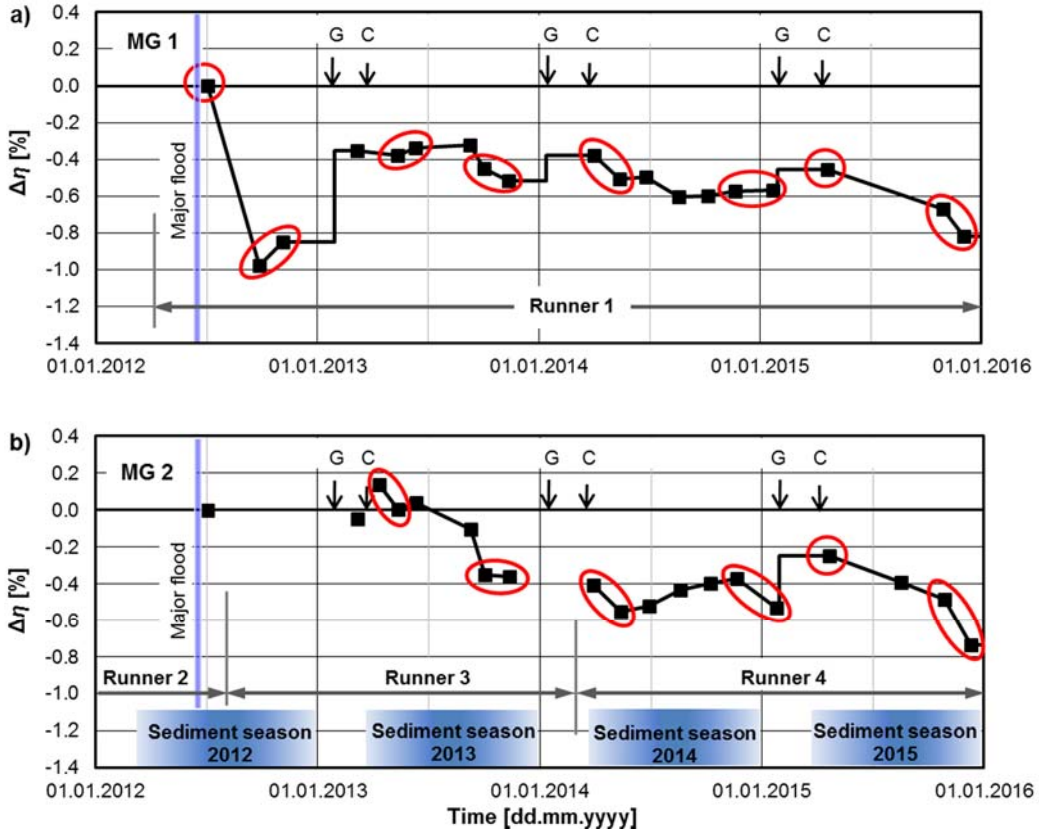

Figure 7-2 Efficiency histories obtained from SNM based on Q_4 at a) MG 1 and b) MG 2; G and C denote revision works as defined in Figure 3-5 (modified from Abgottspon *et al.* 2016b).

Table 7-1 Absolute turbine efficiency differences $\Delta\eta$ from SNM due to erosion over the sediment seasons (SS) as well as due to grinding (G) of splitters and cut-out edges after the SS in HPP Fieschertal.

Year	MG 1			MG 2		
	Erosion during SS		Grinding after SS	Erosion during SS		Grinding after SS
	$\Delta\eta$ [%]	op. hours [h]	$\Delta\eta$ [%]	$\Delta\eta$ [%]	op. hours [h]	$\Delta\eta$ [%]
2012	−0.91	1902	+0.56	no data available due to runner change		
2013	−0.13	2096	+0.04	−0.43	3175	runner change
2014	−0.13	3076	+0.11	+0.03	3126	+0.20
2015	−0.29			−0.36		

7.2 Continuous turbine efficiency monitoring (CEM)

7.2.1 Identification and compensation of variations in s_n-Q-curves

If both MG are running simultaneously, the discharge per MG, which is required for CEM, has to be determined from the respective needle position s_n using the corresponding s_n-Q-curve (Section 3.6.2.2). It was recognized that the s_n-Q-curves obtained from each of the twenty SNM per MG changed occasionally in time (Figure E-2 in Appendix E). Hence the discharge differences ΔQ with respect to the curve of the first SNM on July 4, 2012, were analyzed for all curves (Figure E-3). Three groups of curves were distinguished: (i) the first SNM in July 2012, (ii) from September 2012 to March 2013, and (iii) the other curves. The shift between (i) and (ii) is attributed to a modification in the data acquisition system; the shift between (ii) and (iii) is due to a re-scaling of the needle position sensors' measuring ranges after revision works on the nozzles in spring 2013 (Fig. 3-5). The largest absolute ΔQ among all curves was almost 0.8 m^3/s (Fig. E-3b). In the relevant operation range $40\% \leq s_n \leq 100\%$, i.e. for turbine discharges varying between 3 m^3/s and 7.5 m^3/s, the largest relative discharge difference among all curves was 20% (deviation of ~0.6 m^3/s at $s_n = 40\%$ in Fig. E-3b). For $40\% \leq s_n \leq 100\%$, the standard deviation of the relative differences of the third group of curves (iii) to their average was $< 0.5\%$, i.e. s_n-Q-curves with a good reproducibility were obtained in periods without physical modifications of the system.

With regular updates of the s_n-Q-curves, the uncertainty on the turbine discharge was reduced to an acceptable level which enabled CEM when both MGs were running. This state of operation is the most frequent during the sediment season and hence important for efficiency monitoring in the context of turbine erosion.

7.2.2 Time series of changes in weighted efficiencies

Figure 7-3 shows time series of absolute differences of weighted index efficiencies $\Delta\eta$ obtained from CEM (points) together with those from SNM (lines from Fig. 7-2). The points from CEM represent the available daily averages. The points from CEM scatter more than those from the SNM, but have a higher temporal resolution. The expanded uncertainty on a daily $\Delta\eta$ in Figure 7-3 was estimated as $U_{2\sigma} \approx \pm 0.3\%$. The results of the two methods are in good agreement and contributed to increase the reliability of the efficiency monitoring.

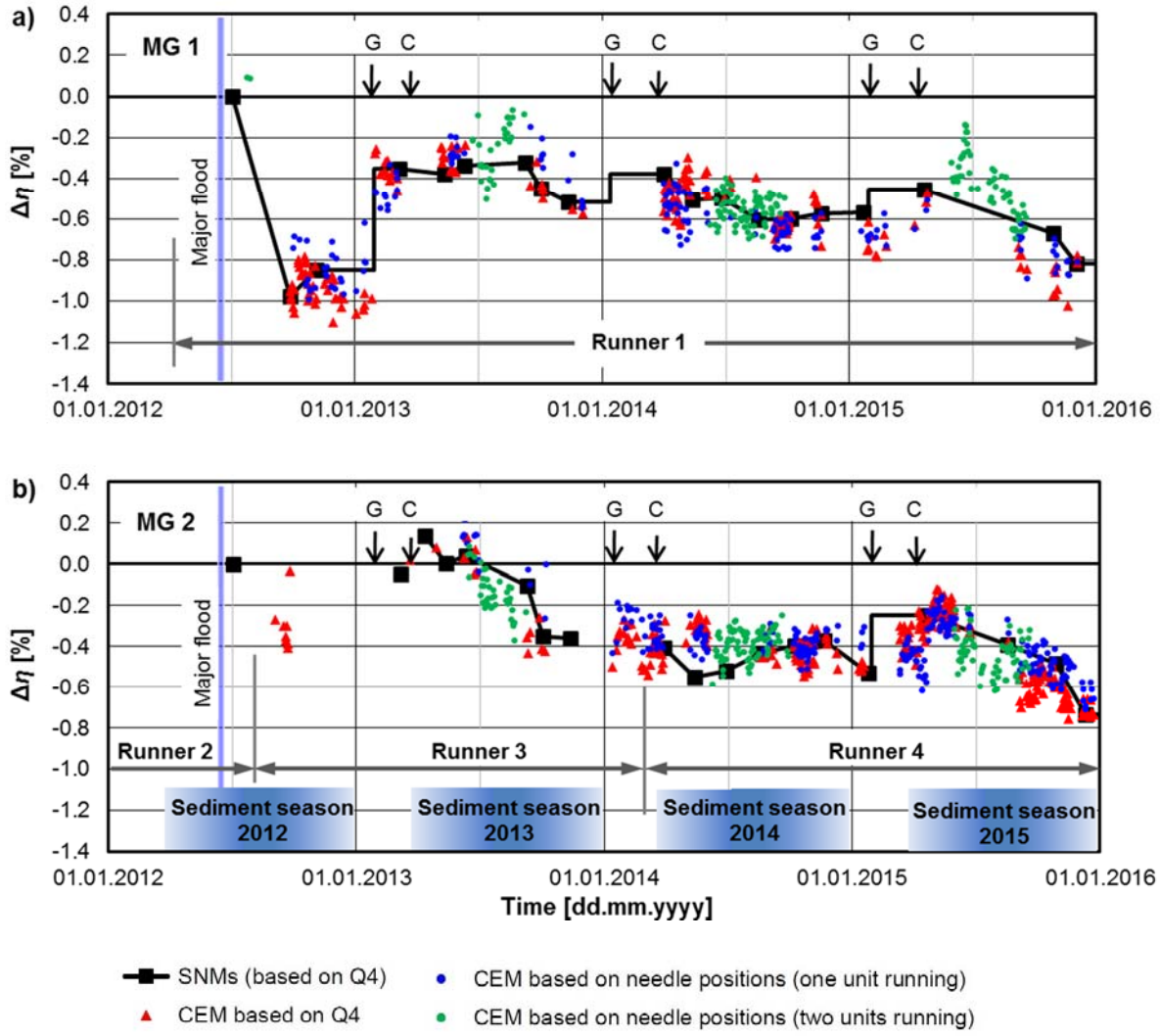

Figure 7-3 Efficiency histories in the years 2012 to 2015 obtained from continuous monitoring (CEM) based on 1 Hz-data compared to those from SNM for a) MG 1 and b) MG 2; G and C denote revision works as defined in Figure 3-5 (modified from Abgottspon *et al.* 2016b).

In Figure 7-3 there are almost no CEM data points before October 2012 because the data acquisition system of the research project was not fully operational before. Hence, archive data with a lower temporal resolution (Section 3.6.2.1) were evaluated for 2012 and 2013 (Figure 7-4). The efficiencies computed from these five-minute-data have a higher uncertainty than those from the 1 Hz-data. The points in Figure 7-4 indicate that there was no clear efficiency reduction from the beginning of the observation period (April 2012) to the first SNM on July 4, 2012, i.e. two days after the major flood and one day before the first re-suspension event after the flood (Fig. 5-26). This means that the turbine efficiencies were not significantly reduced during the flood event as expected a priori, but in the following months – mainly during the transport of coarser particles during re-suspension events (Section 5.7.4). At MG 1, the trend of efficiency increase in the second

quarter 2012 is attributed to partly the polishing of the coating in the buckets (runner installed in April 2012 after a major factory overhaul) and mainly measurement uncertainty. Figure 7-4 shows that data with a temporal resolution of five minutes are not sufficient for reliable continuous monitoring of $\Delta\eta < 1\%$.

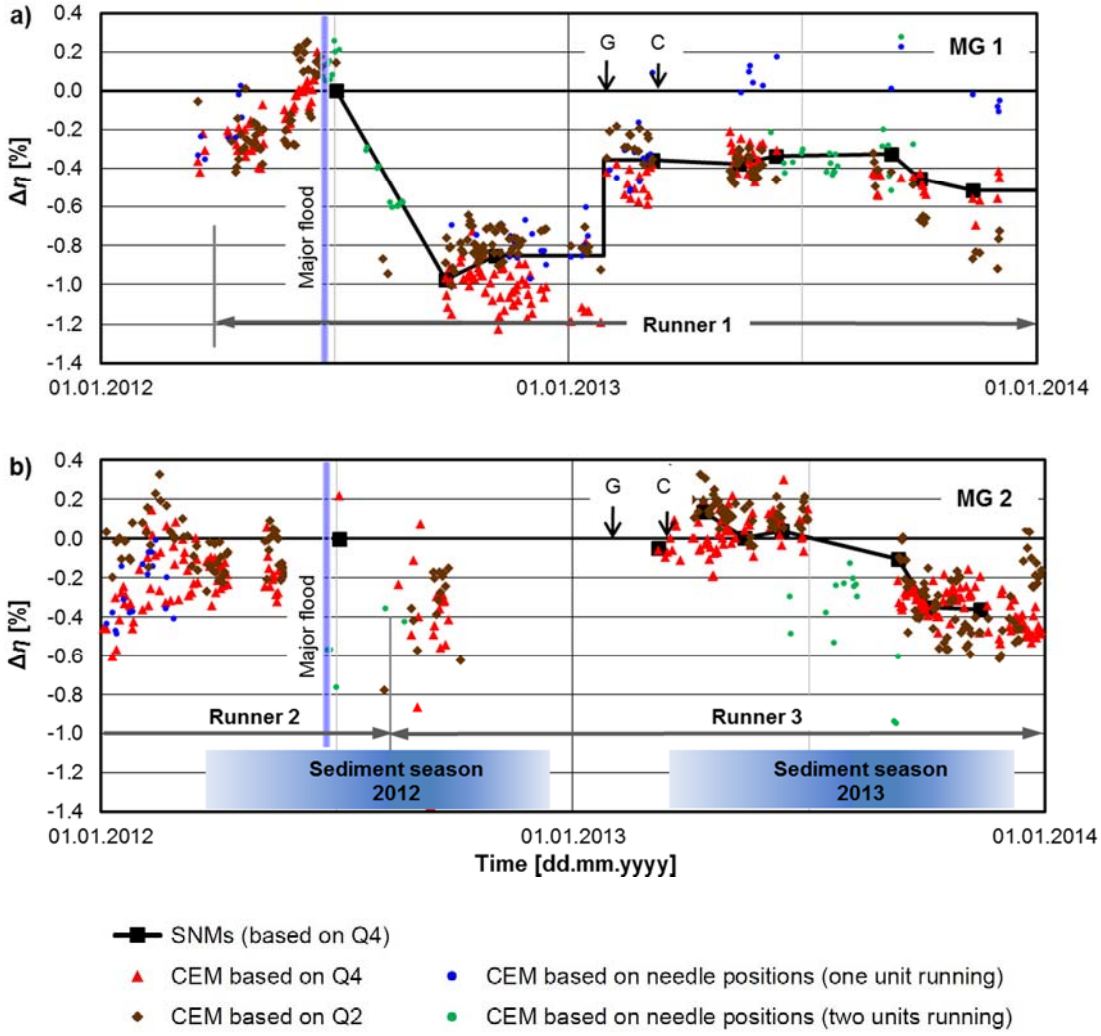

Figure 7-4 Efficiency histories in the years 2012 to 2013 obtained from continuous monitoring (CEM) based on 5-minute archive data compared to those from SNM for a) MG 1 and b) MG 2.

8 RELATIONS BETWEEN SUSPENDED SEDIMENT LOAD, TURBINE EROSION AND EFFICIENCY

In this Chapter, the results from the field study presented in Chapters 5 to 7 (Tasks B to D) are combined. Firstly, the relations between *SSL* or *PL* and turbine erosion at various locations in coated Pelton runner buckets are evaluated and the erosion model according to IEC 62364 (2013) is adapted and partly calibrated. Secondly, the effects of the relative splitter width and the normalized radial splitter tip erosion on turbine efficiency are investigated.

8.1 Turbine erosion

8.1.1 Turbine erosion as function of *SSL* and *PL* over three years

Figures 8-1a to 8-1c show the splitter width s_{centr}, the reduction of splitter height Δh_{max} and the increase of cut-out depth Δc_{max} according to Table 6-3 as a function of the PL_b from the beginning of the year 2012 to 2014 (Section 5.7.2). Approximate *SSL* per turbine are also indicated on the top axes for comparison. It has been shown for the HPP Fiesch-ertal that *PL* and *SSL* are approximately proportional over longer time spans such as at least one year (Fig. 5-32). The lines for MG 2 are interrupted because three different runners were in operation over the three years, while it was always the same runner for MG 1 (Fig. 3-5). The extent of the erosion per season was similar among the MGs, except for 2013 with significant erosion in MG 2 and practically no erosion on MG 1 despite similar PL_b. The higher erosion on MG 2 cannot be explained by initially wider splitters; it might be due to a lower application quality of the coating. The increases of cut-out depths Δc_{max} per season were slightly higher than the reductions of splitter heights Δh_{max} per season (Figs. 8-1b and 8-1c).

Figures 8-1d to 8-1e show the eroded masses of the splitters Δm_{sp} and the cut-outs Δm_{cu}, respectively, again as a function of the PL_b in the three years. The Δm are mass differences per runner (Tables 6-4 and 6-5, Fig. 6-14). Although the Δh of both MGs were similar in 2012, more mass was eroded from the splitters of MG 2 in 2012 because of the wider splitters. These were probably the reason for secondary damages inside the buckets (Section 6.2.2.1), which required to take the runner of MG 2 out of service already during the sediment season for a major factory overhaul. In contrast, the runner of MG 1 had no such damages and remained in operation during four further years (with on-site repairs in

every winter). This shows that the erosion of a runner depends not only on the *PL* and the erosion resistance of the base material and the coating, but also on the buckets' geometry before the exposure period, i.e. their design as well as their erosion and revision status.

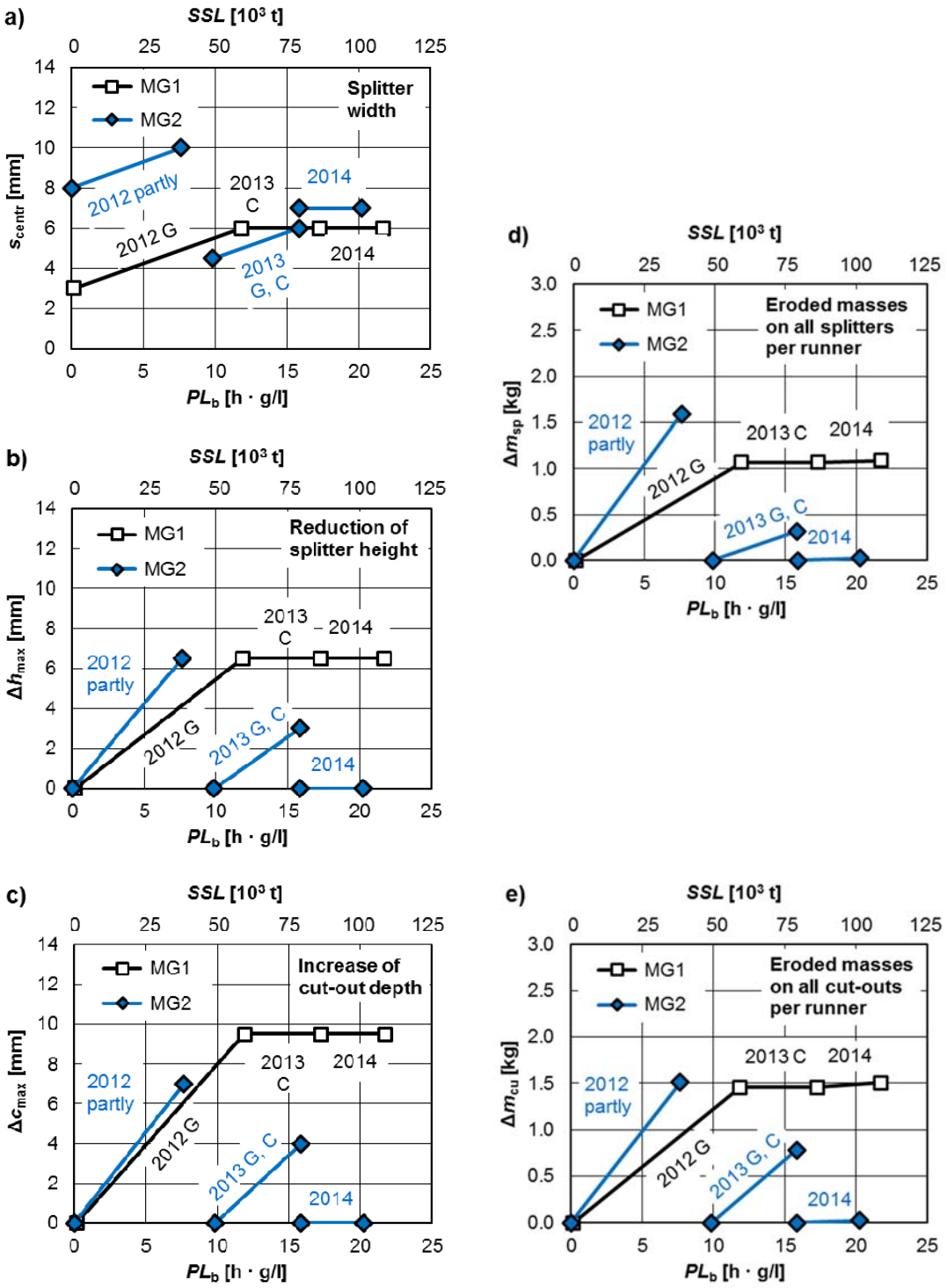

Figure 8-1 Measured geometrical changes (left diagrams) and eroded masses (right diagrams) on splitters (a, b and d) and cut-outs (c and e) of the runners in HPP Fieschertal as a function of the particle load per bucket PL_b and approximate *SSL* since 2012 (a to c modified from Abgottspon *et al*. 2016a, b).

8.1.2 Calibration of adapted IEC erosion model

8.1.2.1 General procedure

The analytical erosion model according to IEC 62364 (2013) given in Equation (2-30) was adapted for the application in the present study. The values of the unknown model parameters were determined from the presented data on PL_b (Chapter 5) and geometrical changes (Chapter 6) for six application cases, i.e. locations in Pelton buckets. In this way, the adapted model was calibrated based on three years of field data from one HPP (Felix *et al.* 2016a).

8.1.2.2 Known and unknown parameters

For HPP Fieschertal, the net head h_n varies between 499 and 515 m. With $h_n \approx 510$ m on temporal average, the characteristic relative velocity in the buckets is $w \approx 50$ m/s (Section 2.3.6.1). IEC 62364 (2013) suggests a velocity exponent of $x = 3.4$ without specifying the turbine type and indicates a range between 2 and 4. In the present study, $x = 3$ was adopted based on Winkler *et al.* (2011a, Section 2.3.4.4), Sulzer Hydro (1996) and other studies, resulting in $w^3 = 125\ 000$ m^3/s^3 for HPP Fieschertal. The reference size RS is the inner bucket width $B = 0.65$ m.

K_f and p are a priori unknown for Pelton turbines (Section 2.3.6.1). K_m is known for the base material ($K_m = 1$ by definition), but is unknown for the coating. To obtain a model applicable for erosion of coating and/or base material, K_m was treated as a generally unknown parameter.

8.1.2.3 Adapted IEC erosion model

Equation (2-31) of the PL for Pelton buckets was inserted in Equation (2-30). The combined equation was solved for the unknowns, resulting in Equation (8-1). The group of unknown parameters was denoted as C_g (Eq. 8-2). This parameter is a normalized 'geometrical' erosion rate.

$$\frac{K_f}{RS^p} K_m = \frac{d_e(t)}{w^x PL_b(t)} \tag{8-1}$$

$$C_g = \frac{K_f}{RS^p} K_m \tag{8-2}$$

For coated runners, two stages of erosion can be distinguished: (1) the erosion of mainly coating and (2) mainly base material. For a given net head and hence w^3, the second stage of erosion begins after a certain threshold on PL_b, denoted as $PL_{b,0}$ in the following. The

$PL_{b,0}$ was inserted in Equation (8-1). With the definition of C_g (Eq. 8-2), Equation (8-3a) resulted, where $w^3 = 125\,000$ m^3/s^3 for the HPP Fieschertal:

$$C_g = \frac{d_e(t)}{w^3 \, (PL_b(t) - PL_{b,0})} \qquad \text{for } PL_b > PL_{b,0} \qquad \text{(units see Table 8-1)} \qquad (8\text{-}3a)$$

$$\text{where} \quad PL_b = \frac{z_0}{z_2} \sum_{i=1}^{(t-t_0)/\Delta t} SSC_i \; k_{size,i} \; k_{shape,i} \; k_{hardness,i} \; \Delta t \qquad [\text{h} \cdot \text{g/l}] = [\text{h} \cdot \text{kg/m}^3] \qquad (8\text{-}3b)$$

8.1.2.4 Model application cases

For the following cases, the values of C_g – and $PL_{b,0}$ if applicable – were determined from the field data on geometrical changes (taken as erosion depths d_e) and PL_b according to Equation (8-3a):

i. Decrease of splitter height Δh_{max}
ii. Increase of splitter width Δs_{centr}
iii. Increase of cut-out depth Δc_{max}
iv. Radial splitter tip erosion Δy_t
v. ΔCT inside the buckets
vi. ΔCT on the splitter crests (Δh within the coating)

The IEC model was developed for the estimation of erosion depths on plane or moderately curved surfaces, as in case (v). Applying such a model to geometrical changes at splitter crests or in cut-outs, as in the other five cases, corresponds to an extension of the original range of application, but is considered to be useful in practice.

Δh, Δc, Δy_t and ΔCT are erosion depths because they are measured approximately in the directions of the erosion. However, Δs is not an erosion depth but a geometrical quantity depending on Δh, the cross-sectional shape of the splitter and the initial splitter width.

8.1.2.5 Determination of C_g- and $PL_{b,0}$-values at splitters and cut-outs

Because the buckets were grinded and fully coated at the beginnings of each sediment season (either factory or on-site re-coating), erosion depths were evaluated per year. The Δh_{max}, Δs_{centr}, Δc_{max} and Δy_t obtained from the measurements are shown as a function of $w^3 \cdot PL_b$ in Figures 8-2a to 8-2d, respectively. The latter quantity reflects the erosion potential per bucket. Approximate *SSL* per turbine are also indicated on the top axes for comparison. The *SSL* refer to the turbine and sediment properties in the investigated case, whereas the $w^3 \cdot PL_b$ is a normalized quantity. The absolute values of the geometrical

changes are given on the left vertical axes, whereas the relative geometrical changes (normalized with the inner bucket width B = 0.65 m) are given on the right vertical axes.

In 2014, the PL_b of both MGs were almost the same and no significant geometrical changes were measured (circular markers on top of each other). The data points in Figures 8-2a to 8-2c show a similar pattern, indicating a systematic dependency of Δh_{max}, Δs_{centr} and Δc_{max} on PL_b (with constant w^3). However, the pattern of the non-zero-values of Δy_t in Figure 8-2d is different: The radial splitter tip erosions are less correlated with PL_b than the other geometrical differences.

For each of the four cases ($d_e = \Delta h_{max}$, Δs_{centr}, Δc_{max} or Δy_t), two types of linear least squares regressions were applied:

- Constrained linear fit passing through the origins of the axes ($PL_{b,0} = 0$), denoted as 'Fit type 1' (dashed lines);
- Unconstrained fit, denoted as 'Fit type 2' (solid lines).

The unconstrained fits were selected because they better represented the data points as seen from Figure 8-2 and by comparison of the R^2. This means that the erosion on the splitter crests and the leading edges of the cut-outs is modelled in two stages:

(1) Erosion of mainly coating (in the sub-millimetre range),
(2) Systematic erosion of mainly base material (in the range of millimetres).

The C_g-values in Equation (8-3) were determined from the slopes in Figures 8-2a to 8-2d, and listed in Table 8-1. The start of the second stage of erosion is quantified by $w^3 \cdot PL_{b,0}$ (Equation 8-3). This corresponds to the horizontal distance from the origin of the axes to the regression line's intersection with the horizontal axis in Figures 8-2a to 8-2d. The $w^3 \cdot PL_{b,0}$-values are listed in Table 8-1 too. The fit parameters are expressed (i) in SI-units units and (ii) in units which are convenient to be used in the context of IEC 62364 (2013), i.e. hours in the PL and millimetres for the erosion depths.

The systematic erosion of mainly base material at the splitter crests and the leading edges of the cut-outs started above $w^3 \cdot PL_{b,0} \approx 1.8 \cdot 10^9$ [kg/s^2] $\approx 5.0 \cdot 10^5$ [m^3/s^3 · h · g/l]. This threshold value corresponds to $PL_{b,0} \approx 4.0$ [h · g/l] with the present net head, and to $SSL \approx 20\,000$ t with the present turbine and sediment particle properties.

The uncertainties in the fit parameters listed in Table 8-1 arise mainly from the uncertainties in the PL_b ($U_{2\sigma} \approx 50\%$ in Section 5.8.2), as seen from the error bars in Figure 8-2. The uncertainties in the geometrical differences are relatively small (Section 6.3.2.2). The uncertainty on w^3 is negligible, because the uncertainty on h_n is < 0.5% and w^3 is proportional to $h_n^{1.5}$ (Section 2.3.2.2).

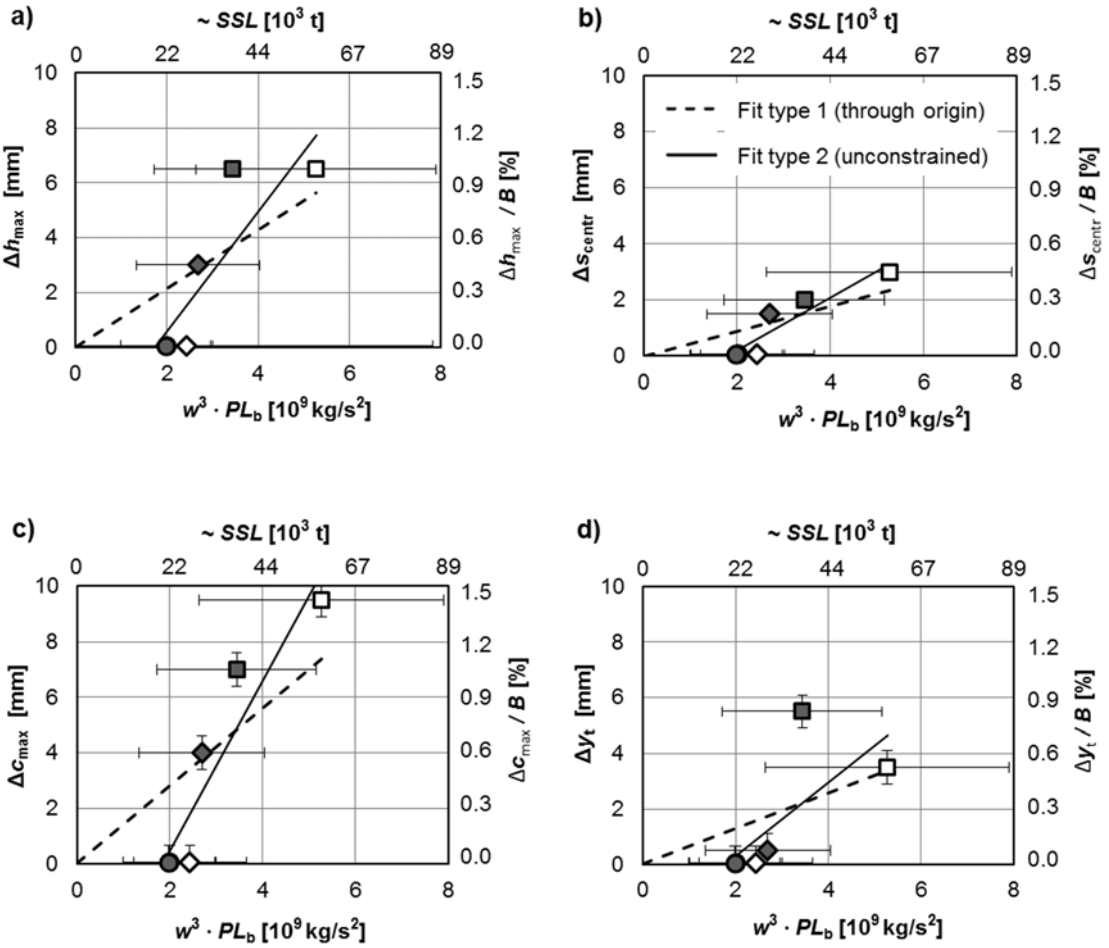

Figure 8-2 a) Measured reduction of splitter height Δh_{max}, b) increase of splitter width Δs_{centr}, c) increase of cut-out depth Δc_{max}, and d) radial splitter tip erosion Δy_t of MG 1 (empty markers) and MG 2 (filled markers) of HPP Fieschertal in the sediment seasons 2012 (□), 2013 (◇) and 2014 (○) as a function of the erosion potential per bucket $w^3 \cdot PL_b$ (with $k_{size} = 0.033$ on average, $k_{hardness} = 0.75$, $k_{shape} = 2$, $z_0 = 2$, $z_2 = 20$, $w = 50$ m/s, $x = 3$) and approximate *SSL* (a to c modified from Felix *et al.* 2016a). The horizontal error bars indicate the estimated uncertainty on the erosion potential at 95% confidence level (2σ); the uncertainty on *SSL* is only half of that.

Table 8-1 Results of the unconstrained linear fits (type 2, solid lines in Fig. 8-2) between measured geometrical changes and the erosion potential per bucket $w^3 \cdot PL_b$ (Eq. 8-3) of Pelton buckets in HPP Fieschertal in the years 2012 to 2014 (modified from Felix *et al.* 2016a).

Application case (location in bucket and direction)	In SI-units		In units referring to IEC 62364		R^2
	$w^3 \cdot PL_{b,0}$ kg/s²	C_g m · s²/kg	$w^3 \cdot PL_{b,0}$ m³/s³ · h · g/l	C_g mm / (h · g/l · m³/s³)	[-]
Reduction of splitter height Δh_{max}	$1.7 \cdot 10^9$	$2.2 \cdot 10^{-12}$	$4.9 \cdot 10^5$	$7.9 \cdot 10^{-6}$	0.75
Increase in splitter width Δs_{centr}	$1.8 \cdot 10^9$	$0.9 \cdot 10^{-12}$	$5.0 \cdot 10^5$	$3.4 \cdot 10^{-6}$	0.87
Increase in cut-out depth Δc_{max}	$1.9 \cdot 10^9$	$3.1 \cdot 10^{-12}$	$5.1 \cdot 10^5$	$11.0 \cdot 10^{-6}$	0.87
Radial splitter tip erosion Δy_t	$1.8 \cdot 10^9$	$1.3 \cdot 10^{-12}$	$4.9 \cdot 10^5$	$4.8 \cdot 10^{-6}$	0.51

The C_g-value for Δs is less than half of that for Δh for geometrical reasons (Fig. 8-3). The ratio of these C_g-values corresponds to a splitter flank angle of ~12° which is in a common range (average along the splitter). The C_g-value for Δc was slightly higher than that of Δh, i.e. the specific geometric erosion rate on the cut-out edges towards the axis of the runner was slightly higher than that on the splitter crests.

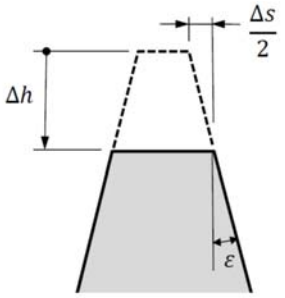

$$\frac{\Delta s}{\Delta h} = \frac{3.4}{7.9} = 0.43$$

$$\frac{\Delta s}{2\,\Delta h} = \tan(\varepsilon)$$

$$\varepsilon \approx 12°$$

Figure 8-3 Geometrical relation between splitter height reduction Δh and increase of splitter width Δs.

8.1.2.6 Determination of C_g-value for erosion of coating in buckets

Figure 8-4 shows the area-averaged ΔCT, i.e. erosion depths of coating inside the buckets obtained from the template-based measurements in 2013 and 2014 as a function of the erosion potential per bucket $w^3 \cdot PL_b$. Approximate *SSL* per turbine are again indicated on the top axis. From a linear fit on these four data points, constrained to pass through the origins of the axes ($PL_{b,0} = 0$), the following C_g-value was obtained:

$$C_g \approx 4 \cdot 10^{-15}\ [\mathrm{m \cdot s^2/kg}] = 1.4 \cdot 10^{-8}\ [\mathrm{mm / (h \cdot g/l \cdot m^3/s^3)}].$$

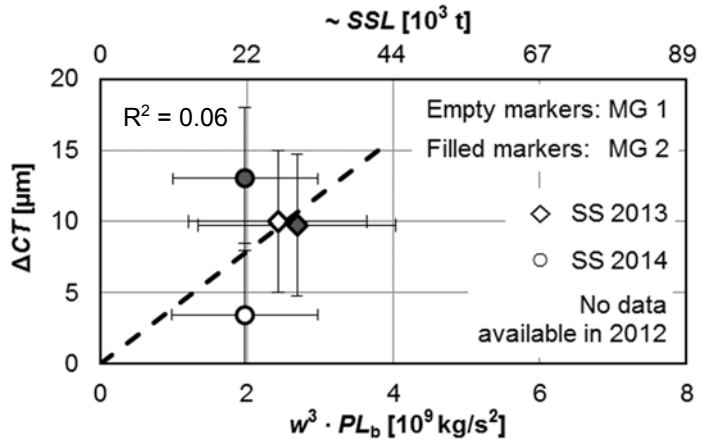

Figure 8-4 Area-averaged measured erosion depth of coating ΔCT inside the runner buckets of HPP Fieschertal in the sediment seasons 2013 to 2014 as a function of the erosion potential per bucket $w^3 \cdot PL_b$ and approximate *SSL*. The horizontal axis and the horizontal error bars are as in Figure 8-2.

Because the measured area-averaged ΔCT were only 0.6 to 2.6 times the measurement uncertainty (± 5 µm according to Section 6.2.1.2), the relative uncertainty of this C_g-value is quite high. However, this is of no concern for practical application, because the erosion of the coating in the buckets in two years without a major flood was small compared to

usual initial *CT*. With blunt splitters however, the C_g-value for erosion of coating inside the buckets may be much higher (Section 6.2.1.3) and the coating erosion inside the buckets may be decisive for the *TBO*.

8.1.2.7 Determination of C_g-value for erosion of coating on splitter crests

The analysis in Section 8.1.2.5 showed that the coating on the splitter crests was systematically eroded after $w^3 \cdot PL_{b,0} \approx 1.7 \cdot 10^9$ [kg/s^2]. Because it was not possible to measure the *CT* on the splitter crests for geometrical reasons (2.4.1.4), the initial *CT* was estimated as 300 to 500 µm. Assuming a homogeneous and linear erosion on the splitter crest, which is a simplification of the real process (Section 6.3.1.1), the following approximate C_g-value resulted with $PL_{b,0} = 0$:

$$C_g \approx (1.8 \text{ to } 2.9) \cdot 10^{-13} \text{ [m} \cdot \text{s}^2/\text{kg]} \approx (0.6 \text{ to } 1.1) \cdot 10^{-6} \text{ [mm / (h} \cdot \text{g/l} \cdot \text{m}^3/\text{s}^3)].$$

The C_g-value and the erosion rate of the coating on the splitter crests are thus 44 to 74 times as high as in the buckets. This is mainly attributed to the effect of the angle of attack α on the erosion rate of brittle material, i.e. higher erosion at $60 < \alpha \leq 90°$ than at small angles (Fig. 2-16). The fact that hard-coatings are particularly resistant to particles impinging at low angles has been mentioned by Gummer (2009).

8.1.2.8 Discussion on different $k_{hardness}$

IEC 62364 (2013) suggests to use different $k_{hardness}$ for uncoated and coated surfaces (Section 2.3.6.1). For HPP Fieschertal, this leads to $k_{hardness} = 0.75$ for base material erosion and $k_{hardness} = 0.31$ for coating erosion (Section 5.1.1). The $w^3 \cdot PL_b$-values in Figures 8-2 and 8-4 as well as the derived fit parameters (C_g and $w^3 \cdot PL_{b,0}$) are based on $k_{hardness} = 0.75$. Using a single $k_{hardness}$-value for the computation of the PL_b has the advantages of (i) a clear common reference in case of erosion on both the base material and the coating and (ii) avoiding iterative calculations if the erosion progresses from the first to the second stage.

Adopting $k_{hardness} = 0.31$ for coating erosion has the following implications:

- The $w^3 \cdot PL_{b,0}$ referring to the erosion of mainly coating in the first stage of erosion are only 0.31 / 0.75 = 41% of those in Table 8-1, i.e. on average ~$7.4 \cdot 10^8$ [kg/s^2];
- The C_g-value for the coating erosion in the buckets is 0.75 / 0.31 = 2.4 times as high as mentioned in Section 8.1.2.6, i.e. ~$1.0 \cdot 10^{-14}$ [m · s^2/kg];
- The C_g-value for the coating erosion on the splitter crests is also 2.4 times as high as mentioned in Section 8.1.2.7, i.e. ~4.1 to $6.8 \cdot 10^{-13}$ [m · s^2/kg].

The difference in $k_{hardness}$ from 0.31 to 0.75 results from the mass fraction of particles with a Mohs hardness above 4.5 to 6.5, i.e. mainly feldspar in the present study. It is expected that these particles contribute more to the coating erosion on the splitter crests and cut-out edges (at high impact angles) than to the coating erosion inside the buckets (at low-impact angles). From the present study it cannot be concluded which definition of $k_{hardness}$ is most suitable to model the erosion in the various cases.

8.1.2.9 Discussion on further parameters of the erosion model

Various C_g-values were determined in the previous Sections for six different cases. C_g involves the parameters K_f, RS^p and K_m (Eq. 8-2). In the following, it is discussed whether it is possible to determine the values of some of these three parameters based on the presented data set.

RS is known (0.65 m), but p is unknown. During the second stage of erosion, i.e. erosion of mainly base material, the coefficient for the properties of the eroded material is known by definition, $K_m = 1$. Thus, the values of the ratio K_f / RS^p are known for the cases (i) to (iv) during the erosion of the base material. From the presented data set, the exponent p, i.e. the effect of RS on the erosion cannot be determined, because runners with only one size have been investigated. Assuming that Δh, Δs and Δc do not significantly depend on RS, i.e. $p \approx 0$ and thus $RS^p \approx 1$, the K_f-values for the erosion of the base material correspond to the C_g-values listed in Table 8-1.

For the erosion of coating or base material on the splitter crests, the K_f / RS^p is approximately the same (both with high impact angle α). The C_g for the erosion of mainly coating (≈ 1.8 to $2.9 \cdot 10^{-13}$ from Section 8.1.2.7 with $k_{hardness} = 0.75$) is lower than the C_g for the erosion of mainly base material (Δh in the second stage of erosion, $2.2 \cdot 10^{-12}$ in the same units and with the same $k_{hardness}$, from Table 8-1) as expected. The ratio of these C_g-values yields $K_m = 1/8$ to $1/13$ for the coating in this situation. In a laboratory investigation by Winkler *et al.* (2011a), the geometrical erosion rate on initially coated splitter crests increased by 5 and 15 times when the coating was eroded on the crests and also on the flanks, respectively (Section 2.3.4.8). Hence, the ratio found in the present field study is in the same order of magnitude as in laboratory investigations.

8.1.3 Eroded masses in relation to *PL* and *SSL*

8.1.3.1 Determination of model parameters

The eroded masses per runner inside the buckets Δm_{cb}, on the splitters Δm_{sp} and on the cut-outs Δm_{cu} for each sediment season are shown in Figure 8-5 as a function of erosion potential per bucket $w^3 \cdot PL_b$ and approximate *SSL*, respectively. The data points on the horizontal axes of Figures 8-5b and 8-5c are the same as in Figure 8-2, and the data points on the horizontal axis of Figure 8-5a are the same as in Figure 8-4. The Δm in relation to the $w^3 \cdot PL_b$ were evaluated by replacing the erosion depth d_e in Equation (8-3) by the Δm:

$$C_m = \frac{\Delta m_i(t)}{w^3 \ (PL_b(t) - PL_{b,0})} \qquad \text{for } PL_b > PL_{b,0} \quad \text{(units see Table 8-2)} \tag{8-4}$$

where w^3 = 125 000 m^3/s^3 for the HPP Fieschertal. C_m stands for a normalized erosion rate by mass, and is the slope of the respective regression line in Figures 8-5a to 8-5c.

Moreover, the ratios *M* of eroded masses (Δm) to erodent masses (*SSL*) were evaluated. Similarly to $PL_{b,0}$, a threshold *SSL* for the start of the systematic erosion of mainly base material was introduced (SSL_0):

$$M = \frac{\Delta m_i(t)}{SSL(t) - SSL_0} \qquad \text{for } SSL > SSL_0 \qquad [-] \tag{8-5}$$

Although *M* is a dimensionless number, it is not directly transferrable to other conditions, because effects of w, k_{size}, k_{shape}, etc. are not considered.

As for the erosion depths, a constrained fit through the origin of the axes was selected for the erosion of coating, whereas unconstrained fits were applied for the erosion of mainly base material on the splitters and cut-outs. The parameters obtained from the fits are listed in Tables 8-2 and 8-3.

The fit parameters in Table 8-2 (C_m and $w^3 \cdot PL_{b,0}$) are based on $k_{hardness}$ = 0.75. Adopting $k_{hardness}$ = 0.31 for coating erosion has the following implications:

- The non-zero $w^3 \cdot PL_{b,0}$ referring to the erosion of mainly coating in the first stage of erosion are only 41% of those in Table 8-2, i.e. on average ~7.0 · 10^8 [kg/s^2];
- The C_m-value for the coating erosion in the buckets is 2.4 times as high as in Table 8-2, i.e. ~1.2 · 10^{-9} [s^2];

The unconstrained fits on the Δm (Figs. 8-5b and 8-5c) yielded slightly lower $w^3 \cdot PL_{b,0}$-values than those on the geometrical changes (Fig. 8-2). The R^2 of the fits on eroded masses (Figs. 8-5b and 8-5c) are lower than those of the fits referring to Δh, Δs and Δc (Figs. 8-2a to 8-2c).

The M-values referring to the erosion of coating inside the buckets and to the erosion of mainly base material at the cut-outs are similar by coincidence. The Δm in the buckets result from small erosion depths (not visible) on a large area, whereas the Δm on the splitters and cut-outs result from localized erosions in the range of millimetres. As for Δc and Δh, the eroded masses at the cut-outs were on average slightly higher than those at the splitters.

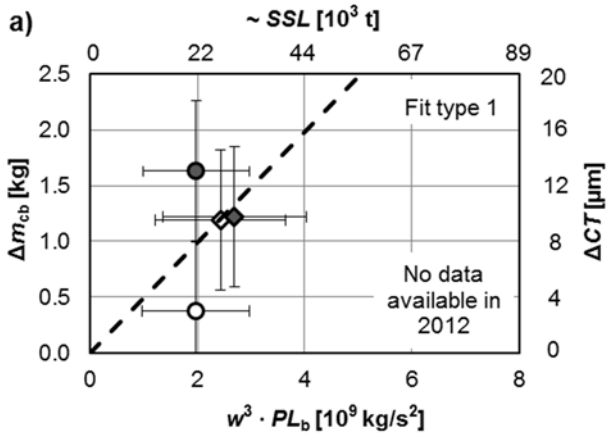

Figure 8-5 Measured eroded masses per runner
a) coating inside the buckets Δm_{cb},
b) on the splitters Δm_{sp} and
c) on the cut-outs Δm_{cu}
as a function of the erosion potential per bucket $w^3 \cdot PL_b$ and approximate SSL of MG 1 (empty markers) and MG 2 (filled markers) of HPP Fieschertal in the sediment seasons 2012 (□), 2013(◇) and 2014 (○) with linear fits. For further information on the horizontal axes and the horizontal error bars see Figure 8-2.

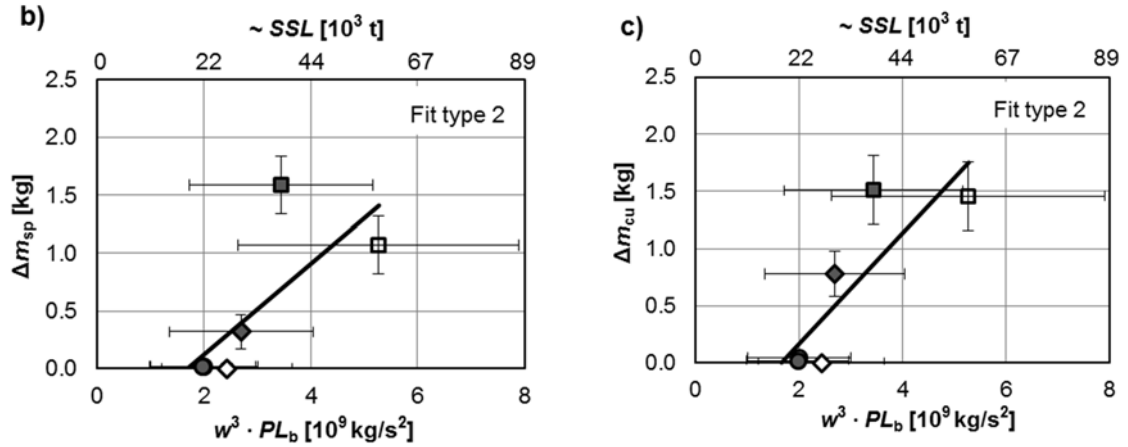

Table 8-2 Results of the fits between measured eroded masses and erosion potential per bucket $w^3 \cdot PL_b$ in Figure 8-5 according to Equation (8-4) of Pelton runners in HPP Fieschertal in the years 2012 to 2014.

Part of the buckets	Stage of erosion, Fit type	In SI-units		In units referring to IEC 62364		R^2
		$w^3 \cdot PL_{b,0}$ kg/s²	C_m s²	$w^3 \cdot PL_{b,0}$ m³/s³ · h · g/l	C_m kg / (h · g/l · m³/s³)	-
In coated buckets Δm_{cb}	1	0	$5.0 \cdot 10^{-10}$	0	$1.8 \cdot 10^{-6}$	0.06
At splitters Δm_{sp}	2	$1.7 \cdot 10^{9}$	$4.0 \cdot 10^{-10}$	$4.7 \cdot 10^{5}$	$1.4 \cdot 10^{-6}$	0.54
At cut-outs Δm_{cu}	2	$1.7 \cdot 10^{9}$	$4.9 \cdot 10^{-10}$	$4.6 \cdot 10^{5}$	$1.8 \cdot 10^{-6}$	0.71

Table 8-3 Results of the fits between measured eroded masses per Pelton runner and *SSL* in Figure 8-5 according to Equation (8-5) at HPP Fieschertal in the years 2012 to 2014.

Part of the buckets	Stage of erosion, Fit type	SSL_0 [t]	$M = \Delta m / (SSL - SSL_0)$ [-]	R^2 [-]
In coated buckets Δm_{cb}	1	0	$4.3 \cdot 10^{-8}$	-0.02
At splitters Δm_{sp}	2	17 500	$3.2 \cdot 10^{-8}$	0.46
At cut-outs Δm_{cu}	2	17 800	$4.2 \cdot 10^{-8}$	0.66

8.1.3.2 Discussion

As seen from Figure 8-5b, the eroded mass on the splitters Δm_{sp} of MG 2 in 2012 was particularly high in relation to the annual $PL_b - PL_{b,0}$. The corresponding splitter width ($s_{0,centr}$ = 8 mm) was also particularly high (Fig. 8-1a). Fig. 8-6 shows the Δm_{sp} normalized with the annual $PL_b - PL_{b,0}$ as a function of the splitter width. The specific eroded masses (including grinding in two cases marked with G) increase with the initial splitter width. Due to the cross-sectional shape of the splitters (Fig. 8-3), a certain Δs or Δh involves the erosion of more material as the splitter is worn down. In laboratory investigations by Winkler *et al.* (2011a, Section 2.3.4.8) on initially fully coated Pelton splitter specimens, increasing eroded masses were measured per unit time. Because *SSC* and PSD were constant in the laboratory, this corresponds to increasing eroded masses per *PL*, as measured in the present study.

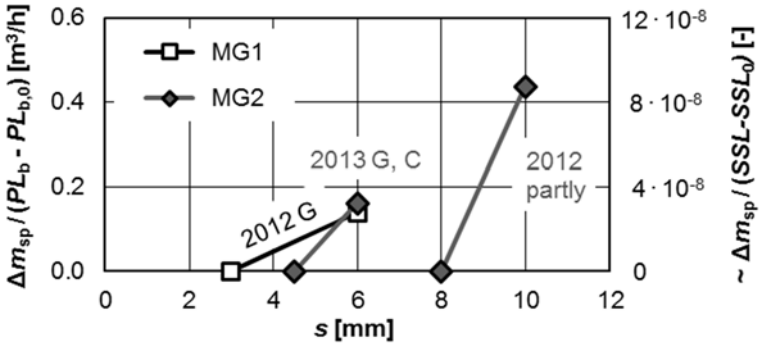

Figure 8-6 Measured eroded masses on the splitters Δm_{sp} normalized with the particle load per bucket PL_b above the threshold $PL_{b,0}$ as a function of the splitter width s of Pelton runners in the HPP Fieschertal.

The approximately linear type of relation between Δs and $PL_b - PL_{b,0}$ found in Figure 8-2b is explained by the two partly compensating non-linear effects mentioned above:

- The Δm_{sp} increases over-proportionally with $PL_b - PL_{b,0}$ as the damages progress;
- The Δs increases under-proportionally with Δm_{sp} for geometrical reasons (Fig. 8-3).

Estimating normalized erosion depths or geometrical changes on the splitter crests and cut-out edges as linear functions of $PL_b - PL_{b,0}$ is practical for engineering applications. Eroded masses are for example of interest for the calibration and validation of numerical models and in more detailed analyses.

8.2 Efficiency decreases

8.2.1 Efficiency decreases as a function of turbine erosion

As described in Sections 2.5.3.2 and 2.5.3.3, efficiency reductions $\Delta\eta$ in Pelton turbines are related to the increase of splitter width Δs and the radial erosion of the splitter tip Δy_t. In the following, the data from the present study are evaluated following these approaches and are compared to published data from other HPPs.

For MG 1 in 2013 and for both MGs in 2014, the splitters and cut-outs were not eroded systematically and no significant $\Delta\eta$ were measured. For MG 2 in 2012, not all required data are available due to the unplanned runner change after the major flood event. In this study, complete data sets on significant Δs, Δy_t and $\Delta\eta$ are available for each MG in one year (Table 8-4). The Δs and Δy_t were normalized with the inner bucket width B and with the jet diameter d_0 as proposed in the mentioned literature.

Table 8-4 Absolute and relative differences of the splitter width Δs_{centr} and of the radial splitter tip positions Δy_t together with absolute reductions of turbine efficiencies $\Delta\eta$ over two years in HPP Fieschertal (extended from Abgottspon *et al.* 2016b).

Year	MG	Runner	RW *	$s_{0,centr}$ mm	Δs_{centr} mm	$s_{end,centr}$ mm	$s_{0,centr}/B$ %	$s_{end,centr}/B$ %	Δy_t mm	$\Delta y_t/B$ %	$\Delta y_t/d_0$ %	$\Delta\eta$ %
2012	1	no. 1	G	3	3	6	0.5	0.9	3.5	0.5	1.5	-0.91 §
2013	2	no. 3	G, C	4.5	1.5	6	0.7	0.9	0.5	0.1	0.2	-0.43

* RW = Revision works: G = Grinding of splitters and cut-outs, C = On-site re-coating of these parts

§ From July 4 to end of 2012 (second part of the sediment season, after the major flood event).

Figures 8-7a and 8-7b show the $\Delta\eta$ as a function of the splitter width and of the normalized splitter width, respectively. The expanded uncertainties on s (±0.2 mm according to Section 6.3.2.2) and on $\Delta\eta$ (±0.15% according to Section 7.1.3) are relatively small. The black lines of both MGs in the present study have similar slopes. Because the runner of MG 2 was not in as-new condition before the sediment season 2013, its efficiency at the beginning of the considered period was probably lower than it was directly after the last major factory overhaul. This means that the line of MG 2 (with the blue markers) would be shifted downwards, if the efficiencies in as-new conditions were consistently taken as the reference for both runners. The shifted line of MG 2 would be closer to that of MG 1.

In addition, data from measurements on three runners in the HPP Dorferbach, Austria (Maldet 2008, and more recent data) are shown in Figure 8-7. Those runners were in operation in the years 2007 to 2009, either for the first time after their commissioning or

after repairs. The first runner was uncoated, the others coated. In contrast to HPP Fieschertal, erosion occurred inside the buckets in the range of several millimetres. The efficiencies of HPP Dorferbach were evaluated from operation data. The bucket width B in HPP Dorferbach is 2.85 smaller than that in the present study. The splitter widths were initially smaller for Dorferbach than for Fieschertal (Fig. 8-7a). However, the relative splitter widths were initially similar for both HPPs (Fig. 8-7b). The slopes of the black lines of HPP Fieschertal in Figures 8-7a and 8-7b are smaller and larger than the average slope of the reference data (grey lines), respectively. The differences in the slopes may be related to (i) scale effects, (ii) other contributions to efficiency depletion such as effects of erosion on cut-outs or inside the buckets, (iii) runner designs, or (iv) different definitions of s.

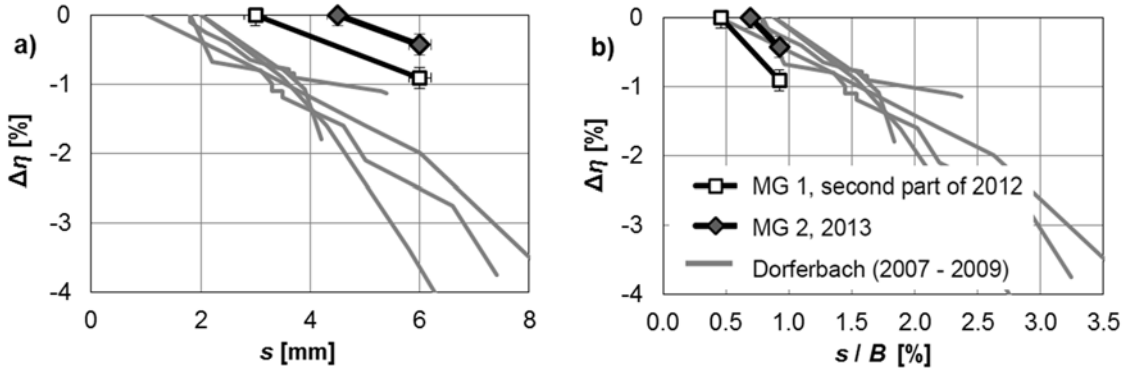

Figure 8-7 Absolute reductions in Pelton turbine efficiency $\Delta\eta$ measured in HPP Fieschertal compared to field data from HPP Dorferbach (Maldet 2008, with updated data as a courtesy of TIWAG-Tiroler Wasserkraft) as a function of a) the splitter width s and b) of the relative splitter width s/B.

Figure 8-8 shows the $\Delta\eta$ measured in HPP Fieschertal as a function of the normalized radial tip erosion y_t. In addition, data of the same type from some other Austrian HPPs reported by Hassler & Schnablegger (2006, Fig. 2-27b) are shown in Figure 8-8. In the present study, the amounts of the $\Delta\eta$ as a function of the normalized radial splitter tip erosions were up to 0.4% higher than the trend of the reference data. These absolute deviations are however similar to the scatter in the reference data.

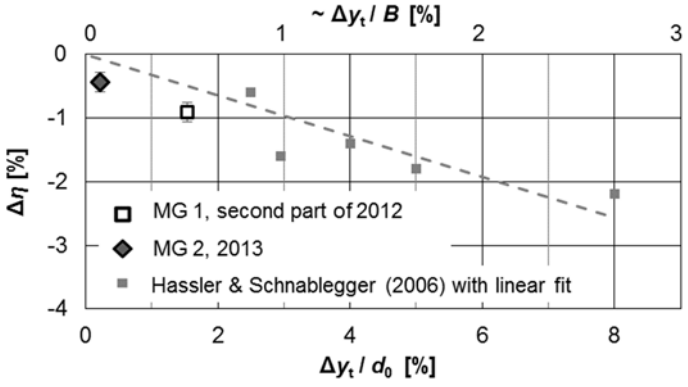

Figure 8-8 Absolute reductions in Pelton turbine efficiency $\Delta\eta$ as a function of the radial splitter tip erosion y_t normalized with the jet diameter d_0 measured in HPP Fieschertal compared to field data reported by Hassler & Schnablegger (2006) from several HPPs in Austria (Verbund AG).

The field data in Figures 8-7 and 8-8 confirm that there are correlations between $\Delta\eta$ and s/B or y_t/d_0 as mentioned in the literature, and they indicate typical orders of magnitude. It appears that s is the more reliable explanatory variable for $\Delta\eta$ than y_t. This might be particularly the case for coated Pelton runners, at which the splitter tips are not always eroded in parallel with the splitter crests and the cut-outs. The question of adequate normalization of geometrical changes in buckets of various sizes with respect to the corresponding $\Delta\eta$ cannot be fully answered based on these data because the number of observations is yet too small and s or y_t are not the only influencing parameters.

8.2.2 Efficiency decreases as a function of *SSL* or *PL*

For both MGs, the time series of the $\Delta\eta$ and the PL_b are shown in the lower and upper parts of Figure 8-9, respectively. Approximate *SSL* are also indicated on the upper left vertical axis. The efficiency levels before and after the sediment seasons resulting from the average of usually two SNM (if available) are indicated by the solid ellipses as in Figure 7-2.

In 2014 there were no significant reductions of η because the annual PL_b was similar to $PL_{b,0} \approx 4$ h · g/l (corresponding to $SSL_0 \approx 20\,000$ t), i.e. the base material on splitter crests and cut-out-edges was not systematically eroded. In 2013, when the PL_b of each MG exceeded the $PL_{b,0}$ by 35 to 50%, $\Delta\eta$ was −0.4% for MG 2 while it was not significant for MG 1 despite similar PL_b. These different $\Delta\eta$ arise from the fact that there was significant base-material erosion on MG 2 only (Fig. 8-1). In 2012 with the major flood event, the PL_b clearly exceeded $PL_{b,0}$ by 150 to 200%, and the highest efficiency reduction of 0.9% was measured in the second part of the year (after the flood). The CEM indicated that there was no significant $\Delta\eta$ before the major flood event (Section 7.2.2). This fits to the fact that the PL_b was below $PL_{b,0} \approx 4$ h · g/l before the flood (Fig. 5-33). The turbine was probably mainly eroded during re-suspension events after the flood, when coarser particles were transported through the turbines (Section 5.5.4).

Figure 8-10 shows the $\Delta\eta$ of each MG per sediment season as a function of the corresponding PL_b (and approximate *SSL*). The $\Delta\eta$ are the differences between the efficiency levels before and after the sediment seasons indicated by the solid ellipses in Figure 8-9.

In the year 2014 for both MGs and in 2013 for MG 1, the $\Delta\eta$ were within the band of estimated uncertainty (0.15%, Section 7.1.3). The PL_b of these points are close to $PL_{b,0}$. In the second part of the year 2012, the efficiency of MG 1was most reduced when PL_b clearly exceeded $PL_{b,0}$. For MG 2 in 2013, the $\Delta\eta$ was also significant. The two points in

the dotted ellipse in Fig. 8-9 give information on the efficiency during the sediment season. The average of these points is shown in Figure 8-10 as an additional point between the initial and final efficiency level. The efficiency decrease was higher towards the end of the season and occurred mainly when $PL_b > PL_{b,0}$. Assuming that geometrical changes are proportional to $PL_b - PL_{b,0}$ (Fig. 8-2), the $\Delta\eta \approx -0.4\%$ of MG 2 in 2013 was high in comparison to the other points. This shows that $\Delta\eta$ cannot be modelled accurately with $PL_b - PL_{b,0}$ only. As mentioned before, the relative splitter width or other geometrical indicators of the erosion status at the beginning of the sediment season should also be considered.

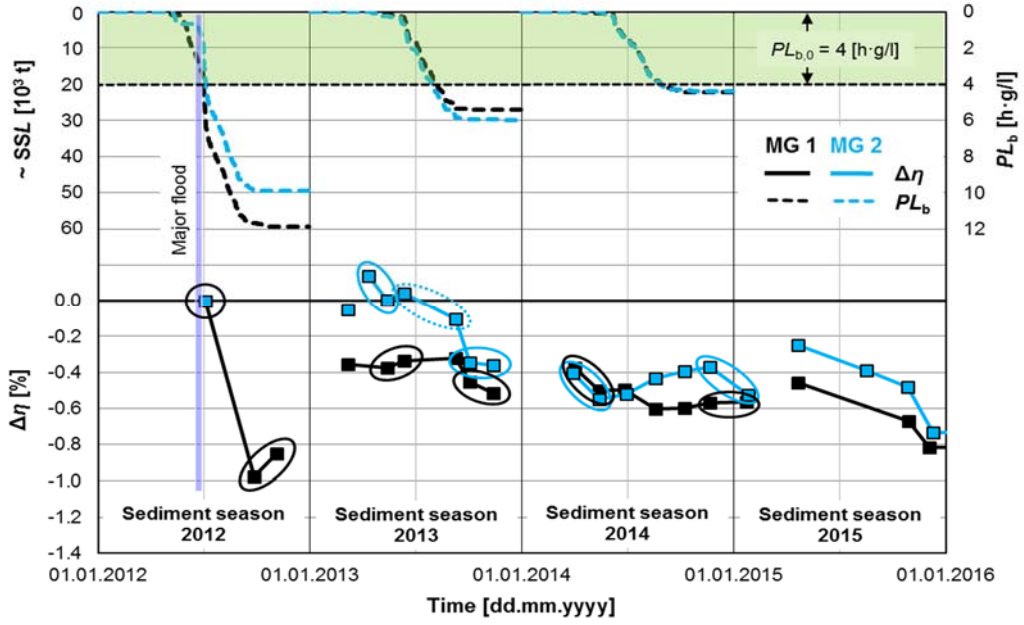

Figure 8-9 Time series of measured absolute turbine efficiency differences $\Delta\eta$ from SNM (lower left vertical axis), annual PL_b (right vertical axis) and approximate annual *SSL* (upper left vertical axis) for both MGs in HPP Fieschertal (modified from Abgottspon *et al.* 2016b). The time series of measured erosion depths and eroded masses are shown in Figure 8-1.

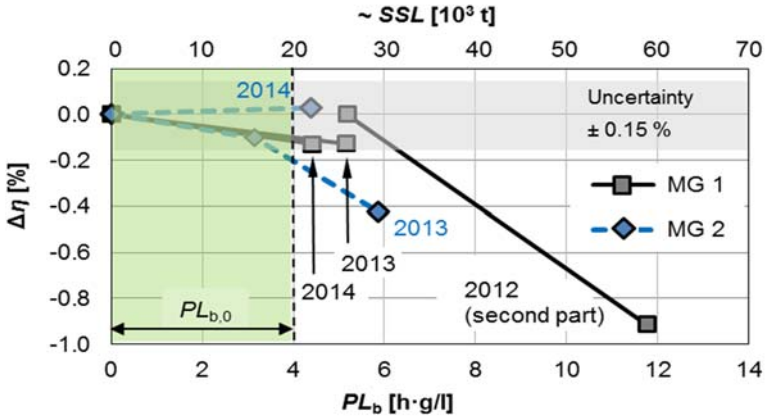

Figure 8-10 Measured absolute turbine efficiency differences $\Delta\eta$ as a function of annual PL_b and approximate *SSL* for both MGs in HPP Fieschertal (modified from Abgottspon *et al.* 2016b).

9 HPP SHUTDOWNS IN PERIODS OF HIGH EROSION POTENTIAL

In this Chapter, the option of temporary HPP shutdowns in periods of exceptionally high erosion potential is addressed. An approach to estimate the shutdown *SSC* is proposed based on a cost-benefit analysis for the example of the HPP Fieschertal. Finally, the financial benefit of a shutdown is demonstrated in a scenario referring to a major flood event in the past.

9.1 Overview

The results in Chapter 5 show that the *SSC* and PSD in the turbine water may vary considerably within hours. This means that the costs and losses induced by fine sediment are also highly variable over time. It might hence be economic to temporarily close intakes and shutdown HPPs when then the sediment-induced costs and losses exceed the revenues from electricity sales. As mentioned in Section 2.7.3, the threshold *SSC* above which the operation of a HPP is not economic with respect to fine-sediment sediments and their consequeces is termed 'shutdown *SSC*'.

To determine the shutdown *SSC* for a specific HPP, data on the *PL*, turbine erosion, $\Delta\eta$ as well as sediment-induced costs and electricity prices are required. For the HPP Fieschertal, the *PL*, turbine erosion and $\Delta\eta$ in the years 2012 to 2014 are reported in the Chapters 5 to 7. The annual revenues from electricity sales and the costs induced by fine sediment are addressed in the following Section.

9.2 Annual revenues and sediment-induced costs

9.2.1 Annual revenues

For simplicity, the electricity price was assumed to be constant at 0.05 €/kWh (50 €/MWh) irrespective of the increasing market pressure in the recent years. With an electricity generation of some 150 GWh per year (Section 3.3.1), the nominal annual revenue was estimated as 7.5 Mio. €.

9.2.2 Annual sediment-induced costs

The average annual costs and losses which are induced by the fine-sediment transport through the turbines were estimated in Table 9-1. The cost estimate is based on data of executed repair works and purchased turbine replacement parts as well as the estimated average annual probabilities of the individual cost elements. For a coated Pelton runner as in HPP Fieschertal, the acquisition cost is between 0.5 and 1 Mio. €, an on-site revision costs typically several 10 000 €, and a major factory overhaul several 100 000 €.

For HPP Fieschertal, where the $\Delta\eta$ are limited by the coating and the annual revisions, the reduction in revenue due to reduced turbine efficiency is relatively small. The annual costs induced by fine-sediment correspond to ~3.7% of the nominal annual revenue (7.5 Mio. €) and are thus economically relevant.

Table 9-1 Average annual costs induced by the fine-sediment load at HPP Fieschertal estimated based on data from 2012 to 2014 for the whole HPP with two turbines (Felix *et al.* 2016e).

Cost or loss item	€/year	€/year	% of annual revenue
Costs of repairs and replacement parts		270 000	3.3%
- Runners	180 000		
- Nozzles and stationary turbine parts	60 000		
- Flushing system of sand trap	30 000		
Electricity generation losses		30 000	0.4%
- Due to reduced efficiency	10 000		
- Due to downtime during runner exchange	20 000		
Total		300 000	3.7%

9.3 Estimation of shutdown *SSC*

9.3.1 Approach and example result

In the following, a linear approach to estimate the shutdown *SSC* is proposed and explained for the example of HPP Fieschertal (Felix *et al.* 2016e).

The long-term average annual load of fine sediment transported through both turbines was estimated as 50 000 tons. This is the average of the annual loads determined from the measurements in the years 2013 and 2014. For the sake of simplicity, it was assumed that the costs induced by the fine sediment are proportional to its mass. With this assumption, specific sediment-induced costs resulted in 300 000 € per year / 50 000 tons per year = 6 €/ton = 0.006 €/kg.

With an average *SSC* of 0.5 g/l = 0.5 kg/m^3, the sediment-induced costs with respect to

the water volume are 0.003 €/m^3. If the *SSC* rises for example to 10 g/l, the fine-sediment induced costs are also 20 times as high as in average conditions, i.e. 0.06 €/m^3.

For HPP Fieschertal, 1 m^3 of water is equivalent to 1.2 kWh of electric energy. Thus, the sediment-induced costs with respect to electric energy is 0.003 €/m^3 / 1.2 kWh/m^3 = 0.0025 €/kWh at average *SSC* of 0.5 g/l. When the *SSC* increases to 10 g/l, the sediment-induced costs rise to 0.05 €/kWh, corresponding to the assumed electricity selling price. It was concluded that the operation of the HPP Fieschertal is not profitable when

$$SSC > 10 \text{ g/l} = \text{shutdown } SSC.$$

9.3.2 Discussion

This shutdown *SSC* is an approximate value because it resulted from a simplified linear approach and a relatively short data set (three years). The value of 10 g/l is higher than most of the published shutdown *SSC* in Table 2-4 referring mainly to Francis turbines.

This procedure based on proportionality can also be formulated in terms of the actual sediment-induced costs vs. the revenue from power sales per unit time as proposed by Agrawal *et al.* (2016). They neglected the effects of reduced efficiency, but introduced a factor accounting for various uncertainties with the aim to avoid economically unjustified turbine shutdowns at too low *SSC*. They presented an example with a relatively high shutdown *SSC* of 55 g/l; without the uncertainty factor it would be 22.5 g/l.

9.4 Shutdown and restart procedure

9.4.1 Warnings and staff action for shutdown

The control system of HPP Fieschertal was programmed to issue a warning when the *SSC* measured at the top of the penstock exceeds 10 g/l for 15 minutes. Preliminary warnings are given from continuous turbidity measurements (i) in the river upstream of the intake and (ii) in the sand trap, offering both a pre-warning time of about one hour (cross-section averaged flow time in the storage tunnel at full load at maximum operation level). The condition of *SSC* threshold exceedance during 15 minutes was added to disregard sharp *SSC* peaks, for which the effort of HPP shutdown and restart would be too high.

The staff member on duty has to confirm the alarm and check via the HPP's control system if the high *SSC* was a consequence of re-suspension of sediment deposits from the storage tunnel, i.e. if the water level in the storage tunnel is low. If this is the case, no shutdown is required, because this sediment transport cannot be avoided (Section 5.5.2).

Otherwise, i.e. if the *SSC* is high due to an external reason for high sediment input into the system (flood, debris flow, glacier outburst etc.), the staff member has the competence to close the intake and to shut down the turbines when required, i.e. after the water in the storage tunnel has been used. No automatic shutdowns are foreseen to avoid false alarms and to allow consideration of additional information like observations (e.g. camera on the river at the intake) and the probable duration of the rain (typical local weather situations and forecast).

9.4.2 Restart

Taking the HPP back to operation is associated with some effort, e.g. de-clogging of cooling water systems, flushing operations and checks. Therefore, it was proposed to resume operation when *SSC* is considerably lower than 10 g/l, say 5 g/l, and when the flood is expected to end soon.

9.5 Shutdown scenario during the 2012 flood

9.5.1 Downtime and avoided *SSL*

The aforementioned proposed rules for HPP shutdown and restart were hypothetically applied to the situation of the major flood event in July 2012. This was the only event in the years 2012 to 2014, in which the shutdown criterion (*SSC* ≥ 10 g/l during ≥ 15 minutes, not due to re-suspension) would have been met. The downtime of the HPP would have been 16 hours. In this period, about 13 000 t of fine sediment would not have passed the turbines (orange fill in Fig. 9-1). This corresponds to 77% of the *SSL* transported trough the turbines during this flood event (Table 5-5). The avoided Δ*SSL* and the corresponding Δ*PL* per MG are summarized in Table 9-2.

The *SSL* entering the power waterway during these 16 h was higher than that measured in the penstock in this period, because a part of the sediment settled in the storage tunnel. These deposited sediments were occasionally re-suspended and transported through the turbines in the months after the flood. The *SSL* which would have been prevented from entering the power waterway if the intake had been closed during these 16 hours is roughly estimated as ~20 000 t based on a part of the increase in the annual *SSL* due to the flood event and its consequences in Figure 5-29b. The 20 000 t correspond to ~19% of the annual *SSL* in 2012 or to ~38% of the average annual *SSL* in the years 2013 and 2014 (Table 9-2). Hence, a single shutdown during a major flood event would have prevented a considerable percentage of the annual *SSL* or *PL* from passing the turbines.

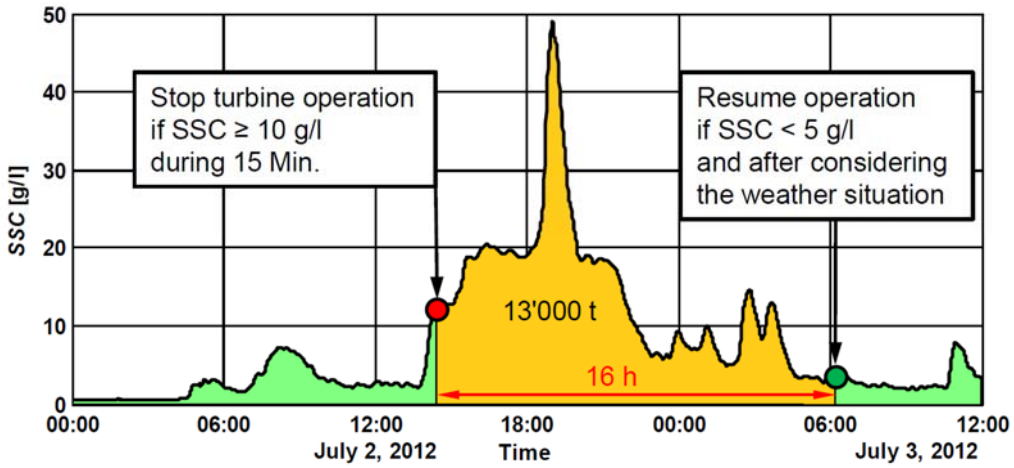

Figure 9-1 Measured *SSC* time series in the turbine water of HPP Fieschertal during the major flood event of July 2012 and shutdown scenario with the proposed rules (Felix *et al.* 2016e).

Table 9-2 Avoided *SSL* and *PL* in the shutdown scenario during the major flood event of July 2012.

		Absolute quantity	% of annual value in 2012	% of annual average in 2013 and 2014
Directly avoided by not operating the turbines during 16 h	*SSL* of both MGs	~13 000 t	12%	25%
	PL of MG 1	12.1 h · g/l	10%	24%
	PL of MG 2	12.1 h · g/l	12%	23%
Avoided in total by closing the intake during 16 h	*SSL* of both MGs	~20 000 t	~19%	~38%

9.5.2 Economic analysis

The economic potential of the HPP shutdown in the described scenario was evaluated and the result is summarized in Table 9-3. A shutdown would have been clearly profitable, with a benefit of roughly 200 000 €, corresponding to ~2.7% of the nominal value of the annually generated electricity. However, in 2012, the data required for the estimation of the shutdown *SSC* had not yet been available and the warnings of high *SSC* had not yet been implemented in the HPP's control system.

Table 9-3 Economic analysis (benefits vs. losses and costs) of the shutdown scenario at HPP Fieschertal (two turbines) during the major flood event in 2012 (Felix *et al.* 2016e).

Benefits	€
Avoided repair costs because of less erosion (rough estimate)	200 000
Avoided generation loss because of less reduced efficiency	30 000
Avoided generation loss because of no runner exchange required	30 000
Total benefits	260 000

Losses and costs	€
Generation loss during shutdown (2 · 32 MW · 16 h ≈ 1 GWh)	−50 000
Potential penalty for non-compliance with the announced generation program	if applicable
Total losses and costs (without penalty)	−50 000

10 CONCLUSIONS AND RECOMMENDATIONS

10.1 Conclusions

10.1.1 Measuring techniques

As a basis for the investigation of quantitative relations between particle load, erosion and efficiency changes on Pelton turbines, various measuring techniques and data evaluation procedures were investigated, further developed and applied.

10.1.1.1 Continuous SSC measurements

The calibrations, sensitivities, measuring ranges and measurement uncertainties of five measuring techniques for continuous real-time *SSC* measurements were assessed in the laboratory and the field during several years. The main conclusions are:

- For tubidimeters, the acoustic system, LISST and CFDM, the conversions of the instruments' outputs to *SSC* need to be based on gravimetrical *SSC* to achieve reasonably low measurement uncertainty on annual *SSL* and *PL*.
- *SSC* from turbidimeters and the single-frequency acoustic attenuation technique may be considerably biased if particle properties vary in time independently of *SSC*.
- The acoustic technique based on ADM installations has the advantages of being insensitive to fouling, requiring practically no maintenance, providing a data series with good spatial averaging and almost no gaps, and being less sensitive to variations in particle properties than turbidimeters.
- With medium silt particles having angular and flaky shapes (granite powder), the LISST with an optical path length of 5 mm and without dilution allows measuring *SSC* with less uncertainty than turbidimeters and the acoustic technique up to ~2 g/l. To overcome this limitation, a LISST model with automatic clear-water dilution is an option.
- The CFDM allows measuring high *SSC* (e.g. 13 g/l) and therefore it is suitable to issue warnings for HPP shutdowns (no parallel bottle sampling required).
- Among the investigated techniques, CFDM with parallel bottle sampling has the lowest relative uncertainty on *SSC* above ~1 g/l.
- The pressure-based technique works for *SSC* above ~2 g/l and does not require bottle sampling for calibration nor additional sensors if the pressure upstream of turbines and the headwater level are already measured. However, this technique has the disadvantage of offering practically no pre-warning time for HPP shutdowns.

- The automatic water sampler triggered by indicators for high *SSC* (turbidity or CFDM density) contributes to a better coverage of rarely occurring high *SSC*, which are particularly important for reliable calibrations of the instruments.

A comparative assessment of the investigated *SSC* measuring techniques is given in Section 5.4.6. The combined use of several instruments (i) improves the data coverage (less data gaps), (ii) increases the reliability of the measurements (redundancy), and (iii) allows for quality and uncertainty assessment of measurement data by comparing the instruments' outputs in overlapping ranges.

10.1.1.2 Continuous PSD measurements

From the laboratory and field investigations, the following conclusions are drawn on the LISST's PSD measurements:

- LISST allows measuring PSDs in the size range which is relevant in turbine water downstream of reservoirs and sand traps (medium silt to fine sand);
- LISST allows measuring PSDs *in-situ* e.g. every minute, which was not affordable before with laboratory LD analyses of bottled water samples;
- LISST PSDs may be biased (particularly at their ends) due to highly non-spherical particles, fouling and other effects;
- For highly non-spherical particles, the diameters d obtained from LISST are higher than equivalent sphere diameters d_{es};
- For known particle shapes, d can be converted to d_{es} based on reference measurements on microscopic images (image analysis).

10.1.1.3 Turbine erosion monitoring

For the monitoring of the coating erosion inside the runner buckets, the optical 3D-survey is not accurate enough and therefore coating thickness (*CT*) measurements are required. A template placed in the buckets for positioning of the probe in repeated measurements reduces the measurement uncertainty.

For the erosion monitoring on the splitter crests and the cut-out edges, *CT* measurements are not possible, but detailed results can be obtained from optical 3D-surveys. The evaluation of such data yields geometrical differences in cross-sections as well as eroded volumes and masses. For routinely runner management outside of a research project, less laborious methods such as measurements with rulers and geometrical templates are sufficient in many cases.

Erosion measurements on turbines of larger run-of-river HPPs are rarely possible during the wet season to avoid production losses, which strongly limits the temporal resolution of the erosion monitoring.

10.1.1.4 Efficiency changes monitoring

Periodically performed Sliding-Needle Measurements (SNM) is a practical technique for systematic efficiency monitoring. Because of the high sediment load and the existing arrangement for pressure measurements, the pressure signals were not reliable enough for the determination of the net head in the case study HPP. Therefore, the net head was determined from the headwater level and the head losses as function of the discharge, which is acceptable at a high-head HPP. The comparison of the various methods for the determination of the turbine discharge showed that

- The discharge based on the measurements of differential pressure on Venturi sections was not reliable enough (was not usable);
- For the determination of discharge based on needle positions, regularly updated relations between needle positions and discharge from ADM are required;
- The ADM at the top of the penstock had higher uncertainty than the ADM at the downstream end of the penstock, probably due to a less homogeneous and less steady flow field near the penstock inlet.

Comparable conditions and long-term stable sensors are of prime importance to determine relatively small efficiency differences which are economically relevant. Therefore, various criteria were developed to check the repeatability and consistency of SNM.

A method for Continuous Efficiency Monitoring (CEM) based on data from normal turbine operation was developed and applied. The results were compared with efficiency histories from SNM. The uncertainty on the efficiency histories from CEM is higher than that from SNM. To reduce the uncertainty on the daily efficiency differences from CEM, cross-checking of the signals' quality (expert system), steady state detection and advanced signal treatment were developed.

In summary, proven measuring techniques are available for the monitoring of *SSC*, particle sizes, turbine erosion and efficiency. Such measurement data are useful for HPP operators and turbine manufacturers to optimize turbine maintenance, check the fulfilment of specifications and contract terms, as well as for other decision making.

10.1.2 Suspended sediment

The detailed results of the suspended sediment monitoring (SSM) showed that the *SSC* and the median particle size d_{50} in the penstock varied quite independently and ranged from 0 to 50 g/l and 10 to 100 µm (medium silt to fine sand), respectively. The transport of coarser particles was associated with higher *SSC* during re-suspension events in the storage tunnel, which are a peculiarity of HPPs with small headwater storages. However, high *SSC* were not always associated with coarser particles, e.g. during floods relatively fine particles were transported through the turbines while coarser ones settled in the storage tunnel at low flow velocities and high water level. Besides high *SSC* due to re-suspension and flood events, a period of higher-than-average *SSC* occurred at the beginnings of the sediment seasons when the discharge from the glacier increased.

The maximum *SSC* of 50 g/l was measured in a flood event with a return period of ~20 years in July 2012. The suspended sediment load (*SSL*) in that year was more than twice the average of the years 2013 and 2014, and coarser particles were transported. The *SSL* and so-called Particle Loads (*PL*) according to IEC 62364 (2013) depend largely on single major flood events. Over longer time periods such as a sediment season, the *PL* were quite proportional to the *SSL*. In re-suspension events, when coarser particles were transported, the k_{size} and the $PL/\Delta t$ reflecting the erosion potential were higher than their respective temporal average values.

The combined use of several instruments for SSM allowed for *in-situ* measurements of the *SSC* and PSD with high temporal resolution (1 minute) and low relative uncertainty. To the knowledge of the author, no comparable time series of fraction-wise *SSC* over three years has been available from any other HPP.

10.1.3 Turbine erosion

The analytical erosion model according to IEC 62364 (2013) in the form of Equation (2-30) was adapted for Pelton runners by considering the effect of the number of jets z_0 and the number of buckets z_2 according to Equation (2-31). For coated runners, two stages of erosion were distinguished: (1) the erosion of mainly coating, and (2) the erosion of mainly base material. The group of unknown parameters was termed C_g (geometrical erosion rate). The C_g-values were determined from linear regressions on the field data for six application cases, i.e. locations within the buckets. In this way, the adapted model has become applicable for the estimation of erosion on coated Pelton buckets.

The regressions between the measured geometrical changes and the erosion potential indicated that the second stage of erosion on the splitter crests and the cut-outs started at an erosion potential per bucket of $\boldsymbol{w^3 \cdot PL_{b,0}} \approx 1.8 \cdot 10^9$ [kg/s^2] $\approx 5.0 \cdot 10^5$ [m^3/s^3 · h · g/l] considering the particles with Mohs hardness > 4.5. This threshold value corresponds in the present case (net head h_n = 509 m, characteristic relative velocity w = 50 m/s) to $PL_{b,0} \approx 4$ [h · g/l] and with the present turbine and sediment particle properties to $SSL \approx$ 20 000 t.

On the splitter crests, the coating slowed down the erosion by a factor of about 10. This is similar to previous results obtained from a jet-type laboratory test rig.

The erosion on the splitter crests and the cut-out edges was decisive for the time between overhauls (*TBO)*. The erosion inside the buckets was only of concern with relatively wide splitters, which lead to secondary damages.

10.1.4 Efficiency changes

Detailed histories of turbine efficiency changes $\Delta\eta$ of two MGs over four years were presented, which have not been available in literature so far. Efficiency reductions due to hydro-abrasive erosion and secondary damages were in maximum 0.9% (in the year 2012 with the major flood event). The η increased by up to 0.6% due to the grinding of blunt splitter crests and cut-out edges between the sediment seasons (Table 7-1). When there was no systematic erosion of base material on the splitter crests and cut-out edges, the $\Delta\eta$ due to grinding was in maximum +0.2%, and the grinding served mainly as a preparation for the coating repairs in these zones. If runners are exposed to erosion and repeatedly grinded, the η reduces over the years. To restore initial η, a major factory overhaul with reconstruction of the planned bucket geometry by welding and grinding is required.

The $\Delta\eta$ were correlated with either the increase of relative splitter width $\Delta s/B$ or the normalized radial erosion of the splitter tip $\Delta y_t/d_0$. The measured $\Delta\eta$ in relation to these geometrical quantities was similar as in previous field studies. For coated runners, the correlation between $\Delta\eta$ and y_t/d_0 is weaker than between $\Delta\eta$ and $\Delta s/B$, because the splitter tip is not always radially eroded when the splitter crests are eroded. For coated runners, the $\Delta\eta$ does not significantly change as long as the PL_b since the last re-coating is smaller than $PL_{b,0}$. Beyond this threshold, η decreases due to the erosion of mainly base material in the range of millimetres. Moreover, the $\Delta\eta$ do not only depend on the $PL_b - PL_{b,0}$, but also on the erosion status of a runner before the exposure period (blunt splitters lead to higher erosion and higher efficiency reductions).

10.1.5 HPP shutdowns in periods of high erosion potential

The proposed approach for the estimation of the shutdown *SSC* is practically applicable and yields an approximate value, which can be improved based on further operation experience. If intakes are closed during sediment transport events (floods), relatively high *SSL* can be prevented from entering the power waterway. In the example of the major flood event in July 2012 at HPP Fieschertal, the peak *SSC* was about five times as high as the shutdown *SSC*. Therefore, a shutdown during less than a day (16 h) would have been clearly profitable. This example shows that an investment on a sediment monitoring system as a prerequisite for temporary HPP shutdowns can be economically justified and is expected to pay off on long-term.

10.2 Recommendations for engineering practice

10.2.1 Suspended sediment measuring techniques

For real-time suspended sediment monitoring (SSM) at HPPs, the following types or combinations of instruments are recommended depending on various conditions:

- If the particle properties are constant or the degree of correlation between *SSC* and d_{50} is high at a certain site, turbidimeters or single-frequency acoustic techniques provide *SSC* with relatively low uncertainty after a calibration period.
- If these site conditions are not met, turbidimeters or single-frequency acoustic techniques may nonetheless be selected if (i) a relatively high uncertainty on *SSC* can be accepted (better a qualitative monitoring than no measurement), (ii) more expensive instruments are not affordable, and (iii) instruments are exposed to natural hazards (e.g. in river beds upstream of intakes). For long-term SSM, only turbidimeter models with automatic cleaning (wiper, air purge or ultrasound) or optical parts being not in contact with the water are recommended to prevent *SSC* bias due to fouling.
- Using ADM installations also for SSM is recommended because the required hardware exists already in many HPPs and the technique is practical. Because the acoustic technique is less sensitive to temporal variations of PSD and particle shapes than turbidimeters, a lower uncertainty on *SSC* can be expected.
- If (i) the PSD vary considerably in time, (ii) the degree of correlation between *SSC* and d_{50} is low at a certain site, and (iii) a low *SSC* measurement uncertainty at low and medium *SSC* is a requirement, the use of a LISST is recommended because the actual PSD is considered in its *SSC*.
- If a HPP operator accepts the lack of PSD data at higher *SSC*, the combination of a standard LISST instrument (without clear-water dilution), a CFDM and an

automatic bottle sampler is seen as an option with good cost-benefit ratio to measure both low and high *SSC* without temporary biases by PSD variations (in the size range of mainly silt) and considering site-specific particle properties. Such instrumentation allows determining annual *SSL* and *PL* with reasonably low uncertainty.

- If detailed PSD data are required at higher *SSC*, the use of a more expensive LISST instrument with automatic clear-water dilution (*LISST-Infinite*) is the only currently available option according to the author's knowledge.
- If the determination of annual *SSL* and *PL* is not a requirement, and only *SSC* above ~5 g/l (without PSD) are of interest, e.g. for temporary HPP shutdowns, the use of a CFDM is sufficient without gravimetric reference *SSC*.

In the present study, linear conversion functions between turbidity and *SSC* or acoustic damping δ and *SSC* were used. To reduce the *SSC* measurement uncertainty of turbidimetry and the acoustic technique, it is recommended to use non-linear conversion functions. Such functions account for (i) potentially non-linear behaviour of the measuring systems at higher *SSC* and (ii) consider potential site-specific correlations between d_{50} and *SSC*.

A further possibility for monitoring of coarser sediment transport at intakes of run-of-river HPPs is to evaluate the temporal evolution of sediment levels in gravel and sand traps. If their flushing is triggered by actual sediment levels, flushing frequencies may be a good indicator for the sediment input at the intake. Moreover, geophones may be used to measure the transport of coarse sediment, i.e. bedload (Albayrak *et al.* 2015).

No generally applicable recommendation on best SSM instrumentation can be given, because the selection of suitable measuring techniques and instruments depends on the measuring task, site conditions, the degree of correlation between *SSC* and d_{50}, available staff, accessibility, cost-benefit trade-offs and various constraints (Felix *et al.* 2016f).

10.2.2 Turbine erosion

For coated Pelton turbine runners, the operating hours until the start of the systematic erosion of base material at splitter crests and cut-out edges can be estimated based on the respective threshold value of the erosion potential per bucket $w^3 \cdot PL_{b,0} \approx 1.8 \cdot 10^9$ [kg/s^2] $\approx 5.0 \cdot 10^5$ [m^3/s^3 · h · g/l]. The relative velocity w between the flow and the Pelton bucket is proportional to the square root of the net head h_n (Section 2.3.2.2). Hence w^3 is proportional to $h_n^{1.5}$, and the $PL_{b,0}$ is over-proportionally lower for higher h_n and vice-versa. The influencing parameters for PL_b and hence $PL_{b,0}$ are summarized in Equation (8-3b). Note that the mentioned threshold value refers to PL_b computed with $k_{hardness}$ equal to the fraction of minerals harder than the base material, i.e. Mohs hardness > 4.5.

If a runner is in good condition before the season and the seasonal PL_b is below $PL_{b,0}$ (for $h_n \approx$ constant), only minor erosion damages in these zones are expected, which can be repaired on-site with limited effort during the low-flow season by local re-coating.

Above $PL_{b,0}$ the coating still contributes to reduce the erosion (inside the buckets and on the splitter flanks), but erosion of mainly base material on splitter crests and cut-out edges has to be expected. The erosion depths and geometrical changes in these zones in the second stage of erosion can be estimated using Equation (8-3) together with the $w^3 \cdot PL_{b,0}$ and C_g-values in Table 8-1.

For practical engineering application, the increase of splitter width Δs is of particular importance because it is highly related to efficiency decreases. The use of the C_g-value for the radial splitter tip erosion is not recommended because of its higher uncertainty. For the application of the regression coefficients listed in Tables 8-1 and 8-2, the following limitations should be noted:

- The number of observations is yet low (three seasons, two identical turbines of one HPP);
- The *PL* with $k_{size} \neq 1$ are largely affected by the definition of the k_{size}-function (Fig. 2-18);
- The *PL* depend on further factors affected by uncertainty (e.g. k_{shape} and $k_{hardness}$);
- Potential scale effects were not experimentally investigated, because the presented data set is based on measurements on turbines of only one size.

Modelling and predicting hydro-abrasive erosion are challenging because of the many parameters involved and their complex interactions. For the planning and design of HPPs with respect to sediment handling and mitigation of turbine erosion, operation experience remains an important source of information.

10.2.3 Efficiency changes

For efficiency monitoring, a combination of both presented techniques (SNM and CEM) is recommended. Discharge-needle position-curves and efficiency-power curves obtained from SNM in single turbine operation mode are used for CEM.

CEM is an attractive option for HPP operators because of the lower effort compared to SNM and no operation constraints, which is particularly important in periods of full load operation (wet season). A further advantage of CEM is the higher temporal resolution compared to periodically performed SNM, which is valuable to detect any turbine degradation as soon as possible.

For the estimation of $\Delta\eta$, a two-step procedure is proposed:

1) Estimate $\Delta s/B$ based on PL_b and w^x (with $\Delta s/B$ proportional to $PL_b - PL_{b,0}$),
2) Estimate $\Delta\eta$ based on $\Delta s/B$ and the initial s/B.

Because turbine erosion cannot be continuously monitored and the prediction of $\Delta\eta$ with the required low uncertainty is challenging or not feasible, efficiency monitoring of each runner remains an important basis for an economically optimized operation and maintenance of HPPs.

10.2.4 Optimisation of HPP operation

10.2.4.1 HPP shutdowns in periods of high erosion potential

For medium- and high-head run-of-river HPPs at sediment-laden rivers, or intakes of water adductions to reservoirs, it is recommended to consider systematic temporary shutdowns if their operation is not economic in periods of high erosion potential or high sediment load, respectively. A real-time system for suspended sediment monitoring is required to issue automatic warnings and to quantify annual *SSL* and *PL* for the estimation of the shutdown *SSC*.

It is recommended to measure *SSC* (or at least an indicator for *SSC* like turbidity) in the river directly upstream of the intake and preferably further upstream in order to increase the pre-warning time for HPP shutdowns and to supply data on the actual sediment load in the river during shutdowns. Moreover, hydro-meteorological forecasts may increase the pre-warning time and serve as a basis for subsequent HPP restart decisions.

Long-term measurements and documentation of sediment loads, turbine erosion, efficiency changes, maintenance actions and costs are highly recommended as a basis for economic and power production optimizations.

10.2.4.2 Increased fine-sediment conveyance through power waterways

In some storage HPP schemes, reservoir sedimentation may become economically more important than turbine erosion on the medium- and long-term. One option to mitigate reservoir sedimentation and to re-establish sediment continuity is to convey fine sediment from reservoirs via power waterways and turbines to downstream river reaches (Sollerer & Matt 2013; Boes & Hagmann 2015; Felix *et al.* 2016e). The fine sediment load in power waterways downstream of reservoirs can be increased by (i) sluicing of sediment-laden water, (ii) reducing the settling in reservoirs (e.g. by jet-induced turbulence,

Jenzer Althaus 2011), or (iii) mobilisation of fine sediment deposits by hydro-suction (Schüttrumpf & Detering 2011, Jacobsen & Chiménez 2015).

With such fine-sediment transport through the power waterway, negative effects of reservoir flushing, i.e. mainly temporarily high *SSC* (BUWAL 1994), are reduced. Other advantages are that no further transport, dewatering and land-based disposal of the sediment are required and no flushing water is lost for electricity generation. Drawbacks are that the costs for mitigation of turbine erosion (turbine design, coatings, separate cooling water systems, etc.) and turbine maintenance may increase, depending on the HPP's head and the particle properties. It is recommended to estimate acceptable increases of *SSC* in the turbine water by economic optimization considering a whole HPP scheme (civil structures and electro-mechanical equipment) over its lifetime.

10.3 Recommendations on further research

10.3.1 Suspended sediment monitoring

Further laboratory and field investigations on techniques for SSM are recommended, in particular:

- Effect of particle size on the density of two-phase flows measured with CFDM;
- Performance of a LISST instrument with automatic clear-water dilution;
- Acoustic backscatter probe with relatively low sensitivity to PSD variations in the range of silt to fine sand (8 MHz, Agrawal *et al.* 2016);
- Acoustic multi-frequency backscatter techniques, possibly in combination with forward scatter;
- Combinations of instruments relying on different physical operation principles;
- Adequate setups for reliable pressure measurements in silt-laden waters.

10.3.2 Suspended sediment yield and transport

Further investigations on the relations between meteorological variables, discharge, *SSC* and PSD of suspended sediment in rivers are recommended, using e.g. advanced models with spatially distributed variables. To improve the knowledge on fine sediment transport processes in HPP schemes, numerical simulations of the sediment-laden flow including deposition and erosion, and/or field and laboratory investigations are recommended for:

- Reservoirs, sand traps and storage tunnels;
- Penstocks and tailwater channels (spatial *SSC* and PSD distributions);
- Penstock bifurcations (potential differences in *SSC* and PSD among turbines).

10.3.3 Turbine erosion

The presented field data set on PL_b, erosion depths and eroded masses may be used to (i) calibrate and/or validate numerical erosion prediction models and (ii) investigate potential scale effects in reduced scale physical model tests. It is recommended to investigate other erosion models in addition to the approach described in IEC 62364 (2013) mainly adopted in this thesis.

To reduce the uncertainty on PL_b (Section 5.8) it is recommended to

- Specify the volume-equivalent sphere diameter d_{es} as the reference (rather than apparent d from LD or hydrometer analyses, which may differ considerably from d_{es} for highly non-spherical particles), and
- Introduce a procedure for the quantification of particle angularity.

For the further development of erosion models for uncoated and coated Pelton runners it is recommended to continue the study at HPP Fieschertal and conduct similar studies on other high-head HPPs on sediment-laden rivers. Further systematic laboratory investigations on jet-type test rigs and numerical simulations are required, because the parameters influencing turbine erosion cannot be investigated individually and the temporal resolution of turbine erosion measurements is limited in field studies. It is recommended to address the following aspects:

- Erosion process of the coating particularly at high impact angles and the interaction with the erosion of base material;
- Effects of the particle size (k_{size}), the particle hardness ($k_{hardness}$), material resistance (K_m) and the flow field (K_f) on low- and high-impact angle erosion of base material and coating;
- Effect of turbine reference size (RS^p) on erosion by investigating turbines with various bucket widths;
- Validation of the velocity exponent $x = 3$ by investigating turbines with various net heads;
- Effect of initial splitter width, in particular with respect to secondary damages;
- Non-linear effects in damage progression;
- Synergy between hydro-abrasive and cavitation erosion (if possible);
- Potential scale effects in physical model tests (e.g. effect of jet diameter);
- Uncertainty and range of applicability of erosion prediction models.

10.3.4 Efficiency changes

Further research is required on the relation between efficiency reductions $\Delta\eta$ and geometrical changes such as $\Delta s/B$ in Pelton turbines. Additional field investigations on turbine erosion and $\Delta\eta$ from HPP Fieschertal and other high-head HPPs are recommended. Moreover, it is recommended to investigate the individual effects of geometrical changes at (i) splitter crests, (ii) cut-out edges including splitter tip, or (iii) inside uncoated and coated buckets on turbine efficiency in a laboratory model study.

10.3.5 HPP shutdowns in periods of high erosion potential

It is recommended to further develop the procedure for the estimation of the shutdown *SSC* considering additionally (i) variable particle sizes and (ii) non-linear relations between *PL*, the extent of erosion and costs – particularly for coated runners.

An approach for (i) is to formulate a threshold value for HPP shutdown with respect to $SSC \cdot k_{size}$ (instead of only *SSC*). This quantity is proportional to $\Delta PL/\Delta t$, similar to Nozaki's equivalent SSC_{eq} (Eq. 2-28). For (ii) improved knowledge resulting from the previously proposed research topics can be included leading to a more accurate switch-off criterion depending on several parameters. However, as for any model, the degree of complexity has to be limited for the sake of practical applicability.

10.4 Final remarks

The mitigation of turbine erosion and reservoir sedimentation involves knowledge in hydrological, sedimentological, hydraulic, mechanical, material, civil and environmental engineering in combination with applied economy. This requires a good collaboration between research institutes, HPP operators, turbine manufacturers, providers of measuring systems, consultants, authorities and other involved parties.

Improved knowledge on turbine erosion, its causes, consequences and possible countermeasures contributes to enhance the sustainable and energy-efficient use of the hydropower potential at medium- and high-head run-of-river HPPs on sediment-laden rivers.

ACKNOWLEDGEMENTS

The conception and realisation of this interdisciplinary research project would not have been possible without the commitment of many parties. I gratefully acknowledge the support from the following persons and institutions:

- Prof. Dr. Robert Boes, head of the Laboratory of Hydraulics, Hydrology and Glaciology (VAW), ETH Zürich, Switzerland, project leader and examiner, for initiation of the present study, his continued support and confidence;
- Dr. Ismail Albayrak, VAW, supervisor and co-examiner, for valuable discussions, scientific input and support;
- Prof. Dr. Thomas Staubli, Hochschule Luzern (HSLU), Competence Center for Fluid Mechanics and Hydro Machines, co-initiator of this study and co-examiner, for scientific input and providing laboratory facilities;
- André Abgottspon, HSLU, for his support in the laboratory tests (including provision of particle material), preparation of installations at HPP Fieschertal, turbine erosion measurements, efficiency monitoring, literature support, and his outstanding commitment for this project;
- Prof. Dr. Peter Gruber, HSLU, for his input on acoustic sediment monitoring;
- Prof. Dr. Helmut Habersack, Universität für Bodenkultur Wien, co-examiner;
- Bernhard Truffer, director of Gommerkraftwerke and Martin Perren, head of operation, enabling this study at HPP Fieschertal, as well as Bernhard Minnig, Erwin Huber, Herbert Jenelten and Romeo Volken for their support on site;
- Ueli Aebi and Daniel Gerber, BKW Energie AG, Bern, for knowledge exchange and supporting the on-site data acquisition;
- Martin von Burg, Philip Stern, André Schwery, Fabian Deschwanden and Patrik Wili as well as Martin Duss of HSLU for their contributions to data evaluation (efficiency, turbine erosion, acoustic sediment monitoring) and the technical support during the laboratory investigations, respectively;
- Swisselectric research as the main funding agency of this work;
- Swiss federal office of energy (SFOE) for the notable financial support in several parts of the project;
- Gommerkraftwerke AG, Ernen, for the financial contribution and the provided support on site;
- Research Fund of the Swiss Committee On Dams, for financial assistance;
- Swiss Competence Center for Energy Research – Supply of Electricity (SCCER-SoE), for project support;
- Dr. Yogesh C. Agrawal, Sequoia Scientific Inc., and Dr. Ole Mikkelsen, for scientific and technical support regarding LISST;

– Dr. Roger Dekumbis, Dr. Kirsten Winkler, Dr. Etienne Parkinson, Matthias Krause, Dr. Jean-Christophe Marongiu, Dr. Magdalena Neuhauser and Wiebke Boden, Andritz Hydro, for exchange of ideas, literature support and reviews;
– Christian Kolb and further collaborators of Endress+Hauser for measuring equipment support (turbidimeters, Coriolis flow– and density meter);
– René Gehri, Sigrist Photometer, for measuring equipment support (*AquaScat*);
– Gerhard Nigg and Mario Rütti, Rittmeyer AG, for measuring equipment support (acoustic sediment monitoring based on ADM);
– Dr. Zhengji Zhang for exchange of ideas and feedback;
– Dr. Michael Plötze and collaborators, Geotechnical Institute, ETH Zürich, for advice and laboratory analyses of sediment samples;
– Daniel Braun, Institute of Environmental Engineering, ETH Zürich, for fruitful discussions on measuring techniques;
– TIWAG-Tiroler Wasserkraft, Kraftwerke Oberhasli (KWO), Repower and other HPP operators as well as engineering consultants, for their input from practice;
– Philipp Grüninger, Tobias Humbel, Semir Ibric, Reto Loosli, Julian Meister, Giacomo Moretti, Mario Ramisberger, Daniel Schaller, Lisa Scheurer, Simone Schmieder and Bandar Secchi, ETH students, for their contributions to data evaluation (suspended sediment, meteorology and run-off);
– Mario Moser and Daniel Gubser, VAW, for IT and electronics support regarding the on-site data acquisition;
– Stefan Gribi, Rolf Meier, Raffael Heini, Robert Pöschl, VAW, for workshop assistance;
– Walter Thürig, Andreas Rohrer, Andreas Schlumpf, VAW, for drawings, illustrations, flyers, photographs and videos;
– Prof. Dr. W. H. Hager, VAW, for literature support;
– Dr. Helge Fuchs, VAW, for coordination with teaching and student works;
– Adriano Lais, VAW, head of the Hydraulic Structures group, for his support and coordination;
– Cornelia Auer and Daniela Addor, VAW, for their contributions to the administration of this project;
– Bernard Feuz and Raoul Felix for reviewing the French résumé of this thesis.

Finally, I would like to also thank all persons not mentioned above, who shared their view in constructive discussions and have supported me in doing this work: friends and relatives (particularly Sylvie Felix and Markus Feldmann), colleagues from VAW, Pöyry (Electrowatt) and Emch+Berger, as well as former teachers. Special thanks go to my parents Heidi Langenegger and Raoul Felix, as well as to my partner Nina Dajcar.

David Felix Mai 2017

ABBREVIATIONS AND NOTATION

Abbreviations

ADM	Acoustic Discharge Measurement installation
BKW	BKW Energie AG, Bern (a Swiss utility and consultant)
CFDM	Coriolis Flow– and Density Meter
CC FMHM	Competence Center for Fluid Mechanics and Hydro Machines of HSLU
CEM	Continuous Efficiency Monitoring
ETH	Eidgenössische Technische Hochschule (Federal Institute of Technology)
FOEN	Swiss Federal Office of Environment
GKW	Gommerkraftwerke AG
HPP	Hydro-electric Power Plant
HSLU	Hochschule Luzern, Technik und Architektur, Switzerland
HVOF	High velocity oxy fuel (spray process for application of hard-coating)
IEC	International Electrotechnical Commission
IMR	Inversion mode for ‘random shaped’ particles (with LISST)
IMS	Inversion mode for spherical particles (with LISST)
LD	Laser diffraction, laser diffractometer
LISST	Laser In-Situ Scattering and Transmissometry (a trademark of Sequoia Scientific Inc., USA)
MeteoSwiss	Federal Office for Meteorology and Climatology
MG	Machine Group = Turbine and Generator (also called Unit)
PSD	Particle Size Distribution
SNM	Sliding-Needle index efficiency Measurement
SS	Sediment Season
SSM	Suspended Sediment Monitoring
SFOE	Swiss Federal Office of Energy

swisstopo	Swiss Federal Office of Topography
VAW	Laboratory of Hydraulics, Hydrology and Glaciology of ETH Zürich
WC-CoCr	Hard-coating (tungsten carbide particles in cobalt-chromium matrix)
1D, 2D, 3D	One-, two- or three-dimensional (in space)
~	Approximately

For abbreviations of particle types used in the laboratory please refer to Table 3-2.

Notation of Parameters

Latin symbols

A	Amplitude of the received pulse (acoustic technique)	[V]
A	Area (projected area of a particle)	[m^2]
A_s	Surface area	[m^2]
a_x	Longest extension of particles, not exceeded by x % of their mass	[µm]
a_c	Centripetal acceleration (Eq. 2-24)	[m/s^2]
B	Inner bucket width of Pelton runner (IEC 61364)	[m]
b_x	Intermediate extension of particles, not exceeded by x % of their mass	[µm]
BVC	Bin Volume Concentrations (with LISST)	[cm^3/l] = 10^{-3} [-]
C	Coefficient (related to settling velocity, drag, or head loss)	[…]
c_x	Shortest extension of particles, not exceeded by x % of their mass	[µm]
c	Cut-out depth of Pelton runner (in top view, Figure 3-13)	[mm]
C_g	Coefficient relating geometrical changes and PL_b (Eq. 8-3a)	[…]
C_m	Coefficient relating eroded masses and PL_b (Eq. 8-4)	[…]
CRF	Cox roundness factor (for particles, Eq. 2-2)	[-]
CSF	Corey shape factor (for particles, Eq. 2-1)	[-]
CT	Coating Thickness	[µm]
D	Pitch circle diameter of a Pelton runner (Figs. 2-7b, 2-8)	[m]
d	Particle diameter	[µm]

d_0	Jet diameter	[mm]
d_e	Depth of erosion	[mm]
$d_{es,x}$	Volume-equivalent sphere diameter of particles, which is not exceeded by x % of their mass	[µm]
d_i	Inner diameter (of a tube, conduit or penstock)	[mm]
d_x	Diameter of graded particles not exceeded by x % of their mass	[µm]
d_{50}	Median diameter of graded particles (50% by mass are finer)	[µm]
F	Force	[N]
f	Frequency	[Hz]
f_c	Correction factor for *SSC* from LISST (mainly particle shape)	[-]
g	Gravitational acceleration	[m/s^2]
h	Water (flow) depth; splitter height difference (Figure 3-13)	[m; mm]
h_n	Net head (of a turbine)	[m]
I	Number of time step; operation mode (MG 1 or 2 running)	[-]
j	Number of particle size class (1 to 5 in fraction-wise *SSC*)	[-]
K_f	Coefficient for the effect of the flow field on erosion (Eq. 2-29)	[…]
K_m	Coefficient for the effect of the target material on erosion (Eq. 2-29)	[-]
$K(t)$	Temporally variable offset to correct *SSC* from CFDM (Eq. 3-3)	[g/l]
K_T	Transducer constant (Eq. 2-17)	[…]
$k_{hardness}$	Coefficient for the effect of particle hardness on erosion (Eq. 2-29)	[-]
k_s	Equivalent sand roughness height (Nikuradse)	[m]
k_{size}	Coefficient for the effect of particle size on erosion (Eq. 2-29)	[-]
k_{shape}	Coefficient for the effect of particle shape on erosion (Eq. 2-29)	[-]
L	Path length (optical or acoustic)	[m]
M	Ratio of eroded mass (Δm) to erodent mass (*SSL*)	[-]
m	Mass (of particles or eroded material)	[g]
n	Number (of samples or data points)	[-]
n	Rotational speed (rpm = revolutions per minute)	[rpm]

n_q	Specific speed (Eq. 2-22a)	[rpm]
n_{QE}	Dimensionless specific speed (Eq. 2-22b)	[-]
P	Probability	[-]
p	Pressure	[Pa]
p	Exponent of the reference size *RS* in the IEC model (Eq. 2-29)	[-]
P_{el}	Electric active power	[W]
P_h	Precipitation height	[mm/day]
P_{hydr}	Hydraulic power (Eq. 2-32)	[W]
PL	Particle Load according to IEC 62364 (2013) (Eq. 2-30)	[h · g/l]
PL_b	Particle Load per bucket (Eqs. 2-31, 8-3b)	[h · g/l]
$PL_{b,0}$	Threshold value for the start of base material erosion (Eq. 8-3a)	[h · g/l]
Q	Volumetric flow rate (discharge)	[m^3/s]
q	Quartz content (by mass, Eq. 2-27)	[-]
r	Radius (of curvature, needle tip, splitter crest)	[m; mm]
R_h	Hydraulic radius	[m]
R^2	Coefficient of determination	[-]
RER	Relative erosion rate	[-]
Re	Reynolds number	[-]
RS	Reference size *RS* in the IEC model (Eq. 2-29)	[m]
S_e	Slope of the energy line (in 1D-flow)	[-]
s	Splitter width of Pelton bucket (Fig. 3-13)	[mm]
s_n	Needle position (degree of opening of a Pelton injector)	[%]
SMD	Sauter Mean Diameter (Eq. 2-4)	[µm]
SSC	Suspended Sediment mass Concentration	[kg/m^3]
SSC_{lim}	Upper limit of *SSC*-measuring range of LISST	[g/l]
SSL	Suspended Sediment Load (Eq. 3-4)	[t]
SSR	Suspended Sediment transport Rate (Eq. 2-15)	[kg/s]

T	Temperature	[°C]
t	Time	[s]
TBO	Time (operating hours) Between Overhauls (of turbines)	[h]
TVC	Total particle Volume Concentration = sum of plausible BVC	[cm^3/l]
U	Depth-averaged flow velocity (in main flow direction)	[m/s]
U_*	Friction velocity	[m/s]
$U_{2\sigma}$	Expanded uncertainty (2σ, at ~95% confidence level)	[…]
V	Volume	[m^3]
v_p	Relative velocity between a particle and the flow	[m/s]
$v_{s,\infty}$	Terminal particle settling velocity in stagnant water	[m/s]
w	Relative velocity between the flow and a turbine part	[m/s]
x	Velocity exponent in erosion models	[-]
x	Coordinate (in bucket Fig. 3-12); distance from transducer	[m]
y	Coordinate (in bucket radially towards runner axis Fig. 3-12)	[m]
y_t	Radial distance from outer runner diameter to splitter tip (Fig. 2-27a)	[mm]
z	Coordinate (vertical in water column, in bucket Fig. 3-12)	[m]
Z	Rouse number (Eq. 2-12)	[-]
Z_0	Average elevation of the intersections of the two jets with the pitch circle diameter (lower reference elevation for the net head)	[m a.s.l.]
Z_1	Headwater level (at downstream end of storage tunnel)	[m a.s.l.]
z_0	Number of jets of a Pelton turbine (IEC 62364)	[-]
z_2	Number of buckets of a Pelton runner (IEC 62364)	[-]

Greek symbols

α	Impact angle (solid particle erosion); angle between the incident light and the receiver (turbidimeters)	[°]
α	Attenuation coefficient (Eq. 2-17)	[1/m]
β	Specific attenuation per unit path length (Eq. 2-18 for acoustic)	[-]

β_2	Relative flow angle at the outlet of a Pelton bucket (Fig. 2-8b)	[°]
Δ	Difference	[...]
$\Delta\eta$	Absolute difference in index efficiency (Eq. 3-9)	[%]
δ	Damping in the acoustic technique (Eq. 3-1)	[-]
ε	Specific acoustic attenuation in non-linear function (Eq. 2-19)	[l/g]
η	Efficiency (index efficiency of an MG, Eq. 2-32)	[%]
θ	Non-dimensional shear stress (Shields parameter)	[-]
θ_c	Non-dimensional critical shear stress (incipent sediment motion)	[-]
κ	Rate of invertible measurements (with LISST)	[-]
λ	Wave length	[m]
μ	Average value (geometric mean) of a quantitiy	[…]
ν	Kinematic viscosity	[m^2/s]
ρ	Density	[kg/m^3]
σ	Standard deviation of a quantitiy	[...]
σ_g	Geometric spreading of PSD (grading of particles, Eq. 2-3)	[-]
τ	Optical transmission	[-]
τ_b	Bottom shear stress in a channel or wall shear stress in a pipe	[N/m^2]
φ	Specific acoustic attenuation in linear function (Eq. 4-2)	[l/g]
ϕ	Normalized particle diameter according to Krumbein (Fig. 2-1)	[-]

Uppercase subscripts

A	*SSC* obtained from the acoustic technique
B	*SSC* obtained by combining the results of several techniques (best estimate)
C	*SSC* obtained from the density measured by CFDM
D	Drag
G	*SSC* obtained by gravimetrical analysis (by weight)
L	*SSC* obtained from LISST; in particular

$SSC_{L0} = TVC \cdot \rho_s$

$SSC_{L1} = TVC \cdot \rho_s \cdot f_c$ with f_c = constant

$SSC_{L2} = TVC \cdot \rho_s \cdot f_c$ with $f_c = f(d_{50})$

P *SSC* obtained from pressure signals

T *SSC* obtained from turbidity

Lowercase subscripts

cb coating inside the buckets (excl. splitter crests and cut-out edges)

centr at the central third of the splitter length

cu at the cut-out

d design (rated)

end end (at the end of the sediment season)

eq equivalent

es equivalent sphere (with particle diameter *d*)

exc (probability or time of) exceedance

f friction

g geometric

inj injector

j jet

m related to mass

max maximum

mix mixture of water and sediment

p particle

ref reference

s solid

sp at the splitter crest (of a Pelton bucket)

w water (pure or clear water)

0 initial (before the sediment season or at the start of the observation period)

REFERENCES

Abgottspon A. (2011). Messung abrasiver Partikel in Wasserkraftanlagen (Measuring abrasive particles in HPPs). *Master thesis* (unpublished), Competence Center Fluid Mechanics and Hydro Machines, Hochschule Luzern, Switzerland (in German).

Abgottspon A., Felix D., Boes R., Staubli T. (2016a). Schwebstoffe, hydro-abrasiver Verschleiss und Wirkungsgradänderungen an Peltonturbinen – Ein Forschungsprojekt am KW Fieschertal (Suspended sediment, hydro-abrasive erosion and efficiency changes on Pelton turbines – a research project at HPP Fieschertal). *Wasser Energie Luft* 108(1): 9–24 (in German).

Abgottspon A., Felix D., Staubli T. (2016b). Erosion of Pelton buckets and changes in turbine efficiency measured in the HPP Fieschertal. *Proc.* 28th IAHR Symp. On Hydraulic Machinery and Systems, Grenoble, France. *IOP Conf. Series: Earth Environ. Sci.* 49, 122008.

Abgottspon A., Staubli T., Felix D., Albayrak I., Boes R.M. (2013a). Hydro-abrasive Erosion of Pelton buckets and Suspended Sediment Monitoring. *Proc*. Hydrovision International, Denver, USA.

Abgottspon A., Staubli T., Felix D., Albayrak I., Boes R.M. (2014). Monitoring Suspended Sediment and Turbine Efficiency. *Hydro Review Worldwide* 22(4): 28–36.

Abgottspon A., Stern P., Staubli T., Felix D., Winkler K. (2013b). Measuring Turbine Abrasion and Efficiency Decrease: First Results of the Case Study at HPP Fieschertal. *Proc*. Hydro Conf., Innsbruck, Austria, paper no. 18.05.

Agrawal Y.C., Mikkelsen O.A., Pottsmith H.C. (2011). Sediment monitoring technology for turbine erosion and reservoir siltation applications, *Proc*. Hydro Conf., Prague, Czech Republic, paper no. 29.09.

Agrawal Y.C., Mikkelsen O.A., Pottsmith H.C., Slade W.H. (2012). Turbine abrasion: one year's experience in real-time sediment monitoring at Hidroagoyan HPP, Ecuador. *Proc*. Hydro Conf., Bilbao, Spain: paper no. 14.08.

Agrawal Y.C. & Pottsmith H.C. (2000). Instruments for particle size and settling velocity observations in sediment transport. *Mar. Geol*. 168: 89–114.

Agrawal Y.C., Slade W.H., Pottsmith H.C., Dana D. (2016). Technologies and experience with monitoring sediments for protecting turbines from abrasion. *Proc.* 28th IAHR Symp. On Hydraulic Machinery and Systems, Grenoble, France. *IOP Conf. Series: Earth Environ. Sci.* 49, 122005.

Agrawal Y.C., Whitmire A., Mikkelsen O.A., Pottsmith H.C. (2008). Light scattering by random shaped particles and consequences on measuring suspended sediments by laser diffraction. *J. of Geophysical Research* 113, C04023.

Albayrak I., Felix D., Hagmann M., Boes R.M. (2015). Suspended Sediment and Bed Load Transport Monitoring Techniques. *Dresdner Wasserbauliche Mitteilungen* 53: 405–414.

Almquist C.W., March P.A., Pearson H.S., Fransen H.W., Whitehead B.H. (1995). The Sliding Gate Method for Hydroturbine Efficiency Testing. *Proc*. WaterPower 1995, American Society of Civil Engineers, New York, USA: 793–801.

Al-Rousan T., Masad E., Tutumluer E., Pan T. (2007). Evaluation of image analysis techniques for quantifying aggregate shape characteristics. *Construction and Building Materials* 21(5): 978–990.

Andrews S.W., Nover D.M., Reuter J.E., Schladow S.G. (2011). Limitations of laser diffraction for measuring fine particles in oligotropic systems: Pitfalls and potential solutions. *Water Resources Research* 47, W05523.

Annandale G. (2013). *Quenching the thirst: sustainable water supply and climate change*. CreateSpace Independent Publishing Platform, North Charleston, South Carolina, USA.

Asarin A.E., Fink A.K., Proudovsky A.M., Seredavkin V.P. (2001). Russian experience in design of dam projects on rivers with heavy sediment load. In Kaushish S.P. & Naidu B.S.K. (eds.), *Proc*. 2nd Intl. Conf. on Silting Problems in HPPs, Bangkok, Thailand: 215-221.

Atkinson C.M. & Kytömaa H.K. (1992). Acoustic wave speed and attenuation in suspensions. *Intl. J. Multiphase Flow* 18(4): 577–592.

Auel C. (2014). Flow Characteristics, Particle Motion and Invert Abrasion in Sediment Bypass Tunnels. *PhD thesis*, *VAW-Mitteilung* 229, Boes R. (ed.), ETH Zürich, Switzerland.

Bachmann P., Schärer C., Staubli T., Vullioud G. (1990). Experimental Flow Studies on a 1-Jet Model Pelton Turbine. *Proc*. 15th IAHR Symp. On Hydraulic Machinery and Cavitation, Belgrade, Serbia.

Bahadur S. & Badruddin R. (1990). Erodent particle characterization and the effect of particle size and shape on erosion. *Wear* 138(1): 189–208.

Bajracharya T.R., Acharya B., Joshi C.B., Saini R.P., Dahlhaug O.G. (2008). Sand erosion of Pelton turbine nozzles and buckets: A case study of Chilime Hydropower Plant. *Wear* 264(3-4): 177–184.

Basse N.T. (2014). A review of the theory of Coriolis flowmeter measurement errors due to entrained particles. *J. of Flow Measurement and Instrumentation* 37: 107–118.

Bergeron P. (1950). Similitude des usures causées par des mixtures liquide-solides (Similitude of wear caused by liquids carrying solid particles). *La Houille Blanche* (spec. issue B): 716–729 (in French).

Bishwakarma M.B. & Støle H. (2008). Real-time sediment monitoring in hydro-power plants. *J. of Hydraulic Research* 46(2): 282–288.

Bitter J.G.A. (1963). A study of erosion phenomena, parts I and II. *Wear* 1963(6): 5–21, 169–190.

Blaser S. & Bühler J. (2001). Werden durchlaufende Sedimentpartikel in hydraulischen Maschinen fragmentiert? (Are sediment particles passing hydraulic machines being fragmented?) *Wasser Energie Luft* 93(11): 305–311 (in German).

Boes R.M. (2009). Real-time monitoring of SSC and PSD in the headwater way of a high-head hydropower plant. *Proc*. 33rd IAHR Congress, Vancouver, Canada: 4037–4044.

Boes R.M. (2010). Kontinuierliche Messung von Schwebstoffkonzentration und –korngrössenverteilung im Triebwasser und Quantifizierung der Hydroabrasion an einer Peltonturbine (Continuous measurements of SSC and PSD in the turbine water and quantification of hydro-abrasive erosion on a Pelton turbine). *Wasser Energie Luft* 102(2): 101–107 (in German).

Boes R.M. & Hagmann M. (2015). Sedimentation countermeasures – examples from Switzerland. *Proc*. 1st Intl. Workshop on Sediment Bypass Tunnels, *VAW-Mitteilung* 232 (Boes R.M., ed.), ETH Zürich, Switzerland: 193–210.

Boes R.M., Felix D., Albayrak I. (2013). Schwebstoffmonitoring zum verschleissoptimierten Betrieb von Hochdruck-Wasserkraftanlagen (Suspended sediment monitoring for wear-optimized operation of high-head HPPs). *Wasser Energie Luft* 105(1): 35–42 (in German).

Bouwman A.M., Bosma J.C., Vonk P., Wesselingh J.A., Frijlink H.W. (2004). Which shape factor(s) best describe granules? *Powder Technology* 146(1-2): 66–72.

Bovet T. (1958). Contribution à l'étude du phénomène d'érosion par frottement dans le domaine des turbines hydrauliques (Contribution to the study of abrasive erosion in hydraulic turbines). *Bulletin technique de la Suisse romande* 84(3) : 37–49 (in French).

Bozic H., Hassler P., Schnablegger W. (2004). Prüfung und Bewertung von Peltonlaufrädern – unter besonderer Bedachtnahme auf den Trend zu geschmiedeten Laufrädern (Testing and assessment of Pelton runners – considering the trend to fully forged runners). *Proc*. Jahrestagung der deutschen, österreichischen und schweizerischen Gesellschaft für zerstörungsfreie Prüfung, Salzburg, Austria. CD published by DGZfP, Berlin (in German).

Brekke H., Wu Y.L., Cai B.Y. (2002). Design of Hydraulic Machinery Working in Sand Laden Water. In Duan C.G. & Karelin V.Y. (eds.), *Abrasive Erosion & Corrosion of Hydraulic Machinery* (pp. 155–233). Imperial College Press, London.

BUWAL (1994). Ökologische Folgen von Stauraumspülungen (Ecological consequences of reservoir flushing). *Schriftenreihe Umwelt* no. 219; Bundesamt für Umwelt, Wald und Landschaft, Bern, Switzerland (in German).

Cateni A., Magri L., Grego G. (2008). Optimization of Hydro Power Plants Performance – Importance of rehabilitation and maintenance in particular for the runner profiles. *Proc*. 7th Intl. Conf. on Hydraulic Efficiency Measurements (IGHEM), Milan, Italy.

Celik I. & Rodi W. (1991). Suspended Sediment-Transport Capacity for Open Channel Flow. *J. Hydraul. Eng*. 117(2): 191–204.

Corey A.T. (1949). Influence of Shape on the Fall Velocity of Sand Grains. *M.S. Thesis*, Colorado Agricultural and Mechanical College, Fort Collins, Colorado, USA, 102 pp. (unpublished).

Costa I., Storti G., Lüscher B., Gruber P., Staubli T. (2012). Influence of solid particle parameters on the sound speed and attenuation of pulses in acoustic discharge measurements (ADM). *J. of Hydrological Eng*. 17(10): 1084–1092.

Cox E.P. (1927). A method of assigning numerical and percentage values to the degree of roundness of sand grains. *J. of Paleontology* 1(3): 179–183.

Czuba J.A., Straub T.D., Curran C.A., Landers M.N., Domanski M.M. (2015). Comparison of fluvial suspended-sediment concentrations and particle-size distributions measured with in-stream laser diffraction and in physical samples, *Water Resources Research* 51, 320–340.

Dahlhaug O.G., Skåre P.E., Mossing V., Gutierrez A. (2010). Erosion resistant coatings for Francis runners and guidevanes. *Intl. J. on Hydropower & Dams* 2010(2): 109–112.

Desale G.R., Gandhi B.K., Jain S.C. (2006). Effect of erodent properties on erosion wear of ductile type materials. *Wear* 261 (7–8): 914–921.

Diepenbroek M., Bartholomä A., Ibbeken H. (1992). How round is round? A new approach to the topic 'roundness' by Fourier grain shape analysis. *Sedimentology* 39: 411–422.

DIN 50320 (1979). Verschleiss; Begriffe, Systemanalyse von Verschleissvorgängen, Gliederung des Verschleißgebietes (Wear; terms, system analysis of wear processes, classification of wear phenomena). *Deutsches Institut für Normung*, Beuth, Germany (withdrawn standard; in German).

DIN EN ISO 7027 (2000). Water quality – Determination of turbidity. Beuth Verlag, Germany.

DIN EN ISO 14688-1 (2013). Geotechnical investigation and testing – Identification and classification of soil – Part 1: Identification and description. Beuth Verlag, Germany.

Doujak E. & Götsch H. (2010). Usage of an axial hydro cyclone as sediment separator. *Proc.* 16th Intl. Seminar on Hydropower Plants. Doujak E. (ed.), Vienna, Austria: 87–95.

Downing J. (2006). Twenty-five years with OBS sensors: The good, the bad, and the ugly. *Continental Shelf Research* 26(17-18): 2299–2318.

Duan C.G. & Karelin V.Y. (eds.) (2002). *Abrasive Erosion & Corrosion of Hydraulic Machinery*, Book series on Hydraulic machinery, Vol. 2. Imperial College Press, London.

Dufour H. (1921). L'usure des turbines hydrauliques et ses conséquences et les moyens d'y parer (Wear of hydraulic turbines, consequences and countermeasures). Grenoble: J. Rey; also published in *La Houille Blanche* 1920(6): 233-237, 1921(1): 18–21, 1921(2): 53–56 and 1921(3): 97–104 (in French).

Durand R. (1951). Transport hydraulique des matériaux solides en conduite: Etudes expérimentales pour les cendres de la centrale Arrighi (The hydraulic transportation of solids in pipes: Experimental studies for the Arrighi power plant ash). *La Houille Blanche* 1951(3): 384–393 (in French).

DVWK 125 (1986). Schwebstoffmessungen, Messrichtlinie (Guideline for measuring suspended sediment). *Regeln zur Wasserwirtschaft*, Deutscher Verband für Wasserwirtschaft und Kulturbau e.V.; Parey, Hamburg Berlin, Germany (in German).

DWA (2006). Entlandung von Stauräumen (Removal of reservoir sediments). Deutsche Vereinigung für Wasserwirtschaft, Abwasser und Abfall e.V., Hennef, Germany (in German).

Edwards T.K. & Glysson G.D. (1999). Field methods for measurement of fluvial sediment. *Techniques of Water-Resources Investigations*, Book 3 (Application of Hydraulics), Chapter C2. U.S. Geological Survey. https://pubs.usgs.gov/twri/twri3-c2/

Elkvik M. (2013). Sediment erosion in Francis turbines. *PhD thesis*, NTNU, Trondheim, Norway.

Endress+Hauser (2003). Turbidity sensor *TurbiMax W CUS 41* – Process and immersion sensor for service water and solids content measurement according to the 90° scattered light method. *Technical Information* TI 177C/24/ae, Endress+Hauser, Germany.

Endress+Hauser (2014). Coriolis flowmeter 'Proline Promass 80F, 83F'. *Technical information*. Endress+Hauser, Germany.

Engelhardt M., Schneider C., Oechsle D. (2001). Real scale performance of advanced erosion protection techniques on water turbines. In Kaushish S.P. and Naidu B.S.K. (eds.), *Proc*. 2nd Intl. Conf. on Silting Problems in HPPs, Bangkok, Thailand: 168–175.

Escudier M.P., Abdel-Hameed A., Johnson M.W., Sutcliffe C.J. (1998). Laminarization and re-transition of a turbulent boundary layer subjected to favourable pressure gradient. *Exp. In Fluids* 25: 491–502.

Espinoza A.M. (2016). Managing Sediment in Peru's Pativilca River Basin [HPP Cahua]. *Hydro Review Worldwide* 24(4): 24–29.

Faletti N. (1934). L'erosione e la corrosione delle turbine idrauliche (Erosion and corrosion of hydraulic turbines) *L'energia elettrica* 11, 277 (in Italian).

Faran J.J. Jr. (1951). Sound scattering by solid cylinders and spheres. *J. Acoustical Society of America* 23(4): 405–418.

Felix D., Abgottspon A., Albayrak I., Boes R.M. (2016a). Hydro-abrasive erosion on coated Pelton runners: Partial calibration of the IEC model based on measurements in HPP Fieschertal. *Proc.* 28th IAHR Symp. On Hydraulic Machinery and Systems, Grenoble, France. *IOP Conf. Series: Earth Environ. Sci.* 49, 122009.

Felix D., Albayrak I., Abgottspon A., Boes R.M. (2016b). Hydro-abrasive erosion of hydraulic turbines caused by sediment – a century of research and development. *Proc.* 28th IAHR Symp. On Hydraulic Machinery and Systems, Grenoble, France. *IOP Conf. Series: Earth Environ. Sci.* 49, 122001.

Felix D., Albayrak I., Abgottspon A., Boes R.M. (2016c). Real-time measurements of suspended sediment concentration and particle size using five techniques. *Proc.* 28th IAHR Symp. On Hydraulic Machinery and Systems, Grenoble, France. *IOP Conf. Series: Earth Environ. Sci.* 49, 122006.

Felix D., Albayrak I., Abgottspon A., Boes R.M. (2016d). Suspended sediment measurements and calculation of the particle load at HPP Fieschertal. *Proc.* 28th IAHR Symp. On Hydraulic Machinery and Systems, Grenoble, France. *IOP Conf. Series: Earth Environ. Sci.* 49, 122007.

Felix D., Albayrak I., Abgottspon A., Boes R.M. (2016e). Optimization of hydropower plants with respect to fine sediment focusing on turbine switch-offs during floods. *Proc.* 28th IAHR Symp. On Hydraulic Machinery and Systems, Grenoble, France. *IOP Conf. Series: Earth Environ. Sci.* 49, 122011.

Felix D., Albayrak I., Boes R.M. (2013a). Laboratory investigation on measuring suspended sediment by portable laser diffractometer (LISST) focusing on particle shape. *Geo-marine Letters* 33(6): 485–498.

Felix D., Albayrak I., Boes R.M. (2013c). Monitoring of Suspended Sediment – Laboratory Tests and Case Study in the Swiss Alps. In *Advances in River Sediment Research*, Fukuoka S., Nakagawa H., Sumi T., Zhang H. (eds), Taylor & Francis Group, London: 1757–1766.

Felix D., Albayrak I., Boes R.M. (2014). Variation des Feinsedimentgehalts im Triebwasser infolge Speicherstollenbewirtschaftung (Variation of suspended sediment load in a penstock due to operation of a storage tunnel). In Boes R.M. (ed.), *VAW-Mitteilung* 227, ETH Zürich, Switzerland (in German): 183–193.

Felix D., Albayrak I., Boes R.M. (2015). Field measurements of suspended sediment using several methods. *Proc*. 36th IAHR World Congress, The Hague, The Netherlands.

Felix D., Albayrak I., Boes R.M. (2016f). Continuous measurement of suspended sediment concentration: Discussion of four techniques. *Measurement* 89: 44–47.

Felix D., Albayrak I., Boes R.M. (2016g). Combining in-situ laser diffraction (LISST) and vibrating tube densimetry to measure low and high suspended sediment concentrations. *Proc.* 13th Intl. Symp. On River Sedimentation, Stuttgart, Germany: 1264–1271.

Felix D., Albayrak I., Boes R.M. (2017). In-situ investigation on real-time suspended sediment measuring techniques: turbidimetry, acoustic attenuation, laser diffraction (LISST) and vibrating tube densimetry. *Intl. J. of Sediment Research* [under review].

Felix D., Albayrak I., Boes R.M., Abgottspon A., Deschwanden F., Gruber P. (2013b). Measuring Suspended Sediment: Results of the first Year of the Case Study at HPP Fieschertal in the Swiss Alps. *Proc.* Hydro Conf., Innsbruck, Austria, paper no. 18.03.

Ferguson R.I. & Church M. (2004). A simple universal equation for grain settling velocity. *J. of Sedimentary Research* 74(6): 933–937.

Finnie I. (1960). Erosion of surfaces by solid particles. *Wear* 1960(3): 87–103.

Flanagan K. (2016). Polymeric Materials Present Alternatives to Traditional Turbine Blade Repair. *Hydro Review Worldwide* 24(4): 14–19.

FOEN (2014). Discharge data at the gauging stations Massa (Blatten), Rhone (Reckingen) and Rhone (Brig). Hydrographical service of the Federal Office of Environment, Switzerland.

Francis J.R.D. (1973). Experiments on the motion of solitary grains along the bed of a water-stream. *Proc. Of the Royal Society of London Series A* 332(1591): 443–471.

García M.H. (ed.) (2008). Sedimentation Engineering: Processes, Measurements, Modeling, and Practice. *ASCE Manuals and Reports on Engineering Practice* 110, American Society of Civil Engineers, USA.

Geilhausen M., Morche D., Otto J.-C., Schrott L. (2013). Sediment discharge from the proglacial zone of a retreating Alpine glacier (Obersulzbachkees, Hohe Tauern, Austria). *Zeitschrift für Geomorphologie* 57, Suppl. 2: 29–53.

Giesecke J., Heimerl S., Emil Mosonyi E. (2014). Wasserkraftanlagen: Planung, Bau und Betrieb (HPP planning, construction and operation). 6th Edition. Springer Vieweg: Berlin, Heidelberg (in German).

Gippel C.J. (1995). Potential of turbidity monitoring for measuring the transport of suspended solids in streams. *Hydrological Processes* 9: 83–97.

GKW (1972). Construction drawings of the HPP Fieschertal (unpublished).

Gorthi S.S. & Rastogi P. (2010). Fringe projection techniques: Whither we are? *Optics and Lasers in Engineering* 48(2): 133–140.

Grasso A., Bérod D., Hefti D., Jakob A. (2011). Monitorage de la turbidité des cours d'eau Suisse (Turbidity monitoring in Swiss rivers). *Wasser Energie Luft* 103(1) : 48–52 (in French).

Grasso A., Bérod D., Hodel H., Jakob A., Lalk P., Spreafico M. (2014). Repräsentativität von Stichproben bezüglich Schwebstoffkonzentration – Erfahrungen der Abteilung Hydrologie bei der Probenahme (Representativity of bottled water samples with respect to suspended sediment concentration – Experiences of the Swiss hydrological service). *Wasser Energie Luft* 106(3) : 224–230 (in German).

Grein H. (1990). Cavitation pitting and rain erosion on Pelton runners. *Proc*. 15th IAHR Symp. On Hydraulic Machinery. Belgrade, Yugoslavia.

Grein H. & Krause M. (1994). Research and Prevention of Hydroabrasive Wear. *Proc*. 17th IAHR Symp. On Hydraulic Machinery. Beijing, China.

Grewal H.S., Agrawal A., Singh H. (2013). Slurry Erosion Mechanism of Hydroturbine Steel: Effect of Operating Parameters. *Tribology Letters* 52(2): 287–303.

Grubbs F.E. (1969). Procedures for detecting outlying observations in samples. *Technometrics* 12(1): 1–21.

Gruber P., Felix D., Storti G., Lattuada M., Fleckenstein P., Deschwanden F. (2016). Acoustic measuring techniques for suspended sediment. *Proc.* 28th IAHR Symp. On Hydraulic Machinery and Systems, Grenoble, France. *IOP Conf. Series: Earth Environ. Sci.* 49, 122003.

GSchG (2009). Bundesgesetz über den Schutz der Gewässer vom 24. Januar 1991, Änderung vom 11. Dezember 2009 (Federal Act on the Protection of Waters of January 24, 1991; amendment of December 11, 2009). Federal Assembly of the Swiss Confederation, Switzerland (in German).

Guangjie P., Zhengwei W., Yexiang X., Yongyao L. (2013). Abrasion predictions for Francis turbines based on liquid-solid two-phase fluid simulations. *Engineering Failure Analysis* 33: 327–335.

Guerrero M., Rüther N., Szupiany R., Haun S., Baranya S., Latosinski F. (2016). The Acoustic Properties of Suspended Sediment in Large Rivers: Consequences on ADCP Methods Applicability. *Water* 8, 13.

Guerrero M., Szupiani R.N., Latosinsky F. (2013). Multi-frequency acoustics for suspended sediment studies: an application in the Parana River. *J. Hydraulic Research* 51(6): 696–707.

Gummer J.H. (2009). Combating Silt Erosion in Hydraulic Turbines. *Hydro Review Worldwide* 17(1).

Habersack H., Haimann M., Kerschbaumsteiner W., Lalk P. (2008). Schwebstoffe im Fliessgewässer, Leitfaden zur Erfassung des Schwebstofftransportes (Suspended sediment in rivers, guideline for measuring suspended sediment transport). *Bundesministerium für Land- und Forstwirtschaft, Umwelt und Wasserwirtschaft BLFUW* (ed.), Vienna, Austria (in German).

Hach Lange (2005). *SOLITAX sc* Betriebsanleitung (Operation manual for turbidimeters of the type *SOLITAX sc*) DOC023.72.03232.Apr05. Hach Lange GmbH, Germany (in German).

Haimann M., Liedermann M., Lalk P., Habersack H. (2014). An integrated suspended sediment transport monitoring and analysis concept. *Intl. J. of Sediment Research* 29(2): 135–148.

Hamblin M.G. & Stachowiak G.W. (1995). A multi-scale measure of particle abrasivity. *Wear* 185(1-2): 225–233.

Hamerak K. (2016). Höhere Lebensdauer von hochbeanspruchten Pelton-Laufrädern durch innovative Herstellungsverfahren (Longer life of Pelton runners due to innovative manufacturing techniques). *Wasserkraft & Energie* 2: 22–32 (in German).

Hassler P. & Schnablegger W. (2006). Pelton runner maintenance and its results at Verbund-Austrian Hydro Power AG. *Proc*. 14th Intl. Seminar on Hydropower Plants, Doujak E. (ed.), Vienna, Austria: 445–454.

Haun S., Kjærås H., Løvfall S., Olsen N.R.B. (2013). Three-dimensional measurements and numerical modelling of suspended sediments in a hydropower reservoir. *J. of Hydrology* 479: 180–188.

Holcomb C.D. & Outcalt S.L. (1998). A theoretically-based calibration and evaluation procedure for vibrating-tube densimeters, *Fluid Phase Equilibria* 150-151: 815–827.

Hsu Y.-S. & Cai J.-F. (2010). Densimetric Monitoring Technique for Suspended-Sediment Concentrations. *J. Hydraul. Eng.* 136(1): 67–73.

Hsu Y.-S., Wei C.-M., Ting Y.-C., Yuan S.-Y., Chang C.-L., Chang K.-C. (2010). Capacitive sensing technique for silt suspended sediment concentration monitoring. *Intl. J. of Sediment Research* 25(2): 175–184.

Hutchings I.M. & Winter R.E. (1974). Particle erosion of ductile metals: a mechanism of material removal. *Wear* 27(1): 121–128.

ICOLD (2009). Sedimentation and sustainable use of reservoirs and river systems. *Bulletin* 147, International Commission on Large Dams, Paris, France.

IEC 60041 (1991). Field acceptance tests to determine the hydraulic performance of hydraulic turbines, storage pumps and pump-turbines, Edition 3.0, *International Electrotechnical Commission* (IEC), Geneva, Switzerland.

IEC 60193 (1999). Hydraulic turbines, storage pumps and pump-turbines – Model acceptance tests. *International Electrotechnical Commission* (IEC), Geneva, Switzerland.

IEC 62364 (2013). Hydraulic machines – Guide for dealing with hydro-abrasive erosion in Kaplan, Francis and Pelton turbines, Edition 1.0, *International Electrotechnical Commission* (IEC), Geneva, Switzerl.

Ilgaz C. (1952). Etude de l'usure d'une surface plane par un jet d'eau chargé de sable (Study of the wear of a plane surface by a sand laden jet of water). *La Houille Blanche* (4): 554–566 (in French).

ISO 11657 (2014). Hydrometry – Suspended sediment in streams and canals – Determination of concentration by surrogate techniques. *Intl. Organization for Standardization*, Geneva, Switzerland.

ISO 2178 (2016). Non-magnetic coatings on magnetic substrates – Measurement of coating thickness – Magnetic method. *Intl. Organization for Standardization*, Geneva, Switzerland.

Jacobsen T. & Jiménez A. (2015). Recent experiences from sediment removal projects. *Proc*. Hydro Conf. Bordeaux, France: paper no. 28.08.

Jahanbakhsh E. (2014). Simulation of Silt Erosion Using Particle-Based Methods. *PhD thesis* no. 6284. Laboratory for Hydraulic Machines, EPF Lausanne, Switzerland.

Jenzer Althaus J. (2011). Sediment evacuation from reservoir through intakes by jet induced flow. *PhD thesis* no. 4927. Hydraulic Constructions Laboratory (LCH), EPF Lausanne, Switzerland.

Jourdin F., Tessier C., Le Hir P., Verney R., Lunven M., Loyer S., Lusven A., Filipot J.F., Lepesqueur J. (2014). Dual-frequency ADCPs measuring turbidity, *Geo-Marine Letters* 34(4): 381–397.

Kalberer A. (1988). Erfahrungen mit neuartigen Beschichtungen im Wasserturbinenbau (experiences with new types of coatings for hydraulic turbines). Intl. Symp. Über Erosion, Abrasion und Kavitation im Wasserbau. In Vischer D. (ed.), *VAW-Mitteilung* 100, ETH Zürich: 245–258 (in German).

Kalotay P. (1999). Density and viscosity monitoring systems using Coriolis flow meters. *ISA Transactions* 38: 303–310.

Karimi A. & Schmid R.K. (1992). Ripple formation in solid-liquid erosion. *Wear* 156(1): 33–47.

Karimi A., Verdon C., Martin J.L., Schmid R.K. (1995). Slurry erosion behaviour of thermally sprayed WC-M coatings. *Wear* 186-187(2): 480–486.

Khanal K., Neopane H.P., Rai S., Thapa M., Bhatt S., Shrestha R. (2016). A methodology for designing Francis runner blade to find minimum sediment erosion using CFD. *Renewable Energy* 87(1): 307–316.

Krause M. & Grein H. (1996). Abrasion research and prevention. *Intl. J. on Hydropower & Dams*, 1996(4): 17–20.

Kresser W. (1964). Gedanken zur Geschiebe- und Schwebstofführung der Gewässer (Thoughts on the bedload and suspended sediment load of rivers) *Österreichische Wasserwirtschaft* 16(1/2): 6–11 (in German).

Krumbein W.C. & Aberdeen E. (1937). The Sediments of Barataria Bay. *J. of Sedimentary Petrology* 7(1): 3–17.

Krumbein W.C. (1941). Measurement and geological significance of shape and roundness of sedimentary particles. *J. of Sedimentary Research* 11(2): 64–72.

Lawn B.R. & Wilshaw T.R. (1975). Indentation fracture: principles and applications. *J. Material Science* 10(6): 1049–1081.

Lazzaro B. & Rossi G. (1995). Effetti del deterioramento sulle prestazioni delle macchine idrauliche (Effects of wear on the performance of hydraulic machines). *L' Energia elettrica.* Associazione elettrotecnica ed elettronica italiana, Milano. 72(4): 49–52 (in Italian).

Le Boursicaud R., Pierrefeu G., Pobanz K. (2015). Monitoring strategy of suspended sediment concentrations on the Upper Rhône. *Proc*. Hydro Conf. Bordeaux, France, paper no. 28.04.

Leguizamón S., Jahanbakhsh E., Maertens A., Vessaz C., Alimirzazadeh S., Avellan F. (2016). Impact erosion prediction using the finite volume particle method with improved constitutive models. *Proc.* 28th IAHR Symp. On Hydraulic Machinery and Systems, Grenoble, France. *IOP Conf. Series: Earth Environ. Sci.* 49, 122010.

Levy A.V. & Chik P. (1983). The effects of erodent composition and shape on the erosion of steel. *Wear* 89(2): 151–162.

Maldet R. (2008). Pelton runner with high erosion caused by glacier sediment: assessment and measures. *Proc*. 15th Intl. Seminar on Hydropower Plants, Doujak E. (ed.), Vienna, Austria: 639–646.

Mann B.S. (2000). High-energy particle impact wear resistance of hard coatings and their application in hydroturbines. *Wear* 237(1): 140–146.

Mei Z.Y. (1996). Review of Research on Abrasion and Cavitation of Silt Laden Flows Through Hydraulic Turbines in China. *Proc.* 18th IAHR Symp. On Hydraulic Machinery and Cavitation, Valencia, Spain: 641–650.

Meister J. (2014). Schwebstoffe im Triebwasser des Wasserkraftwerks Fieschertal im Jahr 2013 (Suspended sediment in the power waterway of HPP Fieschertal in 2013). *Master thesis* (unpublished), VAW, ETH Zürich (in German).

Meng H.C. & Ludema K.C. (1995). Wear models and predictive equations: their form and content. *Wear* 181–183: 443–457.

MeteoSwiss (2014). Data on daily precipitation in Fieschertal, Switzerland. Web-portal for researchers provided by the Federal Office of Meteorology and Climatology, Switzerland.

Mie G. (1908). Beiträge zur Optik trüber Medien, speziell kolloidaler Metallösungen (On the optics of turbid media, in particular colloidal metal solutions). *Annalen der Physik* 25(4): 377–445 (in German).

Moore S.A. (2011). Monitoring flow and fluxes of suspended sediment in rivers using side-looking acoustic Doppler current profilers. *PhD thesis*, Université de Grenoble, France.

Morris G.L. & Fan J. (1998). *Reservoir sedimentation handbook*, McGraw-Hill: New York.

Müller M., De Cesare G., Schleiss A.J. (2014). Continuous Long-Term Observation of Suspended Sediment Transport between Two Pumped-Storage Reservoirs. *J. Hydraul. Eng*. 140(5), 05014003.

Müller P. & De Cesare G. (2009). Sedimentation Problems in the Reservoirs of the KW Sarganserland – Venting of turbidity currents as the essential part of the solution. *Proc*. 23th ICOLD Congress, Q89 R21, Brasilia, Brazil.

Naidu B.S.K. (1999). Developing-Silt Consciousness in the minds of Hydro Power Engineers. In Varma C.V.J, Naidu B.S.K., Rao A.R.G (eds.), *Proc*. 1st Intl. Conf. on Silting Problems in Hydro Power Plants, New Delhi, India (paper no. 1). Rotterdam/Brookfield: Balkema.

Neopane H.P. (2010). Sediment Erosion in Hydro Turbines. *PhD thesis*, NTNU, Trondheim, Norway.

Neopane H.P., Dahlhaug O.G., Cervantes M. (2011). Sediment Erosion in Hydraulic Turbines. *Global J. of researches in Engineering, Mechanical and Mechanics engineering* 11(6)

Nichols G. (2009). *Sedimentology and Stratigraphy*, 2nd edition, Wiley-Blackwell, United Kingdom.

Nozaki T. (1990). Estimation of repair cycle of turbine due to abrasion caused by suspended sand and determination of desilting basin capacity. *Report*. Tokyo, Japan International Cooperation Agency.

Ortmanns C. (2006). Entsander von Wasserkraftanlagen (Desanding facilities of HPPs). *PhD thesis*, *VAW-Mitteilung* 193, Minor H.-E. (ed.), ETH Zürich, Switzerland (in German).

Padhy M.K. & Saini R.P. (2008). A review on silt erosion in hydro turbines. *Renewable and Sustainable Energy Reviews* 12(7): 1974–1987.

Padhy M.K. & Saini R.P. (2009). Effect of size and concentration of silt particles on erosion of Pelton turbine buckets. *Energy* 34(10): 1477–1483.

Padhy M.K. & Saini R.P. (2011). Study of silt erosion on performance of a Pelton turbine. *Energy* 36(1): 141–147.

Padhy M.K., Thatoi D.N., Acharya A.K. (2012). Effect of shape of silt particles on erosive wear of Pelton turbine bucket. *Proc.* IEEE-International Conf. on Advances in Engineering, Science and Management (ICAESM), Nagapattinam, India: 19–24.

Parsons A.J., Cooper J., Wainwright J. (2015). What is suspended sediment? *Earth Surface Processes and Landforms* 40: 1417–1420.

Patent US233692 (1880). Water-Wheel. Invented by Lester A. Pelton, patented on Oct. 26, 1880.

Perrig A., Avellan F., Kueny J.-L., Farhat M., Parkinson E. (2006). Flow in a Pelton Turbine Bucket: Numerical and Experimental Investigations. *J. Fluids Engineering* 128(2): 350–358.

Poudel L., Thapa B., Shrestha B.P., Thapa B.S., Shrestha K.P., Shrestha N.K. (2012). Computational and experimental study of effects of sediment shape on erosion of hydraulic turbines. *IOP Conf. Series: Earth Environ. Sci.* 15, 032054.

Pradhan P.M.S. (2004). Improving sediment handling in the Himalayas. *Proc*. Workshop on Optimal Sediment Handling (OSH) Research, October 2004, Nepal.

Preece C. & Macmillan N.H. (1977). Erosion. *Annual Review of Materials Science* 7: 95–121.

Rai A.K. & Kumar A. (2015). Continuous measurement of suspended sediment concentration: Technological advancement and future outlook. *Measurement* 76: 209–227.

Rai A.K., Kumar A., Staubli T. (2016). Forces acting on particles in a Pelton bucket and similarity considerations for erosion. *Proc.* 28th IAHR Symp. On Hydraulic Machinery and Systems, Grenoble, France. *IOP Conf. Series: Earth Environ. Sci.* 49, 122002.

Rouse H. (1937). Modern Conceptions of Mechanics of Fluid Turbulence. *Trans. ASCE* 102(1): 463–505.

Sauter J. (1926). Die Grössenbestimmung der in Gemischnebeln von Verbrennungskraftmaschinen vorhandenen Brennstoffteilchen (Determination of particle sizes of sprayed fuel in cumbustion engines). *VDI-Forschungsheft Nr. 279* (in German).

Schleiss A., De Cesare G., Jenzer Althaus J. (2010). Verlandung der Stauseen gefährdet die nachhaltige Nutzung der Wasserkraft (Sedimentation of reservoirs compromises the sustaninable use of hydropower). *Wasser Energie Luft* 102(1): 31–40 (in German).

Schorsch S., Ochsenbein D.R., Vetter T., Morari M., Mazzotti M. (2014). High accuracy online measurement of multidimensional particle size distributions during crystallization. *Chemical Engineering Science* 105: 155–168.

Schüttrumpf H. & Detering M. (2011). Innovative sediment handling to restore reservoir capacity. In *Dams and reservoirs under changing challenges*, Schleiss A.J. & Boes R.M. (eds.), CRC Press: 345–352.

Sequoia (2008). LISST concentration limits. *Article* dated August 29, 2008; Sequoia Scientific Inc., www.sequoiasci.com/article/lisst-concentration-limits (last retrieved on Dec. 29, 2016).

Sequoia (2011). LISST bin sizes for inversions based on randomly shaped grains. *Article* dated March 18, 2011; Sequoia Scientific Inc., www.sequoiasci.com/article/lisst-bin-sizes-for-inversions-based-on-randomly-shaped-grains (last retrieved on Dec. 29, 2016).

Shah-Fairbank S.C. & Julien P.Y. (2015). Sediment load calculations from point measurements in sand-bed rivers, *Intl. J. of Sediment Research* 30(1): 1–12.

Shields A. (1936). Anwendung der Aehnlichkeitsmechanik und der Turbulenzforschung auf die Geschiebebewegung (Application of similarity principles and turbulence research to bedload movement). *Mitteilungen der Preussischen Versuchsanstalt für Wasserbau und Schiffbau* Heft 26, Berlin, Germany (in German), also: Hydrodynamics Laboratory Pub. 167, US Department of Agriculture, California Institute of Technology, Pasadena, California, USA (in English).

Sidhu S.S. (1999). Experience of coating and successful field tests of coated guide vanes at Baira Siul HEP. In Varma C.V.J, Naidu B.S.K., Rao A.R.G (eds.), *Proc*. 1st Intl. Conf. on Silting Problems in Hydro Power Plants, New Delhi, India (paper no. 28). Rotterdam/Brookfield: Balkema.

Singh M., Banerjee J., Patel P.L., Tiwari H. (2013). Effect of silt erosion on Francis turbine: a case study of Maneri Bhali Stage-II, Uttarakhand, India. *ISH J. of Hydraulic Eng*. 19(1): 1–10.

Skripalle J., Hies T., Nguyen H.H. (2016). Suspended sediment measurements with multi-frequency backscatter acoustics. *Proc.* 13th Intl. Symp. On River Sedimentation, Stuttgart, Germany: 1289–1294.

Smeltzer C.E., Gulden M.E., Compton W.A. (1970). Mechanisms of Metal Removal by Impacting Dust Particles. *J. Basic Eng.* 92(3): 639–652.

Sollerer F. & Matt P. (2013). Sediment management of reservoirs – sediment discharge in dependence on the suspended load concentration in the run-off water. *Proc*. Hydro Conf. Innsbruck, Austria, paper no. 18.08.

Sommer N. (1980). Untersuchungen über die Geschiebe- und Schwebstoffführung und Transport von gelösten Stoffen in Gebirgsbächen (Investigations on the bedload and suspended load and the transport of dissolved matter in mountian streams). *Proc. Interpreavent,* Bad Ischl (Austria), Volume 2: 69–94 (in German).

Spreafico M., Lehmann C., Jakob A., Grasso A. (2005). Feststoffbeobachtung in der Schweiz – Ein Tätigkeitsgebiet der Landeshydrologie (Monitoring of solid transport – activities of the Swiss hydrological service). *Berichte des BWG*, Serie Wasser Nr. 8, Bern, Switzerland (in German).

Strübin P. & Bussy M. (1988). Erosionserscheinungen im Kraftwerk Mörel der Aletsch AG aus Sicht der Betriebsleitung (turbine wear in HPP Mörel, Switzerland). In Vischer D. (ed.), *VAW-Mitteilung* 100, ETH Zürich, Switzerland: 95–123 (in German).

Sulzer Hydro (1996). Ein semi-empirisches Abrasionsmodell zur Vorhersage von hydroabrasivem Verschleiß an X5 CrNi 13/4 Stahl (a semi-empirical model to predict hydro-abrasive wear on strainless turbine steel). *Bericht* Nr. STT.TB94.020 (in German); partly published in DWA (2006).

Sutherland T.F., Lane P.M., Amos C.L., Downing J. (2000). The calibration of optical backscatter sensors for suspended sediment of varying darkness levels. *Marine Geology* 162: 587–597.

Swisstopo (2015). Swiss geodata portal (https://map.geo.admin.ch). Topographic map, geological map, map of river sub-catchments. Federal Office of Topography, Switzerland.

Tanaka M., Girard G., Davis R., Peuto A., Bignell N. (2001). Recommended table for the density of water between 0 °C and 40 °C based on recent experimental reports. *Metrologia* 38: 301–309.

Thapa B. (2004). Sand Erosion in Hydraulic Machinery. *PhD thesis*, NTNU, Trondheim, Norway.

Thapa B. & Brekke H. (2004). Effect of sand particle size and curvature in erosion of hydraulic turbine. *Proc*. 22nd IAHR Symp. On Hydraulic Machinery and Systems, Stockholm, Sweden.

Thomann P. (1988). Erosion an den Pelton-Rädern der Zentrale Stalden der Kraftwerke Mattmark AG (wear at Pelton runners in HPP Stalden, Switzerland). In Vischer D. (ed.), *VAW-Mitteilung* 100, ETH Zürich, Switzerland: 151–160 (in German).

Truscott G.F. (1971). A literature survey on abrasive wear in hydraulic machinery. *Wear* 20: 29–50.

Uetz H. (1986, ed.). *Abrasion und Erosion; Grundlagen, betriebliche Erfahrungen und Verminderung*. (Abrasion and erosion; fundamentals, operation experience and mitigation). C. Hanser, Munich and Vienna (in German).

Van Rijn L.C. (1984). Sediment transport, Part I: Bed load transport. *J. of Hydraul. Eng*. 110(10): 1431–1456.

Vanoni V.A. (1946). Transportation of suspended sediment by water. *Trans. ASCE* 111: 67–133.

Vanoni V.A. (2006). Sedimentation Engineering: Theory, Measurements, Modeling, and Practice. *ASCE Manuals and Reports on Engineering Practice* 54. American Society of Civil Engineers, USA.

VAW (2011). Gletscher- und Abfussentwicklung im Gebiet des Fieschergletschers 1900–2100 (Evolution of glacier and discharge in the region of the Fieschergletscher, Switzerland). Unpublished report by VAW, ETH Zürich (in German).

Vessaz C., Jahanbakhsh E., Avellan F. (2015). Flow Simulation of Jet Deviation by Rotating Pelton Buckets Using Finite Volume Particle Method. *J. of Fluids Eng.* 137(7) 074501.

Vischer D. & Huber A. (2002). *Wasserbau* (Hydraulic structures). 6th ed. Springer, Berlin (in German).

Vlasak P., Chara Z., Konfrst J., Krupička J. (2015). Experimental investigation of coarse particle conveying in pipes. *EPJ Web of Conferences* 92, 02111.

Wang T. & Baker R. (2014). Coriolis flowmeters: a review of developments over the past 20 years, and an assessment of the state of the art and likely future directions. *J. of Flow Measurement and Instrumentation* 40: 99–123.

Wedmark A. (2014). Living with particle abrasion, *Proc*. Hydro Conf., Cernobbio (Lake Como), Italy, paper no. 08.02.

Weingartner R. & Aschwanden H. (1992). Discharge regime – the basis for the estimation of average flows. Plate 5.2 of the Hydrological Atlas of Switzerland (www.hydrologischeratlas.ch, in German).

Wellinger R. (1949). Sandstrahlverschleiss an Metallen (Sand blasting erosion on metals). *Zeitschrift für Metallkunde (Intl. J. Of Materials Research)* 40: 361–364 (in German).

Wentworth C.K. (1922). A Scale of Grade and Class Terms for Clastic Sediments. *J. of Geology* 30(5): 377–392.

Winkler K. (2014). Hydro-abrasive erosion: Problems and solutions. *Proc*. 27th IAHR Symp. On Hydraulic Machinery and Systems, Montréal, Canada. *IOP Conf. Series: Earth and Environ. Sci.* 22: 052022.

Winkler K., Dekumbis R., Rentschler M., Parkinson E., Garcin H. (2011a). Understanding hydro-abrasive erosion, *Proc*. Hydro Conf., Prague, Czech Republic: paper no. 02.05.

Winkler K., Dekumbis R., Uppal A. (2011b). Coating Minimizes Operational Losses at Nathpa Jhakri in India. *Hydro Review Worldwide* 19(1).

Winkler K., Dekumbis R., Wedmark A. (2010). Finding a way to estimate the amount of abrasion. *Proc*. Hydro Conf., Lisbon, Portugal.

Winter R.E. & Hutchings I.M. (1974). Solid particle erosion studies using single angular particles. *Wear* 29(2): 181–194.

Wittmann H., von Blanckenburg F., Kruesmann T., Norton K.P., Kubik P.W. (2007). Relation between rock uplift and denudation from cosmogenic nuclides in river sediment in the Central Alps of Switzerland. *J. Geophys. Res* 112: F04010

Wren D., Barkdoll B., Kuhnle R., Derrow R. (2000). Field Techniques for Suspended-Sediment Measurement. *J. of Hydraul. Eng.* 126(2): 97–104.

Wulf H., Bookhagen B., Scherler D. (2012). Climatic and geologic controls on suspended sediment flux in the Sutley River Valley, western Himalaya. *Hydrol. Earth Syst. Sci.* 16: 2193–2217.

Zanke U. (1982). *Grundlagen der Sedimentbewegung* (fundamentals of sediment movement). Springer; Berlin, Heidelberg, New York (in German).

Zhang Z. (2016). *Pelton turbines*. Springer, Berlin, Heidelberg, New York.

Zhu H. (2009). Application of Coriolis Mass Flowmeters in Bubbly or Particulate Two-Phase Flows. *PhD thesis*, University of Erlangen-Nuremberg, Germany; Shaker, Aachen.

APPENDIX A: LABORATORY INVESTIGATIONS ON SSM

A1 Setup and instruments

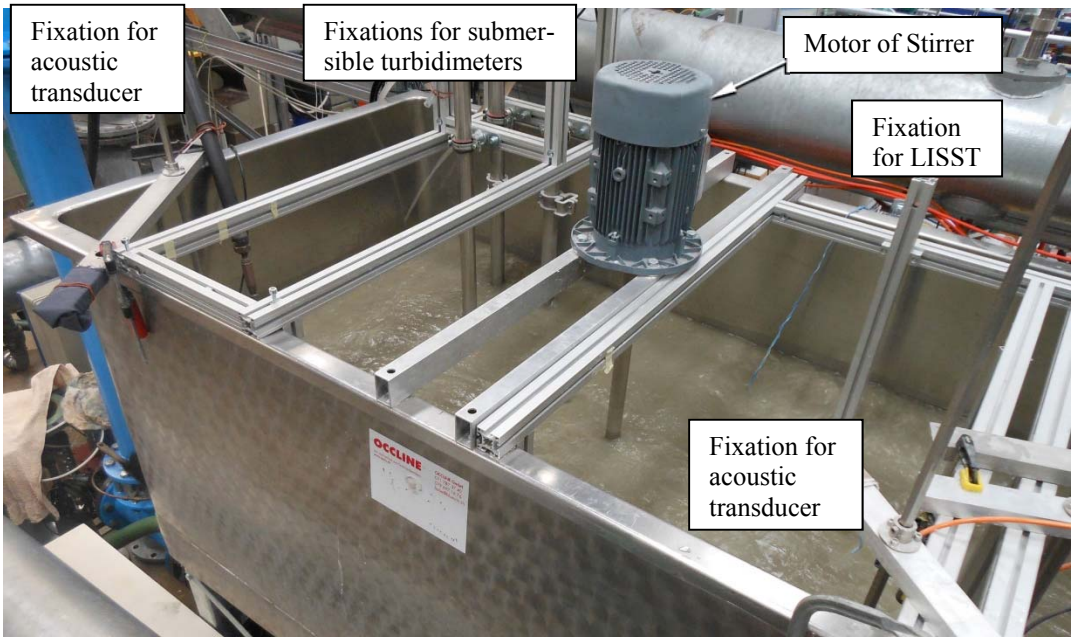

Figure A-1 View on the mixing tank with central stirrer and rods for the fixation of the instruments.

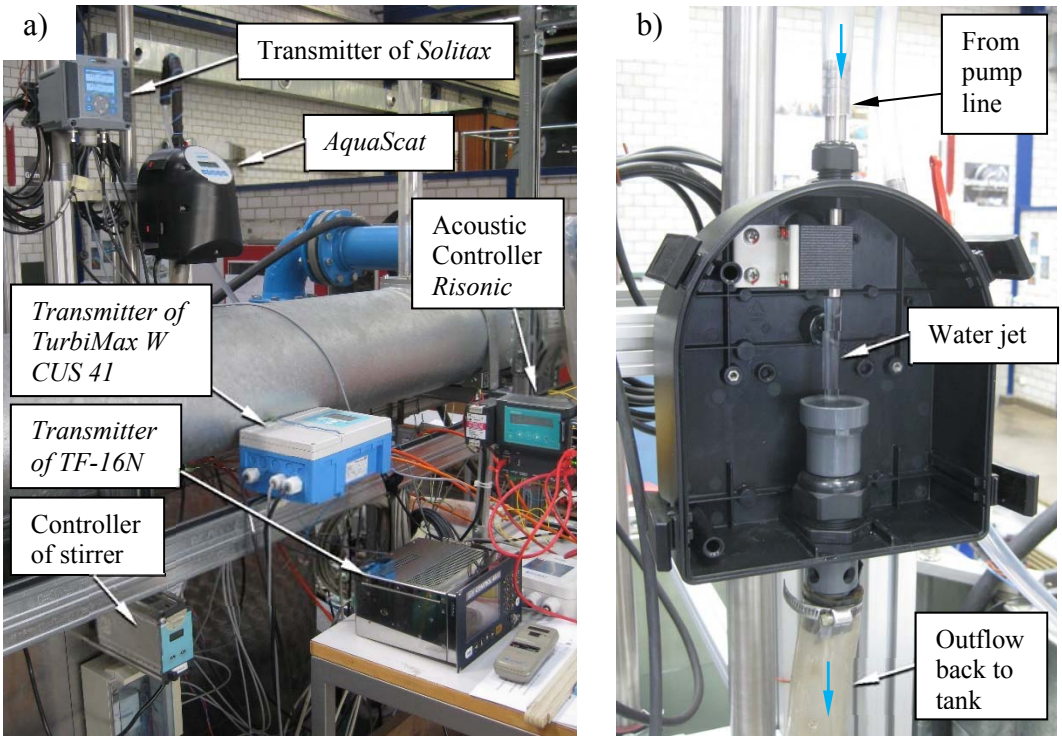

Figure A-2 a) Turbidimeter *AquaScat* installed above the tank and transmitters/controllers of other instruments, b) free-falling water jet in *AquaScat* (front part of instrument removed for photo-graph).

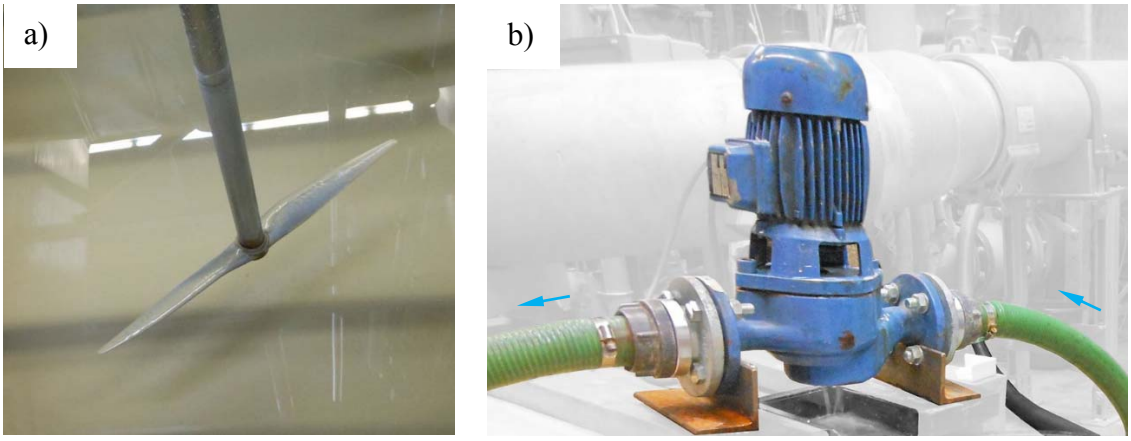

Figure A-3 a) Stirrer in the tank (item no. 8 in Fig. 3-3) with an impeller diameter of 0.51 m and b) pump (item no. 9 in Fig. 3-3) installed on the pump line connected to the tank.

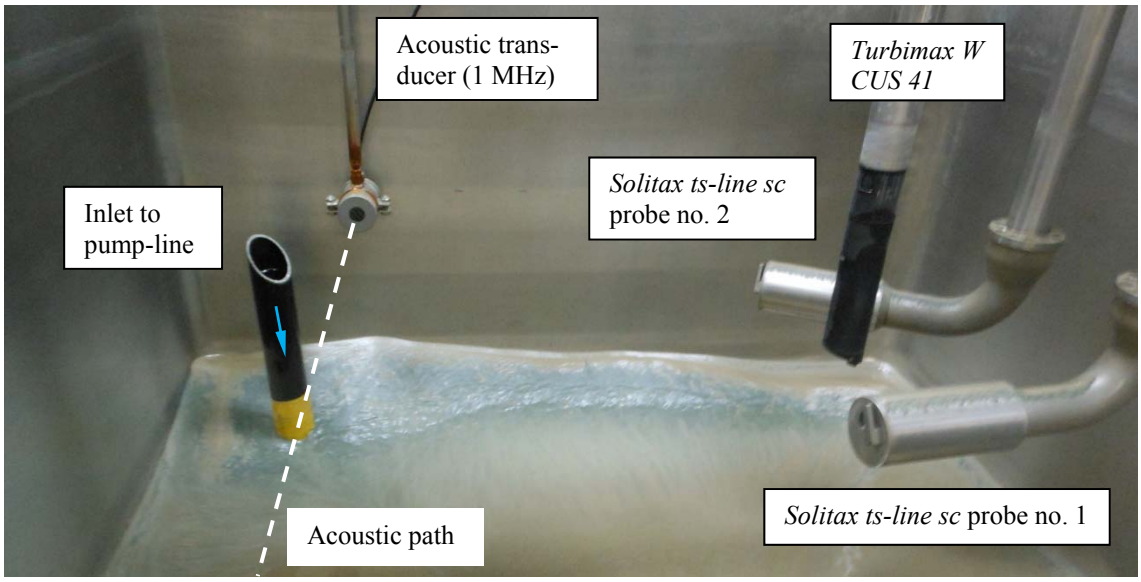

Figure A-4 Dewatered tank after the measurement series with the particles from HPP Stalden (N2).

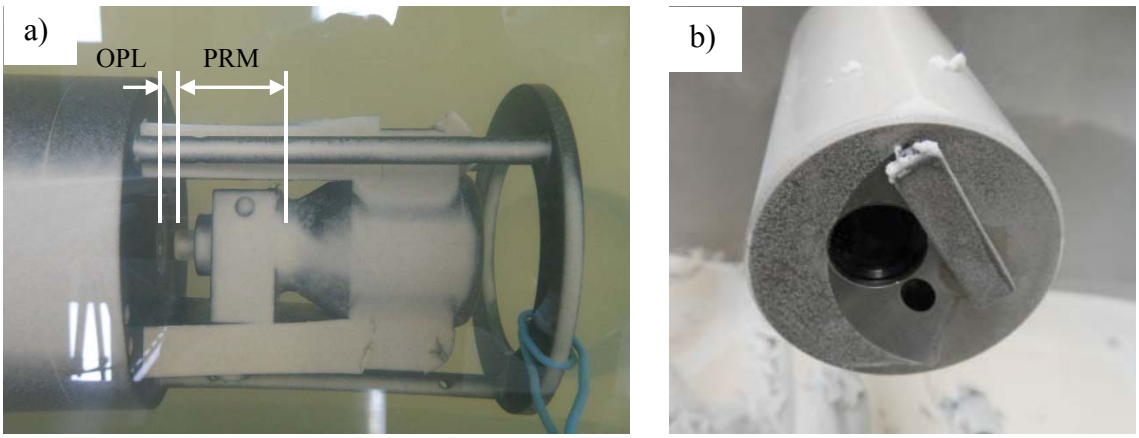

Figure A-5 a) Measuring head of the *LISST-100X* with 90%-path reduction module (PRM) installed leaving an optical path length of 5 mm (OPL) and b) detail of *Solitax ts-line sc* with wiper.

A2 Comparison of gravimetrical and nominal *SSC*

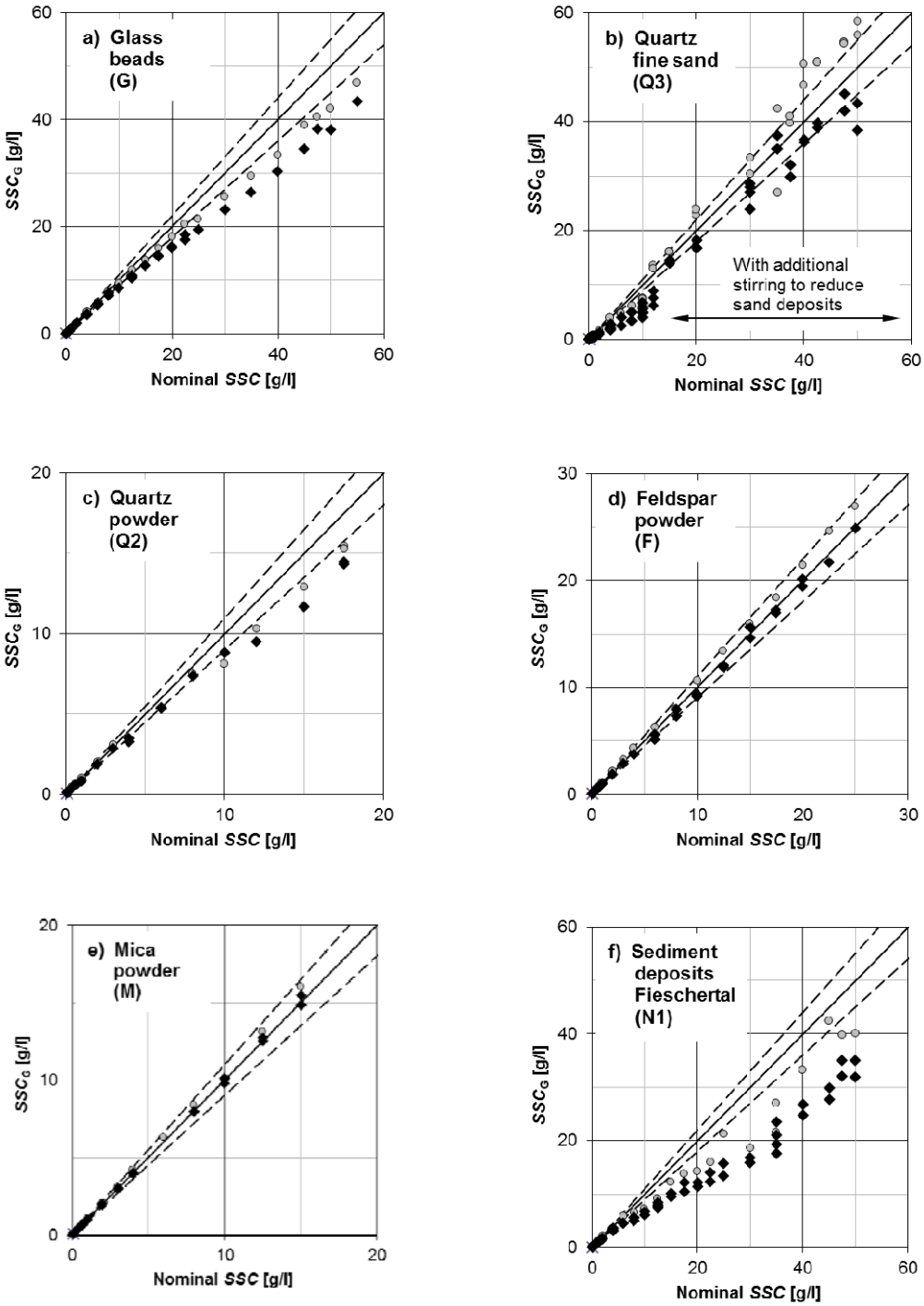

Figure A-6 Gravimetrically measured *SSC* (SSC_G) compared to nominal *SSC* for six types of particles. The circular markers (●) refer to the *SSC* measured at the outlet of the turbidimeter (5) in Figure 3-3, the diamonds (♦) to the *SSC* in the tank on the level of the instruments. The dashed lines indicate a range of ±10%.

A3 Results of turbidity measurements

A3.1 *TurBiScat* – channel no. 1 (scattering at 90°)

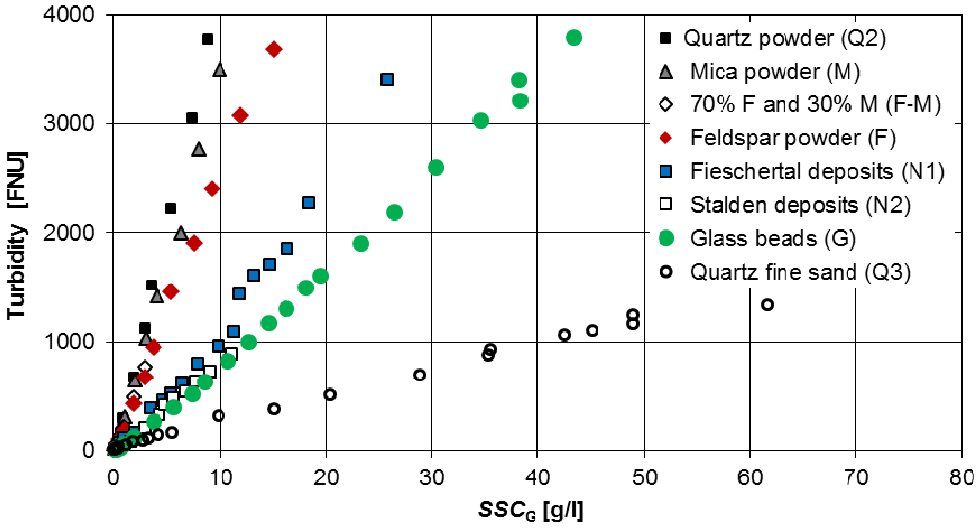

Figure A-7 Turbidity measured with *TurBiScat* at 90° as a function of SSC_G for all measurement series.

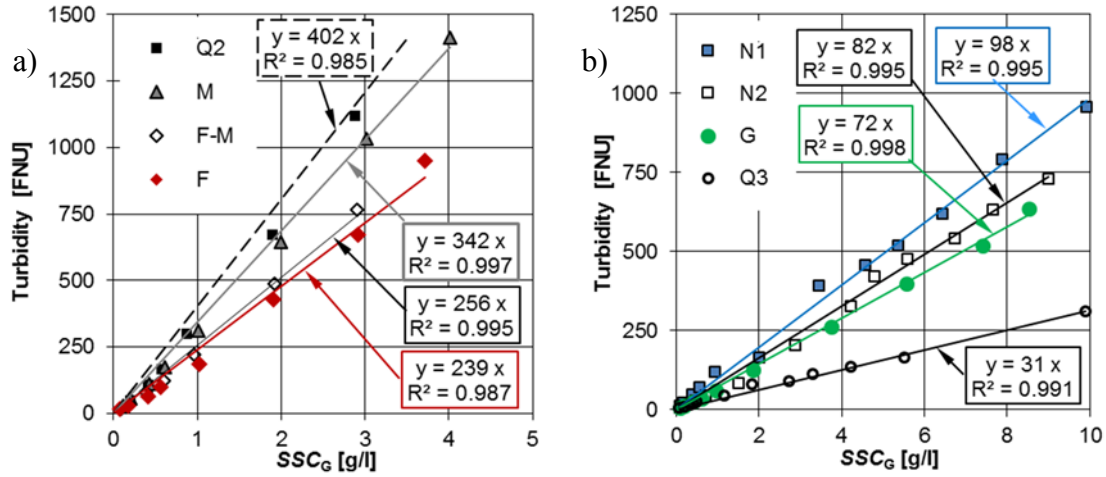

Figure A-8 Turbidity measured with *TurBiScat* at 90° as a function of SSC_G, with linear fits in the ranges up to a) 5 g/l and b) 10 g/l.

A3.2 *TurBiScat* – channel no. 2 (scattering at 25°)

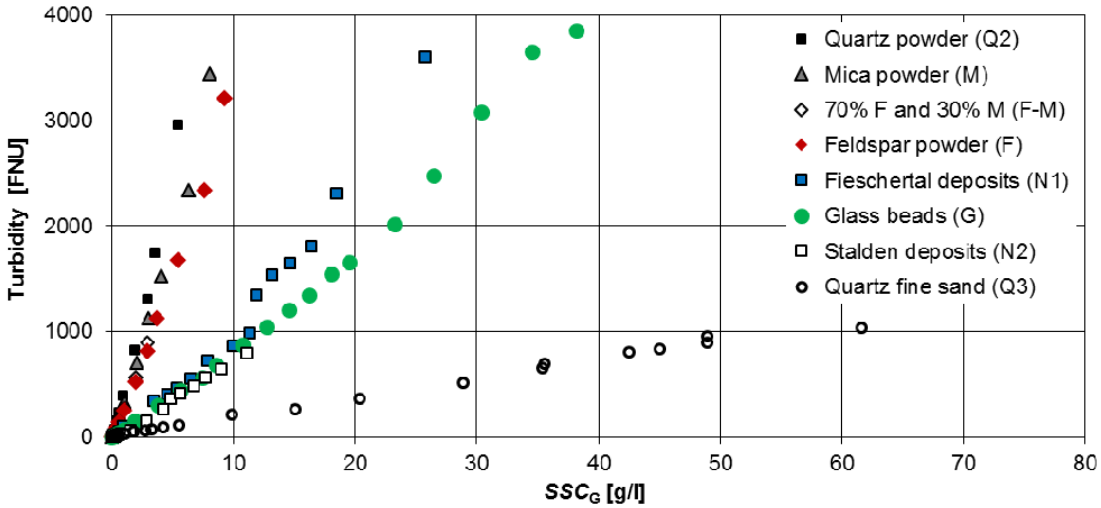

Figure A-9 Turbidity measured with *TurBiScat* at 25° as a function of SSC_G for all measurement series.

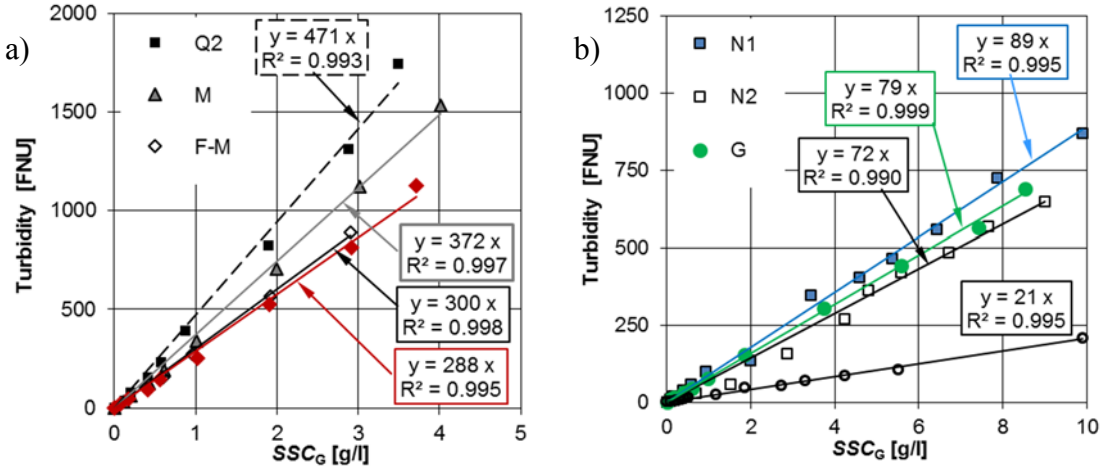

Figure A-10 Turbidity measured with *TurBiScat* at 25° as a function of SSC_G, with linear fits in the ranges up to a) 5 g/l and b) 10 g/l.

A3.3 *Solitax ts-line sc* (90° dual) – probe no. 1

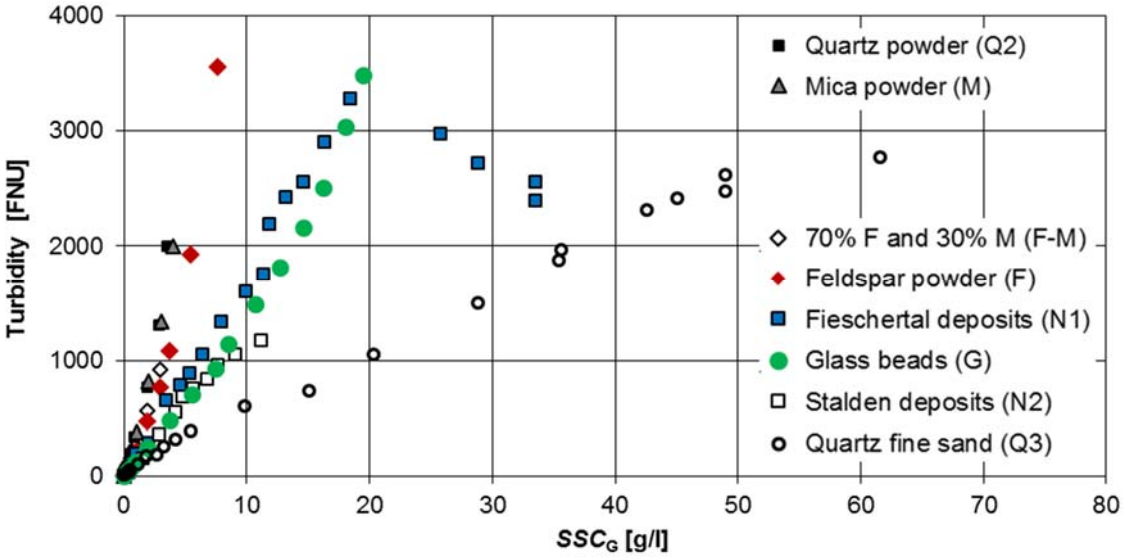

Figure A-11 Turbidity measured with the *Solitax ts-line sc* probe no. 1 (90° dual) as a function of SSC_G for all measurement series.

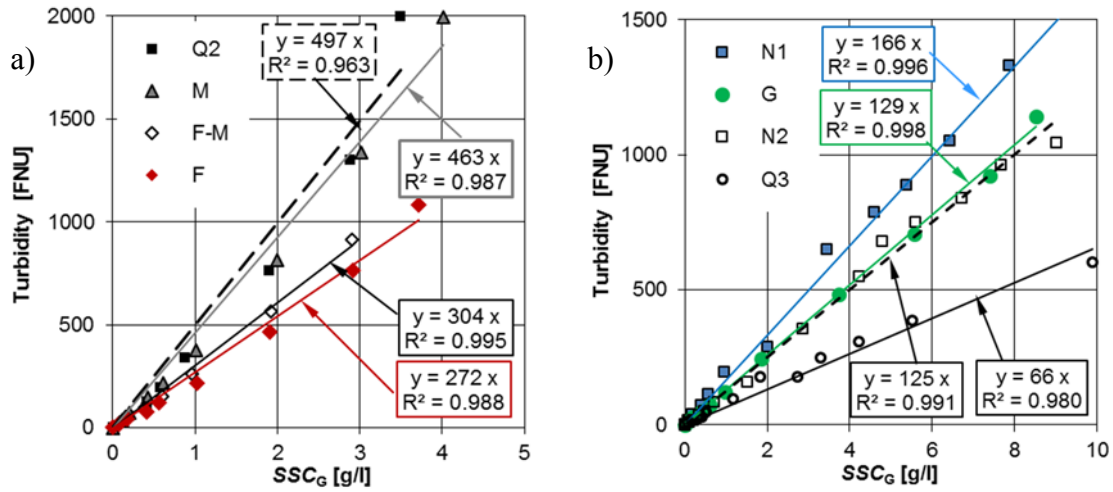

Figure A-12 Turbidity measured with *Solitax ts-line sc* probe no. 1 (90° dual) as a function of SSC_G, with linear fits in the ranges up to a) 5 g/l and b) 10 g/l.

A3.4 *Solitax ts-line sc* (90° dual) – probe no. 2

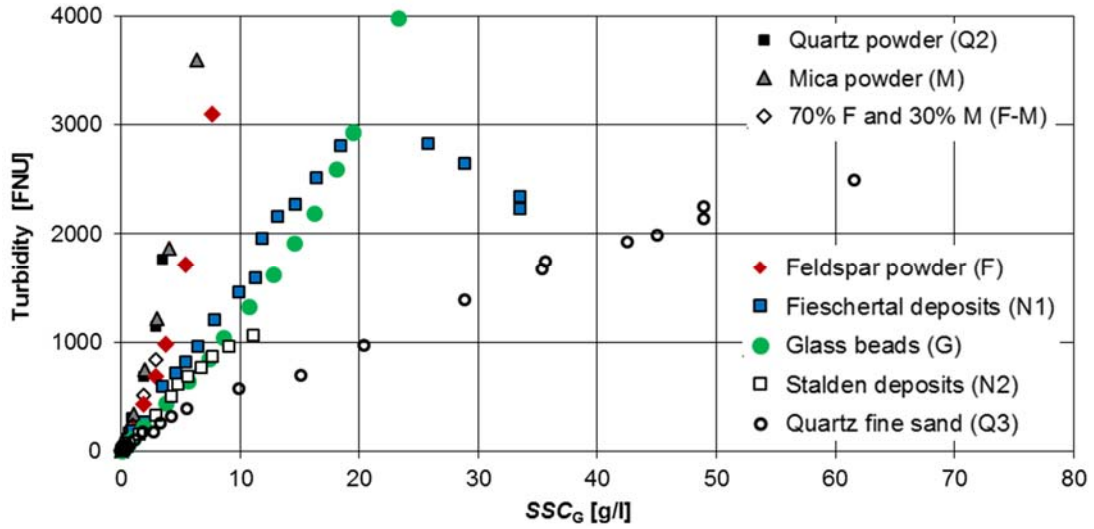

Figure A-13 Turbidity measured with the *Solitax ts-line sc* probe no. 2 (90° dual) as a function of SSC_G for all measurement series.

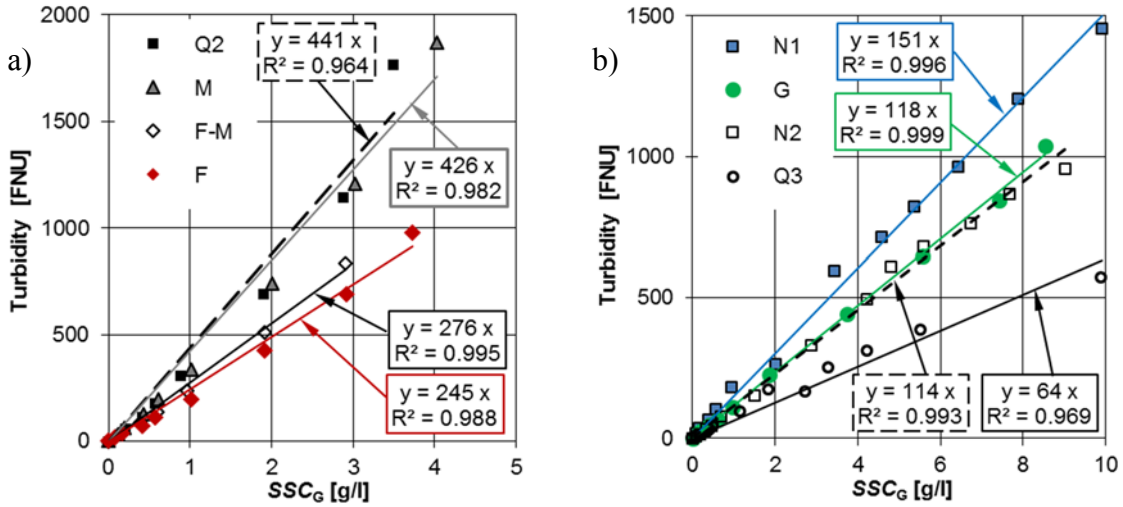

Figure A-14 Turbidity measured with *Solitax ts-line sc* probe no. 2 (90° dual) as a function of SSC_G, with linear fits in the ranges up to a) 5 g/l and b) 10 g/l.

A3.5 Comparison of *Solitax ts-line sc* probes no. 1 and no. 2

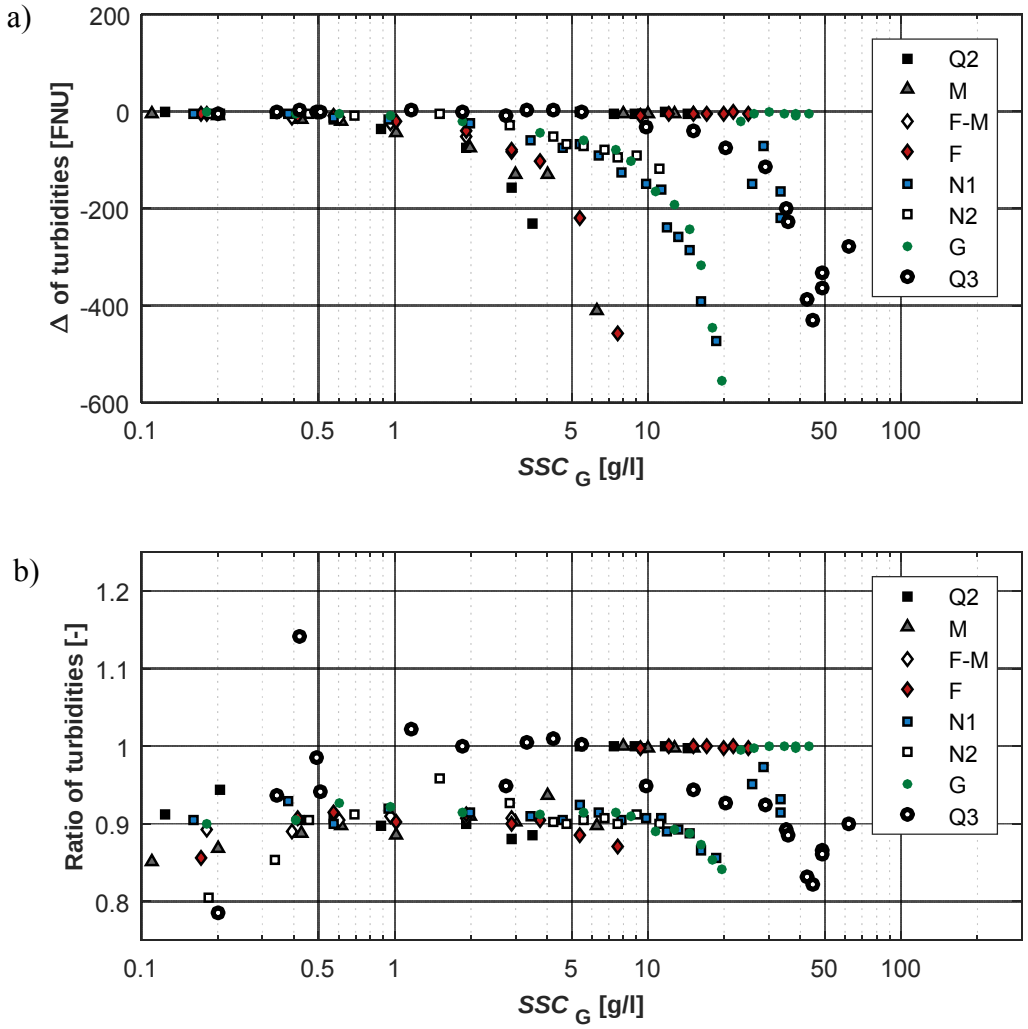

Figure A-15 Comparison of turbidities measured with two *Solitax ts-line sc* probes as a function of SSC_G in the eight measurement series, a) differences and b) ratios.

A3.6 *TurbiMax W CUS 41 (90° dual)*

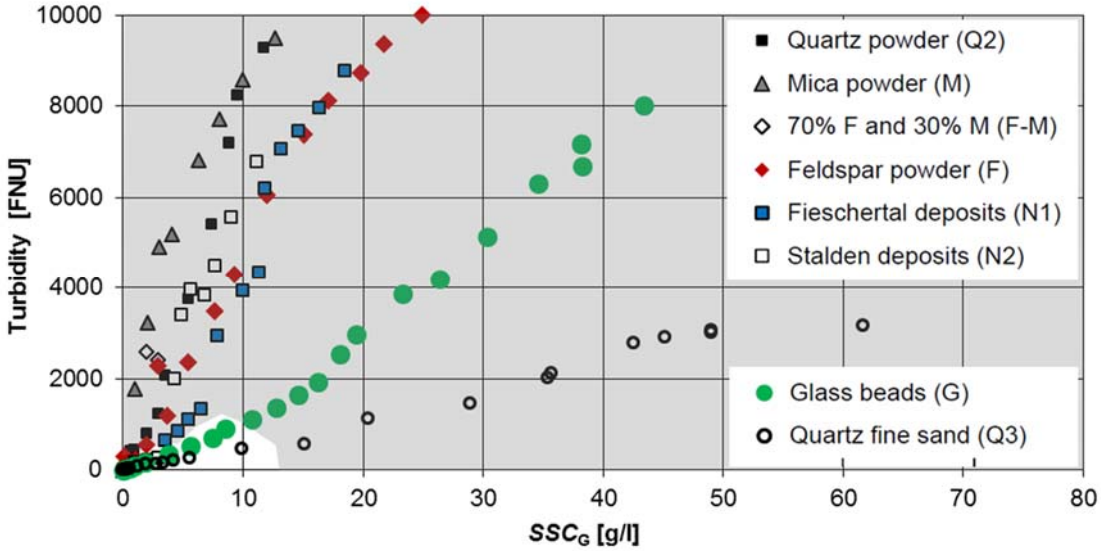

Figure A-16 Turbidity measured with *TurbiMax W CUS 41* (90° dual) as a function of SSC_G for all measurement series. The measurements affected by the occasional sudden increases of the turbidity signal due to the inadequate setting of the 'gas bubble threshold' parameter are marked with the grey fill. These values were not used for the evaluation of the specific turbidities in Figure A-17.

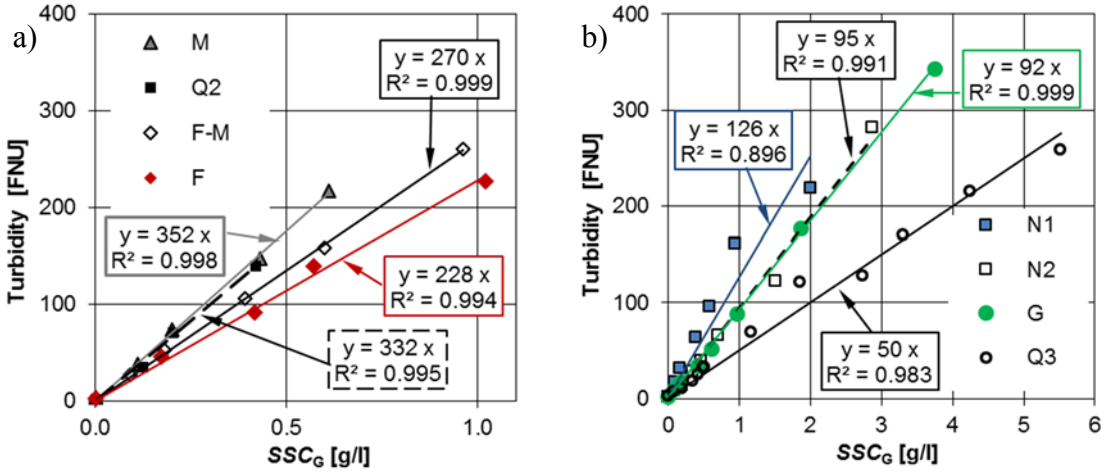

Figure A-17 Turbidity measured with *TurbiMax W CUS 41* (90° dual) as a function of SSC_G, with linear fits in the range below 400 FNU for a) four fine particle types and b) the other particle types.

APPENDIX B: HPP FIESCHERTAL AND SETUP

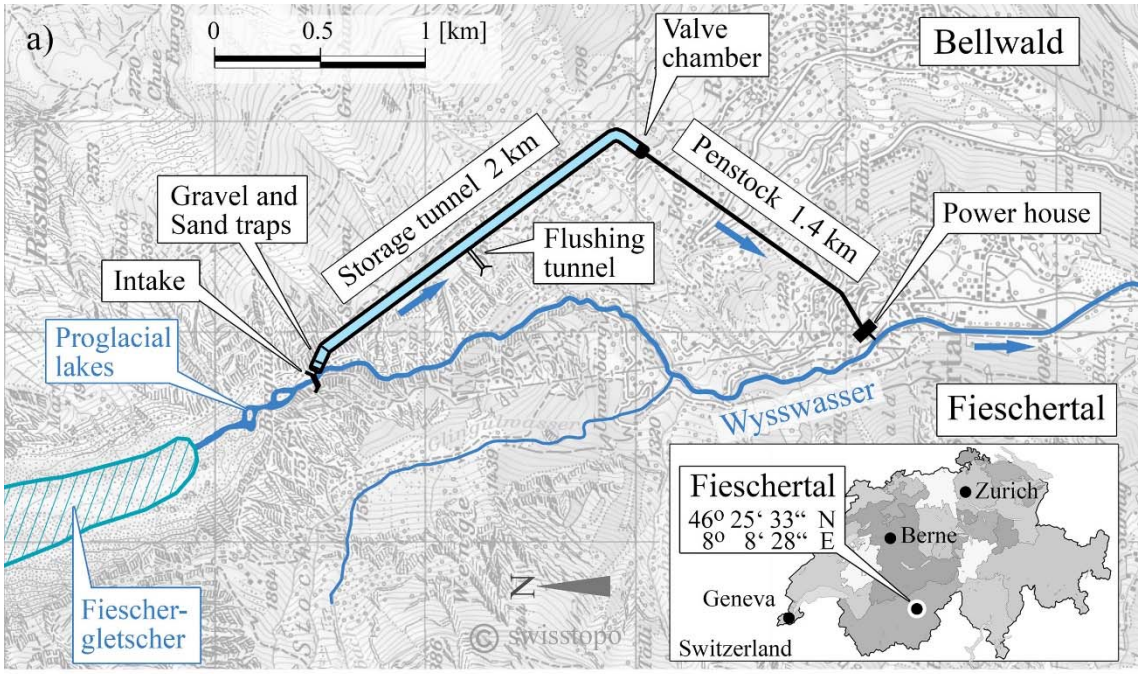

Reproduced with permission from swisstopo (JA100120)

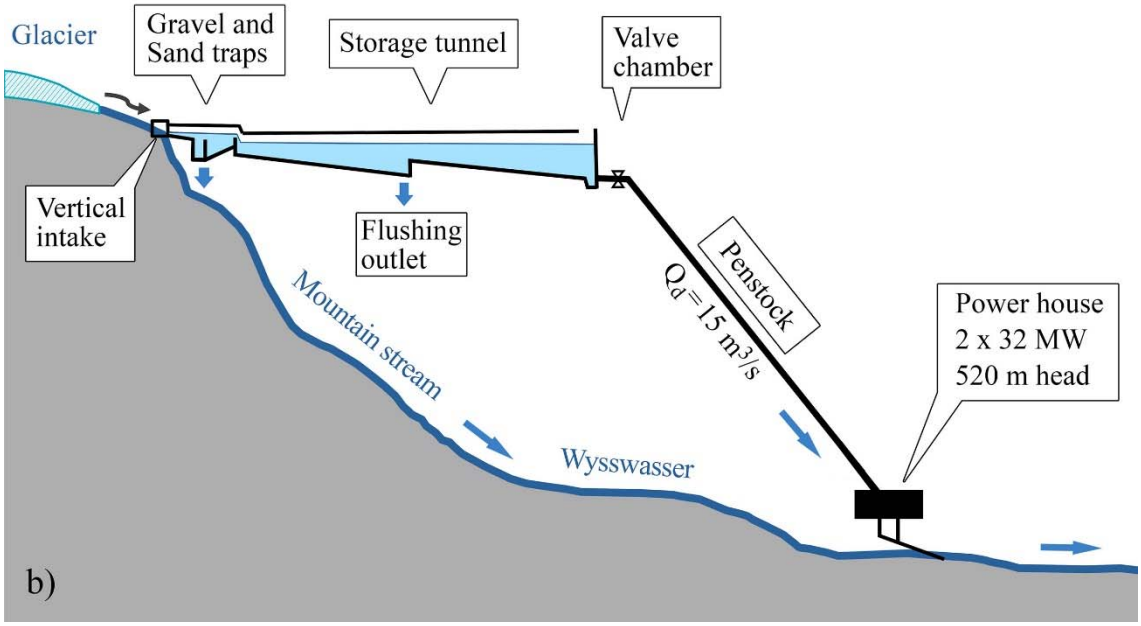

Figure B-1 Layout of the HPP Fieschertal in a) plan view (with location) and b) schematic longitudinal profile (based on construction drawings, GKW 1972).

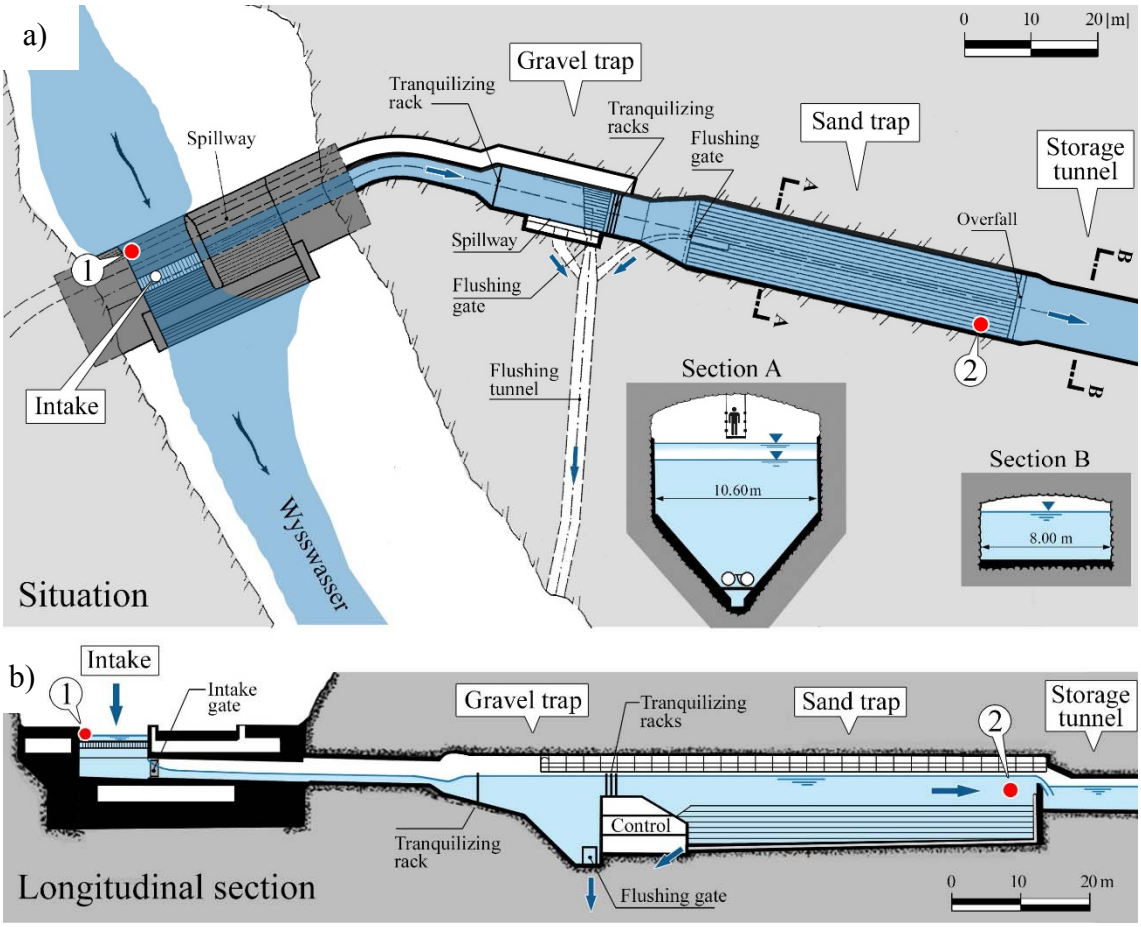

Figure B-2 Layout of the headworks of the HPP Fieschertal in a) plan view and b) longitudinal section (based on construction drawings, GKW 1972); (1) and (2) refer to installed turbidimeters.

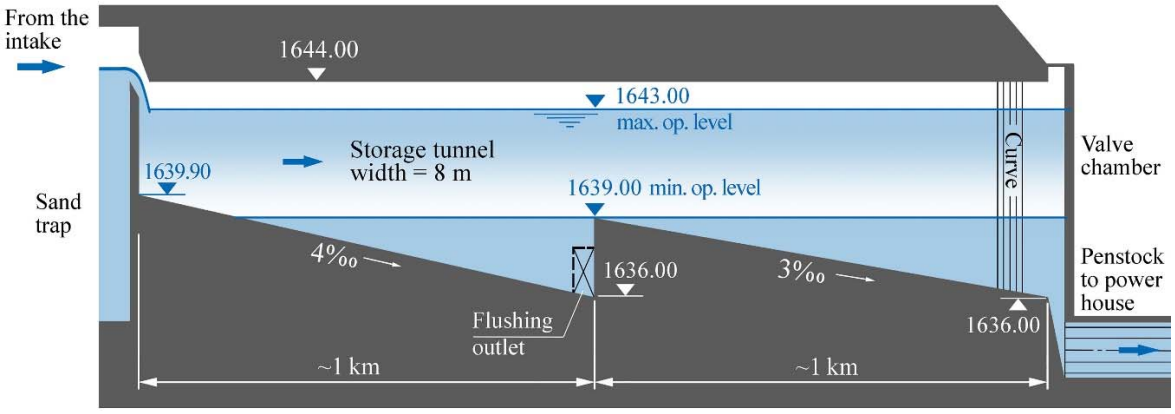

Figure B-3 Schematic longitudinal profile of the storage tunnel of HPP Fieschertal (based on construction drawings, GKW 1972).

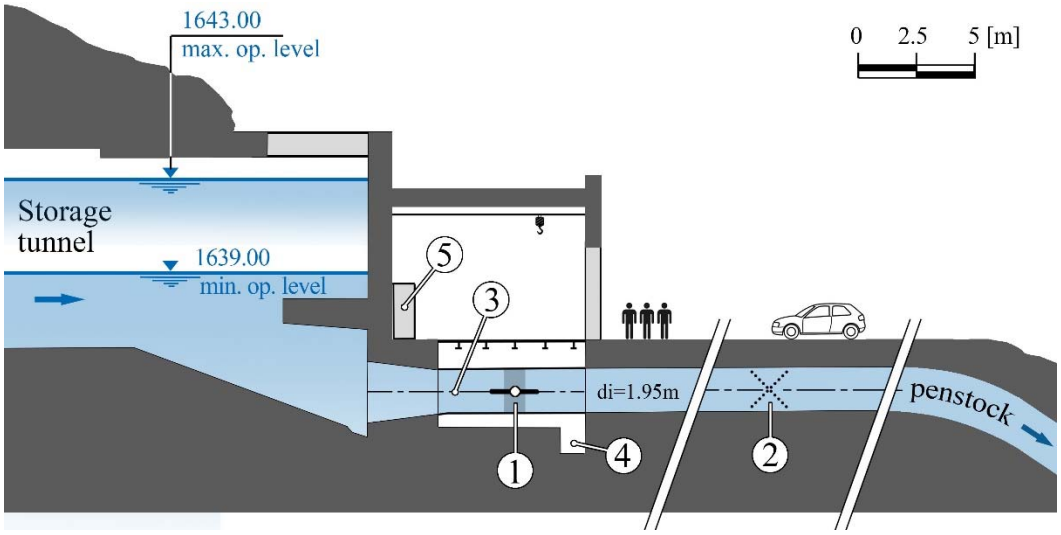

Figure B-4 Vertical section of valve chamber of HPP Fieschertal (based on construction drawings, GKW 1972); (1) butterfly valve, (2) ADM (item 7 in Table 3-1), (3) intake of the water sampling line, (4) pump sump and (5) controls and data acquisition.

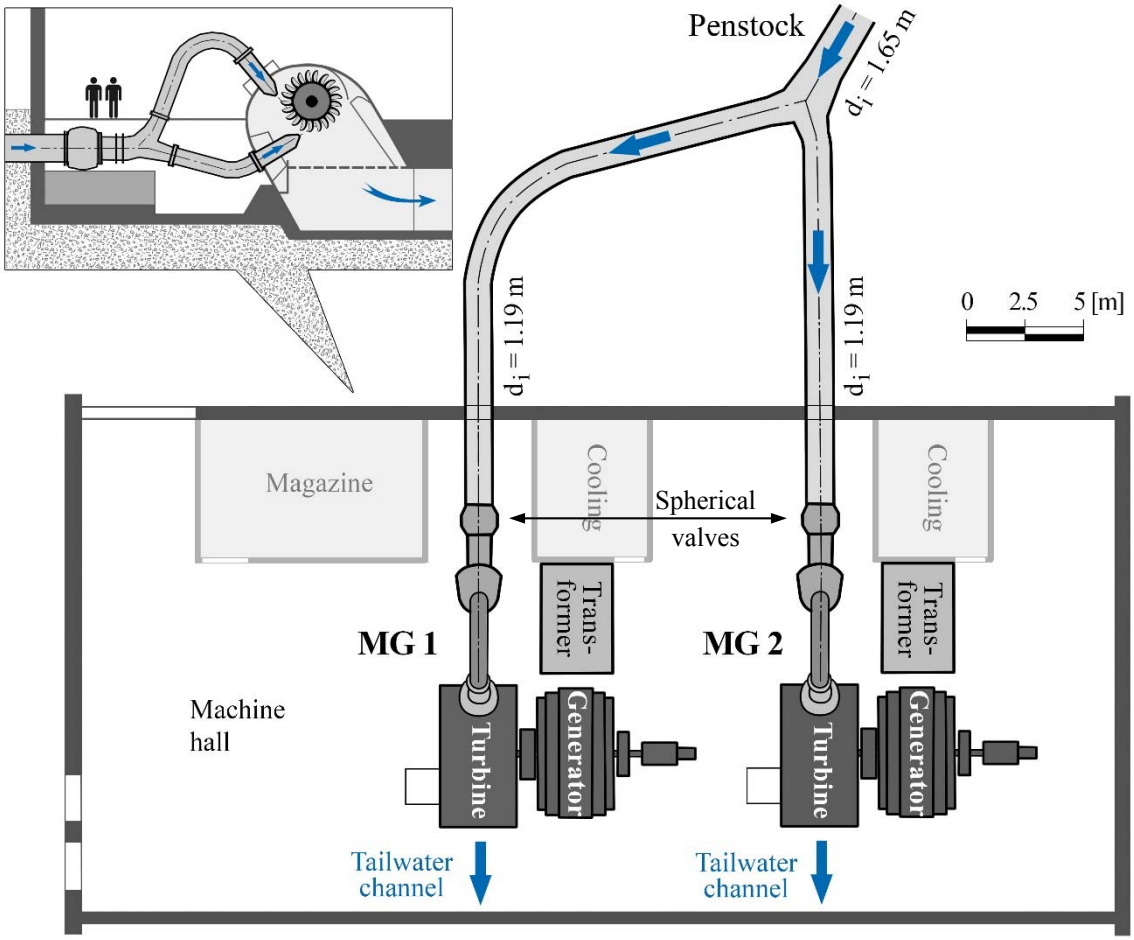

Figure B-5 Layout of the powerhouse and the Pelton turbines of HPP Fieschertal (based on construction drawings, GKW 1972).

APPENDIX C: SSM AT HPP FIESCHERTAL

C1 Overview on SSM field data

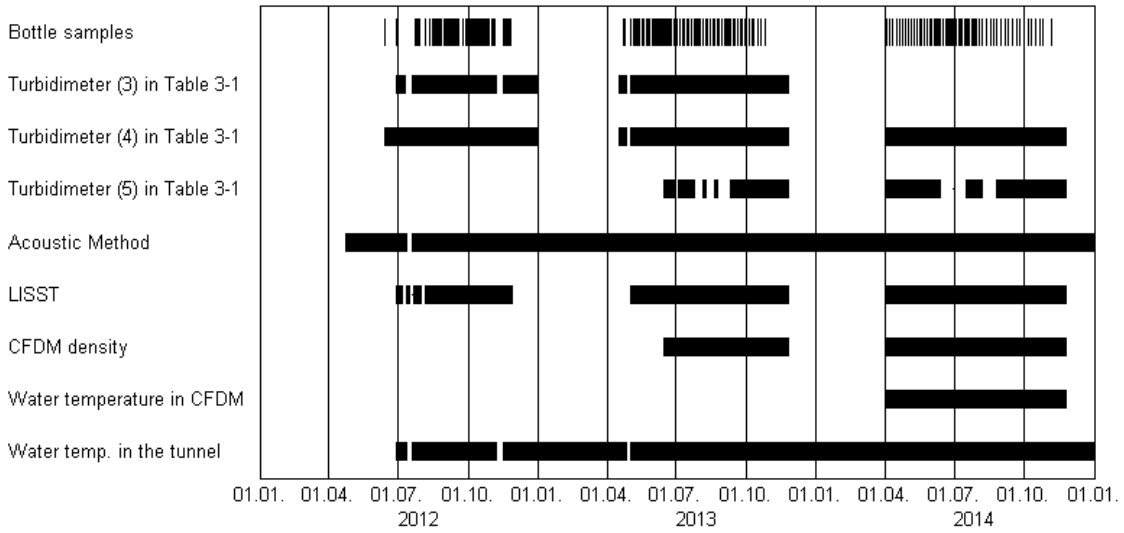

Figure C-1 Available SSM data acquired in the valve chamber of HPP Fieschertal from 2012 to 2014.

C2 General properties of sediment particles

Table C-1 Measured solid densities of sediment particles collected in the HPP Fieschertal.

Sample no.	Sampling location	Date [dd.mm. yyyy]	Provenience of sample material and sample type	Density $\rho_{s,i}$	$\frac{\rho_{s,i} - \rho_{s,m}}{\rho_{s,m}}$
i				[g/cm^3]	[%]
1	Valve chamber	13.06.2012	Deposits in the LISST bucket	2.767	+1.1
2	"	11.10.2013	Deposits on the LISST head	2.735	−0.1
3	"	11.10.2013	Deposits in the LISST bucket	2.743	+0.2
4	"	21.06.2014	Residues of 1 pumped bottle sample	2.708	−1.1
5	"	30.06.2014	Deposits in the LISST bucket	2.708	−1.1
6	"	17.07.2014	Deposits in the LISST bucket	2.706	−1.1
7	"	02.08.2014	Residues of 1 pumped bottle sample	2.709	−1.0
8	"	26.08.2014	Residues of 4 manual bottle samples	2.835	+3.6
9	"	09.09.2014	Residues of 1 pumped bottle sample	2.701	−1.3
10	Intake	29.07.2013	Residues of 3 pumped bottle samples	2.744	+0.3
11	"	23.05.2014	Residues of 3 pumped bottle samples	2.789	+1.9
12	Powerhouse	Jan. 2012	Deposits in tailwater channel	2.699	−1.4
Average of all samples			(σ = 0.037 g/cm^3 = 1.4% $\rho_{s,m}$)	$\rho_{s,m}$ = 2.737	±0.0
Average of samples excl. no. 8			(σ = 0.029 g/cm^3 = 1.1% $\rho_{s,m}$)	2.728	−0.3
Average density (rounded, with expanded uncertainty of ~ ±2 σ)				$\boldsymbol{\rho_s \approx 2.73 \pm 0.07}$	

Table C-2 Mineralogical composition of sediment particles in the HPP Fieschertal (μ and σ denote the average and the standard deviation of all samples, respectively).

Mineral	Mohs' hardness [-]	Mass fractions by weight [%] in sample no.								all samples	
		1	*2*	*3*	*4*	*5*	*6*	*7*	*8*	μ	σ
Quartz	7	37	25	40	47	20	20	28	34	31	10
Epidote	6.5	6	5	6	5	8	8	7	6	6	1
Feldspars (Na-Plagioclase and K-Feldspar)	6	36	31	33	37	41	41	39	39	37	4
Hornblende	5.5	0	2	2	1	1	0	1	1	1	1
Mica (Muscovite and Biotite)	2-3	14	22	14	10	24	24	21	17	18	5
Chlorite, Smectite and other soft minerals	< 3	7	15	6	1	7	7	4	3	6	4
Mass fraction with Mohs' hardness > 4.5 i.e. harder than the turbines' base material		79	63	80	90	69	69	75	80	**76**	8
Mass fraction with Mohs' hardness > 6.5 i.e. harder than the turbines' hard-coating; in the present study this corresponds to the quartz content		37	25	40	47	20	20	28	34	**31**	10

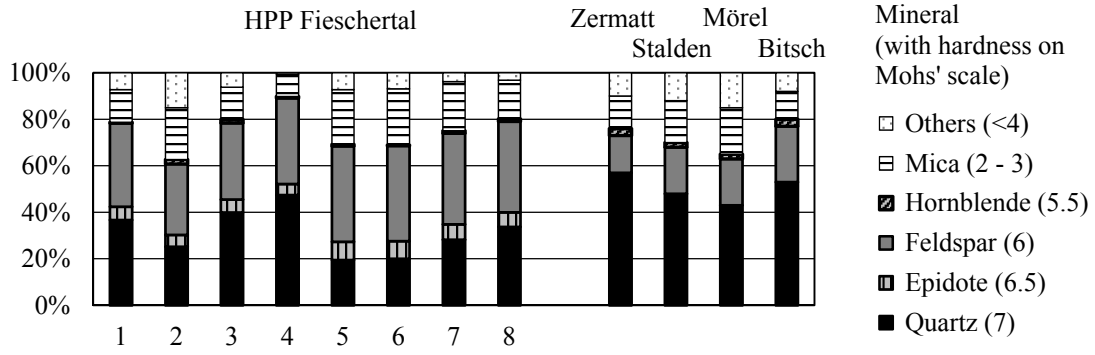

Figure C-2 Mineralogical composition of sediment particles in the HPP Fieschertal (samples 1 to 8 according to Table C-2) and in some other HPPs in the Canton of Valais (Krause & Grein 1996).

Table C-3 Description of samples for the analysis of the mineralogical composition in Table C-2.

Sample no.	Sampling location	Sample type and provenience	Date DD.MM.YYYY	Time CEST	d_{50} µm	SSC_G g/l
1	Valve chamber	Pumped bottle sample	11.08.2012	11:32	37	4.3
2	"	"	25.08.2012	22:11	15	1.1
3	"	"	27.08.2012	03:51	44	3.3
4	Powerhouse	Deposits from tailwater channel	Jan. 2012	As used in SSM lab. test		
5	"	Deposits from bucket of turbidimeter (fed by raw cooling water pumped from the tailwater channel)	26.04.2011	According to Abgottspon (2011)		
6	"		05.05.2011			
7	"		30.05.2011	"		
8	"	"	08.06.2011	"		

C3 Further results of SSM

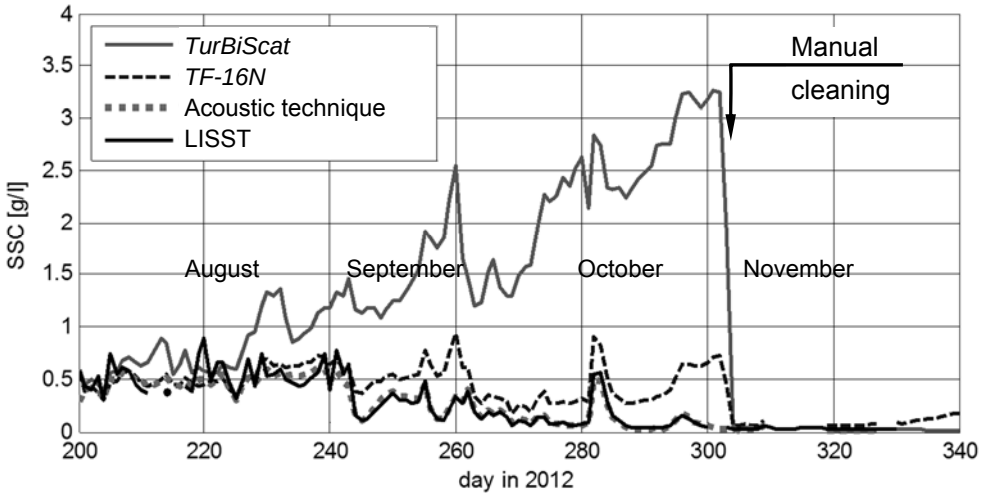

Figure C-3 Preliminary analysis of *SSC* time series showing that some turbidimeter signals were highly affected by fouling (Abgottspon *et al.* 2013a).

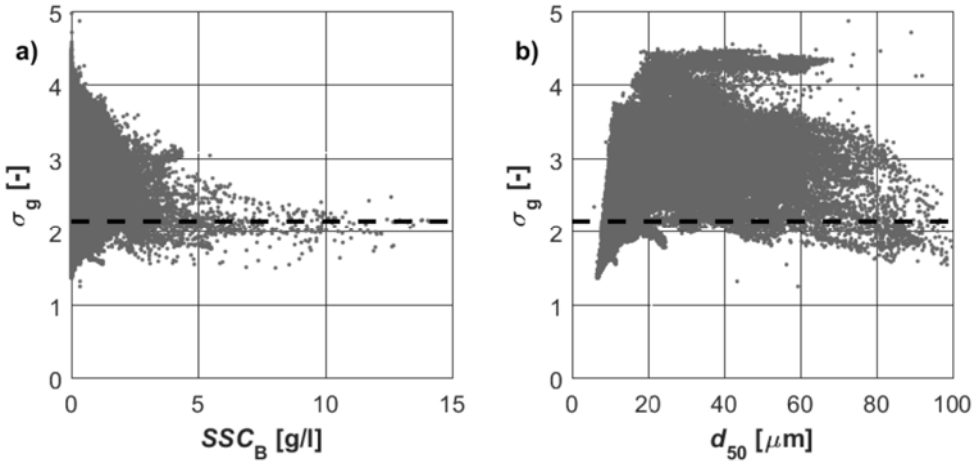

Figure C-4 Spreading σ_g of the PSDs measured in the valve chamber of HPP Fieschertal in 2012 to 2014 as a function of a) *SSC* and b) d_{50}; the dashed lines indicate the median of σ_g.

C4 Precipitation, *SSC* and d_{50} time series

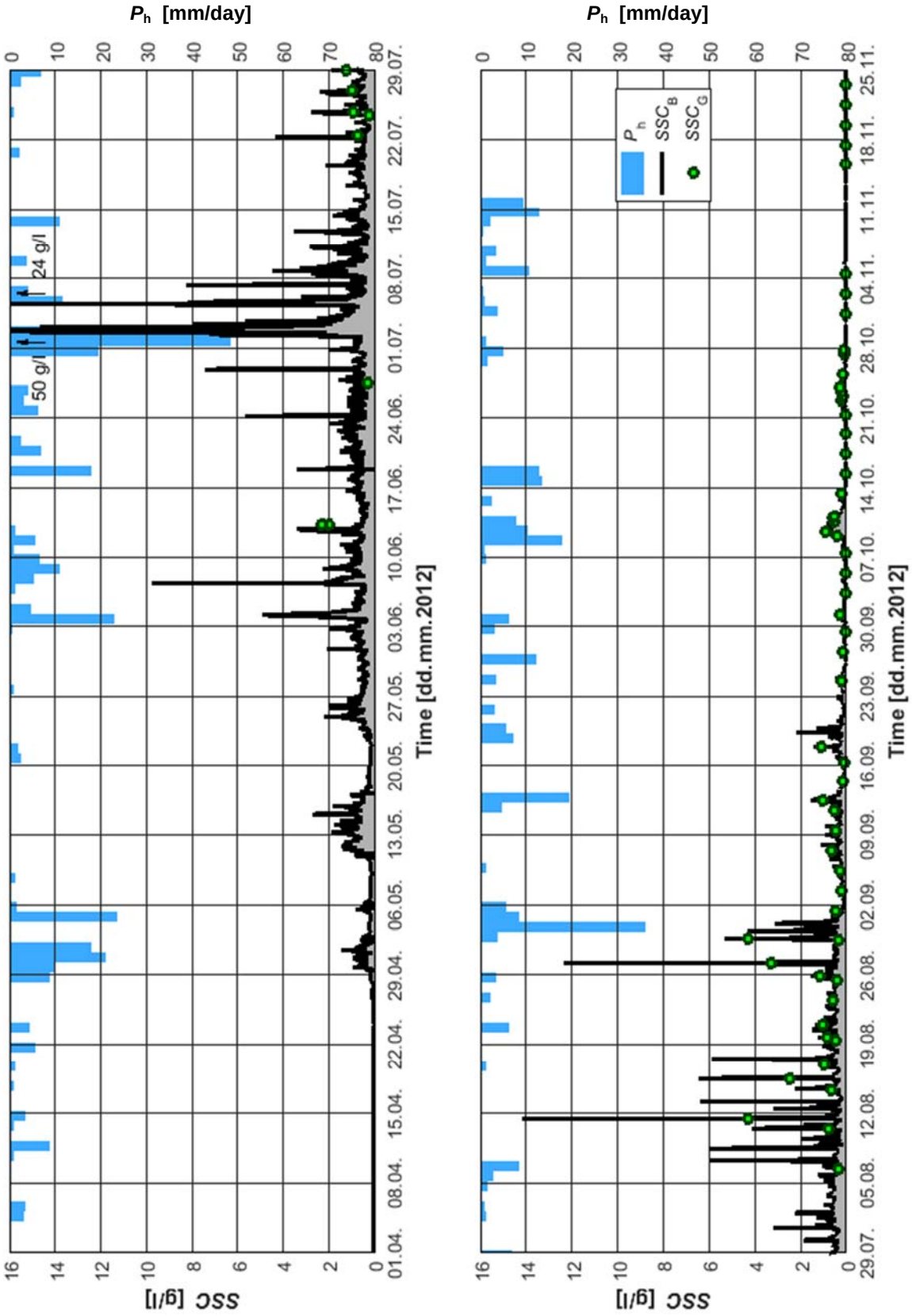

Figure C-5 Time series of *SSC* in the power waterway of HPP Fieschertal and of daily precipitation heights P_h in the village of Fieschertal (MeteoSwiss) during the sediment season 2012.

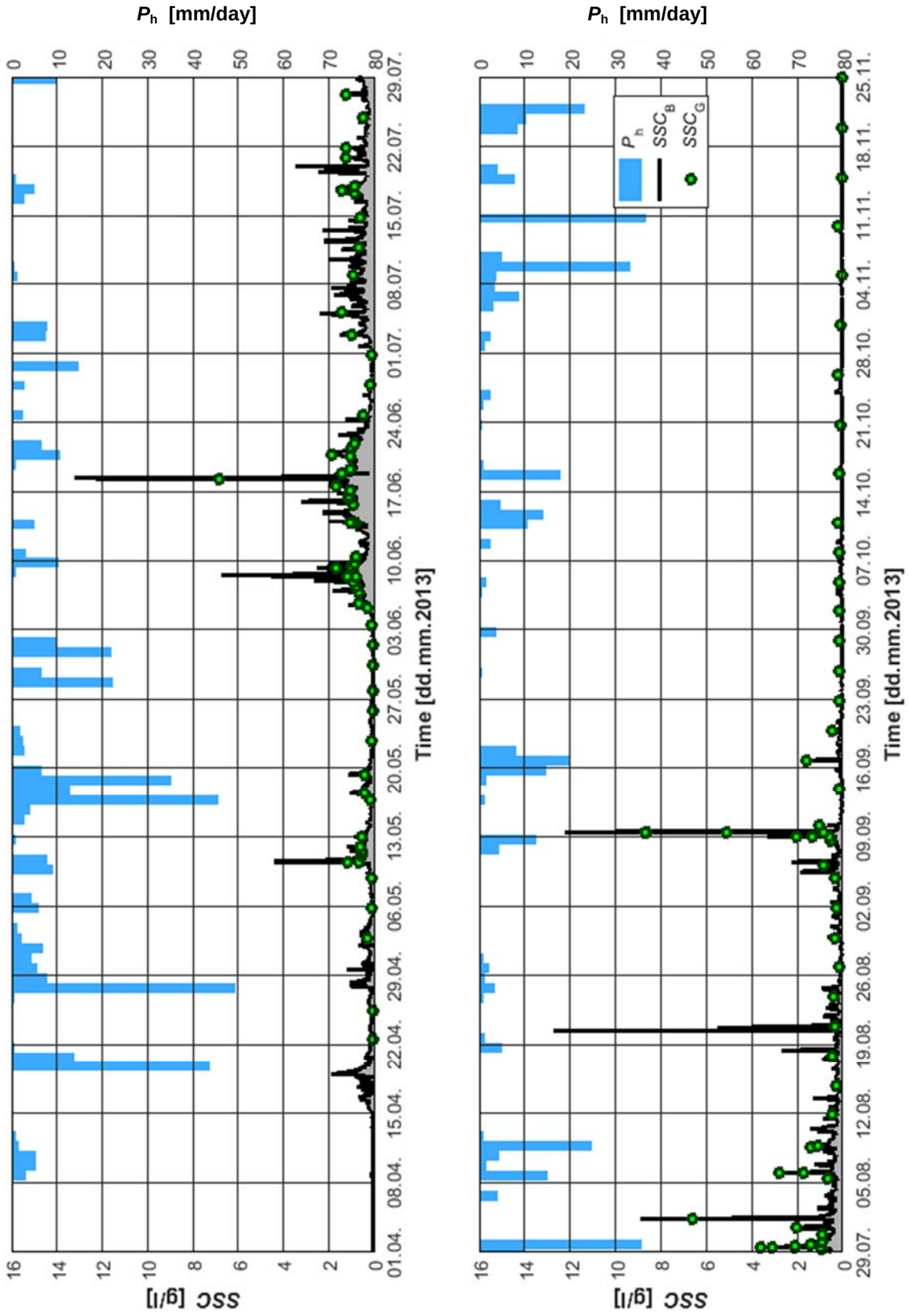

Figure C-6 Time series of *SSC* in the power waterway of HPP Fieschertal and of daily precipitation heights P_h in the village of Fieschertal (MeteoSwiss) during the sediment season 2013.

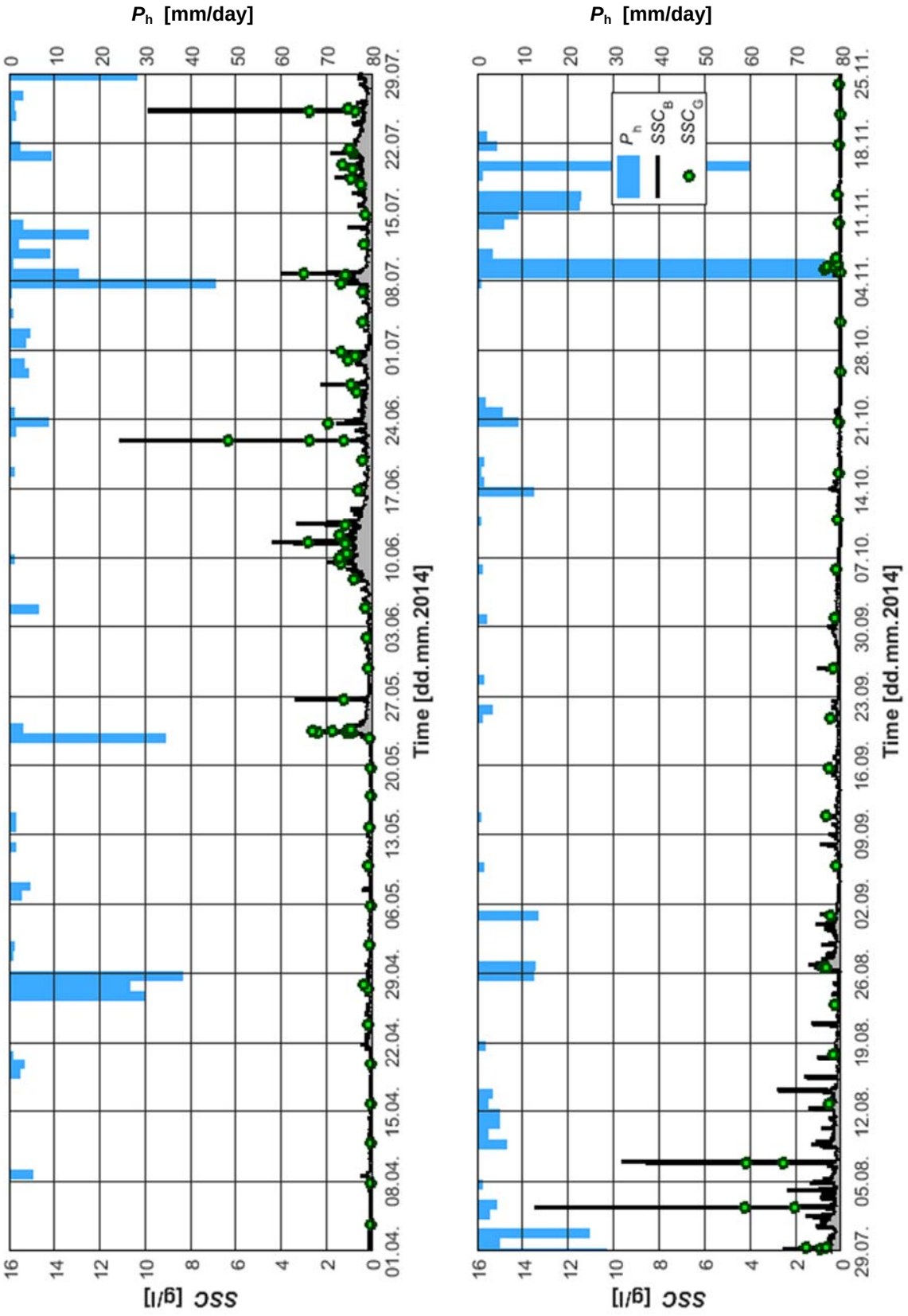

Figure C-7 Time series of *SSC* in the power waterway of HPP Fieschertal and of daily precipitation heights P_h in the village of Fieschertal (MeteoSwiss) during the sediment season 2014.

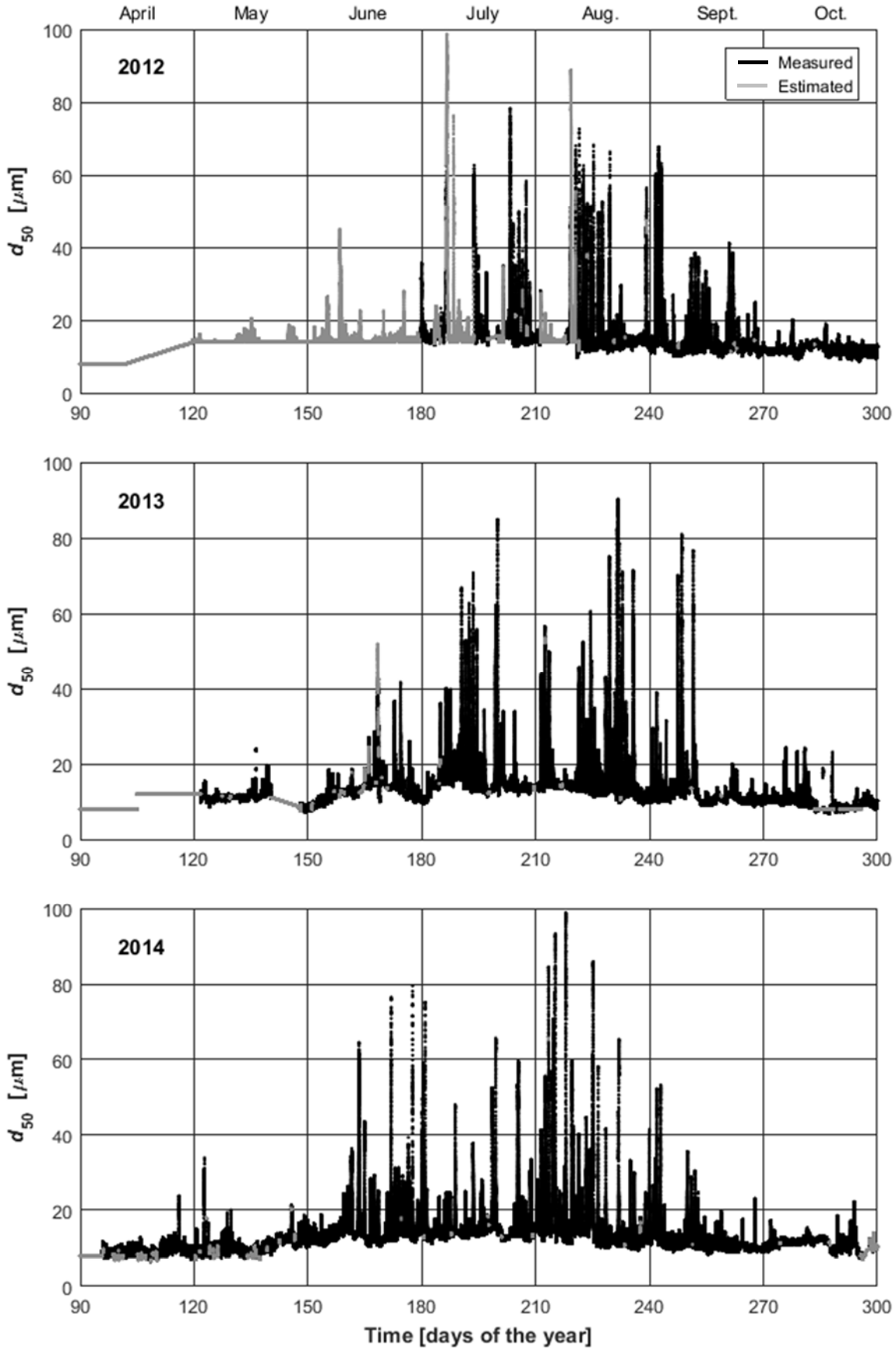

Figure C-8 Time series of d_{50} in the power waterway of HPP Fieschertal during the sediment seasons 2012 to 2014.

C5 Analysis of uncertainties

This part of the Appendix refers to various sources of uncertainty on annual *SSL* and *PL* as introduced in Figure 5-35 in Chapter 5.8. For each source of uncertainty j = 1 to 15, the expanded relative partial uncertainty $U_{2\sigma,j}$ is discussed and estimated on an annual basis. Then, the relative uncertainties on the annual *SSL* and *PL* are calculated.

C5.1 *Uncertainty on SSC reference measurements*

The primary reference values for *SSC*, i.e. SSC_G, are affected by uncertainty due to (i) the weighing and (ii) potential deviations between the water in the bottle samples and that measured by the other SSM instruments. The contribution of (i) was quantified as follows: With a sample volume of ~0.5 l, the absolute expanded uncertainty of gravimetric *SSC* was <0.01 g/l. This corresponds to < 10% for *SSC* > 0.1 g/l, and < 2% for *SSC* > 0.5 g/l. The effect of (ii) was small except for periods when coarser particles were present and *SSC* quickly changed due to the mixing and settling processes in the bucket from where the samples were pumped. The uncertainty due to (ii) was limited by considering only $SSC_G \leq 4$ g/l as references. The expanded relative uncertainty on reference *SSC* was estimated as $U_{2\sigma,1} \approx 4\%$ on temporal average.

C5.2 *Uncertainty in indirect in-situ SSC measurements*

For the uncertainty in *SSL* and *PL*, the time-averaged differences between the indirectly measured SSC_B and gravimetric reference SSC_G are relevant, particularly in the range below 1 g/l. In this range, *SSC* was mostly measured by LISST and otherwise by turbidimeters or the acoustic system. The average differences between indirectly measured *SSC* and SSC_G were analysed in Table 5-1 (μ-values of $SSC_i - SSC_G$). For the combined use of instruments with *SSC* mainly ≤ 1 g/l, the standard deviation σ of the average *SSC* difference was estimated as 0.06 g/l, resulting in 0.12 g/l at 95% confidence level (2σ). With the average *SSC* of ~0.5 g/l (Section 5.6.3), the expanded relative uncertainty on *SSC* due to the indirect *in-situ* measurements was estimated as $U_{2\sigma,2} \approx \pm 24\%$.

C5.3 *Uncertainty on measured SSC due to spatial SSC gradients*

The *SSC* at the sampling pipe inlet may deviate from the average *SSC* in the penstock cross-section due to transversal and mainly vertical gradients.

At a given elevation in the penstock cross-section, the transversal *SSC* distribution is expected to be quite uniform (Section 2.1.4.3), except for the regions very close to the walls. It is estimated that the 10 cm-protrusion of the sampling pipe into the penstock (detail in

Fig. 3-7) contributed to reduce deviation of the *SSC* at the sampling pipe inlet from the average value in the penstock at the sampling elevation.

In quasi-horizontal pipes, vertical *SSC* gradients are generally higher than transversal gradients. To assess the extent of the vertical *SSC* gradient in the penstock in the valve chamber, hydraulic parameters and the Rouse number Z (Eq. 2-12) were calculated for partial to full load operating conditions and a range of particle diameters (Tables C-4 and C-5). The vertical *SSC* gradient is more pronounced at high Z. With sampling at the elevation of the penstock's centre line, a vertical *SSC* gradient does not necessarily cause a large deviation of the local *SSC* from the cross-section averaged *SSC*, because high *SSC* in the lower part of the cross-section are partly compensated by lower *SSC* in the upper part. Due to a lack of specific literature on vertical *SSC* gradients in quasi-horizontal pipes with silt and fine sand particles in the relevant *SSC* ranges, the vertical *SSC* gradient was estimated based on Rouse-type profiles (Section 2.1.4.3). For the lowest 5% of the water column the reference *SSC* at 5% above the bed was taken as an approximation. This estimate indicated that the *SSC* at the elevation of the penstock axis is <0.1%, ~2% or 15% lower than the cross-section averaged *SSC* for $Z = 0.03$, 0.15 or 0.43, respectively. Hence the *SSC* sampling error due to the vertical *SSC* gradient is estimated as follows for various hydraulic conditions and particle diameters *d* (Table C-5):

- In typical summer conditions (both MGs running at full load and transport of silt particles with $d < 60$ µm), the error is negligible (<0.1% with $Z < 0.03$).
- For $d < 150$ µm at full-load operation of both MGs, for $d < 100$ µm at full-load operation of one MG, or for $d < 75$ µm at half-load operation of one MG ($Z < 0.15$), the error is estimated ≤ 2%.
- For medium sand particles $d = 300$ µm at full-load operation of both MGs, the error may amount to 15% ($Z = 0.43$).
- For $d = 300$ µm at discharges below Q_d, the error may be larger.

Hence the *SSC* at the sampling pipe inlet is usually well-representative for the cross-section averaged *SSC* in the penstock. When sand is transported, which is particularly relevant for turbine erosion, the cross-section averaged *SSC* is temporarily underestimated by measurements at the sampling pipe inlet. With fine sand making up < 15% of the annual *SSL* (Section 5.6.2) and assuming that the sampling error due to vertical *SSC* gradients is < 20% for fine sand, the relative uncertainty on *SSC* due to mainly vertical gradients at the sampling location is estimated as $U_{2\sigma,3} \approx \pm 3\%$ on annual average.

Table C-4 Hydraulic conditions in the penstock in the valve chamber of HPP Fieschertal.

Operation mode	Discharge Q [m³/s]	Average velocity U [m/s]	Reynolds number Re [-]	Energy line slope S_e [‰]	Wall shear stress τ_b [Pa]	Friction velocity U_* [m/s]
1 MG at half load	3.75	1.26	$1.8 \cdot 10^6$	0.4	2	0.05
1 MG at full load	7.5	2.51	$3.8 \cdot 10^6$	1.6	8	0.09
2 MGs at full load	15	5.02	$7.5 \cdot 10^6$	5.9	28	0.17

Table C-5 Rouse numbers Z in the penstock in the valve chamber of HPP Fieschertal.

Particle diameter d [µm]	Particle size range	Settling velocity Eq. (2-6) $v_{s,\infty}$ [mm/s]	Rouse number Z [-] according to Eq. (2-12) with assumption $\beta = 1$		
			1 MG at half load	1 MG at full load	2 MGs at full load
10	medium silt	0.1	0.003	0.002	0.001
20	coarse …	0.2	0.011	0.006	0.003
60	… silt	1.9	0.099	0.052	0.027
100	fine …	4.8	0.257 §	0.135	0.070
150		10	0.530 #	0.278 §	0.145
200	… sand	16	0.855 #	0.449 #	0.234 §
250	medium …	23	1.210 #	0.636 #	0.332 §
300 *	… sand ...	30	1.579 #	0.829 #	0.432 #

§ For $Z \geq 0.15$, the sampling error due to vertical *SSC* gradients is estimated > 2%.

For $Z \geq 0.43$, the sampling error due to vertical *SSC* gradients is estimated > 15%.

* Upper limit of particle diameters expected in the penstock (usual limit grain size for sand trap design).

C5.4 *Uncertainty on SSC due to non-isokinetic sampling*

The flow velocity in the inlet of the sampling pipe ranged from 0.3 to 0.5 m/s depending on the tunnel water level (with usual degree of openings of the outlet valves on the sampling pipe), whereas the cross-section averaged flow velocity in the penstock at the sampling location was $U = 1$ to 5 m/s depending in the turbine discharge (Table C-4). With the flow velocity in the sampling pipe inlet being lower than that of the approach flow, *SSC* is overestimated for larger particles (Section 2.2.1.1).

The orientation of the sampling pipe inlet perpendicular to the axis of the penstock (detail in Fig. 3-7) may also give rise to a systematic deviation of the *SSC* in the sampling pipe from the *SSC* in the penstock upstream of the sampling pipe inlet. Such deviations from isokinetic sampling conditions are more pronounced with larger particles (fine sand) and are assumed to be negligible with the usually prevailing fine particles (medium silt).

The *SSC* overestimations due to non-isokinetic sampling are partly compensated by the underestimations due to the vertical gradients discussed in the previous Section. The

additional relative uncertaintiy on *SSC* due to non-isokinetic sampling is estimated as $U_{2\sigma,4} \approx \pm 5\%$ on annual average.

C5.5 *Uncertainty on SSC among MGs*

The *SSC* may differ among the MGs and from the value in the penstock if the particle flux at the penstock bifurcation is not split-up according to the flow rates (particle segregation). In HPP Fieschertal, the branch pipe is symmetrical (Fig. B-5) and none of the MGs is known to suffer systematically from higher erosion. However, secondary currents due to upstream bends in the penstock may cause differences in the *SSC* among the MGs when coarser particles are transported. With fine sand making up < 15% of the annual *SSL* (Section 5.6.2) and assuming that the annual fine sand loads per MG differ by 20%, the relative uncertainties on *SSC* due to differences among the MGs are estimated as $U_{2\sigma,5} \approx \pm 3\%$ on annual average.

C5.6 *Uncertainty on discharges*

The discharge measurement uncertainty of an ADM with four crossed paths in a penstock, located far away from its inlet, as for Q_4 in the present case, is typically less than ±2%. For the *SSL* per turbine, the turbine discharges were obtained from the discharge measured by the ADM in the penstock and the ratio of the electric outputs of the MGs. The relative uncertainty on the turbine discharges is estimated as $U_{2\sigma,6} = \pm 3\%$.

C5.7 *Uncertainty on PL due to k_{hardness}*

The fraction of hard minerals and thus k_{hardness} for the erosion of base material was 76% on average and varied by ±16% (2σ, Section 5.1.1). The expanded relative uncertainty on *PL* due to k_{hardness} is estimated as $U_{2\sigma,7} = \pm 16\% / 76\% = \pm 21\%$.

C5.8 *Uncertainty on PL due to k_{shape}*

With the current state of IEC 62364 (2013), the coefficient k_{shape} for the effect of the particle shape (angularity) on erosion is set to 1 or 2 for rounded or angular particles, respectively. This is based on a qualitative interpretation of microscopic images, implying a quite high uncertainty. With angular particles as in the present case, the relative uncertainty on the *PL* due to k_{shape} is roughly estimated as $U_{2\sigma,8} \approx \pm 25\%$.

C5.9 *Uncertainty of PSD reference measurements*

Reference particle sizes are based on image analysis (Section 3.2.2). The measurement uncertainty on the median volume-equivalent sphere diameter $d_{\text{es},50}$ is relatively low for

close-to-spherical particles with a narrow PSD. For non-spherical particles as in the present case, the *c*/*b*-ratio of the particles (generally not visible on the image) needs to be estimated. In case of wide PSDs, the relative uncertainty increases due to detection problems and limited resolution at fine particles as well as due to the low number of large particles within the image frame. For the particle shape mix in Fieschertal, the uncertainty on the reference particle sizes is estimated as $U_{2\sigma,9} \approx \pm 10\%$ on temporal average and for the particle size range of interest.

C5.10 *Uncertainty of indirect in-situ PSD measurements*

Particle sizes obtained from LISST deviate from the volume-equivalent sphere diameter d_{es} of the primary particles due to (i) non-spherical particle shapes, (ii) flocculation and (iii) fouling.

(i) Based on the comparison of PSD from LISST and image analyses in the laboratory (Section 4.1.2) and considering the particle shapes at HPP Fieschertal (mainly angular and < 39% of fine sheet silicate particles), the $d_{es,50}$ are estimated to be ~35% to 50% smaller than the d_{50} obtained from LISST, depending on the variations of particle shapes (e.g. mica content). For coarser particles (fine sand) which tend to have closer-to-spherical particle shapes and are more relevant for turbine erosion, the bias und uncertainty are expected to be smaller.

(ii) Flocculation might have occurred when there were fine particles (Section 2.1.2.1) and when the water remained in the storage tunnel for several days, as typically in autumns. The floc size measured by LISST is larger than the size of the primary particles. However, this type of overestimation was of no concern when larger, non-cohesive particles were transported, e.g. in re-suspension events which are particularly important with respect to turbine erosion.

(iii) Moreover, fouling might have caused temporary overestimation of primary particles sizes, because agglomerated particles may have stuck on the LISST's measuring windows and effects of fouling were not fully removable in the data treatment.

Due to these three effects, the equivalent sphere diameters of the primary particles (in particular < 60 µm) were probably smaller than those obtained from the LISST measurements. This bias was not compensated because it was not quantitatively known and varies in time. Hence all particle-size related quantities (d_{50}, k_{size}, *PL* with $k_{size} \neq 1$) reported in this thesis refer to apparent particle sizes from LISST (plausible *BVC* using IMR). The relative uncertainty on the particle sizes in the field measurements is estimated as $U_{2\sigma,10} \approx \pm 15\%$.

C5.11 *Effects of spatial PSD gradients in the sampling cross-section*

Similarly to *SSC* (Section C5.3) the PSD at the sampling pipe inlet is generally well-representative for the PSD averaged over the penstock cross-section. However, when fine sand is transported preferrably in the lower part of the cross-section, the cross-section averaged PSD is temporarily underestimated. Due to a lack of specific literature, the sampling error due to vertical particle-size gradients is roughly estimated as 20% for fine sand. With fine sand making up < 15% of the annual *SSL* (Section 5.6.2), the relative uncertainty on particle sizes due to vertical gradients is estimated as $U_{2\sigma,11} \approx \pm 3\%$ on annual average.

C5.12 *Effect of non-isokinetic sampling on PSD*

Due to non-isokinetic sampling, the particle sizes of larger particles are expected to be overestimated similarly to the *SSC* (Section C5.4). Such PSD overestimations are partly compensated by the underestimations due to the vertical gradients discussed in the previous Section. The additional relative uncertaintiy on particle sizes due to non-isokinetic sampling is estimated as $U_{2\sigma,12} \approx \pm 5\%$ on annual average.

C5.13 *Differences in PSD among MGs*

Similarly to *SSC*, the PSD in the turbine water may differ among individual turbines due to particle segregation at the penstock bifurcation (Section C5.5). This potential effect is more pronounced with larger particles. With fine sand making up < 15% of the annual *SSL* (Section 5.6.2) and assuming that the annual fine sand loads per MG differ by less than 20%, the relative uncertainties on particle sizes due to differences among the MGs are estimated as $U_{2\sigma,13} \approx \pm 3\%$ on annual average.

C5.14 *Uncertainty due to invalid or missing measurement data*

Outputs of the instruments were temporarily implausible or invalid, e.g. when the sampling arrangement was clogged or the data acquisition system was disturbed. Such parts of the *SSC* and *PSD* time series were discarded based on visual comparisons with time series obtained from the various employed techniques.

Due to the use of several instruments, at least one valid signal for *SSC* time series was always available. With respect to PSD, LISST data were not always available; hence d_{50} and fraction-wise *SSC* were interpolated or estimated in those periods (Section 3.4.5). With this data treatment, the relative uncertainty $U_{2\sigma,14}$ due to implausible, invalid, or missing measurement data is estimated to be negligible for *SSL* and *PL* with $k_{size} = 1$, and < 20% for annual *PL* with $k_{size} \neq 1$ (due to the higher uncertainty in estimated d_{50}).

C5.15 *Uncertainty on PL due to the calculation of k_{size}*

With wide PSDs, *PL* with $k_{size} \neq 1$ may be inaccurate if calculated based on d_{50} only. The calculation approach adopted in this study, which is based on fraction-wise *SSC* and k_{size}-values for each size class, contributed to reduce this error ($U_{2\sigma,15} < 5\%$).

C5.16 *Uncertainties on annual SSL and PL*

The expanded relative partial uncertainties $U_{2\sigma,j}$ estimated in the Sections C5.1 to C5.15 are summarized in Table C-6. The uncertainty on time measurements (Δt) is negligible and was hence not listed.

As seen from Equations (3-4) and (3-5), the *SSL* and *PL* are the products of the involved variables. The annual *SSL* and *PL* are affected by the uncertainties on these factors (propagation of uncertainty). Assuming that the factors are independent, the total relative uncertainties on the annual *SSL* and *PL* were calculated using Equation C-1:

$$U_{2\sigma} = \sqrt{\sum_j U_{2\sigma,j}{}^2} \qquad [\%] \qquad \text{(C-1)}$$

Table C-6 Analysis of uncertainties on annual *SSL* and *PL* in HPP Fieschertal.

Partial uncertainty		Expanded relative partial uncertainties $U_{2\sigma,j}$ [%]			
No. *j*	Short description	*SSL* in penstock	*SSL* per MG	*PL* with $k_{size} = 1$	*PL* with $k_{size} \neq 1$
1	Reference *SSC*	±4	±4	±4	±4
2	Indirect *SSC* measurements	±24	±24	±24	±24
3	Spatial gradients in *SSC*	±3	±3	±3	±3
4	Non-isokinetic *SSC* sampling	±5	±5	±5	±5
5	*SSC* differences among MGs	-	±3	±3	±3
6	Discharge	±2	±3	-	-
7	Particle hardness	-	-	±21	±21
8	Particle shape	-	-	±25	±25
9	Reference PSD	-	-	-	±10
10	Indirect PSD measurements	-	-	-	±15
11	Spatial gradients in PSD	-	-	-	±3
12	Non-isokinetic PSD sampling	-	-	-	±5
13	PSD differences among MGs	-	-	-	±3
14	Invalid and missing data	±1	±1	±1	±20
15	Calculation of k_{size}	-	-	-	±5
Total expanded relative uncertainty $U_{2\sigma}$		±25%	±25%	±41%	±50%

APPENDIX D: EROSION MONITORING AT HPP FIESCHERTAL

D1 Coating thickness (*CT*) measurements

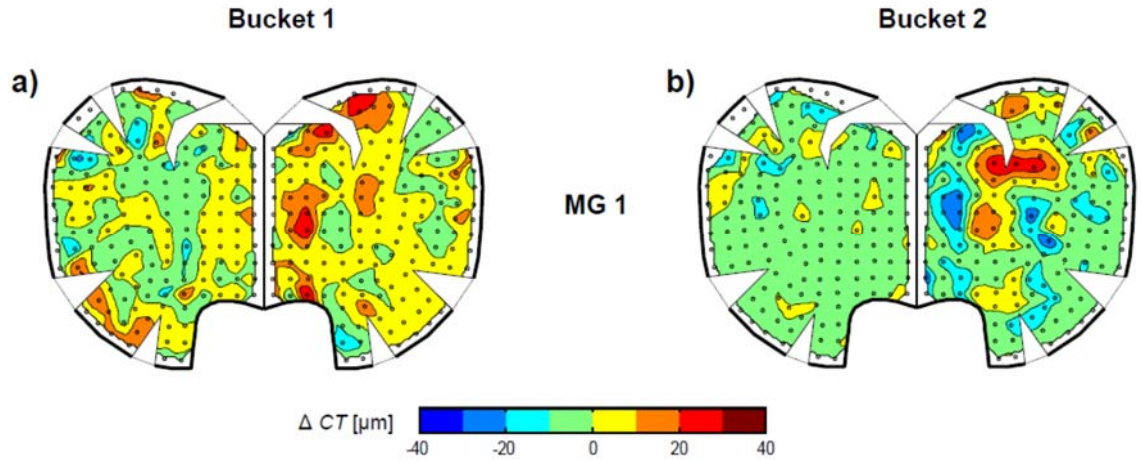

Figure D-1 Maps of *CT* differences in two buckets of MG 1 evaluated from the measurements in May 2014 vs. Nov. 2013, i.e. a period with negligible *SSL* and *PL*.

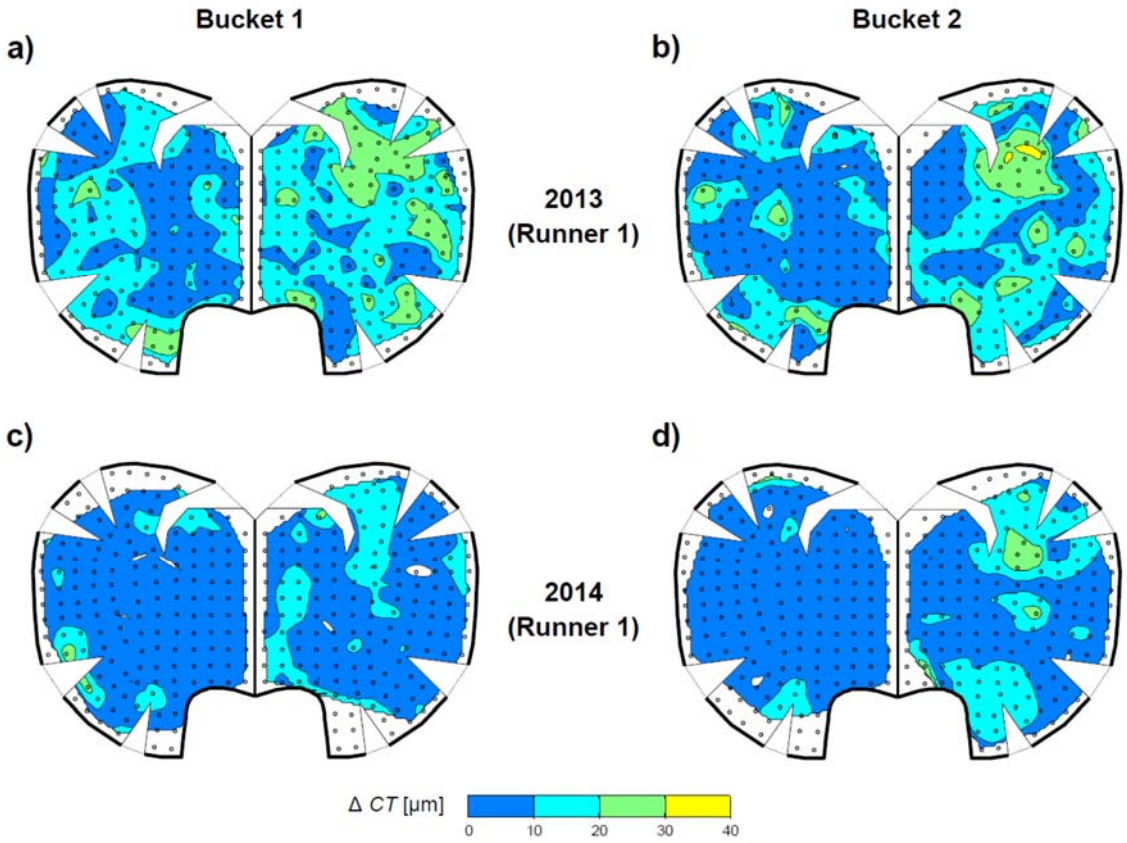

Figure D-2 Maps of *CT* differences in two buckets of MG 1 in the sediment seasons 2013 and 2014.

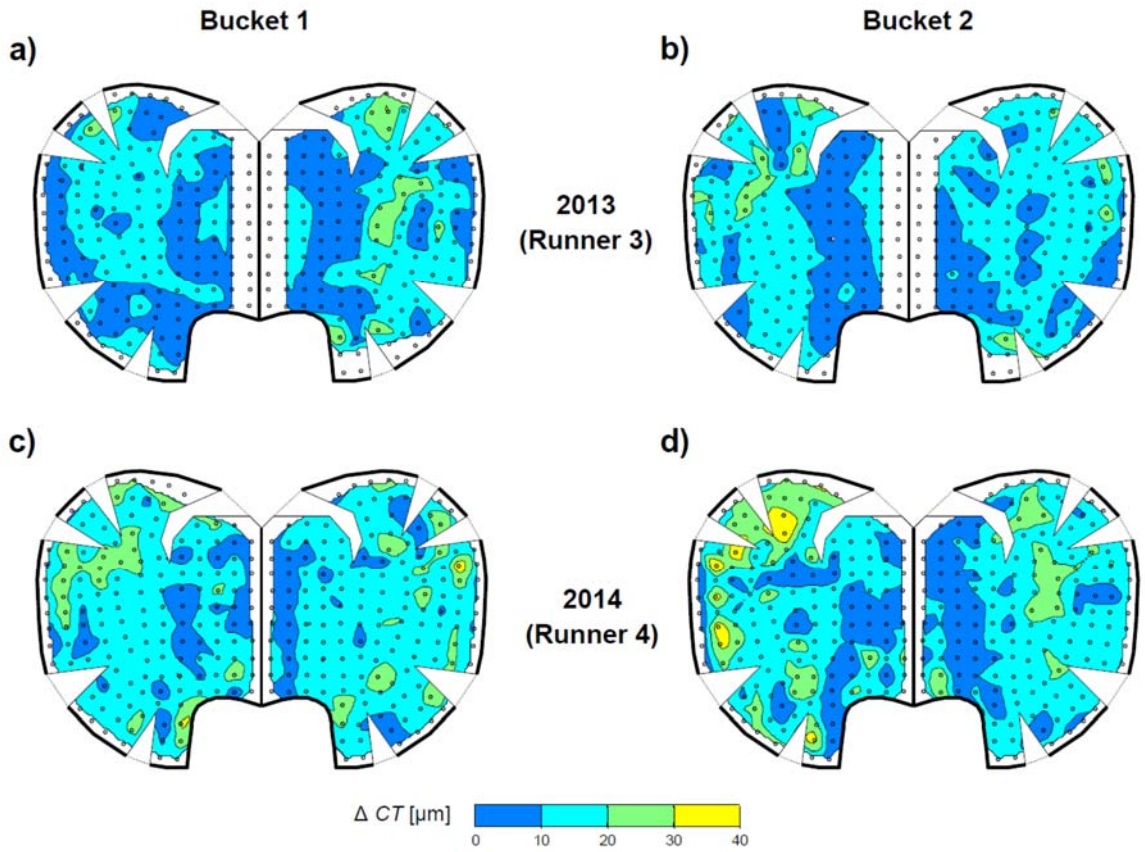

Figure D-3 Maps of *CT* differences in two buckets of MG 2 in the sediment seasons 2013 and 2014.

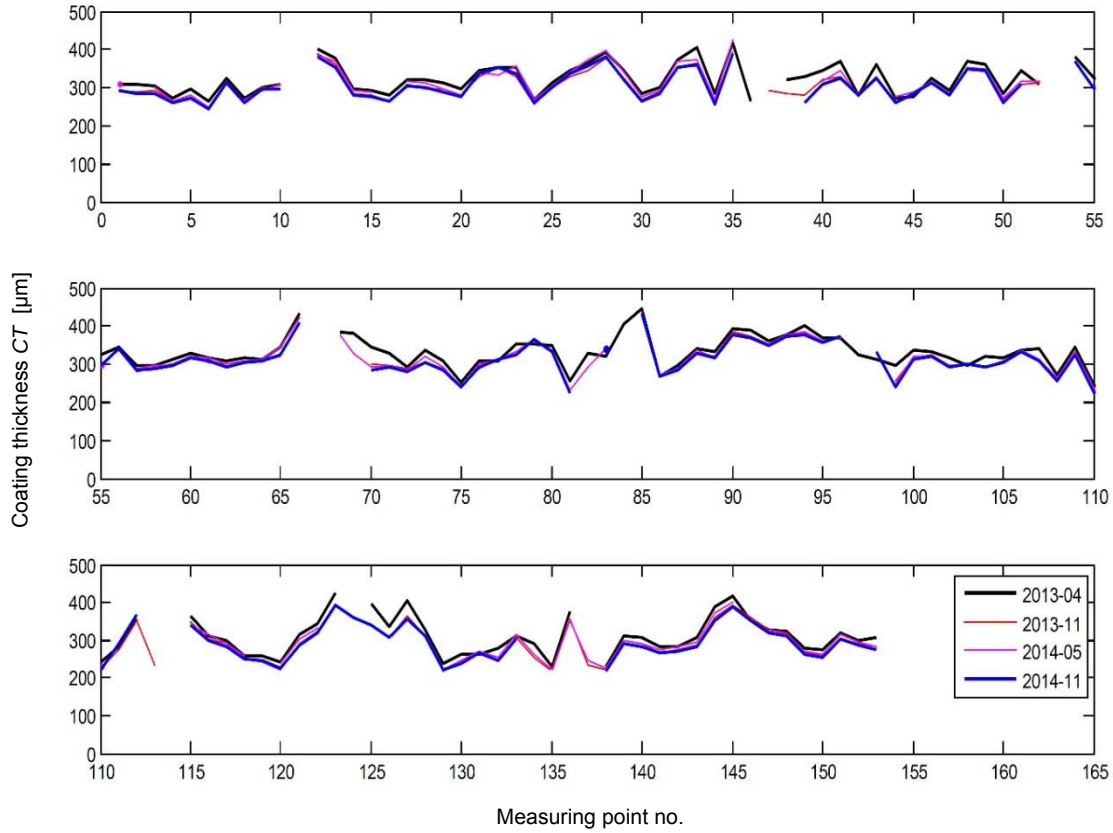

Figure D-4 *CT* at the template's measuring points in the right half of bucket no. 1 in MG 1 at four dates.

D2 Optical 3D-survey (digitizing)

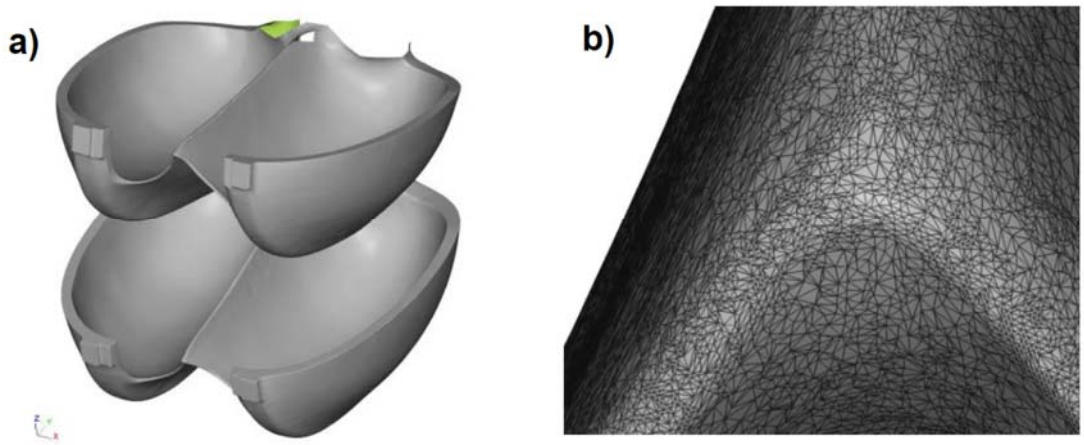

Figure D-5 3D-model of two Pelton buckets of a slightly eroded runner and b) detail of the surface mesh in the region of the splitter tip.

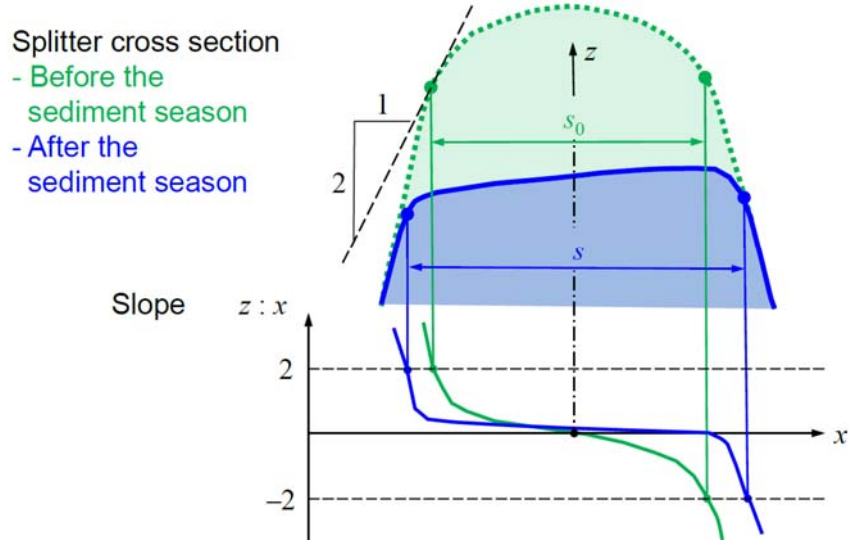

Figure D-6 Determination of the splitter width *s* based on a threshold value of the slope on both sides of the splitter in a cross-section (modified from Abgottspon *et al.* 2013b).

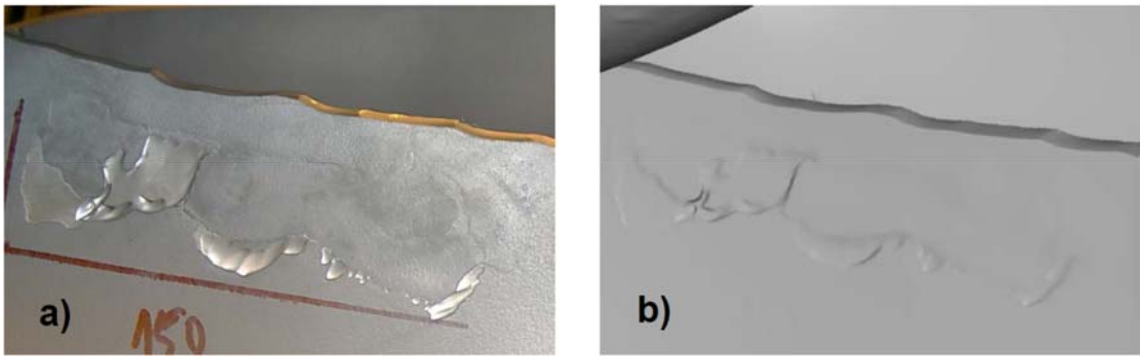

Figure D-7 Splitter of a Pelton runner with local erosion of coating and erosion of base material on its crest and the flanks (bucket no. 1 of MG 2 on August 14, 2012): a) photograph and b) digital 3D-model showing the erosion features. Note that the runner had undergone several on-site revisions before the sediment season 2012 including the major flood event.

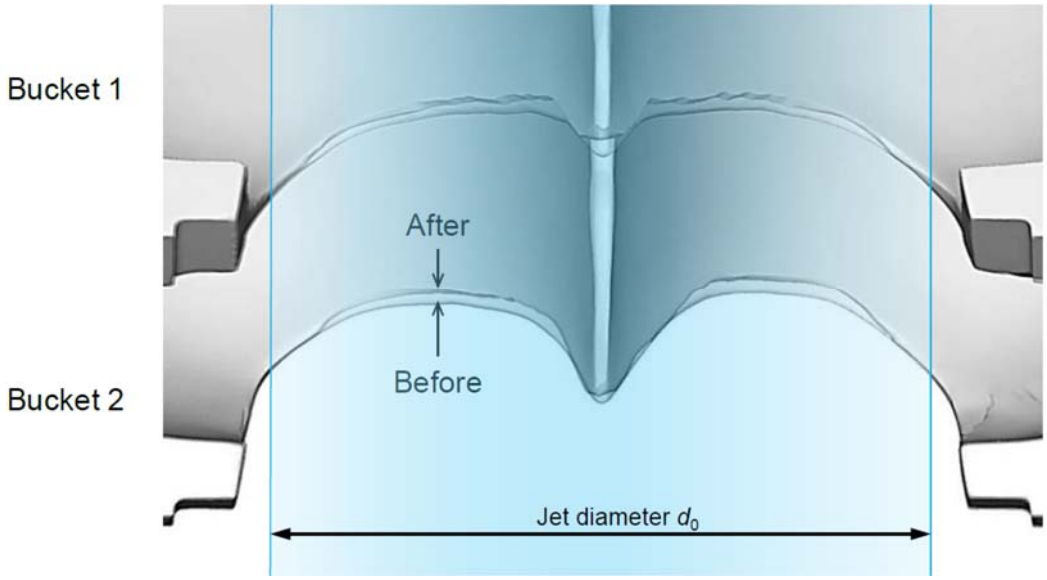

Figure D-8 Overlay of the topview geometries of the cut-outs and splitter tips of two buckets of MG 2 in April and August 2012 (modified from Abgottspon *et al.* 2016b).

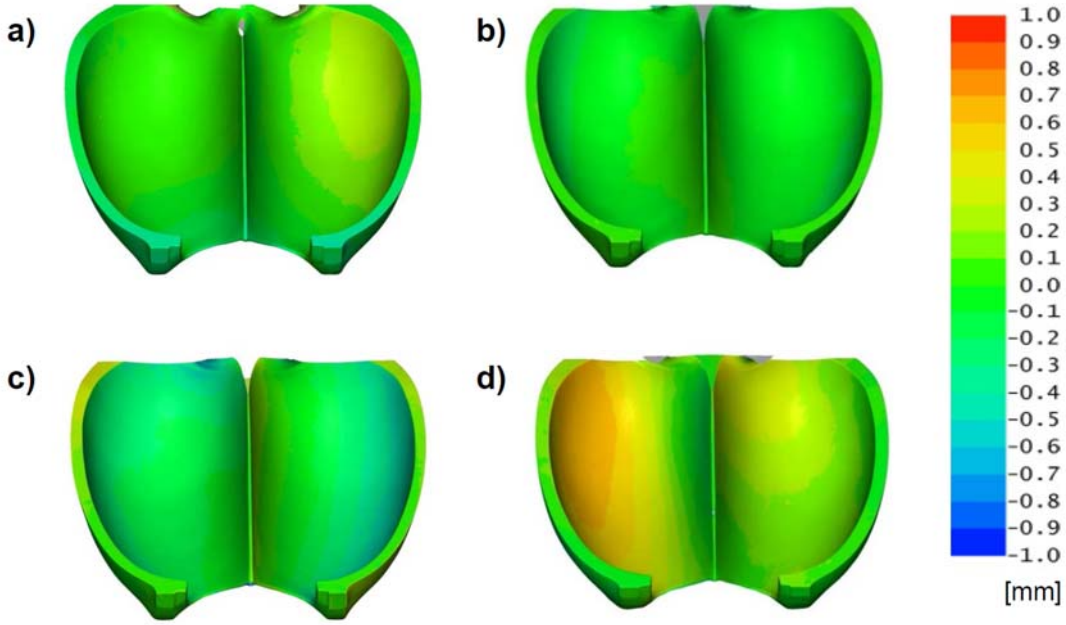

Figure D-9 Differences between two measured bucket geometries: a) repeated measurements in April 2014 on bucket no. 1 of MG 1, as well as measurements in Nov. vs. April 2014 of b) bucket no. 1 of MG 1, c) bucket no. 2 of MG 1, d) bucket no. 1 of MG 2.

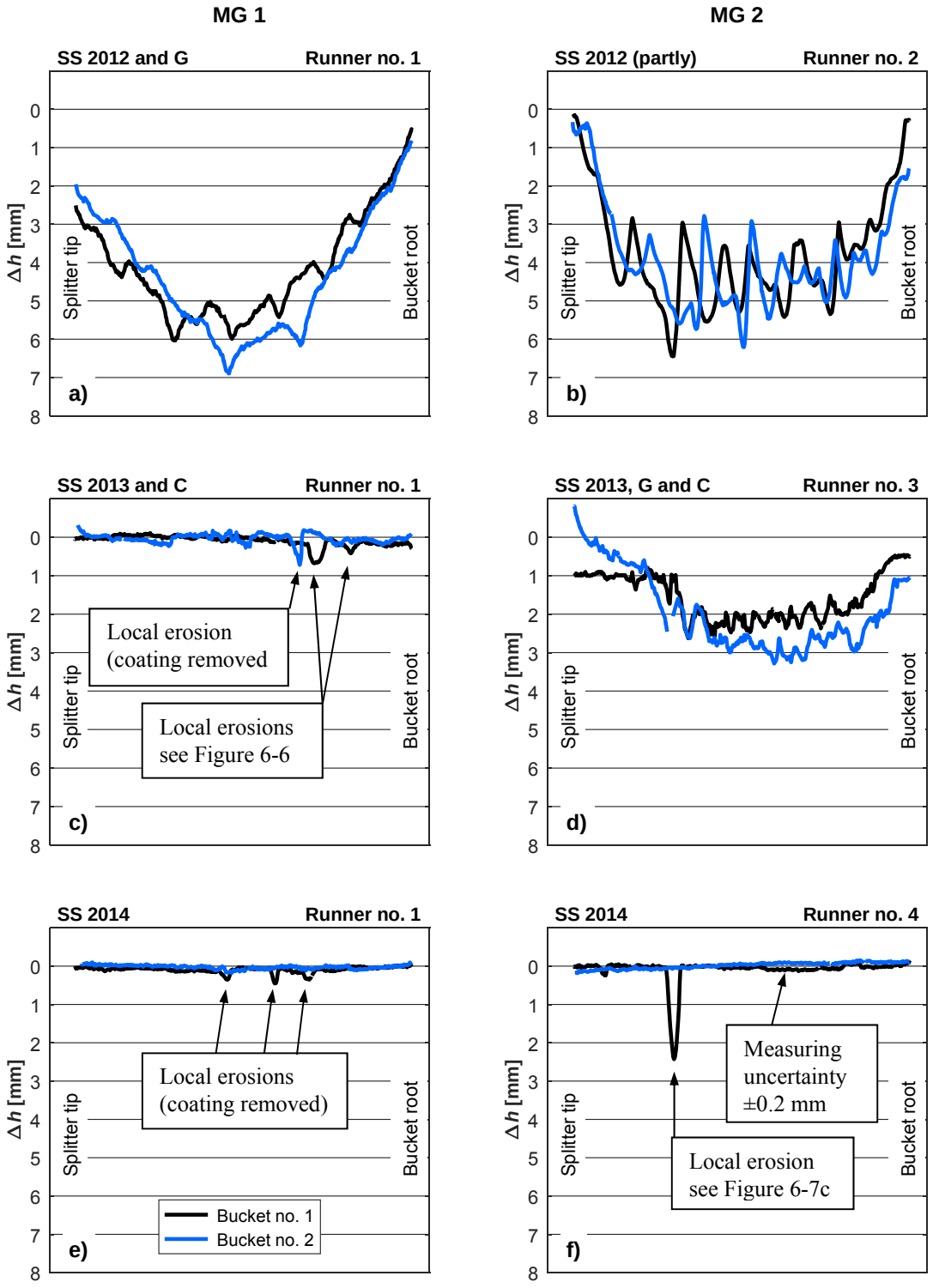

Figure D-10 Reductions of splitter heights Δ*h* along the splitters determined from optical 3D-surveys in the HPP Fieschertal in the years 2012 to 2014. Definition of *h* see Fig. 3-13, SS = sediment season, G = Grinding and C = Local re-coating of splitters and cut-outs.

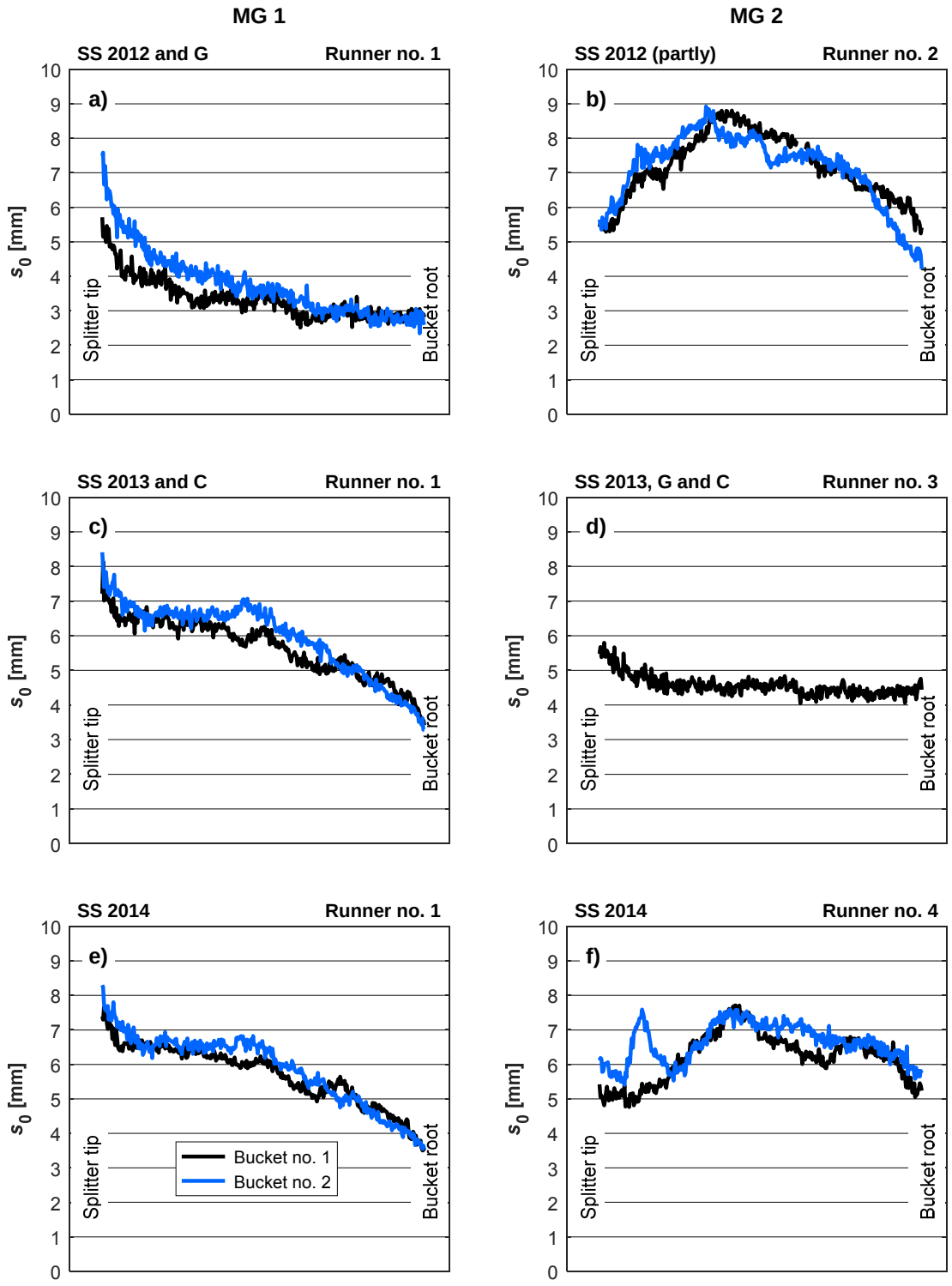

Figure D-11 Splitter widths s_0 along the splitters in the beginnings of the sediment seasons 2012 to 2014 determined from optical 3D-surveys in the HPP Fieschertal. Definition of s see Fig. 3-13, SS = sediment season, G = Grinding and C = Local re-coating of splitters and cut-outs.

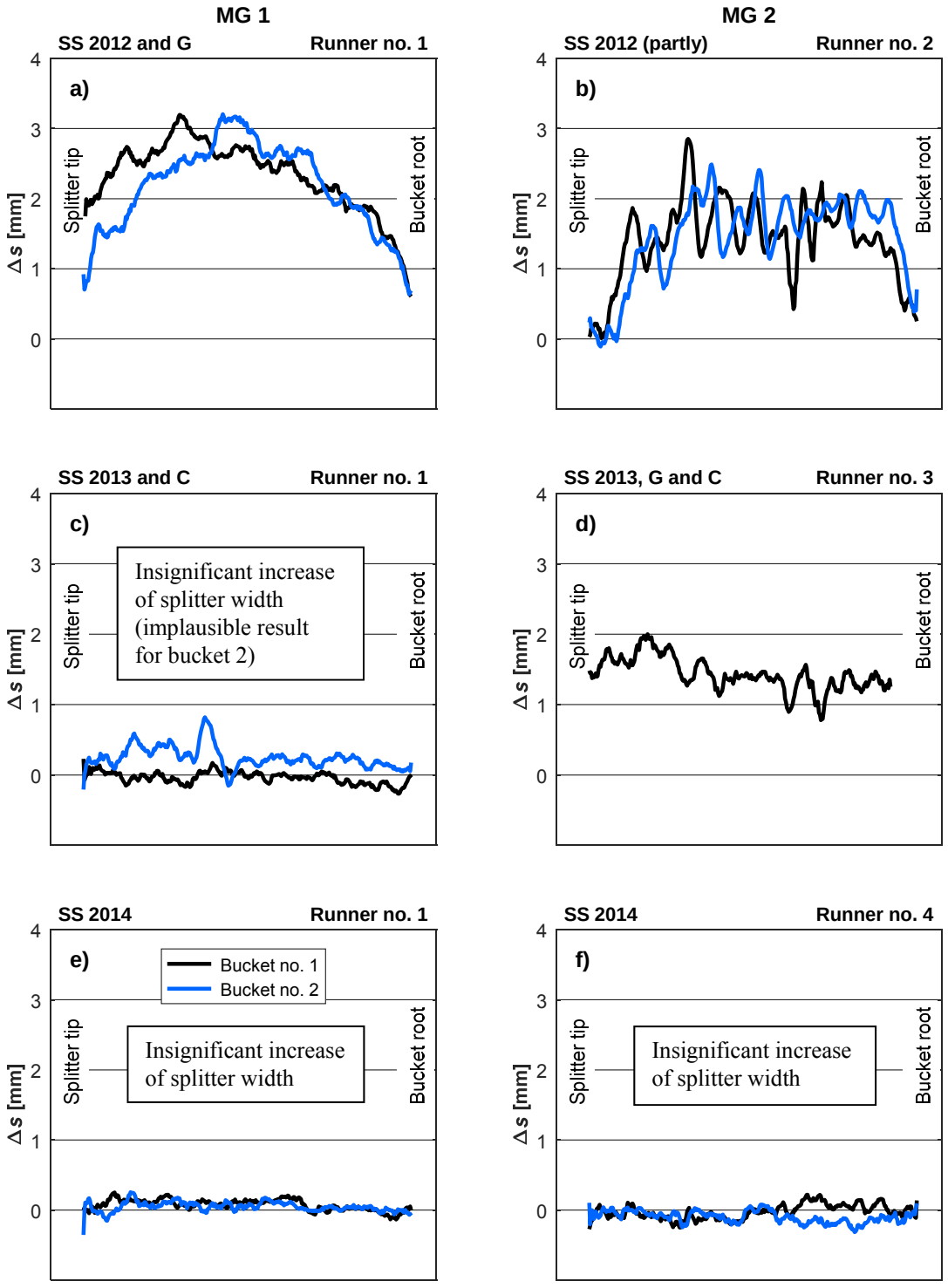

Figure D-12 Increases of splitter widths Δ*s* along the splitters determined from optical 3D-surveys in the HPP Fieschertal in the years 2012 to 2014. Definition of *s* see Fig. 3-13, SS = sediment season, G = Grinding and C = Local re-coating of splitters and cut-outs.

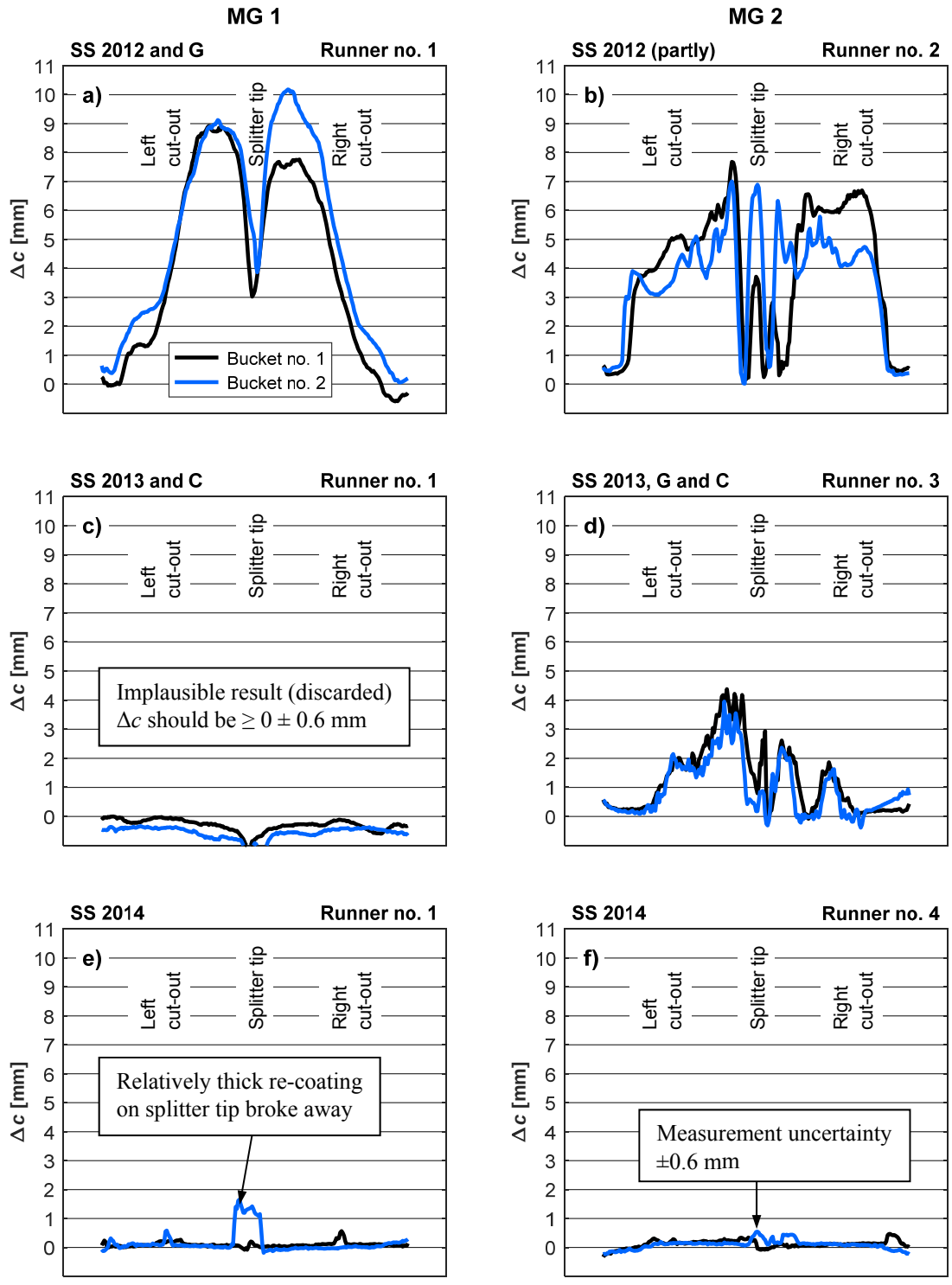

Figure D-13 Increases of cut-out depths Δ*c* (in top-view of buckets) determined from optical 3D-surveys in the HPP Fieschertal in the years 2012 to 2014. Definition of *c* see Fig. 3-13, SS = sediment season, G = Grinding and C = Local re-coating of splitters and cut-outs.

D3 Photographs of turbine inspections

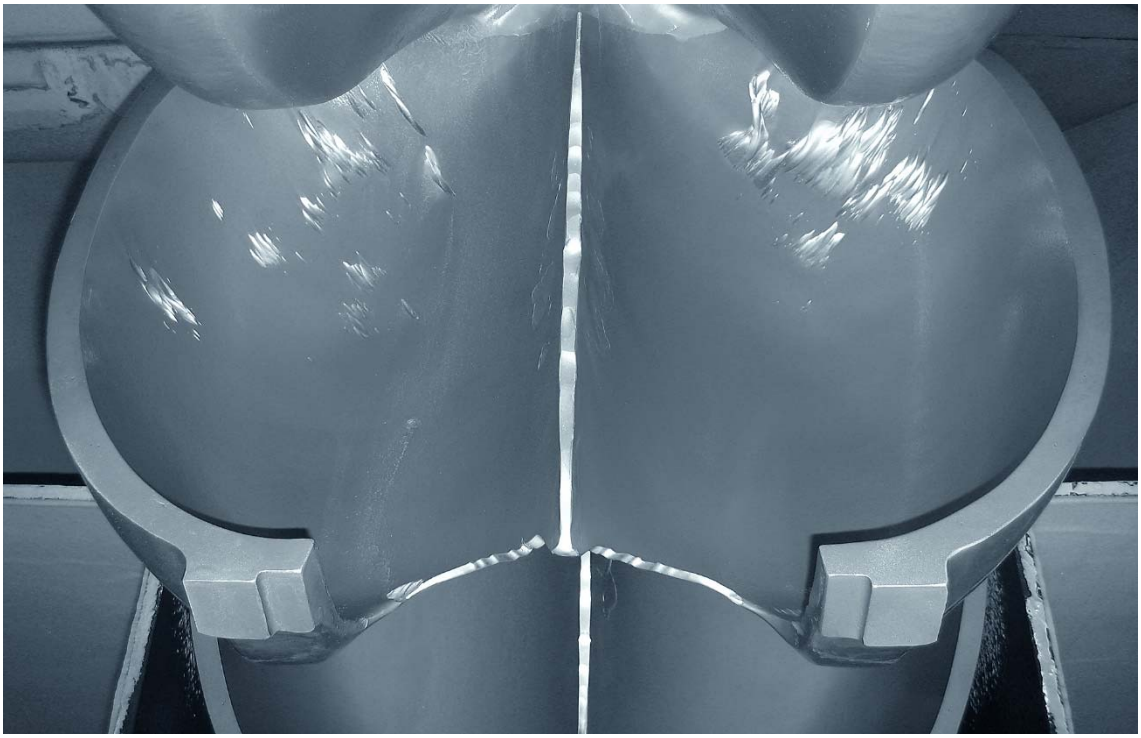

Figure D-14 Local erosion on the splitter and the cut-outs as well as inside a bucket of MG 2 on August 8, 2012, i.e. after the major flood event; the bucket was fully hard-coated at the beginning of the season.

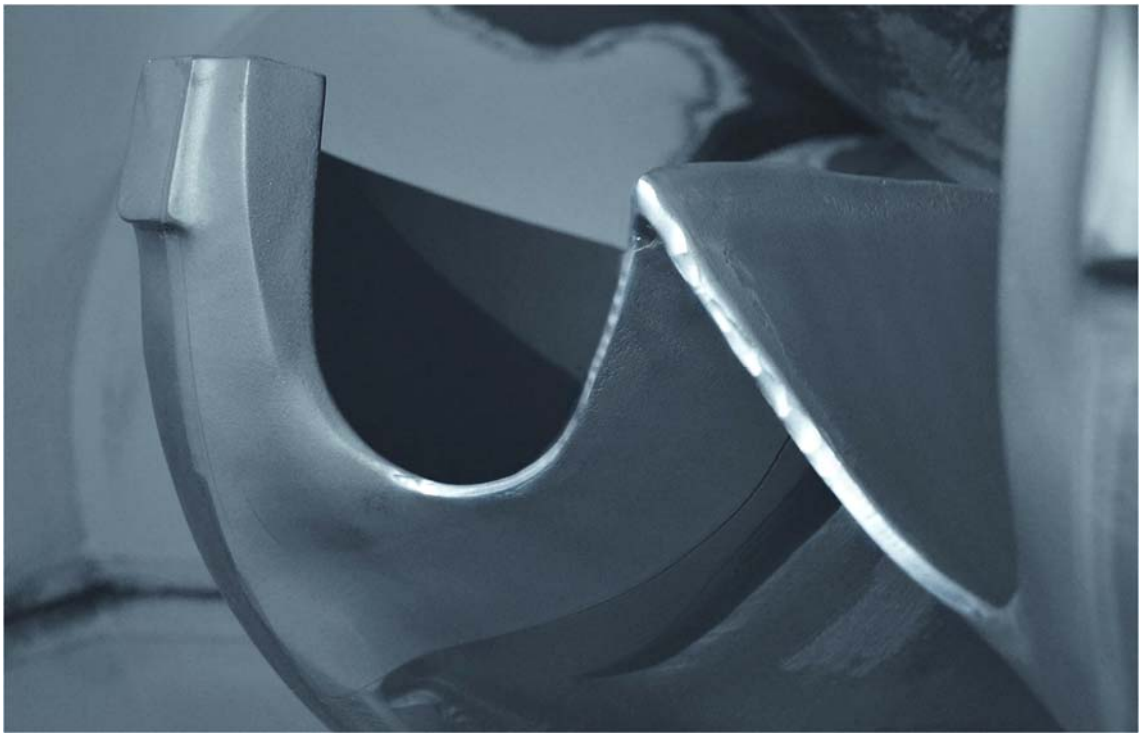

Figure D-15 Eroded cut-outs of bucket no. 14 of MG 1 on November 26, 2014.

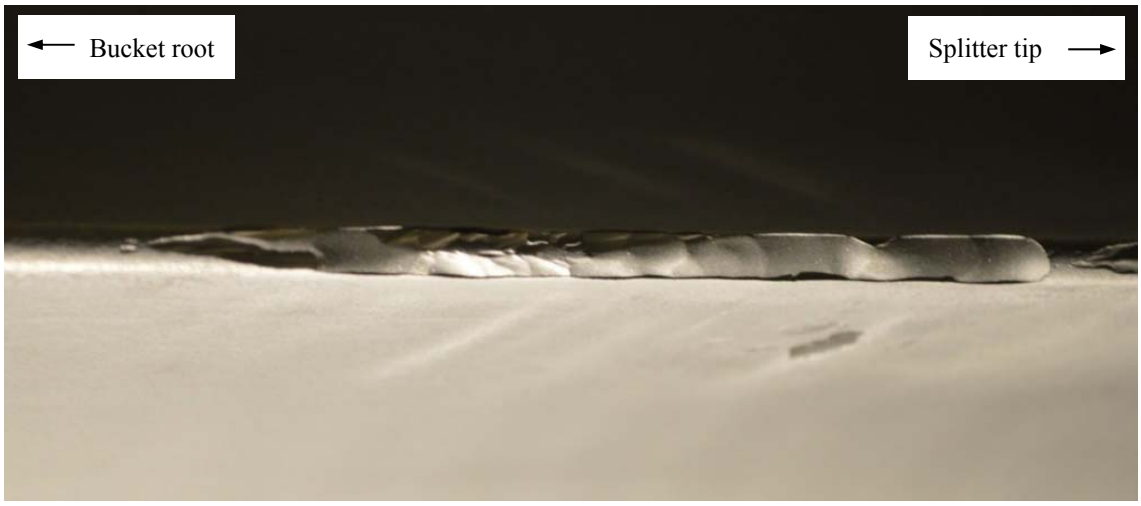

Figure D-16 Detail of eroded splitter crest of bucket no. 19 of MG 2 on November 13, 2014.

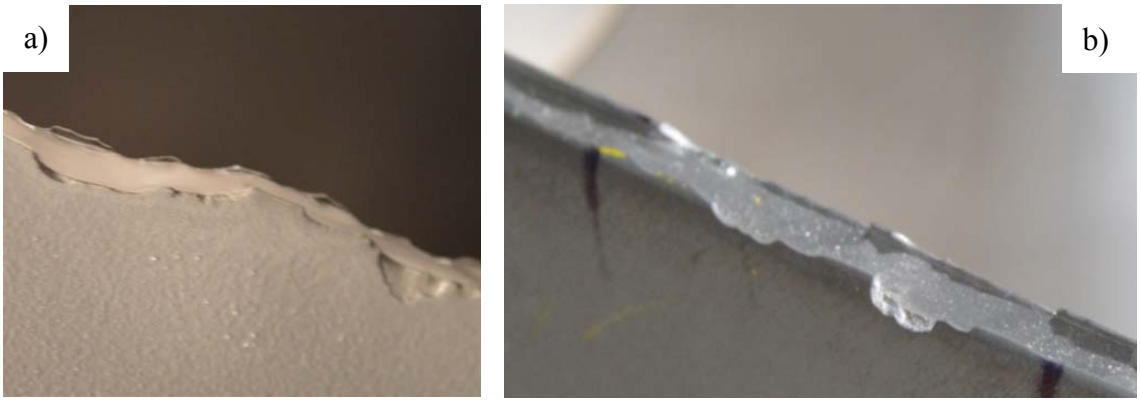

Figure D-17 Details of erosion on initially coated splitters a) bucket no. 1 of MG 1 on August 08, 2012; b) bucket no. 1 of MG 2 on November 15, 2013 (Felix *et al.* 2016a).

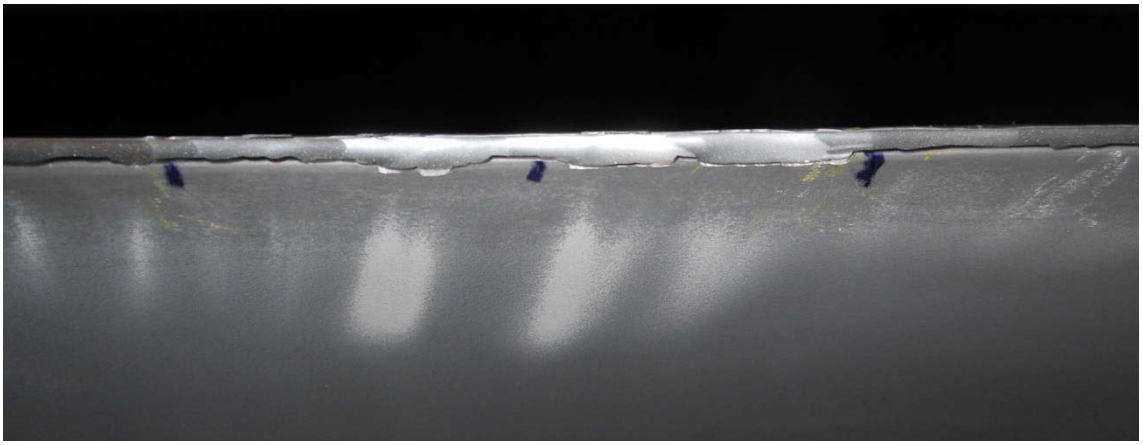

Figure D-18 Detail of eroded splitter crest with erosion traces on the coated splitter flanks downstream of locations where the protruding top parts of the coating layer broke away (bucket no. 1 of MG 2 on November 15, 2013).

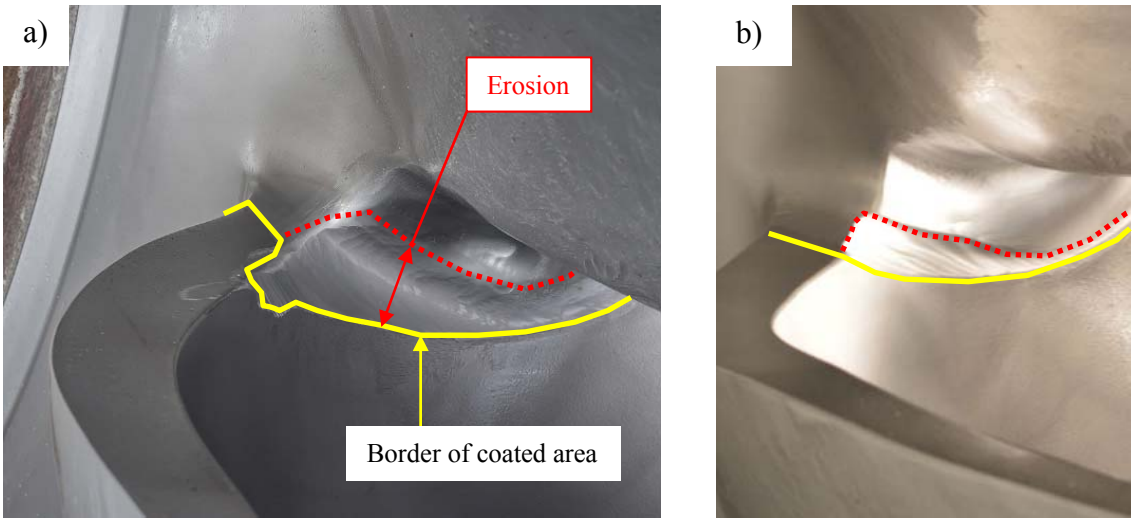

Figure D-19 Local erosion above the coated area at the bucket root close to the bucket outlet a) bucket no. 2 of MG 1 on August 8, 2013; b) bucket no. 1 of MG 1 on August 8, 2012.

Figure D-20 Deflector of lower nozzle of MG 1 a) in original shape in April 2012 and b) with erosion in August 2012 after the major flood event.

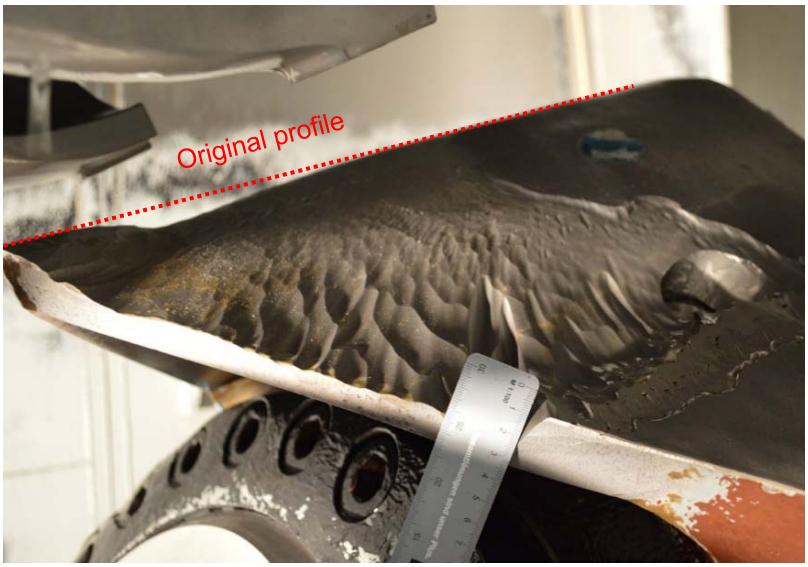

Figure D-21 Eroded shield of the lower nozzle of MG 1 in August 2012 after the major flood.

APPENDIX E: EFFICIENCY MONITORING HPP FIESCHERTAL

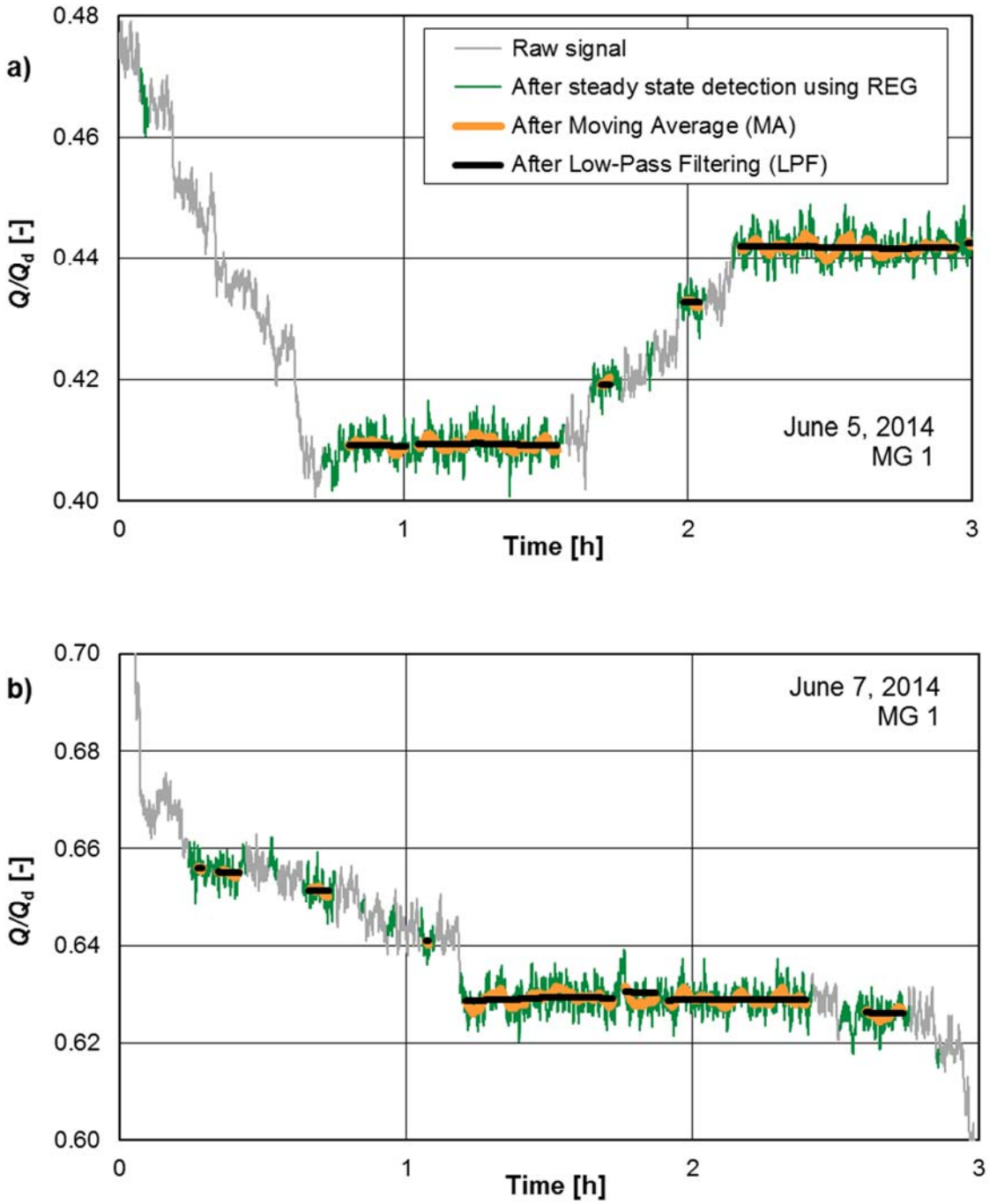

Figure E-1 Examples of steady state detection, smoothing and filtering of a time series of the penstock discharge normalized by the design discharge of one turbine. The pieces of the filtered signal (black lines) were used for the continuous efficiency monitoring (CEM).

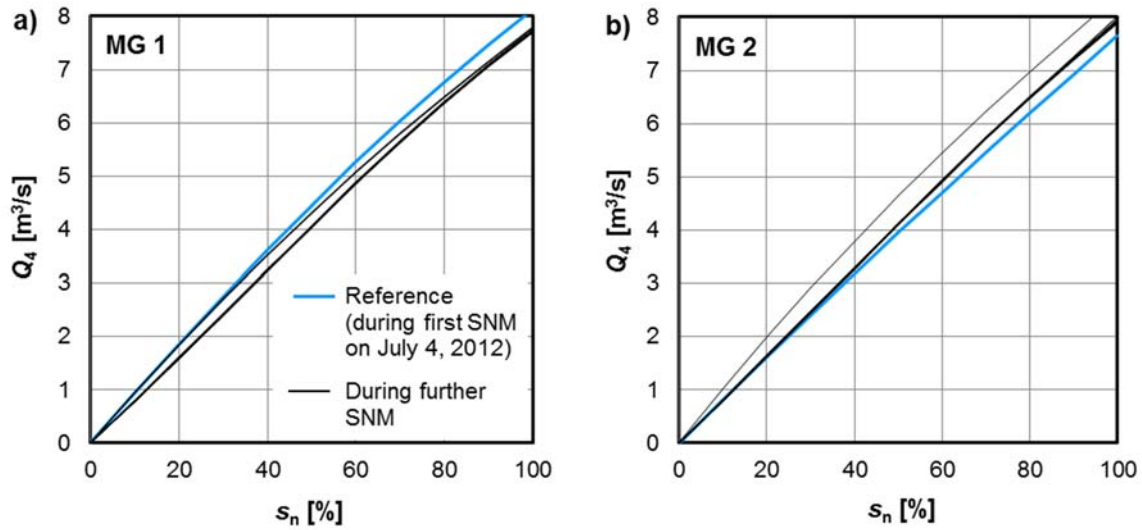

Figure E-2 Relations between needle positions s_n and discharge Q_4 (s_n-Q-curves) during the twenty SNMs in the years 2012 to 2015 for a) MG 1 and b) MG 2 (third-order polynominal fits obtained from measurement data).

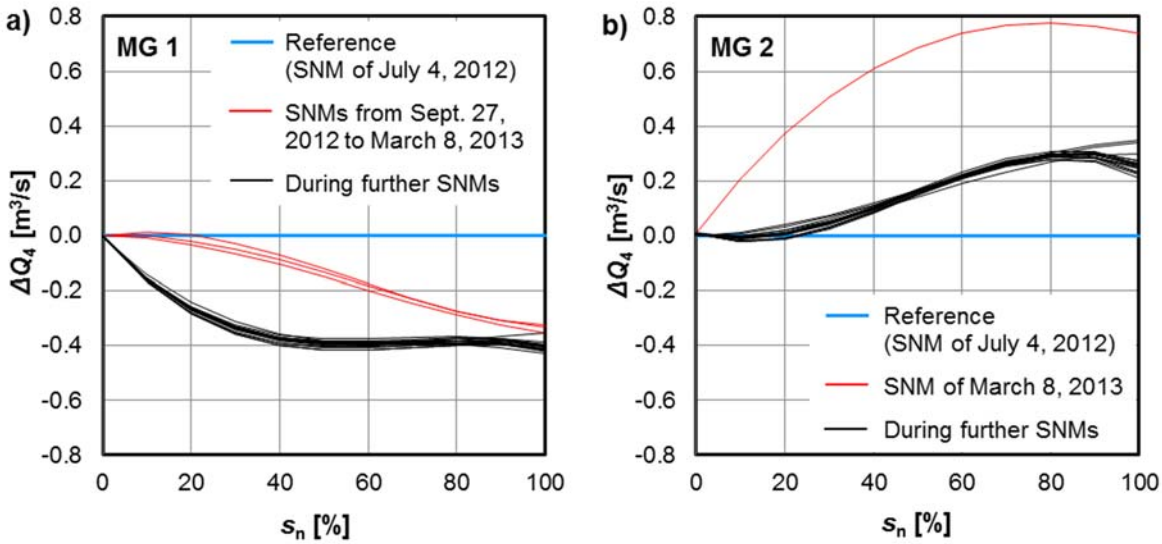

Figure E-3 Differences between the discharge Q_4 measured during each SNM and Q_4 during the first SNM (reference) as a function of s_n for a) MG 1 and b) MG 2.